University of the West of England
BRISTOL

Tuling, S. (2013) ***An engineering method for modeling the interaction of circular bodies and very low aspect ratio cruciform wings at supersonic speeds.*** **PhD, University of the West of England. Available from: http://eprints.uwe.ac.uk/20056**

We recommend you cite the published version.
The publisher's URL is:
http://eprints.uwe.ac.uk/20056/

Refereed: No

(no note)

Disclaimer

UWE has obtained warranties from all depositors as to their title in the material deposited and as to their right to deposit such material.

UWE makes no representation or warranties of commercial utility, title, or fitness for a particular purpose or any other warranty, express or implied in respect of any material deposited.

UWE makes no representation that the use of the materials will not infringe any patent, copyright, trademark or other property or proprietary rights.

UWE accepts no liability for any infringement of intellectual property rights in any material deposited but will remove such material from public view pending investigation in the event of an allegation of any such infringement.

PLEASE SCROLL DOWN FOR TEXT.

University of the West of England
BRISTOL

Tuling, S. (2013) ***An Engineering Method for Modeling the Interaction of Circular Bodies and Very Low Aspect Ratio Cruciform Wings at Supersonic Speeds.*** **PhD, University of the West of England.**

We recommend you cite the published version.
The publisher's URL is https://eprints.uwe.ac.uk/secure/21907/

Refereed: No

(no note)

Disclaimer

UWE has obtained warranties from all depositors as to their title in the material deposited and as to their right to deposit such material.

UWE makes no representation or warranties of commercial utility, title, or fitness for a particular purpose or any other warranty, express or implied in respect of any material deposited.

UWE makes no representation that the use of the materials will not infringe any patent, copyright, trademark or other property or proprietary rights.

UWE accepts no liability for any infringement of intellectual property rights in any material deposited but will remove such material from public view pending investigation in the event of an allegation of any such infringement.

PLEASE SCROLL DOWN FOR TEXT.

University of the West of England
BRISTOL

An Engineering Method for Modeling the Interaction of Circular Bodies and Very Low Aspect Ratio Cruciform Wings at Supersonic Speeds

Sean Tuling

A thesis submitted in partial fulfilment of the requirements of the
University of the West of England, Bristol
for the degree of Doctor of Philosophy

Faculty of Environment and Technology, University of the West of England, Bristol

May 2013

Abstract

An engineering method using a 2D unsteady potential formulation (called the free vortex model or FVM) has been developed to predict the normal force, centre-of-pressure and vortex position for cruciform wing-body combinations in the "plus" orientation, at supersonic speeds and cross flow Mach numbers less than or equal to 0.55 up to angles of attack 20°. The wings are of very low aspect ratio (≤ 0.1), have taper ratios greater than 0.85 (or significant side edges) and have low span to body diameter ratios (≤ 1.5). The method predicts the position and subsequent loads imposed by the vortex along the length on the wing-body combination by determining the shed vorticity using Jorgensen's modified Newtonian impact method. The vortex position is well predicted for angles of attack from 4° until symmetric vortex shedding occurs, whilst the normal force is well predicted from 0°. The centre-of-pressure is predicted further aft at the low angles and further forward at the high angles of attack. If this method is used in combination with the single concentrated vortex of Bryson applied to cruciform wing-body combinations the vortex positions prediction limitations at angles of attack less than 4° can be overcome. An investigation of the lee side flow field of cruciform wing-body configurations was also performed, and revealed that the vortex position is dependent upon the lee side secondary vortex separation characteristics. Other features revealed that symmetric vortex shedding occurs when both the region of flow outside the shed vortex sheet and reverse flow region are supersonic and a termination shock exists. The thesis also investigated the application of the discrete vortex model (DVM) method to cruciform wing-body combinations and found that the potential only formulation overpredicts the normal force, whilst the inclusion of boundary layer separation (and therefore modeling the secondary separation vortex) predicted the normal force very well. The application of the concentrated vortex method of Bryson was also investigated and found to be only applicable at low angles of attack ($< 4°$).

Acknowledgements

I would like to thank my immediate supervisor Laurent Dala for all the questions, guidance, prompting and sterness required to start and finish a doctorate. Also my thanks to my other supervisors Chris Toomer and Mike Ackerman for their guidance.

I would like to thank all the staff at the CSIR who have helped and encouraged, without which this doctorate would not have progressed at all. In particular to Beeuwen Gerryts for putting faith in the doctorate and making time available; to Mauro Morelli and Kaven Naidoo for giving me space and persevering in the process; to Bhavya Vallabh for the invaluable help; Bronwyn Meyers for all the help on the PIV system, and the test teams that have helped get the experimental work done.

To all friends and family that have helped and encouraged and given the time and space.

Finally to my wife Alison, not enough can be said for all she has done.

Statement of Objectives

The objectives of this research are to add to the knowledge of flows over slender bodies with very low aspect ratio wings and develop a theoretical or semi-empirical model of these flows so that they can be used during the preliminary design phases.

All the work in this thesis was performed by the author except for the following:-

- Low speed water tunnel tests that were performed at the University of Málaga by M.A. Arevalo-Campillos, L. Parras and Dr. Carlos del Pino. A paper summarising the work performed is listed in Appendix B.
- The High Speed and Low Speed Wind Tunnel tests at the CSIR were performed by teams because of the industrial nature of the facilities. The author did, however, manage and direct the tests, was a team member setting up and running the tests, performed quality assurance on, and data reduction for both the tests.

This copy has been supplied on the understanding that it is copyright material and that no quotation from the thesis may be published without proper acknowledgement.

Contents

List of Figures

List of Tables

List of Symbols

APC	Aeroprediction Code
AR	Aspect ratio, b^2/S
a	Radius
b	Span
c_{d_c}	Cross flow drag coefficient
C_A	Axial force coefficient, body axes
C_D	Drag coefficient
CFL	Courant-Friedrich-Lewy
C_L	Lft coefficient (wind axes)
C_l	Rolling moment coefficient (body axes)
C_m	Pitching moment coefficient (body axes)
C_n	Yawing moment coefficient (body axes)
C_N	Normal force coefficient (body axes)
$C_{m_{BWT}}$	Pitching moment coefficient for body, wing and tail configuration
$C_{N_{BWT}}$	Normal force coefficient for body, wing and tail configuration
C_{N_B}	Normal force coefficient for isolated body
$C_{N_{B(T)}}$	Normal force coefficient increment of body due to the tail
$C_{N_{T(B)}}$	Normal force coefficient increment of tail due to the body
$C_{N_{B(W)}}$	Normal force coefficient increment of body due to wing
$C_{N_{W(B)}}$	Normal force coefficient increment of wing due to body
$C_{N_{T(W)}}$	Normal force coefficient increment of tail due to wing
C_{N_α}	Normal force coefficient slope (with respect to α)
C_p	Pressure coefficient
$C_{p\rho}$	Non-dimensionalised loss in maximum mainstream dynamic head
CPU	Central Processing Unit
CSIR	Council for Scientific and Industrial Research
C_Y	Side force coefficient, body axes
D	Body diameter
DVM	Discrete Vortex Model
F_A	Axial force, body axes
FAS	Full-Approximation Storage

F_N	Normal force, body axes
F_{N_v}	Normal force due to vortex, body axes
FVM	Free Vortex Model
F_Y	Side force, body axes
HSWT	High Speed Wind Tunnel
i_T	Tail interference factor due to a free vortex
K_{B_W}	Wing-to-body carryover factor
k_B	Fin deflection interference factor, wing-to-body
KE	$\kappa - \epsilon$ turbulence model
K_{W_B}	Body-on-wing carryover factor
k_W	Fin deflection interference factor, body on wing
K_ϕ	Additional loading due to roll angle at constant angle of attack
L	Body length, lift
LSWT	Low Speed Wind Tunnel
M	Freestream Mach number
M_c	Cross flow Mach number, $Msin(\alpha)$
M_N	Mach number normal to the leading edge
n	Vortex shedding rate
q	Freestream dynamic pressure, $1/2\rho V_\infty^2$
Re	Reynolds number
RKE	Realisable $\kappa - \epsilon$ turbulence model
RSM	Reynolds-Stress model
r_o	Radius of the circle in the circle plane
r_B	Radius at the base
S	Reference area, usually $\pi D^2/4$
S_B	Body base area
S_p	Planform area
SA	Sparlat-Allmaras
s	Span of exposed fin/wing
s_m	Wing-body semi-span
SBT	Slender Body Theory
SCV	Single Concentrated Vortex
SOSE	Second Order Shock Expansion
SSB	Stanbrook and Squire Boundary
u	Velocity pertubation in the x-axis direction
u_e	Surface velocity
V	Freestream velocity
V_c	Cross flow velocity $Vsin(\alpha)$
v	Velocity pertubation in the v-axis direction
w	Velocity pertubation in the w-axis direction

x_s	Axial location of start of body vortices, from nose
y_v	Body vortex location in lateral direction
z_v	Body vortex location in vertical direction
α	Angle of attack
α_N	Angle of attack normal to the leading edge
δ	Fin deflection angle
δ_s	Boundary layer vorticity reduction factor
$\Delta\alpha_v$	Induced angle of attack due to a vortex
η	End effect factor
η_n	Half angle of sharp nose
Γ	Vortex strength
Γ'	Non-dimensionalised vortex strength, $\frac{\Gamma}{2\pi V a}$
γ	Specific heat ratio
γ_l	Line vortex strength
Λ	Fin on fin influence factor
Φ	Inertial axes velocity potential
ϕ	Body axes velocity potential
ϕ_x	Roll angle
ρ	Air density
σ	Vortex position (complex) in phyical plane
σ_w	Total incidence/included angle

Chapter 1

Introduction

The prediction of aerodynamic loads of airframes has been the subject of aerodynamicists for over a century. For aircraft type configurations, the Joukowski-Kutta condition and lifting line theory were significant developments in the ability to model and predict aerodynamic loads for wings. For bodies, the primary theory was originally developed by Munk [1] and extended by numerous researchers. Missiles are characterised by slender bodies and low aspect ratio lifting surfaces. For missiles, body wing interactions contribute significantly to the overall aerodynamic loads of the configuration compared to aircraft type configurations. These interactions have, in part, contributed to the creation of the class of fluid flow known as missile aerodynamics.

The primary methods for predicting missile aerodynamics at an engineering level were developed in the late 1950's and early 1960's by numerous investigators such as Morikawa [2], Allen and Perkins [3] and summarised in the first textbook dedicated to missile aerodynamics by Nielsen [4]. These methods relied on potential slender body theory, which is strictly applicable to only low angles of attack ($\leq 4^\circ$), and through insightful 'assumptions' and heuristic analogies extended to moderate ($\approx 10^\circ$) and higher angles of attack ($15^\circ < \alpha < 25^\circ$). These theories have formed the backbone of the predictive methods for slender body configurations. Some major developments have occurred in subsequent decades extending the methods to high angles of attack ($\alpha \geq 25^\circ$). Surprisingly, the use of low angle attached flow slender body theory has been successfully extended to the higher angles where separated flow are required by slender configurations to generate sufficient lift forces. Domains where these extensions break down exist, and together with the body wing interactions are the subject of this thesis.

Before continuing, it should be noted that this thesis is concerned with the interaction of circular bodies of constant diameter and wings whose aspect ratio is less than or equal to 0.1 or alternatively described as very low aspect ratio wings. The very low aspect ratio wings are also commonly called strakes, and both very low aspect ratio wings and strakes shall be used interchangeably throughout the thesis. Furthermore the strakes have limited leading edges or that the taper ratio of these wings is greater than 0.85. The wing span

to body diameter ratio is 1.25. These and other limitations placed on this research are as follows:-

- Strake aspect ratios of the order 0.025 (and less than 0.1)
- Strake taper ratios greater than 0.85
- Strake span to body diameter ratios of 1.25
- Supersonic Mach numbers
- Cruciform wings in the '+' configuration
- Wing-body section of constant body diameter
- Wing length is a significant proportion (>50%) of the overall body length

The angle of attack regime being considered in this thesis is from zero to 25°, and low angles are considered $\alpha \leq 4°$, moderate angles from 4° to 15° and the higher angle of attack regime from 15° to 25°. High angles of attack are traditionally considered as greater than 25° and is the case in this thesis too.

1.1 Thesis

The research question being answered is how can very low aspect ratio wing-body interactions be modeled at an engineering level, and in particular the wing-to-body carryover factor, for engineering prediction purposes. The thesis put forward is that the side edge vortex shed by very low aspect ratio wings with significant side edges, being non-linear in nature, interacts significantly with the body such that the aerodynamics of such configurations needs to be modeled together. This results in the non-linear behaviour of the wing-to-body carryover factor, K_{B_W}, with angle of attack. In particular, the side edge shed vortex is the dominant flow phenomenon whose motion when treated as a Lagrangian fluid particle can predict the motion of the side edge vortex sufficient well for engineering prediction purposes. Finally an integrated method is proposed which forms the basis for the better modeling of K_{B_W}, and therefore extending the previous formulations and which, in first order, account for the non-linear effects.

1.2 Background

The total normal (or lift) force on a slender body-wing configuration has, for one school of thought, been traditionally based on the build up method of configurations (i.e. the addition of wings and/or tails to a slender body) by the linear summation of the individual components (i.e. body alone and wing alone) and their interference factors (i.e. body-on-wing and wing-to-body). For a body-wing-tail combination configuration, the total normal force coefficient, $C_{N_{BWT}}$, can be written as

$$C_{N_{BWT}} = C_{N_B} + C_{N_{W(B)}} + C_{N_{B(W)}} + C_{N_{T(B)}} + C_{N_{B(T)}} + C_{N_{T(W)}} \tag{1.1}$$

where C_{N_B} is the isolated body, $C_{N_{W(B)}}$, the wing in the presence of the body, $C_{N_{B(W)}}$, the increment of the body due to the wing, $C_{N_{T(B)}}$, the tail in the presence of the body, $C_{N_{B(T)}}$, the increment of the body due to the tail, and $C_{N_{T(W)}}$ the effect of the wing on the tail. For a configuration that does not have a tail, which the subject of this thesis is restricted to, the last three terms are excluded.

The wing in the presence of the body, $C_{N_{W(B)}}$, is can be written in terms of the wing alone C_{N_W}, which is made up by combining the two exposed halves of the wing, as has been traditionally defined. The planform characteristics of the wings under consideration are defined in terms of the wing alone. $C_{N_{W(B)}}$ has been traditionally defined in terms of the body-on-wing carryover factor, K_{W_B}, [4] or

$$C_{N_{W(B)}} = K_{W_B} C_{N_W} \tag{1.2}$$

The body-on-wing carryover factor includes the contribution of the wing alone and the incremental or interference effect due to the body. For the interference effect of the wing onto the body, or wing-to-body carryover, this has also been defined in terms of the wing alone characteristics [4], and is defined as

$$C_{N_{B(W)}} = K_{B_W} C_{N_W} \tag{1.3}$$

Equation 1.1 can, for this thesis, be written as

$$C_{N_{BW}} = C_{N_B} + (K_{W_B} + K_{B_W}) C_{N_W} \tag{1.4}$$

The original theories developed to predict the aerodynamics of slender body-wing configurations are based on linear analysis [4]. They assume that the body and the wings have linear characteristics with angle of attack. For bodies at angles of attack larger than 4° non-linear effects start to become significant, primarily due to the shedding of vortices (up to 4° the flow remains attached even though the lee side boundary thickens as the angle of attack increases from 0°). For engineering level predictions, a heuristic model based on the cross-flow concept was proposed by Allen [5] and has been used with considerable success since its introduction such that it remains the starting point for any engineering prediction code such as Missile Datcom and Aeroprediction code (APC). For wings of aspect ratio of the order 1, the normal force can be considered linear up to angles of attack of approximately 40°[4] whereupon non-linear effects (stall and vortex breakdown) dominate. This is because the leading and side edge vortices are not a large contribution to the overall lift force. The theoretical lift curve slope of a low aspect ratio wing with a subsonic leading edge, based on slender body theory, is $AR\pi/2$ [6]. The mostly linear behaviour of wings, in particular, have resulted in the successful use of the body-wing

interaction factors because the wing alone lift characteristics can be formulated based on the linear lift curve slope, or

$$C_{N_W} = \left(\frac{\partial C_{N_W}}{\partial \alpha} \right)_{\alpha=0^\circ} \alpha \tag{1.5}$$

Traditionally the values used to model the the wing-to-body, K_{W_B}, and body-on-wing, K_{B_W}, factors are derived from slender body theory. The effect of afterbodies on these carryover factors have also been considered and are based on two fundamental assumptions, namely that the flow over the wing is conical and that the body is modelled as a plane rather than a circular body [4][7]. This formulation assumed that the aft body is of sufficient length to 'catch' the wing effect. Formulations accounting for zero-, limited- and negative aft bodies were developed in references [8],[9] and [10]. The body-on-wing carryover factor, K_{W_B}, or the "Beskin" upwash factor is due to the induced velocity of the body increasing the effective incidence of the wing, whilst the wing-to-body carryover factor, K_{B_W}, has been essentially interpreted as the body increasingly acting as a reflection plane for the wing as the wing semi-span reduces. The development of the equivalent angle of attack method [11] in the early 1980's accounts for non-linearities in the lift curve slope of wings and extends the low angle of attack method of the previous equations to high angles of attack, and made the component buildup method applicable up to 60°.

A limitation in the previously developed methodologies observed in recent decades has been for the combination of very low aspect ratio wings and slender bodies [12][13], this being the modelling of the wing-to-body interference factor, K_{B_W}. This limitation includes the equivalent angle of attack method. When very low aspect ratio wings (AR=0.067 in reference [13]) are combined with slender bodies having a chord of similar length to the slender body length, the wing-to-body carry over factor, K_{B_W}, is underpredicted by approximately 50% at low and moderate angles of attack. The traditional formulation of K_{B_W} is based on slender body theory; and in the limit of a wing of zero span, the carryover factor is 2.0. These are graphically displayed in Figure 1.1.

One other factor that has been demonstrated to influence K_{B_W} is the cross flow Mach number, $M_c = M \sin \alpha$ [14]. The effect of the cross flow Mach number is that the carryover factors dissipate to 1 for K_{W_B} and 0 for K_{B_W} when the cross flow Mach number is greater than 0.3. The data presented by Simpson and Birch shows neither these effects for K_{W_B} and K_{B_W} for their tests performed at Mach 2.5 (resulting in a cross flow Mach number of 1.05 at an angle of attack of 25°). Indeed K_{W_B} does not drop by more than 20% over the angle of attack range of 25° whilst K_{B_W}, even though underpredicted, does not drop to zero at 25°. The data presented by reference [14] were for wings of aspect ratio AR=0.5. From the available literature the effect very low aspect ratio wings on slender body configurations is not well modeled and the purpose of this body of work is to propose an extended formulation for K_{B_W} that will improve the prediction of the effect of very low aspect ratio wings for slender body configurations.

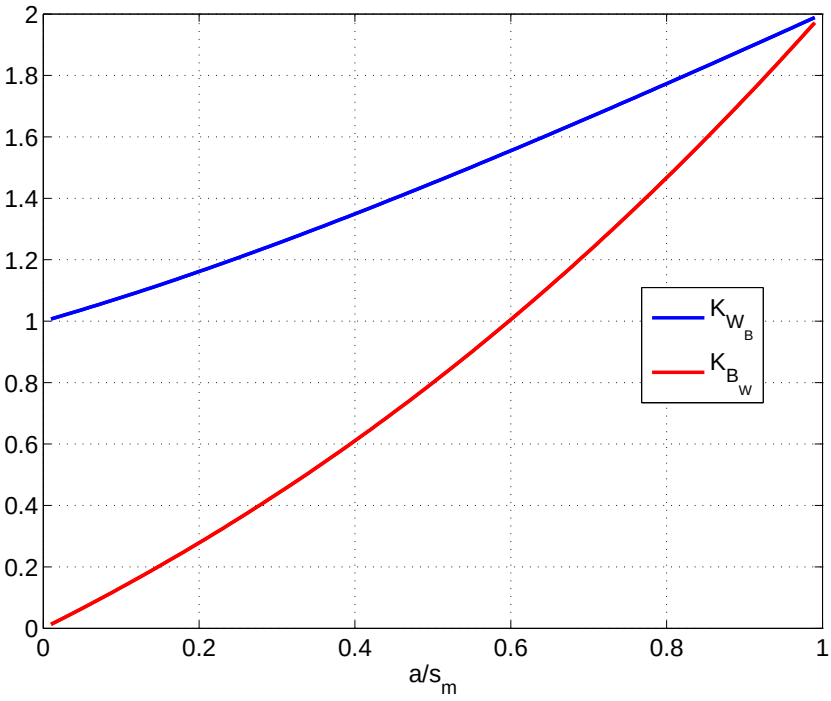

Figure 1.1: Slender body theory wing body interference factors [4]

Wings of very low aspect ratio i.e. less than 0.1, are not uncommon, though fewer practical configurations tend to exist because wings of higher aspect ratio provide a more efficient way of generating lift. The benefits of very low aspect ratio wings for slender bodies have been recognised [15] where lower drag and space constrained configurations are required. At least up until the early 1980's no attempts had been made to develop engineering level methods of predicting the effect of very low aspect ratio wings in slender body configurations. From the late 1980's onwards, attempts to better model the effect of wings on bodies have been based on experimental data, such as those for the Aeroprediction code [16] and Missile Datcom [17][18][19]. APC fits curves to the experimental K_{BW} data as a function of Mach number and angle of attack, while Missile Datcom (post 1999) modifies the cross flow drag coefficient utilising empirical data.

In the past the effect of the wing/strake side edge vortex development in the presence of the body has been noted but not explicitly accounted for. Once free of the lifting surface, the effect of the vortex on downstream surfaces will affect both the store pitching moment and lift characteristics. Two methods have been used in the past. The first, as implemented by Missile Datcom, is to assume that the vortex which is shed from the low aspect ratio wing emanates from the trailing edge at a lateral distance dependent on the spanwise lift distribution [7]. The second is to assume that the side edge vortex leaves the leading edge edge at one half the angle of attack of the wing [20] as defined by Bollay [21]. These two represent two extremes in which the side edge vortex of a strake lies somewhere in between. Configurations where the wings of very low aspect ratio with side edges (i.e.

almost rectangular wings) and not highly swept back leading edges have hitherto not been modeled in the past.

In this thesis it is proposed that this non-linear effect is primarily due to the vortex separation of the side edge that is not accounted for in the original linear formulations or the equivalent angle of attack method. For slender body configurations with very low aspect ratio wings/strakes the side edge vortex created by the wing interacts with, or is influenced by the body, to the extent that the wing and body must be considered together rather than as separate components whose interactions can be accounted for in a linear fashion. Consequently the effect of the side edge vortex on downstream bodies and lifting surfaces will depend on the position and strength of this side edge vortex.

The subject of this thesis is derived directly from industrial applications where the use of very low aspect ratio wings or strakes have and are being considered for short range air-to-air missiles for reasons which include space limitations in stealth platforms. The typical slenderness ratio of such missiles varies from between 17 to 22, while the operational Mach range is 0.6 to 3.0. This thesis is studying the aerodynamics in the supersonic flight regime and the range 2.0 to 3.0 has therefore been chosen whilst the low supersonic limit of 1.5 has been excluded because of limitations in experimental validation capabilities.

1.3 Thesis Outline

The subsequent chapters of the thesis firstly survey the available literature. The core method is then presented after which the aerodynamics of configuration used to develop the method is explored. The 2D potential methods with their extensions that are used to study the configuration are then presented with their predictions after which the engineering method is assessed further by comparing predictions to the limited publically available cases. Finally conclusions are drawn, recommendation made and the contributions to the field listed.

Chapter 2

Literature Survey

The survey will start with a general overview of the background theories and methods used in the preliminary design phase, the potential equation, basic available theories and their applicability. With a view to surveying the interaction of slender bodies and wings, work performed on isolated bodies, isolated wings, and combinations of both, and these within the broader context of engineering methods shall be considered. At this stage it must be mentioned that the cornerstone of most of the available theories for predicting the aerodynamics of slender body configurations is slender body theory (SBT). Slender body theory is applicable over the complete Mach range thus making it suitable for use in engineering methods [4].

2.1 The Use of Analytical and Semi-Empirical Methods in Preliminary Design

The focus of the prediction methods used are analytical and semi-empirical methods. Analytical methodologies are limited in their capabilities because the full Navier-Stokes and even the full potential formulation is not mathematrically tractable. They do, however, provide the basis with which usable semi-empirical methodologies can be developed. The cornerstone of missile preliminary design prediction methodologies is the slender body theory (SBT) [14], whose basis is the potential theory applied to slender bodies.

2.1.1 Design Accuracies

In order to contextualise engineering level prediction methodologies it would be useful to determine their requirements by the users (primarily designers and aerodynamicists) of such methodologies. During preliminary design, the prevailing accuracies required for evaluation of the performance for the airframe are listed in Tables 2.1 and 2.2 [22].

Table 2.1: Computational accuracy requirements [22]

Design Parameter	Value	Unit
Range	10	%
Turn radius	20	%
Turn rate	20	%
Load factor	20	%
Specific Excess Power	100	fps
Fin panel area	20	%
Manoeuver deceleration	20	%
Cruise altitude	1000	ft
Response time	20	%
Center of gravity	2	%body length
Static stability/cross coupling parameters	25	%

Table 2.2: Coefficient accuracy requirements [22]

Coefficient	Value	Unit	Design Parameter
C_L	20	%	Range, load factor
C_m	20	%	Fin size or
	or 2	%length	Static margin
C_A	10	%	Coast range or
	or 0.2	$C_D/(C_A \cos\alpha)$	Turn deceleration

2.1.2 Existing Codes and their Prediction Methodologies

The engineering level codes that have been developed in the past utilise a combination of theoretical and/or experimental data. Numerous codes have been developed in the past, with varying degrees of accuracy in their predictions [22].

The codes predominantly use the slender body theory as a base foundation with unique implementations for the nonlinear regions. Their accuracies in the linear low angle of attack regions are good (within the 20% requirement) and it is in the non-linear (viscous normal force and pitching moment) and interference areas where differences appear as to how these are accounted [22]. For the body alone, they predominantly use the Allen and Perkins (or derivative forms such as that by Jorgensen) viscous cross-flow method to account for viscous effects. The loads for the wings and tails have been determined using a variety of methods (eg. slender body, modified Multhopp). For the complete configuration, the buildup methodology is widely used and algebraically sums the various components and their interference effects [14]. The development of the equivalent angle of attack method has extended this formulation into the non-linear region [11]. A variety of methods are also available for the effect of upstream vortices on wings and fins.

A list of codes that have been developed are

- Missile Datcom
- ESDU
- NSWC I & II (Naval Surface Weapon Center) and Aeroprediction (APC)
- MISSILE I, II & III
- AERODYN
- MAP (Missile Aerodynamics Prediction)
- AEDC High Alpha Code
- Army/Martin High Angle-of-Attack Methodology
- DLCODE
- S/HABP (Supersonic/Hypersonic Arbitrary Body Program)
- NSRDC
- NASA W-B-T
- David Taylor (NSRDC I)
- CAMS (Computer Aided Missile Synthesis)
- MISSILE (ONERA)

Most of these codes are not publicly available. Some may not even be used. These have been predominantly obtained from reference [22] and the subsequent sections detailing their methodologies are also obtained from the same reference.

2.1.3 USAF Missile Datcom

Missile Datcom uses a large number of different theoretical and empirical techniques which are applied to the components that make up the body alone aerodynamics, wing alone aerodynamics and interference factors [23][24].

Table 2.3: Missile Datcom body alone computational methods

Component Mach Number	Subsonic	Transonic	Low Supersonic	High Supersonic
Axial Force ($\alpha = 0$)	Empirical	Empirical & Second Order Van Dyke or Second Order Shock		
Axial Force ($\alpha > 0$)	Modified cross-flow (Jorgensen)			
Inviscid Lift and Pitch Moment	Empirical	Van Dyke Hybrid or Second Order Shock Expansion or Modified Newtonian		
Viscous Lift and Pitching Moment	Modified cross-flow (Jorgensen)			

Table 2.4: Missile Datcom wing and interference computational methods

Component Mach Number	Subsonic	Transonic	Low Supersonic	High Supersonic
Linear Lift	Lowry-Polhamus	Linear Theory		
Linear Pitching Moment	Empirical			
Non-linear Lift and Pitching Moment	Empirical & Panel Centroid			
Wing Body Interference	Slender Body Theory, Empirical & Equivalent AoA			
Wing Tail Interference	Slender Body Theory & Line Vortex Theory			

2.1.4 ESDU

ESDU uses the Pitts, Nielsen and Kaattari slender body theory for the potential flow regime, and a Jorgensen formulation for the viscous component [25][26][27]. The viscous

component is modified with experimental data for the subsonic, transonic and supersonic regimes taking accounting for factors such as end length.

2.1.5 NSWC & APC

The NSWC code utilises basic theoretical methods for many of its components. It also makes significant use of CFD correlated with experimental data. The Aeroprediction code (APC) is the latest code development [16].

Table 2.5: NSWC body alone computational methods [22]

Component Mach Number	Subsonic	Transonic	Low Supersonic	High Supersonic
Nose Wave Drag	-	Euler plus Empirical	Second Order Van Dyke Modified Newtonian	Second Order Shock Expansion Plus Modified Newtonian
Boattail Wave Drag	-	Wu & Aoyoma	Second Order Van Dyke	Second Order Shock Expansion
Skin Friction Drag	Van Driest II			
Base Drag	Empirical			
Inviscid Lift and Pitch Moment	Empirical	Euler or Wu & Aoyoma plus Empirical	Tsien First Order cross-flow	Second Order Shock Expansion
Viscous Lift and Pitching Moment	Allen & Perkins			

Table 2.6: NSWC wing and interference computational methods [22]

Component Mach Number	Subsonic	Transonic	Low Supersonic	High Supersonic
Inviscid Lift and Pitch Moment	Lifting Surface Theory	Empirical	Linear Theory	Shock Expansion Theory
Wing Body Interference	Slender Body Theory and Empirical		Linear Theory, Slender Body Theory and Empirical	-
Wing Tail Interference	Line Vortex Theory			
Wave Drag	-	Empirical	Linear Theory + Modified Newtonian	Shock Expansion + Modified Newtonian Strip Theory
Skin Friction Drag	Van Driest			
Trailing Edge Separation Drag	Empirical			
Body Base Pressure Drag Caused by Tail Fins	Empirical			

2.1.6 MISSILE I, II & III

Missile I, II, III and subsequent developments (M3FLR, M3HAX, M3F3CA) are based on the body buildup methodology. The body alone method uses slender body theory plus cross-flow [28],[29]. The wing and tail fin loads are determined from experimental databases. The equivalent angle of attack method is primarily used to account for interference effects. The codes are heavily dependent on databases and are thus more empirical than the code of NSWC for instance.

2.1.7 AERODYN

The AERODYN code utilises basic theoretical methods with empirical corrections, as summarised in Table 2.7 and 2.8.

Table 2.7: AERODYN body alone computational methods [22]

Component Mach Number	Subsonic	Transonic	Low Supersonic	High Supersonic
Nose Wave Drag	Tangent Ogive - Empirical Table Cone - Semi-Empirical Correlation Von Karman - Empirical Correlation			
Boattail Wave Drag	Empirical Table			
Skin Friction Drag	Van Driest II			
Base Drag	Empirical (NASA)			
Lift (Viscid and Inviscid)	Modified Jorgensen			
Pitching Moment (Viscid and Inviscid)	Empirical Table			

Table 2.8: AERODYN fin and interference computational methods [22]

Component Mach Number	Subsonic	Transonic	Low Supersonic	High Supersonic
Inviscid Lift	Lifting-Line Theory and Datcom Theoretical			
Viscous Lift	Datcom Empirical			
Pitching Moment	Subsonic - Linearised Pertubation Theory Transonic Fairing Supersonic - Lifting Surface Theory			
Wing Body Interference	Slender Body Theory (NACA 1307)		Linear Theory, Slender Body Theory and Empirical (NACA 1307)	
Wing Tail Interference	Line Vortex Theory (NACA 1307)			
Wave Drag	Linear Theory & Empirical			
Skin Friction Drag	Van Driest III			
Vortex Tracking/Shadowing	Line Vortex Theory (NACA 1307)			

2.1.8 MISSILE (ONERA)

The French Aeronautics Research Organisation, ONERA, utilises the basic Allen and Perkins formulation (inviscid and viscous) extended by Jorgensen and modify with experimental data [30]. The interference factors are calculated using the equivalent angle of attack method and experimental correlations which include parameters such as Mach number, taper ratio, angle of attack.

2.1.9 NASA W-B-T

The NASA W-B-T code is the method of Jorgensen of reference [31] and utilises a combination of theoretical methods (Allen and Perkins method extended by Jorgensen), empirical data and the modified Newtonian impact theory. The wings are not modeled separately and the equivalent angle of attack method is not used. Also no vortex tracking to account for the effect of one fin set on a downstream fin set is implemented.

2.2 Basic Aerodynamic Theories

Missile aerodynamics, at least for engineering predictions, uses a wide range of theories. The main equation on which almost all of the engineering level missile aerodynamics is based upon is the potential equation, which describes the velocity potential, Φ, of the flow field.

2.2.1 Nonlinear Potential Equation

The form of the equation is determined by number of conditions namely:

- Compressibility of the fluid
- Coordinate system used
- Velocity of the coordinate system with respect to the far field fuild

For the case where the fluid is stationary and a missile is moving through the fluid field, the full nonlinear equation for the velocity potential, Φ, is

$$\begin{aligned}\left[c_\infty^2-(\gamma-1)\left(\Phi_\tau+\frac{\Phi_\xi^2+\Phi_\eta^2+\Phi_\zeta^2}{2}\right)\right](\Phi_{\xi\xi}+\Phi_{\eta\eta}+\Phi_{\zeta\zeta})\\ =\Phi_{\tau\tau}+(\Phi_\xi^2+\Phi_{\xi\xi}+\Phi_\eta^2\Phi_{\eta\eta}+\Phi_\zeta^2\Phi_{\zeta\zeta})+2(\Phi_\xi\Phi_\eta\Phi_{\xi\eta}+\Phi_\xi\Phi_\zeta\Phi_{\xi\zeta}\\ +\Phi_{\eta\zeta}\Phi_\eta\Phi_\zeta)+2(\Phi_\xi\Phi_{\xi\tau}+\Phi_\eta\Phi_{\eta\tau}+\Phi_\zeta\Phi_{\zeta\tau})\end{aligned}\tag{2.1}$$

The axes system that is fixed to the fluid is ξ,η,ζ. c represents the speed of sound of the fluid in the far field, while τ, is time.

In many cases, the situation that is of interest, is where the missile is stationary with respect to the observer, and the fluid is assumed to be moving at velocity and is parallel and uniform. The axes fixed to the missile, x,y,z, at time t, is such that x is parallel to the fluid traveling at velocity, V. Transforming the potential equation 2.1 using the following equations:

$$\begin{aligned}\bar{x}&=\xi+V\tau\\ \bar{y}&=\eta\\ \bar{z}&=\zeta\\ t&=\tau\end{aligned}\tag{2.2}$$

results in the new velocity potential, ϕ

$$\begin{aligned}\left[c^2+\frac{\gamma-1}{2}V-(\gamma-1)\left(\phi_t+\frac{\phi_{\bar{x}}^2+\phi_{\bar{y}}^2+\phi_{\bar{z}}^2}{2}\right)\right](\phi_{\bar{x}\bar{x}}+\phi_{\bar{y}\bar{y}}+\phi_{\bar{z}\bar{z}})\\ =\phi_{tt}+(\phi_{\bar{x}}^2+\phi_{\bar{x}\bar{x}}+\phi_{\bar{y}}^2\phi_{\bar{y}\bar{y}}+\phi_{\bar{z}}^2\phi_{\bar{z}\bar{z}})+2(\phi_{\bar{x}}\phi_{\bar{y}}\phi_{\bar{x}\bar{y}}+\phi_{\bar{x}}\phi_{\bar{z}}\phi_{\bar{x}\bar{z}}\\ +\phi_{\bar{y}\bar{z}}\phi_{\bar{y}}\phi_{\bar{z}})+2(\phi_{\bar{x}}\phi_{\bar{x}t}+\phi_{\bar{y}}\phi_{\bar{y}t}+\phi_{\bar{z}}\phi_{\bar{z}t})\end{aligned}\tag{2.3}$$

2.2.2 Linearised Potential Equation

The linearised potential equation is derived from the nonlinearised equation by assuming small velocity pertubations u,v,w, and assuming these velocities are significantly smaller,

or at least an order of magnitude smaller than the free-stream velocity. The linearised equation can be written as

$$c^2 \nabla \phi^2 = \phi_{tt} + V_\infty \phi_{\bar{x}\bar{x}} + 2\phi_{\bar{x}t} \tag{2.4}$$

Expressing this in terms of the Mach number M, which equals

$$M = \frac{V}{c} \tag{2.5}$$

The linear potential equation can be written as

$$\phi_{\bar{x}\bar{x}}(1 - M^2) + \phi_{\bar{y}\bar{y}} + \phi_{\bar{z}\bar{z}} = \frac{1}{c_\infty^2}\phi_{tt} + 2\frac{M}{c}\phi_{\bar{x}t} \tag{2.6}$$

which is essentially the equation of linear aerodynamics. The assumptions made in this derivations are:

- Pertubation velocities are very much smaller than the free stream velocity
- Pertubation velocities are of comparable magnitude to each other

For slender bodies or flight speeds near Mach 1.0 or if the changes in the dominant flow direction are slow, the pertubations in the direction of the freestream velocity can be ignored. The equation thus reduces for both sub- and supersonic speeds to the incompressible two dimensional Laplace's equation

$$\phi_{\bar{y}\bar{y}} + \phi_{\bar{z}\bar{z}} = 0 \tag{2.7}$$

2.2.3 Available Theories

In missile aerodynamics a large number of theories are used. Reference [4] has classified them into four categories, namely A,B,C and D. Classes A, B and C are based potential theory, while class D consisting of the Newtonian impact and viscous cross-flow theory are not.

Class A theories are two dimensional and consist of the Ackeret, Busemann, Shock expansion and method of characteristics [4]. All are generally used on aerofoils, except for the method of characteristics which is also used on bodies of revolution. The Mach number range is all supersonic.

Class B theories are also two dimensional and consist of the strip and simple sweep theories. They cover the complete Mach number range [4].

Class C theories are three dimensional and consist of the supersonic wing, conical flow, supersonic lifting line, quasi-cylinder and slender body theories. Except for the slender body theory, all the theories are applied to supersonic flows. They are used on slender shapes, quasi-cylinders and lifting surfaces (wings).

The predominant theory used in the prediction of the aerodynamics of missile-like bodies is slender body theory. The theory is applicable to three dimensional flows and, as its name implies, is useful for slender bodies.

2.3 Bodies

Bodies in isolation have been extensively studied in the past. Of consideration in this research are circular bodies rather than non-circular bodies. Work on cones and non-circular shapes eg. elliptic have also been performed extensively in the past with the following reference being only but a few [32][33][31][34][35] [36][37][38], though these are not subject of this thesis.

2.3.1 Experimental Observations

Experimental observations of flows over slender bodies in isolation show three primary dependencies, these being:

1. Angle of attack
2. Reynolds number
3. Mach number

Each of these is subsequently discussed. The behaviour of the flow over cylindrical bodies in 3D is very similar in behaviour to impulsively started flow in 2D. Much of the flow behaviour is normally explained in this manner. The effect of the nose does, however, limit this analogy [39] but it is none the less extremely useful in this application.

At low angles of attack of less than 4°the flow is attached. As the angle of attack increases separation occurs on the lee side of the body. The location of the separation point as a function from the tip of the nose, at an engineering level, depends on the type of nose (either blunt or sharp). The separation results in two symmetric vortices. As the angle of attack increases, the symmetric vortices become asymmetric resulting in the generation of side forces. The angle of attack at which this occurs depends on the include nose angle and nose type.

For the onset of the symmetric vortices, it is, however, possible to obtain a reasonable non-dimensional correlation of the strength and position of the vortex core as a function of distance from the nose, x, and the angle of attack, α. Basing the correlation on the implusive flow analogy, the resulting non-dimensional parameter against which the non-dimensional vortex strength, $\frac{\Gamma}{2\pi V_\infty a\alpha}$, can be correlated is, $N = \frac{\alpha(x-x_s)}{a}$, where x_S is the location where vortices first start to occur from the nose. Using the available data at the time, reference [4] showed a relatively good correlation and can be used to determine the non-dimensionalised distances, $\frac{y_v}{a}$ and $\frac{z_v}{a}$ in the vertical and lateral directions respectively.

The predominant correlation used subsequent to reference [4] has been derived from reference [20]. The correlation is empirically derived from experimental data. For sharp noses (i.e. nose tip radius < 0.2 of body radius) the following relationship was developed for $4^\circ < \alpha < \eta_n$

$$\frac{x_s}{a} = 32\left[1 - \sqrt{\frac{\alpha - 4^\circ}{\eta_n - 4^\circ}}\right] \tag{2.8}$$

where η_n is the half included angle of the sharp nose. If the angle of attack is greater than the half included angle of the nose, the vortices start at the tip of the nose.

For blunt noses the following relationship was developed

$$\frac{x_s}{a} = 2 + \frac{10^\circ}{\alpha - 4^\circ} \tag{2.9}$$

These relationships form the basis for the separation points for reference [40] on which the Missile Datcom code is based.

For the position and strengths of the vortices, reference [20] and [41] provide correlations for angles of attack up to 50°and transonic and supersonic Mach numbers up to 3.0.

As the angle of attack increases further (generally $\alpha > 60^\circ$), the flow becomes wake like exhibiting 2D like behaviour until the angle reaches 90°.

Reynolds number affects the flow of inclined bodies in the cross flow direction or $M_\infty \sin\alpha$. The complex behaviour is illustrated in Figure 2.1 and is a summary of the graph from reference [42]. The drag coefficient in the cross-flow direction (when one considers the flow in 2D) has a well known sub critical value of 1.2 ($Re < 2 \times 10^5$) with separation occuring at the lateral meridian of 80° to 90°. At critical Reynolds numbers ($2 \times 10^5 < Re < 5 \times 10^5$) a laminar bubble forms where laminar flow separation occurs at 80° to 90°) and transitions to turbulent and reattaches at about 110°, with the turbulent boundary layer finally separating at about 130° to 140°. The drag coefficient drops rapidly to a value of less than 0.3. At supercritical Reynolds numbers the laminar separation bubble disappears, laminar to turbulent transition occurs well before the lateral meridian and the turbulent separation point slowly upwards from 130° to 140° (with a corresponding increase in the drag coefficient) until transcritical Reynolds numbers, where separation occurs at 100° and the drag coefficient plateaus. The boundary layer phenomena that correspond to the drag coefficient dependence on Reynolds number dependence start with potential fully attached flow for very low Reynolds numbers (Re < 5) because viscosity dominates (Stokes flow) [43]. As the cylinder Reynolds number increases beyond 100 regular eddy shedding initiates resulting in the von Karman vortex street. The frequency of the shedding is characterised by the Strouhal number ($S_t = nD/V$), which is approximately 0.2 for cylinders at Mach numbers less than 0.6 [39]. The Strouhal number increases to 0.6 at M_c of 1.6, and is illustrated in Figure 2.2 (which is a summary of the graph from reference [39] and does not include the source data from which the curve was derived).

Once the Reynolds number increases beyond 100000, the wake becomes turbulent.

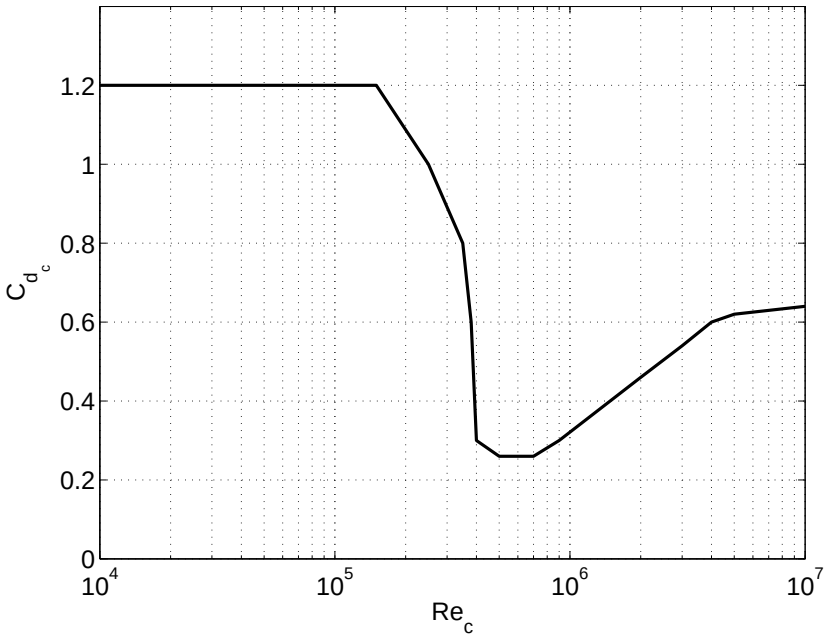

Figure 2.1: Cross flow drag coefficient as a function of Reynolds number for Mach numbers below 0.4 [42]

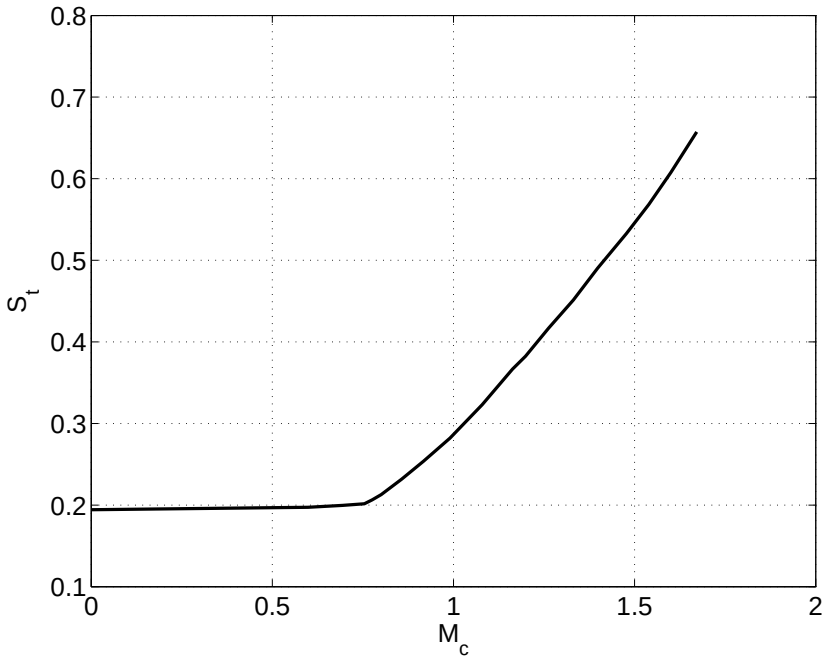

Figure 2.2: Strouhal number variation as a function of Mach number [39]

Inclined circular bodies exhibit similar flow features to the 2D cylinder except that the axial flow component modifies the flow characteristics [43] such that the flow can only be directly analogous to 2D flow at angles of attack above approximately 60° and low angles ($\alpha < 4$) where separation does not occur. For the intermediate symmetric flow pattern, even though multiple asymmetric vortices are shed, the axial flow is sufficiently strong enough to organise the vortices into two single symmetric vortices, whilst in the asymmetric regime the axial flow is only sufficiently strong enough to organise one pair of steady asymmetric vortices [43] resulting in multiple vortices being shed. The expected type of flows for a tangent ogive nose body, and their dependence on angle of attack and Reynolds number base on the body diameter, Re_D, are illustrated in Figure 2.3 [43][44]. Three flow types exist, namely laminar (L), turbulent (T) and short bubble (B), and result in the various illustrated flow regimes. The laminar and turbulent flow regimes correspond to the state of the boundary layer. The short bubble regime (B) is when a laminar separation bubble occurs followed by turbulent reattachment and then turbulent boundary layer separation. The boundaries indicate the transition mechanism, where (1) is due to free shear layer (instability to small disturbances) instability, (2) due to attachment-line (adverse pressure gradient on windward attachment line) instability, (3) due to cross-flow instability (cross flow generated due to centripetal pressure gradient) and (4) due to streamwise-flow (or Tollmien-Schlichting) instability. The laminar flow regime would correspond to subcritical 2D flow, whilst the turbulent flow regime to super- and trans-critical 2D flow. The short bubble flow regime would correspond to critical 2D flow.

The effects of freestream Mach number are normally considered in the cross flow direction or $M \sin \alpha$. As the cross flow Mach number increases, either due to an increase in freestream Mach number or angle of attack, the cross flow behaviour resembles that of subsonic incompressible flow with a lee side separation, until around M=0.43 where the local speed of sound increases beyond sonic around the lateral meridians, terminating in shock waves. At Mach numbers greater than 0.5 the adverse pressure gradients resulting from the shock waves is large enough to cause separation irrespective of whether the boundary layer is laminar, turbulent or transitional [43]. Thus at Mach numbers greater than 0.5, the flow characteristics, and hence drag coefficient, are Reynolds number insensitive and only Mach number dependent.

Figure 2.4 shows the drag coefficient as a function of Mach number, which is a summary of graph presented in reference [42]. None of the experimental data from which the curves were constructed are available and are therefore not plotted.

It has, however, been noted that the drag coefficient varies considerably in the critical, super and transcritical Reynolds number regions [43] [42]. In the critical region the effects of surface roughness, tunnel turbulence, wall boundary layer noise and body motion contribute to variations as large as an order of magnitude. A dependence on Mach number in the supercritical region has also been demonstrated [42]. Asymmetric vortices are not of interest to this thesis because only symmetric vortices are expected for the configuration,

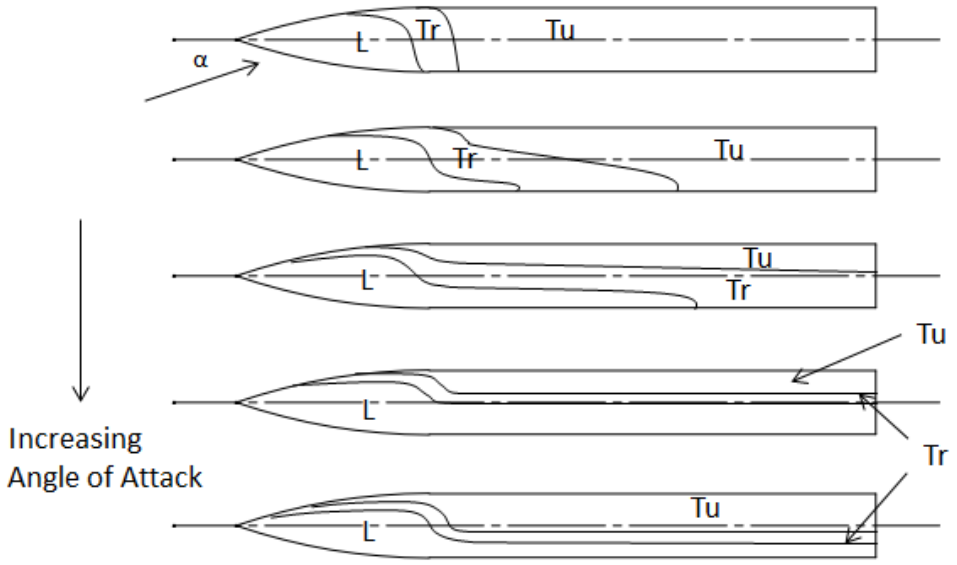

(a) Flow Types (L=laminar, Tr=Transitional, Tu=Turbulent)

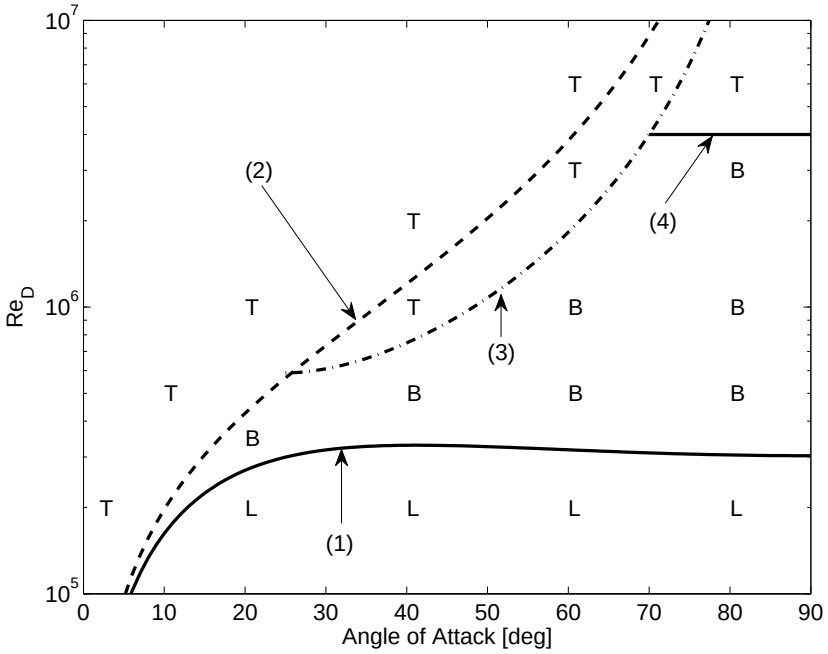

(b) Angle of attack and Reynolds number dependence

Figure 2.3: Types of flows expected for inclined circular bodies and the dependence on angle of attack and Reynolds number.

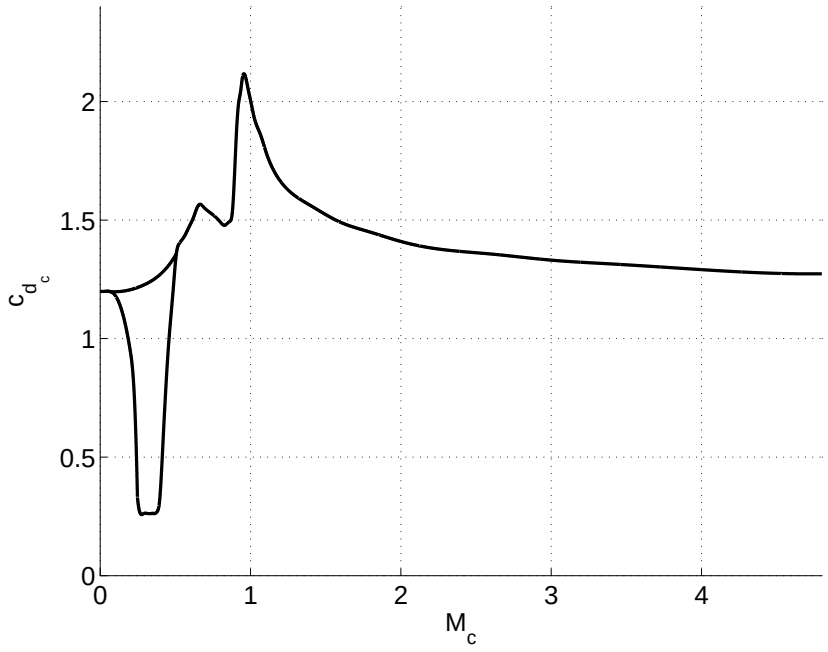

Figure 2.4: Cross flow drag coefficient as a function of Mach number [42]

angle of attack and Mach numbers of interest. Suffice to say, however, that asymmetric vortices result in lateral loads (side force and yawing moment) whose effect drops off as the cross flow Mach number increases beyond Mach 0.4, so that no asymmetric vortices are present at supersonic cross flow Mach numbers [43][44].

The appearance of vortices introduces significant differences between inviscid slender body theory and experiment; this primarily due to the fact that vortices are viscous by nature. For bodies, at angles of attack, the pressure on the windward side decreases as the flow accelerates around the body. On the leeward side the pressure should recover in accordance with inviscid slender body theory because the flow decelerates. In practice, the pressure does not recover because the flow separates from the body, creating vortices. The flow separates due to it being unable to sustain the pressure recovery required. The boundary layer then rolls up into the observed vortices. Because the boundary layer controls the separation, with the boundary layer being viscous by nature, analytically predicting the nature and characteristics of the vortex precisely is not possible due to the dependence of the boundary layer behaviour on body shape, Mach number, Reynolds number and so forth.

The transient behaviour of 2D cylinders is also of interest. When observing 2D cylinders that are started impulsively, the flow at very low speeds is Stokes like in nature. As the speed increases, the flow separates, creating vortices. The drag force experienced by the cylinder has been experimentally measured and its behaviour is similar to an impulse imparted on a second order underdamped system [45]. The maximum drag coefficient experienced is approximately 1.6 and reduces to the steady state value of 1.2. The devel-

opment of separated flow over inclined cylinders or bodies of revolution can again be viewed in the cross flow planes using the analogy of an impulsively started 2D cylinder. Thomson [46][39] has also extended this analogy to account for favourable pressure gradients and base effects in an approximate way.

2.3.2 Theoretical Methods

The available theoretical methods for slender body configurations fall into four broad categories

1. Linear
2. Cross flow analogy
3. Vortex clouds (or discrete vortex models) and concentrated vortices
4. Higher order numerical methods

2.3.3 Linear Methods

The linear theories used to determine the inviscid lift of a slender body can be classified into the following categories:-

1. Potential methods
2. Method of characteristics
3. Shock expansion

Potential methods include slender body theory and Van Dyke's second order potential method [47][48]. Slender body theory for supersonic speeds which was solved by the method of Ward [49], whilst the subsonic speed analogy is explained in reference [4]. Shock expansion methods include the second order shock expansion method (SOSE) [50] and a conical-shock-expansion method by Eggers and Savin [51]. The method of characteristics, whilst accurate, has never really been used in engineering methods due to its complexity and computational cost [52].

Using the method of Ward for supersonic flow yields for the side and normal forces

$$\begin{aligned} \frac{F_Y}{q} + i\frac{F_Z}{q} &= 2i\alpha S(x) \\ \frac{F_Y}{q} &= 0 \\ \frac{F_Z}{q} &= 2\alpha S(x) \end{aligned} \tag{2.10}$$

where $S(x)$ is the cross sectional area at a given axial location.

2.3.4 Loads

The lift coefficient with the base area as reference area for a body of unit length is thus

$$C_L = \frac{F_Z}{qS} = 2\alpha \tag{2.11}$$

or simply put, the lift curve slope of a slender body is two, based on its base area.

The center of pressure of a slender body of revolution is

$$x_{cp} = \frac{\int_0^L xS(x)dx}{\int_0^L S(x)dx} = \left(1 - \frac{V}{S_B}\right) L \tag{2.12}$$

where S_B is the base area, and V is the volume of the body.

2.3.5 Non-Linear Effects : Vortices

The predominant method used to determine the non-linear forces and moments on a slender body is the cross-flow drag concept as initially developed by Allen [5] and refined by Allen and Perkins [3].

Allen developed the equations in their generalised form but presented the slender body potential component in reference [3] as low angle of attack equations i.e. less than 5°, due to the approximate nature of the the method [3] [5]. The small angle of attack approximation formulae are shown below.

The cross-flow normal force per unit length developed by a normal infinite cylinder of radius, a, at an angle of attack, α, with a drag coefficient of c_{d_c}, is defined as

$$\frac{dF_{N_v}}{dx} = c_{d_c}(2a)q\alpha^2 \tag{2.13}$$

Adding this to the lift generated by the slender body theory results in

$$\frac{dF_{N_v}}{dx} = 2q\alpha\frac{dS}{dx} + c_{d_c}(2a)q\alpha^2 \tag{2.14}$$

where S is the cross-sectional area. By integration, the normal force is thus

$$F_N = 2q\alpha S_B + c_{d_c}q\alpha^2 S_p \tag{2.15}$$

where S_B is the body base area, S_p is the body planform area subject to viscous cross-flow.

Equation 2.15 correlates fairly well with experimental data for high slenderness ratio configurations [4] at low to moderate angles of attack.

The two components which make up the normal force are thus the potential component, which is proportional to the angle of attack and base area; and the viscous component, which is proportional to the square of the angle of attack.

The basic concept of Allen and Perkins has been generalised to angles of attack ranging from 0° to 180° since its application is limited to low and moderate angles of attack (i.e.

less than 20°angle of attack). This was performed by Jorgensen [42] [53]. The small angle of attack approximations have been removed and the full form equations presented. The representation for angles of attack from 0° to 90° are listed.

The normal force is expressed as:

$$C_N = \frac{S_B}{S} \sin(2\alpha) \cos\left(\frac{\alpha}{2}\right) + \eta c_{d_c} \frac{S_C}{S} \sin^2(\alpha) \tag{2.16}$$

where η is the cross flow drag proportionality factor or cross flow drag coefficient ratio of finite to infinite length cylinders.

The pitching moment is expressed as:

$$C_m = \left[\frac{V - S_B(L - x_{mrc})}{SD}\right] \sin(2\alpha) \cos\left(\frac{\alpha}{2}\right) + \eta c_{d_c} \frac{S_p}{S} \left(\frac{x_{mrc} - x_c}{D}\right) \sin^2(\alpha) \tag{2.17}$$

where V is the volume of the body, L is the length of the body, and x_c is the centroid of the planform area of the body. The axial force is expressed as:

$$C_A = C_{A_{\alpha=0^\circ}} \cos^2(\alpha) \tag{2.18}$$

The aerodynamic center is expressed as:

$$x_{ac} = \left(\frac{x_{mrc}}{D} - \frac{C_m}{C_N}\right) D \tag{2.19}$$

Various methods are used to calculated the cross-flow drag coefficient, c_{d_c}. In the original formulation of Allen and Perkins, c_{d_c} was calculated using a cross section diameter of D' which is derived from the expression

$$D' = \frac{S_p}{L} \tag{2.20}$$

where S_p is the cross sectional area exposed to the cross flow, and L is the body length.

The drag coefficient was then calculated from the resulting Reynolds number and Mach number, which for the two cases presented was 1.2 since the cross-flow Reynolds number was below critical. Corrections to the value of 1.2 were made for the bodies being finite cylinders instead of infinite cylinders, resulting in ratios of 0.755 and 0.692 for the two bodies used.

Jorgensen [42] provided a comprehensive survey of the prediction methodologies used for the cross flow drag coefficient including end effects at the available time when the article was published. The infinite length cross flow drag coefficient is dependent on two primary non-dimensional parameters, namely Reynolds number and Mach number. These have been discussed in the experimental observations section.

The cross flow drag proportionality factor, η, has only been measured at low cross flow Mach numbers for different slenderness ratios [42]. The author did, however, indicate that these values have been used successfully for engineering purposes even though the data were scarce.

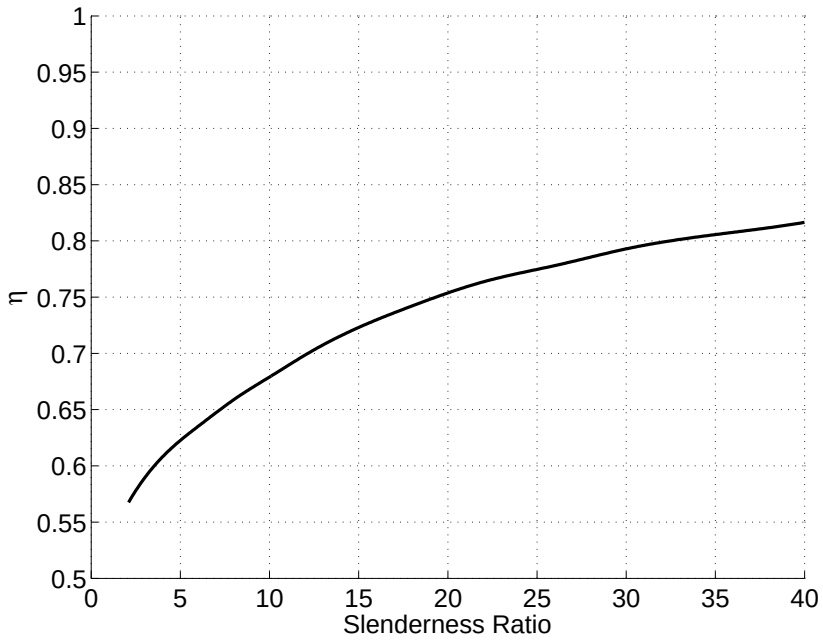

Figure 2.5: Cross flow drag proportionality factor as a function of slenderness ratio [42]

Jorgensen updated the proportionality factor in reference [53]. Figure 2.6 shows the product ηc_{d_c} as a function of the cross flow Mach number obtained at high angles of attack, while Figure 2.7 shows the dependence of η only. For both figures, the experimental data used to construct the curves by reference [53] has not been shown, and only the curves have been reproduced. As indicated by reference [53], more data are required around $M_c = 1$, though the sharp drop at $M_c = 1$ was obtained from experimental data.

The value of $\eta = 1$ for most supersonic cross-flow Mach numbers have been validated from past investigations [42][53]. Figure 2.7 is consistent when one considers that at high cross flow Mach numbers the flow is completely supersonic essentially nullifying the end effects that are seen at the lower cross flow Mach numbers.

The effect of roughness on the cross flow drag coefficient has been demonstrated by a number of authors [54], [43] [55]. Reference [54] showed that the critical Reynolds number decreases as the roughness increases, also resulting in higher drag coefficients.

2.3.6 Vortex Models

A number of investigators have attempted to model the wake region of an inclined body of revolution by either a concentrated vortex with and without feeding sheets or discrete vortex elements in a cloud. The "NACA Vortex Model" was one of the earlier methods developed [56] where two line vortices are attached to the inclined body. Extensive use of experimental data was required to position the vortices and predict vortex strengths.

Some refinements such as modelling viscous cores or using feeding sheet representations have been adopted such as that of Mello [57]. Bryson [56] represents one of the first

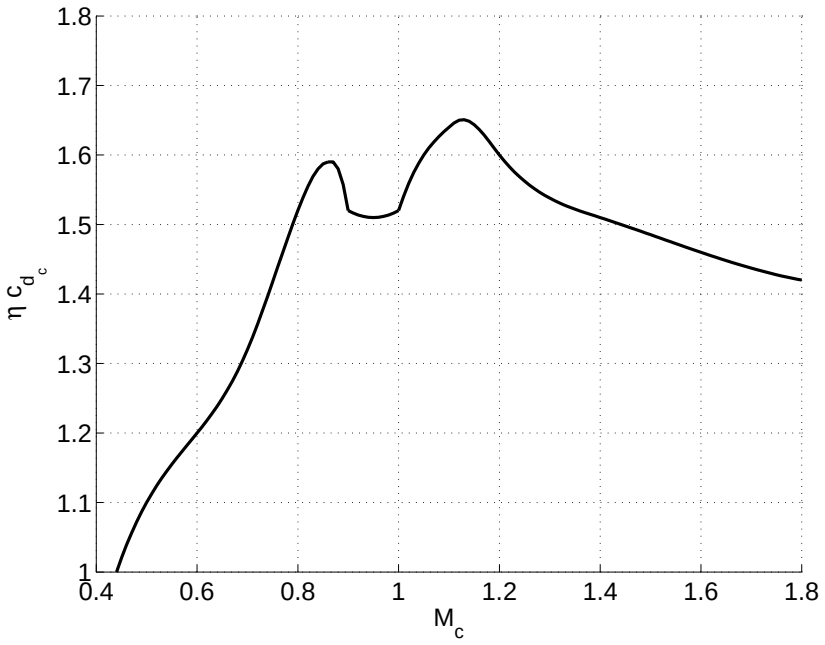

Figure 2.6: Product of cross flow drag and proportionality factor as a function of Mach number [53]

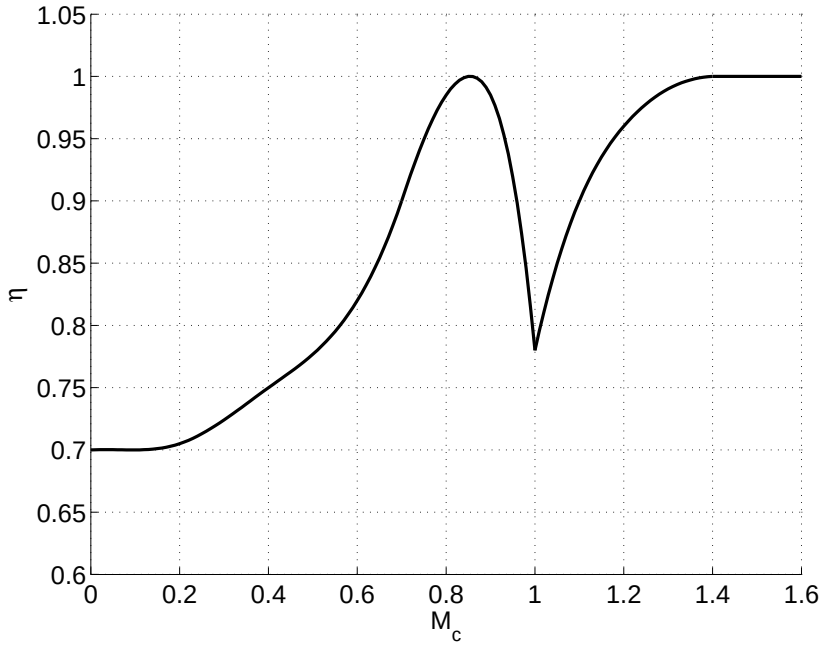

Figure 2.7: Cross flow drag proportionality factor as a function of cross flow Mach number [53]

attempts to model the separated wake using a concentrated vortex and a feeding sheet of vanishing strength. The position of the vortices were determined to be where the net force on the vortex and feeding sheets were zero. Wardlaw [58], and Fidler and Bateman [59] extended Bryson's model to asymmetric vortices, this in an attempt to model the more diffuse nature of the leeside flow.

The later models were developed as a consequence of the wake being more complex in structure than the NACA Vortex Model or two line vortex representation. These include discrete vortices placed in a prescribed shape to represent the feeding sheet [60].

Angelucci [61] and Marshall and Deffenbaugh [62] adopted the alternative approach of multiple elementary discrete vortices being shed into the wake region or more generically known as the Discrete Vortex Model (DVM) or vortex cloud methods. Mendenhall refined these concepts in his implementation of vortex clouds [63] [64] [65] to include compressibility effects, boundary layer separation, viscous vortex cores and non-circular bodies. Mostafa has also applied the DVM method to unsteady flows for bodies and cambered plates [66].

2.3.7 Higher Order Methods

It is worth mentioning higher order methods even though they are not used in engineering level codes due to their cost and complexity, more as an example of the limited nature in which codes have and can be applied for engineering level use. From the full Navier-Stokes formulation, two major levels of simplification occur namely ignoring viscous effects which result in Euler codes and then rotationality resulting in potential codes. The level of codes used in engineering level applications are only the lowest level, this being the incompressible 2D potential formulation. Most Navier-Stokes methods are based on the finite volume method.

Full potential methods examples include the code NCOREL [67] and those by Rakich [68]. These methods already require the flow domain to be discretised and an example of the simplifications employed is where only the flow within the bow shock is modeled and a boundary condition placed at the bow shock. The addition of entropy to the full potential methods allows shocks to be captured [67].

2.4 Wings

Of concern to the subject of this thesis are wings of very low aspect ratio ($AR < 0.1$) rather than low to moderate aspect ratio. Wings of aspect ratio of order of magnitude 1 have been used in the past [69] and remains the predominant aspect ratio employed. The wings are also generally of simple cross section [69] such as diamond or hexagonal (primarily due to their application being of short duration) and are applied mostly in a cruciform configuration.

Delta wings, or variations to this such as cropped deltas, arrows or trapezoids, are used predominantly for slender body winged configurations and have been the subject of much research. They exhibit separated flow at low to moderate angles of attack and are also amenable to linear analysis or slender body theory.

2.4.1 Experimental Observations

The flow over delta wings have been catergorised into 2 distinct regimes, these as a function of the Mach number and angle of attack in a plane normal to the leading edge (M_N and α_N respectively) [70]. Of particular importance is the Stanbrook and Squire boundary (SSB) [71]. Within the M_N and α_N space, 6 or 7 distinct flow regimes exist for thin or thick delta wings respectively [72] (see Figure 2.8). Most of the work has been for wings with sharp leading edges, though some data are available for rounded leading edges such as the Shuttle [70]. Rounded leading edges broaden the SSB [70]. Delta wings at very low angles of attack have attached flow for both sub- and supersonic speeds. For subsonic leading edges at moderate angles of attack, separation occurs at the leading edge separation such that on the leeward side a primary vortex exists with a feeding vortex sheet. In addition a secondary separation vortex exists between the primary vortex and the leading edge. Thin delta wings with supersonic leading edges at moderate angles of attack, exhibit attached flow over the leading edge due to an expansion fan, whilst a shock induced vortex occurs at a span somewhat inboard from the leading edge. For thick delta wings at low supersonic leading edge speeds ($M_N < 1.5$) , leading edge separation occurs without a secondary vortex forming. On the leeward side an attached or detached shock exists depending on the leading edge Mach number and leading edge angle of attack.

At higher angles of attack, vortex bursting occurs for delta wings. Experimental correlations for when these occur have been developed [72].

The lift characteristics of delta wings depends primarily on the aspect ratio and Mach number. Reference [73] reports on the aerodynamic characteristics for a wide range of low aspects ratios at supersonic Mach numbers. A summary of this follows. As the Mach number increases from subsonic through to transonic speeds, the stalling characteristics are dominated by the vortex breakdown phenomena. At supersonic speeds the windward side flow increasingly dominates the force contribution resulting in a distinct Mach number dependence in low angle characteristics. No obvious stall or vortex breakdown is noticeable, probably because of the smaller contribution to wing normal forced by the leeward side.

As the aspect ratio of delta wings is reduced the lift curve slope decreases at both sub- and supersonic Mach numbers, and the normal force becomes increasingly second order in characteristic with respect to angle of attack. At subsonic speeds the effect of vortex breakdown and wing stall dominate the moderate to higher angles of attack behaviour.

For rectangular wings at subsonic speeds complex vortex features exist at the leading

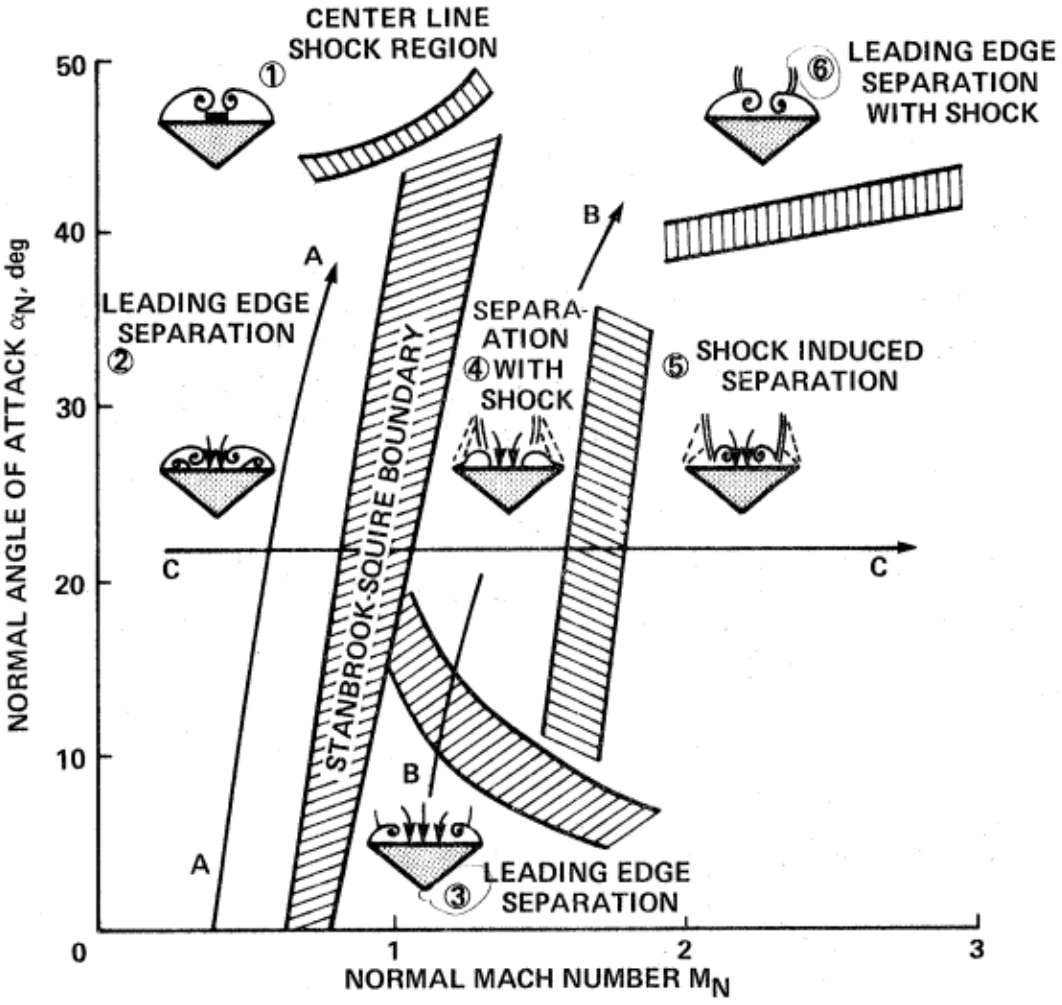

Figure 2.8: Delta wing flow regimes [72]

edge, whilst the rest of the flow is dominated by a vortex that separates from the side. At supersonic Mach numbers the spanwise pressure distribution is relatively uniform [73] when compared to the patterns at subsonic speeds because the suction peaks are lower at supersonic speeds. Work by Winter [74] showed that the normal force for a rectangular wing becomes increasingly nonlinear as the aspect ratio decreases such that at aspect ratio of AR=0.033, the response is essentially a $\sin^2$ function for angles of attack up to 35 degrees, where as for AR=1.5 or 2.0, the response is linear at low to moderate angles of attack, with the normal force curve displaying characteristics typical of a 2D higher aspect ratio wing. The tests performed by Winter were, however, only subsonic. At subsonic speeds the separated flow vortex structures are complex [72] and unsteady [75]. In addition to the side edge vortex, a leading edge and horseshoe exists because of the zero sweep leading edge. This is graphically illustrated in Figure 2.9. Wickens [76] performed some tests on rectangular plates of aspect ratio 0.25 showing that the side edge shed vortices are diffuse and rolled up at an angle of $\alpha/2$ which is consistent with that modeled by Bollay [21] using horseshoe vortices. The normal force coefficient displays the non-linear second order characteristic as demonstarted by Bollay and Winter.

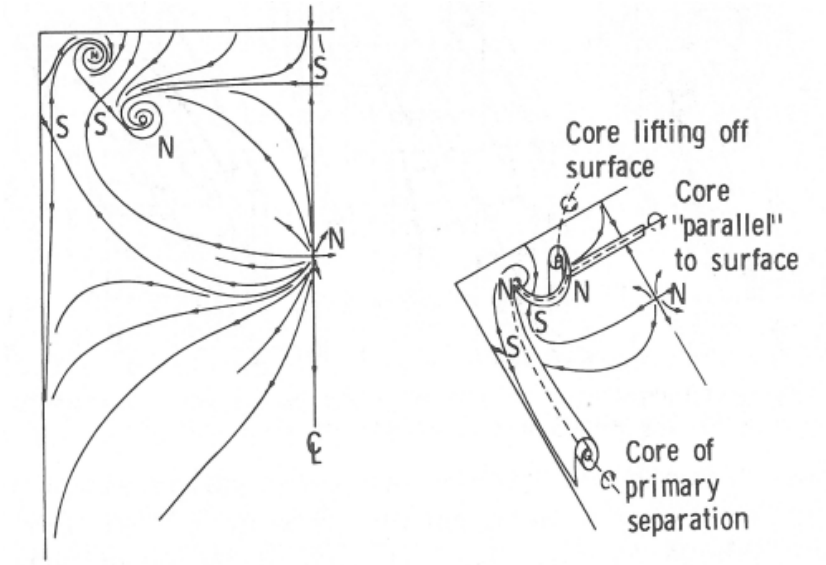

Figure 2.9: Subsonic rectangular wing flow structures [77]. S and N denote saddle and nodal singular points of separation or reattachment as interpreted by reference [77].

Cropped delta wings created by sweeping the leading edge of a rectangular wing to some finite less than 90° for aspect ratios of order 1, show changes in normal force and centre-of-pressure to be essentially the same as that of a rectangular wing [73]. The leading edge vortex at subsonic speeds (for the leading edge that is) is unsteady [75] for leading edge sweep angles less than 45°. For leading edges that are supersonic (the leading edge is in front of the Mach line), no leading edge vortex is shed.

Wings with leading edges strakes are the last major category of planform. They are

essentially trapezoidal wings or deltas that have a tip with high leading edge sweep. For trapezoidal wings the primary driver for the strakes is that the leading edge separation for moderately swept planforms is unsteady and erratic [69]. Wings with strakes exhibit significant differences to either the wing without the strake, the strake itself or a linear combination of the two. A synergistic effect due to the strake vortex helps to stabilise the increase both the maximum lift coefficient realised and the angle of attack before stall occurs for subsonic speeds by keeping the flow attached to the root of the wing. At supersonic speeds the windward side starts to dominate the flow field, with a resulting drop-off in the effect of the strake [73].

As for inclined circular bodies, the 2D analogy has been employed in the past to determine the loads on slender wings using the cross flow concept. Flat plates inclined at 90° to the flow exhibit, like a circular cylinder, a separated flow region with two dominant vortices in the lee side. Sarpkaya in his work on impulsively started flows also examined the loads on a flat plate [45][78]. The behaviour is similar to cylinders but has distinctly differently characteristics. The first is that the impulse peaks at a drag coefficient of 2.5 which occurs sooner than for a cylinder. Subsequently the drag drops below the steady state value and peaks again at 2.4 before settling down to the steady state value of 1.9.

2.4.2 Theoretical Methods

One of the earliest attempts at modeling separated flow over delta wings from a theoretical perspective was by Legendre [79] who modeled the flow as a concentrated vortex and imposed the Joukowski-Kutta condition at the leading edge. This led to reasonably accurate results at moderate angles of attack ($10^\circ \leq \alpha \leq 20^\circ$), but predicted negative lift at low angles and also multi-valued solutions. Adams [80] and Brown and Michael [81] refined this formulation by introducing a branch cut between the separation point and the concentrated vortex, which solved the negative lift with Legendre's formulation. This was further refined by Edwards [82] by ensuring that both the vortex and feeding sheet are force free which solved the multi-valued problem. Whilst Legendre, Adams, Brown and Michael, and Mangler and Smith employed the Joukowski-Kutta condition, Pershing [83] forced the concentrated shed vortices to form at an angle of $\alpha/4$ with the wing plane. Sacks [75], however, modeled the vortex feeding sheet and rollup of the sheet using a discrete number of concentrated vortices while imposing the Joukowski-Kutta condition, which is the DVM method that was applied to bodies. The linear lift curve slope of a slender delta wing that is within the Mach cone is $AR\pi/2$ [6], which is based on slender wing theory and is only really applicable for vanishing aspect ratios.

The other class of planform are rectangular wings. One of the earliest attempts to model the flow of a rectangular wing at subsonic speeds was performed by Bollay [21]. Bollay used multiple horseshoe vortex elements along length of the chord. The vortex elements were allowed to separated from the edge of the wing, thus resulting in an ap-

proximate angle of $\alpha/2$. Subsequent improvements have been performed by Scholtz [84] and Gersten [85]. At low angles of attack, the linear lift curve slope was determined by Schlichting [86] to be a function of Mach number because the leading edge of the wing is supersonic. Gersten [85] extended his model by including a non-constant spanwise distribution. Extension to arbitrary planforms have been performed by Gersten [87], Berlotserkovskiy [88] and Yermolenko [89].

Global gross load prediction methodologies utilise the summation of potential and separation or vortex type components. Aside from vortex lattice methods, the only simplified global gross load prediction methodology is the leading section suction analogy, originally developed by Polhamus [90][91][92] and extended by Lamar [93][94][95]. The suction analogy does, however, rely on the assumption that the separated flow reattaches fully. Mendenhall and Nielsen [20] utilised the concept of the side edge vortex for wings with finite tips i.e. cropped deltas of aspect ratio 0.1 to 5, where they assumed that all (or semi-empirically correlated fraction) of the full side edge suction was converted to lift.

2.4.3 Semi-Empirical Methods

Semi-empirical methods are employed during the design phase and in engineering level codes because of the requirement for speed. Of particular interest in this thesis are low and very low aspect ratio wings. The normal force behaviour of these wings has already been touched upon in the previous section. Missile Datcom uses supersonic linear theory for low to moderate angles of attack [23], whilst APC uses a fourth order polynomial model for angles of attack from 0° to 180° [96] correlated against experimental data.

2.5 Body and Wing Combinations

2.5.1 Experimental Data and Databases

Empirical or semi-empirical methods using experimental databases (mostly utilising polynomial or similar type functions) to model wing body combinations (and wings with very low aspect ratios) are from three primary sources. They are White [97], Sigal and Blake [98][18][19] (Missile Datcom) and Moore [16][16][99][100] [101] (Aero Prediction Code). Other models have been developed by Nelson [12], Baker and Aiellio. Of these methods, only the APC code has correlated, within its empirical database, the wing-to-body carryover factor as a function of angle of attack. The rest utilise consider the wing and body as one configuration.

The data used for these methods is in the most part not readily available. Some publicly data are, however, available for these purposes or for validation of numerical models. The most extensive of these are by Jorgensen [102][103] and Allen [104]. Jorgensen has performed work on bodies with planar strakes [103] with aspect ratio 0.0285 and strake span to body ratios of 1.2 though the primary objective of the report was to determine the

effect of strakes on the side forces of these configurations. Allen [104] has performed tests on bodies and cruciform strakes though the aspect ratios of the strakes were only 0.153 with a strake span to body ratio of 1.77. Other sources of data are by Simpson and Birch [13], Spearman and Trescot [105] and Robinson [106]. Simpson and Birch performed tests on bodies of revolution with planar strakes of aspect ration less than 0.1. The Simpson and Birch configuration was a wing of aspect ratio 0.067 and wing span to body diameter of 1.6. Robinson tested rectangular wings of aspect ratios 0.077 and 0.154 with wing span to body diameter ratios of 1.33 and 2.11 respectively, whilst Spearman and Trescot extended the tests performed by Robinson to other Mach numbers.

Other experimental work performed on circular wing-strake combinations was by Macha [107], but these were performed at angles of attack of 90° only i.e. 2D, and not for inclined slender body configurations. The visualisation results from these tests were extremely poor and limited to only one Schlieren photograph for a span to body ratio of 1.55 and freestream or cross flow Mach number of 1.0. No defining features of the separated wake can be discerned. The other Schlieren photographs were of the circular cylinder alone [108] which shows the change in the vortex structures for transonic Mach numbers.

Configurations with very slender delta wings have been performed by Simpson and Birch [13] and Spearman and Robinson [109]. Very slender delta wings interact with bodies of revolution differently to that of wings with side edges [13]. Cones with strakes have been studied by Jorgensen [110]. The only other experimental investigation of the interaction of body vortices and wing vortices was performed by Jeane [111] looking at the change in the vortex generation of the body of a slender body and its subsequent effects.

With regards to flow visualisation, Werle [112] has performed work on body and strake configurations at low speed in a water tunnel for a chine like configuration with a strake span to body diameter ratio of 1.74 and a circular body and strake configuration with strake span to body diameter ratio of 2.16 and strake length of 5.9D. Jorgensen has for the configuration used in reference [31] performed laser vapour screen visualisation and is of particular interest because of its similarity to that being used in this thesis. The Mach numbers considered were 0.6, 0.9 and 2.0. The lee side flow structures of three locations were imaged namely at the start of the strakes, midway down the strakes and at the end of the strakes. The angles of attack were 10° to 50°, in 10° intervals. The report was, however, more concerned with the alleviation of side force and yawing moment at the higher angles due to asymmetric vortices than with the detailed understanding of the lee side flow field which explains the lack of detail and interpretation of the observed flow fields. No other publically available flow visualisation data are available, except for a single plane in the flow field at an angle of attack of 8° by Simpson and Birch.

2.5.2 Body-Wing Interference Modeling

Various methods or models have been developed in the past to calculate the mutual interference for engineering methods and fall into three main categories, these being:

- Linear
- Non-linear
- Newtonian impact theory [31]
- Semi-empirical correlations [113]

The semi-empirical correlations have been discussed in the previous subsection (see subsection 2.5.1).

For the linear methods, two broad classes exist namely exact and approximate. The exact methods include W-function and multi-pole methods [114], fourier analysis [115], conical boundaries [116], upwash and slender body theory [7][117], [118], [119] and the Volterra method [120]. Approximate methods include a wing-alone method [121], component method by Flax and Lawrence [122] and Lennertz method by Schneider and Nikolitsch [123]. These methods are amenable to determining the influence of the body on the wing and/or vice versa. The linear methods have in the past [113] been classified as those belonging to the class of P-N-K or Pitts, Nielsen and Kaattari as enunciated in reference [7]. The linear methods do, however, result in the mutual interference effects being constant with angle of attack as exemplified by that of slender body theory [7]. Lamar and Luckring [124] have applied the leading edge suction analogy method, quasi-vortex-lattice potential flow method and a free vortex sheet method to body and wings and combinations thereof.

The component buildup methodology takes into account the combination of wings and bodies through interference factors and both linear and slender body theory facilitate this methodology. These interference factors as mentioned in the introduction account for the effect of the body due to the wing and vice versa, or more commonly known as K_{B_W} and K_{W_B} respectively. The equivalent angle of attack method represents the most significant development for component buildup methods since their orginal formulation in the 1950's. This formulation allows the non-linear behaviour of wings to be included in the original linear formulations. Because of its significance and importance, this method is elucidated in the next subsection by itself.

The Newtonian method of Jorgensen [31] does not fall into the same category as the component build up methodologies and considers the body and strake as one entity, utilising the Allen cross flow concept extended to body and strakes. The cross flow coefficient based on the equivalent diameter, which for cylinder strake configuration is the same as the cylinder diameter. The Newtonian method developed differs to the data presented by Macha in that it underpredicts the cross flow drag coefficient [18]. The work by Sigal and Blake [18][19], in developing a "unified" cross flow concept, is similar to that of the

Jorgensen Newtonian method except that correction factors obtained from experimental data (in the form of ratios) are used. The model is the same as that of Jorgensen in that it utlises the heuristic Allen cross flow concept but employs the empirical database of body-strake combinations at 90°to the flow of tests performed by Macha [107] at various transonic Mach numbers.

The non-linear methods represent a class of methods that have previously not been explicitly acknowledged because they have not been used for determining the interference effects, but rather overall flow phenomena. They have evolved from been used primarily in the past to model the separated leading edge vortex of slender wings, method which have already been mentioned in section on wings. Two sub-categories of methods exist namely concentrated vortex models and discretised vortex models. For concentrated vortex models, Levinsky *et al* [125][33] have used the Mangler and Smith model [126] as a starting point and extended the theory to include non-conical flows, whilst Mendenhall and Nielsen used a combination of the leading edge suction analogy and Bollay's side edge vortex model for modelling wing-body-tail combinations [20]. One of the earliest implementations of the discretised vortex model (DVM) methods was by Sacks [75] where his work on slender wings using discrete vortices also included the body in his application. Mendenhall provides the only application of the vortex cloud method to so called winged-body configurations [127]; these being forebodies with chines at subsonic speeds. The discretised vortex model was originally proposed by Rosenhead [128] in his paper on unsteady vortex sheets and was subsequently employed by numerous investigators including Westwater [129] for the rollup of trailing edge vortices. The DVM method is not without its problems, one of these being that the vortices tend to coalesce together if they come too close together.

Only the semi-empirical databases and non-linear vortex methods currently represent ways of modelling non-linearities at an engineering level; this being analogous to the Allen and Perkins analogy for viscous effects for bodies in isolation. Simplifying the non-linear methods for use in engineering applications does, however, represent a challenge to the methodologies used in the past.

In completing this subsection of the literature survey, other related, though not directly associated with wing-to-body carryover effects are presented.

The effect of bodies on wing panels have been modelled by Oberkampf in a series of papers [130][131][132] where the body vortex is represented as a concentrated vortex with feeding sheets made up discrete low strength vortices positioning in a prescribed shape. The position and strengths were, however, determined experimentally and the simplified model only used to model the interaction of body vortices on wings.

Work has also been performed for non-circular bodies such as ellipses [133][134][34][12].

2.5.3 Equivalent Angle of Attack Concept

One of the first attempts to account for mutual interference effects due to non-linear aerodynamics was by Flax and Lawrence [122]. The equivalent angle of attack concept, though distinctly different falls into the same category. The angle of attack concept was developed to overcome the inherent limitations of slender body theory and extend the theory to increase accuracy and provide a comprehensive component buildup methodology for flows ranging from subsonic to hypersonic and from low to very high angles of attack. A short summary taken from references [14] and [11] is given here. The method has the ability to account for arbitrary bank angles and fin deflections in its formulation and represents the largest development since reference [7] for the component buildup methodology. The effect of bank angle and fins deflections are not explored in this survey.

The traditional manner for determining the loads eg. normal force and pitching moment on an airframe are:

$$C_{N_{BWT}} = C_{N_B} + C_{N_{W(B)}} + C_{N_{B(W)}} + C_{N_{T(B)}} + C_{N_{T(W)}} + C_{N_{W(T)}} \quad (2.21)$$

$$C_{m_{BWT}} = C_{m_B} + C_{m_{W(B)}} + C_{m_{B(W)}} + C_{m_{T(B)}} + C_{m_{T(W)}} + C_{m_{W(T)}} \quad (2.22)$$

The influence of the tail on the wing can normally be neglected for high speed tactical missiles unless the two are closely coupled because the flows remain predominantly supersonic. The view that the normal force and pitching moment can be seen as a linear supersposition of flow fields is only strictly true if the flow is linear, which is only true for low to moderate angle of attack [4],[7]. This method has been extended to determine nonlinear aerodynamic characteristics [11].

The method derives its name from the modification of the angle of attack term, α, to α_{eq}, when determining the contribution of a component in terms of the isolated component itself i.e.

$$C_{N_{W(B)}} = \frac{\partial C_{N_W}}{\partial \alpha} \alpha_{eq} \quad (2.23)$$

For missile like configurations slender body theory predicts no (or little in practical circumstances) lift for cylindrical portions of the body. For wing-body sections, the lift is thus entirely due to the wings. Extending the slender body theory originally developed by Munk [1] for wing-body sections resulted in the normal force coefficient for the winged section as:

$$C_{N_{W(B)}} + C_{N_{B(W)}} = \frac{2\pi\alpha s_m^2}{S}\left(1 - \frac{a^2}{s_m^2}\right)^2 \quad (2.24)$$

where a is the local body radius and s_m is the maximum semi-span. The above equation is furthermore independent of Mach number.

Ward [49], Morikawa [2], and Nielsen and Kaattari [117] all suggested using the above equation to obtain the interference between the wing and body by using the linear theory

or data for the exposed wing alone composed of the two exposed fins joined together at their root chords. The wing alone component is thus defined as

$$C_{N_W} = \frac{2\pi\alpha s^2}{S} = \frac{2\pi\alpha\left(s_m - a\right)^2}{S} \tag{2.25}$$

where s is the span of the exposed fin i.e. it excludes the body radius.

Dividing equation 2.24 by 2.25 gives

$$\frac{C_{N_{W(B)}} + C_{N_{B(W)}}}{C_{N_W}} = \left(1 + \frac{a}{s_m}\right)^2 \tag{2.26}$$

The above equation is called the modified slender body theory method. Equation 2.26 can be rewritten as:

$$C_{N_{W(B)}} + C_{N_{B(W)}} = (K_{W_B} + K_{B_W})\frac{\partial C_{N_W}}{\partial \alpha}\Big|_{\alpha=0}\alpha \tag{2.27}$$

where

$$\begin{aligned} K_{W_B} &= \frac{C_{N_{W(B)}}}{C_{N_W}}; \alpha \neq 0, \delta = 0 \\ K_{B_W} &= \frac{C_{N_{B(W)}}}{C_{N_W}}; \alpha \neq 0, \delta = 0 \\ K_{W_B} + K_{B_W} &= \left(1 + \frac{a}{s_m}\right)^2 \end{aligned} \tag{2.28}$$

The values of K_{W_B} and K_{B_W} as determined above by slender body theory can be replaced by other analyses such as semi-empirical, numerical or experimental values, thereby improving the overall results. The slender body theory results for K_{W_B} and K_{B_W} are shown in Figure 2.10 and is adequate for component buildup predictions as long as the wing-body combination is sufficiently downstream of the influence of the nose [7]. The effect of increasing Mach number tends to reduce the total body carryover effect and moves the center of pressure aft. As mentioned previously modifications to the predictions have been performed to account for Mach number effects [4] and afterbodies of finite length [9][10].

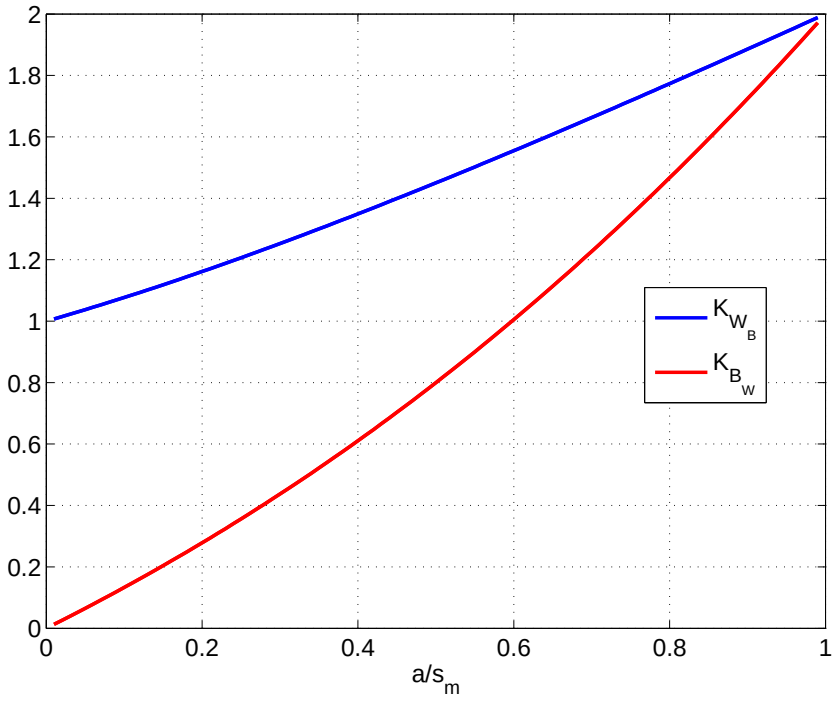

Figure 2.10: Slender body theory wing body interference factors [4]

The contribution of the tail section (i.e. tail-wing interference) is handled in same way as for the wing-body. The tail contribution in the presence of the wing can be expressed as:

$$C_{N_{T(W)}}\Big|_{fins} = \frac{\partial C_{N_T}}{\partial \alpha}\Big|_{\alpha=0} \Delta\alpha_v \tag{2.29}$$

where $\frac{\partial C_{N_T}}{\partial \alpha}$ is the slope of the tail-alone normal force coefficient curve at zero angle of attack and $\Delta\alpha_v$ is the effective upwash angle generated by the vortices of the wing, which is nonlinearly dependent on the wing load, geometry, configuration incidence angle and wing deflection angle.

Since $\Delta\alpha_v$ is the average upwash angle of the exposed fin span, it can be equated to an effective fin deflection angle as

$$\Delta\alpha_v = k_W \delta_{eff} \tag{2.30}$$

The tail-body contribution due to the wing vortices is thus

$$C_{N_{T(W)}} = (1 + \frac{k_B}{k_W})\Delta\alpha_v \frac{\partial C_{N_T}}{\partial \alpha}\Big|_{\alpha=0} \tag{2.31}$$

The normal force coefficient for the complete configuration is thus

$$C_{N_{BWT}} = C_{N_B} + [(K_{W_B} + K_{B_W})\sigma_w + (k_W + k_B)\delta]_{wing} \frac{\partial C_{N_W}}{\partial \alpha}\Big|_{\alpha=0} + [(K_{W_B} + K_{B_W})\sigma_w + (k_W + k_B)\delta + (1 + \frac{k_B}{k_W})\Delta\alpha_v]_{tail} \frac{\partial C_{N_T}}{\partial \alpha}\Big|_{\alpha=0} \quad (2.32)$$

where σ_w is the total incidence angle.

The pitching moment is simply obtained by summing the product of each contribution with its appropriate center of pressure.

The key to extending equation 2.32 into the nonlinear range is to consider the contribution of the wing and tail panel or fins loads separately from those acting on the body, which allows this method to maintain the existing forms yet have applicability over a large range of angles of attack and flow regimes. The normal force acting on one of the horizontal wing panels of a finned section in the "plus" attitude is

$$C_{N_{B(W)}} = (K_{W_B}\sigma_w + k_W\delta + \Delta\alpha_v)\frac{\partial C_{N_W}}{\partial \alpha}\Big|_{\alpha=0} \quad (2.33)$$

From this the equivalent angle of attack, α_{eq}, can be defined as

$$\alpha_{eq} \equiv K_{W_B}\sigma_w + k_W\delta + \Delta\alpha_v \quad (2.34)$$

and

$$C_{N_{B(W)}} = \frac{\partial C_{N_W}}{\partial \alpha}\alpha_{eq}$$

The formulation for the equivalent angle of attack for fin i is thus:

$$\alpha_{eq_i} = K_{W_B}\sigma_w \cos\phi + \frac{2}{AR}K_\phi \sigma_w^2 \sin(2\phi) + \sum_{j=1}^{4} \Lambda_{ji}\delta_j + \Delta\alpha_{v_i} \quad (2.35)$$

where Λ_{ji} is the interference of the deflection of fin j on fin i.

For the symmetric low angle attack case, the wing vortex interference component, $\Delta\alpha_{v_i}$, can be estimated using by the influence coefficient method of reference [7]. For all other cases reference [14] indicates that only empirical correlations and vortex tracking methods could be used. This is because it is necessary to first determine the distribution of the flowfield vorticity in the cross-flow planes cutting through the finned section. Secondly the spanwise and chordwise distribution of upwash induced on the fins must be computed based on flowfield distribution. Finally, the effective angle of attack for each fin due to the upwash is determined.

Typically only the spanwise upwash distribution at a representative chord is calculated and appears to give accurate enough results assuming the vorticity moves in the freestream direction [14]. The simplest and most popular method is to compute the arithmetic average of the local induced angle of attack [14].

The equivalent angle of attack formulation (see equation 2.35) was obtained by linearly adding the various contributing components. For angles of attack above 20°, the velocity components should be summed rather than the angles of attack [14],[11]. This results in:

$$\tan\hat{\alpha}_{eq_i} = K_{W_B}\tan\sigma_w\cos\phi + \frac{2}{AR}K_\phi\tan\sigma_w\sin\sigma\sin(2\phi_i) + \tan\Delta\alpha_{v_i} \tag{2.36}$$

where

$$\alpha_{eq_i} = \hat{\alpha}_{eq_i} + \sum_{j=1}^{4}\Lambda_{ji}\delta_j \tag{2.37}$$

and $\hat{\alpha}_{eq_i}$ is the equivalent angle of attack for no fin deflection. For the non-rolled (and hence zero banked) case

$$K_{W_B} = \frac{\tan\hat{\alpha}_{eq_i}}{\tan\sigma_w} \tag{2.38}$$

which is identical to the equation 2.28.

It should be noted that K_{W_B} varies with angle of attack [4].

The assumptions made up to this point in the equivalent angle of attack method have included

1. Nonlinear effects can be accounted for using the equivalent angle of attack formulae and wing alone data
2. Interference factors K_{W_B}, K_{B_W} and K_ϕ are angle of attack independent
3. Dynamic pressure and Mach number of the flow near the fins are near the freestream values

This is true for linear theory, but not when the angle of attack relative to the freestream increases. It has been shown from experimental data that K_{W_B} is a function of the total incidence angle, σ_w [14] and also dependent on Mach number. A single family of curves can, however, be obtained plotting the data against $M\sin\sigma_w$ instead of σ_w. The trend in the data seems to indicate that compressibility is a primary cause in the loss of favourable body-fin interference. Additional correlations are available from the work done for the Aeroprediction code (APC) [99][16].

2.6 Downwash, Wakes and Vortices

In the component build up methodology the shedding of wakes and vortices need to be accounted for. The wake has been calculated by various methods in references [135],[136],[137] and [138]. Of particular interest to this thesis, however, are free and bound vortices and their effect on lifting surfaces and bodies, which is discussed in the next section. In addition to this, the effect of attached vortices (vortices with feeding sheets) on close coupled lifting surfaces have not been explicitly considered.

2.6.1 Vortex Trajectories

The effect of a free vortex on a lifting surface is to change the angle of attack along the span of the surface. An example of this is the effect of a body or canard vortex on a tail. Methods used in the past include slender body theory and strip theory [7] and that by Alden and Schindel [7] and Sacks [139].

The position of a vortex shed when it encounters the tail after being shed from the trailing edge of an upstream lifting surface (or the trajectory that it follows from being shed) has also been the subject of research. The use of potential theory to determine the trajectory of free vortices has been performed in the past both for bodies and wing-body combinations [4]. A free vortex, because it cannot support a force, must move as a Lagrangian fluid point in the flow field. The subsequent movement is thus simply determined using an ordinary differential equation solver such as the Runge-Kutta-Merson, Runge-Kutta-Felberg or the plethora of other available schemes depending on the stiffness of the problem and accuracy required.

One of the original theoretical developments was performed by Spahr [140]. The method has been used in various applications since its inception for predicting the aerodynamic performance of a family of slender body configurations in engineering codes [20][141][41][40]. Previous applications of this method have been to track vortices for cruciform wings [142][143] and their effect on tails [144] and also for induced rolling moments [141][145].

Continued development of vortex tracking and afterbody vortex shedding methodologies have led to the development of methods to predict vortex shedding from circular and non-circular bodies in both subsonic and supersonic flow [63] [65][64][37], and at high angles of attack [146]. The prediction of shedding and tracking of body vortices from both non-circular and circular bodies is based on reducing a three dimensional steady flow problem to a two dimensional unsteady separated flow problem i.e. parabolising the potential flow domain. This approach originated from the analogy of a two dimensional unsteady flow past a body and the steady three dimensional flow past an inclined body [63].

The application of vortex tracking to cruciform wing-body combinations has been performed for low aspect ratio triangular wing body combinations [75] and forebodies with chines [127] (whose work was based on [75]). The work for both of these was performed at subsonic Mach numbers.

The work performed by Mendenhall and Lesieutre [127] modeled forebodies with chines as a non-circular body with sharp edges, rather than a circular body with low aspect ratio wings. Consequently the forebody chine configuration is thus represented as an equivalent asymmetric body with the same cross-sectional area as the actual body. The work performed by Sacks [75] uses a form of the discrete vortex model where the vortex sheet is represented by a discrete number of vortices emanating from the leading edge such that the Joukowski-Kutta condition is met at the edge. The minimum number of

vortices that needed to be shed to ensure convergence was determined to be 24 for the semi-empirical implementation and 30 for the theoretical method. This is in contrast to the later work by Mendenhall and his co-workers on body (and forebody chines) vortex shedding which allows the accuracy requirements of the stepwise integration to be met thus requiring the use of a variable number of vortices. The modeling by Sacks thus discretises the sheet and primary vortex into a finite number of discrete vortices, while Mendenhall does not assume that a primary vortex necessarily forms or exists. Multiple groupings of vortices may possibly form. Mendenhall, on his work with forebody chines [127], assesses the effect of representing the vortex cloud as a single concentrated vortex by summing the vortices strengths and placing it at the centroid of the cloud, and also the vortex sheet using 5 discrete vortices. It was found that the single concentrated vortex did not model the flow at the edge of the chine well especially as the number of shed vortices increased. Modeling the vortex feeding sheet improved results, though with only limited fidelity. It should be noted that the comparisons were performed by combining vortices in the cloud rather than performing the simulations with the single concentrated vortex or limited number of vortices. This makes the vortex cloud methods computationally expensive. It was noted by Mendenhall on his work on chines that they included secondary vortex separation simulation capabilities due to its importance in asymmetric vortex cases.

2.7 Summary

Slender body theory and the linearised potential equation remain the cornerstone of theoretical methods employed in engineering level predictions codes [4]. The limitations of these methods to low angles of attack are extended to higher angles using the heuristic method of Allen and Perkins [3] which have been extended by subsequent investigators [31], with semi-empirical corrections improving the predictions [27][25][44][26][29]. Similarly the wing-body interactions have been developed from slender body theory and are essentially low angle of attack formulations that can be extended to higher angles of attack due to the lift characteristics of the isolated wings. For component buildup formulations, the equivalent angle of attack method [11] has extended the low angle of attack formulation to high angles of attack. The modeling of separated flow phenomena are accounted for by using the method of Allen and Perkins which utilises the cross-flow drag concept, or more specifically the vortices themselves, either as a single concentrated vortex (as originally proposed by Bryson [56]), or as discrete vortices (discrete vortex model - DVM - method of Rosenhead [128]).

The methods used for wing-body combinations have been developed for wings with aspect ratios from 0.25 to 4. Limited methods have been developed for wings with aspect ratios less then 0.1. The unified cross flow concept of Sigal and Blake, and Jorgensen's modified Newtonian cross-flow method essentially extend the Allen and Perkins cross-flow drag method to wings with very low aspect ratio and do not simulate the separated

flow topology as would the DVM method or method of Bryson. The application of these methods have been limited to conical configurations (Levinsky *et al* [33]), bodies only [56][147][45][61], wings only [79][81][126], bodies with wings of aspect ratio higher than 0.1 [75] or chine-like configurations [127].

Chapter 3

Modeling Method

3.1 Introduction

The approach adopted to developing the proposed engineering method of modeling the lee side flow for cruciform body strake configurations at supersonic speeds is based on the 2D slender body theory concept that a 3D steady compressible flow problem can be reduced to an unsteady 2D incompressible problem, or alternatively put, the flow along the body in the primary direction of the flow is analogous an impulsively started infinite 2D configuration. Any other extension in the third dimension increases the complexity of the model beyond that which engineering codes can process in a reasonable time. As shall be shown, even 2D methods can also be too computing intensive for engineering purposes. Furthermore, the full viscous Navier-Stokes equations are reduced to the simplest linearised potential equation. This method of modeling has, and remains a challenge because the fully separated compressible flow in the lee side of the body and strake configuration can only be solved accurately using the full Navier-Stokes formulation. This and previous attempts are essentially using the lowest complexity order model to solve the highest complexity order problem. In order to model the lee side separated flow 2D line vortices are used, either as single concentrated vortices or distributed vortices depending on the method.

As seen from the literature survey, two broad classes of methods have been used in the past namely the single concentrated vortex (SCV) (i.e. Bryson [56] and Legendre [79]) and discretised vortex model (DVM) . Both these methods are applied to the cruciform body configuration. A third or approximate method, based on the concept of a free vortex is subsequently extended and applied and is developed from the two previous methods. The method first presented is SCV method because it is the simplest. Secondly the DVM method is presented and finally the free vortex method. In summary, three methods have been extended from their originating theories and applied to the cruciform circular body configuration.

For each method, after an introduction, the theoretical development is presented including extensions required for the cruciform circular body. The method is then applied

over the angle of attack range of interest and the results are compared to the CFD simulations. The body vortex or vortices present at angles of attack above 15° are simulated for all the methods except the SCV method.

The assumption made for all the methods employed is that the complex 3D steady flow can be simplified to a 2D unsteady flow problem. Implicit in these methods is the use of the 2D impulse flow analogy, where the flow along the body can be modeled as a time dependent impulsively started solution. Before any of these methods are presented, the basis of these methods is developed in the subsequent section.

3.2 Theoretical Development of the Basic 2D Method

The basic 2D method is presented in this section and forms the basis for all the subsequent methods and is presented here for brevity. In developing methods for assessing the aerodynamic loads of slender bodies, theories such as slender body theory and the 2D potential flow model employed in this analysis seek to exploit features of the flow and/or configuration. It should be noted that the methods used in this thesis have an extensive theoretical basis and the primary development in this thesis are extensions of the theoretical basis to, and application to cruciform wing-body configurations.

For the slender configurations and supersonic flow regime under consideration, the problem at hand can be solved in a two dimensional plane with the incompressible formulation of Equation 2.7, or

$$\phi_{\bar{y}\bar{y}} + \phi_{\bar{z}\bar{z}} = 0$$

This is based on the assumption that the flow in the plane perpendicular to the freestream flow direction changes slowly and is derived from Equation 2.6 by assuming a time steady formulation. This results in

$$\left(1 - M^2\right) \frac{\partial^2 \phi}{\partial x^2} + \frac{\partial^2 \phi}{\partial y^2} + \frac{\partial^2 \phi}{\partial z^2} = 0 \tag{3.1}$$

where the complex potential is

$$W(\sigma) = \phi + i\psi \tag{3.2}$$

The flow is treated as two dimensional such that incompressible potential flow formulations can be used. This allows a 3D steady problem to thus be reduced to a 2D unsteady problem. To predict the flow in the physical 2D plane for various configuration whether they be wing, planar wing body configurations, cruciform, elliptical and so forth, a transformation needs to be made to a suitable plane where analysis can be performed. For the series of methods employed in this thesis, the circle plane is used.

The axes system employed in these analyses are illustrated in Figure 3.1. The physical plane is denoted by the complex plane $\sigma = y + iz$, while the circle plane to which transformations are made is denoted by the complex plane $\nu = \tau + i\lambda$.

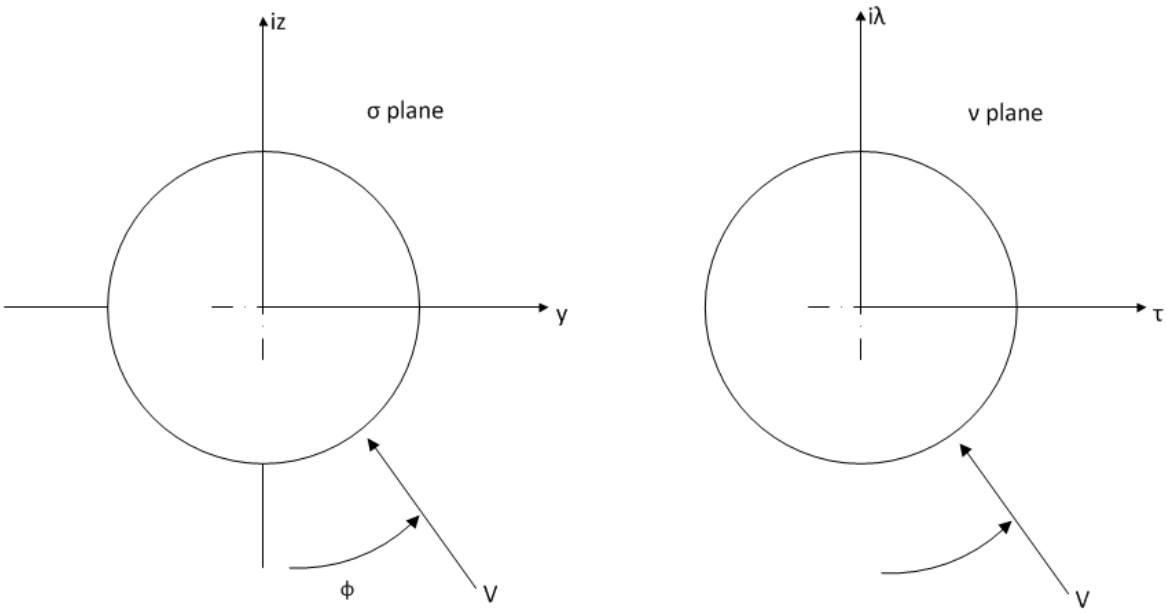

Figure 3.1: Cross flow physical and transformed axes systems

The geometries being considered are wings, planar wing-body combinations and cruciform wing-body configurations. This implies that the bodies are circular and that the wings are thin. The transformation is written in the form of

$$\nu = \nu(\sigma) \tag{3.3}$$

and is interpreted to mean that any point in σ plane can be transformed to point in the ν plane, and the inverse transformation

$$\sigma = \sigma(\nu) \tag{3.4}$$

can be interpreted to mean that any point in ν plane can be transformed to point in the σ plane. The transformations of the type used in this thesis do not cause any distortions in the planes at infinity and take the form

$$\nu = \sigma + \sum_{n=1}^{\infty} \frac{c_n}{\sigma^n} \tag{3.5}$$

$$\sigma = \nu + \sum_{n=1}^{\infty} \frac{k_n}{\nu^n} \tag{3.6}$$

where the constants c_n and k_n may be complex. For the complex potential W, the velocity components parallel to the y and z axes are denoted v and w respectively.

The configuration used in this thesis is the cruciform wing-body configuration. The transformation and its derivatives from the physical to the circle plane, with a circle of radius r_o in the ν plane are:

$$\sigma^2\left(1+\frac{a^4}{\sigma^4}\right)=\nu^2\left(1+\frac{r_o^4}{\nu^4}\right) \tag{3.7}$$

$$r_o^2=\frac{1}{2}s^2\left(1+\frac{a^4}{s^4}\right) \tag{3.8}$$

$$\frac{d\nu}{d\sigma}=\frac{\sigma}{\nu}\left(\frac{1+\frac{a^4}{\sigma^4}}{1+\frac{r_o^4}{\nu^4}}\right) \tag{3.9}$$

$$\frac{d^2\nu}{d\sigma^2}=\frac{d\nu}{d\sigma}\left[\frac{1}{\nu}\left(3-\frac{4}{1-\frac{r_o^4}{\nu^4}}\right)\left(\frac{d\nu}{d\sigma}\right)-\frac{1}{\sigma}\left(3-\frac{4}{1-\frac{a^4}{\sigma^4}}\right)\right] \tag{3.10}$$

3.3 Transverse Velocities of Vortices

For the 2D methods under consideration, the movement of vortices, whether shed by the body or free, can be modeled as Lagrangian fluid particles. The theoretical development is well established and the formulation employed in this analysis is a summary of [140] and [141] and is reproduced for clarity.

Consider the complex potential for the flow in the transformed (ν) plane for two vortices designated 1 and 2 of strength Γ_1 and Γ_2. This can be written as

$$W(\nu)=-iV\sin\alpha e^{-i\phi_x}\left(\nu-\frac{r_o^2e^{i2\phi_x}}{\nu}\right)-\frac{i\Gamma_1}{2\pi}\ln\left(\frac{\nu-\nu_1}{\nu-\frac{r_o^2}{\bar{\nu_1}}}\right)-\frac{i\Gamma_2}{2\pi}\ln\left(\frac{\nu-\nu_2}{\nu-\frac{r_o^2}{\bar{\nu_2}}}\right) \tag{3.11}$$

The assumption made is that the body is of uniform radius and that no image vortices are at the centre of the body.

The complex potential $W_1[\nu(\sigma)]$ for the complex velocity v_i-iw_i for the vortex, Γ_1, in the σ plane is the total complex potential $W(\nu)$ for the flow including the vortices minus the singularity at vortex Γ_1, or

$$\begin{aligned}W_1[\nu(\sigma)] &= -iV\sin\alpha e^{-i\phi_x}\left(\nu-\frac{r_o^2e^{i2\phi_x}}{\nu}\right)-\frac{i\Gamma_1}{2\pi}\ln\left(\frac{1}{\nu-\frac{r_o^2}{\bar{\nu_1}}}\right)-\frac{i\Gamma_2}{2\pi}\ln\left(\frac{\nu-\nu_2}{\nu-\frac{r_o^2}{\bar{\nu_2}}}\right)\\ &\quad+\frac{i\Gamma}{2\pi}\ln\left(\frac{\sigma-\sigma_1}{\nu-\nu_1}\right)\end{aligned} \tag{3.12}$$

The complex velocity of the vortex, Γ_1, in the σ plane is simply

$$v_1-iw_1=\frac{dW_1}{d\sigma}\,|_{\sigma=\sigma_1} \tag{3.13}$$

From reference [4] it can be shown that

$$\frac{d}{d\sigma}\ln\left(\frac{\sigma-\sigma_1}{\nu-\nu_1}\right) = -\frac{1}{2}\left(\frac{d\sigma}{d\nu}\right)\left(\frac{d^2\nu}{d\sigma^2}\right)_{\sigma=\sigma_1} \tag{3.14}$$

The complex velocity is thus

$$\begin{aligned} v_1 - iw_1 &= \frac{d}{d\sigma}\left[-iV\sin\alpha e^{-i\phi_x}\left(\nu - \frac{r_o^2 e^{i2\phi_x}}{\nu}\right) + \frac{i\Gamma_1}{2\pi}\ln\left(\nu - \frac{r_o^2}{\bar{\nu_1}}\right) - \frac{i\Gamma_2}{2\pi}\ln\left(\frac{\nu-\nu_2}{\nu-\frac{r_o^2}{\bar{\nu_2}}}\right)\right] \\ &\quad -\frac{i\Gamma_1}{4\pi}\left(\frac{d\sigma}{d\nu}\right)\left(\frac{d^2\nu}{d\sigma^2}\right)_{\sigma=\sigma_1} \end{aligned} \tag{3.15}$$

Evaluating this at $\sigma = \sigma_1$ yields

$$\begin{aligned} v_1 - iw_1 &= \left[-iV\sin\alpha e^{-i\phi_x}\left(1 + \frac{r_o^2 e^{i2\phi_x}}{\nu_1^2}\right) + \frac{i\Gamma_1}{2\pi}\ln\left(\frac{1}{\nu_1 - \frac{r_o^2}{\bar{\nu_1}}}\right)\right. \\ &\quad \left. -\frac{i\Gamma_2}{2\pi}\left(\frac{1}{\nu_1-\nu_2} - \frac{1}{\nu_1 - \frac{r_o^2}{\bar{\nu_2}}}\right)\right]\left(\frac{d\nu}{d\sigma}\right)_{\sigma=\sigma_1} \\ &\quad -\frac{i\Gamma_1}{4\pi}\left(\frac{d\sigma}{d\nu}\right)\left(\frac{d^2\nu}{d\sigma^2}\right)_{\sigma=\sigma_1} \end{aligned} \tag{3.16}$$

Expanding this to n vortices yields

$$\begin{aligned} v_1 - iw_1 &= \left[-iV\sin\alpha e^{-i\phi_x}\left(1 + \frac{r_o^2 e^{i2\phi_x}}{\nu_1^2}\right) + \frac{i\Gamma_1}{2\pi}\left(\frac{1}{\nu_1 - \frac{r_o^2}{\bar{\nu_1}}}\right)\right. \\ &\quad \left. -i\sum_{k=1}^{n}\frac{\Gamma_k}{2\pi}\left(\frac{1}{\nu_1-\nu_k} - \frac{1}{\nu_1 - \frac{r_o^2}{\bar{\nu_2}}}\right)\right]\left(\frac{d\nu}{d\sigma}\right)_{\sigma=\sigma_1} \\ &\quad -\frac{i\Gamma_1}{4\pi}\left(\frac{d\sigma}{d\nu}\right)\left(\frac{d^2\nu}{d\sigma^2}\right)_{\sigma=\sigma_1} \end{aligned} \tag{3.17}$$

Generalising this for the j^{th} vortex results in the following expression

$$\begin{aligned} v_j - iw_j &= \left[-iV\sin\alpha e^{-i\phi_x}\left(1 + \frac{r_o^2 e^{i2\phi_x}}{\nu_1^2}\right) + \frac{i\Gamma_j}{2\pi}\left(\frac{1}{\nu_j - \frac{r_o^2}{\bar{\nu_j}}}\right)\right. \\ &\quad \left. -i\sum_{k=1}^{n}\frac{\Gamma_k}{2\pi}\left(\frac{1}{\nu_j-\nu_k} - \frac{1}{\nu_j - \frac{r_o^2}{\bar{\nu_2}}}\right)\right]\left(\frac{d\nu}{d\sigma}\right)_{\sigma=\sigma_j} \\ &\quad -\frac{i\Gamma_j}{4\pi}\left(\frac{d\sigma}{d\nu}\right)\left(\frac{d^2\nu}{d\sigma^2}\right)_{\sigma=\sigma_j} \end{aligned} \tag{3.18}$$

The equations of motion for the j^{th} vortex is

$$\frac{dy_j}{dt} = v_j \text{ and } \frac{dz_j}{dt} = w_j \tag{3.19}$$

The cross-flow plane is moving down the body at a speed of $V\cos\alpha$. Thus

$$\frac{dx}{dt} = V\cos\alpha \tag{3.20}$$

The rate of change of the j^{th} vortex with body axial position is thus

$$\frac{dy_j}{dt} = \frac{v_j}{V}\frac{1}{\cos\alpha} \text{ and } \frac{dz_j}{dt} = \frac{w_j}{V}\frac{1}{\cos\alpha} \tag{3.21}$$

3.4 Vortex Induced Loads and the Vortex Impulse Theorem

The vortex impulse theorem was first proposed by Sacks in reference [148] and essentially states that the loads imposed on a section of a slender body and wing configuration by a vortex is due to the change in the position of the vortex in the circle plane. This can be written as

$$F_Z - iF_Y = \rho V\Gamma\nu_r \tag{3.22}$$

where ν_r is the complex distance between the vortex and its image in the circle plane. A good example of this, and one which is directly applied in this thesis, is when a vortex sheet or concentrated vortex is shed from the body. The total complex force on the body of interest is simply the complex distance of the vortex and its image in the circle plane at the plane at the end of the body. The total moment is the integral of the change in force along the length of the body. In coefficient form,

$$C_N - iC_Y = 4\Gamma'\nu'_r \tag{3.23}$$

where $\Gamma' = \frac{\Gamma}{2\pi aV}$ and ν' is non-dimensionalised by the body radius, and assuming the reference area is the area of the base of the body i.e. πa^2.

3.5 Component Buildup Method

When modeling the loads on a configuration, and in particular, those due to a specific phenomena such as a vortex, the question arises as to how to account for this phenomena, and the vortex impulse theorem provides a convenient way to account for this phenomena without having to resort to integrating surface pressures. Utilising the concept of Allen [5], the total load is therefore the sum of the the attached potential flow and the vortex load. This concept was used in reference [75]. Mathematically:-

$$C_N = C_{N_{attached}} + C_{N_{vortex}} \tag{3.24}$$

As mentioned previously, the configurations being considered in this thesis are cruciform wing-body combinations, but no configurations with multiple sets of wings. Alternatively put, only two components make up such configurations namely a slender circular

body and a single cruciform wing of very low aspect ratio. Considering equation 1.4 the total lift over the cruciform wing-body section is therefore

$$C_{N_B} + (K_{W_B} + K_{B_W})C_{N_W} = C_{N_{attached}} + C_{N_{vortex}} \tag{3.25}$$

where C_{N_B} is the body alone lift for the wing-body section only, $C_{N_{attached}}$ is the attached potential flow component and $C_{N_{vortex}}$ is the vortex induced component, which can, and for this thesis, is calculated using the vortex impulse theorem.

It should be noted that the formulation method is different to the widely used equivalent angle of attack method where the normal force of wing-body is cast in terms of the normal force at the equivalent angle of attack. In the slender body theory development of the interference factors, K_{W_B} and K_{B_W} the total lift of the wing body section is derived as a function of the geometry (see Equation 2.24), and the interference factors are a consequence of this derivation. The equivalent angle of attack method is essentially a method to account for the non-linearity of the fin only loads. The method proposed in this thesis is the same as the equivalent angle of attack method in that the total lift of the wing-body section is calculated. On the other hand, because the method proposes a summation of linear and vortex lift components, no equivalent angle of attack needs to be calculated. The method assumes that the separated flow vortex load, due to shed vortices and their interactions with the body, is all captured by the 2D methods that is the subject of the research being undertaken.

The attached flow component of the wing-body section consists of only the isolated wing because the body is of a constant diameter (see the limitation placed on the method in Chapter 1). This equation is simply

$$\begin{aligned} C_{N_{attached}} &= (K_{W_B} + K_{B_W})C_{N_W} && (3.26)\\ &= (K_{W_B} + K_{B_W})C_{N_\alpha} \sin\alpha \cos\left(\frac{\alpha}{2}\right) && (3.27) \end{aligned}$$

The lift curve slope of the wing can be obtained from any sufficiently accurate source. If no accurate data are available, the slope as defined by Jones [6] of $\pi AR/2$ can be used. The lift curve slope used in this thesis is that derived from CFD simulations rather than $\pi AR/2$.

Finally, if a configuration consisting of a forebody, cruciform wing-body section and aftbody is considered, the total lift is defined as

$$\begin{aligned} C_{N_T} &= C_{N_{B_{forebody}}} + C_{N_{attached}} + C_{N_{vortex}} + C_{N_{B_{aftbody}}} && (3.28)\\ &= C_{N_{B_{forebody}}} + (K_{W_B} + K_{B_W})C_{N_{W_\alpha}} \sin\alpha \cos\left(\frac{\alpha}{2}\right) + C_{N_{vortex}} + C_{N_{B_{aftbody}}} && (3.29) \end{aligned}$$

This formulation is different to the method used by codes such as Missile Datcom, APC and Dave Taylor where the complete body alone load is used rather than only the parts

where the body does not contain a wing, and is the same as that used by reference [141]. This is because the configurations under consideration have a very low aspect ratio wing-body section of significant length of the overall body length. The method proposed by this thesis takes into account the complete loads (body, wing and the interaction between the two) of the wing-body section, and including the body alone loads for this section would therefore result in an overprediction of the overall loads. The method of Missile Datcom assumes that the body continues to generate vortices in the body sections after a set of wing or canards and that the influence of a wing set on the body vortices is negligible. This assumption is not unreasonable for wings of low aspect ratio rather than very low aspect ratio because the wing sets comprise the smaller percentage of the overall body length whereas the wing-body configurations being considered in this thesis comprise the majority percentage of the overall body length.

It should be noted that the methods used in this thesis do not predict the wing-to-body carryover factor explicitly. It should also be remembered that the SBT method also does not predict this explicitly. Instead the total lift of the wing-body section and body-on-wing factor are predicted. The wing-to-body factor is simply the difference between the total and body-on-wing factor. This holds true for the factors determined by the SBT method.

3.5.1 Fore- and Aftbody Load Prediction Method

For the purposes of this thesis, whose objective is to develop an engineering wing-body interference method, any suitably accurate method for determining the forebody and aftbody loads will be used. This may be experimental, validated CFD simulations or the plethora of available engineering methods. Where available, experimental or CFD simulations will be used. In an engineering code, the accuracy of the loads for a complete configuration will be a function of the method used, with engineering methods being less accurate than experimental and (generally) viscous Navier-Stokes finite volume methods.

For the fore- and aftbody, where no CFD or experimental data are available, the loads are based on the engineering method of Jorgensen [31], which is a refinement or extension of the concept of Allen. These take the form of the sum of a potential and non-linear component i.e. the same as equation 3.24. The formulae presented here assume that the body has a constant diameter (or cylindrical) and that the reference area, S, is based on the body cross sectional area ($S = \pi D^2/4$). The potential or linear component is defined as:-

$$C_{N_{potential}} = \frac{C_{N_\alpha}}{2} \sin(2\alpha) \cos\left(\frac{\alpha}{2}\right) \tag{3.30}$$

where the normal force slope is 2 based on slender body theory. A correction for Mach number effects based on ESDU 89008 [25] is applied for tangent ogive bodies. As shall be seen, almost all configurations used in this thesis are have tangent ogive noses.

The non-linear component represents all non-potential effects. It is equivalent to $C_{N_{vortex}}$ but is not limited to only shed vortices as for the wing-body section. The Allen and Perkins formulation encompasses the non-linear effects in the crossflow drag coefficient and as for the wing-body section assumes the effect is due to shed vortices. From Jorgensen [42] this is:-

$$C_{N_{non-linear}} = \eta c_{d_c} \frac{S_p}{S} \sin^2 \alpha \tag{3.31}$$

where η is the end effects factor for finite length bodies (and is set to 1 because the flow is supersonic [42][53]), c_{d_c} is the cross-flow drag coefficient, and S_p is the planform area of the forebody or aftbody.

The cross flow drag coefficient, c_{d_c}, uses the data of the MISSILE code (reference [29]) and is tabulated as follows:-

Table 3.1: Cross flow drag coefficient

$M \sin \alpha$	0	0.2	0.4	0.5	0.6	0.8	1	1.2	1.6	2	2.4	3.2	8
c_{d_c}	1.2	1.2	1.23	1.3	1.37	1.62	1.72	1.67	1.47	1.4	1.37	1.3	1.3

The pitching moment is:-

$$C_{m_{potential}} = \left[\frac{V - A\,(L - x_{mrc})}{SD}\right] C_{N_{potential}} \tag{3.32}$$

$$C_{m_{non-linear}} = \left(\frac{x_{mrc} - x_c}{D}\right) C_{N_{non-linear}} \tag{3.33}$$

where V is the volume of the forebody or aftbody, L is the length of the fore- or aftbody, and x_c is the centroid of the planform area.

3.5.2 Body Shedding Vortex Prediction Method

Where vortices are shed by a body i.e. the non-linear component, the position and strength of the vortices may need to be determined for inclusion in determining the cruciform wing-body loads. As for the fore- and aftbody loads, where no CFD or experimental data are available empirical data are used. These data have been obtained from reference [41] and [20] and is the same model as used in reference [40]. The model only predicts a single vortex and its position is a function of Mach number and angle of attack. From reference [41] for the angle of attack range $20^\circ \leq \alpha \leq 50^\circ$ at Mach 2.0, the lateral position, y_v, is defined as

$$\frac{y_v}{a} = 1.119 - 0.0169\alpha \tag{3.34}$$

Chapter 4

Very Low Aspect Ratio Cruciform Wing-Body Aerodynamics

4.1 Introduction

Before the various 2D methods are introduced, the aerodynamics of slender bodies with very aspect ratio wings are studied. The aerodynamics of very low aspect ratio wing-body configurations with low semi-span to body radius ratios, and wings with side edges rather than highly swept back leading edges, at supersonic speeds, is dominated by the side edge vortex, and body vortex where appropriate. This is in contrast to moderate ($AR \approx 4$) and low aspect ratio wings ($AR \approx 1$), where the side edge vortex contribution is small or non-existent (such as for taper ratios of $\lambda = 0$). Higher wing semi-span to body radius ratios reduce the influence of the body on the side edge vortex. An indicator of this is illustrated by the interference lift ratios for panel-to-panel interference for cruciform and planar configurations. At low semi-span to body radius ratios (between 1 and 1.4) the interference ratio, K_ϕ, for both configurations coincide and only deviate at higher ratios [4], thus indicating the dominant influence of the body on even slender body potential flow wing-body interference aerodynamics.

The configuration chosen to study this side edge vortex is a body of constant diameter of length 16D with a 3D tangent ogive nose, resulting in an overall length of 19D. This body configuration was chosen because most short range air-to-air missiles have slenderness ratios of the order 17 to 22 and the geometry has been previously used in studies [13]. The nose profile is, however, different from reference [13] in that a third order polynomial described the nose profile, whereas a tangent ogive was used for this study.

The very low aspect ratio wings or strakes are rectangular wings with a leading edge of 45° and a straight trailing edge. The semi-span of the wing alone is 0.25 of the radius, and the root chord starts at 4.75D from the nose. The root chord is 11.25D in length (or 59% of the overall configuration length), resulting in an afterbody of 3D. The wing has a finite thickness of 5mm at the root. The location of the start of the strakes was chosen to

result in an afterbody of 3D, thus ensuring an effective infinite afterbody for the strakes or wings for the Mach numbers under consideration. Finally the body diameter is 80mm.

The geometry of the configuration, including the strake thickness definition, are shown in Figure 4.1.

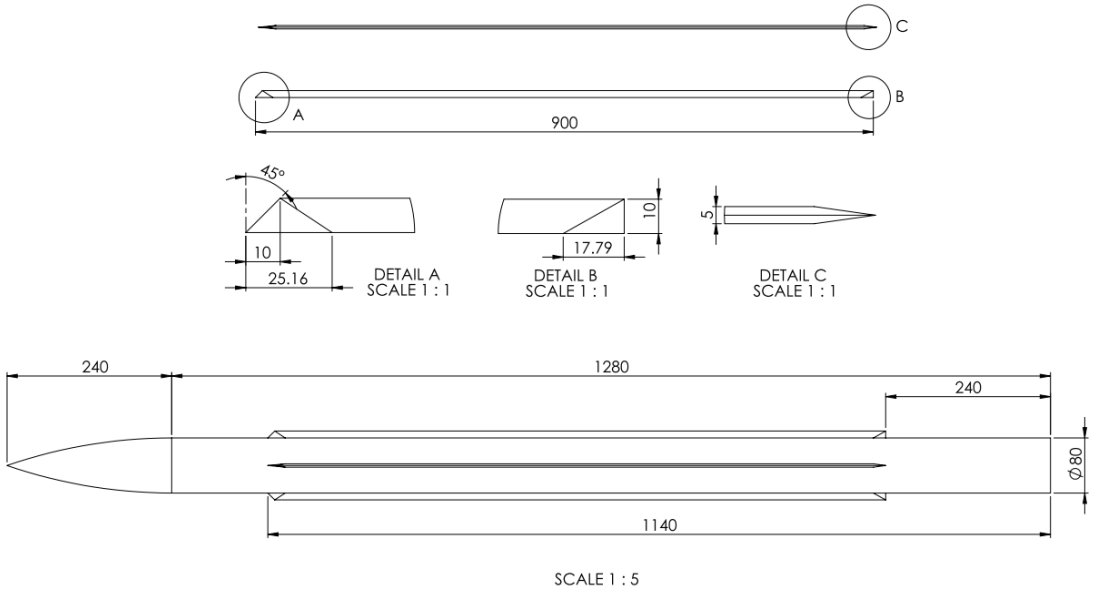

Figure 4.1: Configuration Geometry, dimensions in mm

Of particular interest in this thesis are the aerodynamics of the various components of the configuration namely, the body, the strakes and combination or interaction of the two.

4.2 Expected Flow Features

Before the numerical or experimental simulations are presented, a discussion of the expected topographical features of the flow, especially in the lee side, helps in the interpretation of these simulations. For the body alone, the flow is expected to remain attached and only separate at angles of attack greater than 4°. The separated flow results in vortex sheets which roll up into two symmetric concentrated vortices. Because the nose is sharp i.e. not blunted, these vortices will eventually emanate from the nose at an angle of attack equal to the total included angle of the nose. For the start location, non-dimensionalised to the body radius, Figure 4.2 illustrates the empirical method developed by Hemsch *et al* [40], which is described by the equation

$$\frac{x_s}{a} = 32\left[1 - \sqrt{\frac{\alpha - 4}{\eta_n - 4}}\right] \tag{4.1}$$

where η_n is half the total nose angle.

The angle at which the vortices emanate from the nose is half the total included angle of the nose, which for this configuration is 18.92°. At the higher angles of attack under

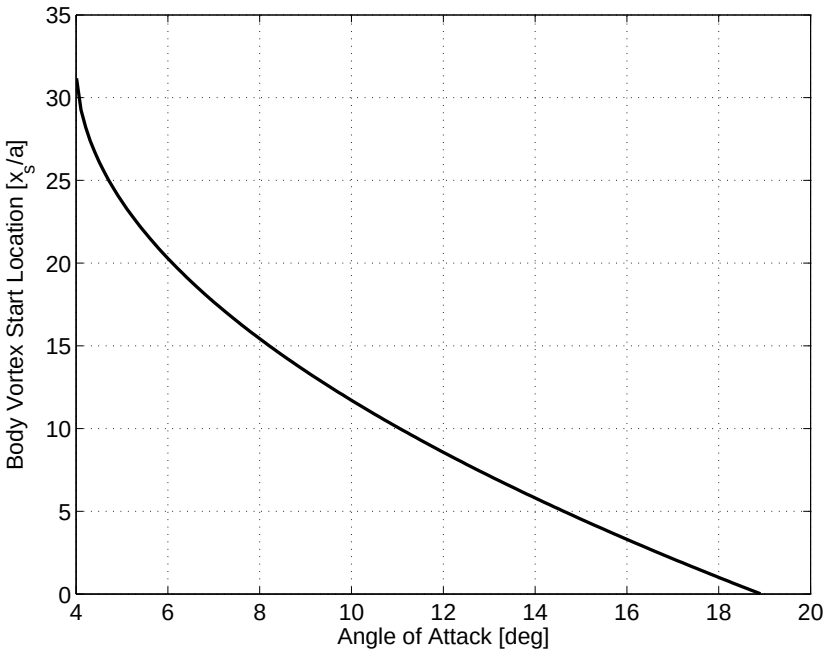

Figure 4.2: Body Alone Vortex Start Location

consideration multiple vortices are expected, and the behaviour of the vortices is expected to resemble impulsively started flow [56]. The number and spacing of these vortices is, however, dependent on the cross flow Mach number and nose configuration. For the Mach numbers and angles of attack under consideration, using the data from reference [39], at least two symmetric vortices are expected. The angle at which asymmetric vortices starts when the angle of attack exceeds the total included angle at the apex, which for this configuration is 37.85° [43], which is above the angle of attack range ($0° \leq \alpha \leq 25°$) being considered in this thesis.

For the strake, the flow is expected to separate almost immediately as the angle of attack is increased from zero because of the long side edge. No leading edge vortex is expected because the Mach numbers under consideration (2.0 to 3.0) results in the leading edge being supersonic (leading edge sweep is 45°). Similar to the body alone, the flow is expected to create multiple vortices at the higher angles of attack [149].

According to Figure 4.2 or Equation 4.1, the flow for the body-strake configuration is expected to remain attached to the nose section until 11.4° because the leading edge of the strakes start at an axial location of $x_s/a = 9.5$ or 4.75D. This limit was, however, derived from data which showed significant scatter and therefore body vortices appearing before the angle of attack of 11.4° is not unexpected. For the strake, the flow is expected to separate from the side edge at all non-zero angles of attack. Where a body vortex is present, it is expected to interact with the side edge vortex. It should be noted that the strake will experience an increased angle of attack compared to the freestream because of the upwash from the body. The behaviour of the side edge vortex, by itself and when

interacting with the body vortex is the subject of this thesis.

4.3 Numerical Simulations

A numerical finite flow volume method was used to establish the primary force and moment and flow field database from which subsequent analyses are performed and the proposed engineering method is developed. These simulations were, however, validated experimentally, and is presented in the next section. The specific numerical tool used was ANSYS Fluent V13. Simulations were performed for the body alone, the strakes and the full configuration. The Mach numbers simulated were 2.0, 2.5 and 3.0. The spatial discretisation scheme employed was the second order upwinding scheme. The solver used was the coupled-implicit density based formulation whilst the Roe convective flux-difference splitting scheme was used. The total pressure used for the simulations was 129kPa and a total temperature 288K. The freestream turbulence was set to 0.1% with a characteristic length of 10μm, typical values for a wind tunnel. The turbulence model used was Spalart-Allmaras (SA) with near wall treatment. Symmetry was used for all the configurations because the onset of asymmetric vortices for the body is only expected at angles of attack greater than 25°. The cell count for the body alone was 580000, whilst the full configuration was approximately 3340000, and the strake alone 4200000. The mesh design for the body alone and body-strake configurations did not include the base region because the speed regime is supersonic. Figure 4.3 and Figure 4.4 show schematics for the body-strake, and strake alone configurations. The body-strake configuration forebody mesh is the same as the body alone configuration mesh, except that for the body alone configuration the forebody mesh is extended to the end of the body.

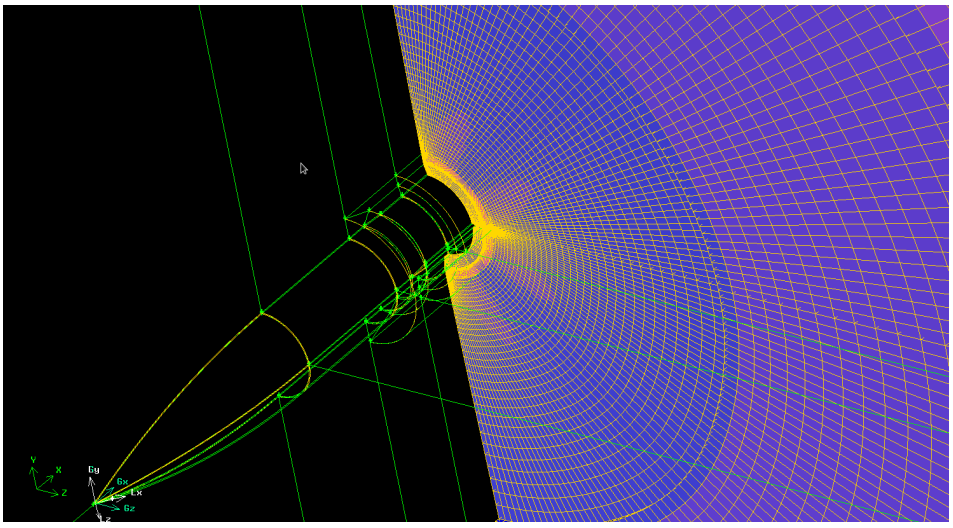

Figure 4.3: Body and strakes CFD mesh

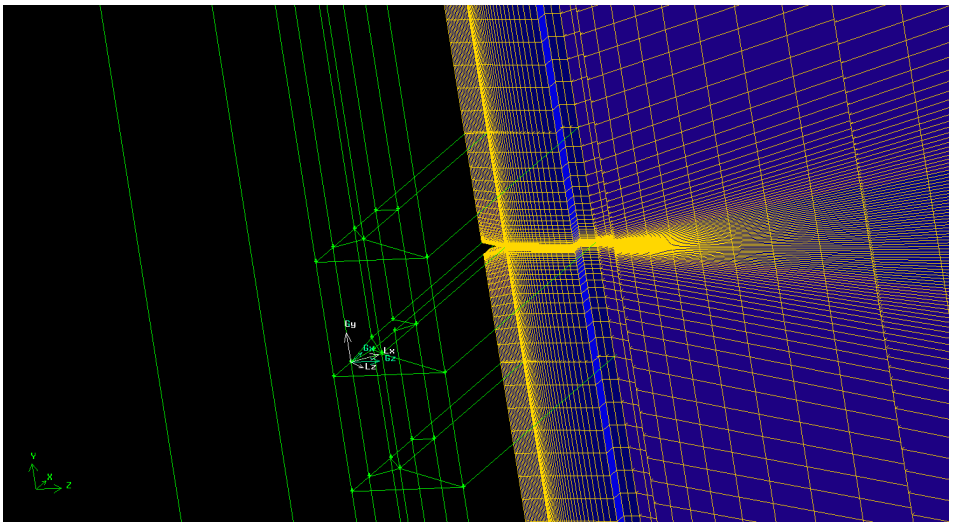

Figure 4.4: Strake CFD mesh

Simulations were initialised with the Fluent provided Full-Approximation Storage (FAS) pre-solver and run until the primary variables (which included turbulent viscosity) reduced by at least three orders of magnitude, and the primary variables and loads asymptoted to constant values. The typical number of iterations to convergence required for the full configuration was 4000 using a CFL number of 5. Because near wall treatment was employed in the simulations, at least 15 cell layers were placed in the boundary layer by calculating the expected boundary layer displacement thickness using simple flat plate theory. As an additional check, the y^+ was observed to remain within the order of 1 (the maximum y^+ was no more than 2). A comparison of the normal force, pitching moment, axial force and centre-of-pressure for the body alone, body-strake, and strakes alone for the three Mach numbers 2.0, 2.5 and 3.0 are shown in Figure 4.5 to Figure 4.7. The coefficients are normalised to the body cross sectional area and diameter for the body and body-strake configurations, whilst the strake coefficients are normalised to the strake planform area and average aerodynamic chord i.e. 895mm. The moment reference centre for the body, and body-strake configuration is 9.5 calibers from the nose, whilst for the strake configuration it is the wing apex.

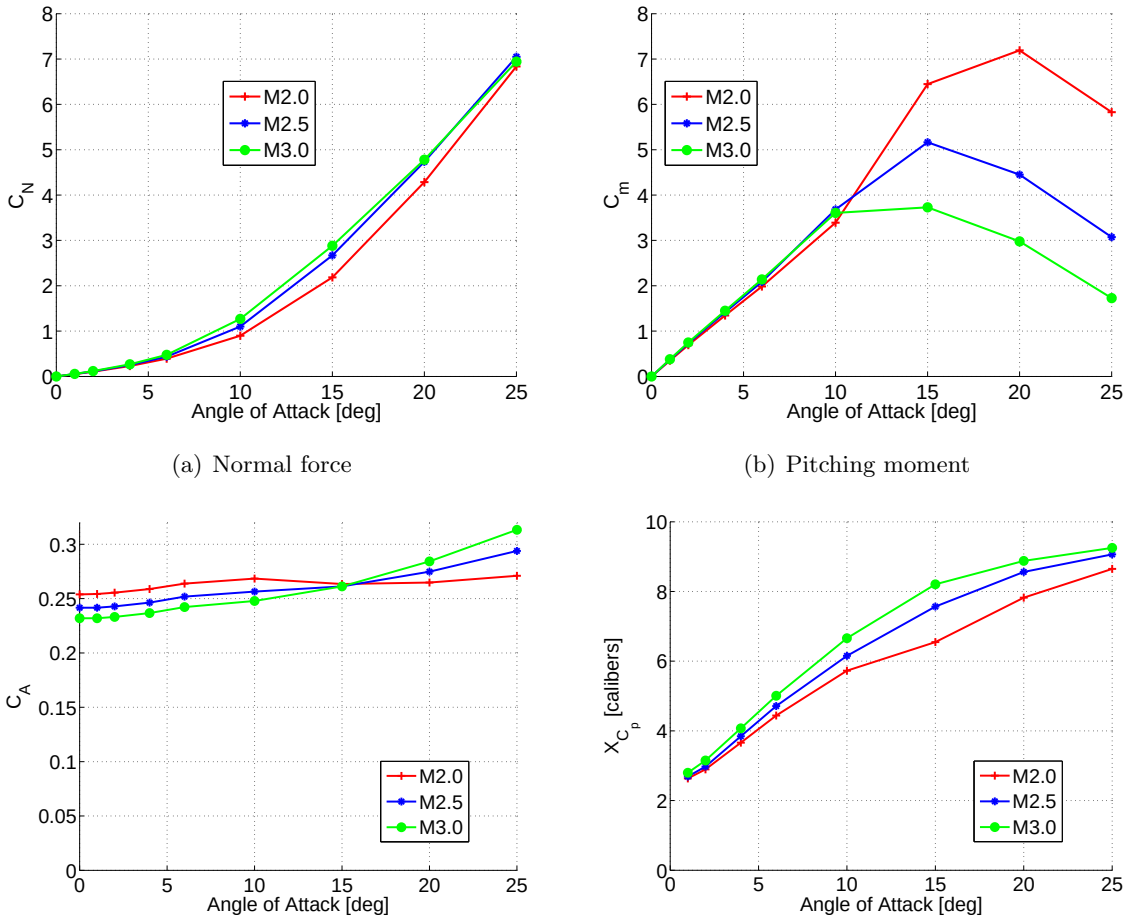

(a) Normal force

(b) Pitching moment

(c) Axial force

(d) Centre-of-pressure

Figure 4.5: Body alone CFD Mach number comparison

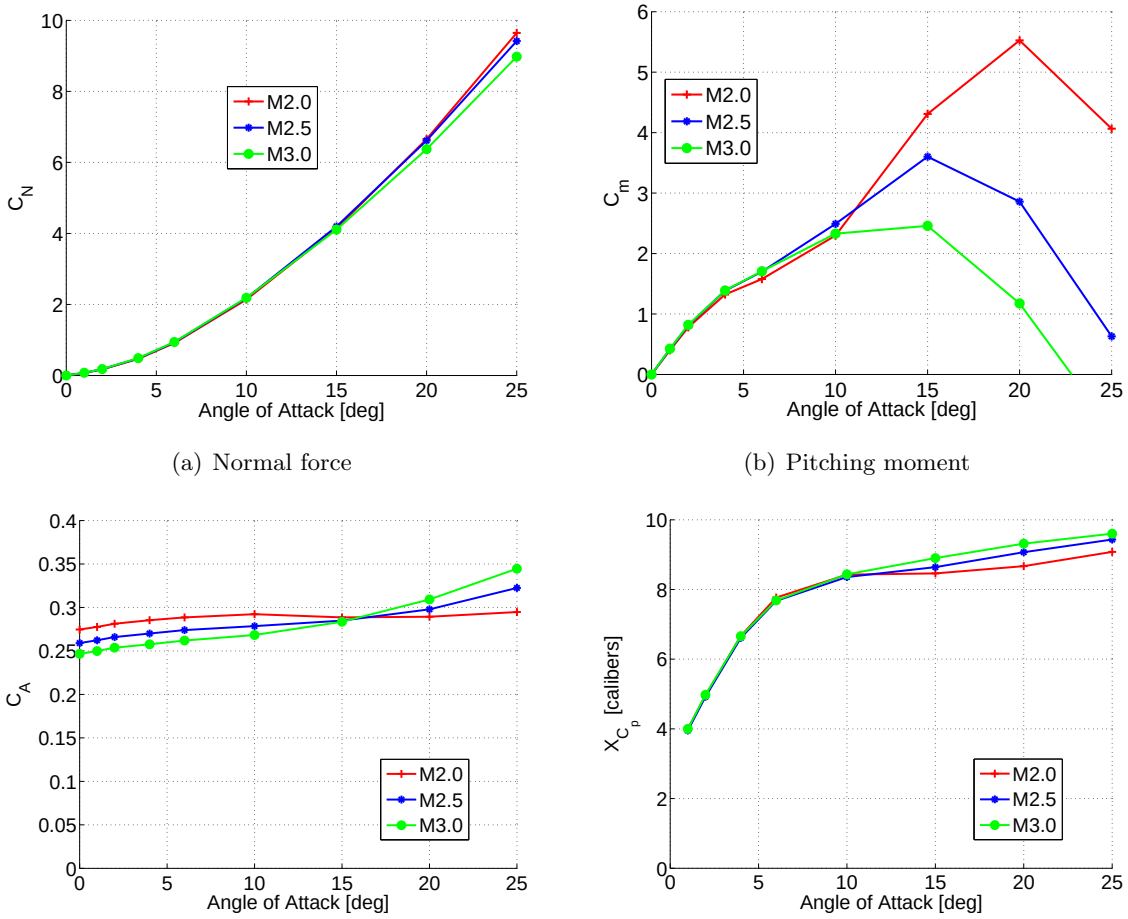

(a) Normal force

(b) Pitching moment

(c) Axial force

(d) Centre-of-pressure

Figure 4.6: Body and strake CFD Mach number comparison

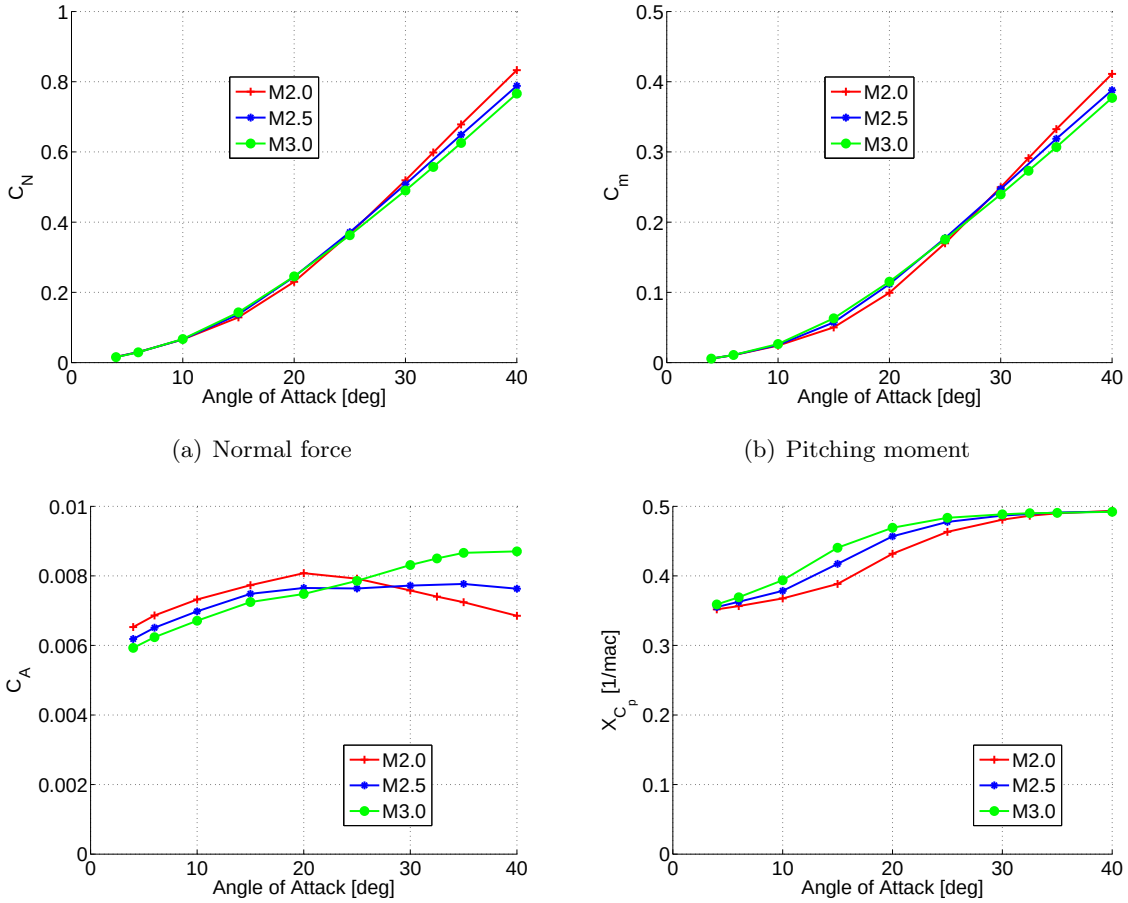

(a) Normal force

(b) Pitching moment

(c) Axial force

(d) Centre-of-pressure

Figure 4.7: Strakes alone CFD Mach number comparison

Grid sensitivity studies were performed for all the configurations by increasing the cell count outside the near wall or attached flow boundary layer and the two other orthogonal directions parallel to a wall by at least 1.5. The cell count in each orthogonal direction parallel to the wall for the body alone was doubled because of the initial lower cell count than the body-strake configuration. An additional grid size was executed for the body alone configuration where the cell count in orthogonal direction parallel to the wall was increased by 1.5 times. The former grid is designated the high density grid, whilst the latter, the medium density grid. This study was only performed at Mach 2.0 with the Spalart-Allmaras turbulence model. Figure 4.8 show the difference between the existing and high density grids for the body alone configuration, whilst the body-strake configuration comparison is shown in Figure 4.9, and the strakes alone are shown in Figure 4.10. The grid sensitivity studies indicated that the original discretisation was sufficient and possibly even finer than the minimum required, given that the differences only manifest themselves in the axial force. A reduction in the number of the cells was not considered.

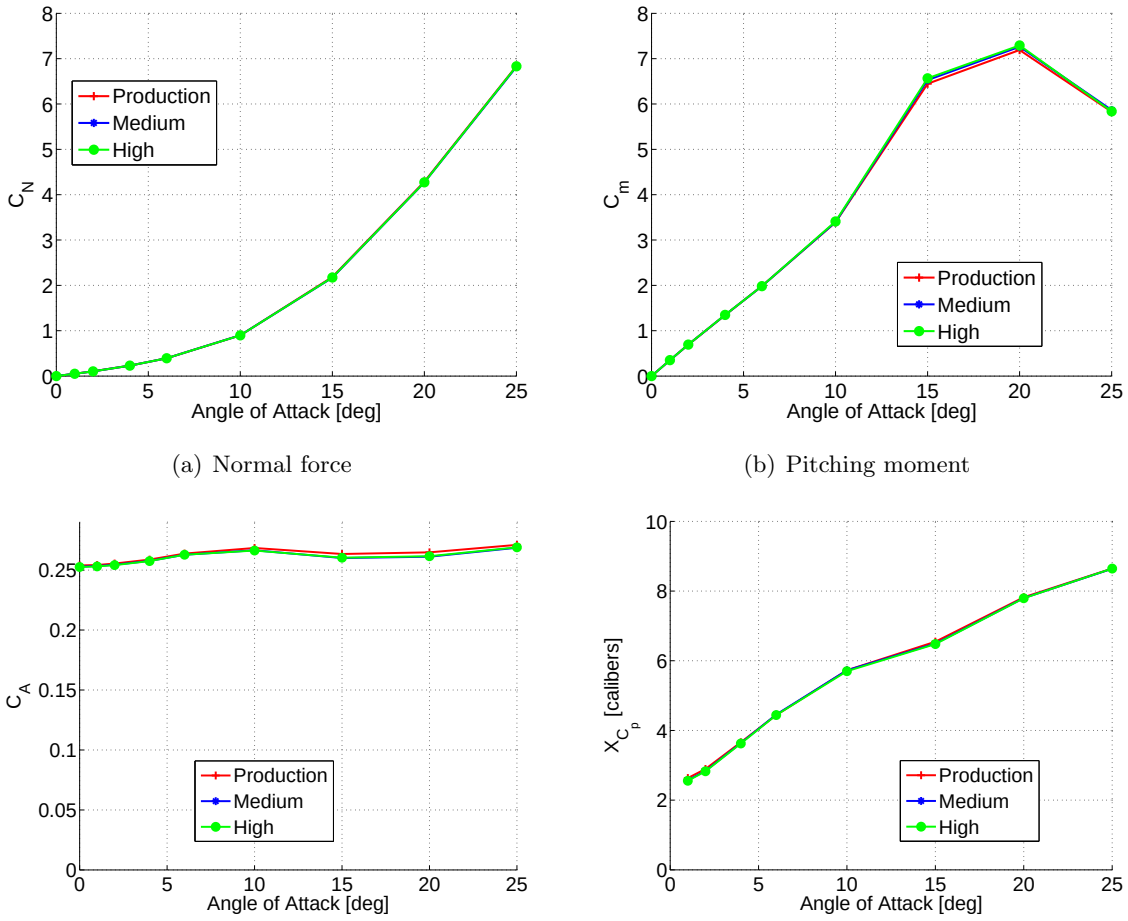

(a) Normal force

(b) Pitching moment

(c) Axial force

(d) Centre-of-pressure

Figure 4.8: Body alone CFD grid sensitivity comparison, Mach 2.0

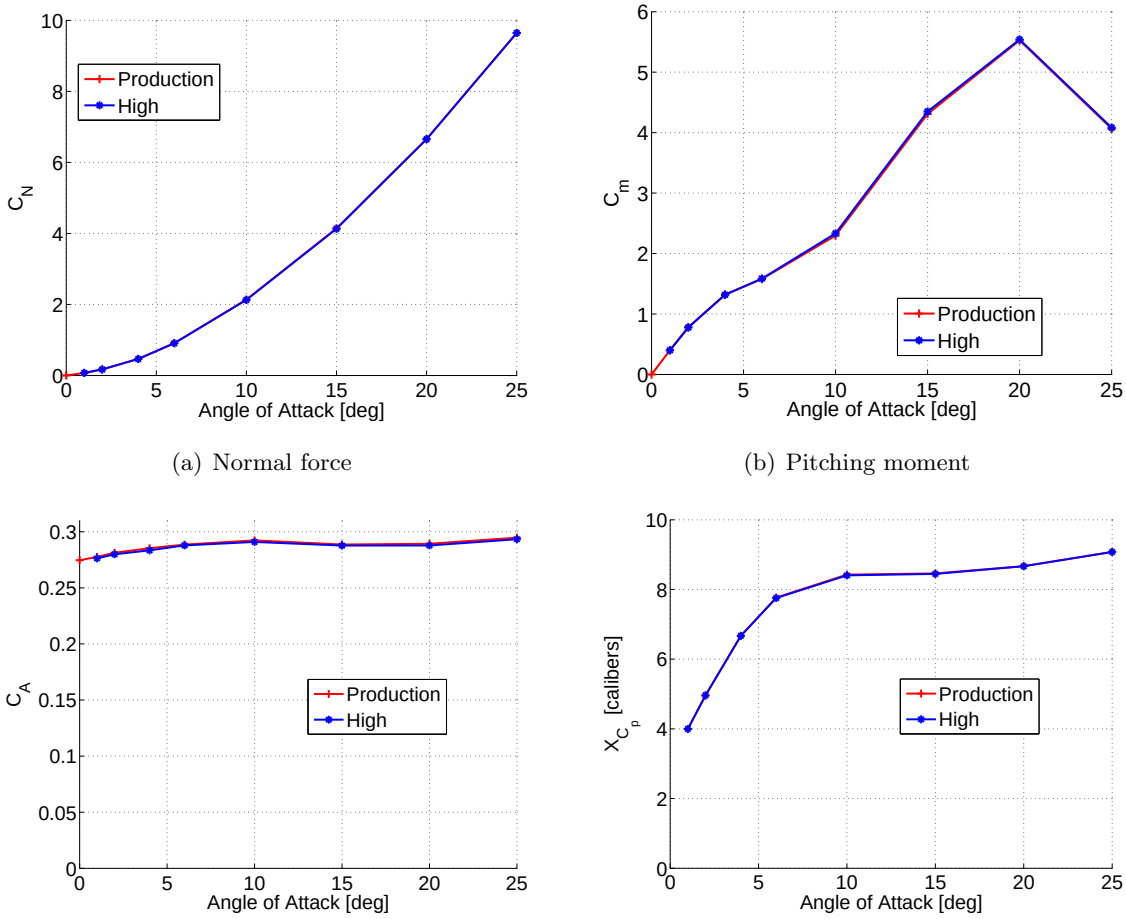

(a) Normal force

(b) Pitching moment

(c) Axial force

(d) Centre-of-pressure

Figure 4.9: Body and strake CFD grid sensitivity comparison, Mach 2.0

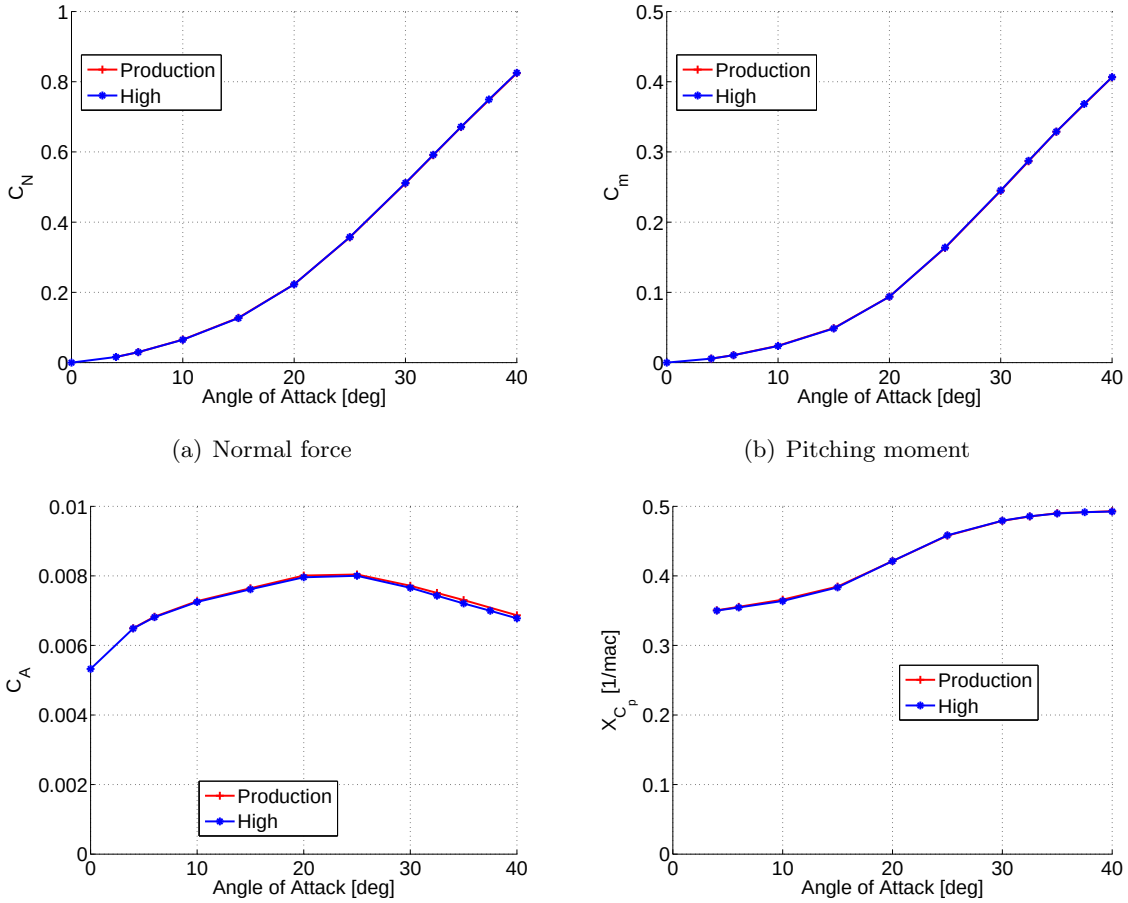

(a) Normal force

(b) Pitching moment

(c) Axial force

(d) Centre-of-pressure

Figure 4.10: Strakes alone CFD grid sensitivity comparison, Mach 2.0

At the higher angles of attack, because the flow in the leeside of the body is fully separated and symmetrical, high strain rates are experienced in the flow in this region. The Spalart-Allmaras turbulence model is only a first-order model and utilises the Boussinesq hypothesis that the turbulent viscosity is an isotropic scalar quantity. Its modeling of the flow may therefore not be sufficiently accurate given the high axial velocities and rolled up shed vortex sheets at the higher angles of attack. To gain some insight into this, additional simulations were performed using the $\kappa - \epsilon$ (KE), Realisable $\kappa - \epsilon$ (RKE) and Reynolds-Stress model (RSM) for Mach 2.0 for the body and body-strake configurations, though the Reynolds-Stress model model was only implemented for the body alone configuration and not the body-strake configuration. The $\kappa - \epsilon$ and Realisable $\kappa - \epsilon$ formulations are two equation models with the Realisable $\kappa - \epsilon$ model overcoming some of the problems associated with the $\kappa - \epsilon$ model by modeling some of the Reynolds stress constraints making the formulation more physical. The Reynolds Stress model calculates the individual Reynolds stresses i.e. it solves the transport equations for each stress tensor. Of the Reynolds averaged models the anisotropy of the turbulent viscosity can only be modeled by the Reynolds Stress model for highly swirling flows and stress driven secondary flows. In its implementation by Fluent the Realisable $\kappa - \epsilon$ method is also suitable at lower swirl flow numbers (i.e. <0.5) [150]. In Fluent, the RSM model uses the $\kappa - \epsilon$ formulation for wall treatment, and its inclusion for comparison is more by way of process because the Realisable $\kappa - \epsilon$ and Reynolds-Stress model solution process used the KE solutions as starting estimates.

The results of these simulations are shown in Figure 4.11 to Figure 4.12. The body alone comparison indicates that the Reynolds-Stress model turbulence model shows a small shift in the centre-of-pressure when compared to the Spalart-Allmaras model. Because the difference manifests itself at low angles of attack, the discrepancy is due to the difference in the recovery of pressure in the aft section of the body as illustrated in Figure 4.13 for the angle of attack of 2°, along a slice of 1mm from the centreline. The Reynolds-Stress model simulations generate a lower pressure than the SA simulations in the rear half of the body therefore resulting in a more aft centre-of-pressure than the SA simulations. The difference is, however, no more than half a caliber. The difference is probably due to the growth in the boundary layer being different between the Spalart-Allmaras and Reynolds-Stress model models because the Reynolds-Stress model formulation uses the $\kappa - \epsilon$ formulation. Interestingly the $\kappa - \epsilon$ and Realisable $\kappa - \epsilon$ do not show the same centre-of-pressure shift. The difference in the normal force is, however, not discernable. For the purposes of developing an engineering method, the Spalart-Allmaras model is therefore sufficiently accurate given the interest in only the normal force and pitching moment components.

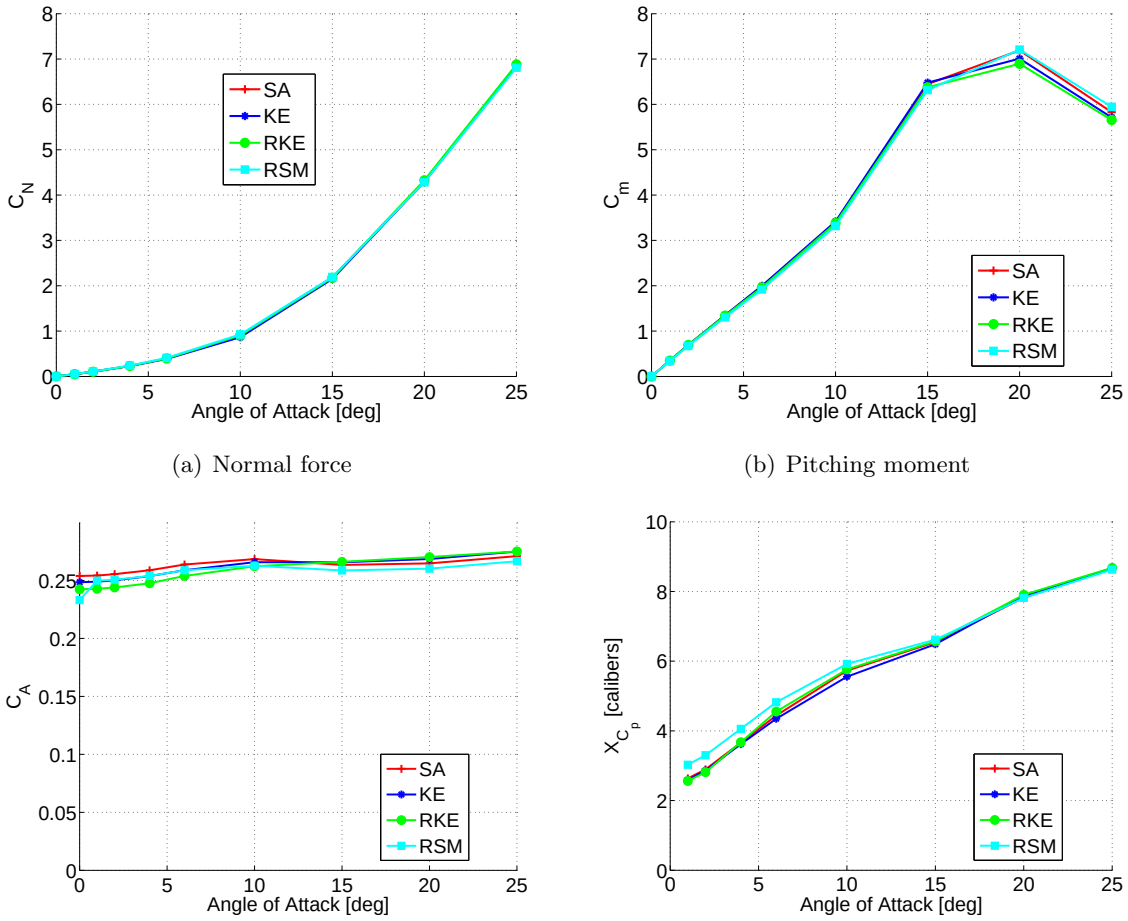

(a) Normal force

(b) Pitching moment

(c) Axial force

(d) Centre-of-pressure

Figure 4.11: Body alone CFD turbulence model comparison, Mach 2.0

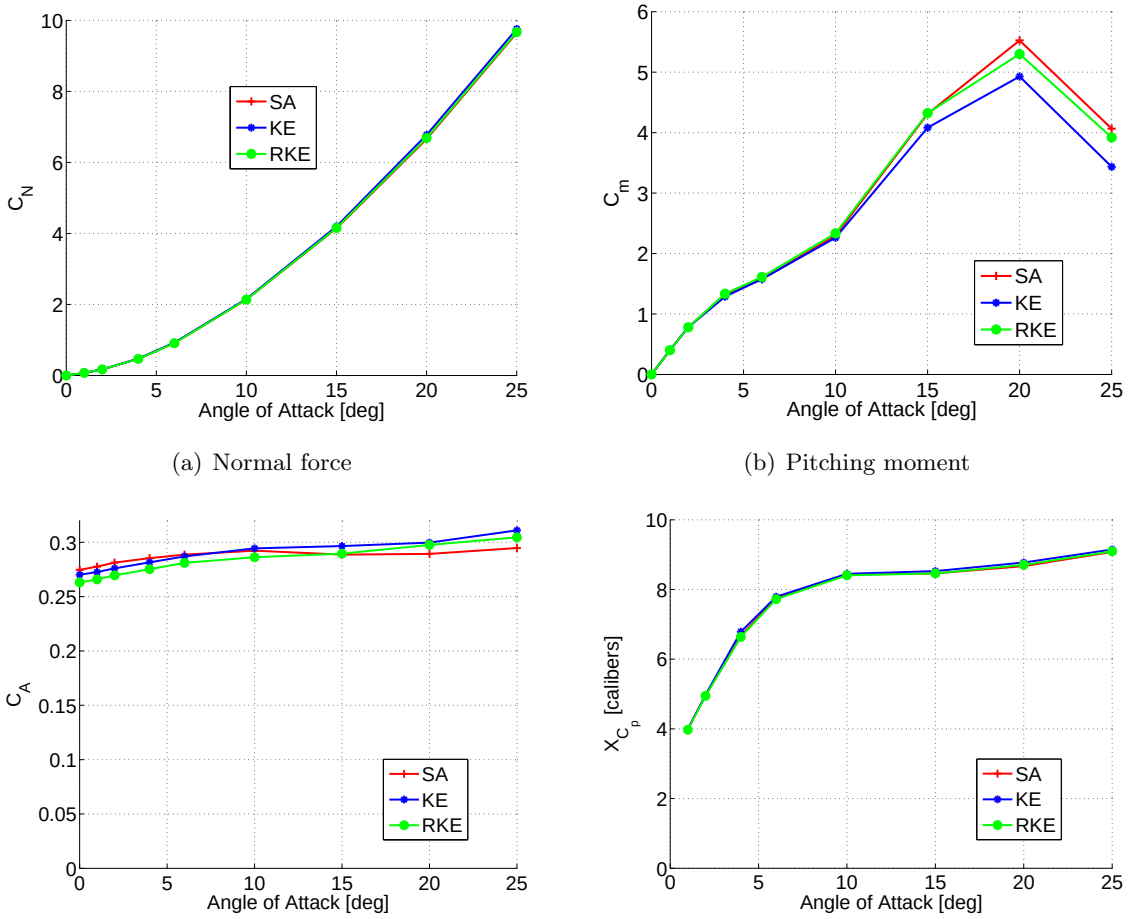

(a) Normal force

(b) Pitching moment

(c) Axial force

(d) Centre-of-pressure

Figure 4.12: Body and strake CFD turbulence model comparison, Mach 2.0

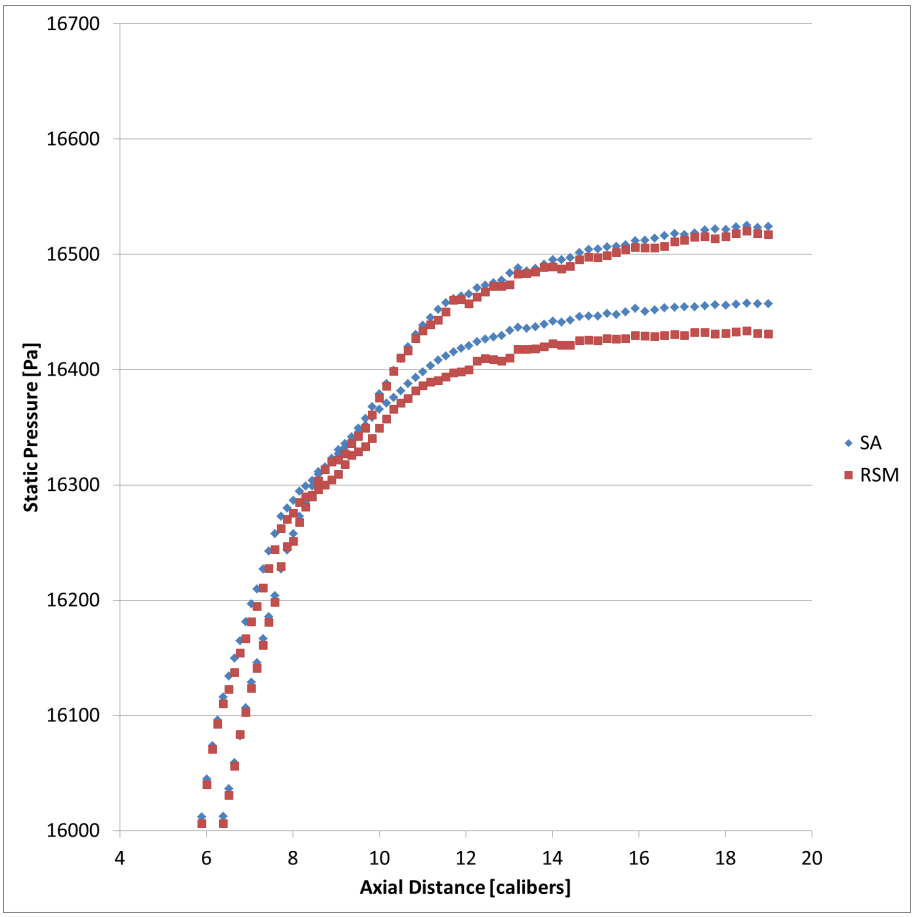

Figure 4.13: Body alone pressure difference between SA and RSM turbulence models, α=2°

4.3.1 Flow Field Properties

The CFD simulations have been used to determine the position of vortices because of the availability of the flow field data. Of particular interest to this thesis are the rolled up vortex sheets shed by both the body and the strake. The vortex sheets shed from the body and strake roll up into concentrated vortices, and the identification of these vortices can be performed using at least three Galilean invariant criteria (Q-criterion, Δ-criterion, and λ_2-criterion). A study on the most suitable criterion is detailed in Appendix A. For this thesis, the λ_2-criterion is used from which the position of a vortex is determined by locating the local minimum.

4.4 Experimental Validation

Given the separated nature of the flow, especially in the lee side of the configuration, experimental validation of the gross configuration force and moments was deemed necessary. These validation tests were performed in the High Speed Wind Tunnel (HSWT) of the CSIR. The industrial facility has a 450mm x 450mm test section resulting in the use of a model with diameter of 25mm (i.e. 31.25% scale model).

Unlike the numerical predictions, the isolated strakes were not tested due to the difficulty in performing experimental tests for wings of aspect ratio of the order 0.025. Full span wings cannot accommodate a suitable balance without significantly changing the configuration and the stiffness would be too low for practical tests. Similarly half-span tests have the difficulty of boundary layer growth which results in the boundary layer being a significant proportion of the span of the span of the strake at the trailing edge, thus questioning the validity of the results. Experimentally compensating for the boundary layer through wall suction raises the question of the extent of compensation by the boundary layer suction and the consequent changes to the overall aerodynamics of the flow over the strake. Lastly the use of a boundary layer island or peniche to limit the effects of boundary layer growth destroys the half-span concept because the body, no matter how thin, effectively increases the span of the strakes.

The experimental test conditions were different to that of the numerical predictions. Even though the total pressures were higher than those used in the numerical predictions, the experimental Reynolds numbers were lower than for the numerical predictions. The freestream Reynolds number for the HSWT tests is 580000 based on the body diameter at Mach 2.0, whereas it is 1.33 million for the CFD simulations. From references [43] and [44] (reproduced in Figure 2.3), the boundary layer is expected to be turbulent throughout the angle of attack range for the Mach numbers 2.0 to 3.0 for both the CFD simulations and HSWT tests. The lee side boundary separation is therefore expected to be similar for both the CFD simulations and HSWT tests.

The test matrix executed is shown in Table 4.1, including the dynamic pressures. Both

body alone and body-strake configurations were run at the same total pressures to ensure that no Reynolds number difference between the two configurations were present.

Table 4.1: Experimental test conditions

Mach No.	P_T kPa	T_T K	q kPa	Re_D
2.03	180.5	301	63.5	580000
2.5	293.5	301	75.4	740000
3.0	490	301	84.2	956000

The force and moment data presented in the next subsection was corrected for flow angularity and model offsets. No wall corrections were performed because the flow is supersonic and the model was always within the shock rhombus. Flow visualisation by way of colour Schlieren was performed. This was used to also determine the location of the lee side vortices in the vertical plane. No other flow visualisation or measurement techniques were available in the facility for determining the shed vortex location in the lateral direction.

The maximum estimated uncertainty of the normalised coefficients and other parameters for each Mach number are listed in Table 4.2. The uncertainties were estimated using the industry standard method defined by references [151] and [152]. The uncertainty in the centre-of-pressure is less than 0.2 of a caliber for angles of attack greater than 2°. At the moderate and high angles the uncertainty is at least half the value of the maximum for each Mach number.

Table 4.2: Experimental test accuracies

Parameter	M2.0	M2.5	M3.0	Units
C_N	0.0532	0.0806	0.126	-
C_m	0.0484	0.0783	0.137	-
C_Y	0.00523	0.00461	0.00483	-
C_n	0.0116	0.0114	0.0126	-
C_l	0.0315	0.0293	0.0337	-
C_{A_f}	0.00978	0.00952	0.0122	-
α	0.163	0.168	0.181	°
q	0.358	0.715	1.179	kPa
Mach	0.00982	0.0126	0.0169	-
X_{C_P} $\geq 2°$	0.19	0.15	0.13	-

Some grounding was experienced because the length of the model limited the available gap between the sting and the inside of the model. For the body alone configuration, grounding only occurred above 22° for Mach 3.0. Grounding for the body-strake configuration unfortunately occurred at lower angles of attack, but was still higher than 19° for

Mach 2.0 and 2.5. For Mach 3.0, grounding occurred above 15°. The centre-of-pressure trend at the higher angles is, however, captured.

4.4.1 Loads and Centre of Pressure

For the three Mach numbers for the body alone and body-strake configurations, good correlation of the CFD simulations with the experimental was obtained, therefore validating the CFD simulations and especially the use of the Spalart-Allmaras turbulence model. The comparisons are shown in Figure 4.14 to Figure 4.19. For the body alone configuration, the normal force predictions are very well predicted by the CFD, except for the Mach 3.0 body alone simulations (see Figure 4.16), where the CFD loads are lower than the experimental. The deviations occur at a cross flow Mach numbers greater than 0.5, and may point towards a poorer numerical prediction in the loss of dynamic pressure due to the bow shock. The centre-of-pressure predictions are very good for angles of attack above 15° for all the Mach numbers, and are predicted further forward at the lower angles of the Mach numbers 2.0 and 2.5. The change in centre-of-pressure movement at 10° at Mach 2.0 and 2.5 points towards a change in the topology of the vortex structures. The higher angle of attack trends are however well captured. The differences in centre-of-pressure manifest themselves in the pitching moment differences, whose effect is amplified because the moment reference centre is at 9.5 calibers. The CFD centre-of-pressure predictions are no more than half a caliber different to the experimental data for Mach 2.0 and 3.0 for angles of attack from 4°.

For the body-strake configuration, the normal force is, as for body alone configuration, well predicted for Mach 2.0. The Mach 2.5 predictions are under predicted by 8%, whilst the Mach 3.0 predictions shows better correlation than for the body alone configuration, within the limited experimental range available. The centre-of-pressure are very well predicted by the CFD and as for the body alone within half a caliber. The trends are also well predicted. As for the body alone, the pitching moment differences are a consequence of the differences between the normal force and centre-of-pressure.

The axial force comparison presented is the forebody force which excludes the base drag. This is because the CFD mesh did not extended beyond the end of the body. The axial force predictions are less well predicted by the CFD, both in absolute values and their trends with angle of attack. The axial force is, however, not of interest in this thesis.

From the correlations between the CFD simulations and experimental data it can be concluded that the CFD simulations are validated and can be used for further analyses.

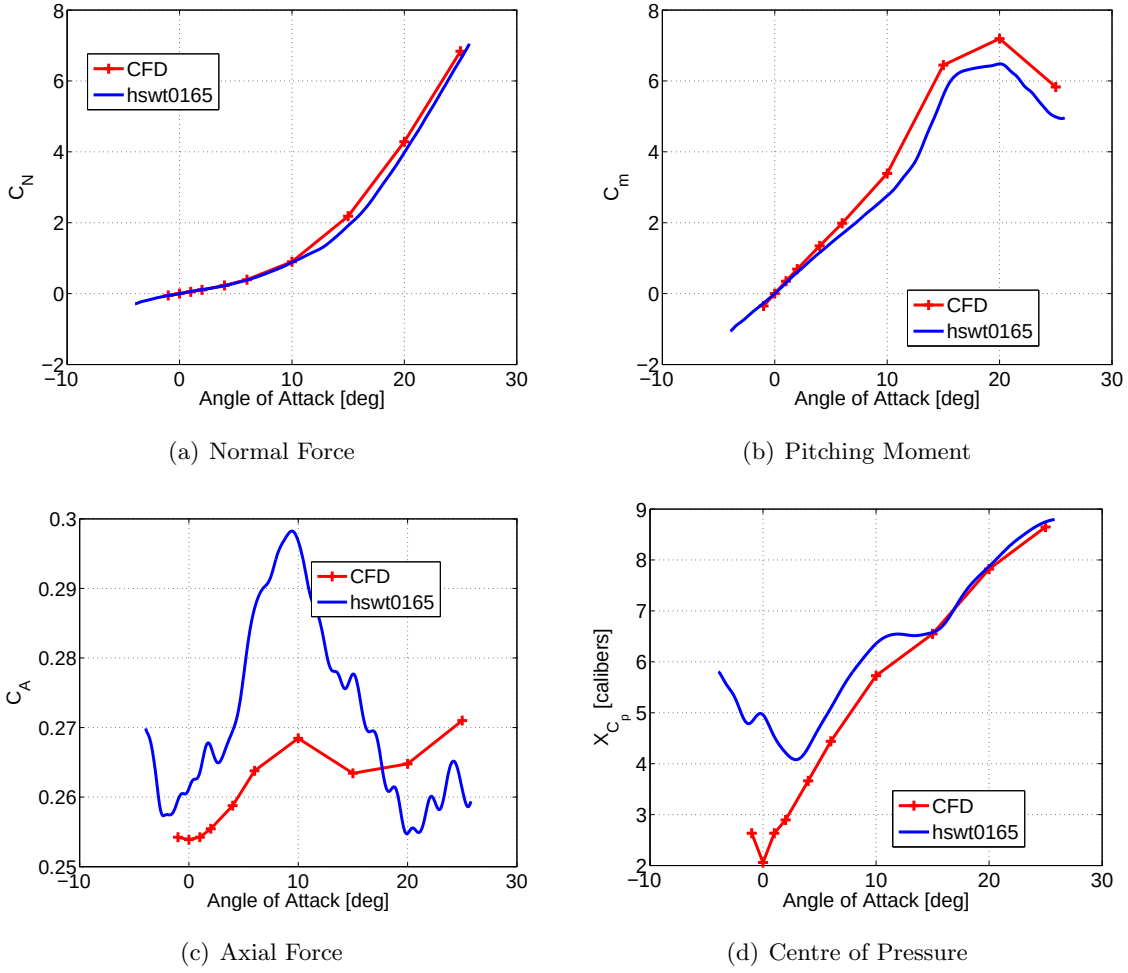

(a) Normal Force

(b) Pitching Moment

(c) Axial Force

(d) Centre of Pressure

Figure 4.14: Body alone CFD and experimental normal and axial force and pitching moment comparison, Mach 2.0

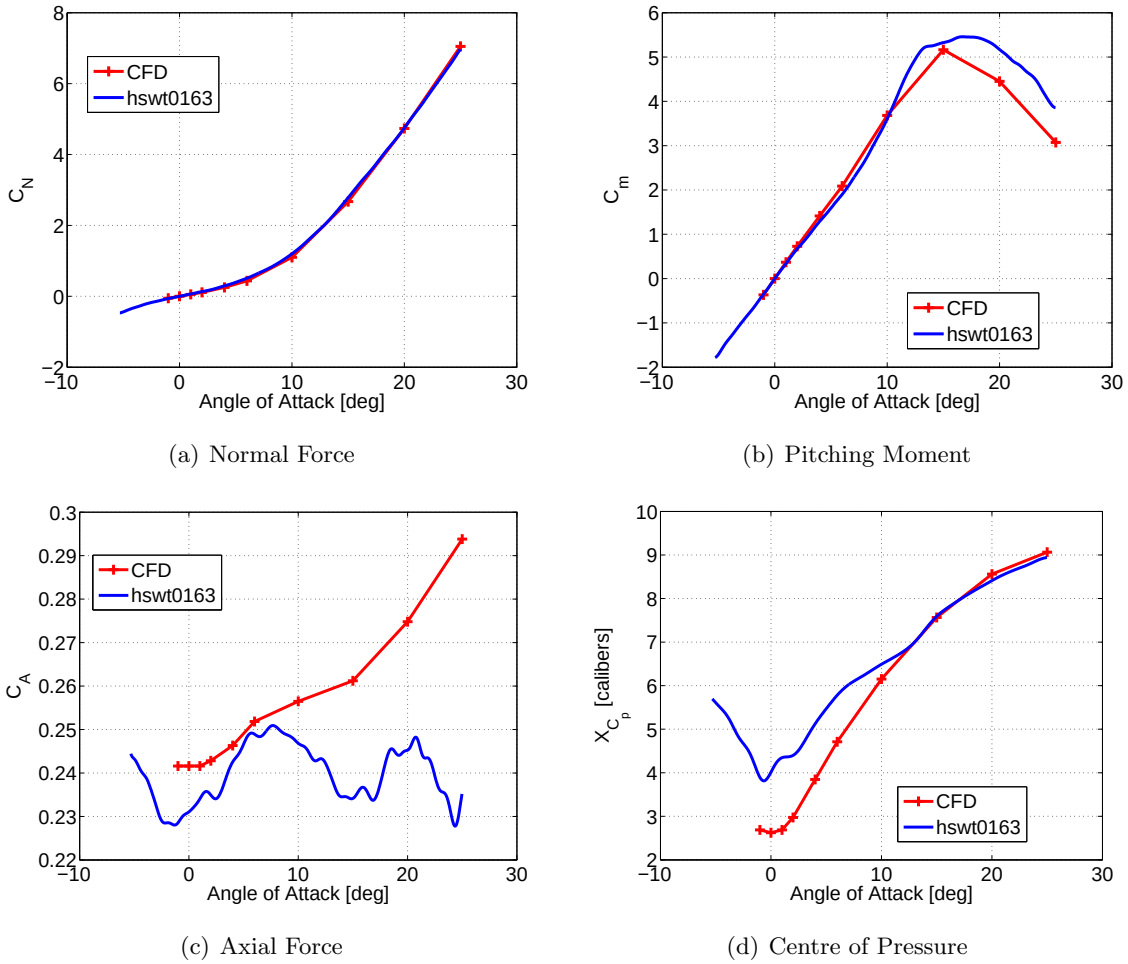

(a) Normal Force

(b) Pitching Moment

(c) Axial Force

(d) Centre of Pressure

Figure 4.15: Body alone CFD and experimental normal and axial force and pitching moment comparison, Mach 2.5

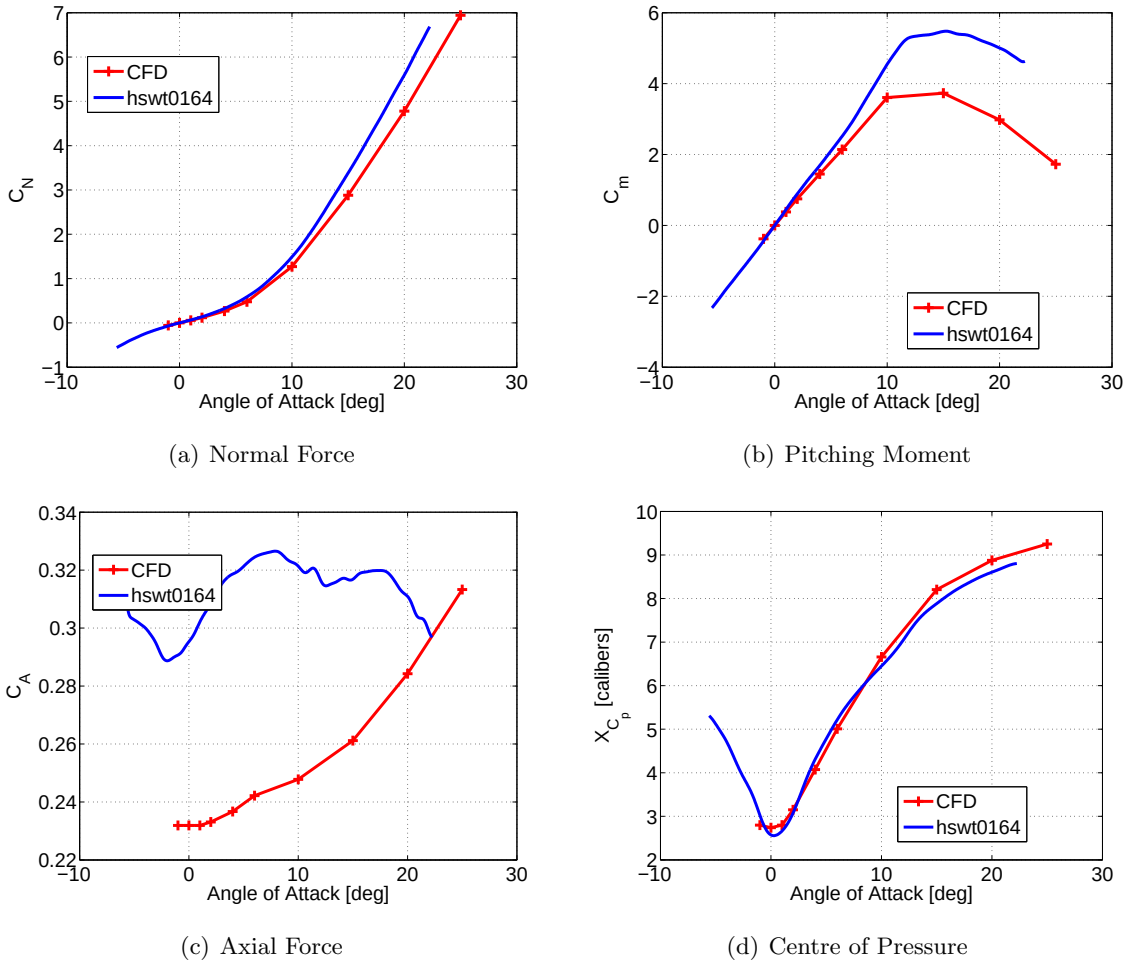

(a) Normal Force

(b) Pitching Moment

(c) Axial Force

(d) Centre of Pressure

Figure 4.16: Body alone CFD and experimental normal and axial force and pitching moment comparison, Mach 3.0

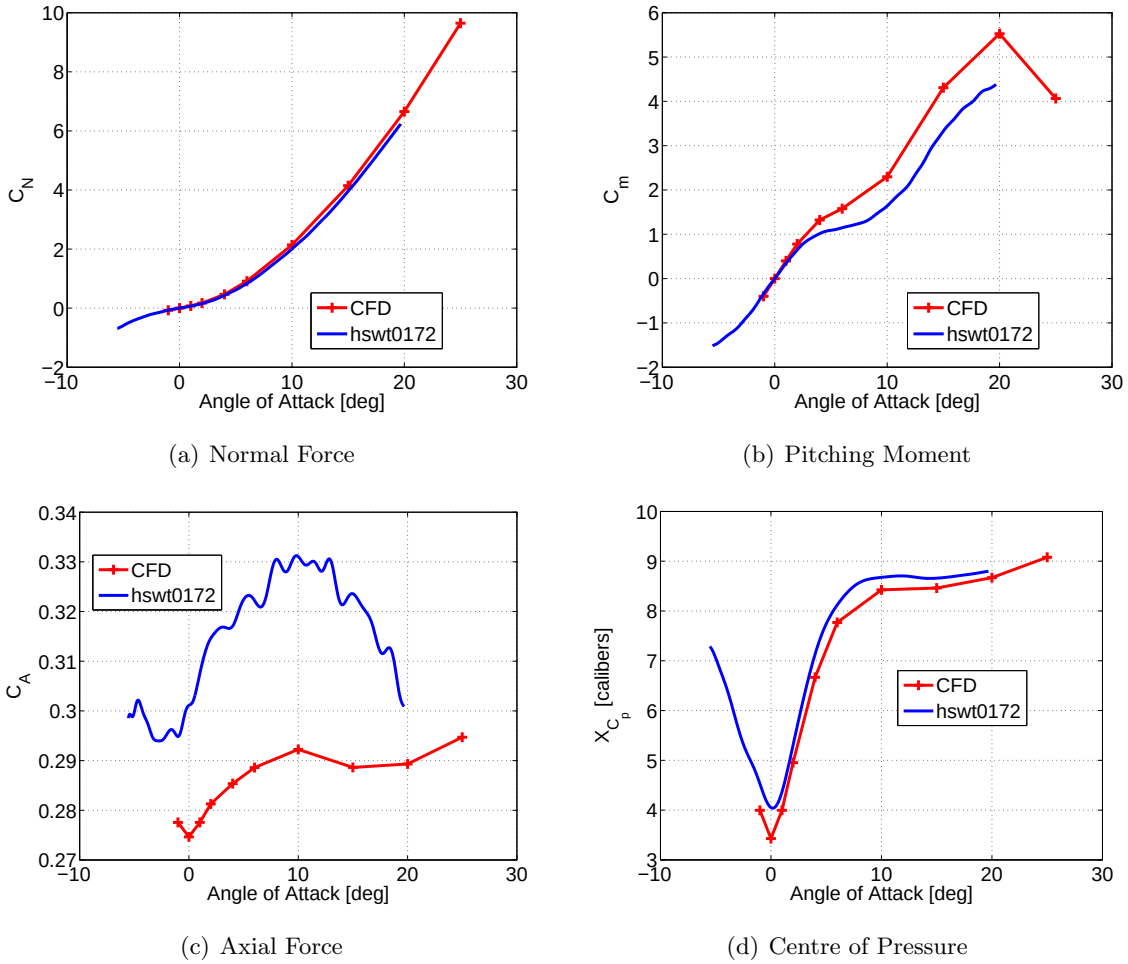

(a) Normal Force

(b) Pitching Moment

(c) Axial Force

(d) Centre of Pressure

Figure 4.17: Body and strakes CFD and experimental normal and axial force and pitching moment comparison, Mach 2.0

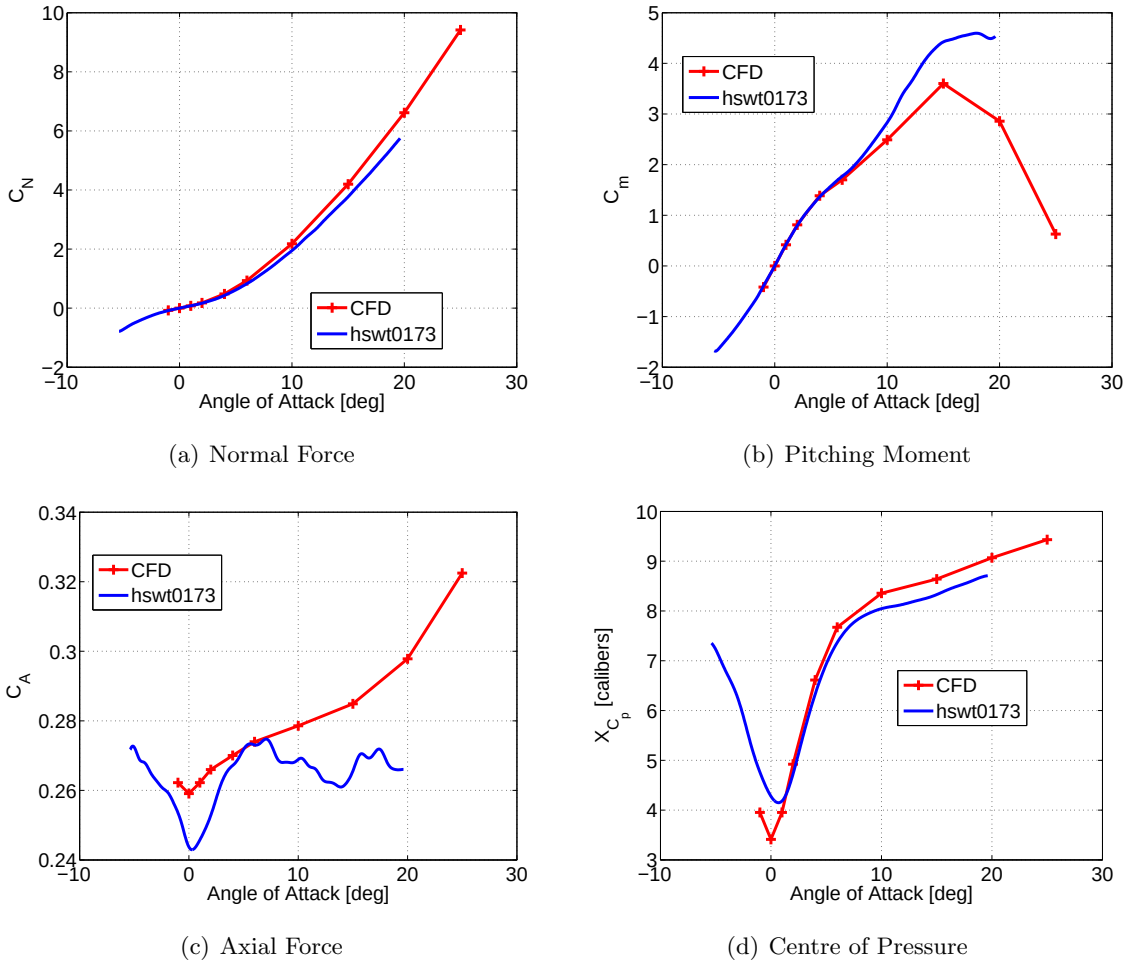

(a) Normal Force

(b) Pitching Moment

(c) Axial Force

(d) Centre of Pressure

Figure 4.18: Body and strakes CFD and experimental normal and axial force and pitching moment comparison, Mach 2.5

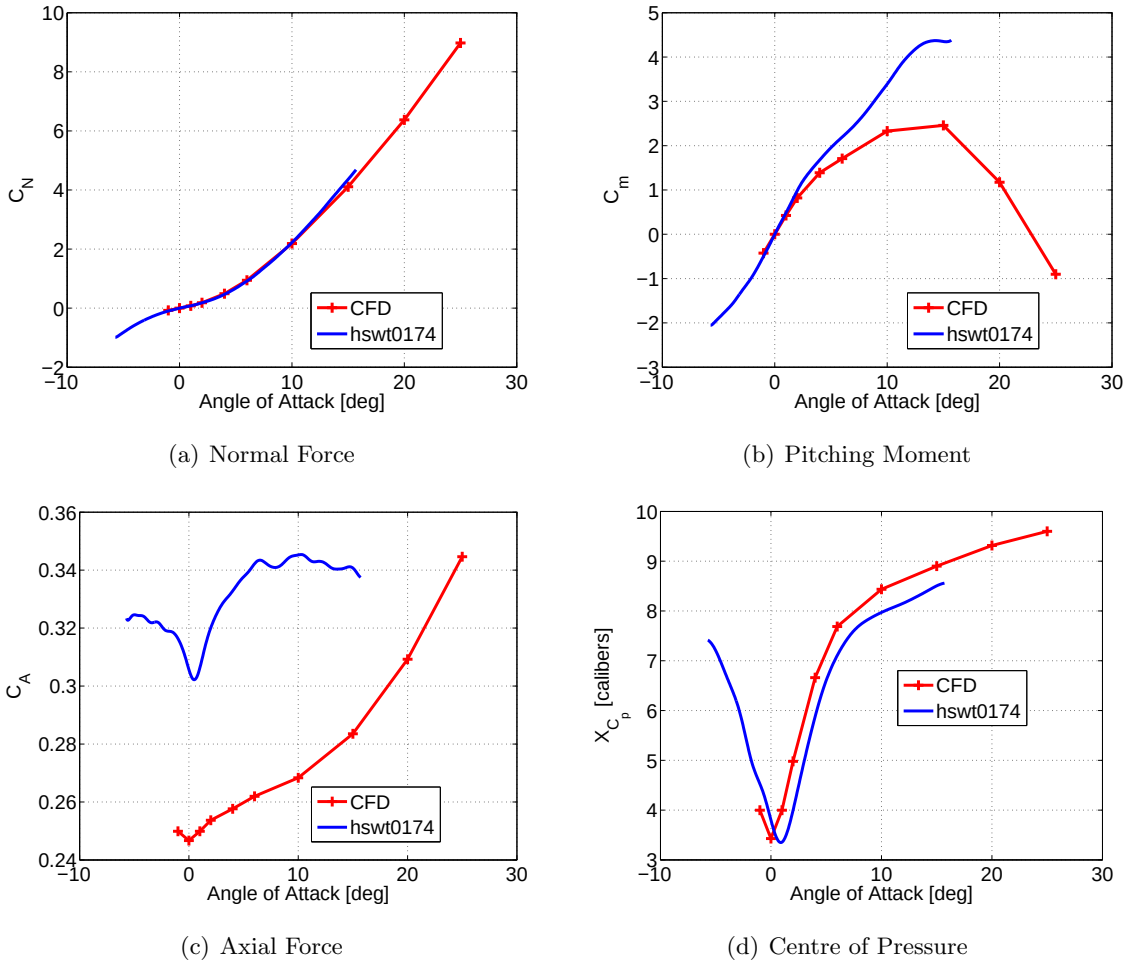

(a) Normal Force

(b) Pitching Moment

(c) Axial Force

(d) Centre of Pressure

Figure 4.19: Body and strakes CFD and experimental normal and axial force and pitching moment comparison, Mach 3.0

The lateral loads (side force, yawing moment and trolling moment) to did not show significant deviation from the nominal zero. Deviations are evident upon the onset of body or strake vortices but are due to manufacturing asymmetries and indicate that the shed vortices are symmetric. These deviations are illustrated in Figure 4.20 and Figure 4.21. For the body alone configuration, the deviations in the side force, yawing moment and rolling moment is only indicative of model manufacturing asymmetries rather than the onset of asymmetric vortices. For both configurations, the side force coefficient is no larger than 0.15, or 2.5% of the maximum body alone normal force.

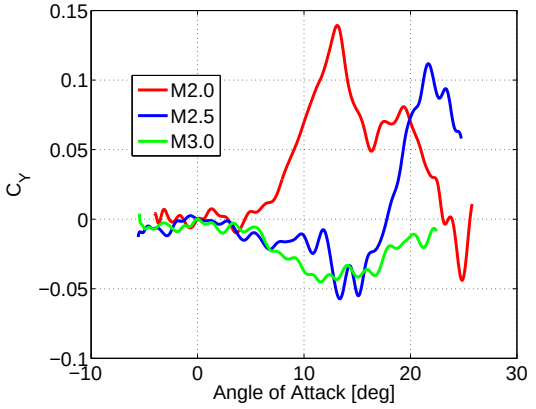

(a) Side Force

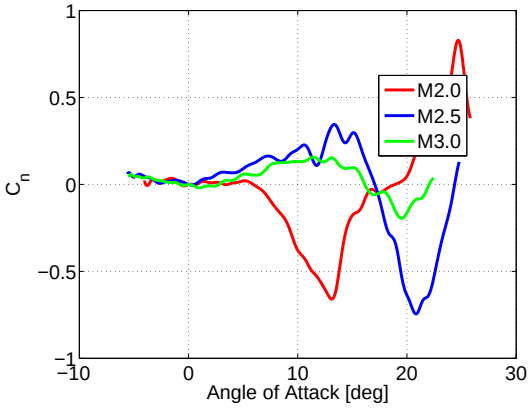

(b) Yawing Moment

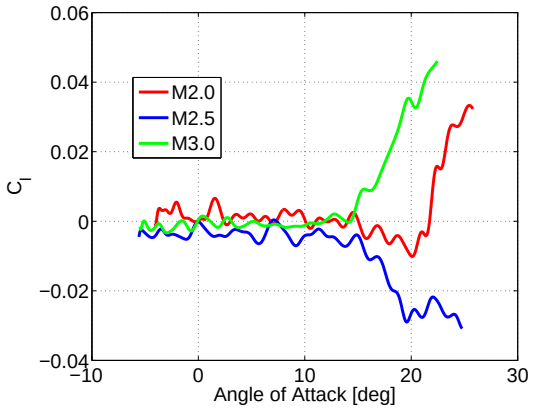

(c) Rolling Moment

Figure 4.20: Body alone lateral loads deviation

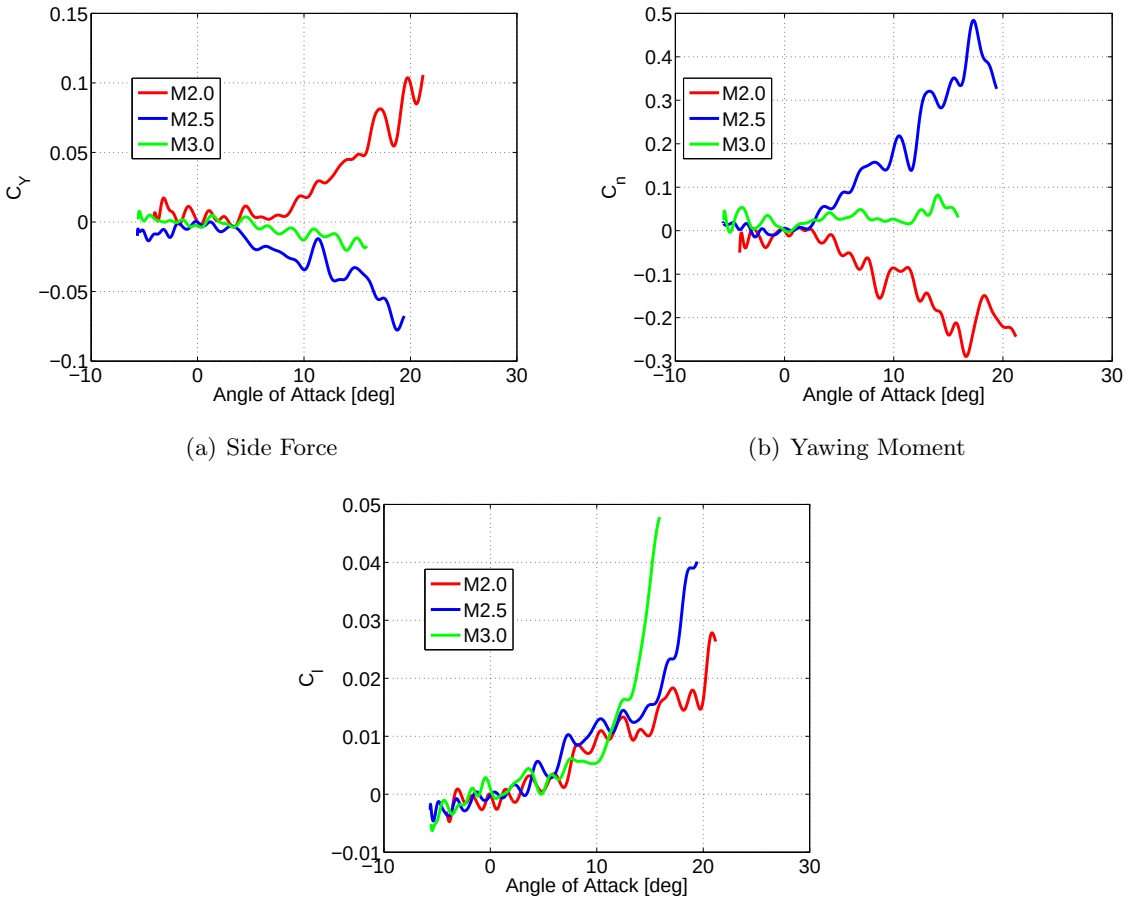

(a) Side Force

(b) Yawing Moment

(c) Rolling Moment

Figure 4.21: Body and strakes lateral loads deviation

4.4.2 Flow Visualisation

As mentioned previously colour Schlieren was performed during the force and moment tests. These visualisations were used to determined the position of the lee side vortices in the vertical plane. A sensitive colour mask was used during the tests with the resultant identification of low density gradients in the flow which made the identification of vortices easier.

The leeside flow separation is shown for the body only configuration in Figure 4.22 to Figure 4.24. For angles of attack below 6°, no noticeable leeside separation is observable, except possibly at the end of the body. For angles above 6°, the vortex structures toward the end of the body are less distinct. At the higher angles, more than two vortices are not distinctly identifiable. The nose vortex is distinctly visible. The second shed vortex, starting near the nose, is located close to the body and does not seem to shed, nor is a third vortex distinctly identifiable. Given the sensitivity of the Schlieren used (because the weaker nose vortex is distinctly visible), little possibility exists that a third vortex is present.

For the body-strake configuration, only the angles of attack higher than 10° were able to yield any information on the location of the vortices because at angles of attack less than 10° the vortex core was in the shadow of the body. Figure 4.25 to Figure 4.27 show the Schlieren for angles of attack 10°, 15°, 20° and 25°, for the Mach numbers 2.0, 2.5 and 3.0 respectively. The location of the vortex was measured from the Schlieren photographs. The accuracy of the measurements for the angle of attack is 0.2°, and the position is 0.2 calibers.

Because the Schlieren method shows density gradients, care was taken during the measurement of the vortex locations to ensure that the vortex core was identified rather than what was perceived to be the vortex core. Allen and Perkins [3] and Thomson and Morrison [39] indicated that the vortex centre is the region of low light intensity adjacent to a region of high light intensity; this because "the rapid change in light intensity is a direct result of the change in sign of the density gradient at the centre of the vortex".

At the angles of attack above 15°, the vortex structure shows vortex shedding for all the Mach numbers, and for Mach 2.5 and 3.0 shedding occurs from 15°. It is evident from the Schlieren images that the strake vortex and body vortices combine initially before vortex shedding occurs (resulting in two vortices). The perceived vortex shedding is also evident on the body alone configuration at the higher angles of attack.

It should also be noted that no vortex asymmetry is identifiable in the Schlieren pictures, confirming the force and moment data, and the existing understanding of the onset of asymmetric vortices.

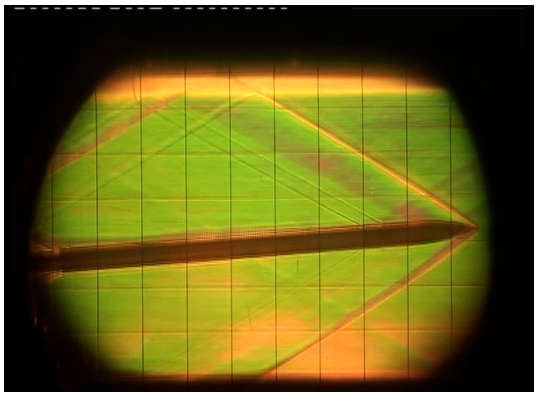

(a) 4°

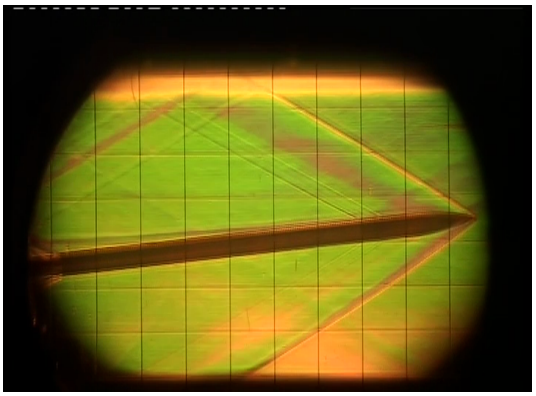

(b) 6°

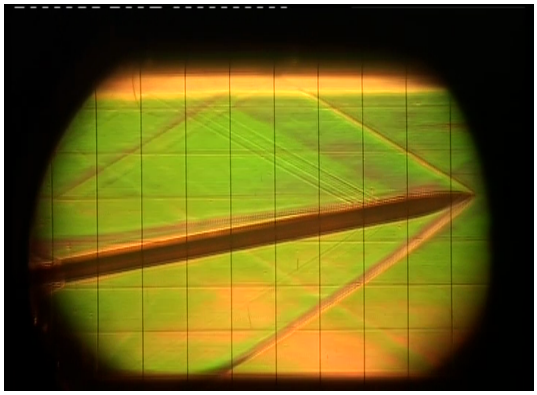

(c) 10°

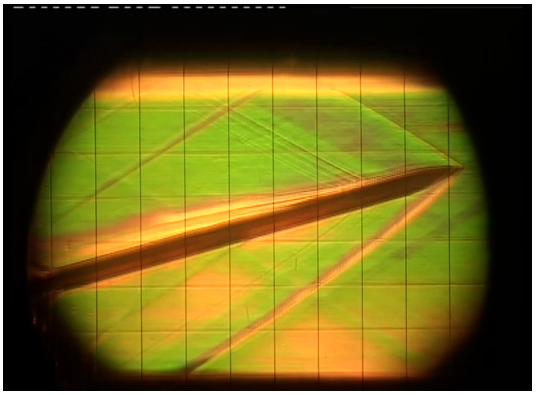

(d) 15°

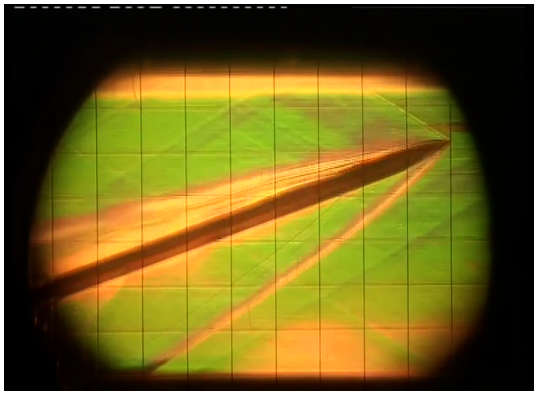

(e) 20°

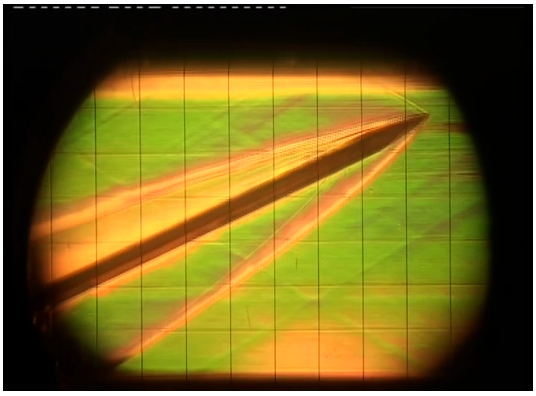

(f) 25°

Figure 4.22: Schlieren of body alone at M2.0

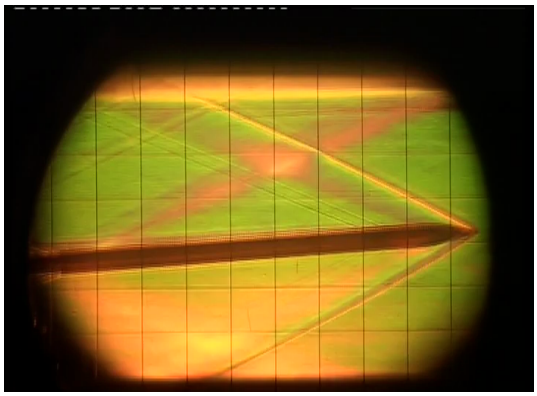

(a) 4°

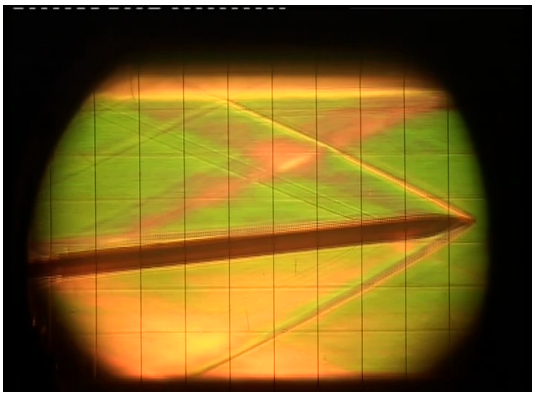

(b) 6°

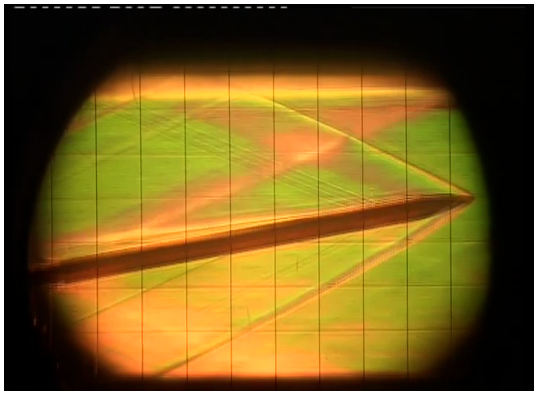

(c) 10°

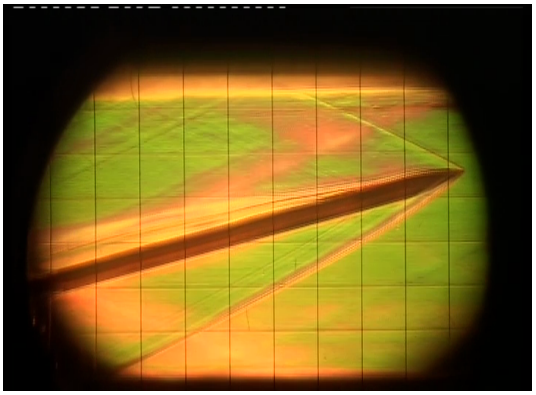

(d) 15°

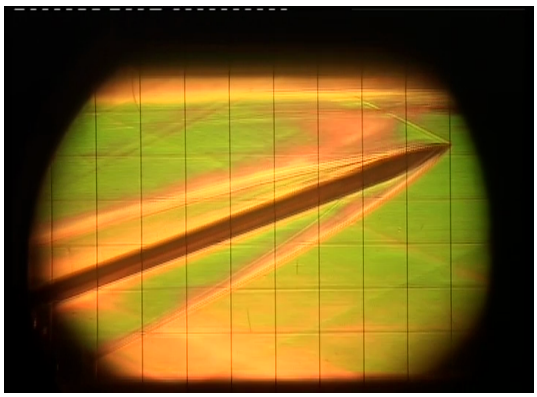

(e) 20°

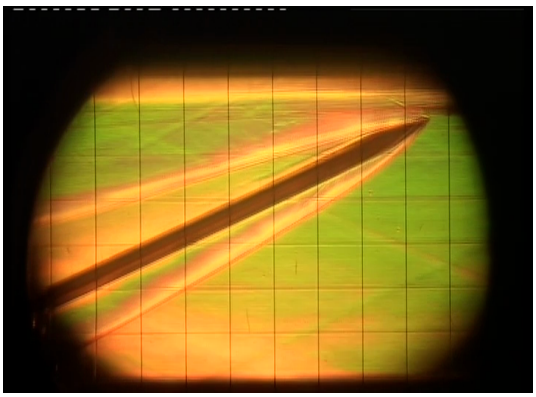

(f) 25°

Figure 4.23: Schlieren of body alone at M2.5

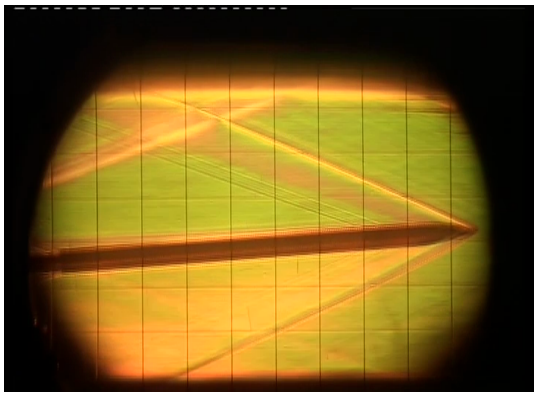

(a) 4°

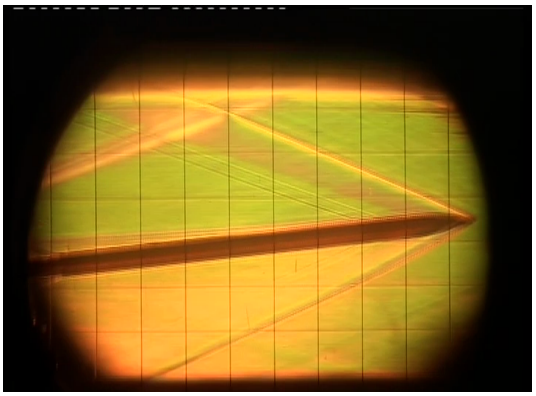

(b) 6°

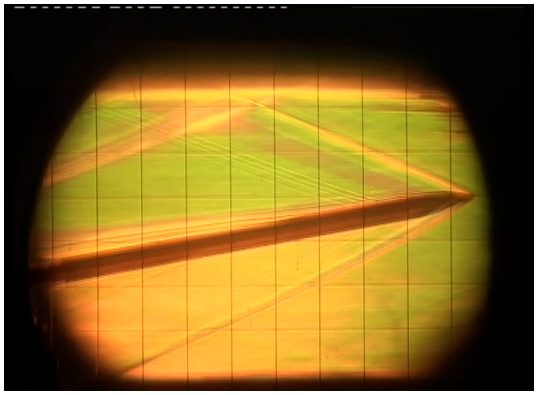

(c) 10°

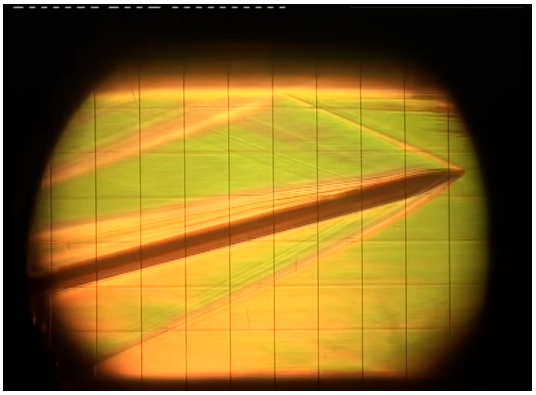

(d) 15°

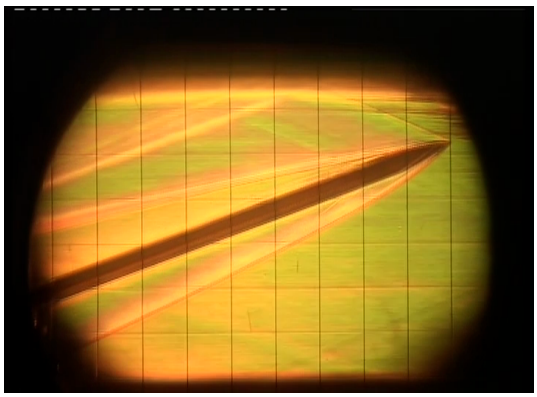

(e) 20°

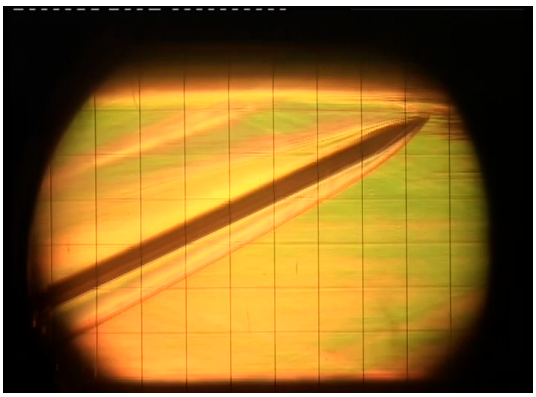

(f) 25°

Figure 4.24: Schlieren of body alone at M3.0

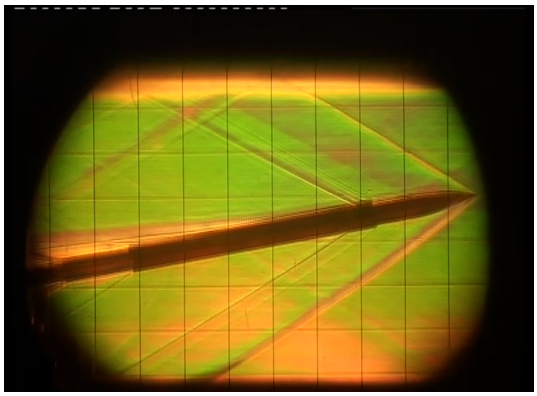

(a) 10°

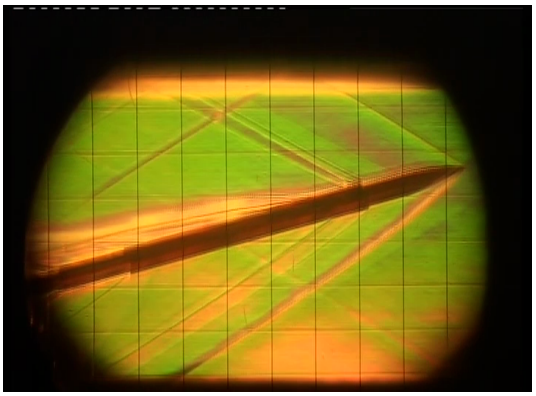

(b) 15°

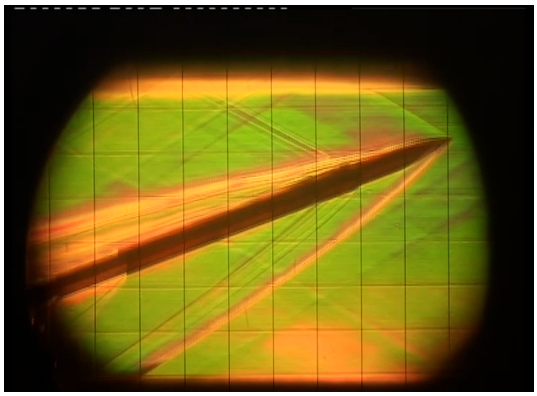

(c) 20°

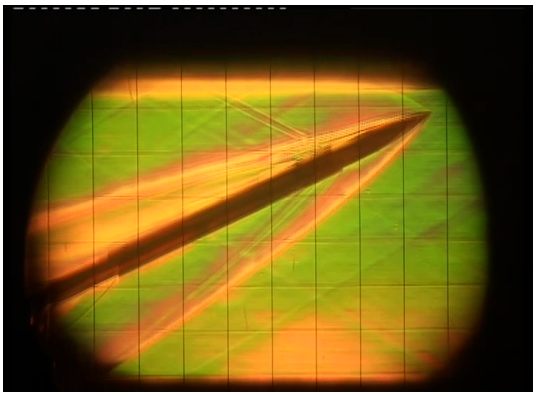

(d) 25°

Figure 4.25: Schlieren of body and strake at M2.0

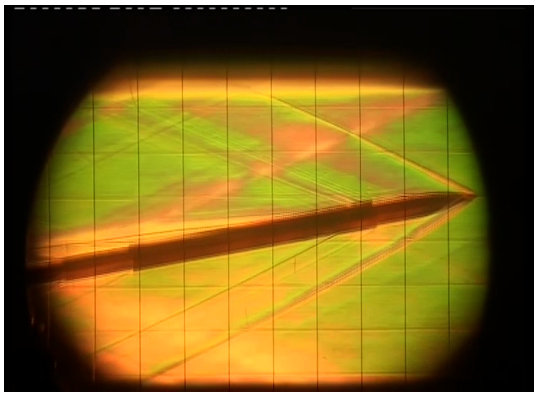

(a) 10°

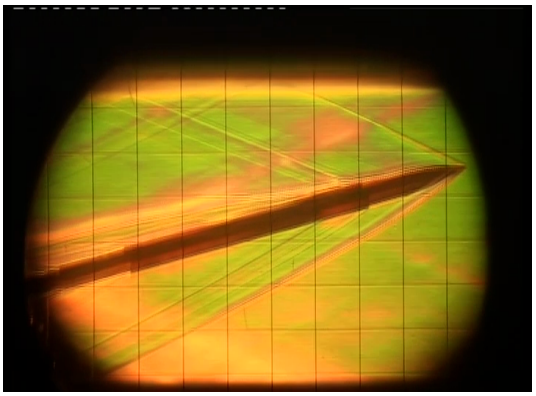

(b) 15°

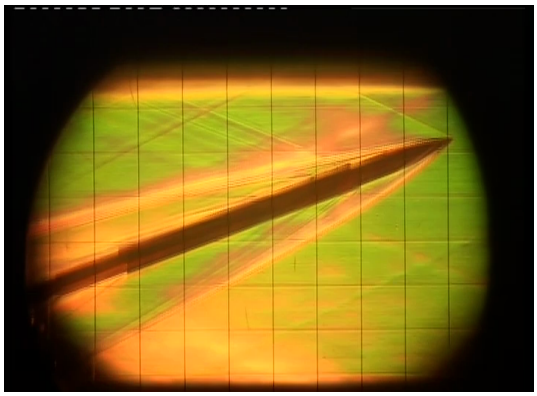

(c) 20°

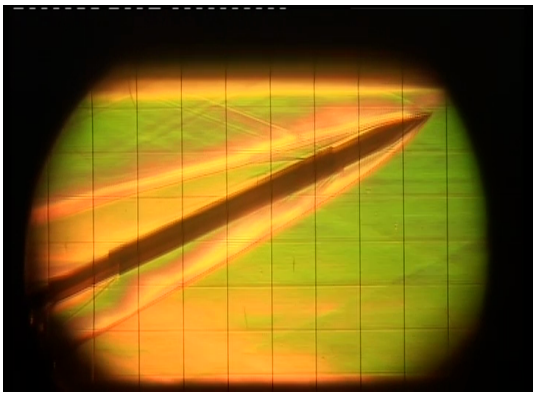

(d) 25°

Figure 4.26: Schlieren of body and strake at M2.5

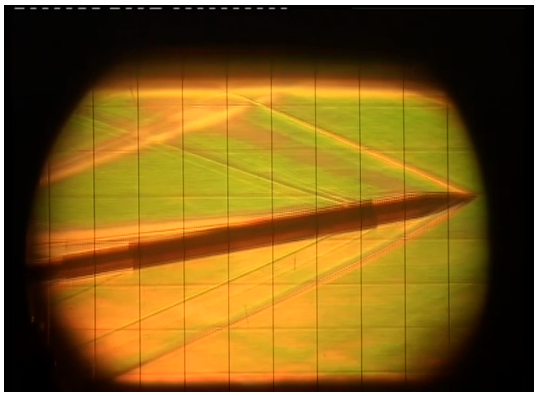

(a) 10°

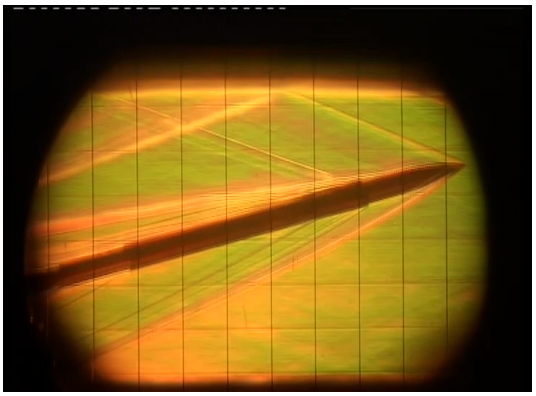

(b) 15°

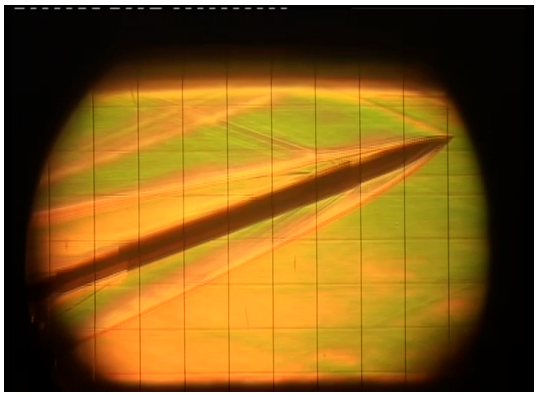

(c) 20°

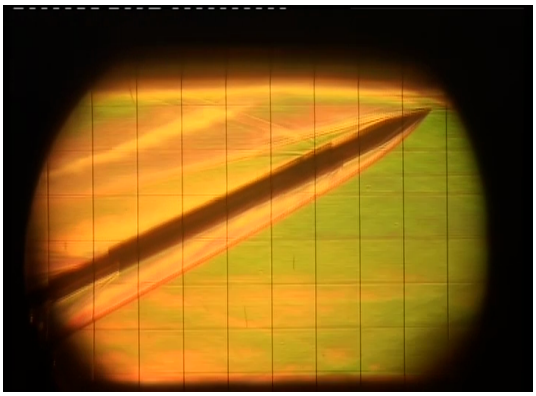

(d) 25°

Figure 4.27: Schlieren of body and strake at M3.0

4.4.3 Low Speed Flow Visualisation

In order to gain more confidence in the CFD predictions low speed tests were performed using two tests. The first test series was a water tunnel test performed at the University of Málaga by M.A. Arevalo-Campillos, L. Parras and Dr. Carlos del Pino in a water tunnel using flourescent dye. The tests covered the angle of attack range 6.5° to 27°. The tests did not cover the very low angles of attack because the illumination at the low angles was poor and the dye was applied to the forebody of the model. The second test series was a low speed air test performed by the author at the Low Speed Wind Tunnel (LSWT) of the CSIR using a printed model, laser light sheet and smoke to generate particles for the light sheet. For these tests the phenomena of interest are the higher angle of attack vortex structures because the second vortex close to the body, for both the body and body-strake configurations are less distinct in the Schlieren images.

Whilst the low speed flow visualisation tests at both the CSIR and the University of Málaga were incompressible with a Mach number of essentially zero, these results can be applied to the supersonic speed regime using Equation 2.7 which based on the well established assumption that the flow parallel to the freestream flow direction changes slowly, or repeated as

$$\frac{\partial^2 \phi}{\partial y^2} + \frac{\partial^2 \phi}{\partial z^2} = 0$$

Following slender body theory, no Mach dependence is predicted for flows in the y-z plane.

University of Málaga Tests

The experiments were carried out in a water towing tank with a working section of 0.5m x 0.5m and 5m long, installed at the Laboratory of Aero-Hydrodynamics of Vehicles at the University of Málaga. The test section is made of Plexiglas to allow for optical visualisation. A sketch of the experimental set up is depicted in Figure 4.28.

The values of the angle of attack were nominally the ones used in this thesis. Due to support system deflection the model angles of attack were 6.5°±0.3, 11°±0.3, 16°±0.2, 22°±0.05 and 27°±0.05. The velocity of the missile was 57 mm/s ±1 mm/s. The water temperature was measured with a PT100 probe to within ±0.1 °C. The Reynolds number is defined as $Re = \rho V D/\mu$ and reaches a constant value of 1040 ±3 . Special care was taken to obtain a steady velocity with no fluctuations. The missile was thus smoothly accelerated until it reached a constant velocity and the results were checked to ensure that they were not dependent on the acceleration.

Flow visualisation was carried out using a green fluorescent dye (Rhodamine 6G) mixed with a retardant gel. The dye was applied on the forebody zone. This area was found to better highlight the fluid dynamics. The test area was illuminated normal to the mean

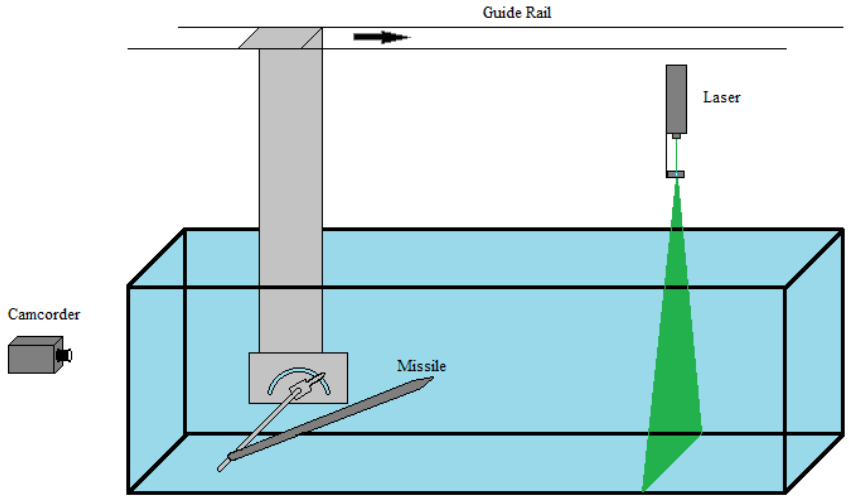

Figure 4.28: Water tunnel tests overview

flow with a laser sheet from a green laser of 500mW (wavelength = 532nm). A set of lens and optics were used to create a thin laser sheet.

A 1Mpixel video-camera was used to capture the vortex images at a frame rate of 1/25s. The frame rate was found to be well suited to have enough accuracy in the axial resolution of the flow structures which can be resolved to within 0.15D. The processed images were extracted from a video and then post-processed to quantify the vortex core position from both the body and the strakes.

Further details of the particular tests are detailed in reference [153].

The tests at 6.5° were not successful due to the location of the application of the dye. Only the results of 11° to 27° revealed sufficient information to be able to track the trajectories of the vortices. Because the angles were not at the nominal values collected in previous tests, further numerical simulations were performed to directly compare the CFD simulations to the water tunnel tests. These were performed at Mach 2.0 at the same conditions as in section 4.3 using the Spalart-Allmaras turbulence model as for the original numerical simulations.

CSIR Tests

The model for the LSWT tests had a body diameter of 45mm instead of the 25mm of the high speed model. This was to increase the available resolution of the flow visualisation over the high speed model. The speed of the flow was 11±1m/s, whilst the total temperature was 301±1K and the ambient pressure 87kPa. The Reynolds number based on

the body diameter was 27000. The tests were performed in the Low Speed Wind Tunnel (LSWT) of the CSIR, a 7'x5' low speed facility. The printed model was sanded by hand and three layers of paint were applied to ensure a smooth finish. The configuration used during these tests is shown in Figure 4.29. The flow was visualised by using an Aerotech smoke generator, Model SGS-90, and the flow illuminated with a laser.

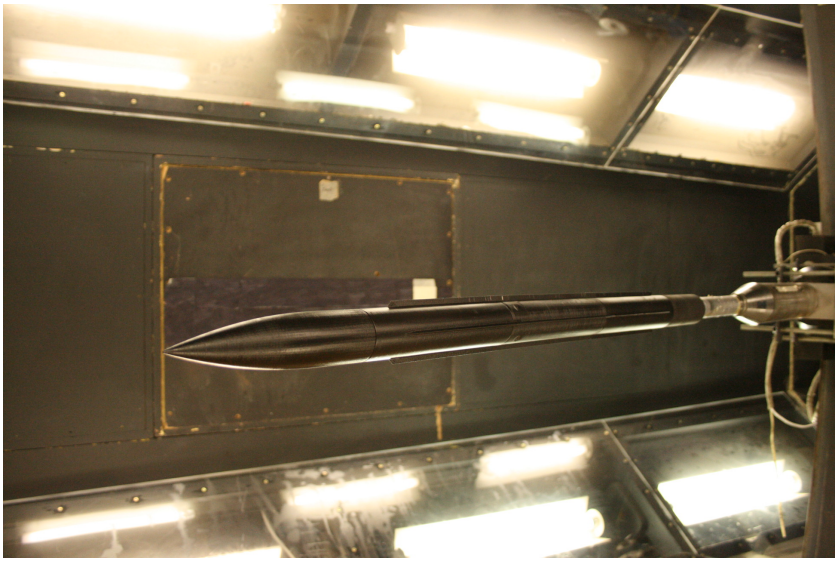

Figure 4.29: LSWT model in test section

The separated flow in the lee side of the body-strake configuration is shown in Figure 4.30 and Figure 4.31 for various angles of attack. For the angles of attack below 20° the plates are at the axial station of 15.75D from the nose, or 11D along the strake. For the angles of attack lower than 20° the model and laser sheet was pitch together, while for the angles of attack of 20° and 25°, the support system was yawed such that the laser sheet was perpendicular to the air flow or using the same configuration as for the water tunnel tests. The location of the rolled up vortex sheet was then measured from the pictures, after correcting for lense abberations and camera location perspective using a calibrated target. Where the vortex has less strength such as nearer the start of the strakes, the location of the vortex was much more difficult to identify. Therefore the location of the vortex was not measured along the complete length of the strake. This does not, however, limit the validation of the CFD simulations because the later vortex roll up position is dependent on the initial stages. The error in measurement of the position is estimated to be 0.1D or 4.5mm model scale and is due to the manual selection of the vortex core. The uncertainty in measurement in the lateral direction therefore translates to 40% of the semispan of the strakes. The non-smoothness of the smoke is due to the smoke generator not producing a sufficiently continuous stream of smoke and the stream being of small diameter. This does not, however, detract from identifying the centre of the rolled up vortex sheet. No discernable secondary vortex separation was identified in the strake body junction; this

again due to the non-smoothness of smoke generator.

(a) 6° at 15.75D

(b) 10° at 15.75D

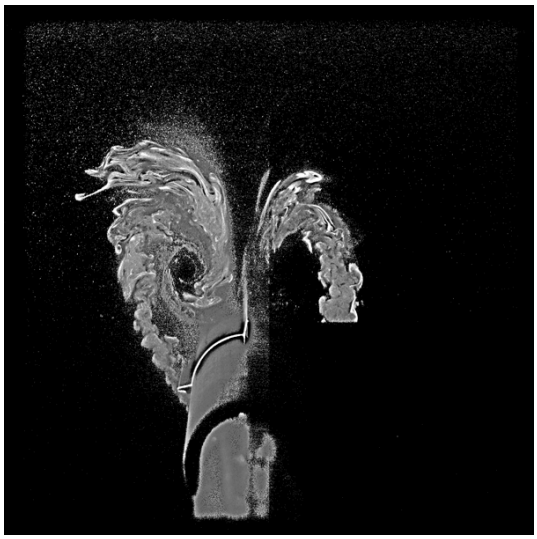

(c) 15° at 15.75D

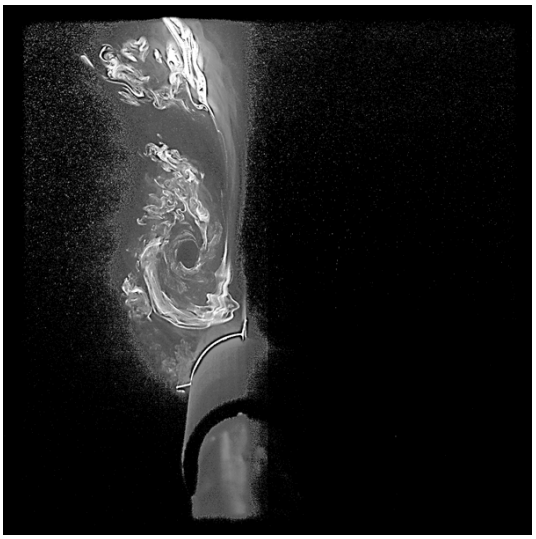

(d) 17° at 15.75D

Figure 4.30: Vortex sheet roll up for LSWT tests for angles lower than 20°

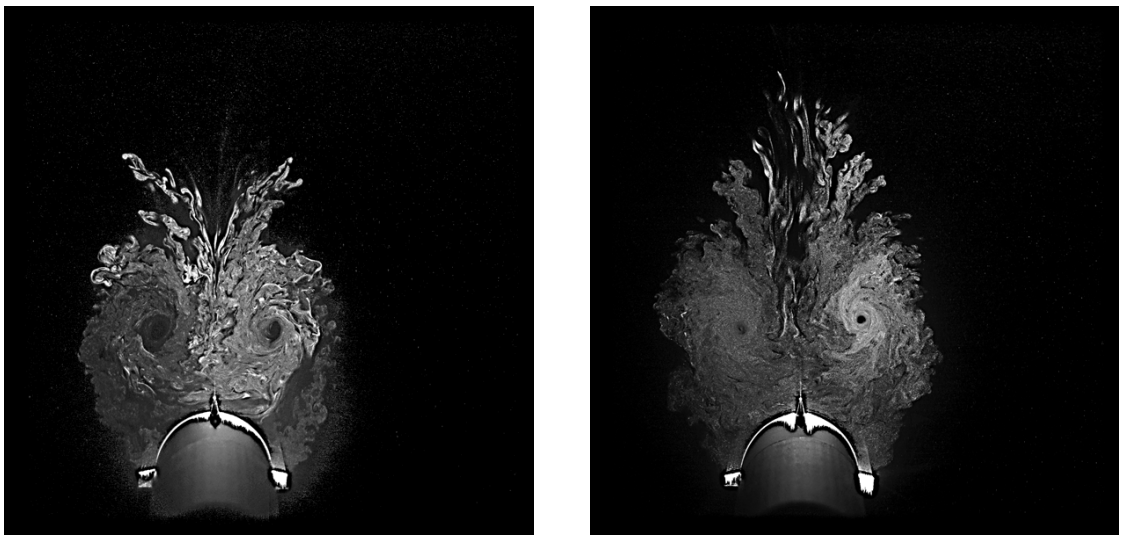

(a) 20° at 14.58D (b) 25° at 14.30D

Figure 4.31: Vortex sheet roll up for LSWT tests at angles greater than 17°

At angles of attack greater than 10°, both the Málaga and CSIR tests exhibit the body vortex rolling into and coalescing with the strake vortex sheet. This is illustrated in Figure 4.32 for the LSWT tests and is demonstrated in the vortex tracking of Figure 4.33 to Figure 4.36. Only a single vortex is therefore present for the subsonic tests in contrast to the high speed tests and CFD predictions for angles greater than 15°.

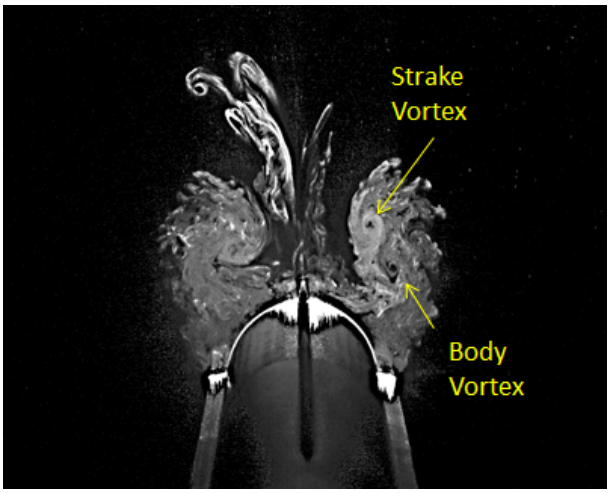

Figure 4.32: Body and strake vortex sheet roll up for 20°

Subsonic Flow Visualisation Comparison

A comparison of the CFD simulations at Mach 2.0 and the experimental tests (both Málaga and LSWT tests) are shown in Figure 4.33 to 4.36 for the angles of attack of 11° to 27°. The lateral, vertical and 3-dimensional trajectories are plotted. The 3-dimensional trajectories were not symmeterised, whilst only the starboard side are used for the lateral and vertical graphs. The plots for the experimental Málaga tests reveal the resolution limitations of the images from which the data were extracted and indicates uncertainties of 0.1 of the body radius or 0.05 of a caliber. Given the method used to collect data for the Málaga tests, more data are obviously available than for the LSWT tests.

It should be remembered that the LSWT tests were performed at lower angles of attack than the Málaga tests and CFD simulations. This is exemplified in the vortex position being higher in the CFD predictions than the LSWT tests (see Figure 4.33).

The largest discrepancy between the Málaga and LSWT tests are for the nominally 10° case (see Figure 4.33), with the Málaga tests showing a drop in the centre of vortex as it travels along the body length i.e. the strake vortex after interacting and combining with the body vortex travels closer to the body. Furthermore, the LSWT tests indicate a consistently higher vortex position in the vertical direction than the Málaga tests. Both the experimental tests show a body and strake vortex coalescing into a single vortex. The coalescing process is evident in the spiral trajectory of both vortices and is exemplified by the Málaga observations because of the axial resolution. The 20° LSWT case also demonstrates the spiral trajectory but is not as pronounced as the observations from the Málaga tests because of the greater resolution in the axial direction of the Málaga tests. No explanation can be given for the differences between the Málaga tests and the LSWT tests, and it is currently assumed that an unknown factor is present in the Málaga tests and the results are only used for qualitative purposes.

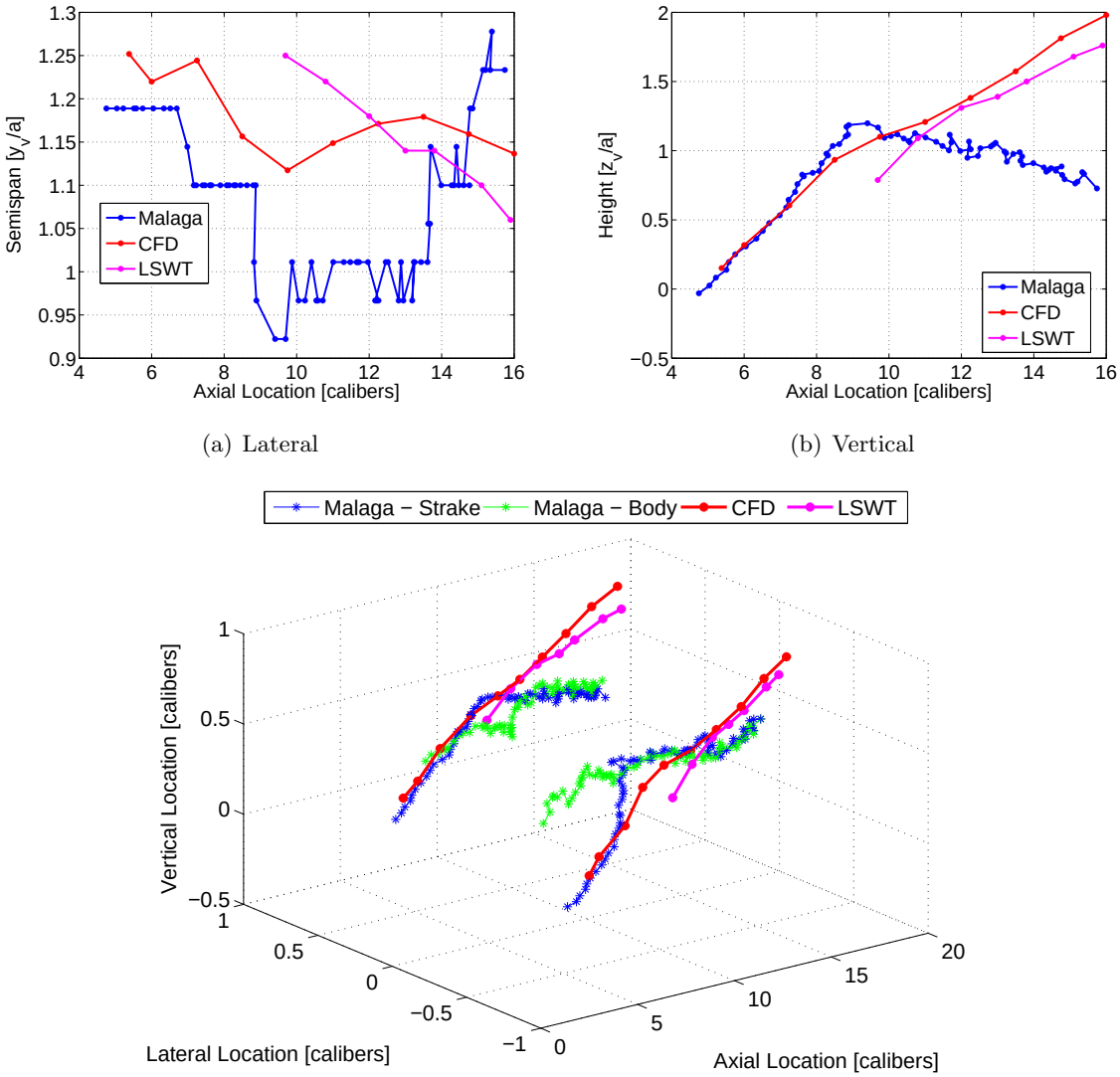

(a) Lateral

(b) Vertical

(c) 3D

Figure 4.33: Vortex trajectories at 11°

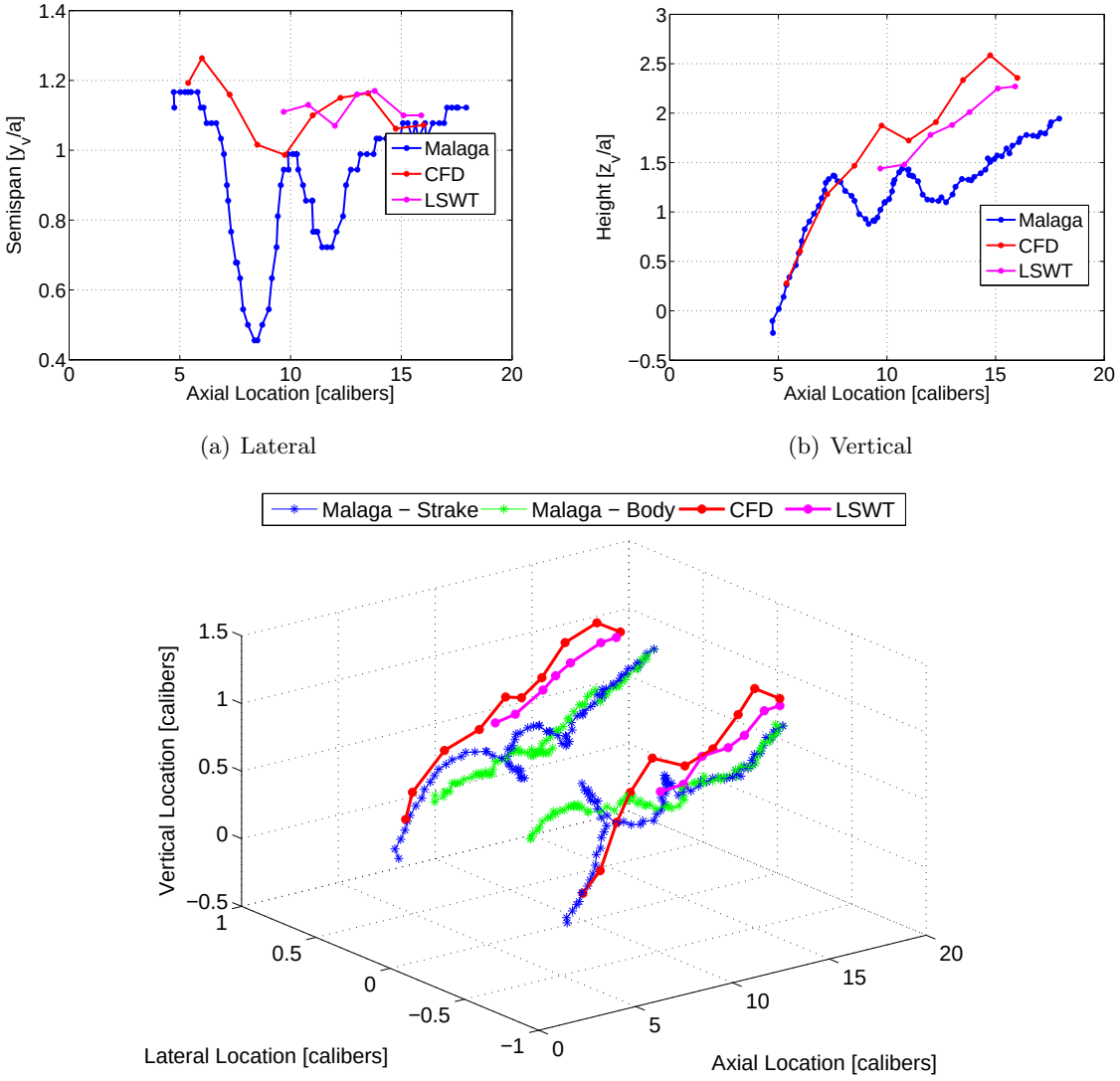

(a) Lateral

(b) Vertical

(c) 3D

Figure 4.34: Vortex trajectories at 16°

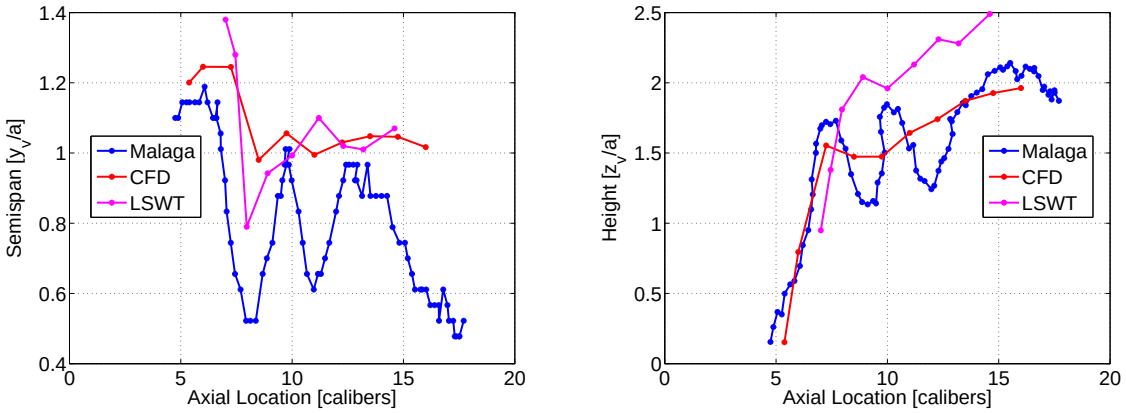

(a) Lateral

(b) Vertical

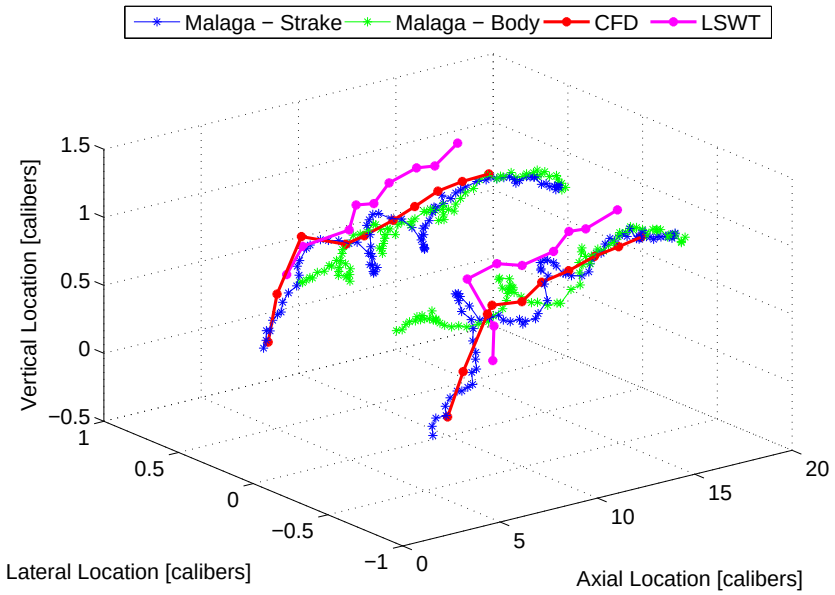

(c) 3D

Figure 4.35: Vortex trajectories at 22°

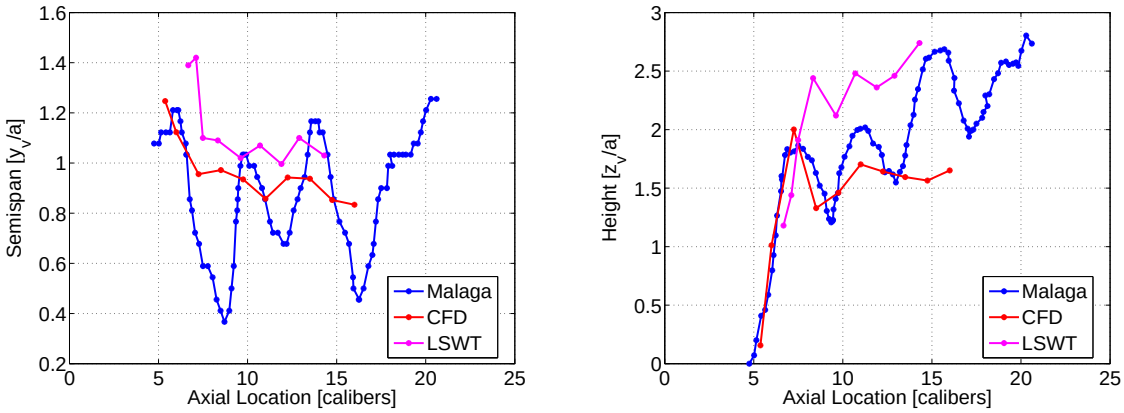

(a) Lateral

(b) Vertical

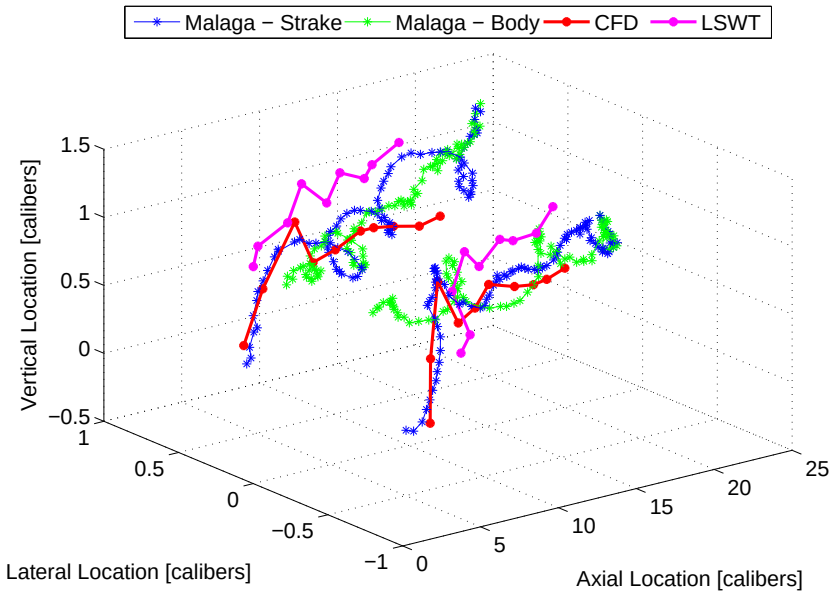

(c) 3D

Figure 4.36: Vortex trajectories at 27°

4.4.4 Vortex Position Comparison

The position of the vortices in the lateral and vertical directions as predicted by the CFD are shown in Figure 4.37 to Figure 4.46 for the angles of attack 6° to 25°. For the angles of attack above 10° two concentrated vortices were identified and these are displayed as the body vortex (upper shed vortex) and strake vortex (lower vortex). Where appropriate (6° and higher) the HSWT and LSWT experimental data are plotted. The figures illustrated the good correlation between the HSWT vertical positions and the CFD predictions for all the Mach numbers. Evident is the Mach number dependency of the body nose vortex at 20° and 25°. At the low angles i.e. 2° to 6°, the CFD simulations indicate that a small dependence on Mach number exists, though this only starts approximately half way down the strake and is only in the vertical direction. At 6° and 10° this effect is more pronounced, and also evident in the Schlieren images of the 10° case.

The LSWT tests show good correlation with the HSWT tests for the angles of attack of 6°, 10° and 15°. The LSWT positions show a marginally lower vertical position than the Mach 2.0 HSWT tests for the angles of attack of 6° and 15°. At 10° the position correlates with the HSWT position. The marginally lower position for the LSWT tests would be consistent with the trend of the position with Mach number i.e. position is higher as the Mach number increases, with the LSWT tests representing a lower limit.

Returning to the number of vortices shed at the higher angles of attack, the most distinct feature between the high speed and low speed tests is the interaction of the body-strake edge vortices. For the higher angles of attack i.e. 15° and above, the body vortices roll up into the shed strake vortex sheet in the low speed tests. For the high speed tests, from the Schlieren images, it is evident that the strake vortex first combines with the body vortex as for the incompressible case, and from this single vortex two vortices emanate or vortex shedding occurs, whereas for the LSWT tests the vortex does not split into two. No asymmetric vortices are observed indicating that the shed vortex is symmetric (in contrast to asymmetric vortex shedding prevalent at higher angles of attack for bodies). From the Schlieren images the body and strake vortices combine at anything between six to eight calibers (from the nose). For the figures of 4.41 to 4.46 the shed vortex is labeled as the body vortex even though the body vortex originally combines with the strake vortex simply because the shed vortex is observed from the Schlieren images as a continuation of the body vortex. The vortex that remains close to the body is labeled the strake vortex.

From the correlations between the HSWT test, LSWT tests and CFD simulations it can be concluded that not only are the CFD simulations validated by the normal force and centre-of-pressure correlations (see subsection 4.4.1), but also in their vortex positions and allows the flow fields of the CFD simulations to be used for further analysis purposes.

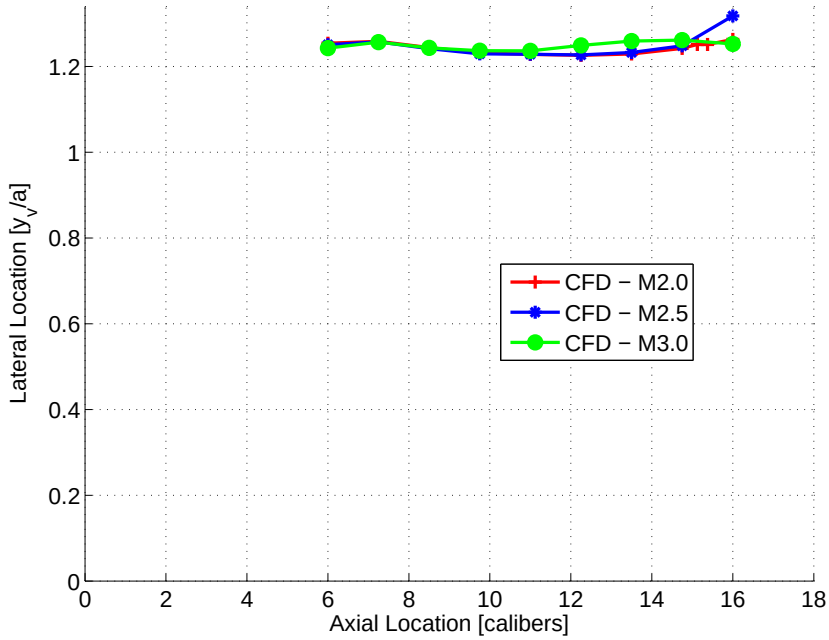

(a) Lateral

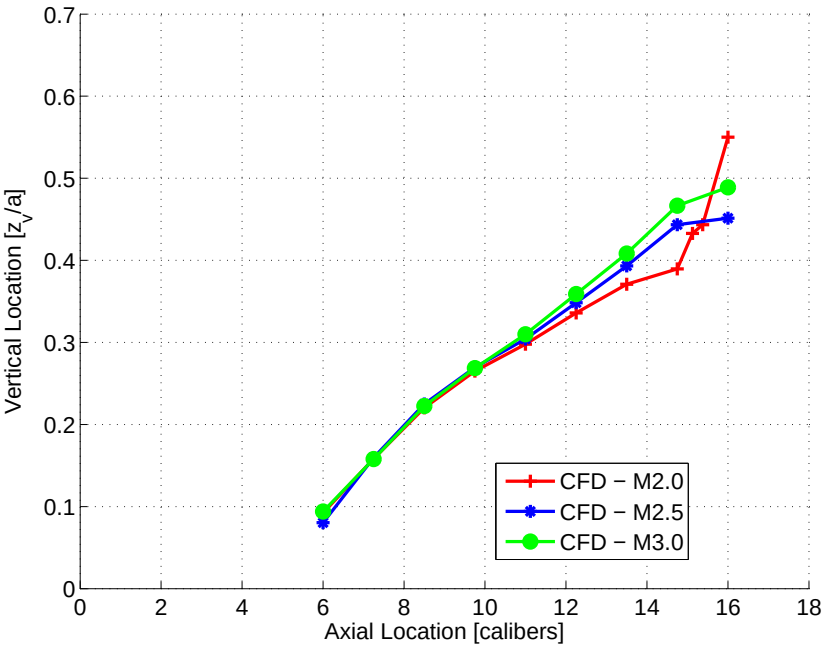

(b) Vertical

Figure 4.37: CFD concentrated vortex positions at $\alpha = 2^\circ$

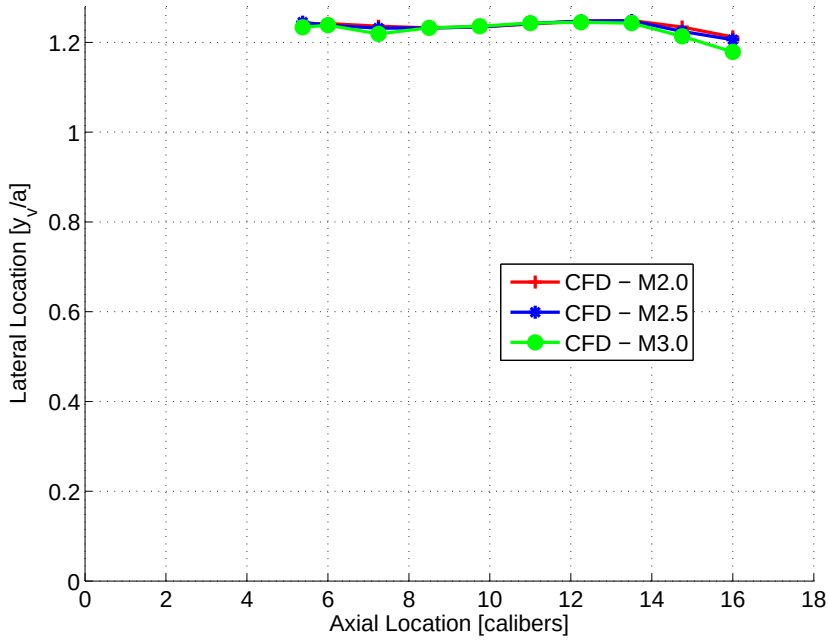

(a) Lateral

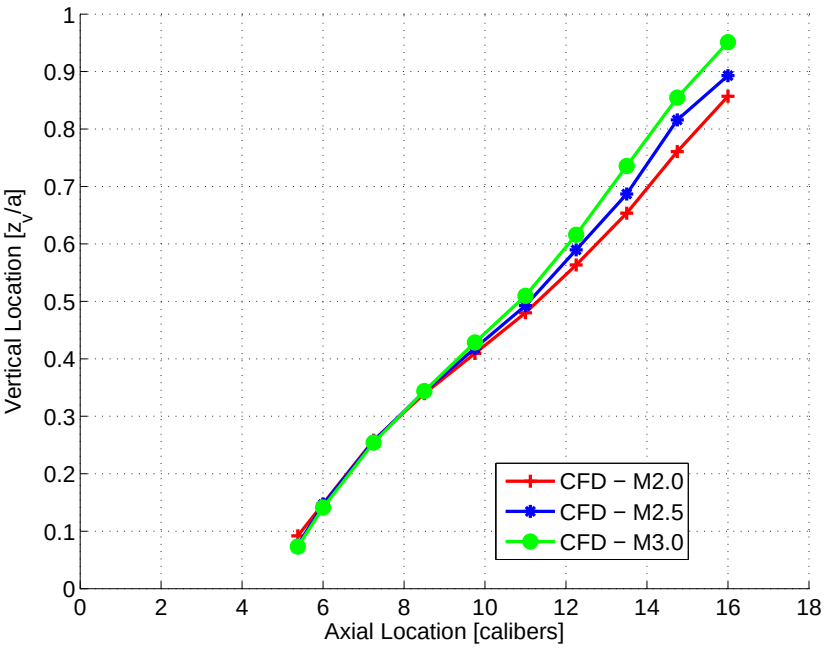

(b) Vertical

Figure 4.38: CFD concentrated vortex positions at $\alpha = 4°$

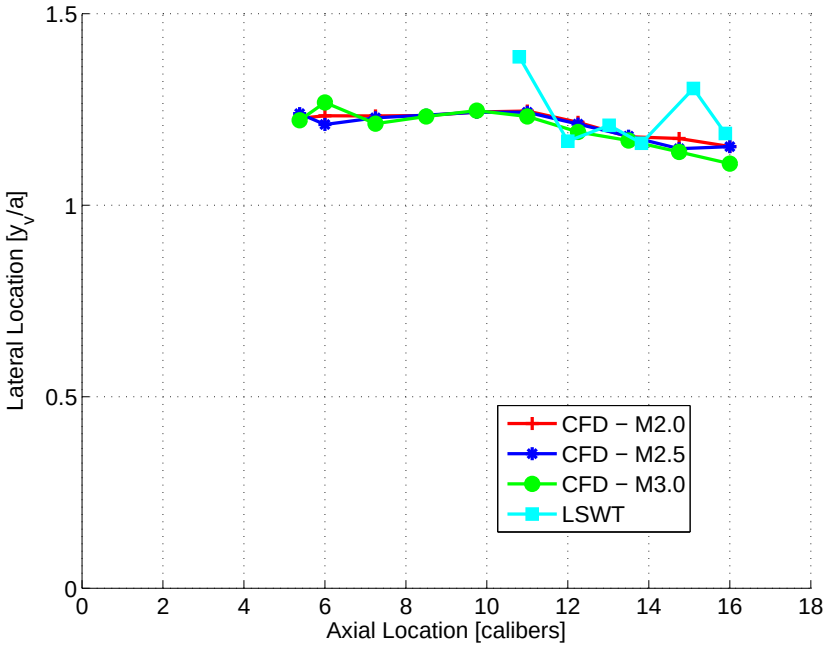

(a) Lateral

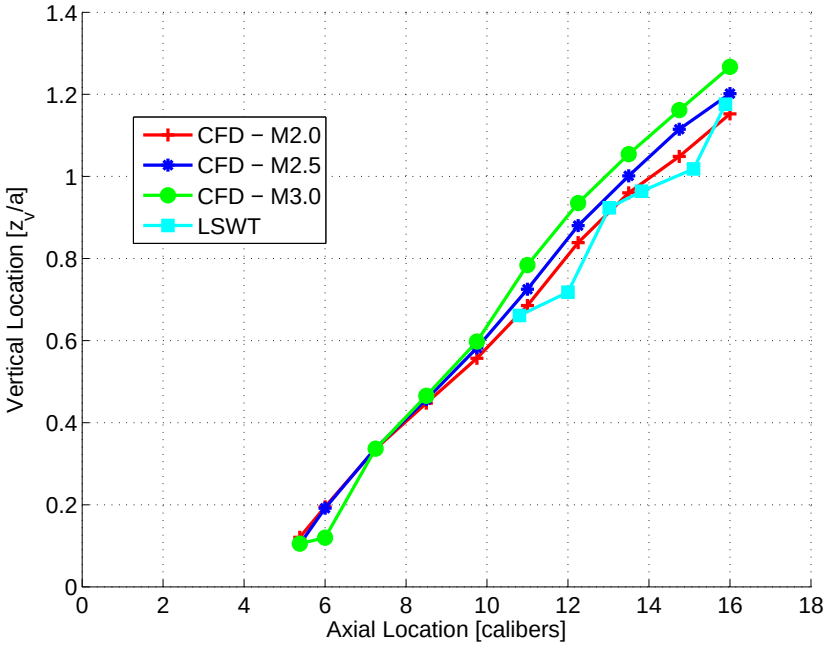

(b) Vertical

Figure 4.39: CFD and experimental comparisons of concentrated vortex positions at $\alpha = 6^\circ$

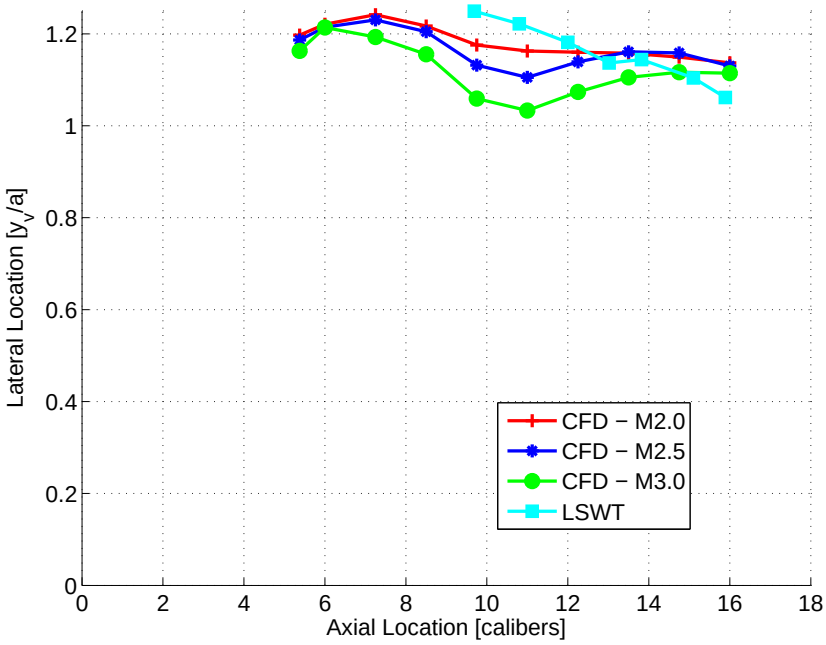

(a) Lateral

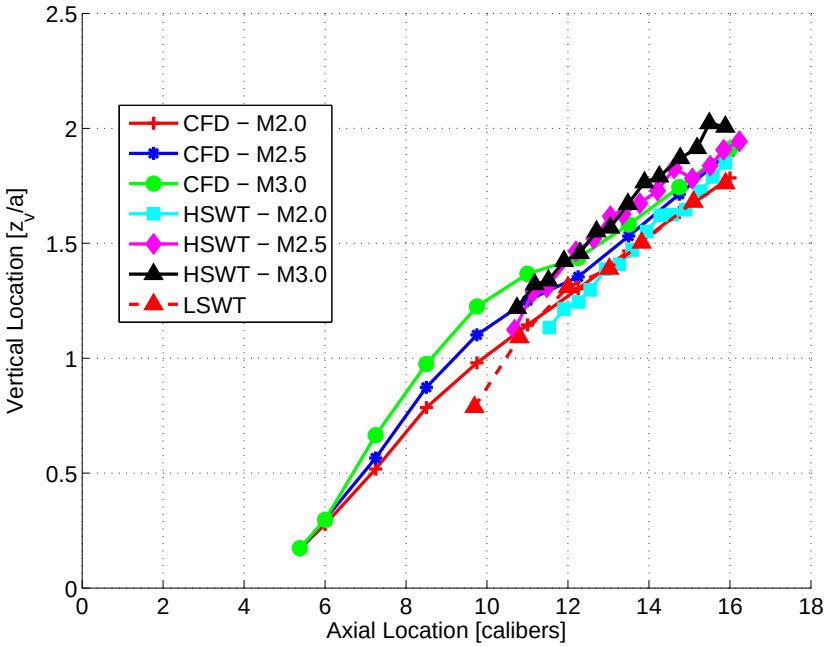

(b) Vertical

Figure 4.40: CFD and experimental comparisons of concentrated vortex positions at $\alpha = 10°$

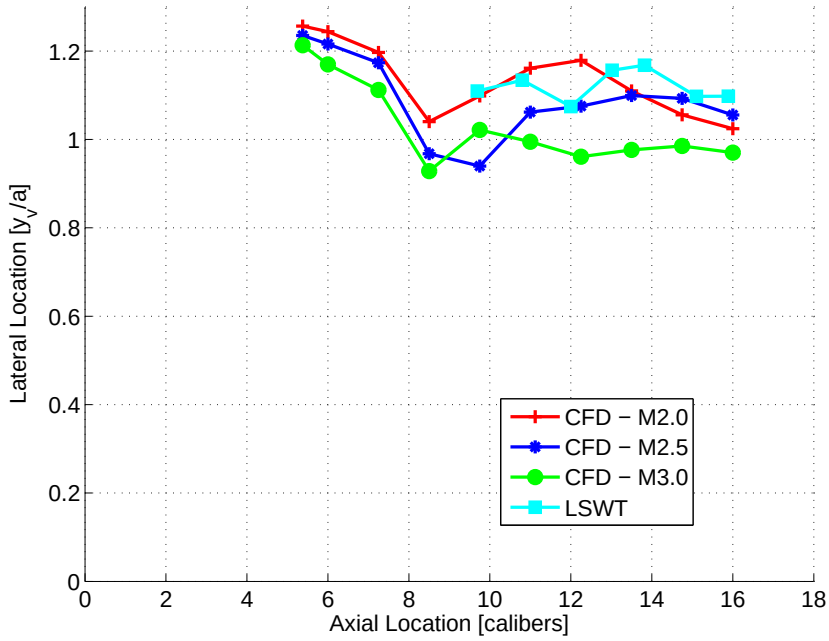

(a) Lateral Strake

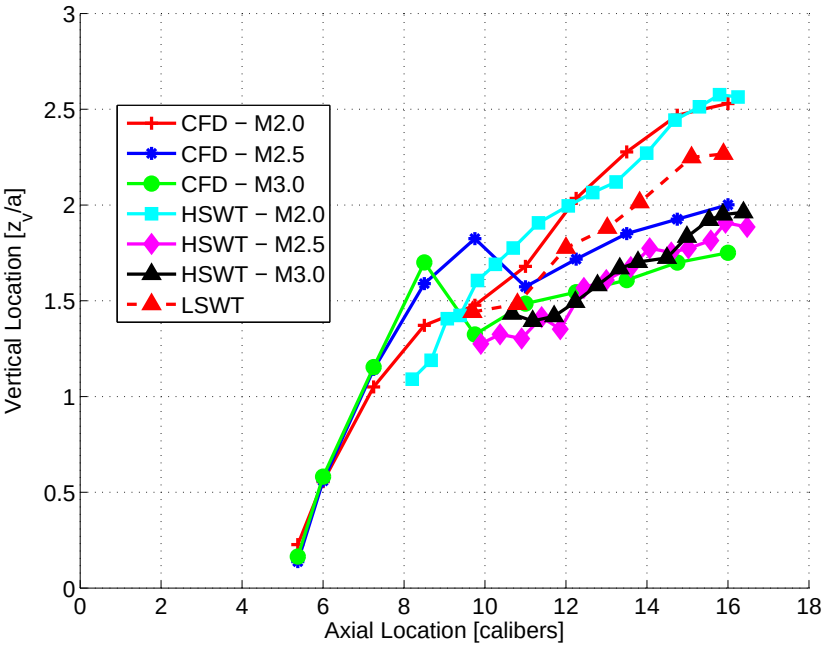

(b) Vertical Strake

Figure 4.41: CFD and experimental comparisons of concentrated strake vortex positions at $\alpha = 15°$

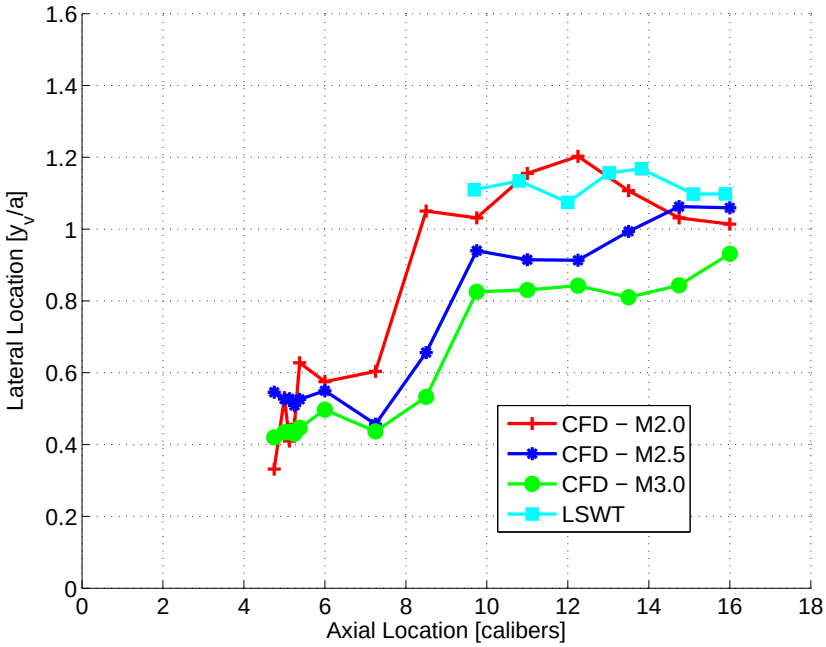

(a) Lateral Body

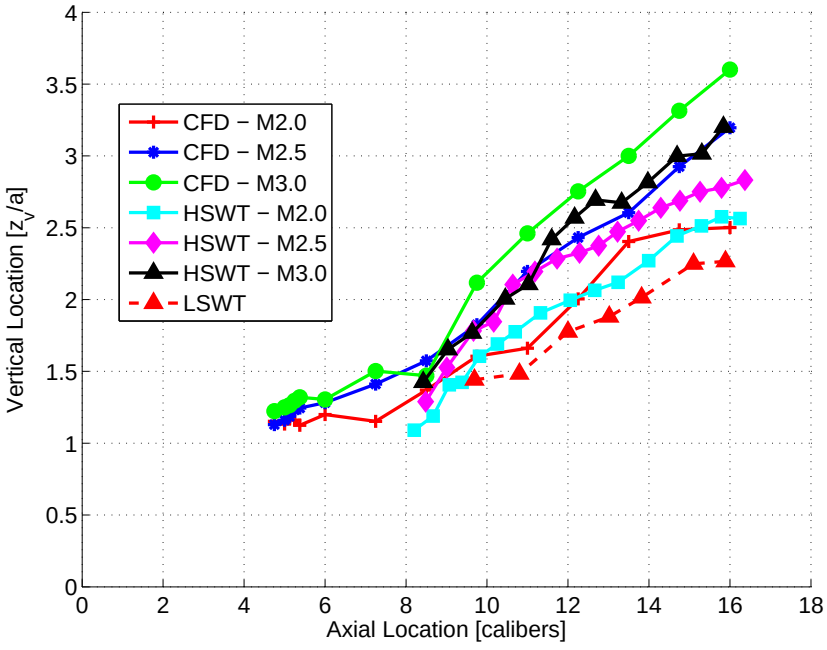

(b) Vertical Body

Figure 4.42: CFD and experimental comparisons of concentrated body vortex positions at $\alpha = 15°$

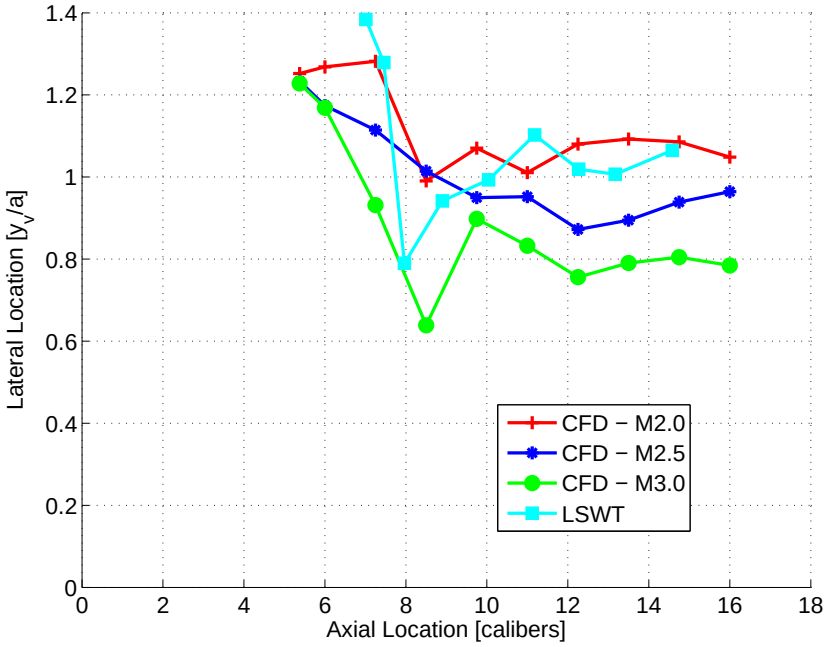

(a) Lateral Strake

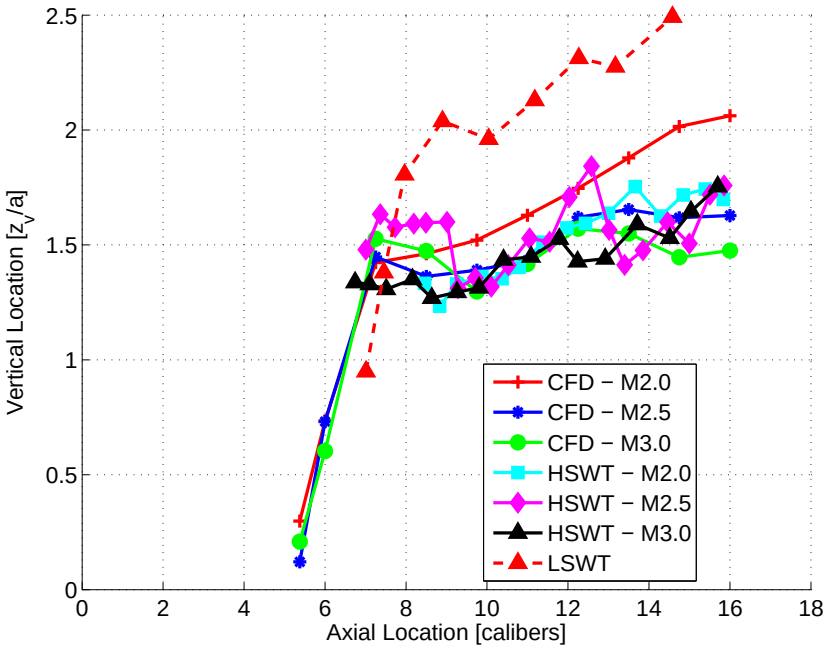

(b) Vertical Strake

Figure 4.43: CFD and experimental comparisons of concentrated body vortex positions at $\alpha = 20°$

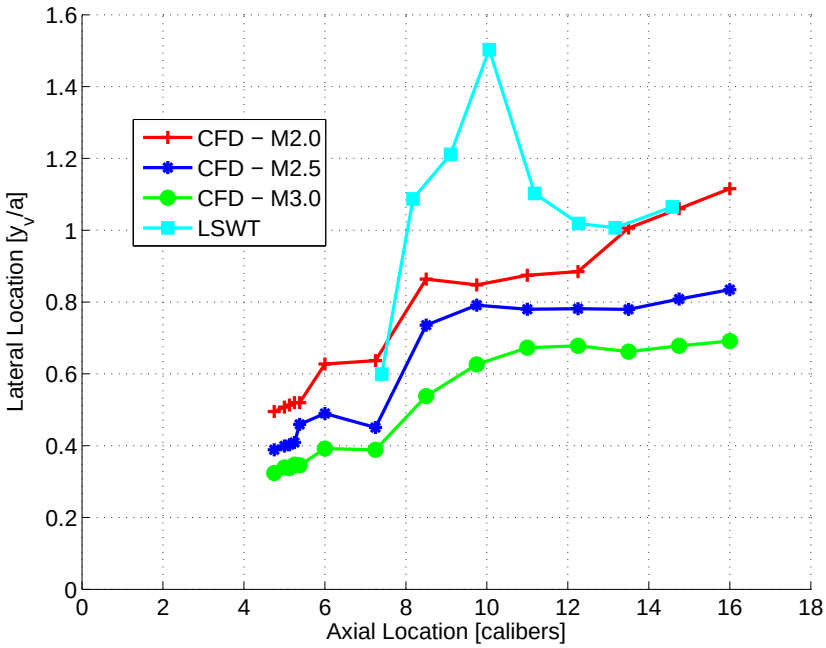

(a) Lateral Body

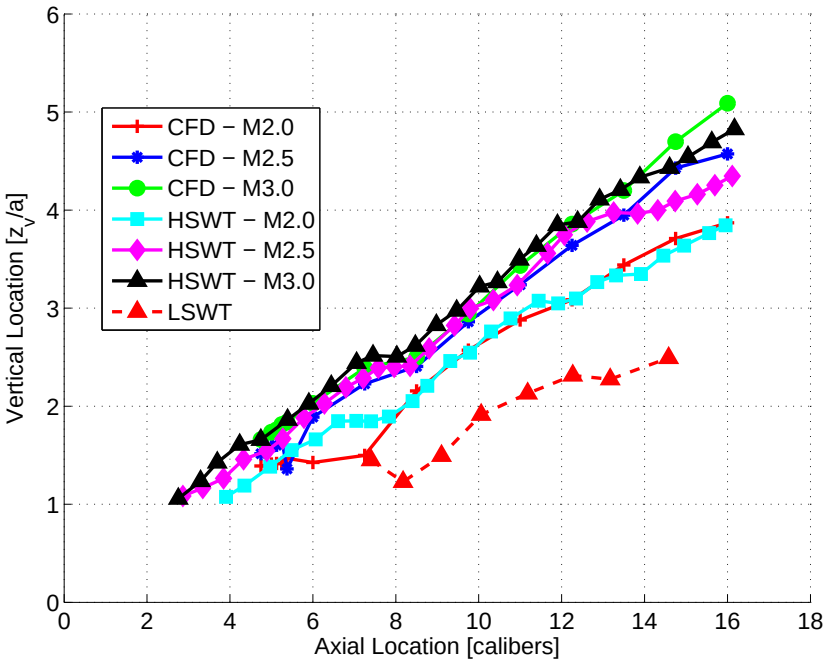

(b) Vertical Body

Figure 4.44: CFD and experimental comparisons of concentrated body vortex positions at $\alpha = 20°$

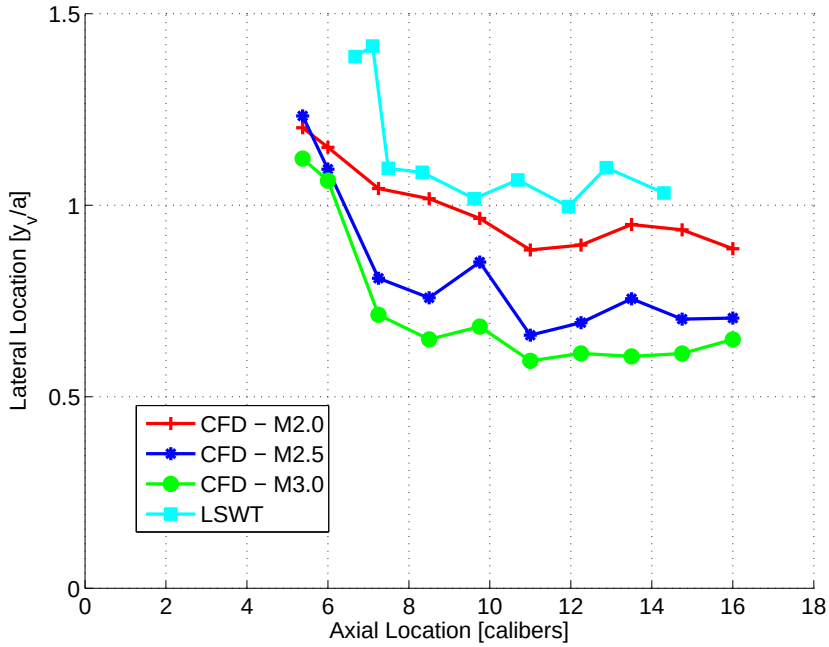

(a) Lateral Strake

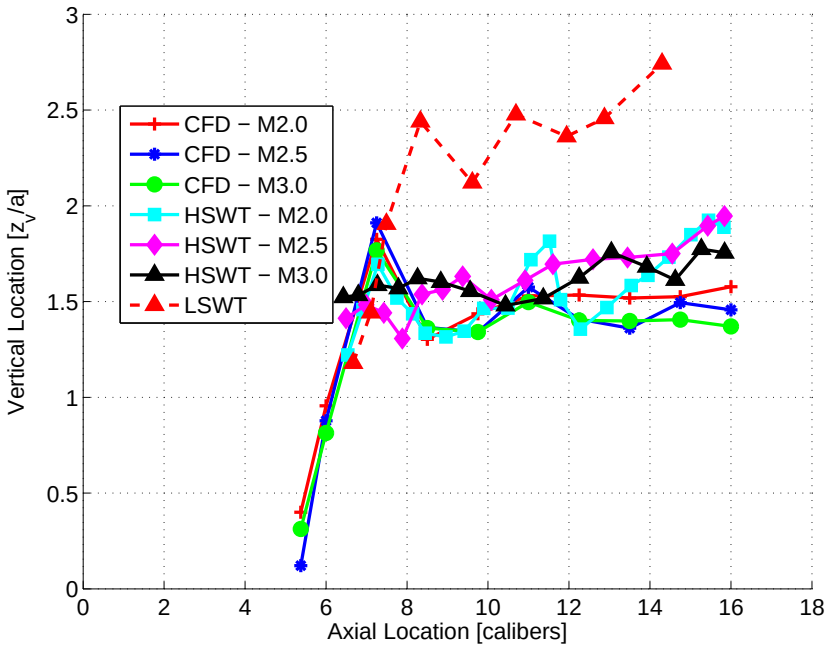

(b) Vertical Strake

Figure 4.45: CFD and experimental comparisons of concentrated strake vortex positions at $\alpha = 25°$

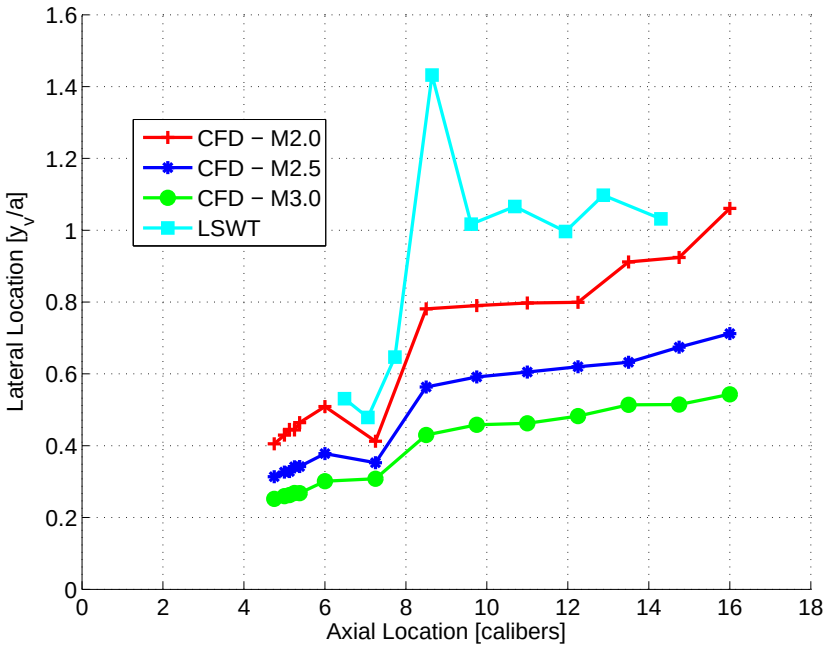

(a) Lateral Body

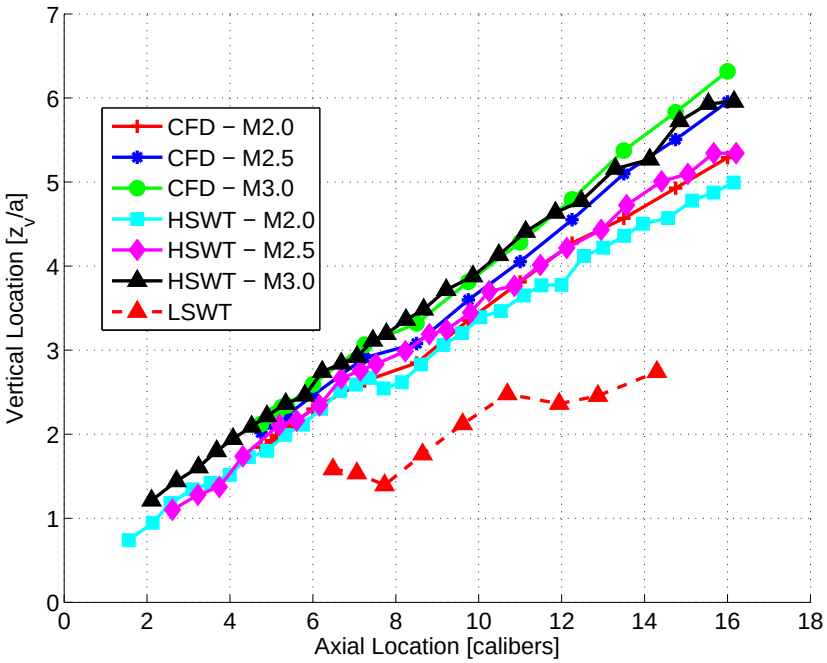

(b) Vertical Body

Figure 4.46: CFD and experimental comparisons of concentrated body vortex positions at $\alpha = 25°$

4.5 Body Aerodynamics

The body alone loads do not exhibit any particularly extraordinary features not identified by existing literature (see Figure 4.5). Of interest is the increase in normal force as the Mach number increases from 2.0 to 3.0. This is explained by viewing this from a 2D perspective, where there is an increase in the cross flow drag coefficient at cross flow Mach numbers of $M_c \approx 0.43$ and peaks at $M_c = 0.9$ (see Figure 2.5). At a freestream Mach number of 3.0 the peak corresponds to a cross flow Mach number of $M_c = 1.03$.

From the CFD simulations, the first symmetric vortices appear at the start of the strake axial location i.e. axial location of 4.75D, only at angles of attack above 10° which correlates with the empirical method of reference [20]. This is shown in Figure 4.47, which compares the 6°, 10° and 15° simulations at the axial location where the strakes start for Mach 2.0. The λ_2-criterion is used to determine the location of vortices. At 6° no vortices appear at the axial location of the start of the strakes whilst at 10° a weak vortex forms, whereas at 15° a vortex is fully present. The vortex at 15° is initiated by a termination shock on the lee side of the body as shown in Figure 4.48, where contours of cross flow Mach number are plotted with the contour of λ_2-criterion (of -5×10^6) to outline the vortex position. The body vortex at 10° at the axial location of 4.75D is therefore arguably a thickened boundary layer.

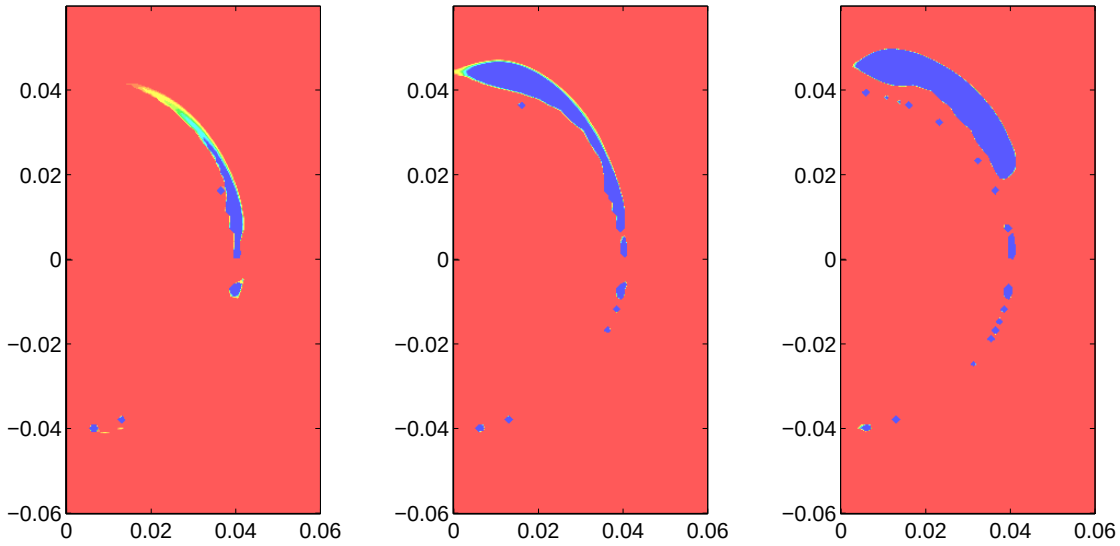

(a) 6° (b) 10° (c) 15°

Figure 4.47: Body vortex comparison for angles of attack of 6°, 10° and 15° at 4.75D

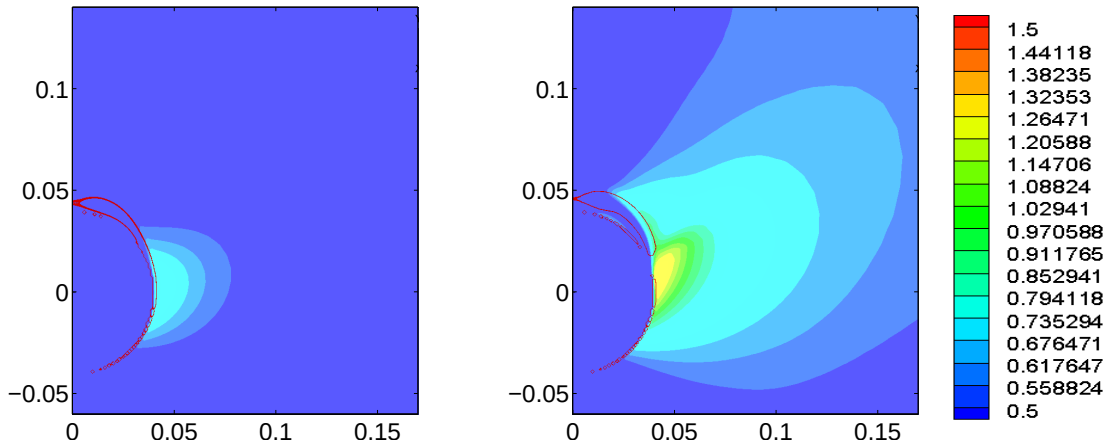

(a) 10° (b) 15°

Figure 4.48: Body vortex and cross flow Mach number comparison for angles of attack of 10° and 15° at 4.75D

The high speed supersonic tests, even though not clearly visible due to camera resolution limitations, do not reveal a vortex at the location of the start of the strakes at angles of attack below 15° (see Figure 4.25) therefore validating the CFD predictions. The formation of vortices from the apex of the nose at angles of attack from 20° onwards is also confirmed by the Schlieren of the high speed tests. The vortices remain symmetric as confirmed by the force and moment data of the validation tests and as expected by the asymmetry criteria of reference [43].

Of interest is the change in vortex structure for the flow at angles of attack greater than 10°. This is due to the onset of the shedding of multiple vortices and is intimated to by the change shift in centre of pressure (see Figure 4.14). At an angle of attack of 15° two different structures exist at Mach 2.0, 2.5 and 3.0. For Mach 2.0 the shed vortex sheet rolls into a single vortex sheet along the complete length of the body, whilst at Mach 2.5 and 3.0 the first vortex sheds establishing a second vortex. At the angle of attacks of 20° and 25° only two vortices are established for all the Mach numbers. When referring to the vortex shedding work by Thomson and Morrison [39] no indication of the vortex structures can be inferred for symmetric vortices because their study was focussed on asymmetric vortex shedding (which can be modeled by the impulsively started flow analogy or yaw cylinder). Symmetric vortices are also observed from the Schlieren images. Therefore only when the angle of attack increases beyond the total nose angle are asymmetric vortices shed [43] which for this configuration is 38.75°. For this configuration no definitive evidence exists for more than two vortices being shed and that the shed vortices become asymmetric i.e. they remain symmetric.

4.6 Strake Aerodynamics

The normal force of the strake, non-dimensionalised to the area of the strake, and the centre-of-pressure in semispan units, has already been shown in Figure 4.7. A small Mach number effect is noticeable. Note that the length of the strake is 45 times the length of the span, and hence 90 times the length of the semispan. The normal force displays the non-linear nominally second order characteristic whilst the centre-of-pressure starts (non-dimensionalised to the root chord) at approximately 1/3rd from the nose and asymptotes to the area centroid of the strake (which is just aft of half the length of the strake because the strakes has a 45° leading edge sweep) as the flow becomes more 2D in nature as the angle of attack increases.

The aerodynamics of the strake are dominated by the separation at the side edge. The leading edge of the strake is supersonic for the Mach numbers of interest ($M \geq 2.0$), resulting in no leading edge vortex being shed. At low angles of attack, the flow that separates at the side edge rolls up into a single concentrated vortex. At higher angles of attack ($\alpha > 20°$) multiple vortices are shed. This progression is shown in a series of subfigures in Figure 4.49, by plotting iso contours of the λ_2-criterion for Mach 2.0 of -5×10^6. This is also shown in selected cross planes for Mach 2.0 for the angles of attack 10° to 30° in Figure 4.54 to Figure 4.50. The initiation of vortex shedding is illustrated in Figure 4.55 for Mach 2.5 and 3.0. At Mach 2.5 and 3.0, the angle of attack at which multiple vortices are shed is increasingly lower, pointing to it being dependent on the cross flow Mach number.

Of particular interest is the observation that the side edge vortex remains attached to the strake until the higher angles of attack.

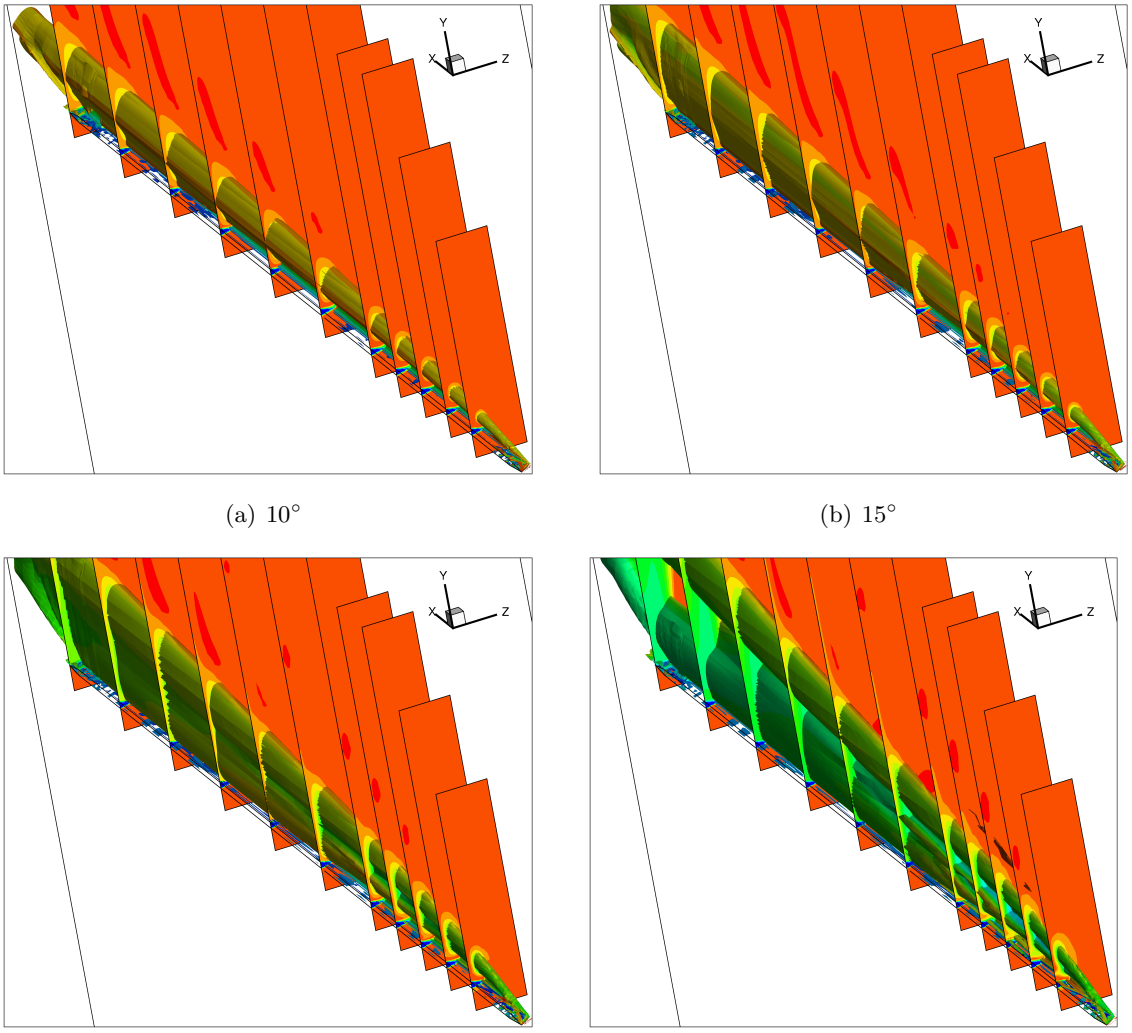

(a) 10°

(b) 15°

(c) 20°

(d) 25°

Figure 4.49: Side edge vortex development as a function of angle of attack

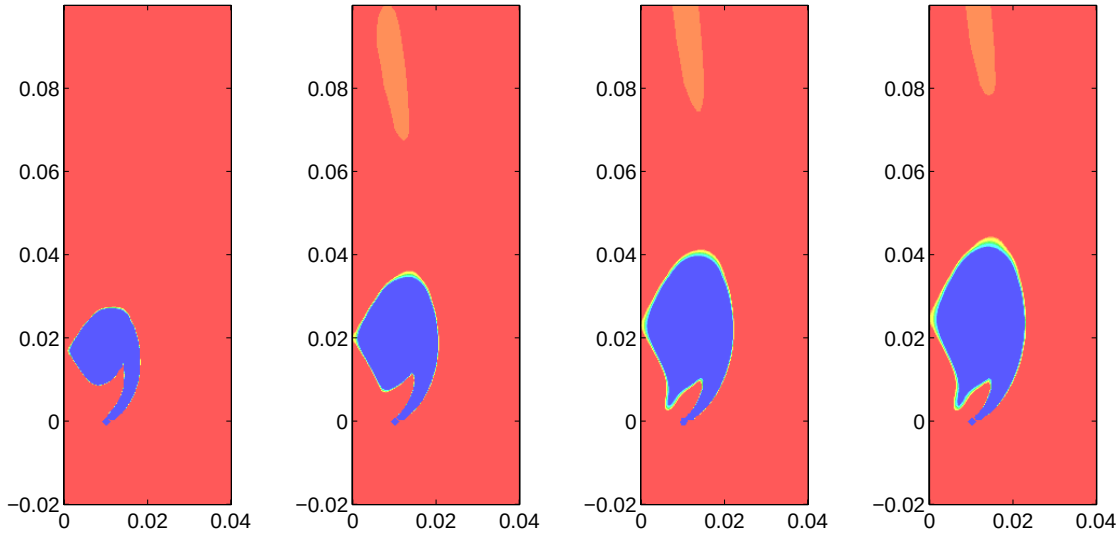

(a) 30ss (b) 50ss (c) 70ss (d) 80ss

Figure 4.50: Vortex development for strake only for $\alpha = 10°$ at Mach 2.0

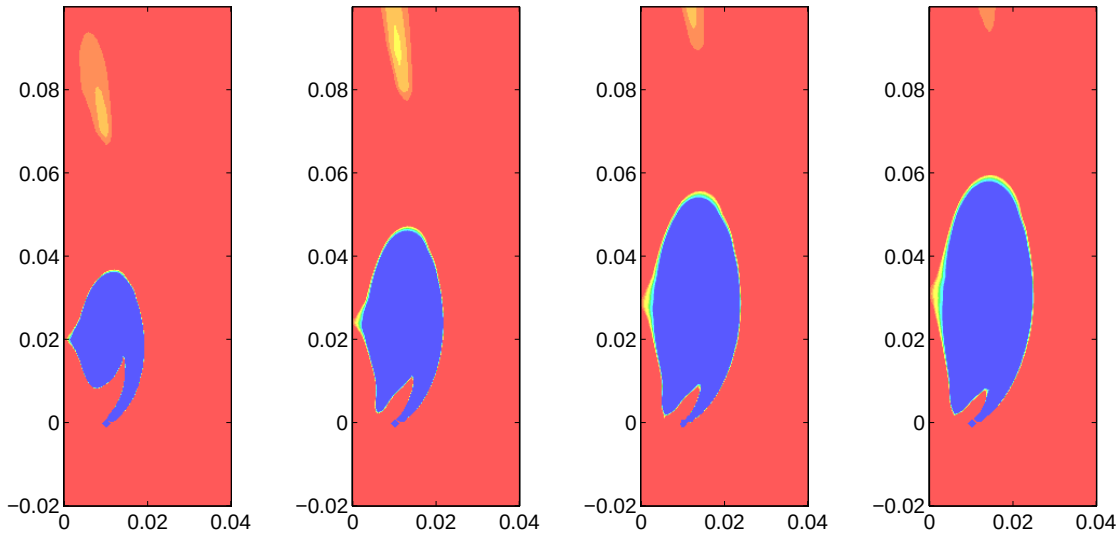

(a) 30ss (b) 50ss (c) 70ss (d) 80ss

Figure 4.51: Vortex development for strake only for $\alpha = 15°$ at Mach 2.0

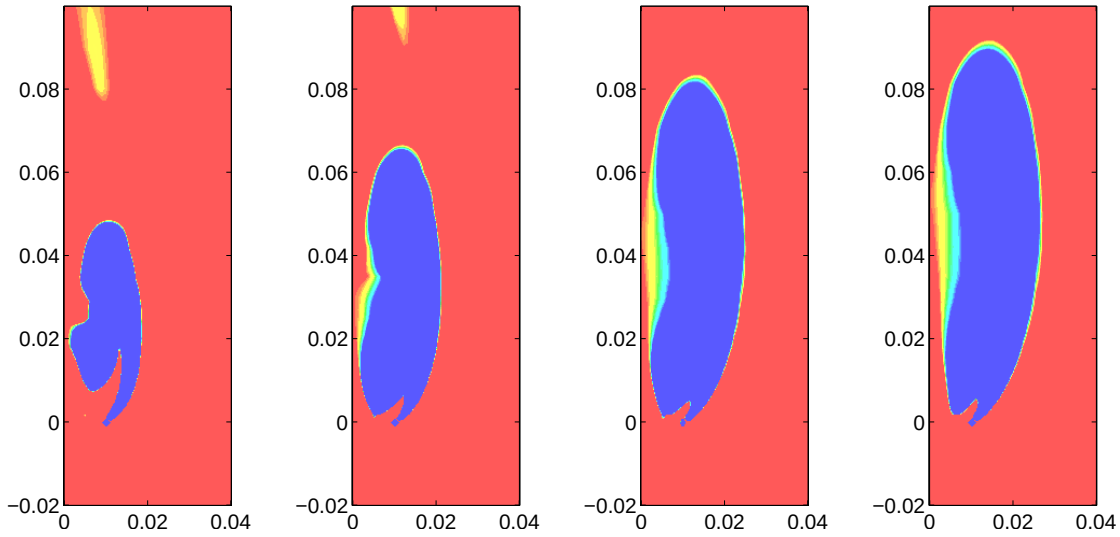

(a) 30ss (b) 50ss (c) 70ss (d) 80ss

Figure 4.52: Vortex development for strake only for $\alpha = 20°$ at Mach 2.0

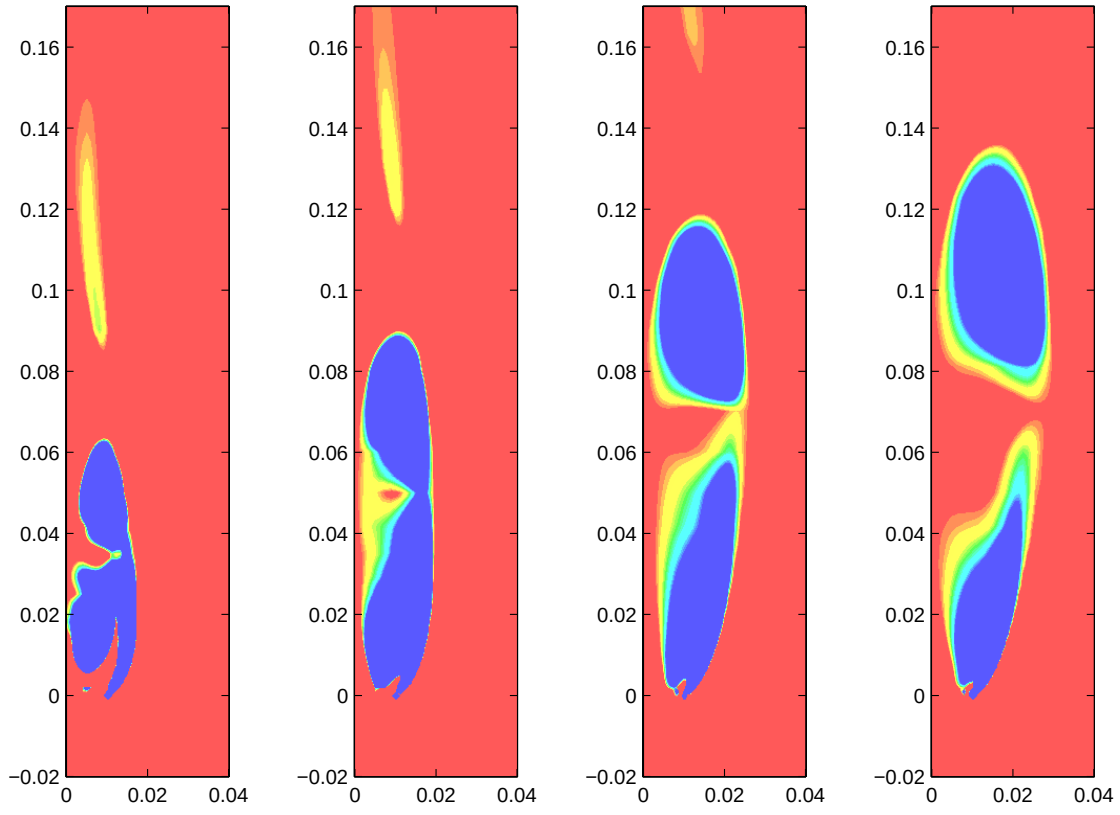

(a) 30ss (b) 50ss (c) 70ss (d) 80ss

Figure 4.53: Vortex development for strake only for $\alpha = 25°$ at Mach 2.0

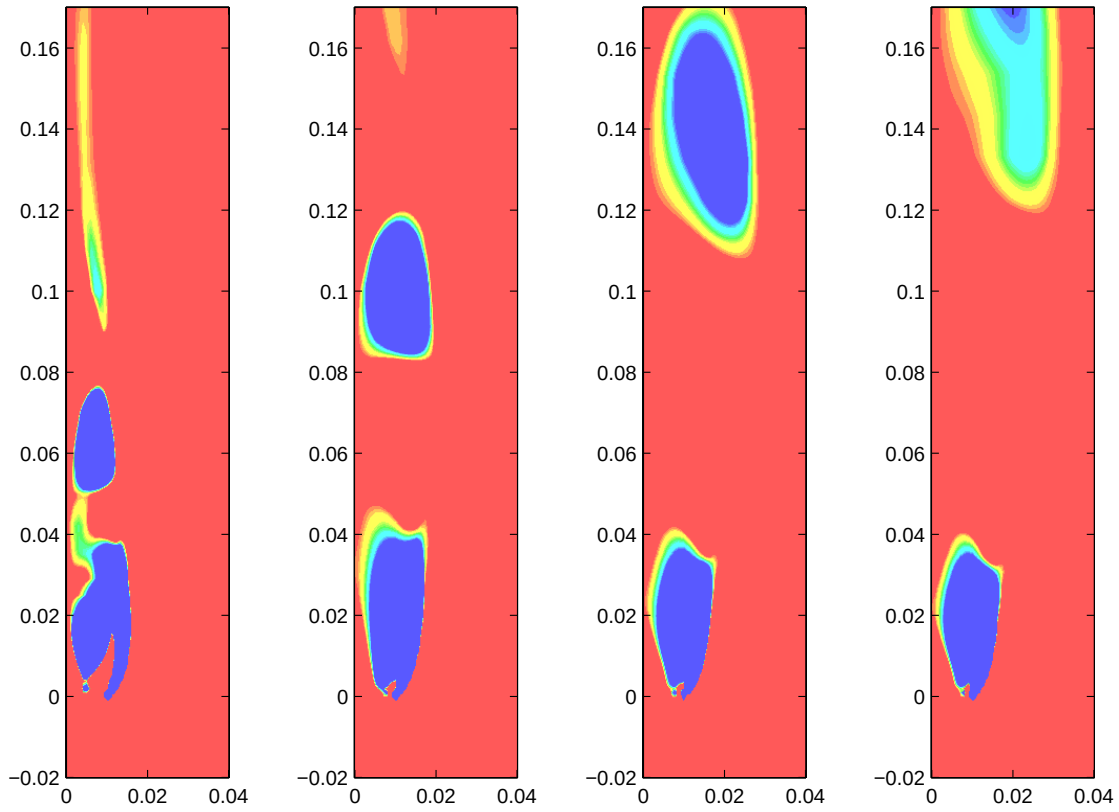

(a) 30ss (b) 50ss (c) 70ss (d) 80ss

Figure 4.54: Vortex development for strake only for $\alpha = 30°$ at Mach 2.0

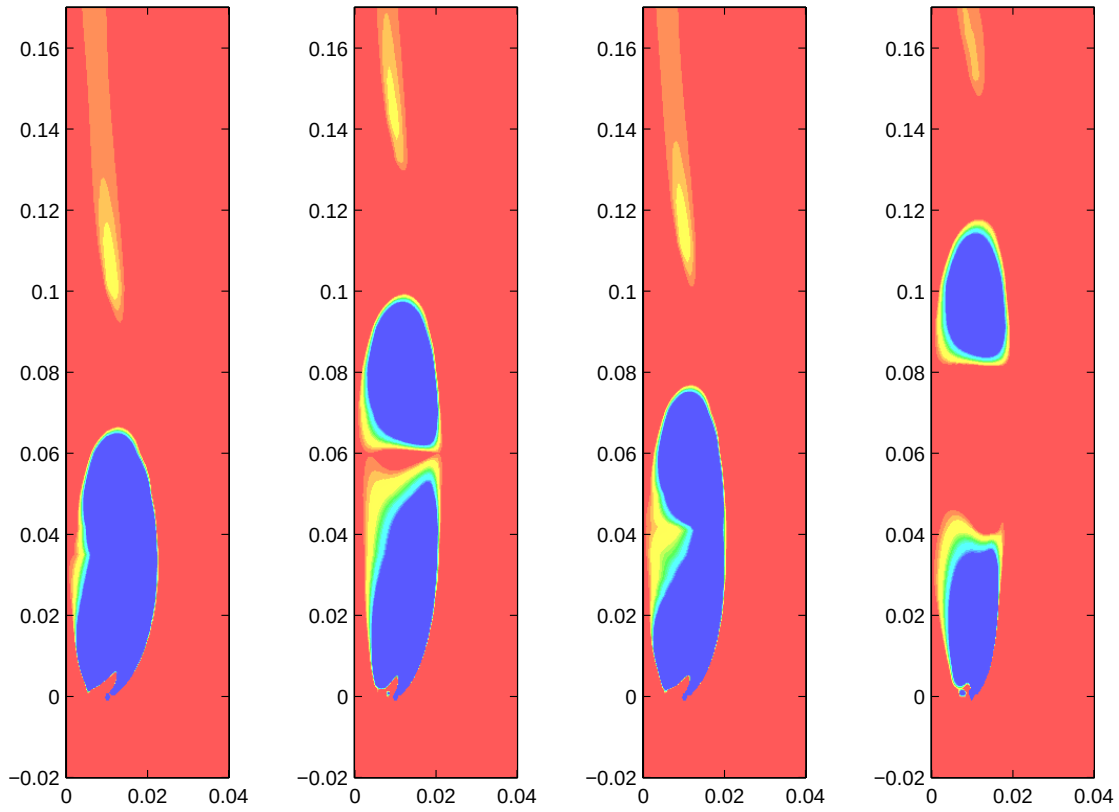

(a) Mach 2.5, 15° (b) Mach 2.5, 20° (c) Mach 3.0, 15° (d) Mach 3.0, 20°

Figure 4.55: Vortex development for strake only at Mach 2.5 and 3,0

4.7 Body-Strake Aerodynamics

The aerodynamics of circular bodies with very low aspect ratio wings are dominated by the side edge vortex, and at higher angles of attack the interaction of the side edge and body vortex or vortices.

4.7.1 Force and Moment Results

The normal force and centre-of-pressure for the body-strake configuration have already been illustrated in Figure 4.6. A small Mach number effect is noticeable for the body-strake configuration, with the normal force reducing at the higher angles at the higher Mach numbers, pointing towards a possible Mach number effect. The effect of the strake i.e. body plus strake less the body alone, on the gross loads, C_{N_S}, is shown in Figure 4.56. More clearly noticeable than on the body-strake configuration is the effect of Mach number. For Mach 2.0 and 2.5, and Mach 3.0 and angles of attack below 20°, this is due to the increase in normal force of the body only configuration (see Figure 4.5) rather than the reduction in normal force of the body-strake configuration (see Figure 4.6). The reduction for Mach 3.0 at angles above 15° is not easily identified since both the body alone and body-strake normal forces decrease relative to the Mach 2.5 and 2.0 cases. This may be indicative of a distinctive Mach number effect which only starts at Mach 3.0.

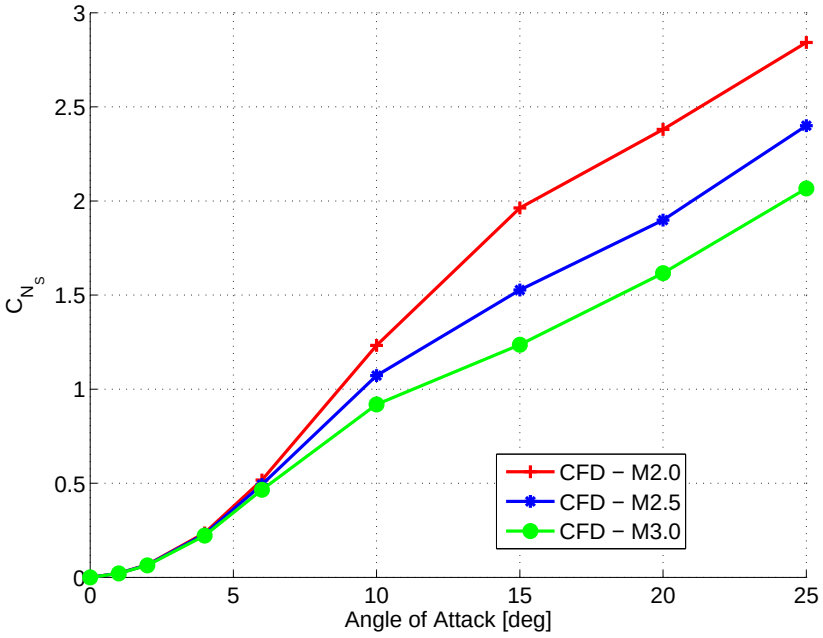

Figure 4.56: Strake effect on full configuration normal force as a function of angle of attack

4.7.2 Strake Vortex Dynamics

The side edge vortex development for angles of attack of 4°, 10°, 15° and 25° are shown in Figure 4.57 to Figure 4.60 by plotting iso contours of the λ_2-criterion of -5×10^6 for Mach 2.0. Two views are shown to illustrate the complex structures especially at moderate angles of attack. At low angles of attack (up to 4°) the vortex remains attached to the strake. As the angle of attack increases, the vortex sheet exhibits tearing, yet the vortex sheet rolls into a single vortex. This is similar to the body alone behaviour where the axial velocity organises the rolled up vortex sheets into two symmetric vortices. Above 15°, vortex shedding occurs (as characterised by Figure 4.60).

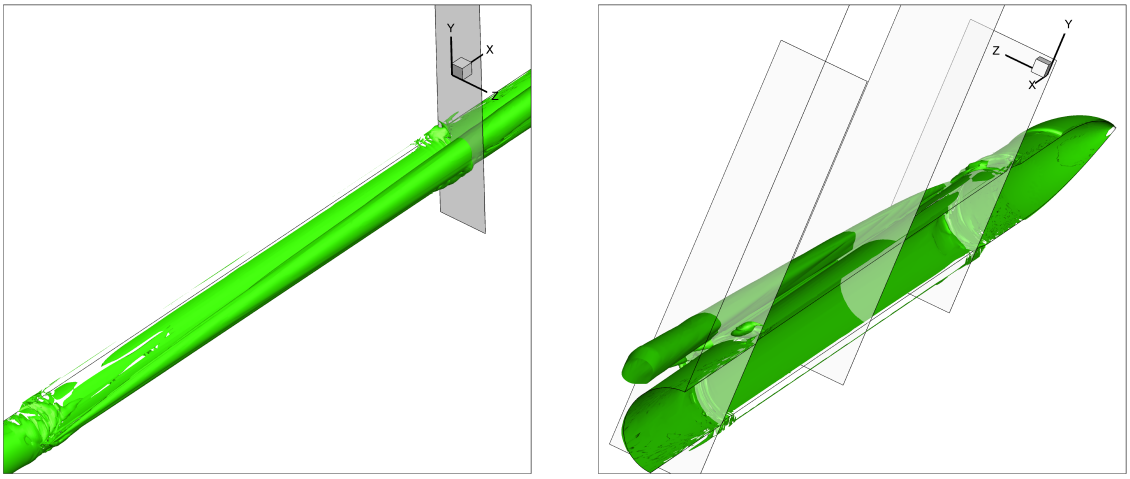

Figure 4.57: Body and strake side edge vortex at $\alpha = 4°$

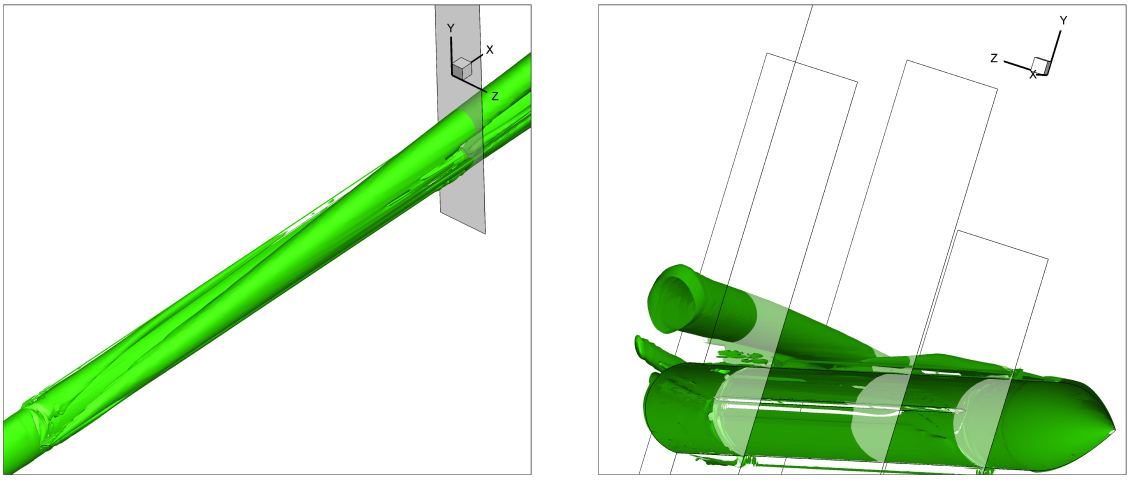

Figure 4.58: Body and strake side edge vortex at $\alpha = 10°$

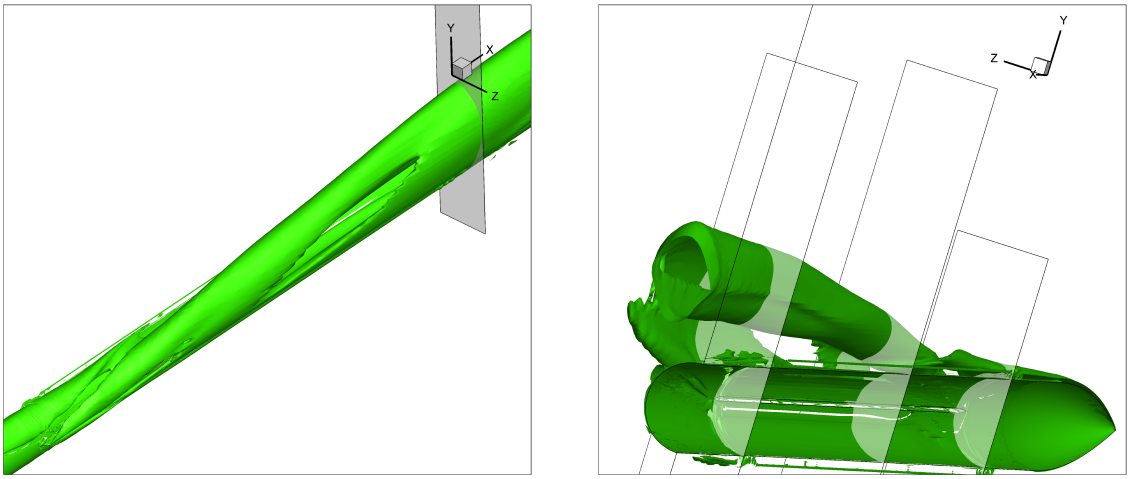

Figure 4.59: Body and strake side edge vortex at $\alpha = 15°$

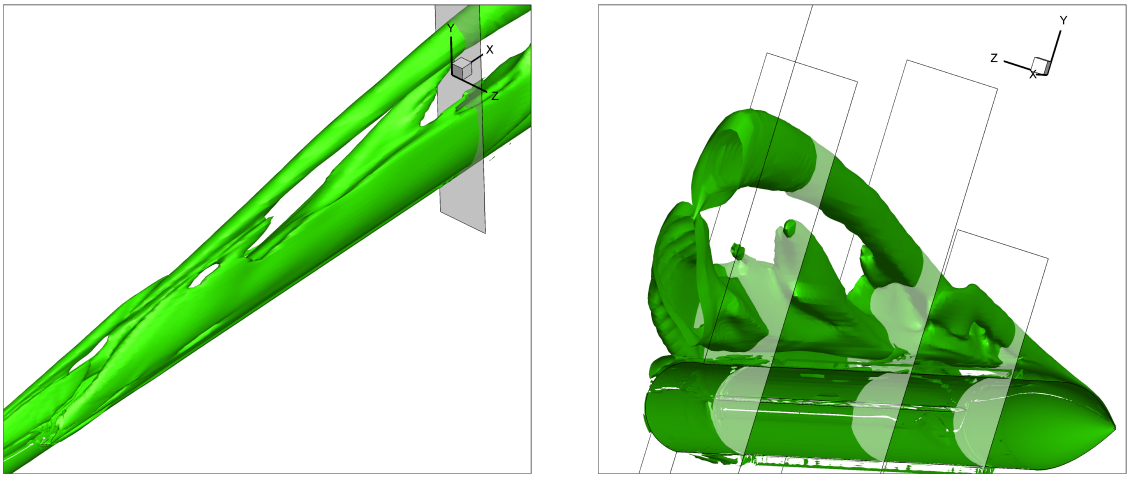

Figure 4.60: Body and strake side edge vortex at $\alpha = 25°$

A comparison of the lee side vortex development of the body alone, and body-strake configuration is shown in Figure 4.61 to Figure 4.68. As can be seen, at the low angles, the side edge vortex dominates where at angles of attack below 6° no body vortex exists. From angles of attack 6° to 15° the single vortex of the body is similar to the single vortex of the body and strake. At angles of attack below 20° the shed vortex sheet at the edge of the strake rolls up into only one single concentrated vortex, even though the side edge sheet exhibits tearing. At the angles of attack where a body vortex exists, the body vortex initially coalesces with the side edge vortex sheet. At the higher angles of attack two separate vortices result from the single coalesced vortex, with the lower vortex being locationally closer to the body than at lower angles of attack.

In contrast to the strake only, the side edge vortex separates from the strake at moderate angles of attack i.e. $\geq 4°$. This is a distinct difference compared to the strake alone vortex dynamics and shows the influence of body and therefore the wing-body interaction and its effect on the rolled up vortex.

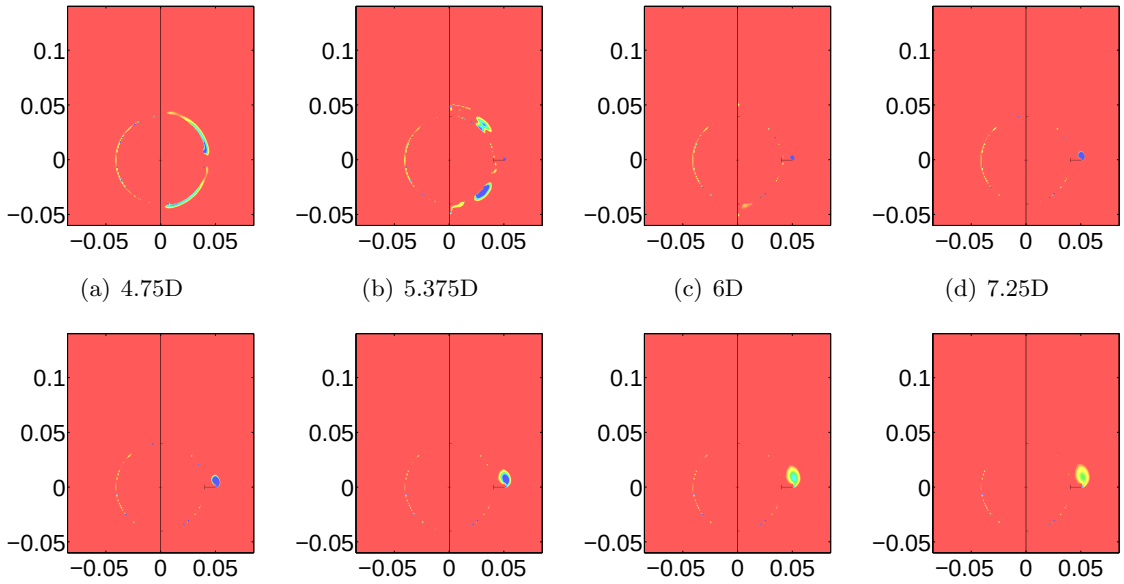

(a) 4.75D (b) 5.375D (c) 6D (d) 7.25D

(e) 8.5D (f) 11D (g) 13.5D (h) 14.75D

Figure 4.61: Vortex development for $\alpha = 1°$, body compared to body and strake at Mach 2.0

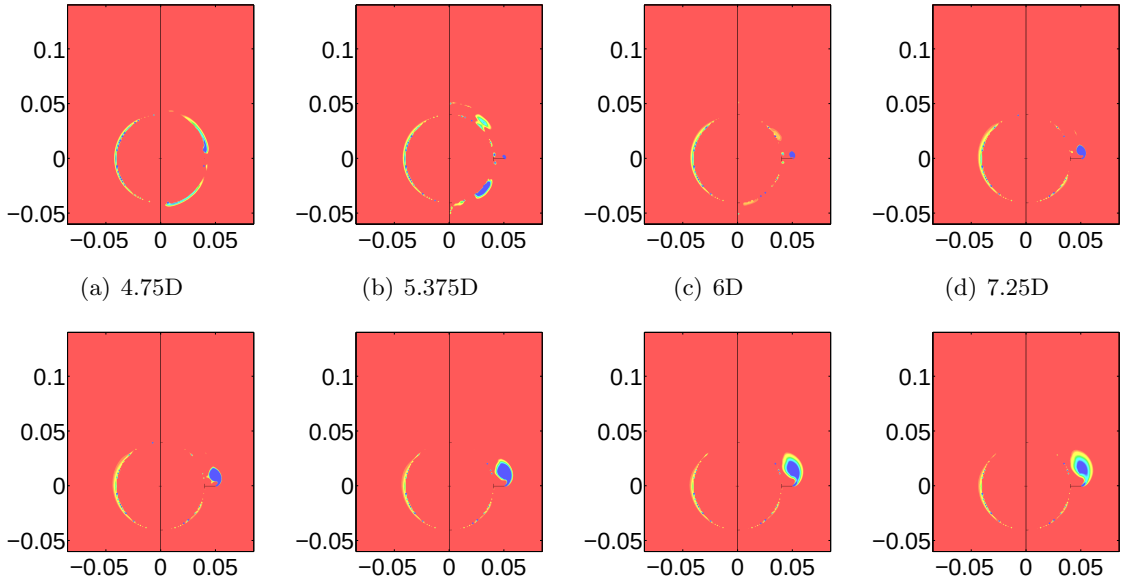

(a) 4.75D (b) 5.375D (c) 6D (d) 7.25D

(e) 8.5D (f) 11D (g) 13.5D (h) 14.75D

Figure 4.62: Vortex development for $\alpha = 2°$, body compared to body and strake at Mach 2.0

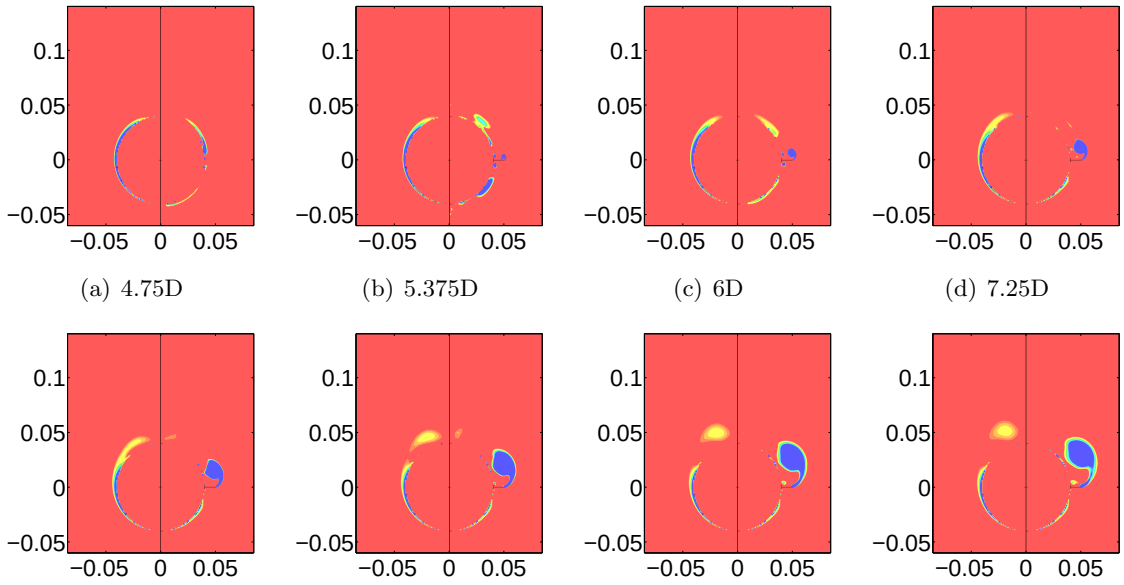

(a) 4.75D (b) 5.375D (c) 6D (d) 7.25D

(e) 8.5D (f) 11D (g) 13.5D (h) 14.75D

Figure 4.63: Vortex development for $\alpha = 4°$, body compared to body and strake at Mach 2.0

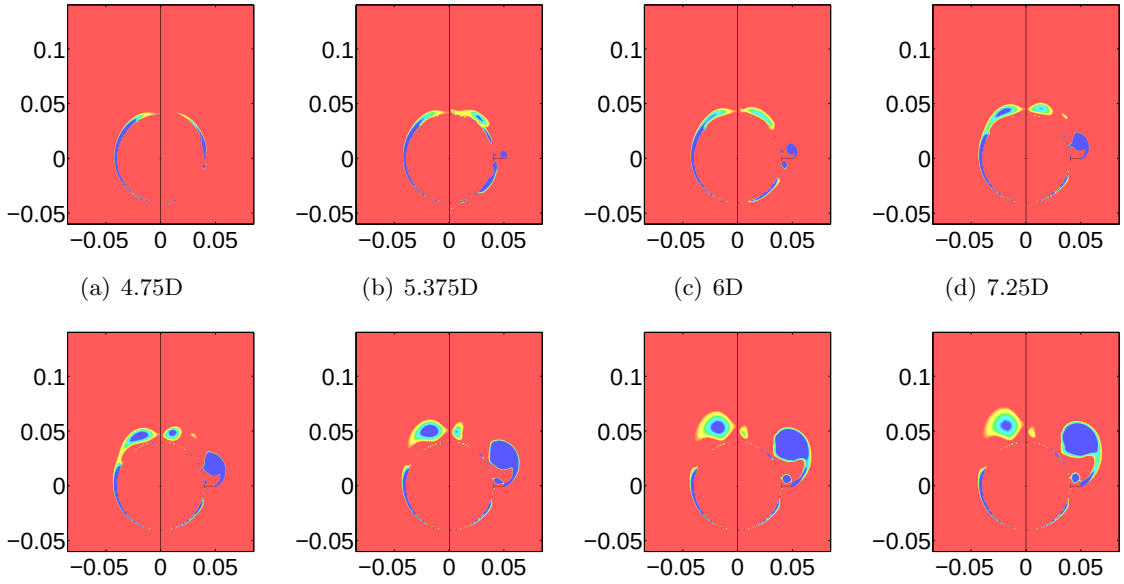

(a) 4.75D (b) 5.375D (c) 6D (d) 7.25D

(e) 8.5D (f) 11D (g) 13.5D (h) 14.75D

Figure 4.64: Vortex development for $\alpha = 6°$, body compared to body and strake at Mach 2.0

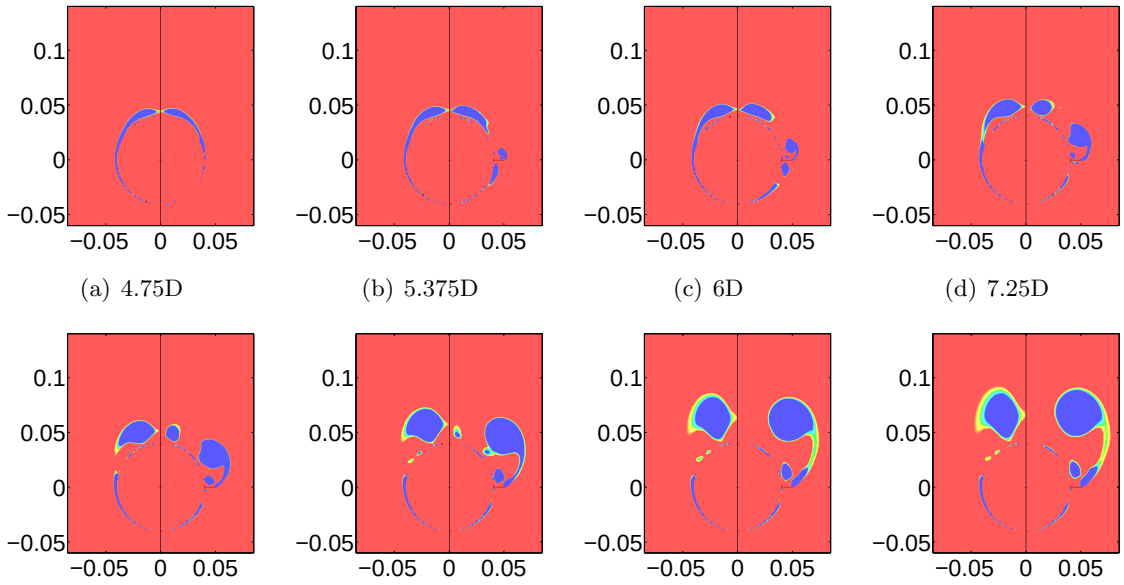

(a) 4.75D (b) 5.375D (c) 6D (d) 7.25D

(e) 8.5D (f) 11D (g) 13.5D (h) 14.75D

Figure 4.65: Vortex development for $\alpha = 10°$, body compared to body and strake at Mach 2.0

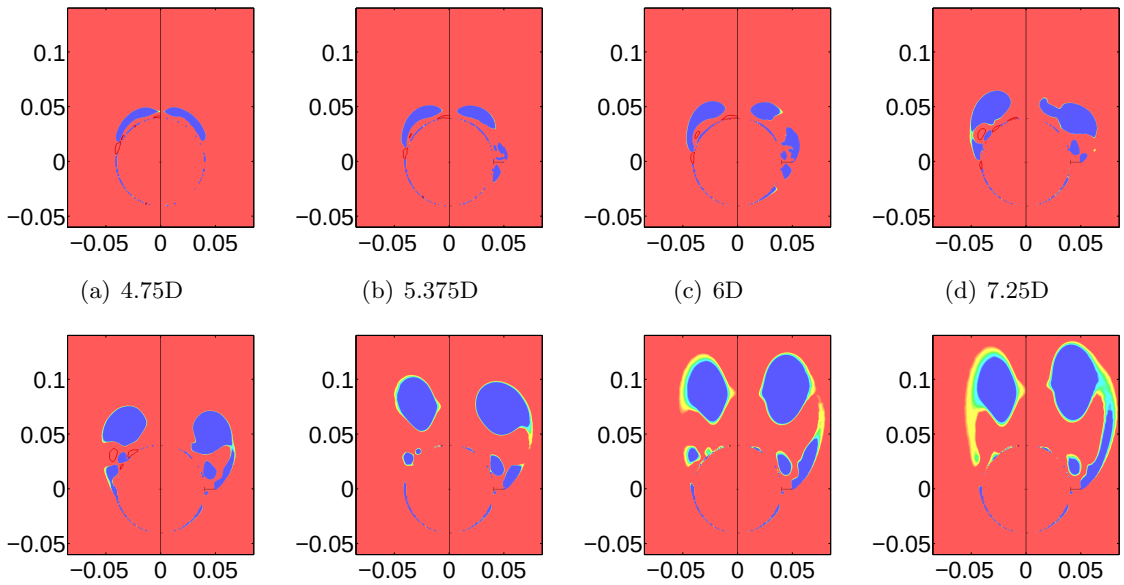

(a) 4.75D (b) 5.375D (c) 6D (d) 7.25D

(e) 8.5D (f) 11D (g) 13.5D (h) 14.75D

Figure 4.66: Vortex development for $\alpha = 15°$, body compared to body and strake at Mach 2.0

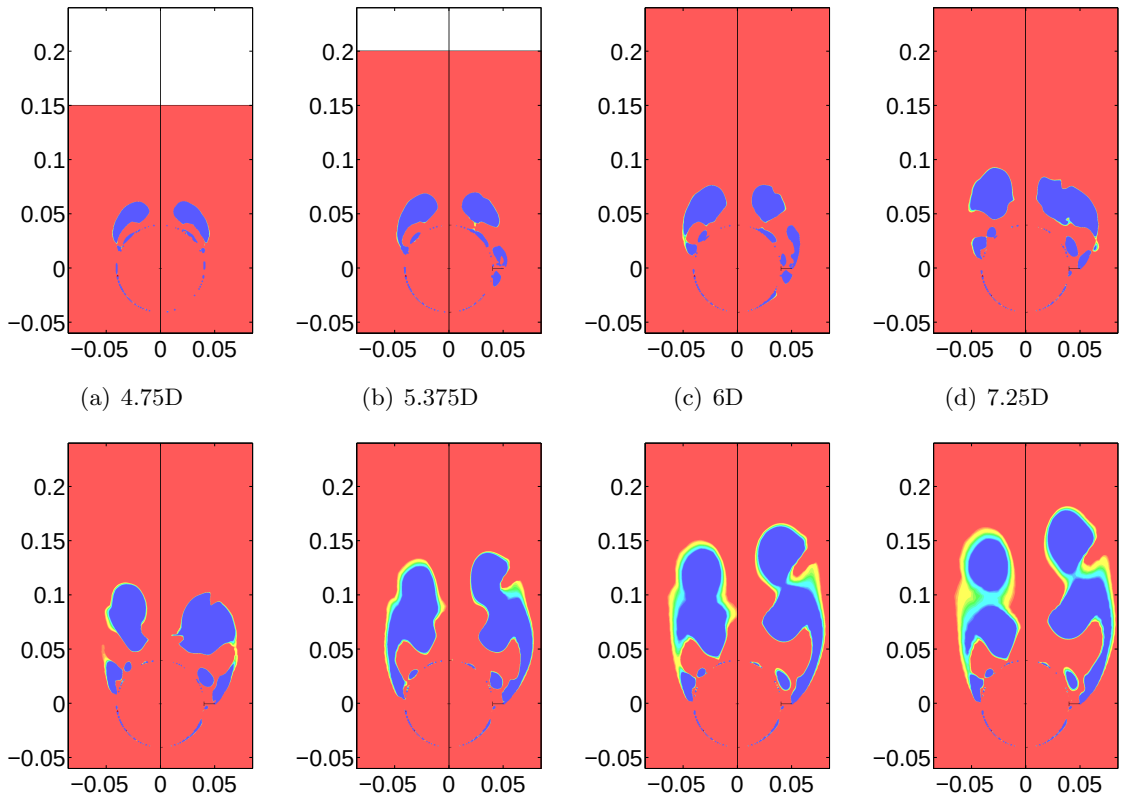

(a) 4.75D (b) 5.375D (c) 6D (d) 7.25D

(e) 8.5D (f) 11D (g) 13.5D (h) 14.75D

Figure 4.67: Vortex development for $\alpha = 20°$, body compared to body and strake at Mach 2.0

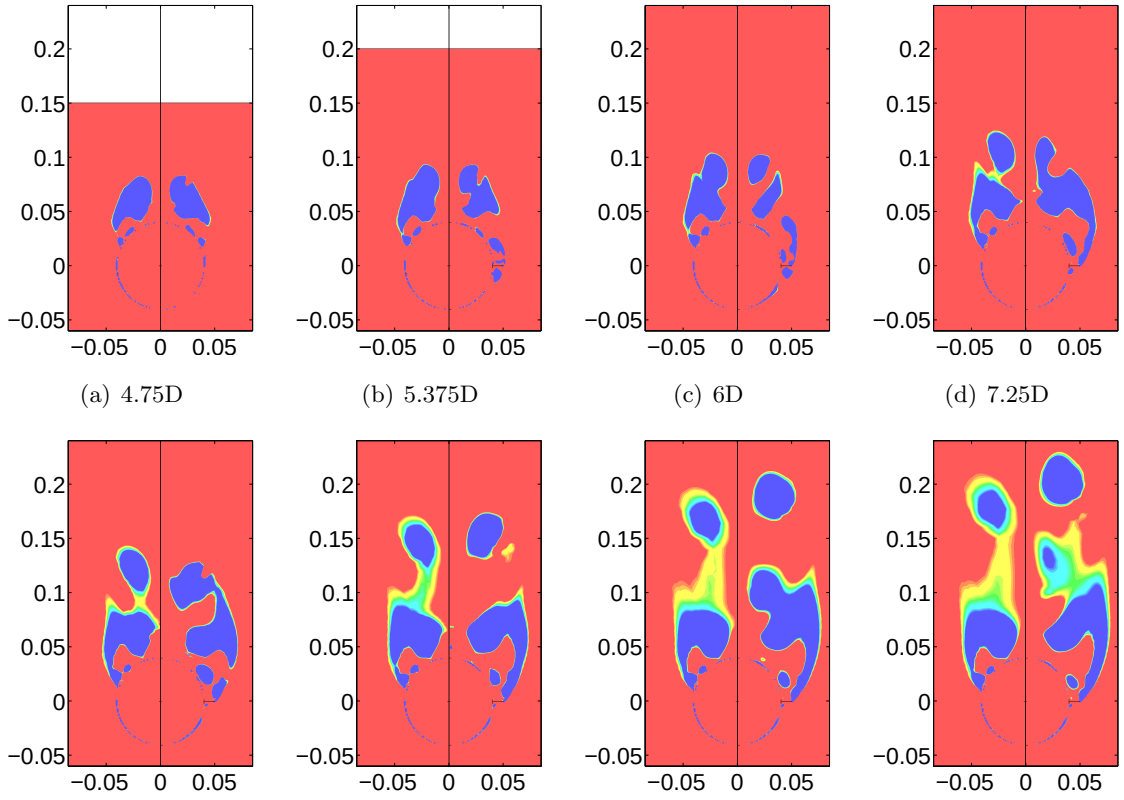

(a) 4.75D (b) 5.375D (c) 6D (d) 7.25D

(e) 8.5D (f) 11D (g) 13.5D (h) 14.75D

Figure 4.68: Vortex development for $\alpha = 25°$, body compared to body and strake at Mach 2.0

4.7.3 Body-on-Wing Carryover Factor

The body-on-wing carryover factor, K_{W_B} is predicted well by both the slender body theory and the corrections used by Missile Datcom for the semi-span to body diameter ratios being considered [13]. The predictions by Missile Datcom are shown in Figure 4.69 for the Mach number under consideration. A small Mach number effect is present. From the CFD simulations no direct measurement of the body-on-wing factor can be obtained. The accuracy of body-on-wing effect can, however, be assessed by comparing the wing alone normal force in the presence of the body, $C_{N_{S_I}}$. These were extracted from the CFD simulations and compared to the product of the strake alone normal force and K_{W_B}. This is illustrated in Figure 4.70. A good correlation is demonstrated and is due to the short span of the wings compared to the body diameter. This good correlation is expected because the variation in velocity across the span is small when compared to wings of larger span to diameter ratios. The Datcom predictions include the induced velocity due to the body vortex at higher angle of attack. This is averaged over the length of the strake and is reasonable in its prediction when compared to the CFD simulations.

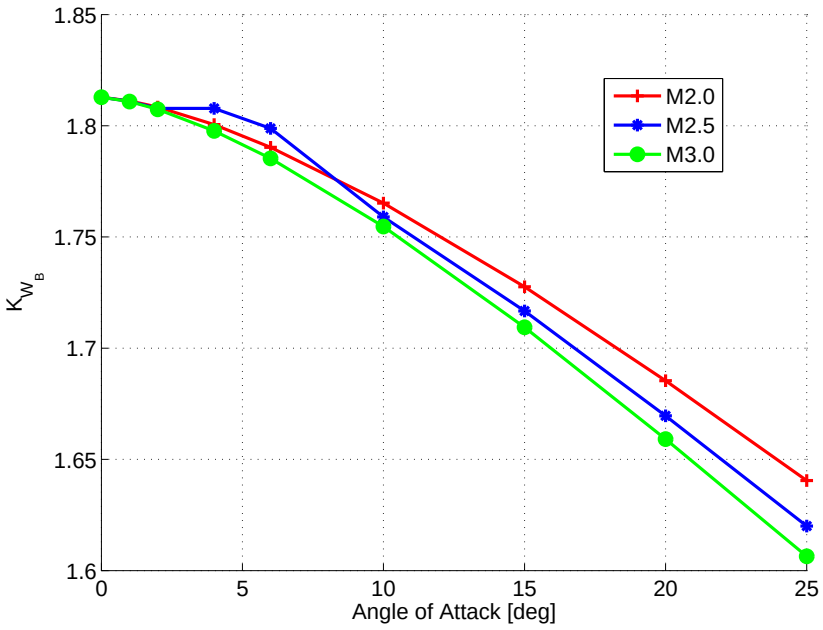

Figure 4.69: Body-to-wing carryover factor, K_{W_B}, as predicted by Missile Datcom

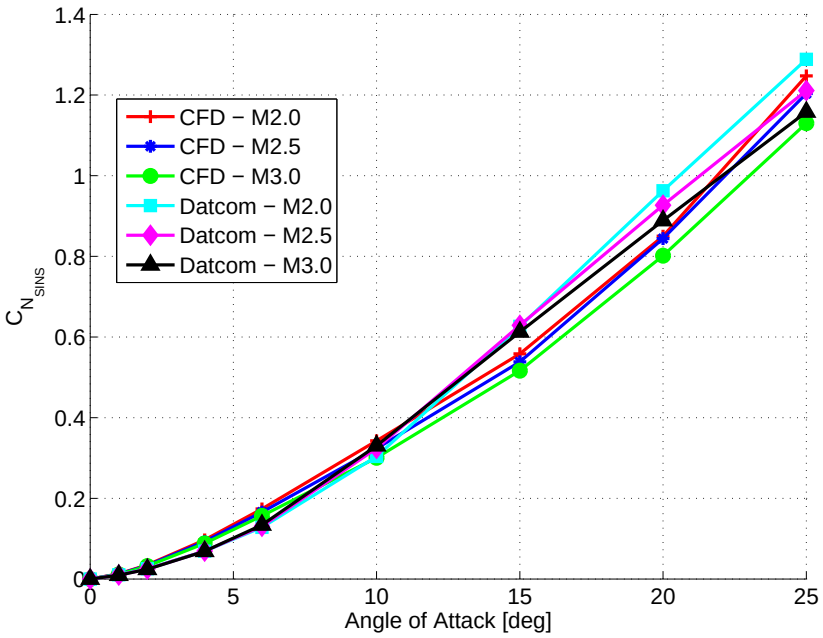

Figure 4.70: Installed strake normal force comparison

4.7.4 Wing-to-Body Carryover Factor

The wing-to-body carryover factor, K_{W_B}, was calculated using the equivalent angle of attack method because the strake normal force is not linear with angle of attack in the range under consideration ($0 < \alpha < 40$). K_{B_W} is thus calculated using the local induced angle of attack as determined by the body-on-wing carryover factor, K_{W_B}. K_{B_W} is not well predicted by slender body theory even though the equivalent angle of attack method is used, which is in contrast to K_{W_B}. The correlation would be completely incorrect if the linear formulation of Equation 1.5 were used because the zero angle of attack strake normal force slope is very low (0.00244 /° for Mach 2.0). As already indicated in the literature survey, other analytical methods have been developed. These methods are based on linear theory, potential flow assumptions or use slender body carryover factors. Figure 4.71 shows K_{B_W} as a function of angle of attack for the numerical simulations and experimental tests, with the slender body theory prediction (which is independent of angle of attack).

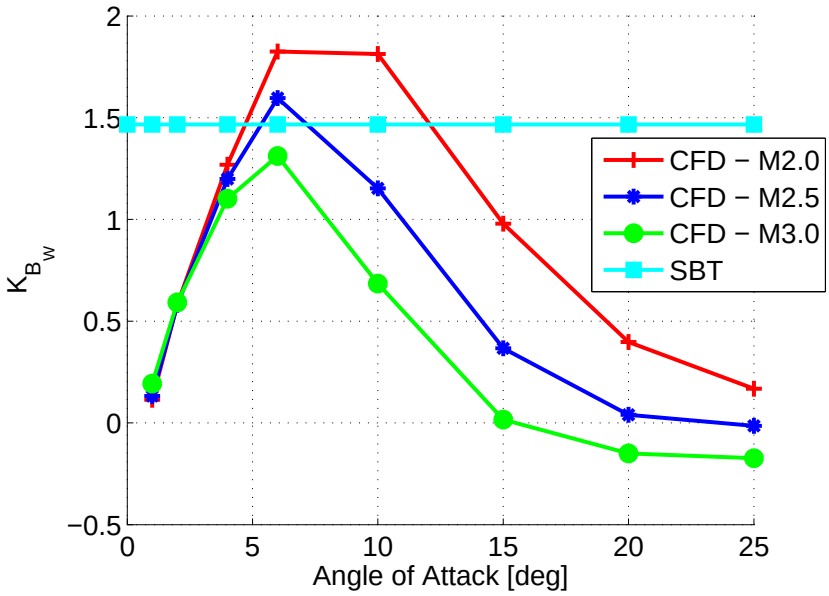

Figure 4.71: Wing-to-Body carryover factor

The results show a complex response of K_{B_W} with angle of attack. At low angles of attack, K_{B_W} is a relatively linear function of angle of attack for the Mach numbers being considered, with the wing carryover effect increasing as the angle of attack increases. At higher angles of attack this effect drops off to low or even negative values. A Mach number effect is also present and is a direct result of the increase in normal force with Mach number as discussed in the forces and moments subsection (see subsection 4.7.1).

4.8 Aftbody Vortex Shedding

Due to the relatively short aftbody length it is not certain whether vortex shedding occurs because no direct evidence exists from the Schlieren images. The CFD simulations do however predict vortex shedding whose position is very close to the body and not above the body and therefore confirming its absence in the Schlieren images. Figure 4.72 shows the shed vortex shed at 25° at Mach 2.0 and aftbody loads as a function of angles of attack. The aftbody therefore represents just less than 10% of the overall load for the body-strake configuration.

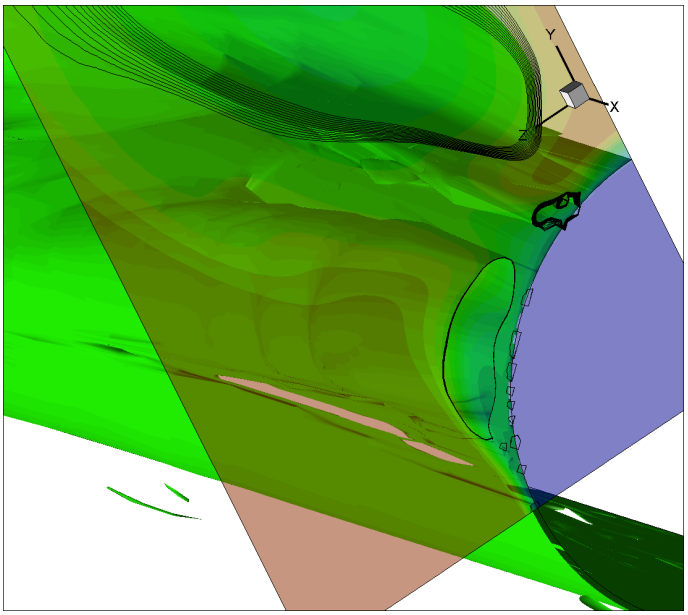

(a) Vortex Position

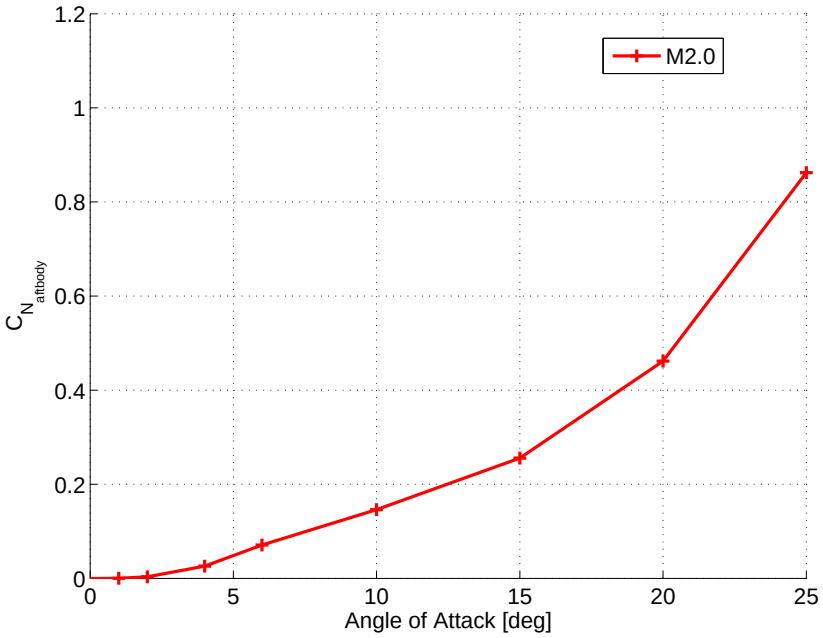

(b) Loads

Figure 4.72: Aftbody vortex shedding at 25° at Mach 2.0

4.9 Vortex Shedding Characteristics

For the three configurations simulated, the initiation of vortex shedding characteristics is particularly interesting. For the body-strake configuration this occurs at cross flow Mach numbers greater than 0.55. The strake alone configuration shows vortex shedding at higher angles of attack or that corresponding to the cross flow Mach number greater than 0.8.

Thomson and Morrison [39] indicated that the onset of the vortex shedding for body alone configurations was due to the establishment of shock waves in the lee side of the body. For this configuration it occurs at a cross flow Mach number of Mach 0.65 rather than 0.43 (the critical Mach number where the flow becomes Reynolds number insensitive and the drag coefficient starts to rise because shock waves trigger the separation of boundary layer [43] rather than the incompressible adverse pressure gradient). Figure 4.73 to Figure 4.75 show the development of shed vortices for Mach 3.0 for various angles of attack at selected body stations. The figures plot the cross-flow Mach number and contours of λ_2-criterion to show the vortex (ranging from -1×10^7 to -1×10^6). At 10° no vortex shedding occurs, but occurs at 15° and higher. From these figures it can be seen that vortex shedding is associated when supersonic cross flow is established (at Mach 3.0 and 10° the cross flow Mach number is 0.52) in the outer side region the vortex sheet and not just the body. Further investigation reveals that the vortex shedding is triggered by the recovery cross flow shock waves for both the flow in the region outside the vortex sheet and the reverse flow region along the symmetry plane (as seen at Mach 2.0 @ 20°). Both shocks interact with the vortex precipitating the vortex shedding. For the body alone configuration this only occurs at higher cross flow Mach numbers compared to the body-strake configuration.

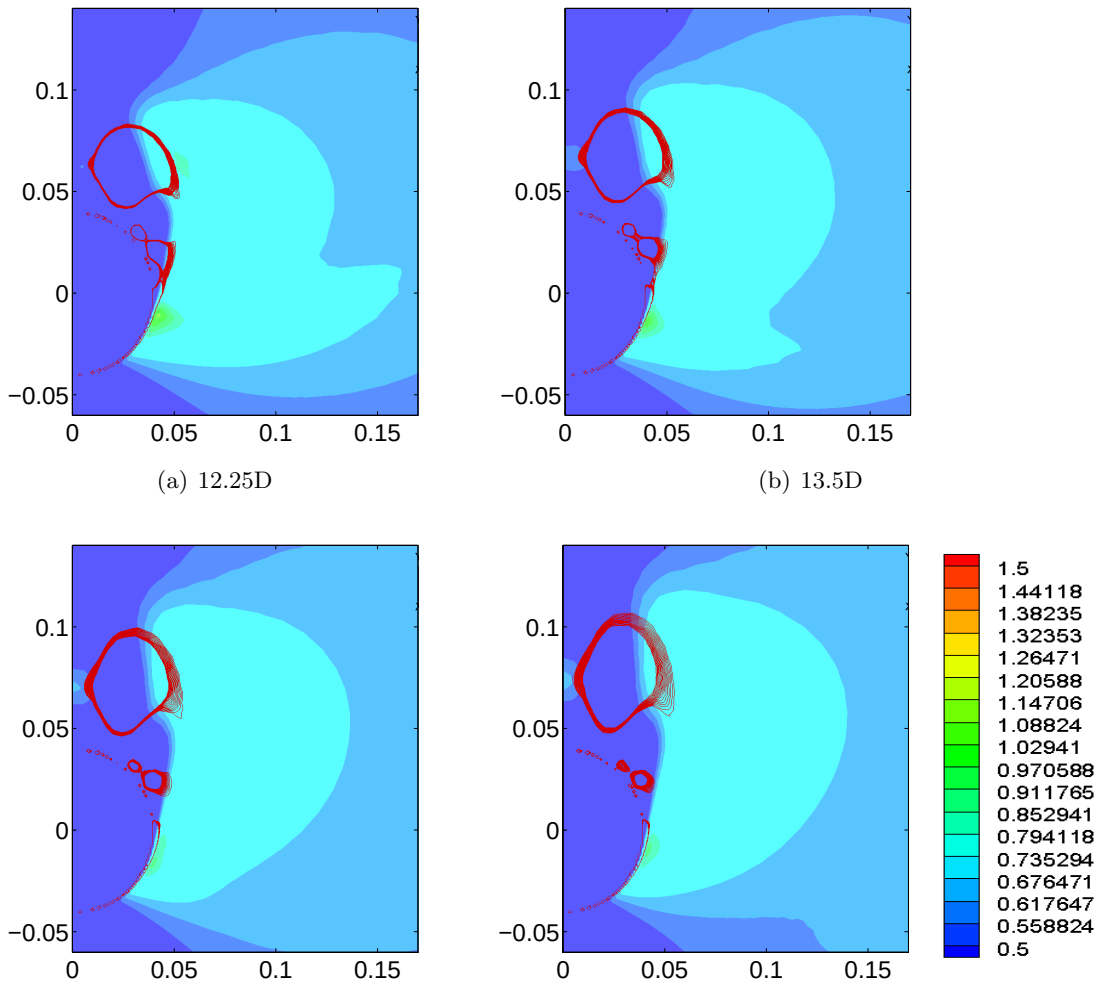

(a) 12.25D

(b) 13.5D

(c) 14.75D

(d) 16D

Figure 4.73: Body alone cross flow Mach number and vortex position at Mach 3.0 at $\alpha = 10^{\circ}$

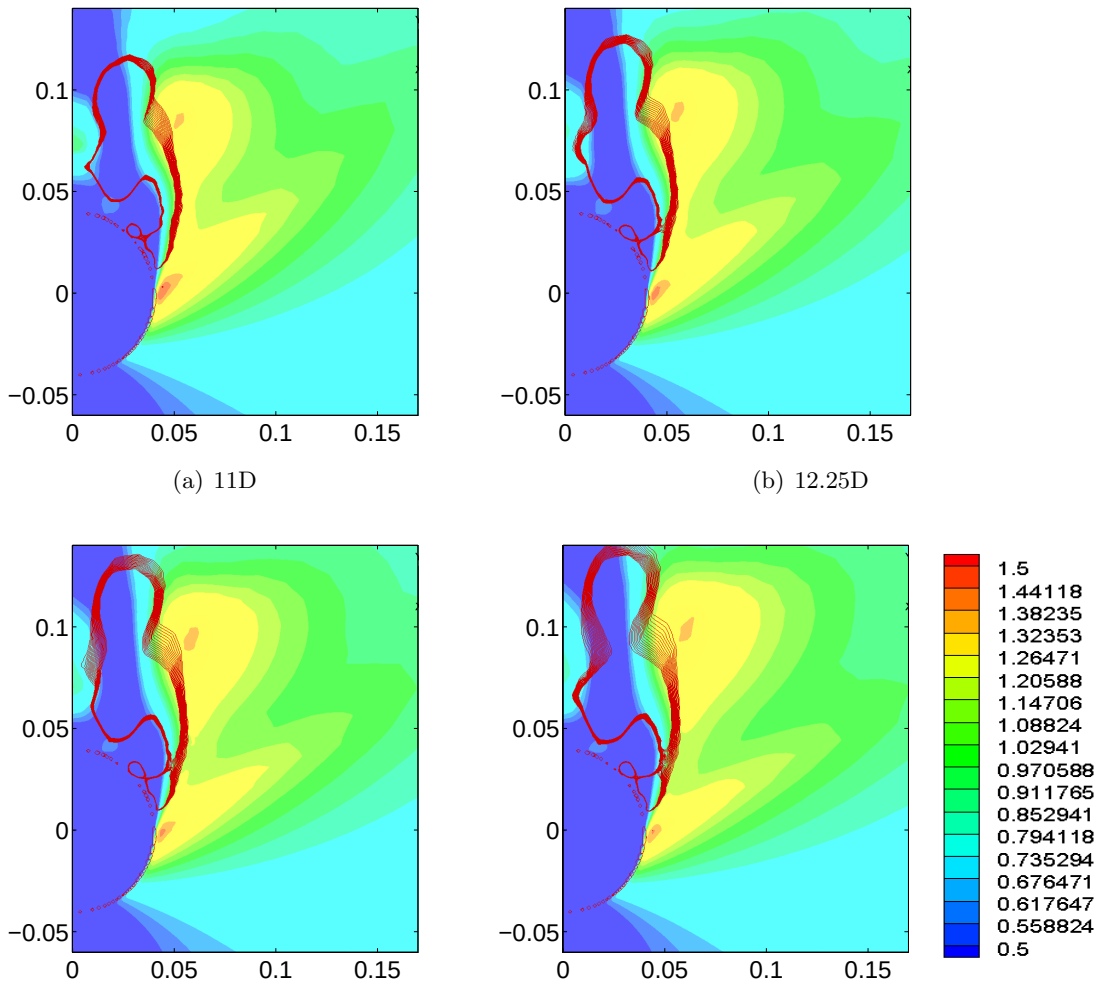

(a) 11D

(b) 12.25D

(c) 13.5D

(d) 14.75D

Figure 4.74: Body alone cross flow Mach number and vortex position at Mach 3.0 at $\alpha = 15°$

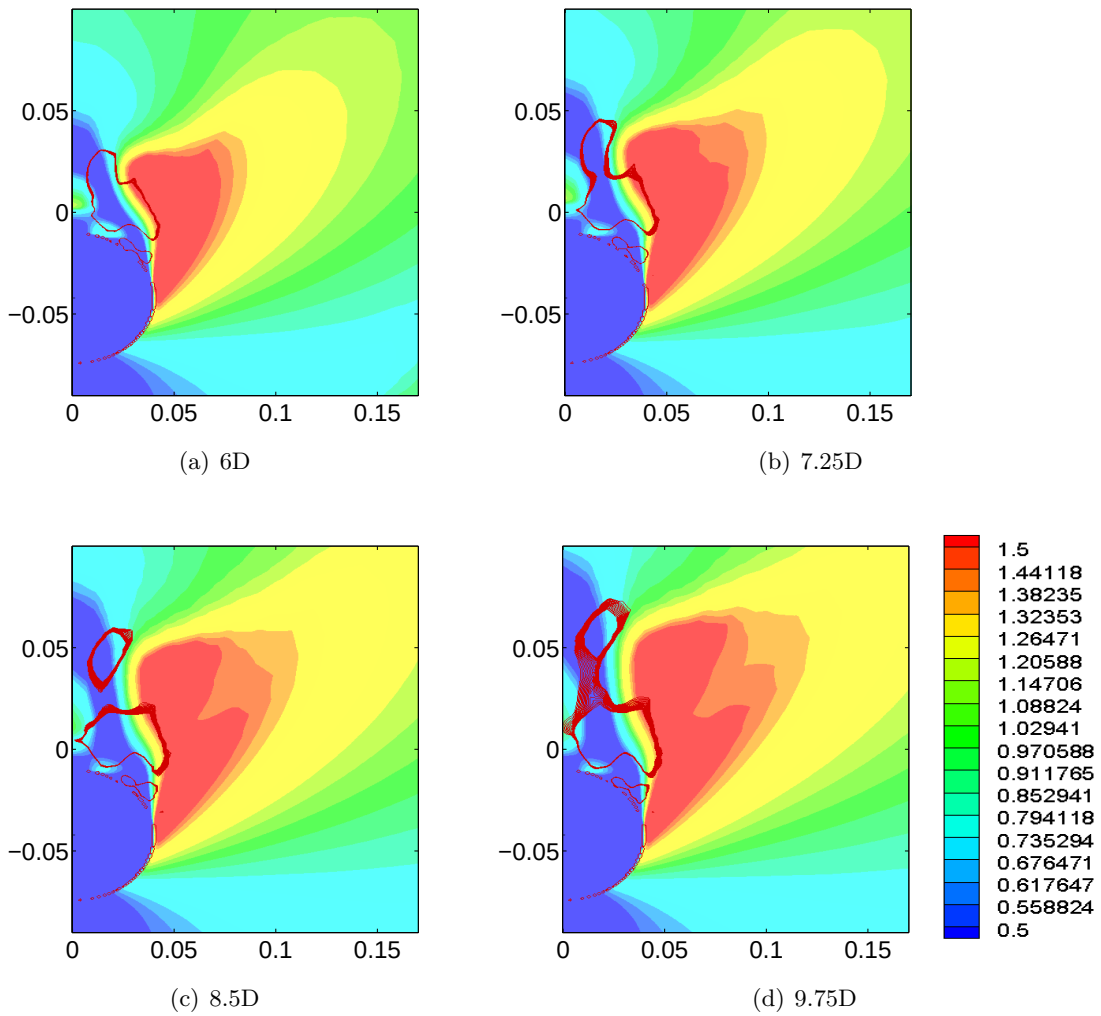

(a) 6D

(b) 7.25D

(c) 8.5D

(d) 9.75D

Figure 4.75: Body alone cross flow Mach number and vortex position at Mach 3.0 at $\alpha = 20°$

For the strake configuration, Figure 4.76 to Figure 4.78 show the development of shed vortices for Mach 2.0 for various angles of attack at selected body stations. The figures plot the cross-flow Mach number and contours of λ_2-criterion to show the vortex (ranging from -1×10^7 to -1×10^6). The simulations reveal the same mechanism for vortex shedding as for the body alone configuration. For the strake configuration, this corresponds to the cross flow Mach number of approximately 0.8.

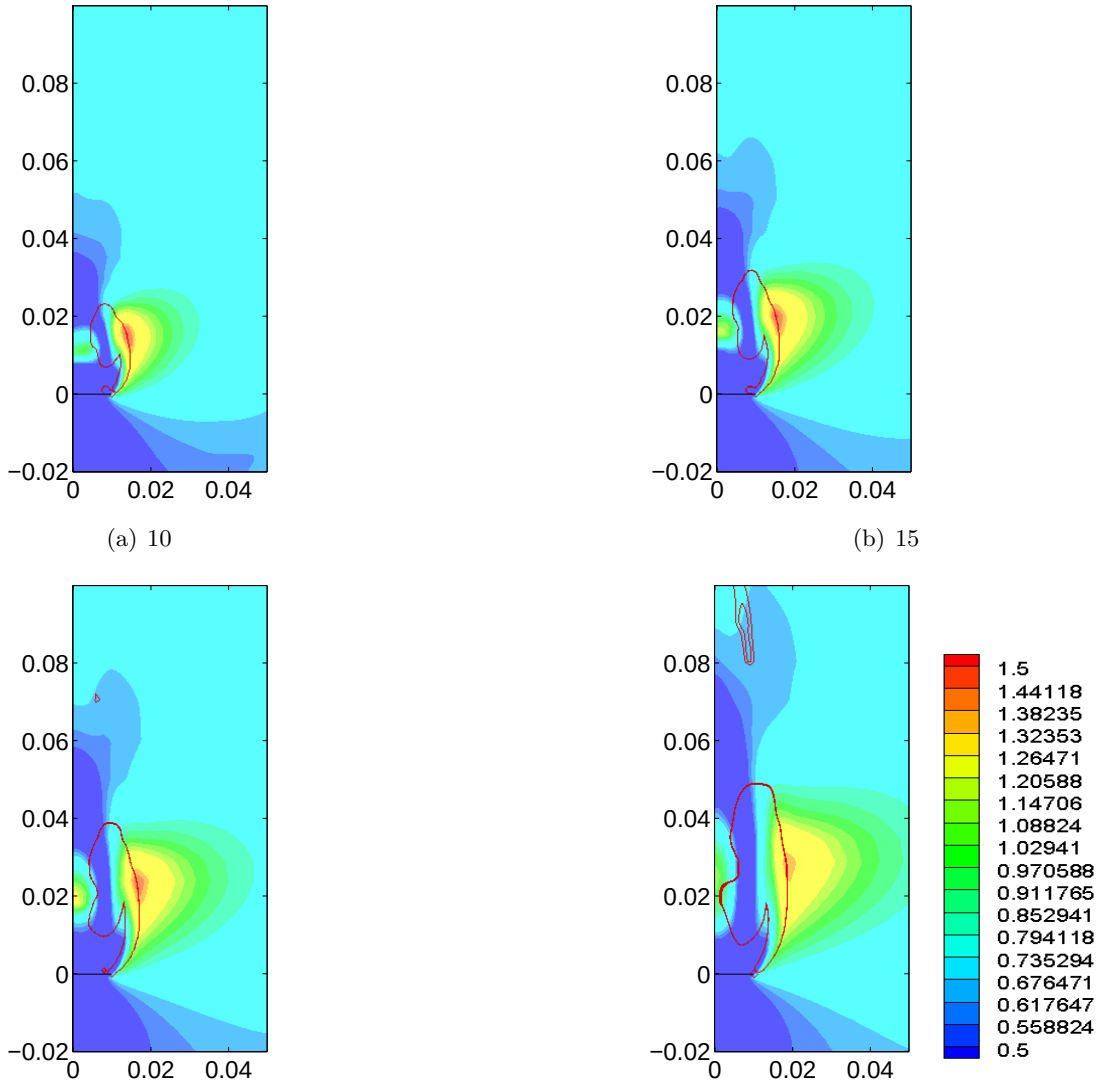

(a) 10

(b) 15

(c) 20

(d) 30

Figure 4.76: Strake cross flow Mach number and vortex position at Mach 2.0 at $\alpha = 20°$

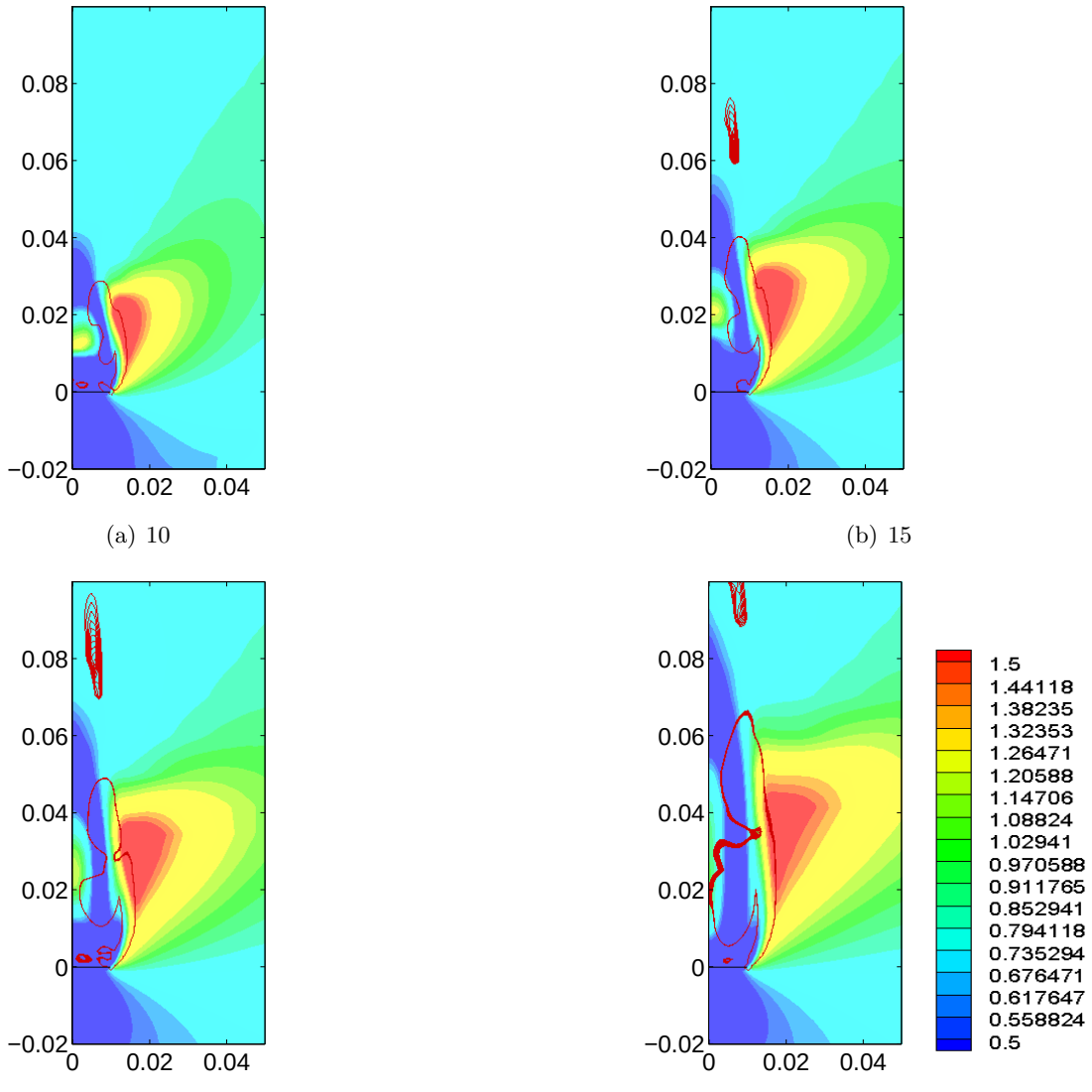

(a) 10

(b) 15

(c) 20

(d) 30

Figure 4.77: Strake cross flow Mach number and vortex position at Mach 2.0 at $\alpha = 25°$

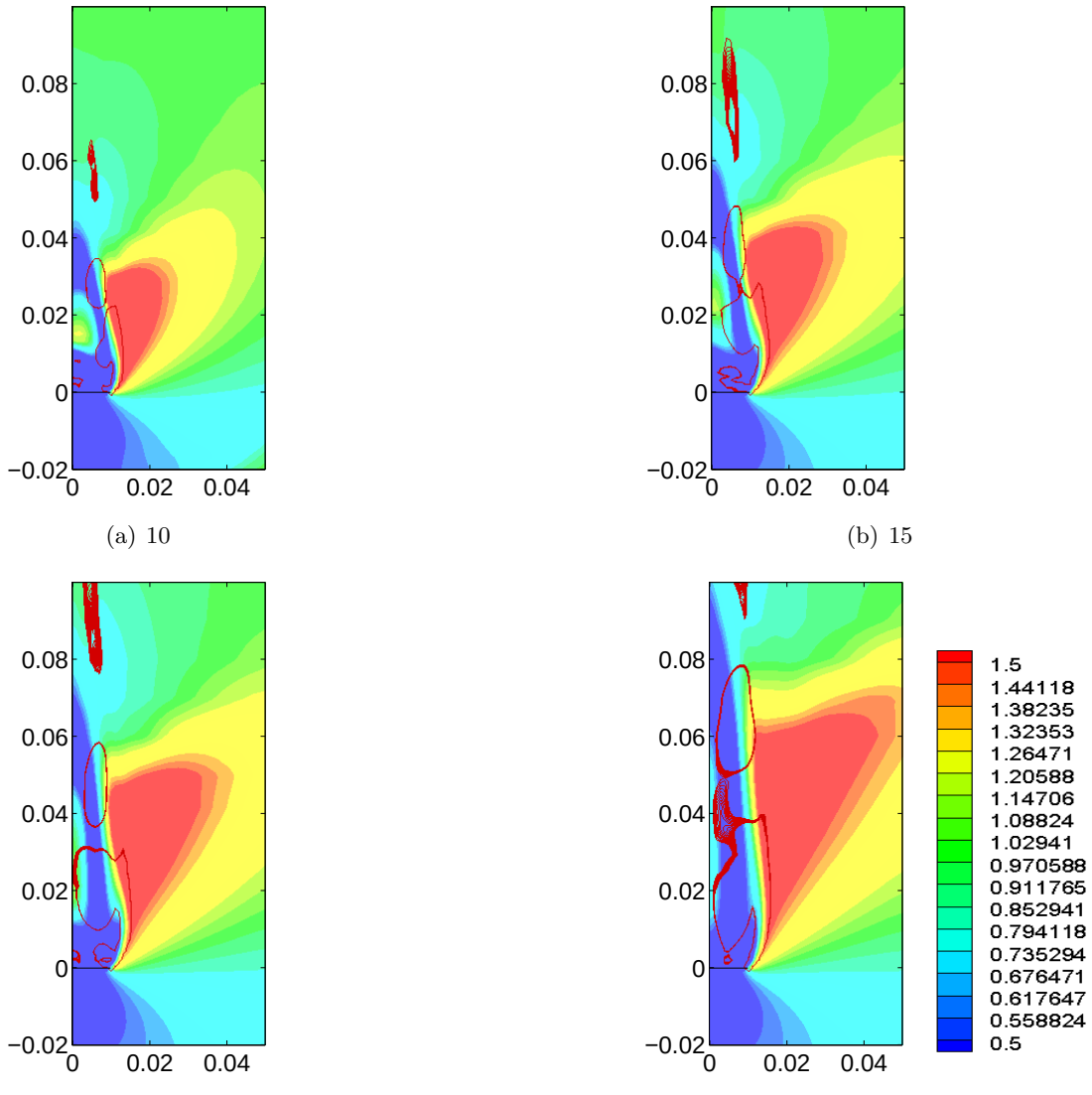

(a) 10

(b) 15

(c) 20

(d) 30

Figure 4.78: Strake cross flow Mach number and vortex position at Mach 2.0 at $\alpha = 30°$

For the body-strake configuration, Figure 4.79 to Figure 4.81 show the development of shed vortices for Mach 3.0 for various angles of attack at selected body stations. The figures plot the cross-flow Mach number and contours of λ_2-criterion to show the vortex (ranging from -1×10^7 to -1×10^6). The simulations reveal the same mechanism for vortex shedding as for the body alone and strake alone configuration. For the body-strake configuration, this corresponds to the cross flow Mach number of approximately 0.55. With the vortex shedding being initiated by terminating shock waves, the low speed tests in Málaga and the CSIR are necessarily different because the crossflow remains subsonic.

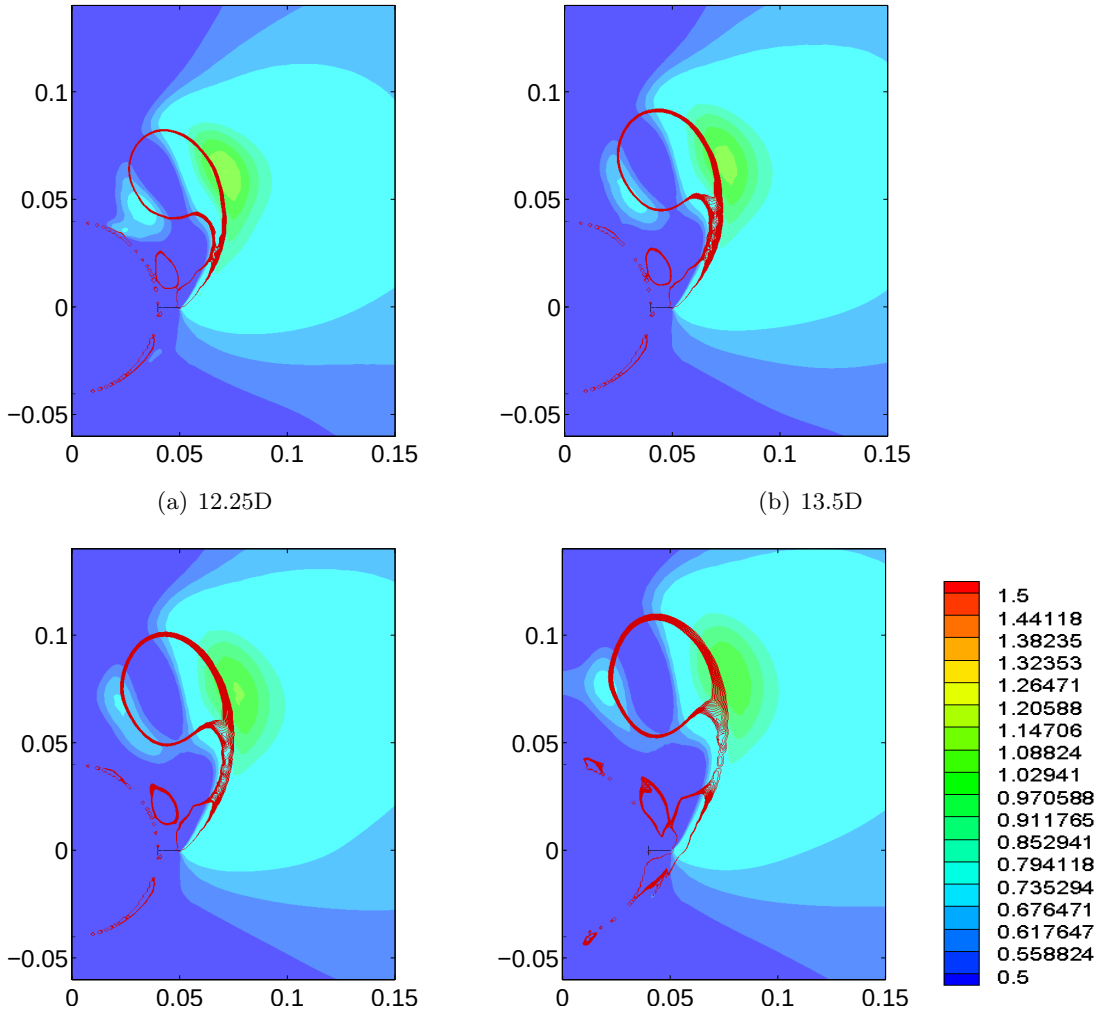

(a) 12.25D (b) 13.5D

(c) 14.75D (d) 16D

Figure 4.79: Body and strakes cross flow Mach number and vortex position at Mach 3.0 at $\alpha = 10°$

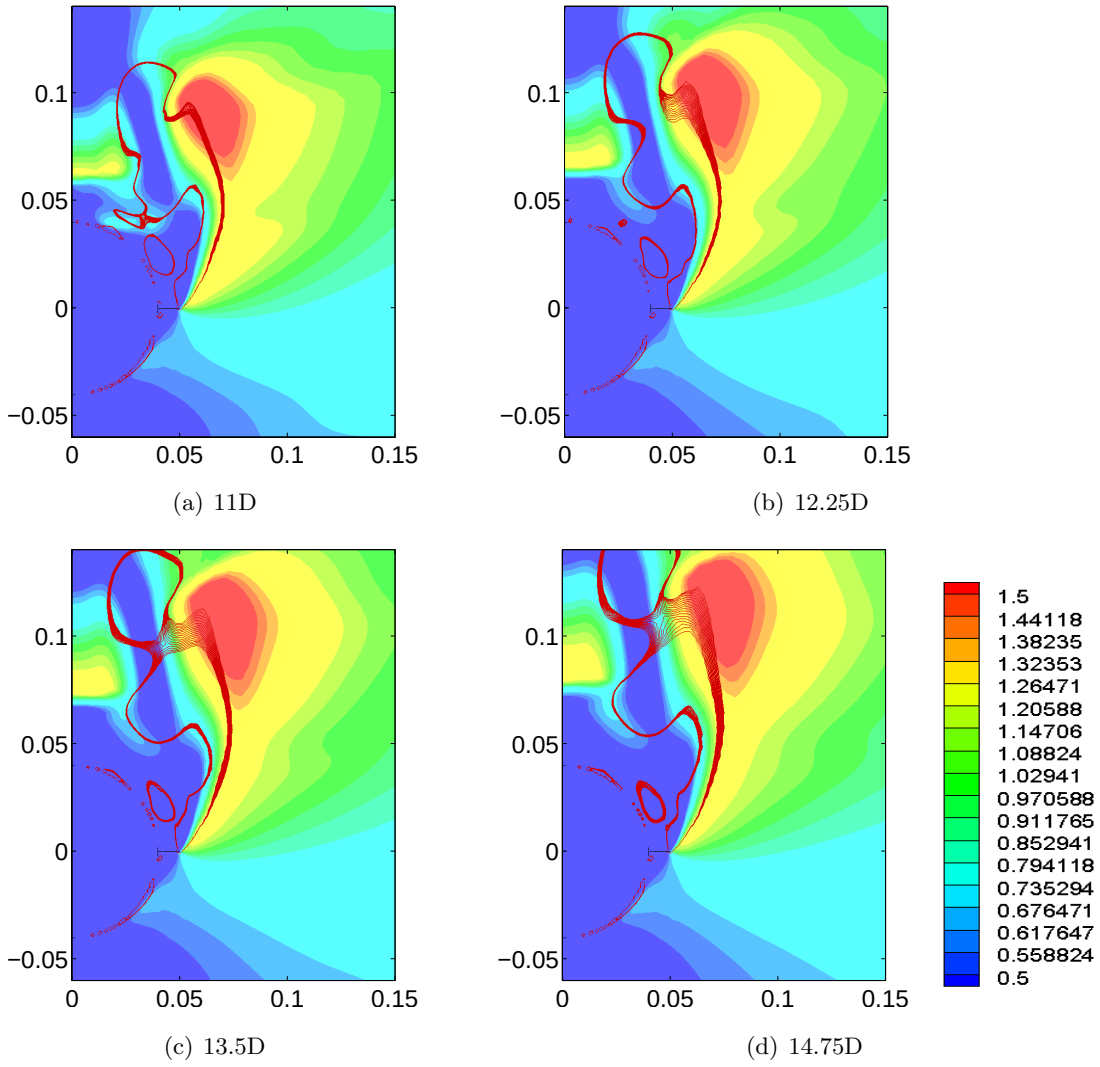

(a) 11D

(b) 12.25D

(c) 13.5D

(d) 14.75D

Figure 4.80: Body and strakes cross flow Mach number and vortex position at Mach 3.0 at $\alpha = 15°$

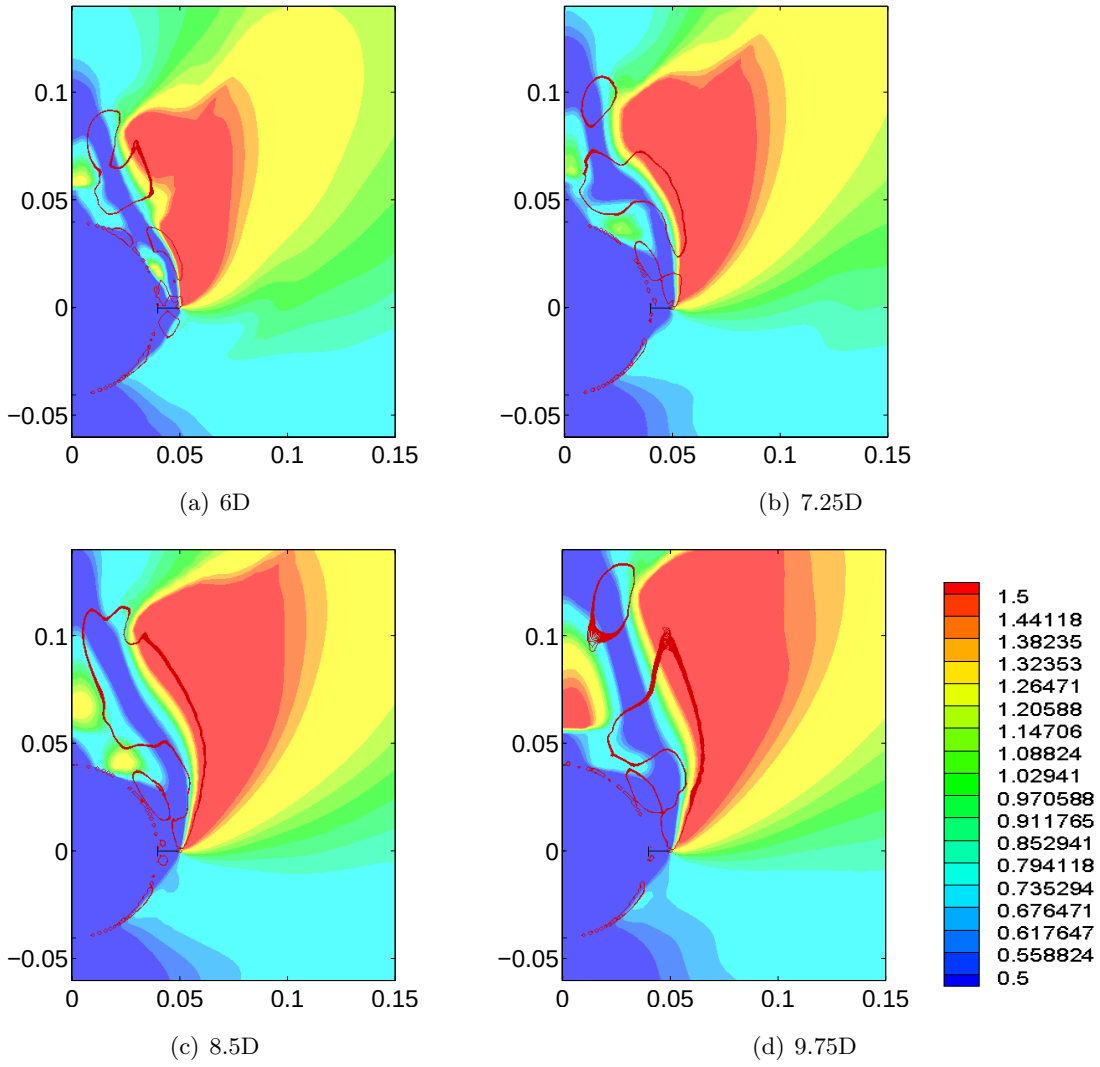

(a) 6D

(b) 7.25D

(c) 8.5D

(d) 9.75D

Figure 4.81: Body and strakes cross flow Mach number and vortex position at Mach 3.0 at $\alpha = 20°$

4.10 Secondary Vortex Characteristics

For both the body alone and body-strake configurations, secondary vortices are shed in the lee side of the configurations under consideration. The body alone configuration is of less interest in this particular section. For the body-strake configuration, the secondary vortex is caused by the adverse gradient at the body strake junction. Whilst secondary vortices are created at the body wing junctions for all four strakes, those on the ventral and dorsal strakes are small and do not affect the development of the side edge vortex. The development of the secondary vortex with angle of attack for various body axial locations are shown in Figure 4.82 to Figure 4.85 for the angels of attack, 2°, 4°, 6°and 10°. The figures plot the total pressure, velocity vectors and contours of λ_2-criterion to show the vortex (ranging from -1×10^7 to -1×10^6).

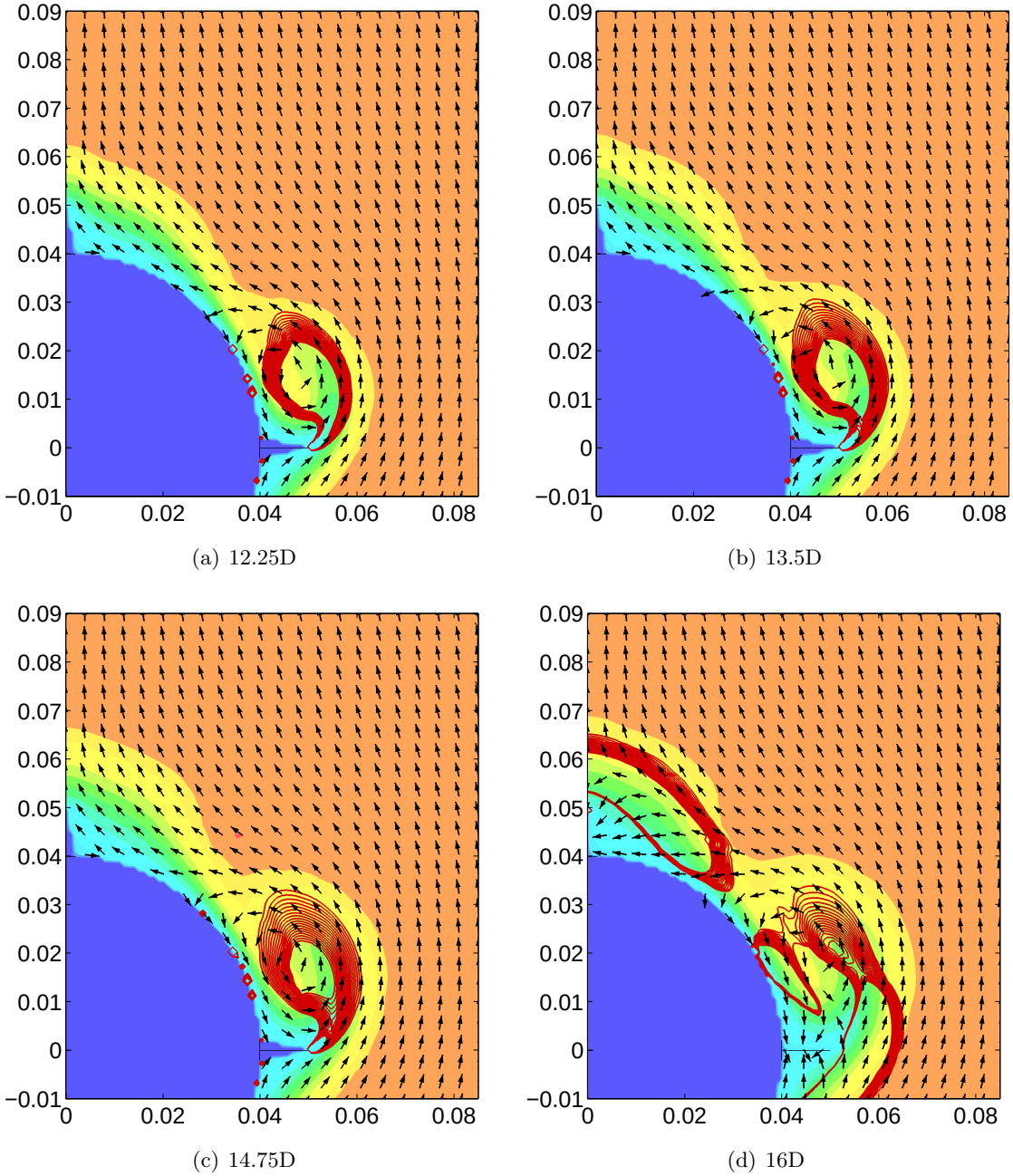

(a) 12.25D

(b) 13.5D

(c) 14.75D

(d) 16D

Figure 4.82: Lee side body strake junction secondary vortex at Mach 2.0 at $\alpha = 2°$

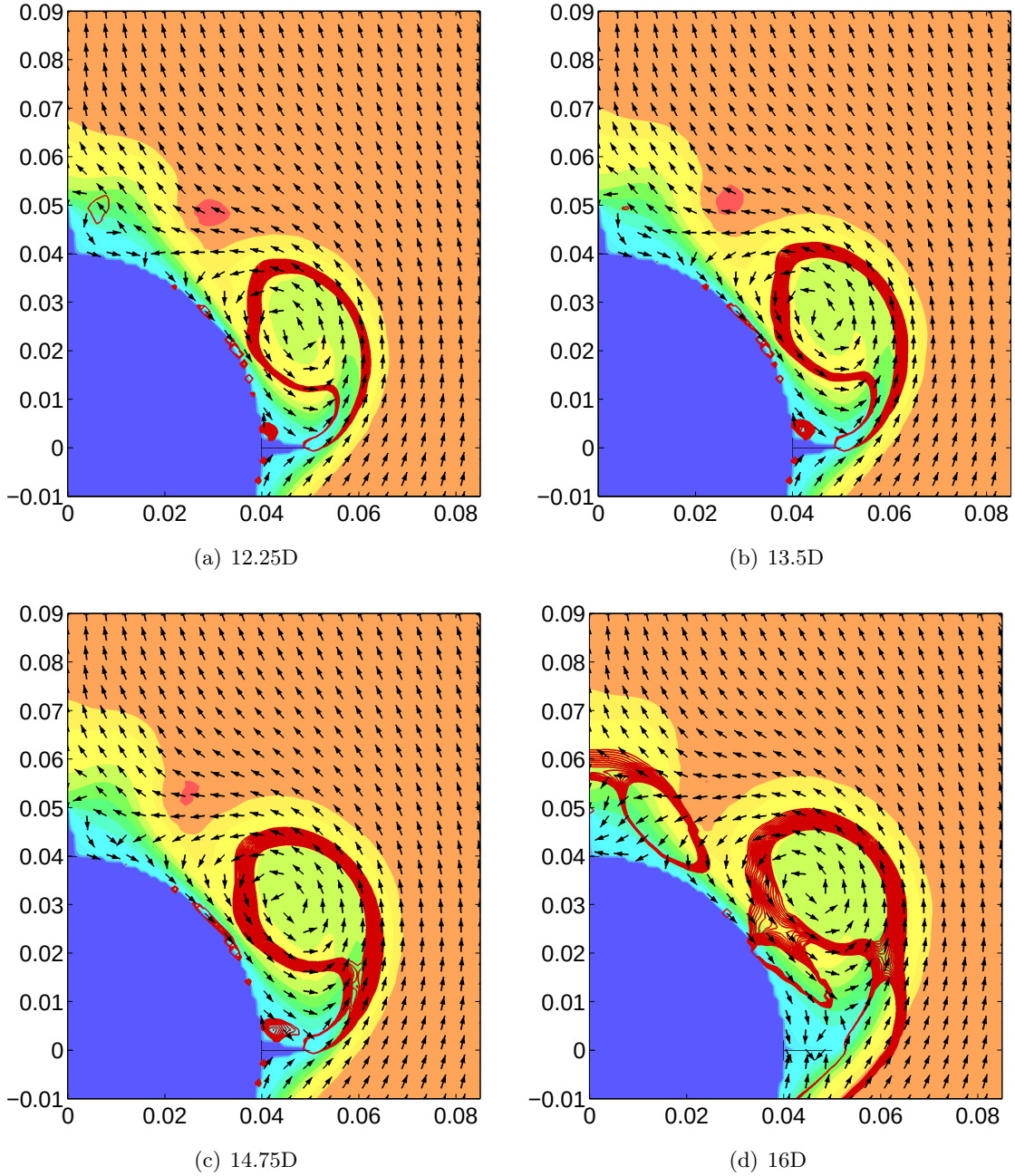

(a) 12.25D

(b) 13.5D

(c) 14.75D

(d) 16D

Figure 4.83: Lee side body strake junction secondary vortex at Mach 2.0 at $\alpha = 4°$

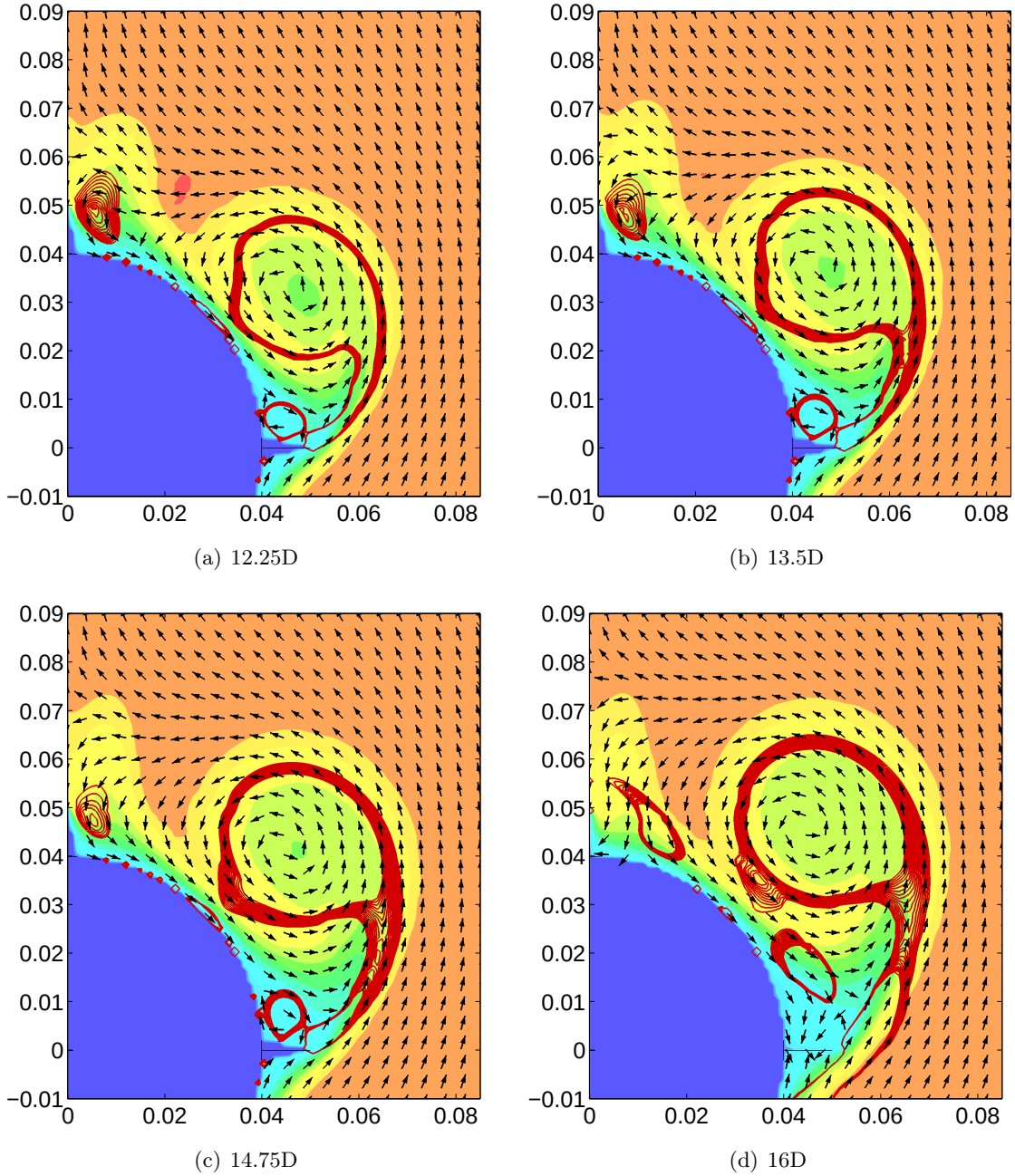

(a) 12.25D

(b) 13.5D

(c) 14.75D

(d) 16D

Figure 4.84: Lee side body strake junction secondary vortex at Mach 2.0 at $\alpha = 6°$

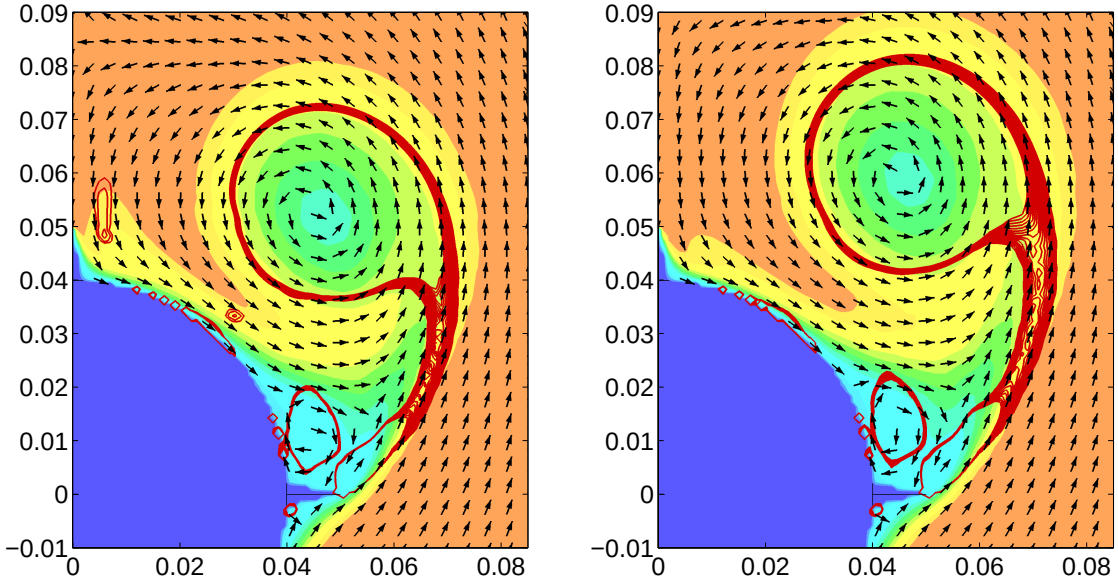

(a) 12.25D

(b) 13.5D

(c) 14.75D

(d) 16D

Figure 4.85: Lee side body strake junction secondary vortex at Mach 2.0 at $\alpha = 10°$

The secondary vortex is created at angles of attack above 2° (see Figure 4.82 and Figure 4.83). At 10° (see Figure 4.85) the secondary vortex influences the flow over the lee side of the strake. Once the secondary vortex is created the flow over the lee side of the strake, the vortex seems to change the local flow conditions near strake edge by introducing a flow vector in the opposite direction to the tangential flow needed to enforce the Joukowski-Kutta conditions. This reduces the vorticity shed by the side edge because the flow essentially starts to behave like it has turned the 180° strake edge. This also reduces the normal force generated because the vorticity shed is reduced. The emergence of the possible effect of the secondary vortex on the strake edge is different to that indicated by Mendenhall on his work on chines where secondary vortices were deemed only important when asymmetric vortices were shed [127].

4.11 Discussion

The flow over the body, strakes, and body-strake configuration is dominated by the large separated flow regions in the lee side of the body, strakes, and body-strake configuration respectively. The flow for the body alone configuration conforms to that which has already been observed by past investigators, with vortex shedding manifesting itself at a cross-flow Mach number of 0.65.

The flow for the strake alone configuration is dominated by the side edge vortex and due to the length of the strakes resembles more of a flat plate in 2D flow or flow over a cylinder than a typical swept back low aspect ratio wing. Vortex shedding occurs at angles of attack greater than 15° depending on the Mach number (which also coincides with the cross flow Mach number of 0.8), before which the rolled up side edge vortex sheet remains attached to the strake.

The body and strake separated flow regions, at low angle of attack, are dominated by the vortex that forms from the separation of the flow from the side edges of the strakes. This effect is prevalent at all non-zero angles of attack. This differs to the body alone configuration which exhibits attached flow at angles up to 4° (see Figure 4.63). When the cross flow Mach number exceeds 0.55 vortex shedding occurs.

The flow structures for the configuration studied is similar in some ways, and yet different to the that of circular cones with strakes [125] even though the study was performed at subsonic speeds. At low angles the strake dominates the separated flow features, which is the same for the configuration being studied in this thesis. At moderate angles of attack the body vortex coalesces with the strake vortex whereas a cone and strake configuration exhibits a body and a strake vortex which are separate, with the strake vortex remaining attached to the strake. In other words, the intermediate phase observed in cone and strake configurations does not exist for the configuration being studied with the single vortex not being attached to the strake. This is also different to the strake only vortex dynamics. The higher angle of attack flow structure for the configuration studied exhibits vortex

shedding and is due to compressibility effects.

The body-strake configuration shows a distinct difference in the rolled up side edge vortex sheet and its interaction with body vortices when compared to the expected flow for a component build up method. In a component build up method, it would be expected that the strake vortex remains separate from the body vortex and that the two only influence each other rather than combine. This is the case at the very low angles of attack where the strake vortex remains attached to the strake. At the moderate and higher angles of attack the flow structures are different, with the flow resembling that of an isolated body because the body and side edge vortex coalesce rather than only influence each other (see Figure 4.67). This distinctive feature in the flow, which is prevalent throughout the speed range including at incompressible Mach numbers, indicates the need to consider the flow structures of the body and strake in combination when considering the contribution of the side edge vortex to the interaction of the body and the strake.

4.11.1 Side Edge Vortex Trajectory Interference

The position and strength of the side edges vortices affect the overall loads for configurations with fins downstream of the very low aspect ratio wings. This is due to the interference of the vortex on the downstream fins. Their effect on the normal force of a fin could, in first order, be calculated using methods such as those developed by Pitts, Nielsen and Kaattari (strip theory) [7] or Alden and Schindel [154]. Graphs of the reduction in loads are graphically illustrated in reference [7] and result in a reduction in the normal force the closer the vortex is to the fin. This has two effects, the first being a possible reduction in pitching moment for the overall configuration should the fins be toward the rear of the body, and a reduction in the loading on the fins. If the predicted vortex position is closer to the fin than what physically occurs, the tail fins may be sized larger than required to achieve a given stability margin during the preliminary design phase, leading to more significant changes as the design process progresses. Should the fins be interdigitised compared to the strakes, an additional effect of the vortex inducing opposite effects depending on whether the fin is on one or the other side of the fin may be present, resulting in a more complex control algorithm than predicted if the vortex positions were incorrectly predicted.

As an example for this configuration, consider a set of non-interdigitised cruciform fins placed 2 calibers from the end of the strakes for an angle of attack of 10°, and the fins have a semispan to body diameter of 2.5 and no taper. Also assume that the strake edge trailing edge vortices travel along the freestream vector rather than as Lagangian fluid particle. The traditional method of considering the vortex interference over the set of fins would result in the core of the vortex passing over the fins at a height of 0.35 calibers, whilst the experimental and CFD simulations for this configuration indicate the core of the vortex would pass over the fins at a height of 1.24 calibers. Estimating the tail interference factor

i_T from reference [7] Chart 7(c), the traditional method predicts $i_T = -0.9513$ whilst the CFD simulations predict $i_T = -0.5434$. This represents a reduction in the interference factor by 43%, or the fin becomes more effective and the fin size can be reduced in order to achieve a given pitching moment. If the fins are primarily used for pitch control, these fins can therefore be smaller with the consequential reduction in drag.

4.12 Summary

From the extensive analysis of the configuration chosen, the flow features for circular slender body and very low aspect ratio wing combinations can be summarised as follows:-

- The lee side flow structures for the body-strake configuration differ to a summation of the body and strakes for the moderate and higher angles of attack. The side edge vortex resembles the flow over a circular body rather than of a body and a strake added together. This is particularly evident at angles of attack where a body vortex exists.

- The overall behaviour of the separated flow is dominated by the side edge vortex, and at higher angles of attack the effects of compressibility (by way of terminating shocks) on the vortex by splitting the vortex into two separate vortices

- At the higher angles of attack, at least one vortex is shed into the freestream. From the CFD simulations, this is due to the terminating shocks on both the outer and inner flows regimes of the shed vortex. Consequently, the flows between the freestream supersonic and subsonic flow regimes are expected to be different, indicating the limitations of the linearised small disturbance potential equation

- For the configuration being researched symmetric vortex shedding occurs above a cross flow Mach of 0.65 for a tangent ogive body, for strakes above Mach 0.8 and for the body-strake configuration above Mach 0.55

- At moderate angles, secondary vortex separation in the lee side is exhibited, caused initially by the adverse pressure gradient of the wing-body junction. This vortex is large enough to cover the complete span of the strake. This secondary vortex starts to manifest itself at relatively low angles (4°) for the configuration being researched.

- The CFD simulations with the Spalart-Allmaras turbulence model have been validated by the experimental tests, not only in the gross forces and moments, but also the lee side vortex positions. The CFD simulations are, therefore, used in the development of the engineering method as the baseline data set.

- The Spalart-Allmaras turbulence model is a suitable model for the supersonic flows over slender bodies with very low aspect ratio wings, requiring less computational

effort than the two-equation algebraic models, and increasing the robustness of the simulations.

4.12.1 Recommendations

The recommendations that follow from this CFD simulation and experimental validation phase are:

- Study different nose length configurations to determine the body vortex roll up with strake vortex sheet i.e. initiate body vortices at lower angles of attack.
- Perform a validated incompressible CFD simulation to complete the subsonic simulations
- Develop a half model or sidewall test technique for wings of very low aspect ratio

Chapter 5

Single Concentrated Vortex Model

5.1 Introduction

As mentioned previously in the literature survey, one of the simplest categories of method used in the past to model the flow in the lee side of bodies is that of a single concentrated vortex, or "lumped-vorticity" concept. For circular bodies this was also known as the "NACA Vortex Model". This concept was first implemented by Bryson [56] for cylinders and cones, and subsequently expanded upon by Levinsky et al [125][33] for conical bodies. The method Bryson employed to position the symmetric vortices was to assume that the vortex is force free. The model is simple and consequently has features which are non-physical. The first of the two significant consequences is that no vortex feeding sheet is modeled. Subsequently a pressure jump or discontinuity exists across the infinitesimally thin vortex feeding sheet which does not physically occur. The second feature is that whilst the vortex is force free, a moment acts upon the vortex. One of the physical results of the simple model is that the cross-flow drag on a cylinder as a function of time is reasonably predicted in the initial stages i.e. at the start of the impulse of the cylinder or cone. Once the drag coefficient peaks at around $C_D = 1.6$, instead of the drag coefficient asymptoting to $C_D = 1.2$, it drops off to zero. This is due to the vortices travelling towards the Foppl points, where it was observed by Bryson that the rate of change of vorticity dropped below zero i.e. the vortex started to reduce in strength. It was conjectured by Bryson that at this point the vortex was released into freestream as a free vortex, thus forming the expected vortex street. Levinsky employed a model where the vortex sheet was explicitly modeled as a limited number of discrete elements (normally six) and the discretised sheet was attached to the vortex through a cut. The model has its origin in modeling the flow over slender wings, this originally performed by Legendre [79] and subsequently by Brown and Michael [81], and Mangler and Smith [126]. Bryson was the first to apply the Brown and Michael model to bodies rather than wings only. Levinsky *et al*, improved the model and applied it to conical and elliptical cones with and without strakes of varying aspect ratio, and later to conical bodies with double delta wings and wings with curved leadings edges, and conical bodies with curved noses.

The previously mentioned limitations not withstanding, the concept has been used to model and study flows in the lee side of bodies and wings. The simplicity of the model, does however, appear attractive to modeling the interaction of very low aspect ratio wings with bodies. Indeed, Levinsky has already employed the extended model to circular and elliptic cones with very low aspect ratio strakes. The uniqueness of this application is its application at supersonic Mach numbers and to a cylinder of constant diameter where the side edge is parallel to the primary flow direction (non-conical flows) rather than for conical bodies and triangular type or delta wings.

For the configurations and flow regimes under consideration, the vortex behaviour is expected to remain within the initial impulse phase of the two dimensional flow over a cylinder, and the reduction of the rate of change of vorticity to zero is only expected at the higher angles of attack.

The presentation of the method as developed by Bryson is first presented and it application to the cruciform wing-body configuration is then expounded. The resulting formulation is applied to the angles of attack of interest where upon the results are compared to the validated CFD simulations.

5.2 Single Concentrated Vortex Model

The "lumped-vorticity" or single concentrated vortex model (SCV) is developed in this subsection. The development is based on the work presented by Bryson [56] and naturally reproduces this work before extensions are made for the configuration under consideration. Consider a 2D cylinder with two symmetric vortices outside the boundary layer. The condition that satisfies the no-net-force requirement on the vortices is

$$\dot{\nu_1} + (\nu_1 - \nu_{sp}) \frac{\dot{\Gamma}}{\Gamma} = W_1 \tag{5.1}$$

where ν_1 is the complex velocity of the vortex, W_1 is the fluid velocity at the vortex excluding the singularity of the vortex, Γ is the strength of the vortex, and ν_{sp} is the location where the vortex is being fed from i.e. the separation point on the body. This relationship is derived by considering the discontinuity in the the potential, ϕ, due to the circulation Γ. This results in a pressure discontinuity across the branch line or vortex sheet of $\rho\dot{\Gamma}$, and a resulting total force of $i\rho\dot{\Gamma}(\nu_1 - \nu_{sp})$. The force on the concentrated vortex is $-i\rho\dot{\Gamma}(W_1 - \nu_1)$. The sum of these two forces must be zero, thus resulting in the above relationship. This relationship is thus applicable for not only circular bodies, but bodies of arbitrary shape.

The fluid motion or velocity, W_1, at the one vortex assuming symmetry is defined by considering the potentials due to the freestream, cylinder, vortices and their images. This results in the following expression

$$\overline{W}_1 = v - iw = -iV\sin\alpha\left[1 + \frac{a^2}{\nu_1^2} + \lambda a\left(\frac{1}{\nu_1 + \frac{a^2}{\nu_1}} - \frac{1}{\nu_1 - \frac{\nu_1}{\overline{\nu}_1}} - \frac{1}{\nu_1 + \overline{\nu}_1}\right)\right] \tag{5.2}$$

where $\lambda = \frac{\Gamma}{2\pi V a \sin\alpha}$.

At the separation points, the fluid velocity is zero. Combining the two equations and satisfying the separation condition results in the following expression for the strength of the symmetric pair of vortices

$$\lambda = \frac{(\nu_1 - \nu_{sp})(\overline{\nu}_1 - \overline{\nu}_{sp})(\nu_1 + \overline{\nu}_{sp})(\overline{\nu}_1 + \overline{\nu}_{sp})}{(\nu_1\overline{\nu}_1 - a^2)(\nu_1 + \overline{\nu}_1)} \tag{5.3}$$

The extension of the work done by Bryson to cruciform wing-body combinations (or other transformable configurations) requires that the above relationships be modified to account for the transformation from the physical to the circle plane (for which the work by Bryson is applicable). The only term affected in the no-net-force equations is the fluid velocity term, W_1. This term is modified by the transformation relationship $d\nu/d\sigma$. The expression for the strength of symmetric pair of vortices remains the same because in the circle plane the separation condition remains the same i.e. $dW/d\nu = 0$.

Firstly, the transformation and its derivatives from the physical to the transform plane of a cruciform wing-body combination in the σ-plane into a circle of radius r_o in the ν-plane are:

$$\sigma^2\left(1 + \frac{a^4}{\sigma^4}\right) = \nu^2\left(1 + \frac{r_o^4}{\nu^4}\right) \tag{5.4}$$

$$r_o^2 = \frac{1}{2}s^2\left(1 + \frac{a^4}{s^4}\right) \tag{5.5}$$

$$\frac{d\nu}{d\sigma} = \frac{\sigma}{\nu}\left(\frac{1 + \frac{a^4}{\sigma^4}}{1 + \frac{r_o^4}{\nu^4}}\right) \tag{5.6}$$

$$\frac{d^2\nu}{d\sigma^2} = \frac{d\nu}{d\sigma}\left[\frac{1}{\nu}\left(3 - \frac{4}{1 - \frac{r_o^4}{\nu^4}}\right)\left(\frac{d\nu}{d\sigma}\right) - \frac{1}{\sigma}\left(3 - \frac{4}{1 - \frac{a^4}{\sigma^4}}\right)\right] \tag{5.7}$$

For a symmetric pair of vortices, or a roll angle of $\phi_x = 0$, by utilising the preceding relationships and non-dimensionalising to the body radius, the fluid velocity of the one vortex is therefore

$$\overline{W}_1 = -iV\sin\alpha\left[1 + \frac{r_o^2}{\nu_1^2} + \lambda\left(\frac{1}{\nu_1 + \frac{r_o^2}{\nu_1}} - \frac{1}{\nu_1 - \frac{\nu_1}{\overline{\nu}_1}} - \frac{1}{\nu_1 + \overline{\nu}_1}\right)\right]\frac{d\nu}{d\sigma} - \frac{iV\sin\alpha\lambda}{2}\frac{d\sigma}{d\nu}\frac{d^2\nu}{d\sigma^2} \tag{5.8}$$

5.3 Test Matrix

The conditions for which simulations were performed are the angles of attack of 1°, 2°, 4°, 6°, 10°, 15°, 20°and 25°. These are the same angles of attack as the CFD simulations. No body vortex was included for these simulations and the angles of attack above 10° are therefore not comparable to the other methods.

5.4 Results

An example of the trajectory of the concentrated vortex is shown in Figure 5.1. This is for the angle of attack of 10°. The trajectory is typical for all the angles of attack considered given that the flow in axial direction is modeled using the impulsively started 2D configuration. Of interest is the outward movement of the vortex as the angle of attack increases, and is a consequence of the imposition of the Joukowski-Kutta condition at the strake edge.

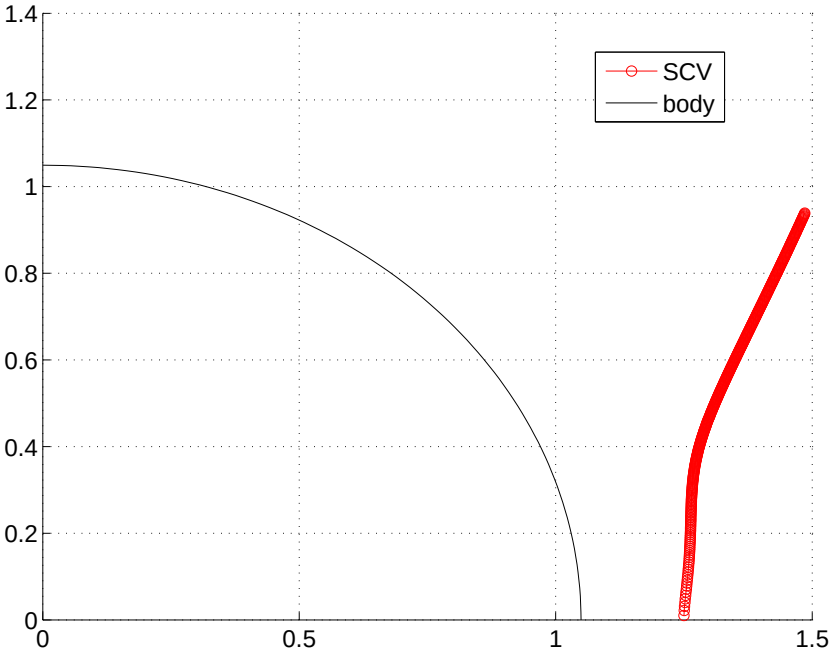

Figure 5.1: Vortex path for angle of attack 10° (in the circle plane)

5.4.1 Global Loads

The normal force and centre-of-pressure comparison of the overall configuration is shown in Figure 5.2. The SCV predictions for Mach 2.0 are compared against CFD simulations for the Mach numbers 2.0 to 3.0. It should be remembered that the SCV normal force is composed of the SCV predicted loads, wing in the presence of the body SBT linear load, wing-to-body carryover linear SBT load, and fore- and aftbody loads. The fore- and aftbody loads are directly extracted from the CFD simulations, rather than using less accurate engineering methods. The Mach 2.5 and 3.0 SCV predictions were not illustrated because the variation in the contribution of the forebody and aftbody from M2.0 to M3.0 is no greater than 2.7% throughout the angle of attack range. It should be remembered that the SCV method does not predict any Mach number dependency. As can be seen, the single concentrated vortex method over predicts the normal force load with increasing angle of attack. The low angle of attack predictions (up to 4°) are, however, well predicted. The centre-of-pressures are reasonably well predicted, with the possible exception of the lower angles of attack where the centre-of-pressure is predicted further back than the CFD.

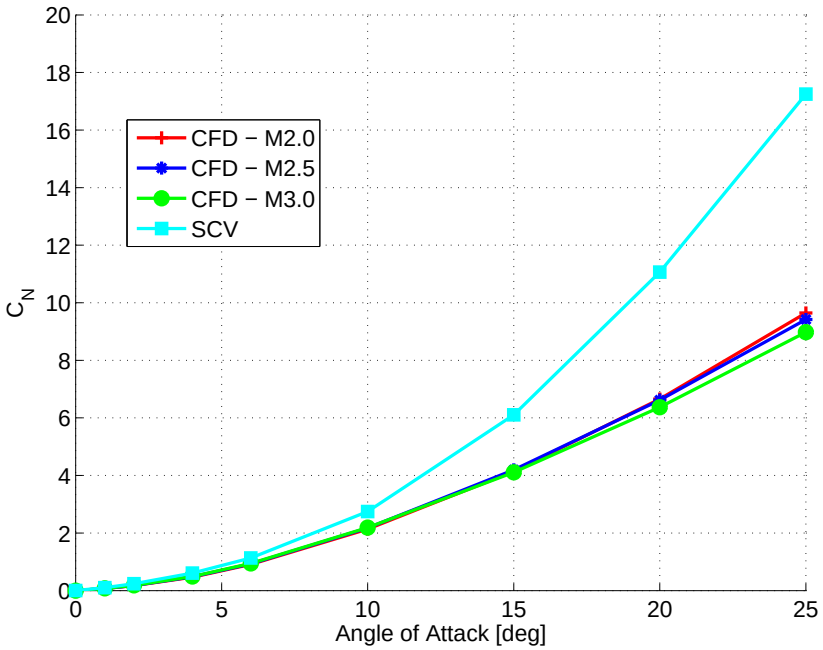

(a) Normal force

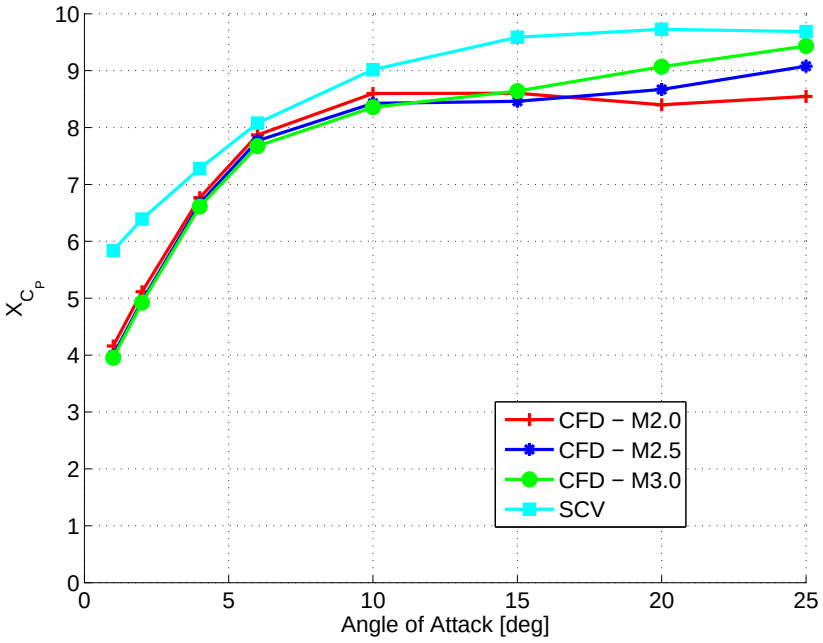

(b) Centre-of-pressure

Figure 5.2: CFD and SCV normal force and centre-of-pressure comparison

5.4.2 Detailed Flow Field

The flow field results of the simulations are shown in Figure 5.3 to Figure 5.10 and plots the position of the vortex for various axial locations in comparison to the CFD predictions for Mach 2.0. The location of the concentrated vortex is denoted by the ◊ symbol. At 1° (see Figure 5.3) the vortex position is very well predicted. This prediction becomes progressively poorer as the angle of attack increases. The prediction is still good at 2° (see Figure 5.4, but is predicted lower than the CFD simulations above 4° (see Figure 5.5 to Figure 5.10). The predictions are, however, reasonable at the start of the strake i.e. from the axial location of 4.75D to 5.375D (these are illustrated in the sub-figure (b) of Figure 5.3 to Figure 5.10). The poor prediction of the lateral location of the concentrated vortex is exemplified at the higher angles of attack i.e. 15° and higher, where the SCV method predicts the position to be further from the body centre than the CFD simulations.

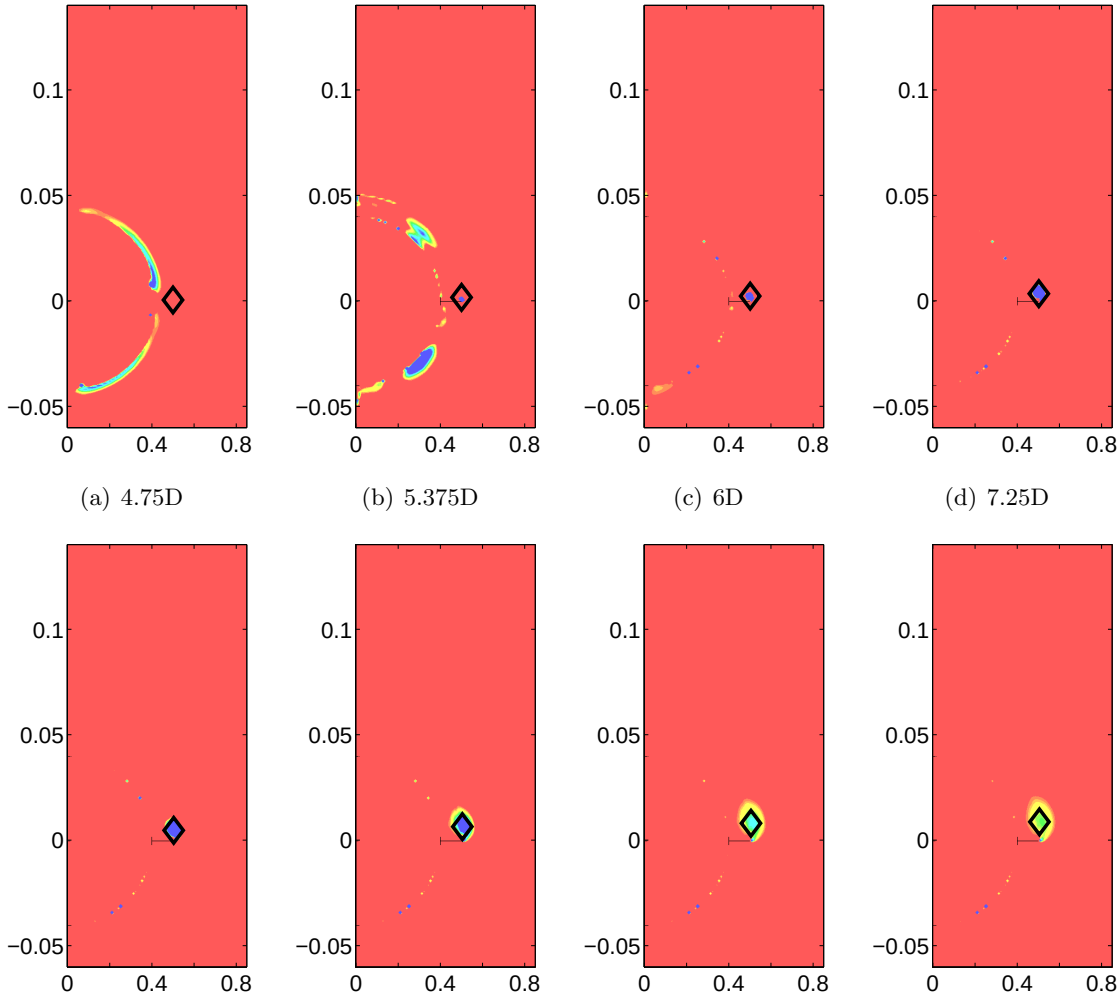

(a) 4.75D (b) 5.375D (c) 6D (d) 7.25D

(e) 8.5D (f) 11D (g) 13.5D (h) 14.75D

Figure 5.3: Vortex development for $\alpha = 1°$, SCV

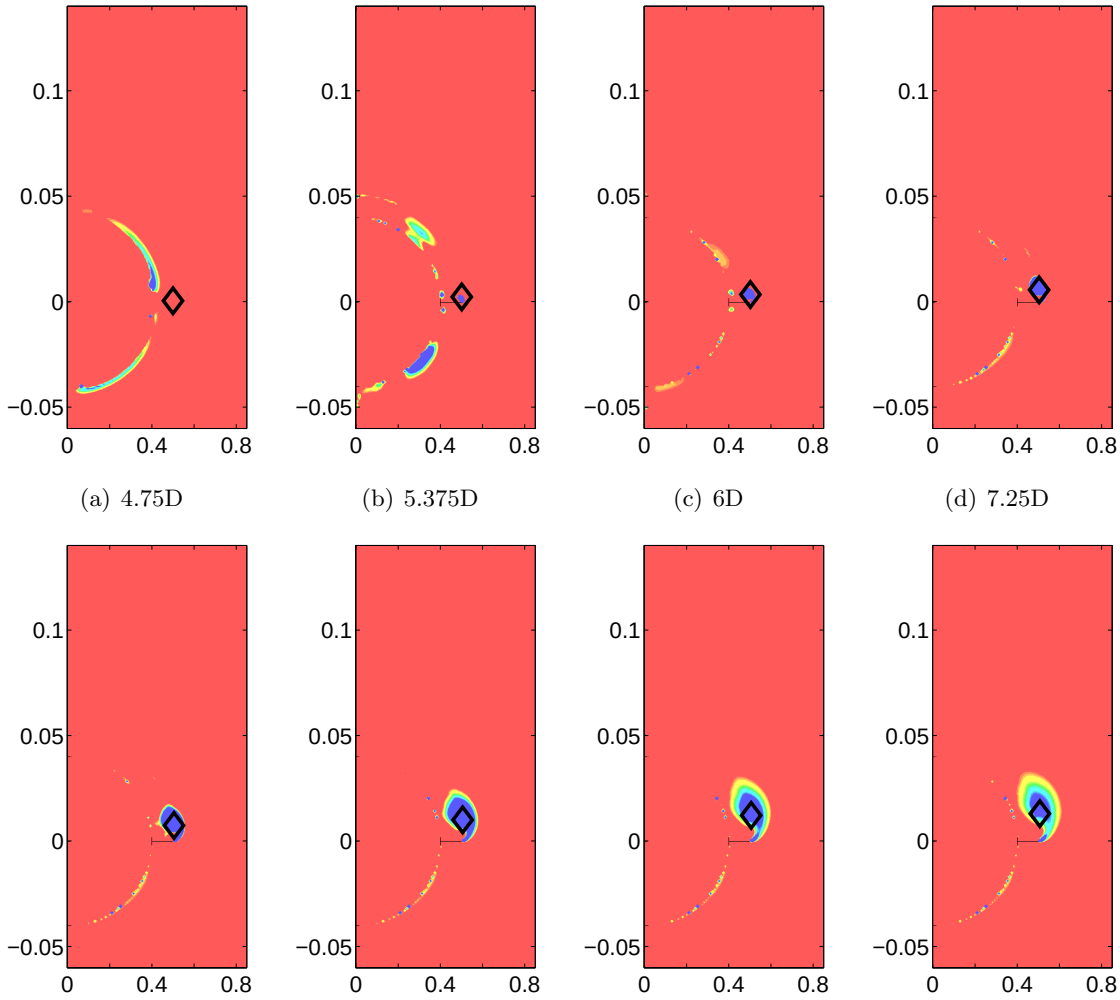

(a) 4.75D (b) 5.375D (c) 6D (d) 7.25D

(e) 8.5D (f) 11D (g) 13.5D (h) 14.75D

Figure 5.4: Vortex development for $\alpha = 2°$, SCV

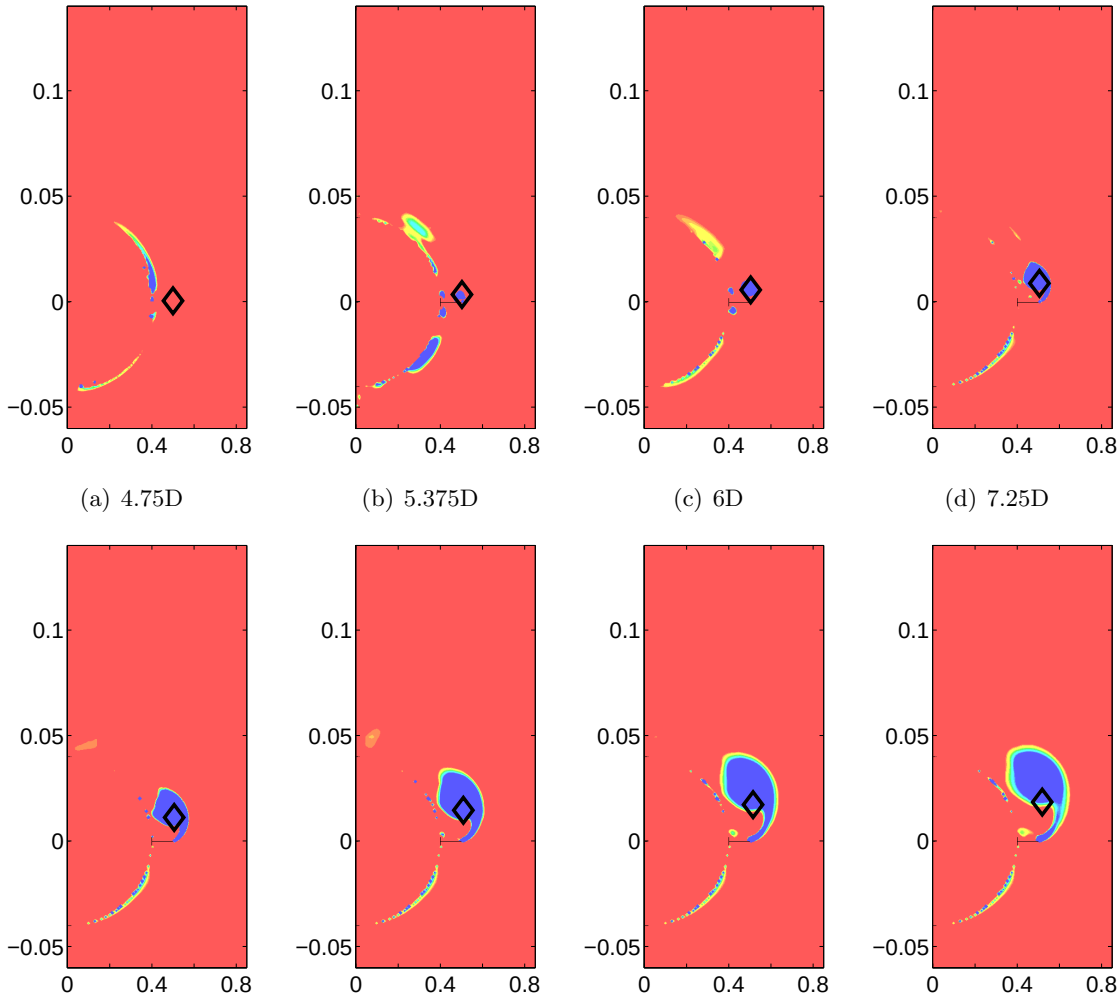

(a) 4.75D (b) 5.375D (c) 6D (d) 7.25D

(e) 8.5D (f) 11D (g) 13.5D (h) 14.75D

Figure 5.5: Vortex development for $\alpha = 4°$, SCV

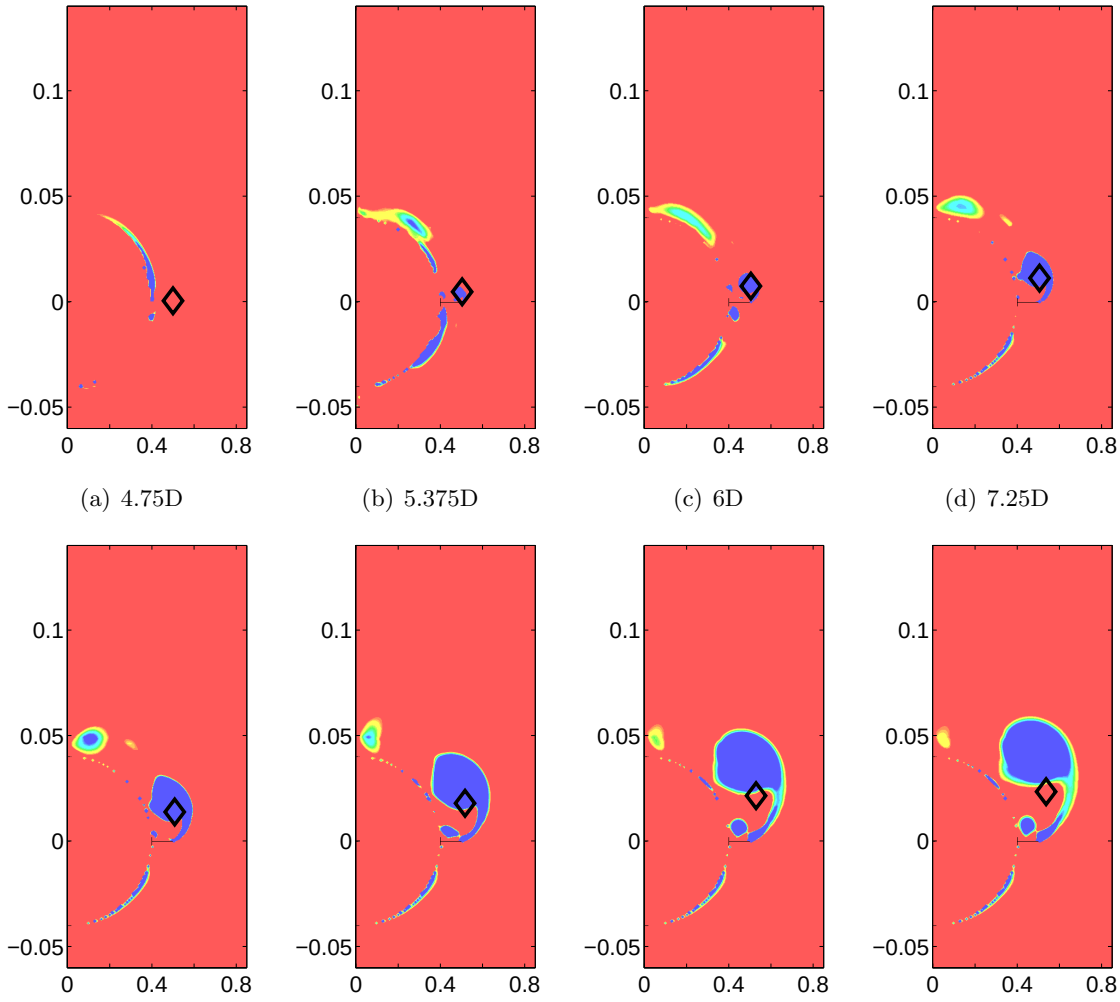

(a) 4.75D (b) 5.375D (c) 6D (d) 7.25D

(e) 8.5D (f) 11D (g) 13.5D (h) 14.75D

Figure 5.6: Vortex development for $\alpha = 6°$, SCV

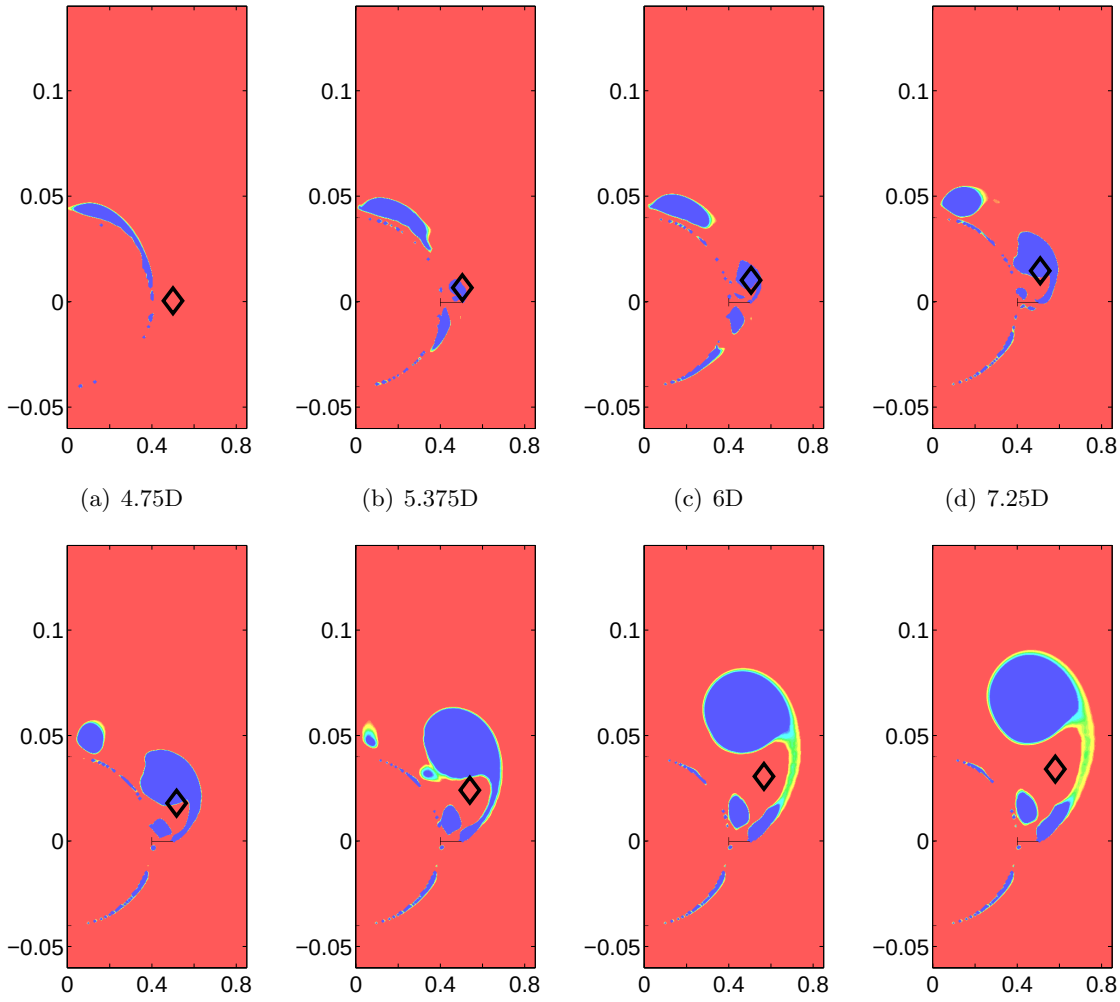

(a) 4.75D (b) 5.375D (c) 6D (d) 7.25D

(e) 8.5D (f) 11D (g) 13.5D (h) 14.75D

Figure 5.7: Vortex development for $\alpha = 10°$, SCV

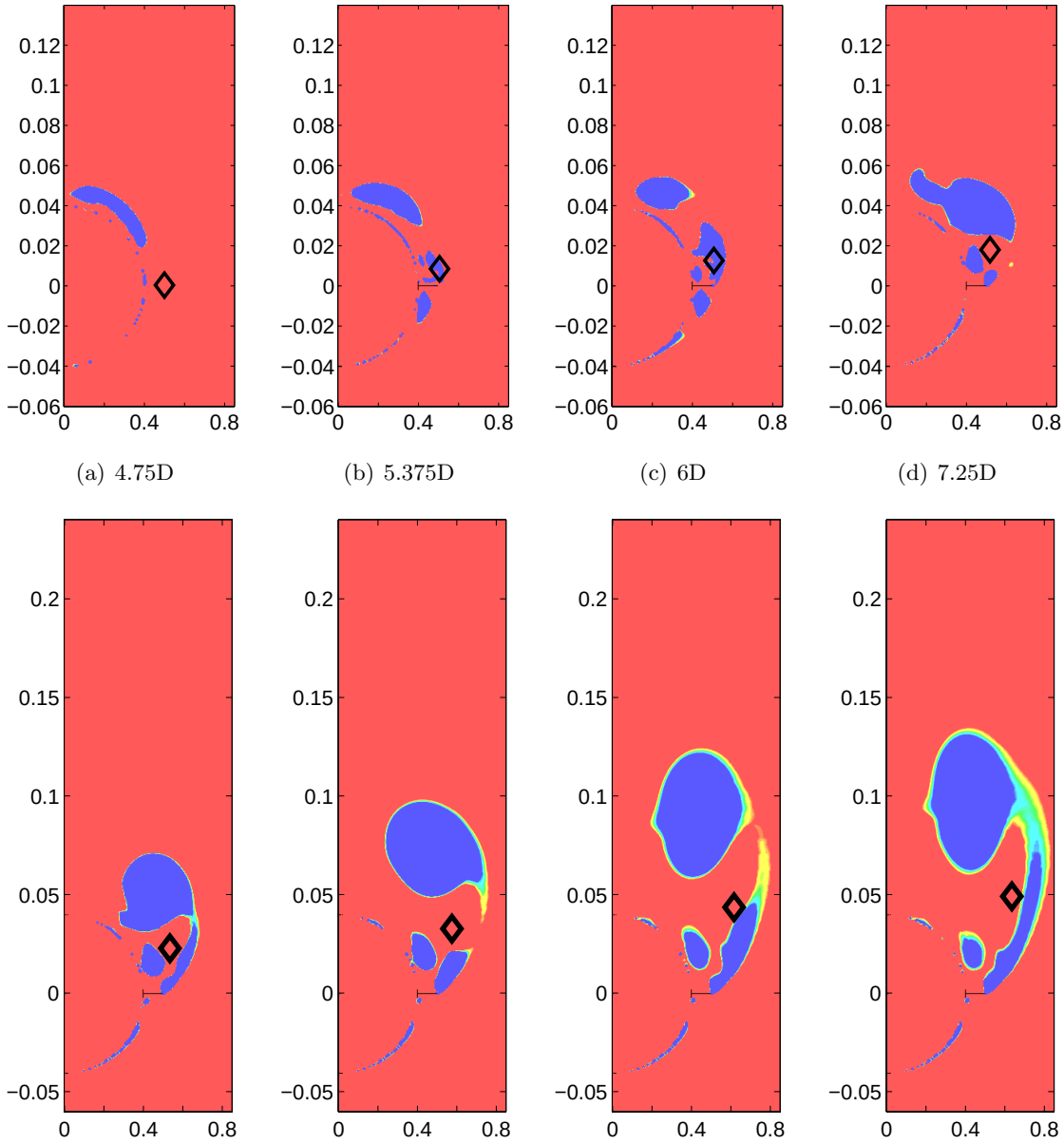

(a) 4.75D (b) 5.375D (c) 6D (d) 7.25D

(e) 8.5D (f) 11D (g) 13.5D (h) 14.75D

Figure 5.8: Vortex development for $\alpha = 15°$, SCV

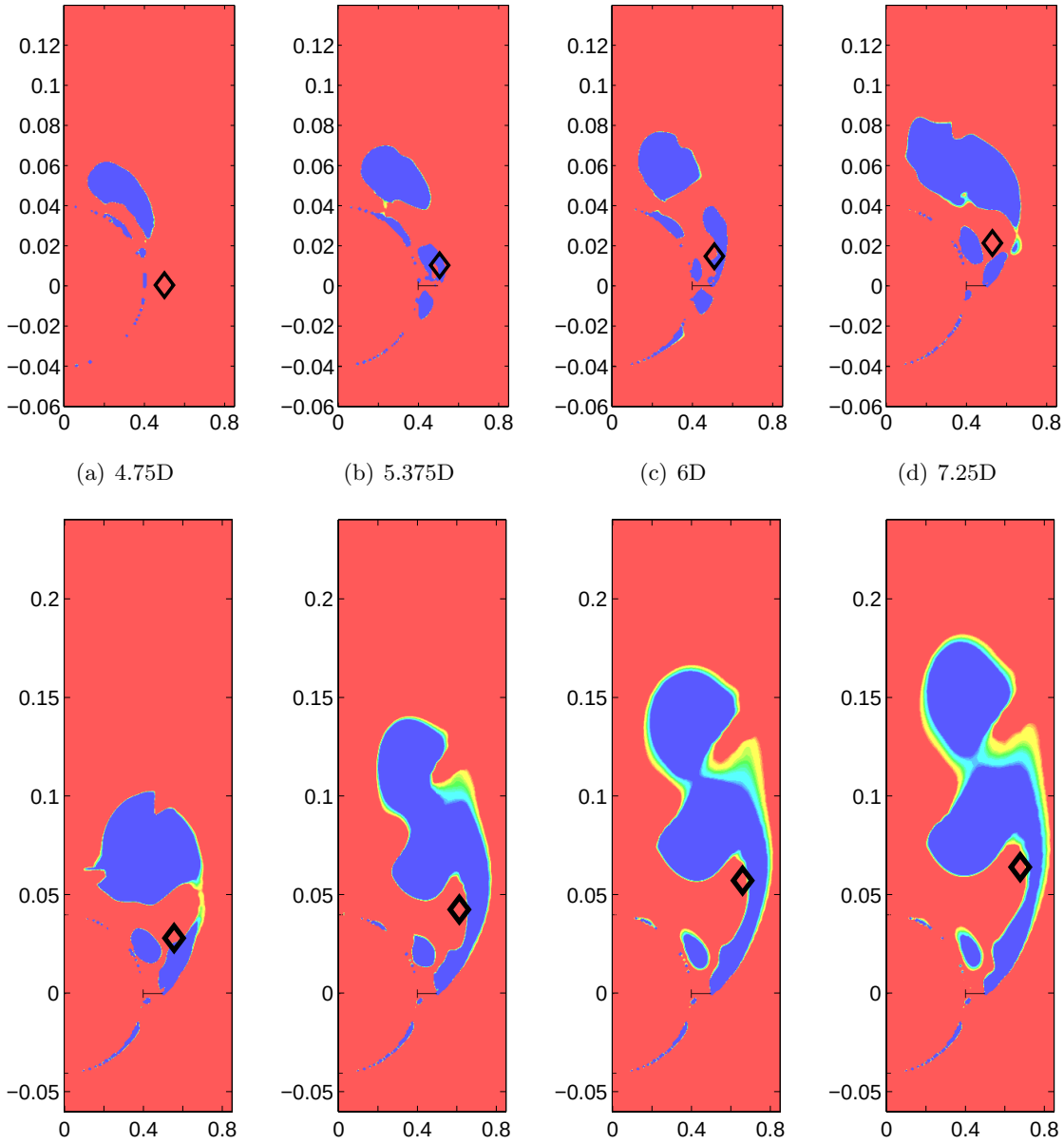

(a) 4.75D (b) 5.375D (c) 6D (d) 7.25D

(e) 8.5D (f) 11D (g) 13.5D (h) 14.75D

Figure 5.9: Vortex development for $\alpha = 20°$, SCV

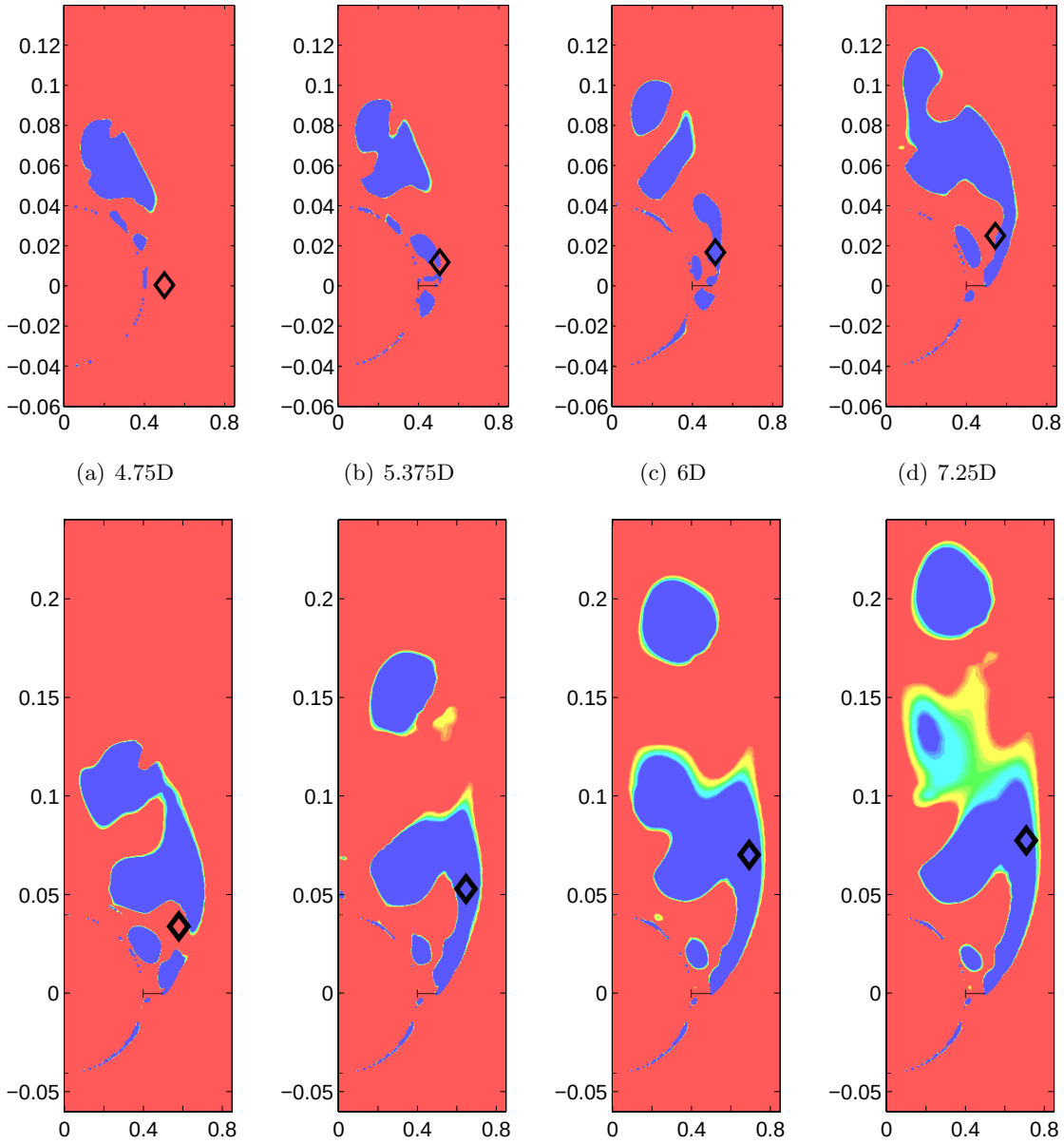

(a) 4.75D (b) 5.375D (c) 6D (d) 7.25D

(e) 8.5D (f) 11D (g) 13.5D (h) 14.75D

Figure 5.10: Vortex development for $\alpha = 25°$, SCV

An alternative method of viewing the vortex position is shown in Figure 5.11 to Figure 5.13. The growing deviation of the concentrated vortex is illustrated. The deviation is acceptable for 2° and still usable at 4°. The angles of attack greater than 6° are not shown simply because the deviation is already too large and not worth illustrating. As mentioned, one characteristic of the SCV method is that the position of the vortex is predicted increasingly further away from the centreline as the angle of attack increases, which is in direct contrast to the CFD simulations and experimental correlations. This outward movement of the vortex is expected as it is the mechanism which enforces the Joukowski-Kutta condition at the side edge. At 2° (see Figure 5.11) the CFD predicts a change in the trend in the vortex position at 15 calibers. This is because of the change in the profile of the strake (resulting in expansion waves) which interacts with the shed vortex because of the low vortex strength.

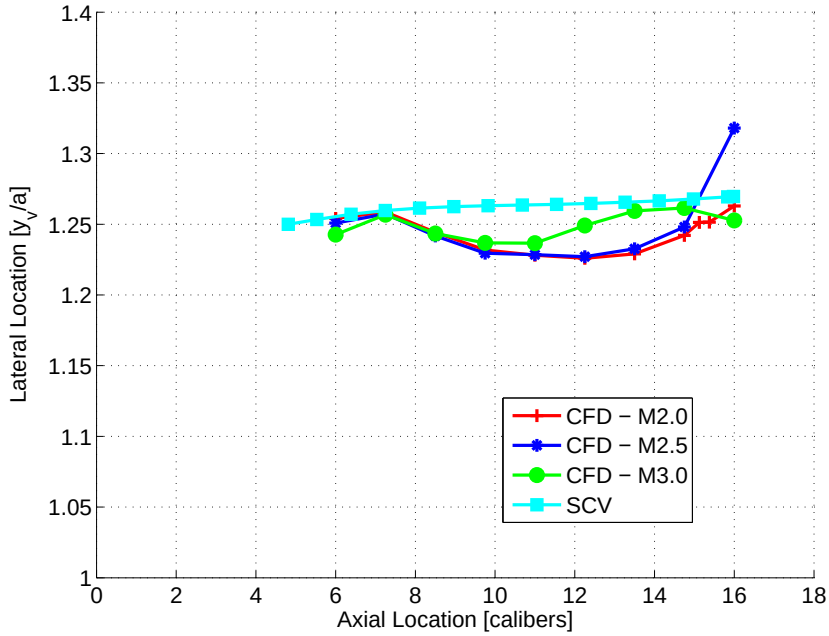

(a) Lateral

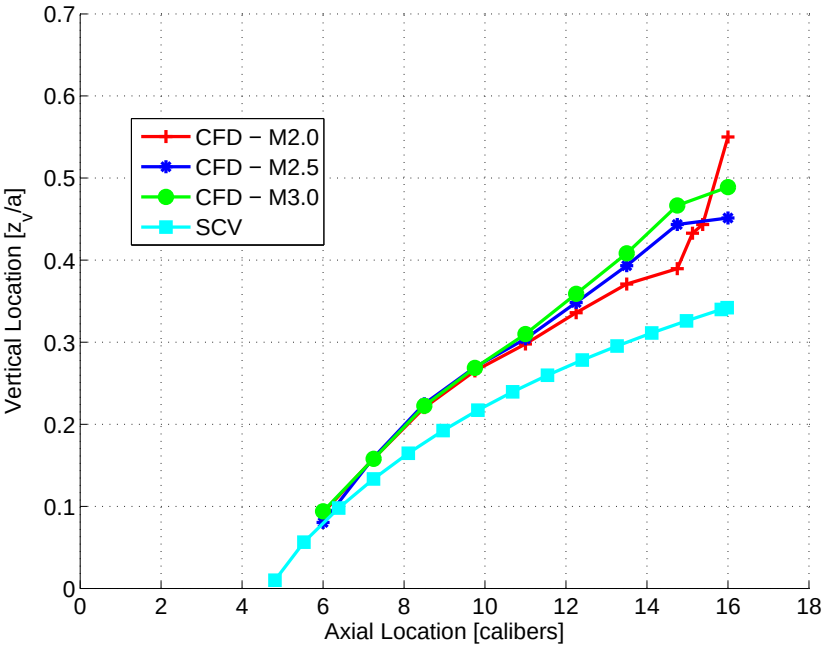

(b) Vertical

Figure 5.11: CFD and SCV concentrated vortex position comparison at $\alpha = 2°$

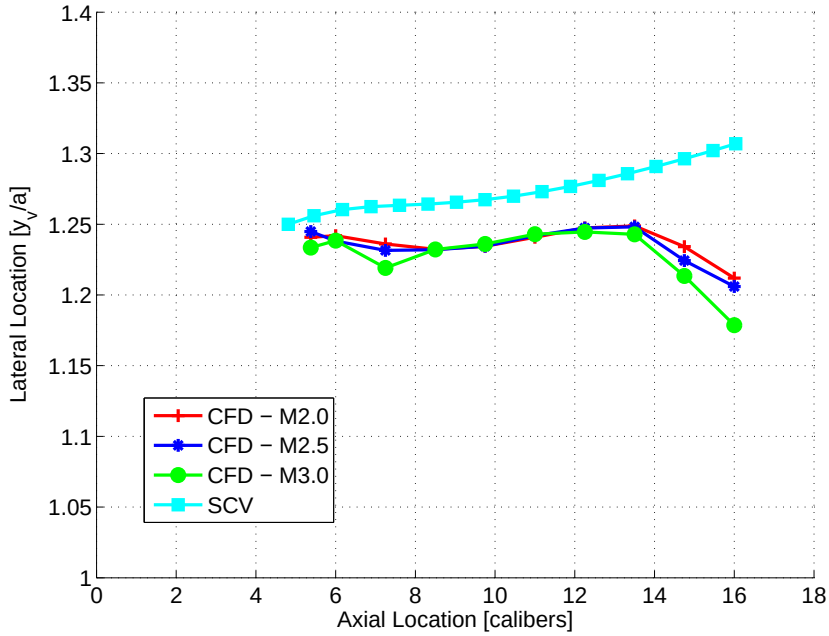

(a) Lateral

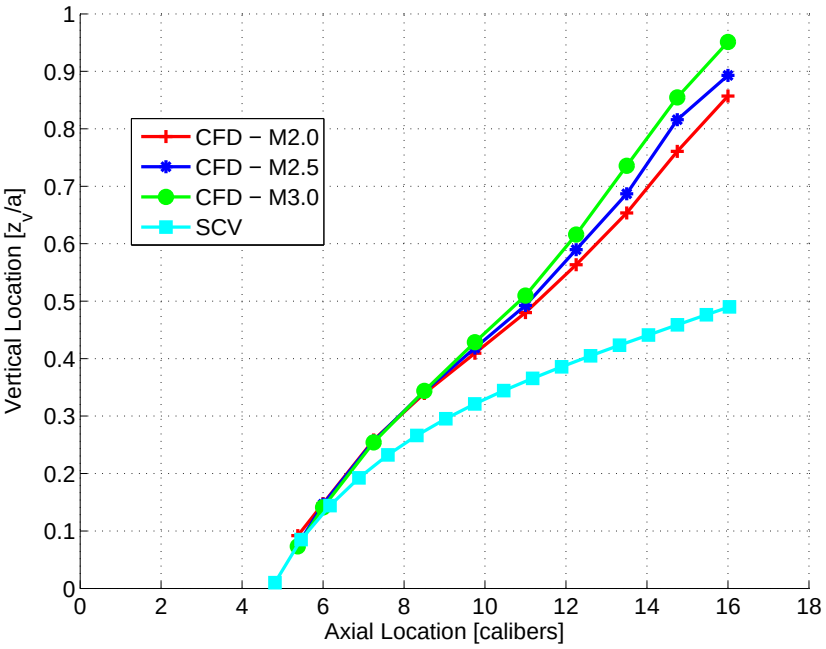

(b) Vertical

Figure 5.12: CFD and SCV concentrated vortex position comparison at $\alpha = 4°$

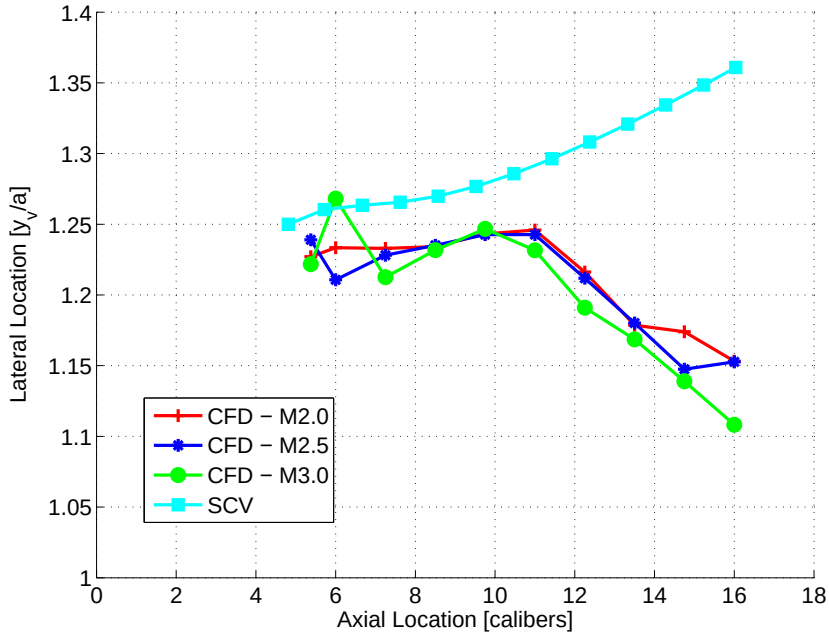

(a) Lateral

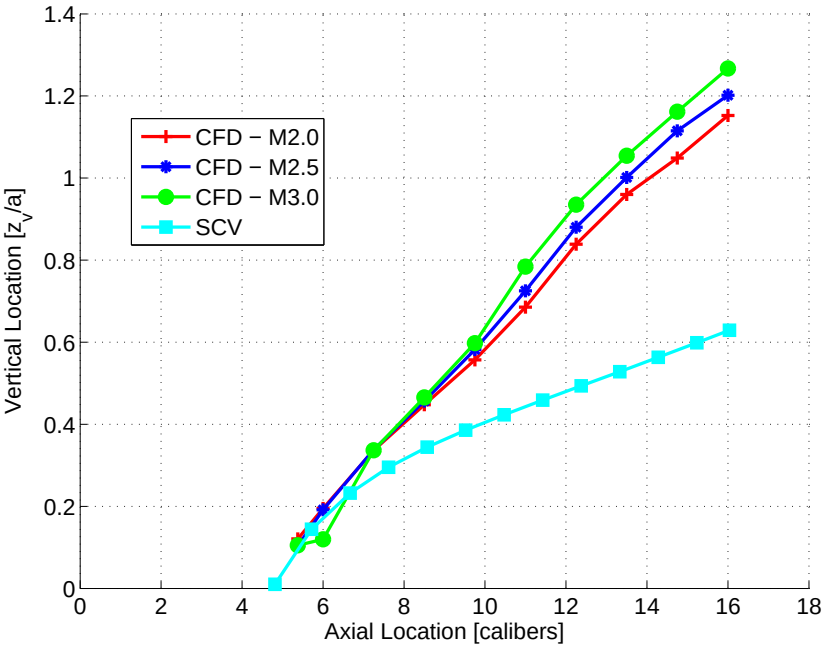

(b) Vertical

Figure 5.13: CFD and SCV concentrated vortex position comparison at $\alpha = 6°$

As a further validation of the SCV simulations, the concentrated vortex strength, Γ', is compared to that measured from the CFD simulations. Figure 5.14 and Figure 5.15 plot the CFD simulations against the SCV predictions for the angles of attack from 2° to 6°. The higher angles have been excluded because the prediction of the vortex position and loads start to diverge at 6°. The concentrated vortex strength compares well with, though higher than the CFD simulations indicating the suitability of the SCV method to predicting the side edge flows at the low angles. The change in position of the vortex at 2° for Mach 2.0 is also reflected in the vortex strength which decreases considerably, and is because of the influence of the change in profile at the end of the strake. A drop in the vorticity towards the end of the strake for the 4° and 6° cases indicates the effect of the secondary vortex and the increasing inability of the SCV method to model the flow features faithfully.

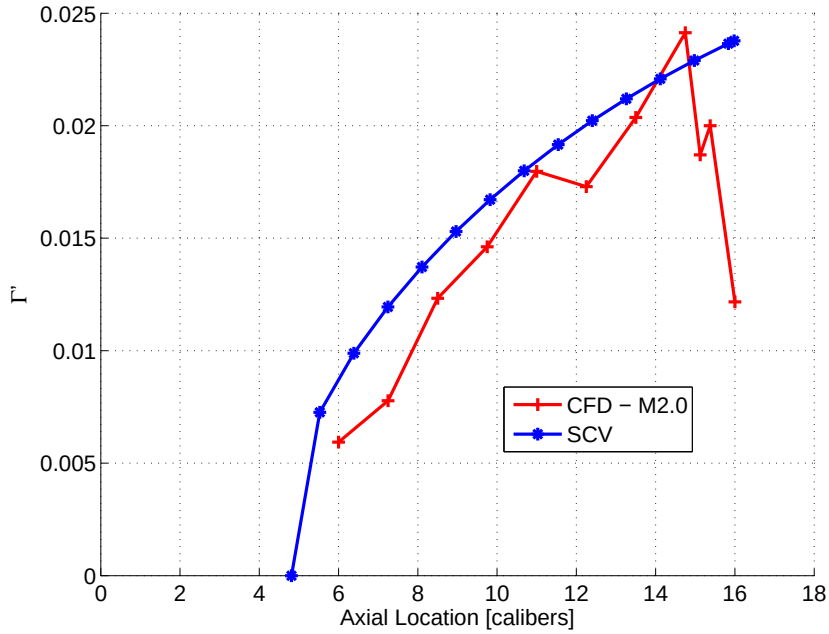

(a) 2°

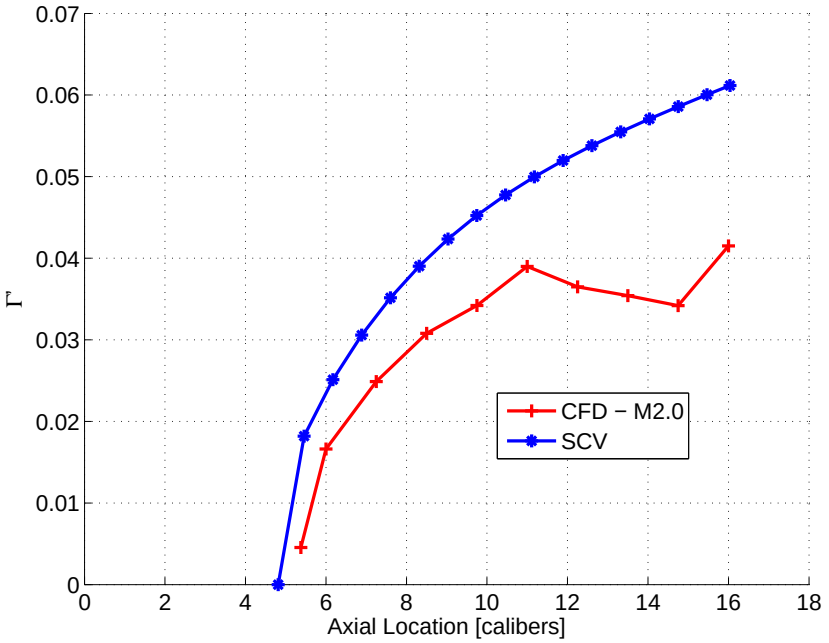

(b) 4°

Figure 5.14: CFD and SCV comparisons of the non-dimensionalised concentrated vortex strength for 2° and 4°

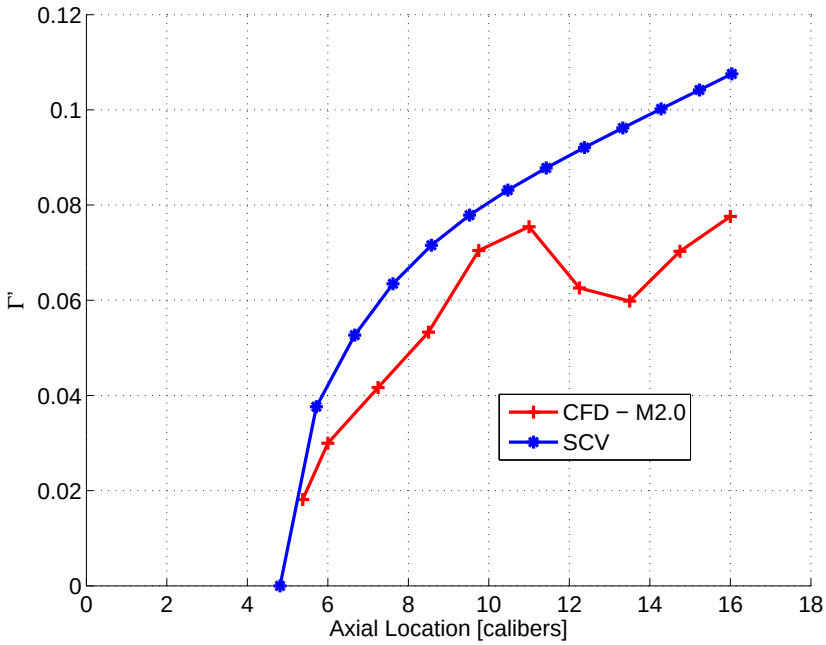

Figure 5.15: CFD and SCV comparisons of the non-dimensionalised concentrated vortex strength for 6°

5.5 Discussion

From the simulations performed it can be seen that the single concentrated vortex model of Bryson only captures the effects of the shed side edge vortex accurately at low angles of attack i.e. <4°. From the implementation of this method it is clear that the flow physics of the lee side separated flow i.e. rolled up vortex sheet into a single concentrated vortex, is governed by more than the Joukowski-Kutta condition at the moderate and higher angles of attack. Not only is it possible, but it is recommended that the SCV method be used at low angles of attack because the vortex position is also well predicted.

The deviation of the SCV method at low angles corresponds to the emergence of the secondary vortex and is not a compressibility effect. The secondary vortex modifies the Joukowski-Kutta condition which is the same as for a sharp edged delta wing [83]. The applicability of the method to angles less than 4° is in contrast to delta wings, where the single concentrated vortex model of Legendre [79] and its subsequent modifications [80][81] were applicable from 0° to 20°.

The SCV method whilst still providing solutions above 4° angles of attack is recommended to only be used at low angles of attack ($\leq 4°$).

Chapter 6

Discretised Vortex Model

6.1 Introduction

The method presented in this chapter builds upon the initial formulation of Chapter 3, where the transformations from the physical to circle plane and the equations of motion of vortices were developed. The method employed in this chapter falls into the class of the discretised vortex model (DVM) methods. The primary feature of this methods is that multiple elemental vortices are shed from separation points and these are convected into the fluid at the local fluid velocity. This method has its origins in the proposal by Rosenhead in the study of unsteady vortex sheets. Subsequent investigators have utilised this method to study the flow over bodies, wing-body combinations and plates. The wing-body combinations have been limited to wings of swept back leading edge and large span to body ratios. The application to wing-body combinations of low span to body ratios and wings with substantial side edges has not been previously performed. The closest application to configurations similar to that used in this thesis has been for chine configurations and at subsonic speeds. The presentation of the method and it application to the configuration at hand starts with the continued theoretical development of the DVM method as applied to cruciform wing-body configurations and is subsequently applied to the angles of attack of interest where upon the results are compared to the validated CFD simulations.

6.2 Vortex Shedding for Cruciform Wing-Body Configurations

6.2.1 Boundary Conditions

Three conditions need to be satisfied to define the shed vortex namely its position in two orthogonal directions and its strength. In the potential flow formulation, at the side edge, the velocity is infinite, which is physically untenable and separation occurs. The nature of the edge is more suitable defined by the Joukowski-Kutta condition, as a

number of investigators have applied. For the application of a two dimensional linearised potential flow solution this Joukowski-Kutta condition is adequate. For slender delta wings, this conditions has been identified as not entirely satisfactory, though still adequate [79][80][82][83][75]. For the potential $W(\sigma)$ the Joukowski-Kutta condition specifies that at the side edge in the circle plane that a stagnation condition exists, or

$$\frac{dW(\nu)}{d\nu} = 0 \tag{6.1}$$

Specifying a condition such as the Joukowski-Kutta condition at the side edge thus leaves the shed vortex strength to be specified before the position of the vortex can be determined.

6.2.2 Joukowski-Kutta Condition

From chapter 3, the complex potential is

$$W(\nu) = -iV\sin\alpha e^{-i\phi_x}\left(\nu - \frac{r_o^2 e^{i2\phi_x}}{\nu}\right) - \sum_{k=1}^{n}\frac{i\Gamma_k}{2\pi}\ln\left(\frac{\nu-\nu_k}{\nu-\frac{r_o^2}{\bar{\nu_k}}}\right) \tag{6.2}$$

The complex velocity, $\frac{dW}{d\sigma}$, is

$$\frac{dW}{d\sigma} = \frac{dW(\nu)}{d\nu}\frac{d\nu}{d\sigma} \tag{6.3}$$

or

$$\frac{dW}{d\sigma} = \left[-iV\sin\alpha e^{-i\phi_x}\left(1 + \frac{r_o^2 e^{i2\phi_x}}{\nu^2}\right) - \sum_{k=1}^{n}\frac{i\Gamma_k}{2\pi}\left(\frac{1}{\nu-\nu_k} - \frac{1}{\nu-\frac{r_o^2}{\bar{\nu_k}}}\right)\right]\frac{d\nu}{d\sigma} \tag{6.4}$$

As mentioned, at the side edges, $\pm s_m$, $\frac{d\nu}{d\sigma}$ is undefined because $\nu = \pm r_o$ and the flow at a physical level is expected to turn through an angle of 2π, which is physically untenable. Physically the flow separates, while in the circle plane, a stagnation condition exists, or repeating equation 6.1

$$\frac{dW(\nu)}{d\nu} = 0$$

From equation 6.4 the Joukowski-Kutta condition is:

$$-iV\sin\alpha e^{-i\phi_x}\left(1 + \frac{ro^2 e^{2i\phi}}{\nu_{sp}^2}\right) = \frac{i}{2\pi}\sum_{k=1}^{n}\Gamma_k\left(\frac{1}{\nu_{sp}-\nu_k} - \frac{1}{\nu_{sp}-\frac{r_o^2}{\bar{\nu_k}}}\right) \tag{6.5}$$

where ν_{sp} is the position in the circle plane where separation occurs.

6.2.3 Shed Vortex Strength and Vortex Sheet Model

The previous methods used to determine the strength of the shed vorticity is reviewed in fair detail by reference [127]. Almost all of the methods used concentrate their efforts on configurations with delta-wing or triangular wings, where as [127] seems to be the only method concerned with chines or configurations that have significant side edges.

The method used for smooth bodies as defined in references [62], [63] and [65] is:

$$\frac{\Gamma}{V} = \frac{u_e^2}{2V^2}\frac{\Delta x}{\cos\alpha}\delta_s \tag{6.6}$$

where δ_s is the reduction factor, u_e is the surface velocity in the cross-flow plane and Δx is the axial distance increment. For supersonic speeds the reduction factor is normally chosen as 1.0, while at subsonic speeds the value of 0.6 is used. This formulation is obtained by considering the vorticity in the boundary layer at the separation point.

Reference [127] indicates that for sharp edges the smooth body criterion does not seem applicable. One criteria used is to assume that the flow is conical [79][81][126], thus defining the position of the vortex and the strength of the vortex is a result of the Joukowski-Kutta condition and the conical flow assumption.

Reference [83] modified the Joukowski-Kutta condition for delta-wings by effectively discarding it, whilst maintaining the conical flow assumptions, and postulates that the leading edge vorticity is shed at an angle of $\alpha/4$. This was necessary to account for the lack of modelling the secondary vortex.

The method of Sacks [75] assumes that the velocity at the point of initial separation on a sharp edge is $v = 0.5V\alpha$ and the shed vortex is convected outward along the wing span axis for a distance $v\Delta t$. The fundamental derivation of this starting condition does not seem to be clearly elucidated from the text, other than a possible derivation from water tank studies, where the velocity, v, is derived from the average of the upper and lower surface velocities, ψ_u and ψ_l, respectively, or:

$$v = \frac{V}{2}\left(\psi_u + \psi_l\right) \tag{6.7}$$

Reference [75] did, however, indicate that the water tank experiments were unsuccessful. The shed line vorticity is then replaced by a single vortex placed such that the Joukowski-Kutta condition is satisfied. Subsequent shed vorticity is determined from the local v-velocity at the (finite) limiting value at the strake edge.

For chines, reference [127] utilised the same procedural methodology as reference [75] but calculates the velocity at the point of separation as the average of the v-velocity over the outer 10 percent of the chine, excluding the singularity. During the development of the methods employed by reference [127] an alternative method to start the solution which models the chine as a single panel lifting surface was attempted. A vortex is placed on the single lifting panel, at half semispan, from which the initial vortex strength can be determined and subsequent shed vorticity is determined using the outer 10 percent

v-velocity method. The problem with the single panel method is that the initial shed vortex is of much lower strength leading to a lag in the shed vorticity. An additional, but unsuccessful method was to determine the shed vorticity strength using the vorticity in the boundary layer as for smooth bodies by using the average of the velocity distribution tangent to the lower surface of the chine near the outer 10 percent of the semispan.

The method employed in this thesis uses the method of Sacks simply because it is theoretically based and utilises less numerical calculations.

6.2.4 Joukowski-Kutta Condition due to Shed Vortex Sheet

As the free vortices move as Lagrangian fluid particles, the Joukowski-Kutta condition is satisfied by the shed vortex sheet at each time step. Equation 6.5 can thus be rewritten as:

$$\begin{aligned} -iV\sin\alpha e^{-i\phi_x}\left(1+\frac{r_o^2e^{2i\phi_x}}{\nu_{sp}^2}\right) &= \frac{i}{2\pi}\sum_{k=1}^{n}\Gamma_k\left(\frac{1}{\nu_{sp}-\nu_k}-\frac{1}{\nu_{sp}-\frac{r_o^2}{\bar{\nu_k}}}\right) \\ &\quad +\frac{i}{2\pi}\sum_{l=1}^{m}\int\gamma_l\left(\frac{1}{\nu_{sp}-\nu_l}-\frac{1}{\nu_{sp}-r_o^2/\bar{\nu_l}}\right)ds \quad (6.8) \end{aligned}$$

where γ_l is the line vortex strength. If the length, ds, and shape of the vortex sheet is defined, the strength of the line vortex, γ_l, can be determined. The shape of the sheet is a straight line, whilst the length is simply the product of the velocity of the velocity at the Joukowski-Kutta edge and the incremental time step.

6.2.5 Shed Velocity at the Joukowski-Kutta Edge

The local velocity at the Joukowski-Kutta edge, can be determined from the velocity potential

$$v-iw=\left.\frac{dW}{d\sigma}\right|_{\nu=\nu_{sp}}=\left.\frac{dW}{d\nu}\frac{d\nu}{d\sigma}\right|_{\nu=\nu_{sp}} \quad (6.9)$$

The transformation factor $\frac{d\nu}{d\sigma}$ is undefined at the separation locations. This does not, however, prevent us from determining the edge velocities as L'Hopitals rule can be applied.

Using Equation 6.4 this can be generalised as

$$\frac{dW}{d\sigma}=\left[-iV\sin\alpha e^{-i\phi_x}\left(1+\frac{r_o^2e^{i2\phi_x}}{\nu^2}\right)-\sum_{k=1}^{n}\frac{i\Gamma_k}{2\pi}\left(\frac{1}{\nu-\nu_k}-\frac{1}{\nu-\frac{r_o^2}{\bar{\nu_k}}}\right)\right]\frac{d\nu}{d\sigma}$$

Inserting the Joukowski-Kutta condition from Equation 6.5, and evaluating at the a Joukowski-Kutta location yields

$$
\begin{aligned}
v - iw &= \frac{-i}{2\pi}\frac{d\nu}{d\sigma}\sum_{k=1}^{n}\Gamma_k\left[\frac{1}{\nu-\nu_k} - \frac{\bar{\nu_k}}{\nu\bar{\nu_k} - r_o^2}\right. \\
&\left. + \frac{\nu^2 + r_o^2 e^{2i\phi_x}}{\nu^2\left(1 + \frac{r_o^2 e^{2i\phi_x}}{\nu_{sp}^2}\right)}\left(\frac{1}{\nu_{sp}-\nu_k} - \frac{\bar{\nu_k}}{\nu_{sp}\bar{\nu_k} - r_o^2}\right)\right]
\end{aligned} \tag{6.10}
$$

If the conformal transformation scaling factor $\frac{d\nu}{d\sigma}$ is defined as

$$
\frac{d\nu}{d\sigma} = X\frac{Y}{Z} \tag{6.11}
$$

the velocity at the Joukowski-Kutta location can be rewritten as

$$
\begin{aligned}
v - iw &= \frac{-i}{2\pi}\sum_{k=1}^{n} X\frac{Y}{Z}\Gamma_k\left[\frac{1}{A} - \frac{\bar{\nu_k}}{B} + \frac{C}{\nu_{sp}^2 F}\left(\frac{1}{D} - \frac{\bar{\nu_k}}{E}\right)\right] \\
&= \frac{-iX}{2\pi}\sum_{k=1}^{n}\frac{Y}{Z}\Gamma_k\left[\frac{F\left(BDE\nu^2 - \nu^2 ADE\bar{\nu_k} - ABC/F(E - \bar{\nu_k}D)\right)}{\nu^2 ABDEF}\right] \\
&= \frac{-iX}{2\pi}\sum_{k=1}^{n}\frac{f(\nu)}{g(\nu)}
\end{aligned}
$$

where

$$
\begin{aligned}
A &= \nu - \nu_k \\
B &= \nu\bar{\nu_k} - r_o^2 \\
C &= \nu^2 + r_o^2 e^{2i\phi_x} \\
D &= \nu_{sp} - \nu_k \\
E &= \nu_{sp}\bar{\nu_k} - r_o^2 \\
F &= 1 + \frac{r_o^2 e^{2i\phi_x}}{\nu_{sp}^2}
\end{aligned}
$$

Applying L'Hopitals rule yields

$$
\begin{aligned}
\frac{df(\nu)}{d\nu} &= YF\left[2\nu DE(B - \bar{\nu_k}A) - \frac{E - \bar{\nu_k}D}{F}\left(BC + \bar{\nu_k}AC + 2\nu AB\right)\right] \\
\frac{dg(\nu)}{d\nu} &= \frac{dZ}{d\nu}\nu^2 ABDEF
\end{aligned} \tag{6.12}
$$

For a planar wing-body combination

$$\begin{aligned} \frac{d\nu}{d\sigma} &= \left(1-\frac{a^2}{\sigma^2}\right)\left(\frac{\nu^2}{\nu^2-r_o^2}\right) \\ X &= \left(1-\frac{a^2}{\sigma^2}\right) \\ Y &= \nu^2 \\ Z &= \nu^2 - r_o^2 \end{aligned} \tag{6.13}$$

and for a cruciform wing-body combination

$$\begin{aligned} \frac{d\nu}{d\sigma} &= \frac{\sigma}{\nu}\left(\frac{1-a^4/\sigma^4}{1-r_o^4/\nu^4}\right) \\ X &= \sigma\left(1-\frac{a^4}{\sigma^4}\right) \\ Y &= \nu^3 \\ Z &= \nu^4 - r_o^4 \end{aligned} \tag{6.14}$$

6.3 Vortex Impulse Loads

The loads due to the shed vortices imposed on the wing-body combination are calculated using the vortex impulse theorem [148][75], which states that the lift, L, due to a vortex and its image is proportional to the product of the strength, Γ, of the vortex and the distance between vortex and its image, ν_r, or:

$$L = \rho V \Gamma \nu_r \tag{6.15}$$

The incremental lift, ΔL, at each time step, x_i, is the change in the distance between vortex and its image, ν_r, between the start and end of the time step Δx, or

$$\Delta L = \rho V \sum_{k=1}^{n} \Gamma_k \left(\nu_k - \frac{r_o^2}{\bar{\nu}_k}\right) \tag{6.16}$$

The incremental pitching moment is

$$\Delta M = \Delta L \left(x_i - x_{mrc}\right) \tag{6.17}$$

At each time step, the incremental lift for the vortices and shed vortex sheet is

$$\Delta L = \rho V \left[\sum_{k=1}^{n} \Gamma_k \left(\nu_k - \frac{r_o^2}{\bar{\nu}_k}\right) + \sum_{l=1}^{m} \int_{s_m}^{s_m+ds} \gamma_l \left(\nu_{sp} - \frac{r_o^2}{\bar{\nu}_l}\right) ds\right] \tag{6.18}$$

where ds is the length of the vortex sheet. Recasting in the ν plane yields

$$\Delta L = \rho V \left[\sum_{k=1}^{n} \Gamma_k \left(\nu_k - \frac{r_o^2}{\bar{\nu}_k}\right) + \sum_{l=1}^{m} \int_{\nu_{sp}}^{\nu_{sp}+d\nu} \gamma_l \left(\nu_{sp} - \frac{r_o^2}{\bar{\nu}_l}\right) \frac{ds}{d\nu} d\nu\right] \tag{6.19}$$

6.4 Imposition of the Joukowski-Kutta Condition During Vortex Tracking

The Joukowski-Kutta condition is only imposed by Sacks in his implementation of the method at the start of each time step step rather than throughout the time stepping process. This limitation is overcome by replacing the circle formulation used by Sacks with the Joukowski-Kutta condition derived in Equation 6.5, or:-

$$-V \sin\alpha e^{-i\phi_x} = \frac{1}{2\pi\left(1+e^{2i\phi_x}\right)} \sum_{k=1}^{n} \Gamma_k \left(\frac{1}{r_o - \nu_k} - \frac{1}{r_o - \frac{r_o^2}{\overline{\nu_k}}} \right) \tag{6.20}$$

6.5 Secondary Boundary Layer Separation Simulation

The simulation of secondary separation due to the boundary layer has been previously modeled in 2D potential codes by Mendenhall [63] for circular and non-circular bodies at subsonic and supersonic speeds. The criterion used for secondary separation was that developed by Stratford for both laminar [155] and turbulent boundary layers [156]. The boundary layer for secondary separation on the lee side of the configuration was assumed to be laminar (the same as implemented by Mendenhall). To keep the separation physically realistic, separation was limited to the body only, and thus no separation was allowed on the strakes.

The simplified Stratford laminar separation criterion states that separation occurs when the following criterion is met

$$\left[C_{p\rho} \left(x \frac{\partial C_{p\rho}}{\partial x} \right)^2 \right] = 7.64 \times 10^{-3} \tag{6.21}$$

where $C_{p\rho}$ is the loss in non-dimensional maximum mainstream dynamic head and x is the distance from a stagnation point for a zero pressure gradient flow field.

This is the same criterion used by reference [63], though only for research purposes. Given that initial favourable gradients will exist when calculating the separation point, the equivalent distance, x_0, needs to be calculated. This is calculated using the Thwaites' or Energy Equation implemented by Stratford and is defined as

$$x_0 = \int_0^{x_0'} \left(\frac{U_1}{U_0} \right)^5 dx' \tag{6.22}$$

where x' is the actual distance from a stagnation point along the surface of the body in the lee side of the flow.

The non-dimensionalised loss in maximum mainstream dynamic head, $C_{p\rho}$, is defined by U_1/U_0, and the mainstream dynamic head corresponds to the point where the maximum velocity occurs from the stagnation point of interest.

The strength of the discrete vortex that is shed from the boundary has already been determined by reference [63] by considering the vorticity flux across the boundary and was listed as Equation 6.6 and reiterated here

$$\frac{\Gamma}{V} = \frac{u_e^2}{2V^2}\frac{\Delta x}{\cos\alpha}\delta_s$$

The vortex is positioned such that the velocity induced by the vortex cancels the surface velocity at the separation point. This yields a distance, dr, being the distance between the body and the surface of the body as

$$dr = \frac{2\Gamma a}{2\pi u_e a - \Gamma} \tag{6.23}$$

Mendenhall experienced numerical difficulties in the trajectory calculations of vortices that were placed too close to body, and therefore placed the shed vortex well outside the boundary layer at an arbitrary distance of 5% of the local radius from the surface to prevent the vortex from being trapped in the boundary layer. This particular limit was not implemented in this thesis. An upper limit of 15% of body radius was placed on a shed vortex because it was found that, on occasion, other vortices that were close to the shed vortex would result in the calculated distance being inordinately large. This is a difficulty of the DVM method because the vortices are essentially singularities at their centres and unrealistically high velocities are generated near the vortex core if a realistic viscous core is not modeled.

Lastly, not all the vortices were used to determine when separation occurred. When a vortex is placed close to the surface, the movement of the vortex from one time step to the next is insufficient, which results in a rapid and unrealistic forward movement of the separation point from one time step to the next. This is because the separation point remains essentially the same from one time step to the next and the location of maximum velocity or peak dynamic head as required by the Stratford criterion is predicted more forward that physically possible. Viewed alternatively, for a flat plate, the separation point over a long time period should remain at the same position. Placing a vortex at the separation point pushes the prediction of subsequent peak dynamic pressure forward because the flow must decelerate to zero at the predicted separation point, rather than maintaining the same separation point. The determination of where separation occurs is primarily determined by the external potential flow. For a 2D cylinder in incompressible flow at sub-critical Reynolds numbers, the separation point is between 80°–90° from the stagnation point. From a potential flow perspective, the flow must separate at an angle greater than 90° because the peak dynamic pressure is at 90°. The reason the flow separates slightly earlier is because the separated flow in the lee side modifies the potential flow field resulting in a slightly more forward separation point. Choosing to use the potential flow field will therefore result in a later separation point and leaving the vortex at its chosen position results in a rapid unrealistic forward movement of the separation point. The method of

placing the vortex at 5% of the body radius does overcome this.

This thesis uses a different method to overcome these limitations. A heuristic method was employed; this being to ignore vortices that are too close to the body surface. This method was used so that the boundary layer shed vortices would not be convected by the potential flow but create a secondary separation region. The heuristic method effectively simulates the thickening of the boundary layer. In essence, by ignoring vortices close to the surface, the separation criteria becomes more realistic and achieves the same effect as placing the vortex at a minimum distance of 5% from the surface.

6.6 Numerical Procedure

The numerical procedure employed is as follows:

1. Start the time stepping by assuming the edge velocity is $v_{sp} = V \sin \alpha/2$ from which the shed line vortex strength can be determined and an initial vortex can be placed
2. Calculate the length of the vortex sheet, ds in the physical and then circle plane using the edge velocity
3. Calculate the strength of the shed line vortex, γ_l, whilst satisfying the Joukowski-Kutta condition
4. Calculate the position of a shed concentrated vortex (which has the same strength as the shed line vortex) by satisfying the Joukowski-Kutta condition
5. Calculate the Joukowski-Kutta edge velocity
6. When the number of vortices exceeds a specified number, the second last vortex is combined with the last vortex to form the concentrated vortex. The strength of the vortex is the sum of the second last and last vortex, whilst its position is determined such that the vortex impulse of the separate loads is the same as the combined vortex. For this thesis the number chosen was 5 (the same as reference [65])
7. Calculate the loads imposed on the configuration using the vortex impulse theorem
8. Calculate the new positions of the vortices at the next chordwise station by integrating over the interval Δx and repeat steps 2 to 7

6.7 Body Vortex Simulation

For angles of attack above 10° a body vortex is predicted by both the CFD simulations and the engineering method of references [40] and [20]. In the simulation performed using the DVM method and for comparison to the validated CFD simulations, the position and strength of the body vortex was estimated from the CFD simulations using an average for

the vortex strength between the axial locations 4.75D and 5.25D. For the angle of attack of 10° the vortex was not simulated because its strength is small and does not affect the overall simulations. The positions and strengths of the body vortex for the various angles of attack are listed in Table 6.1. They were estimated by performing closed line integrals around points within a selected region outside the vortex core for the Mach 2.0 simulations. At 25° two vortices were identified.

Table 6.1: Estimated CFD Body Vortex Positions and Strengths

Angle of Attack	y_v/a	z_v/a	Γ'
15°	0.6277	1.124725	0.018109
20°	0.5199	1.469	0.084987
25°	0.558	1.27	0.256
	0.414	1.87	0.0879

6.8 Test Matrix and Execution

6.8.1 Grid Sensitivity

As for all discretised methods, the solution for a DVM method is in some way dependent on the number of discrete vortices or alternatively put, the number of steps employed along the strake edge. Since this particular implementation was derived from reference [75], the obvious starting point for the number of vortices shed was obtained from reference [75] which found that a 45 vortices was sufficient to model the flow over a body with a delta wing. A number of simulations were run to determine whether the 45 vortices shed would be sufficient. It was found that the 45 specified by Sacks was inadequate. At least 100 or double that specified by Sacks was required. This study was performed for an angle of attack of 10°, and is illustrated in Figures 6.1 to 6.3. The potential method excluding the boundary layer simulation was used to assess the grid sensitivity. From the concentrated vortex position and Joukowski-Kutta velocities (see Figures 6.1 and 6.3) it is evident that 120 or 240 vortices is required. The concentrated vortex strength shows a difference in the vorticity generated by the side edge depending on the number of vortices. As the number of steps are increased, the deficit in vorticity is evident for the smaller number of vortices. This is reflected in the Joukowski-Kutta velocity (Figure 6.3) where the vorticity generated for the 60 step case shows lower vorticity than for 120 steps and higher. The minimum number of steps of 120 was used for the subsequent simulations.

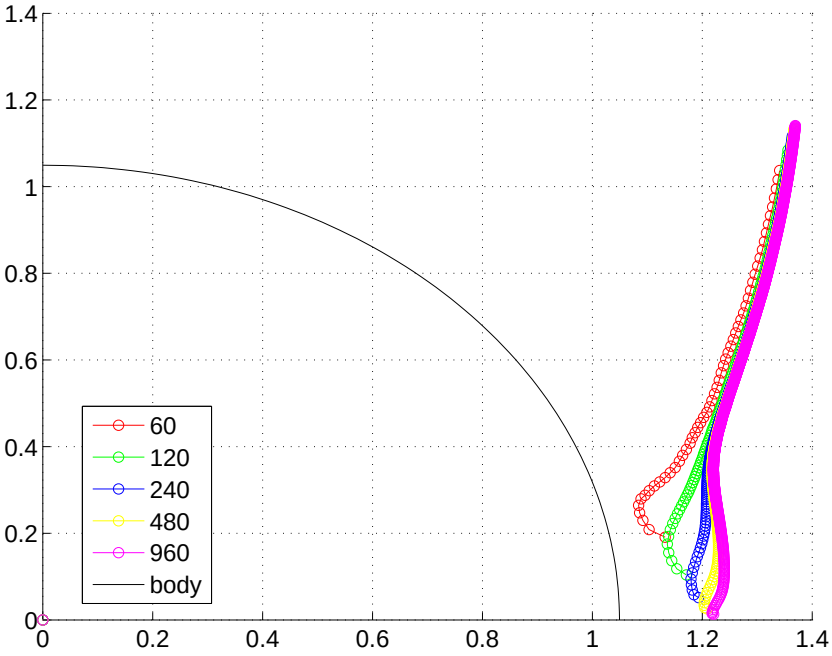

Figure 6.1: Vortex path as a function of step size (in the circle plane)

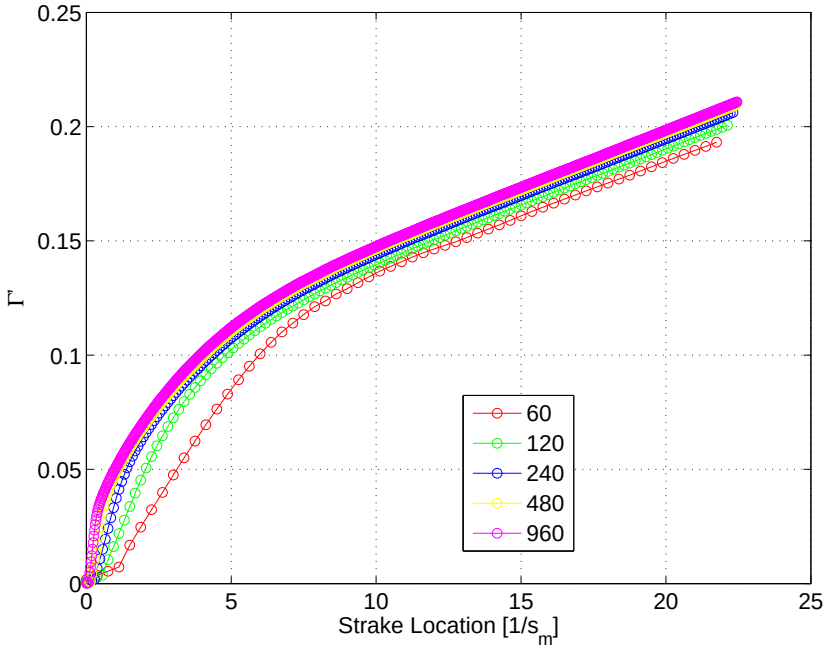

Figure 6.2: Vortex strength as a function of step size

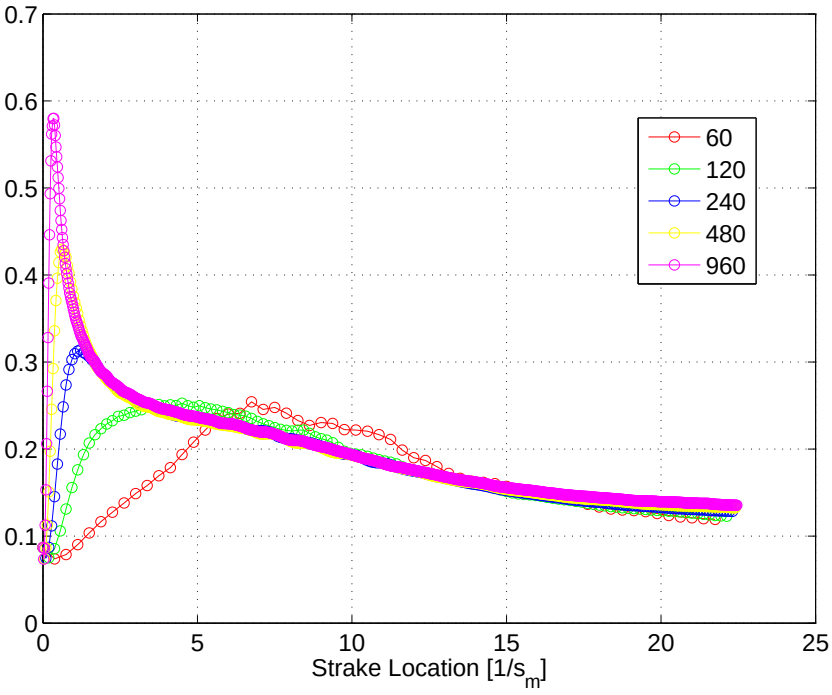

Figure 6.3: Kutta edge velocity as a function of step size

For this configuration of very low aspect ratio wings with side edges in combination with a circular body, it is interesting to note that a larger number of vortices is required to model the vortex behaviour sufficiently compared to a delta wing configuration. This is probably due to the vortex remaining attached for delta wings whereas the vortex for a side edge separates from the wing, or the gradients for the strake are higher than for a delta wing, thus requiring smaller steps to adequately capture the flow phenomenology.

6.8.2 Test Matrix

The test matrix was performed for the following configurations

- Potential
- Potential + Boundary Layer
- Potential + Boundary Layer @ 0.05r

The angles of attack simulated were 1°, 2°, 4°, 6°, 10°, 15°, 20° and 25° i.e. the same as the SCV and CFD simulations. It should be remembered that the simulations are only applicable for Mach 2.0 for the angles of attack above 10° because the vortex positions and strengths were obtained for this Mach number.

6.9 Results

6.9.1 Global Loads

The normal force and centre-of-pressure comparison of the overall configuration is shown in Figure 6.4. As for the SCV method, the discrete vortex method does not predict any Mach number dependency. As can be seen, the potential only method overpredicts the loads at angles of attack above 10°. The methods which model the boundary layer predict the effects better, with the deviations only manifesting themselves at the higher angles of attack (>15°). The centre-of-pressure prediction is very good at the moderate angles of attack, though as for the SCV method, the low angles of attack centre-of-pressure is predicted further back than the CFD simulations. At the higher angles of attack, the three methods diverge amongst each other when compared to the CFD simulations.

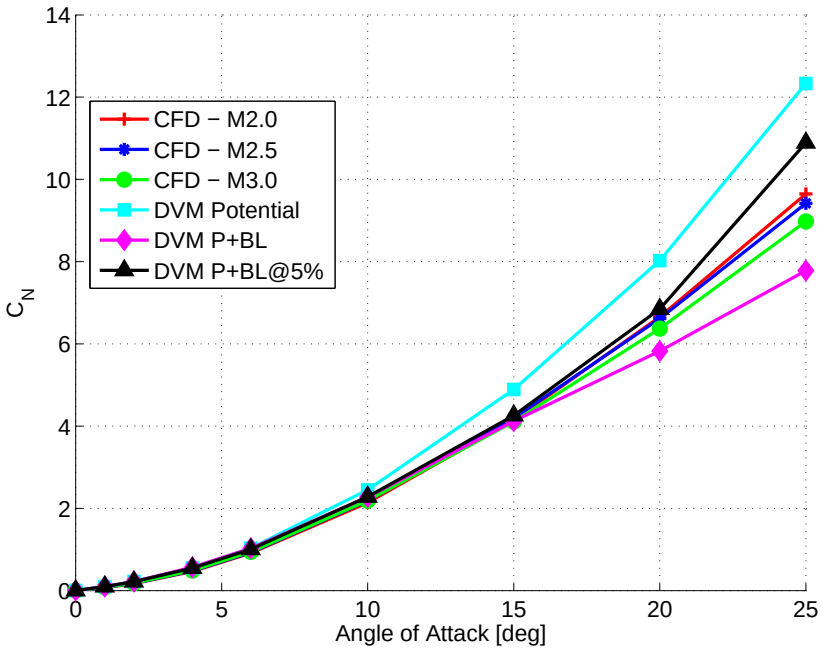

(a) Normal force

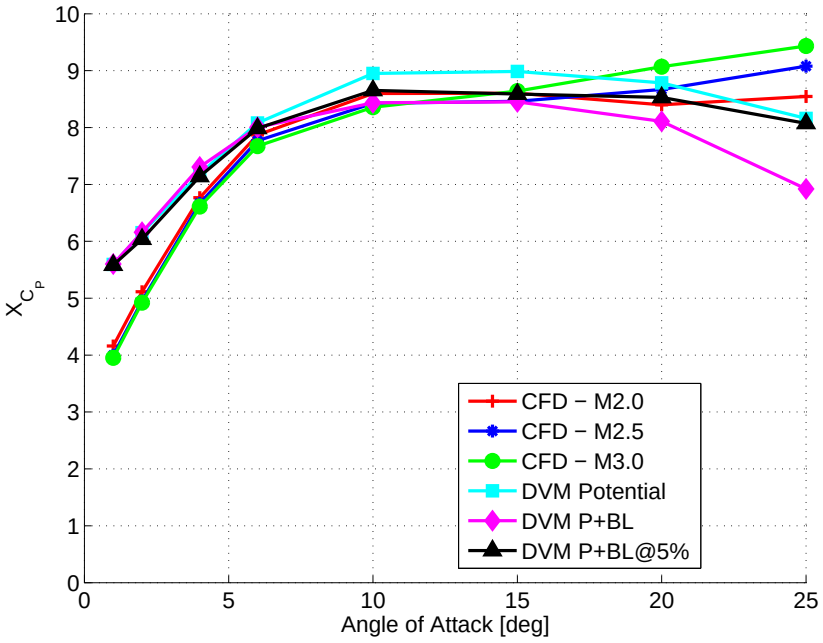

(b) Centre-of-pressure

Figure 6.4: CFD and DVM normal force and centre-of-pressure comparison

6.9.2 Detailed Flow Field

The differences and similarities observed in the interference loads can be seen in the detailed flow fields. Figure 6.5 to Figure 6.12 show selected 2D slices along the axial location of the body-strake configuration for the various angles of attack from 1° to 25° for the potential method. Figure 6.13 to Figure 6.20 show selected 2D slices along the axial location of the body plus strake configuration for the various angles of attack from 1° to 25° for the potential plus boundary layer method. The comparisons for the potential plus boundary layer separation vortices at 5% are shown in Figure 6.21 to Figure 6.28. For the cases with body vortices, the motion of these vortices are denoted by the large □ and + symbols. The vortices generated by boundary layer separation i.e. secondary vortices, are identified separately from those shed from the side edge. They are denoted by the light blue ∗ symbol, whilst the side edge vortices are denoted with a small black ∗ symbol.

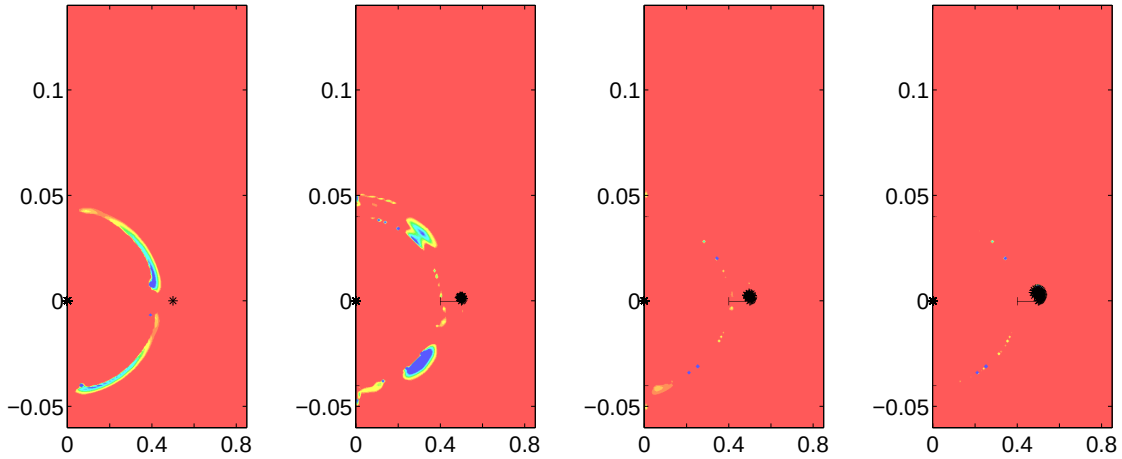

(a) 4.75D (b) 5.375D (c) 6D (d) 7.25D

(e) 8.5D (f) 11D (g) 13.5D (h) 14.75D

Figure 6.5: Vortex development for $\alpha = 1°$, potential only

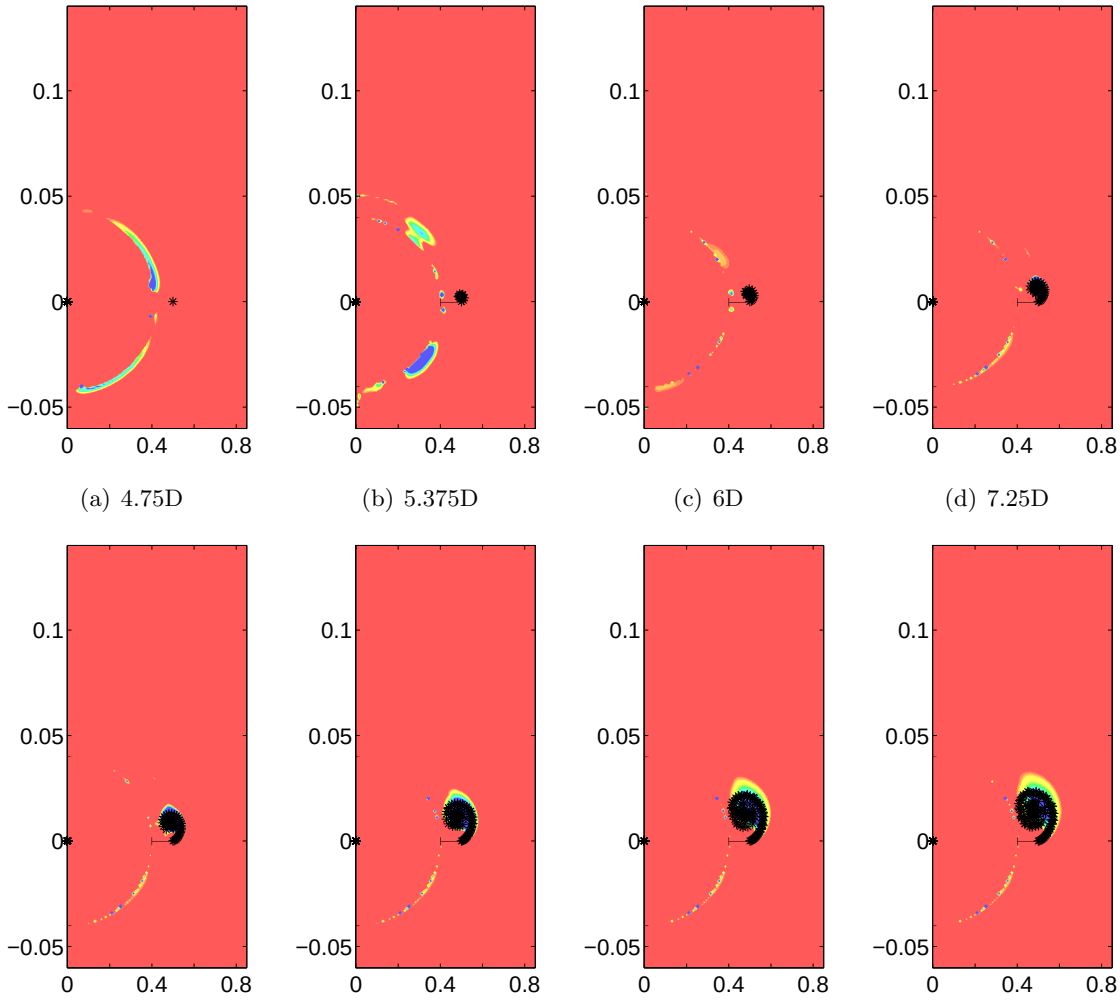

(a) 4.75D (b) 5.375D (c) 6D (d) 7.25D

(e) 8.5D (f) 11D (g) 13.5D (h) 14.75D

Figure 6.6: Vortex development for $\alpha = 2°$, potential only

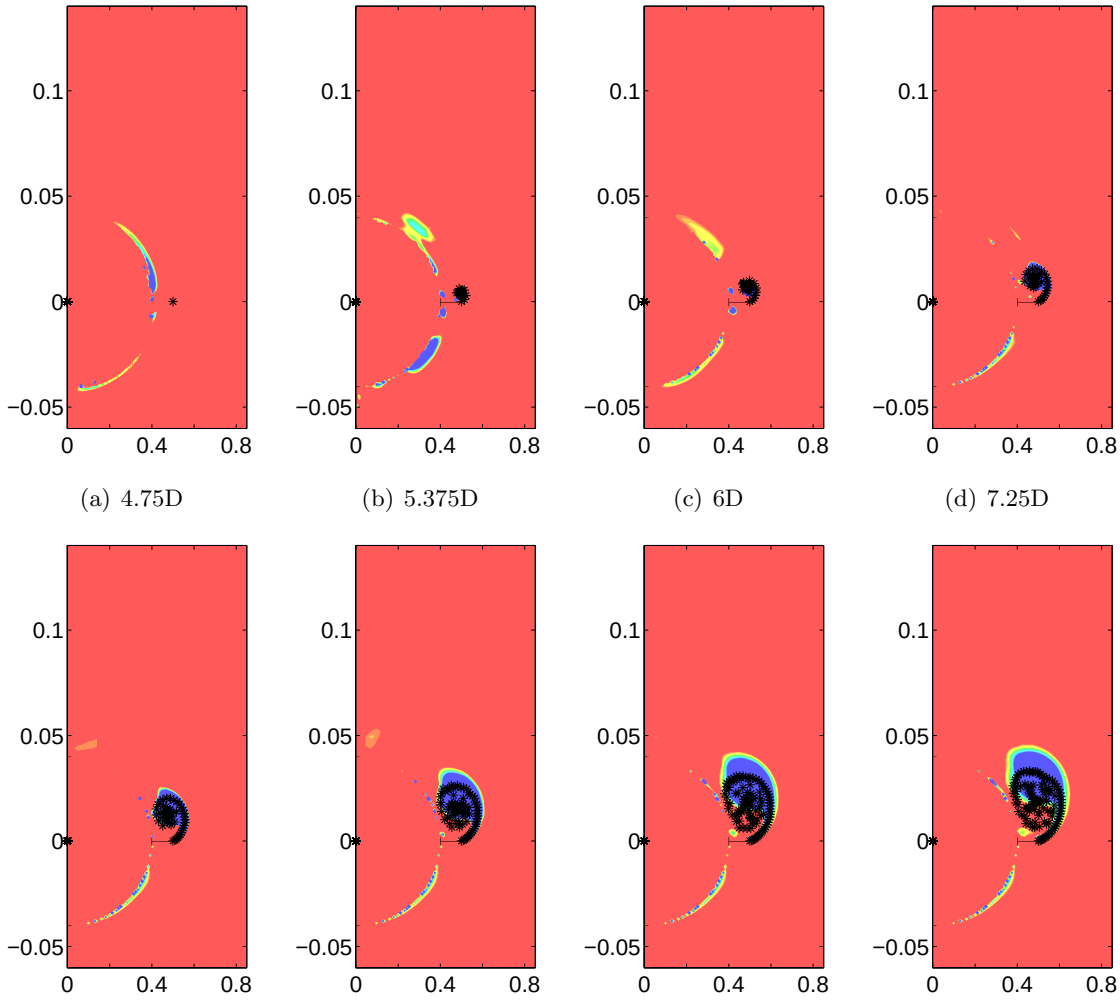

(a) 4.75D (b) 5.375D (c) 6D (d) 7.25D

(e) 8.5D (f) 11D (g) 13.5D (h) 14.75D

Figure 6.7: Vortex development for $\alpha = 4°$, potential only

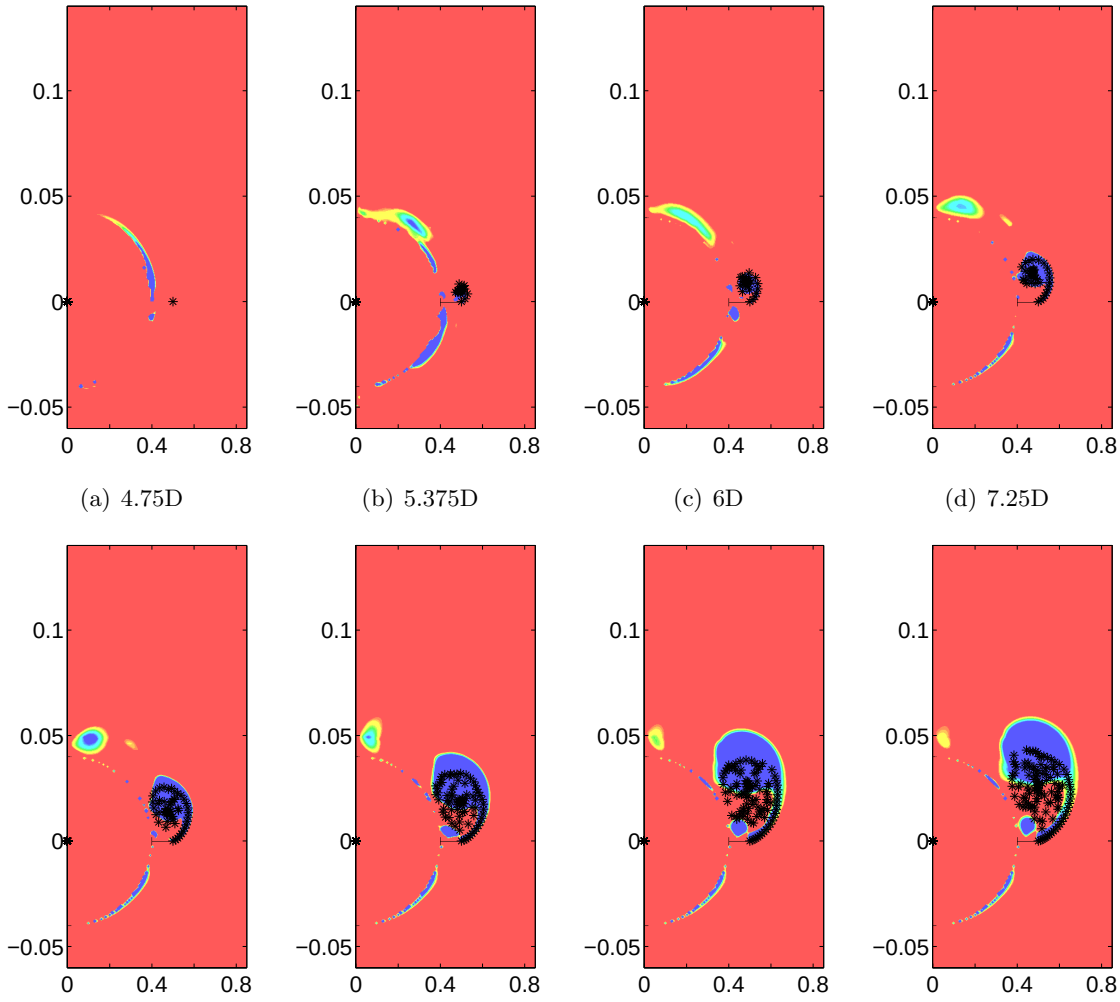

(a) 4.75D (b) 5.375D (c) 6D (d) 7.25D

(e) 8.5D (f) 11D (g) 13.5D (h) 14.75D

Figure 6.8: Vortex development for $\alpha = 6°$, potential only

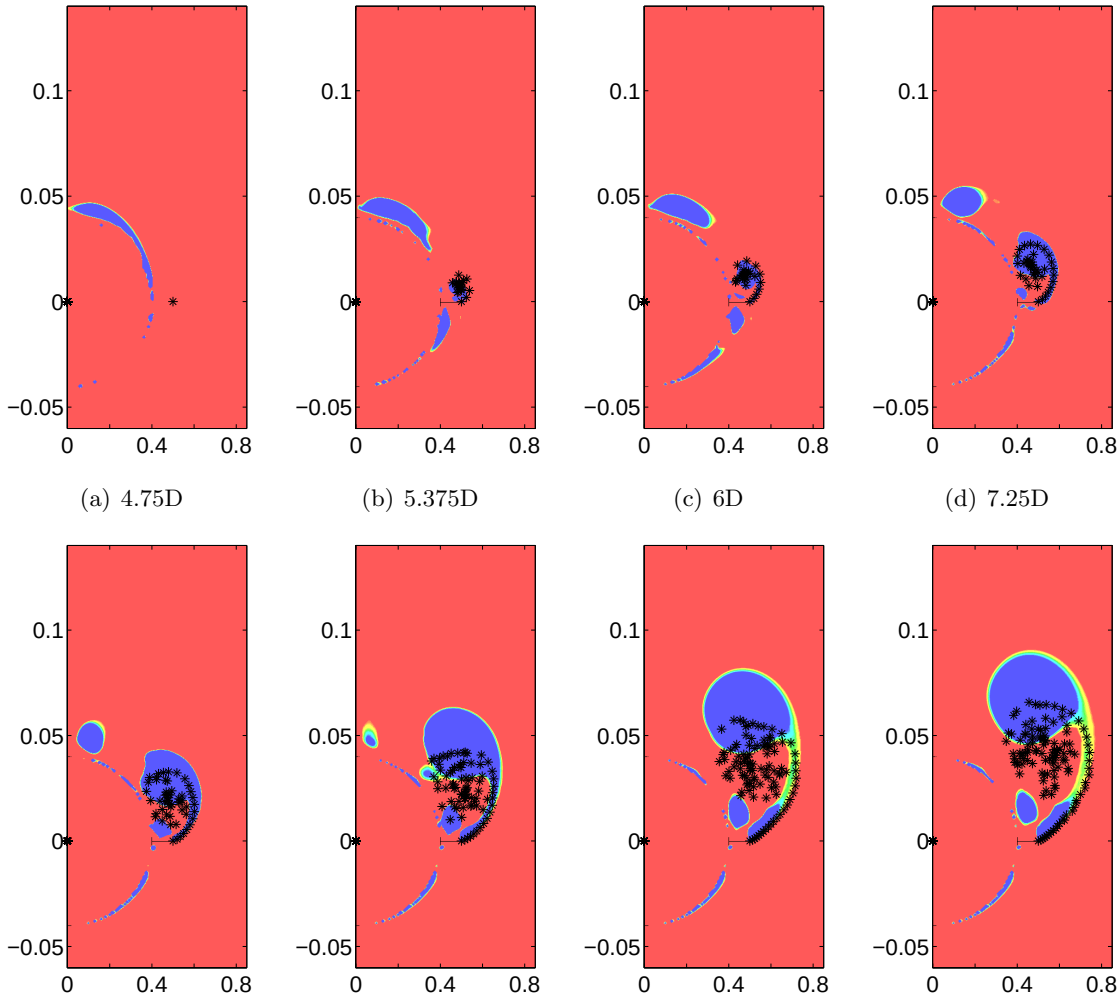

(a) 4.75D (b) 5.375D (c) 6D (d) 7.25D

(e) 8.5D (f) 11D (g) 13.5D (h) 14.75D

Figure 6.9: Vortex development for $\alpha = 10°$, potential only

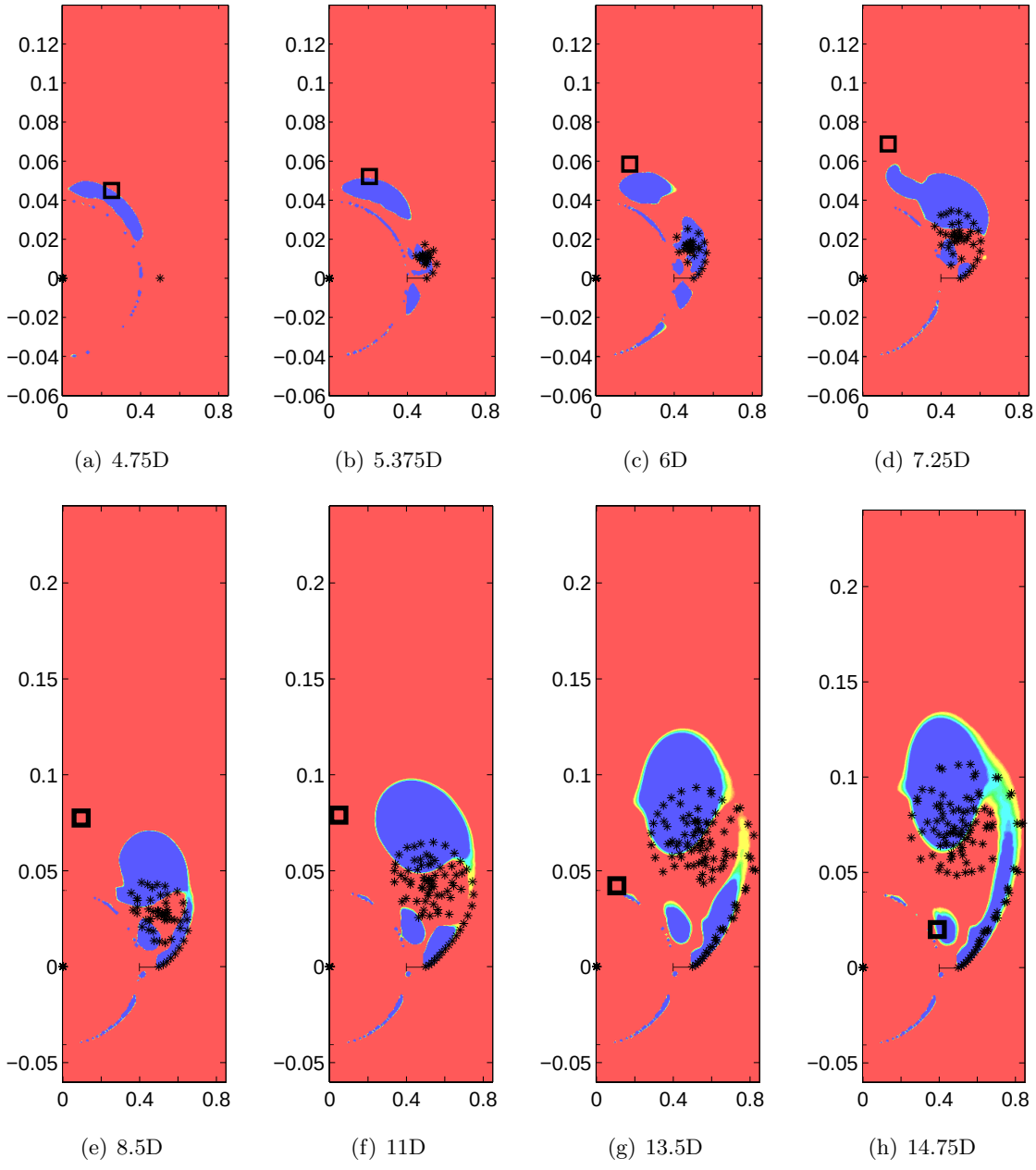

(a) 4.75D (b) 5.375D (c) 6D (d) 7.25D

(e) 8.5D (f) 11D (g) 13.5D (h) 14.75D

Figure 6.10: Vortex development for $\alpha = 15°$, potential only

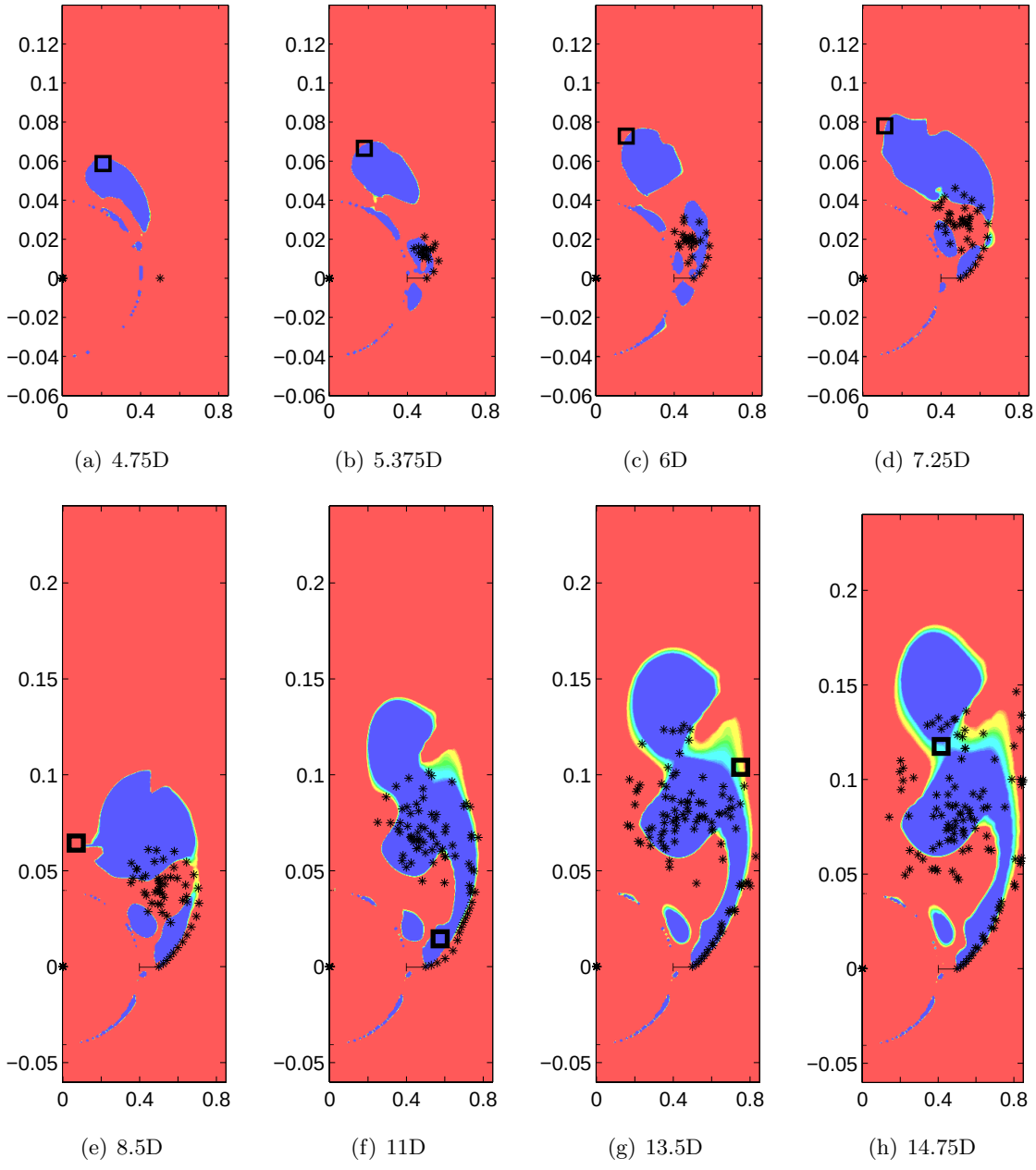

(a) 4.75D (b) 5.375D (c) 6D (d) 7.25D

(e) 8.5D (f) 11D (g) 13.5D (h) 14.75D

Figure 6.11: Vortex development for $\alpha = 20°$, potential only

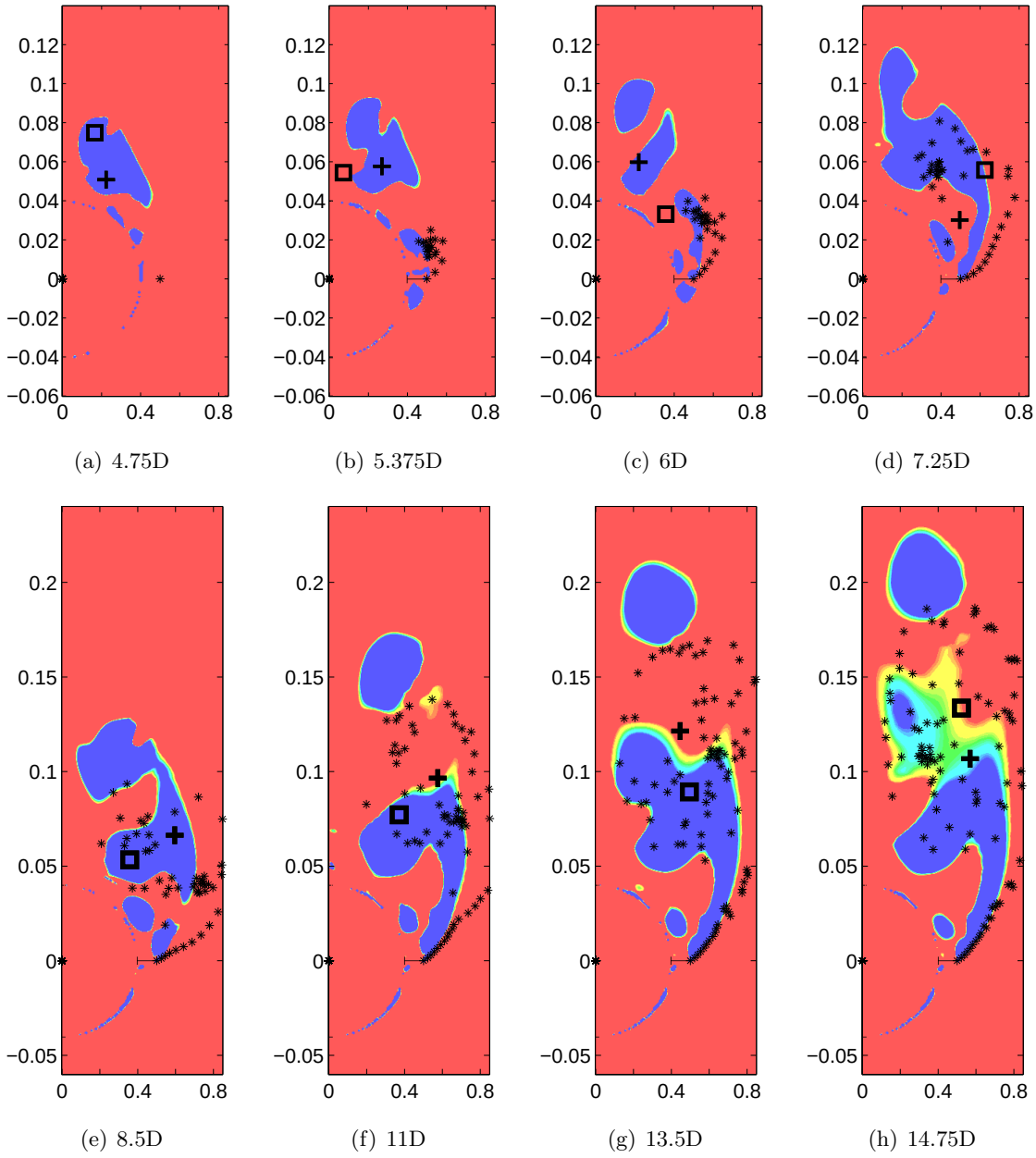

(a) 4.75D (b) 5.375D (c) 6D (d) 7.25D

(e) 8.5D (f) 11D (g) 13.5D (h) 14.75D

Figure 6.12: Vortex development for $\alpha = 25°$, potential only

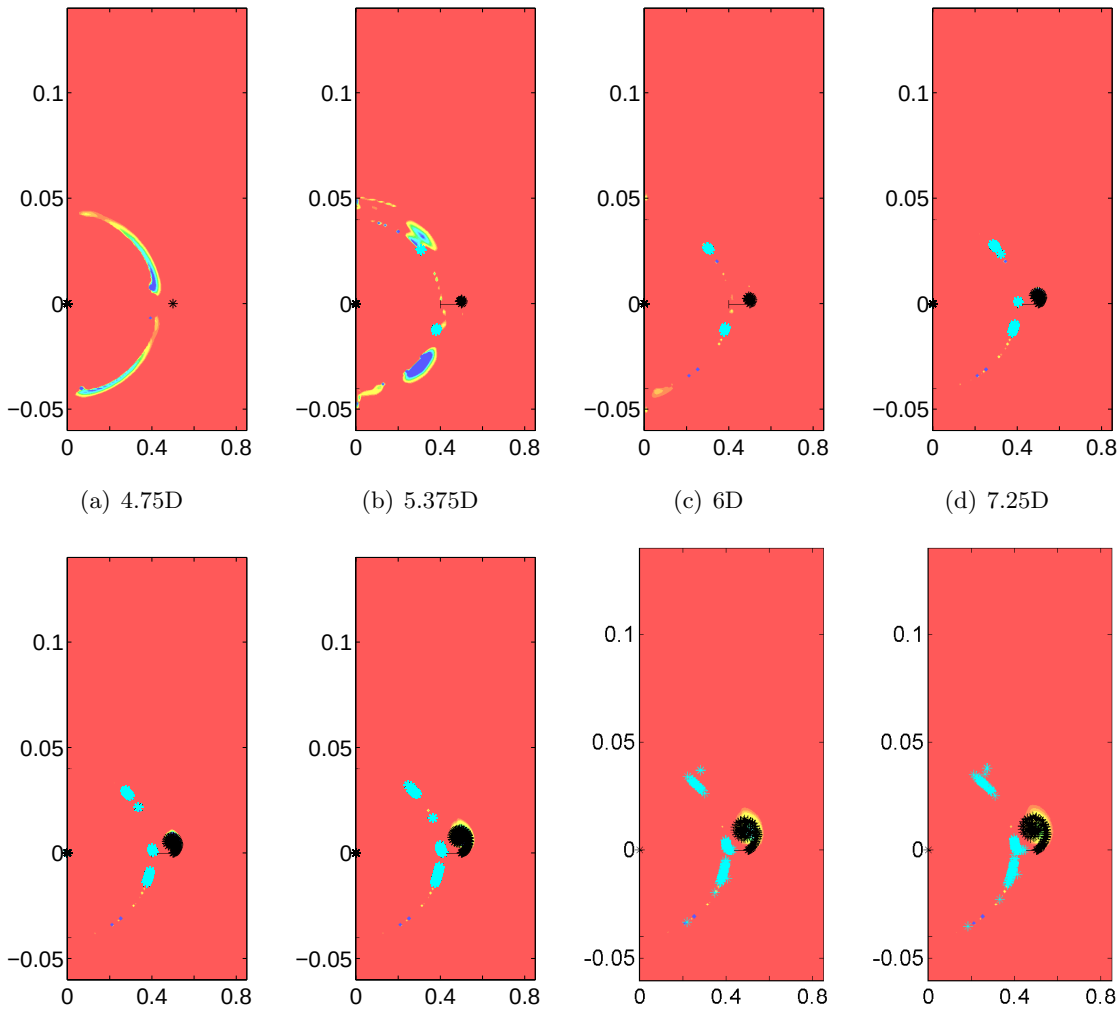

(a) 4.75D (b) 5.375D (c) 6D (d) 7.25D

(e) 8.5D (f) 11D (g) 13.5D (h) 14.75D

Figure 6.13: Vortex development for $\alpha = 1°$, potential+boundary layer

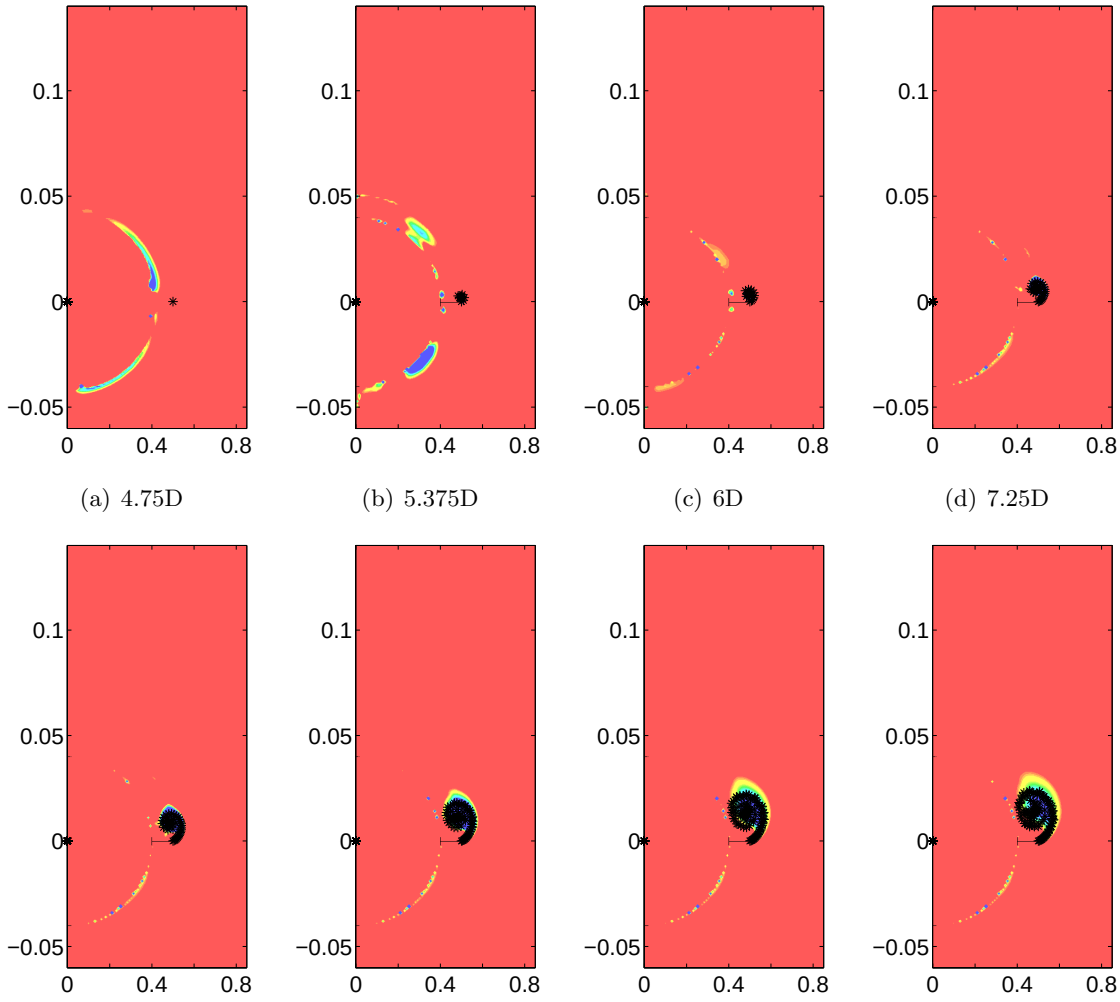

(a) 4.75D (b) 5.375D (c) 6D (d) 7.25D

(e) 8.5D (f) 11D (g) 13.5D (h) 14.75D

Figure 6.14: Vortex development for $\alpha = 2°$, potential+boundary layer

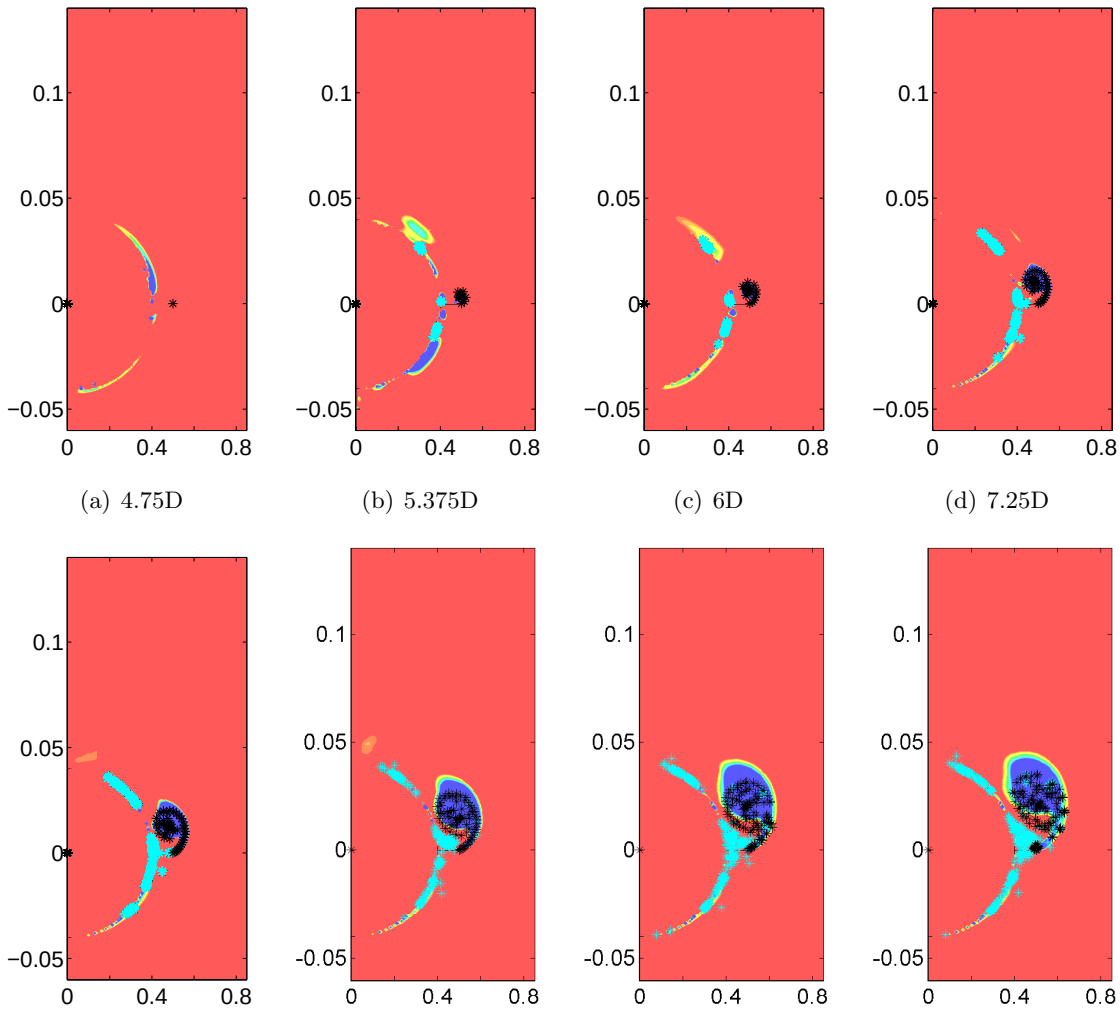

(a) 4.75D (b) 5.375D (c) 6D (d) 7.25D

(e) 8.5D (f) 11D (g) 13.5D (h) 14.75D

Figure 6.15: Vortex development for $\alpha = 4°$, potential+boundary layer

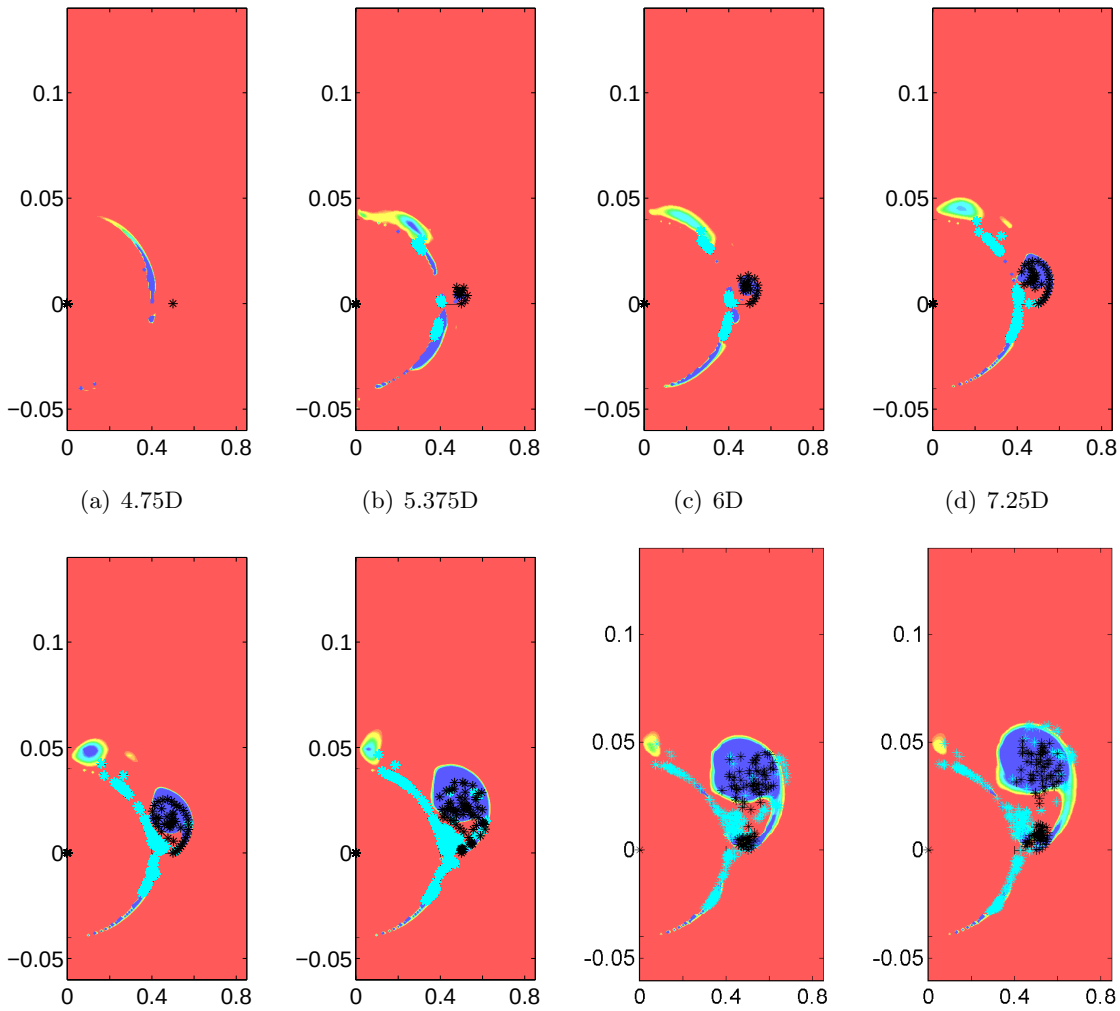

(a) 4.75D (b) 5.375D (c) 6D (d) 7.25D

(e) 8.5D (f) 11D (g) 13.5D (h) 14.75D

Figure 6.16: Vortex development for $\alpha = 6°$, potential+boundary layer

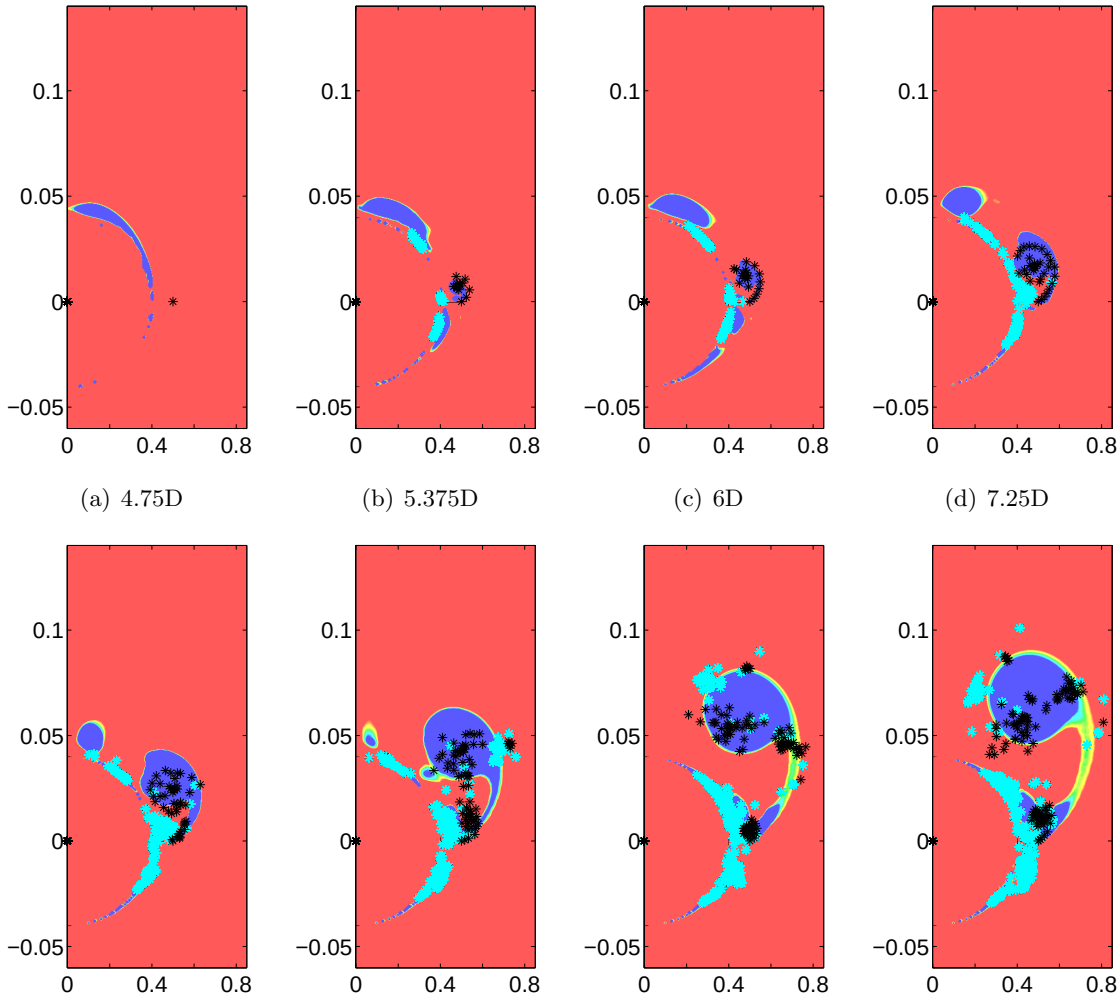

(a) 4.75D (b) 5.375D (c) 6D (d) 7.25D

(e) 8.5D (f) 11D (g) 13.5D (h) 14.75D

Figure 6.17: Vortex development for $\alpha = 10°$, potential+boundary layer

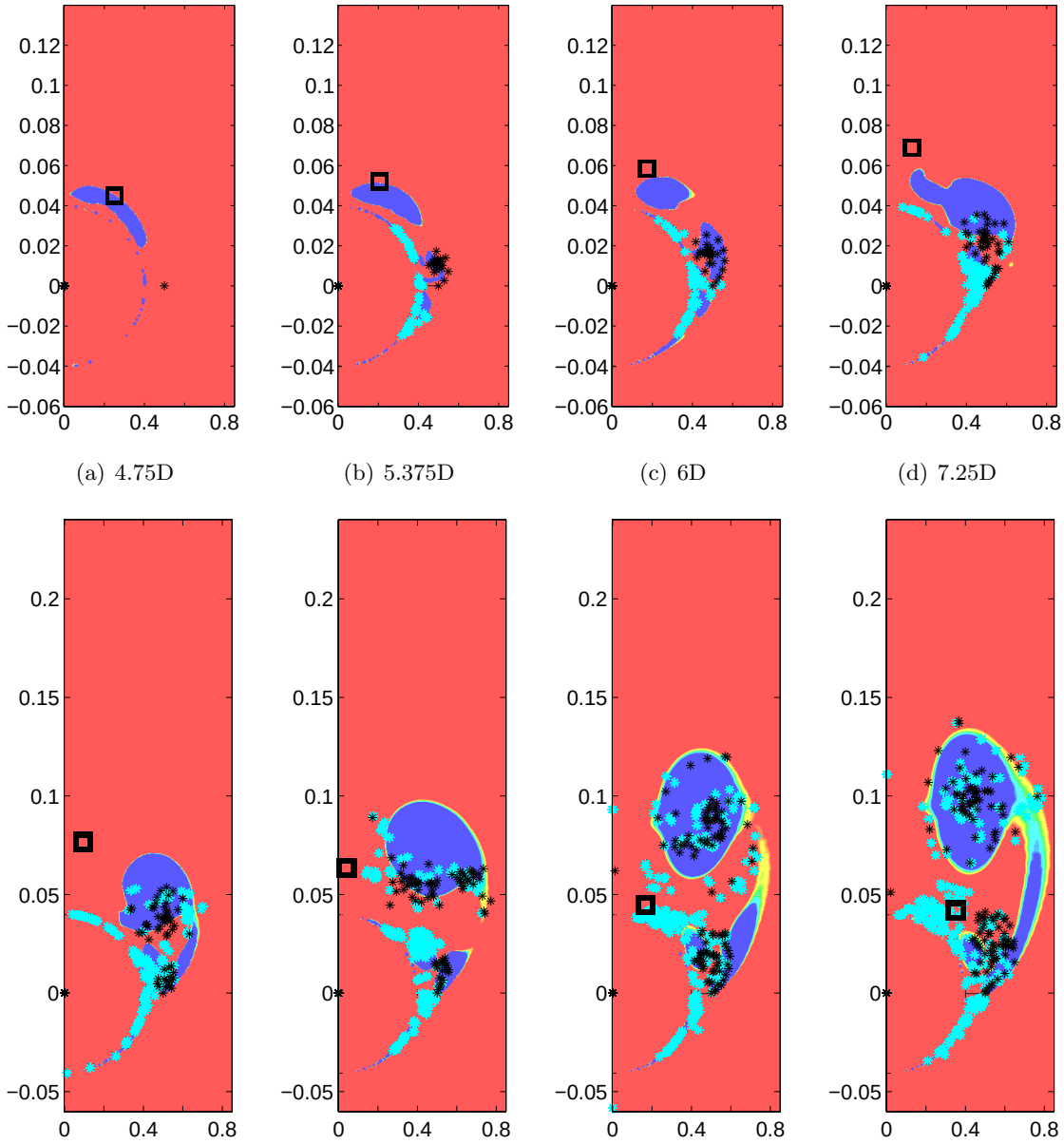

(a) 4.75D (b) 5.375D (c) 6D (d) 7.25D

(e) 8.5D (f) 11D (g) 13.5D (h) 14.75D

Figure 6.18: Vortex development for $\alpha = 15°$, potential+boundary layer

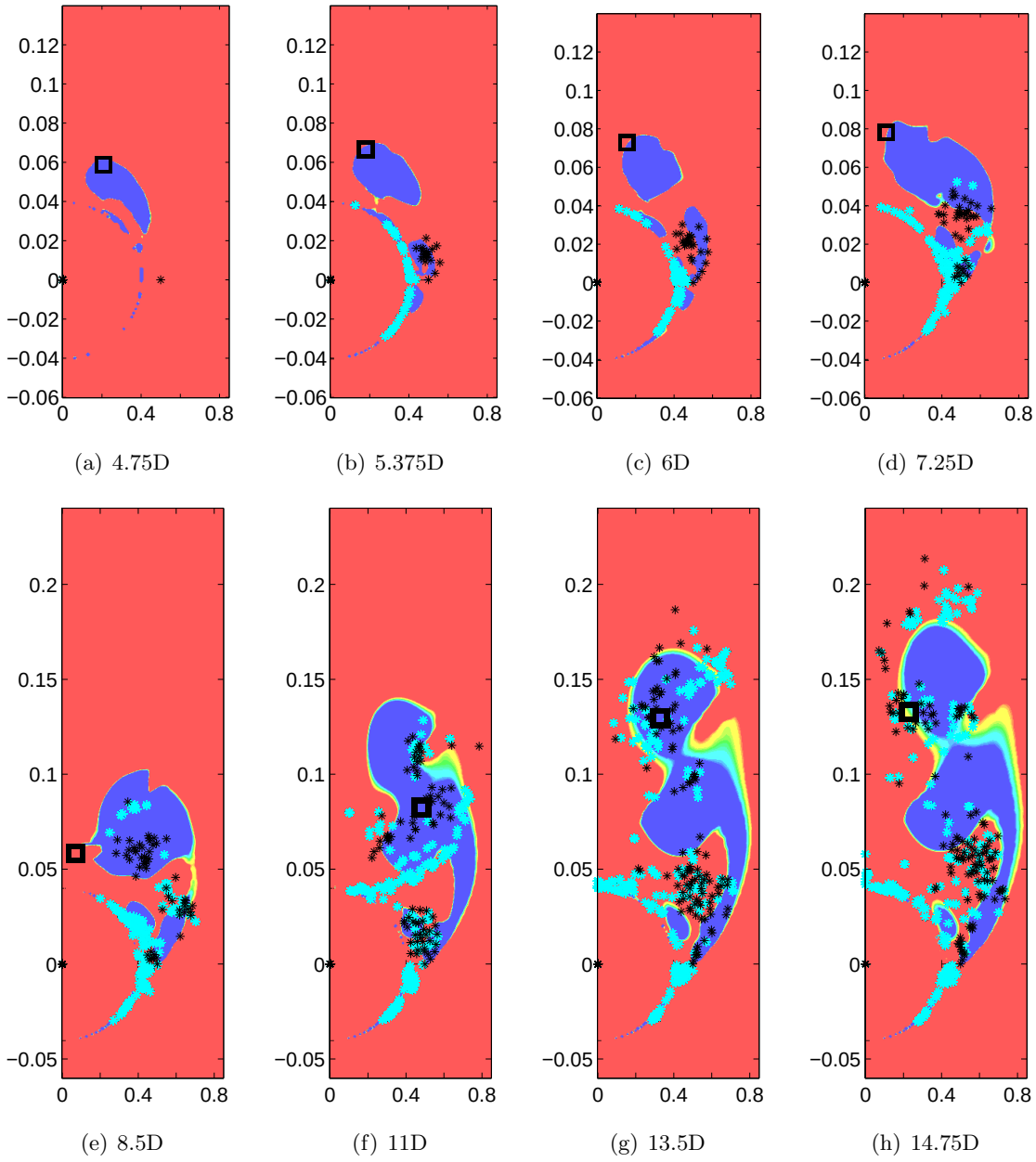

(a) 4.75D (b) 5.375D (c) 6D (d) 7.25D

(e) 8.5D (f) 11D (g) 13.5D (h) 14.75D

Figure 6.19: Vortex development for $\alpha = 20°$, potential+boundary layer

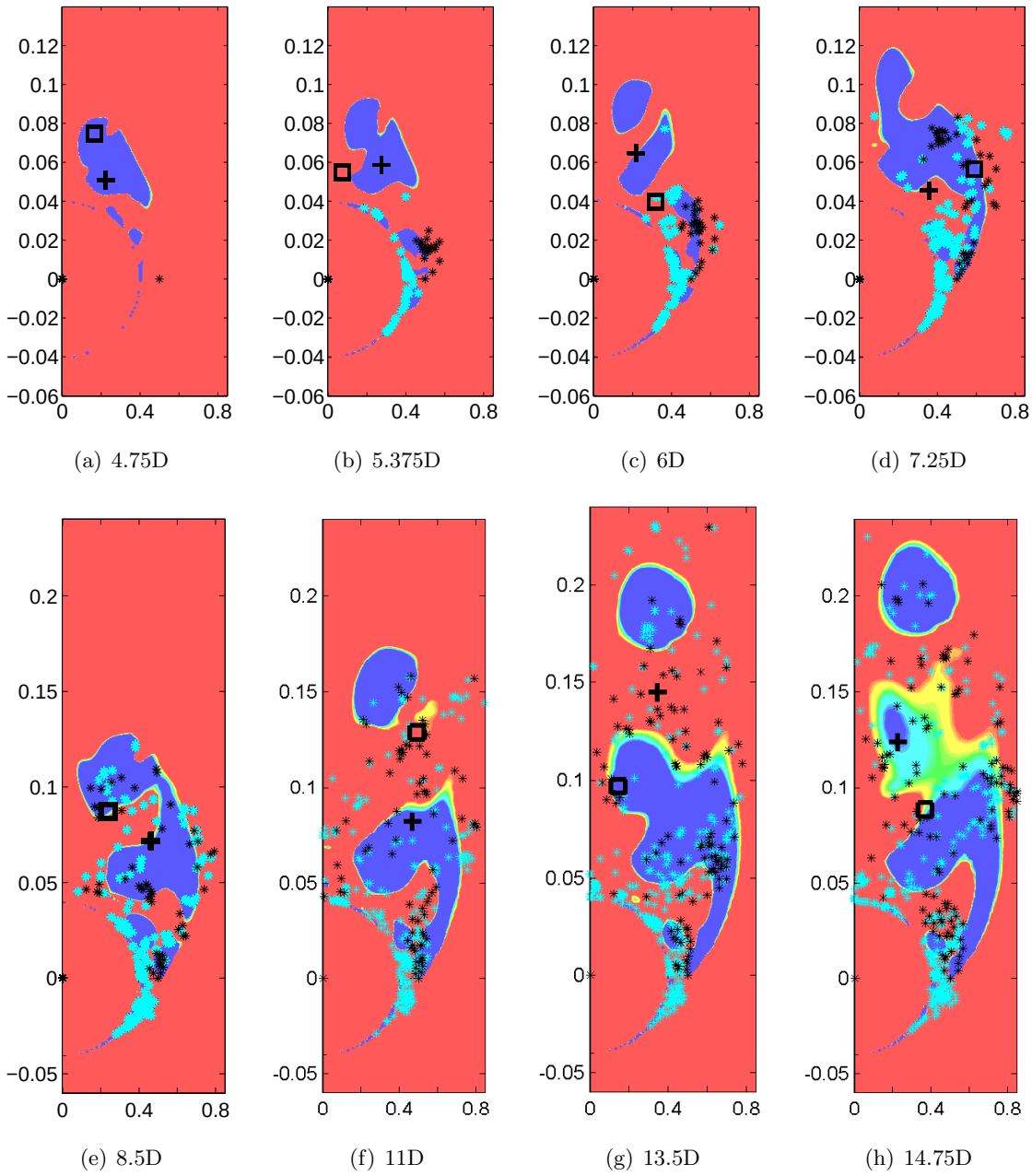

(a) 4.75D (b) 5.375D (c) 6D (d) 7.25D

(e) 8.5D (f) 11D (g) 13.5D (h) 14.75D

Figure 6.20: Vortex development for $\alpha = 25°$, potential+boundary layer

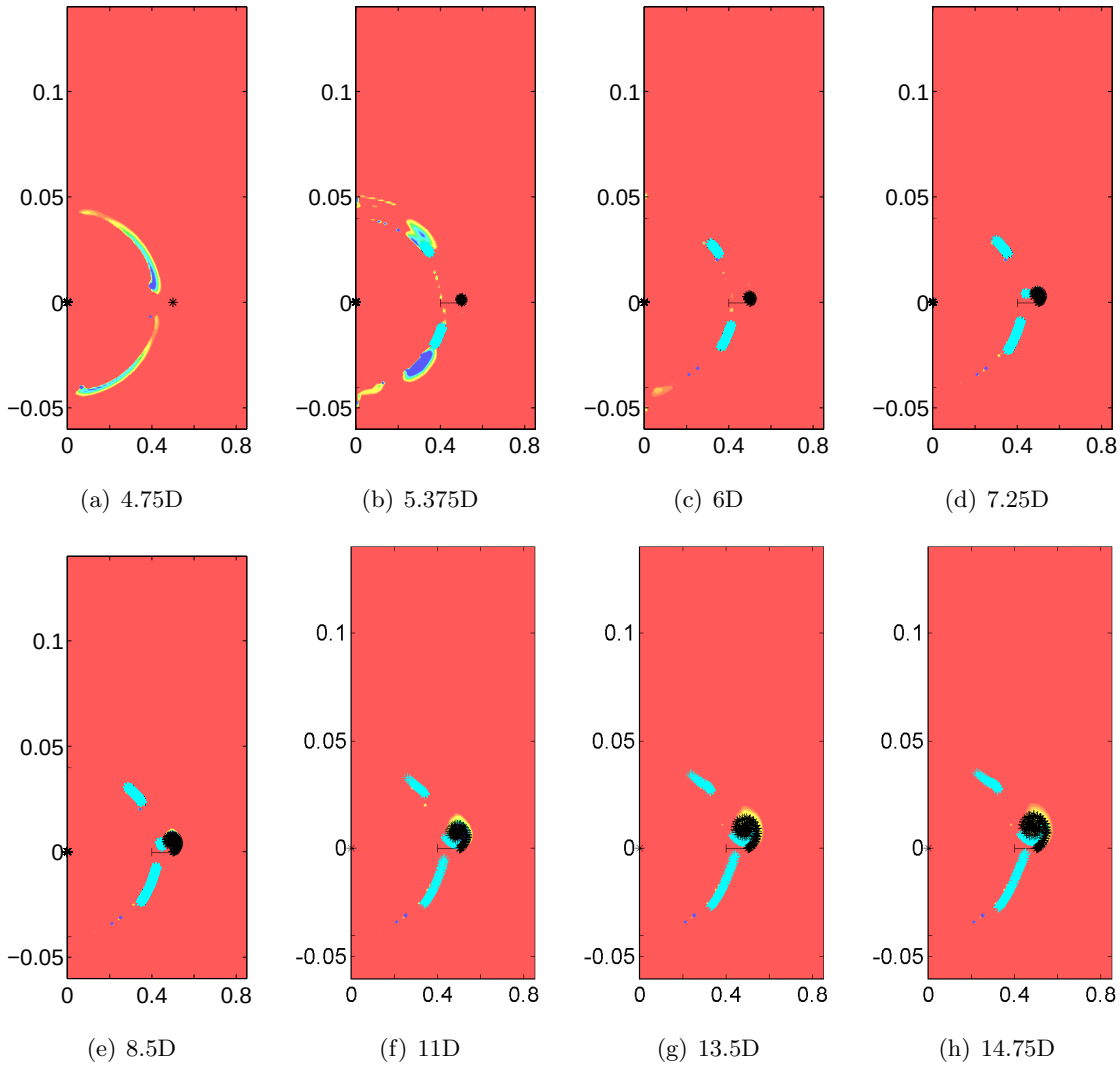

(a) 4.75D (b) 5.375D (c) 6D (d) 7.25D

(e) 8.5D (f) 11D (g) 13.5D (h) 14.75D

Figure 6.21: Vortex development for $\alpha = 1°$, potential+boundary layer at 5%

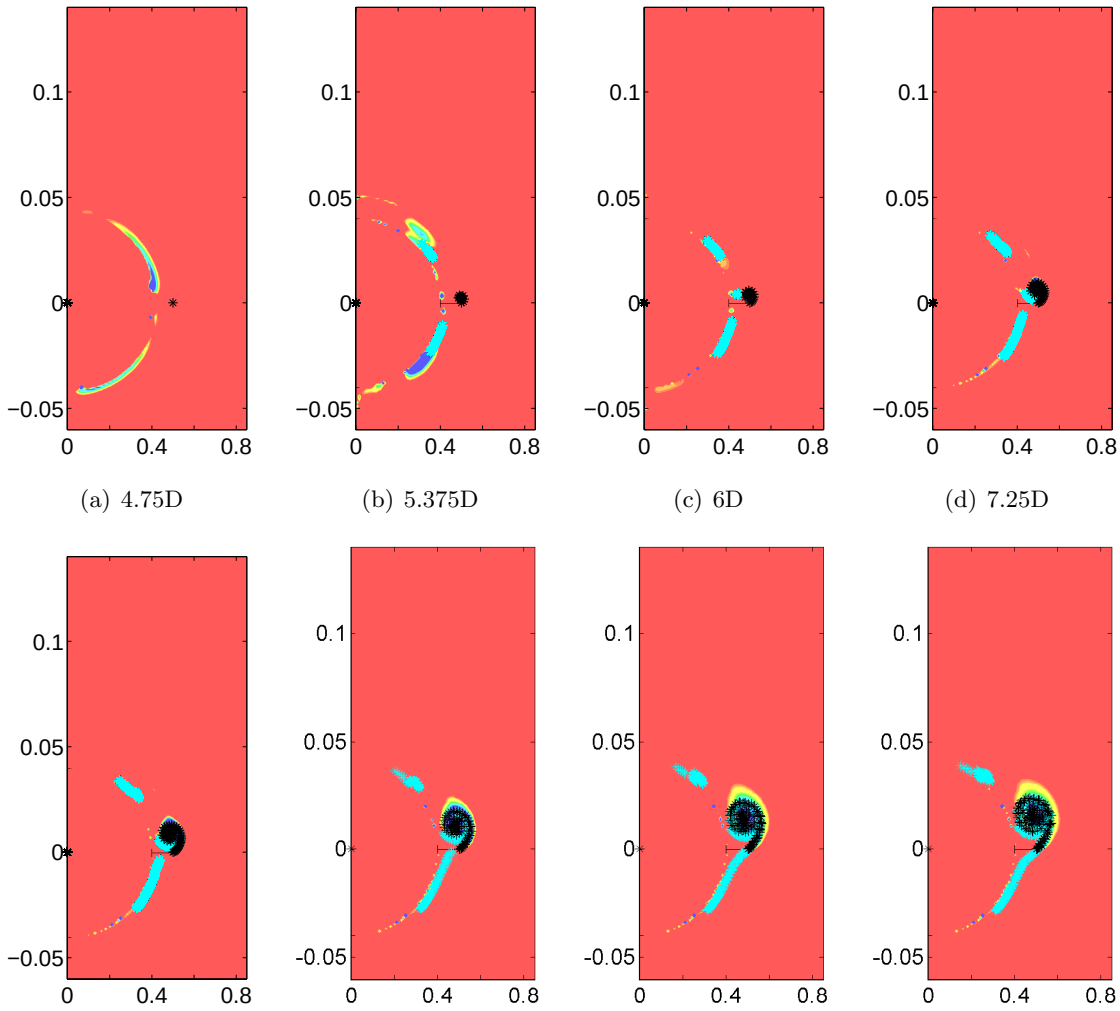

(a) 4.75D (b) 5.375D (c) 6D (d) 7.25D

(e) 8.5D (f) 11D (g) 13.5D (h) 14.75D

Figure 6.22: Vortex development for $\alpha = 2°$, potential+boundary layer at 5%

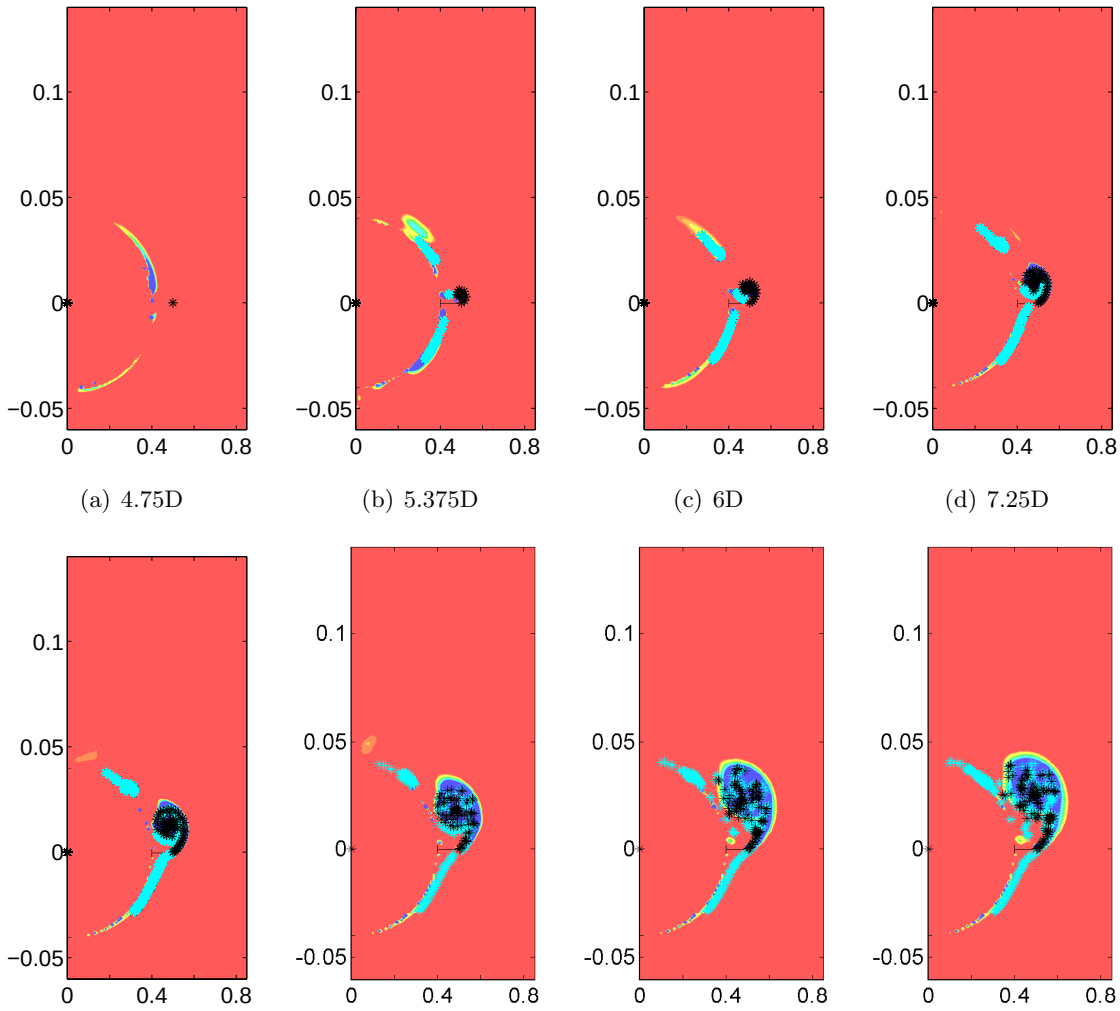

(a) 4.75D (b) 5.375D (c) 6D (d) 7.25D

(e) 8.5D (f) 11D (g) 13.5D (h) 14.75D

Figure 6.23: Vortex development for $\alpha = 4°$, potential+boundary layer at 5%

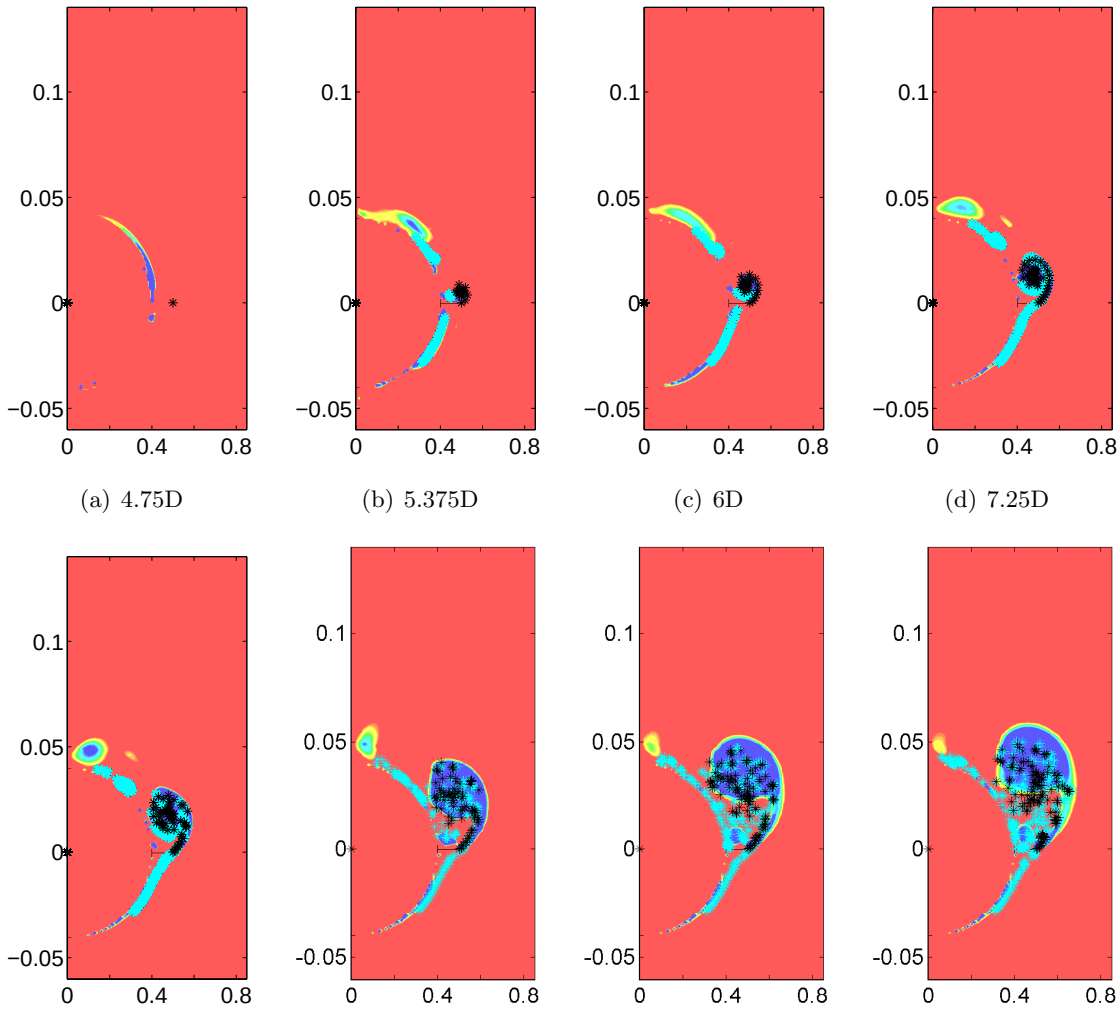

(a) 4.75D (b) 5.375D (c) 6D (d) 7.25D

(e) 8.5D (f) 11D (g) 13.5D (h) 14.75D

Figure 6.24: Vortex development for $\alpha = 6°$, potential+boundary layer at 5%

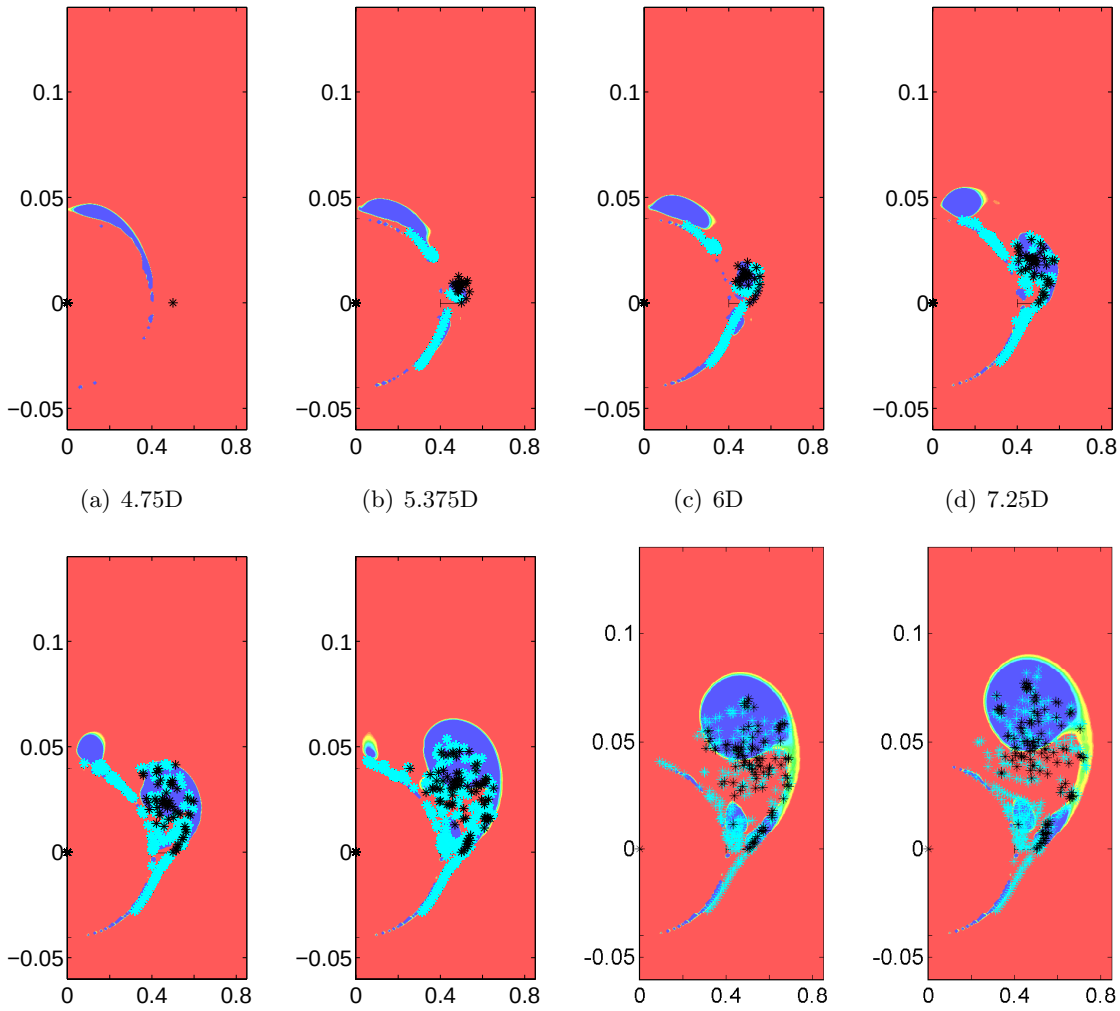

(a) 4.75D (b) 5.375D (c) 6D (d) 7.25D

(e) 8.5D (f) 11D (g) 13.5D (h) 14.75D

Figure 6.25: Vortex development for $\alpha = 10°$, potential+boundary layer at 5%

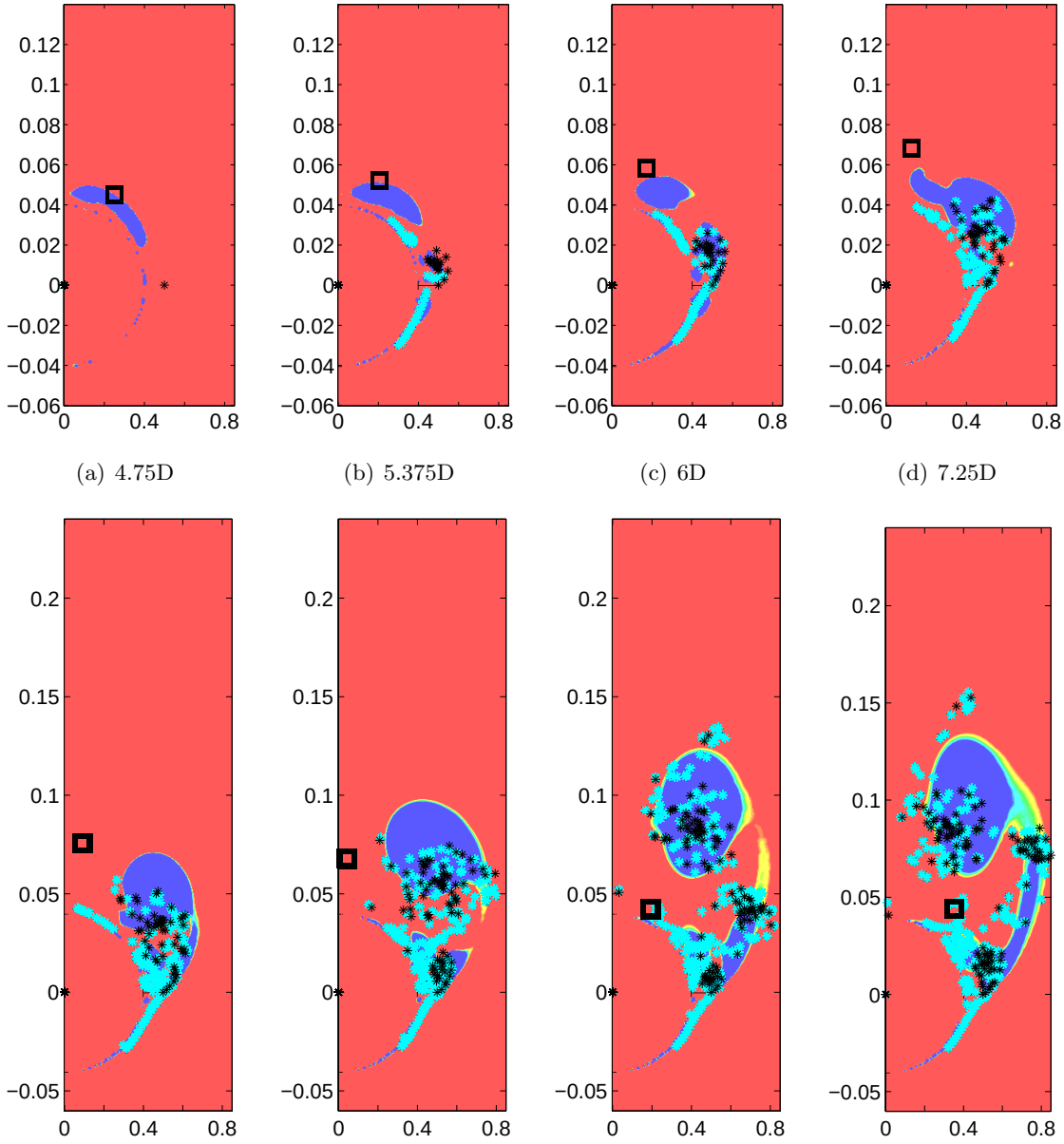

(a) 4.75D (b) 5.375D (c) 6D (d) 7.25D

(e) 8.5D (f) 11D (g) 13.5D (h) 14.75D

Figure 6.26: Vortex development for $\alpha = 15°$, potential+boundary layer at 5%

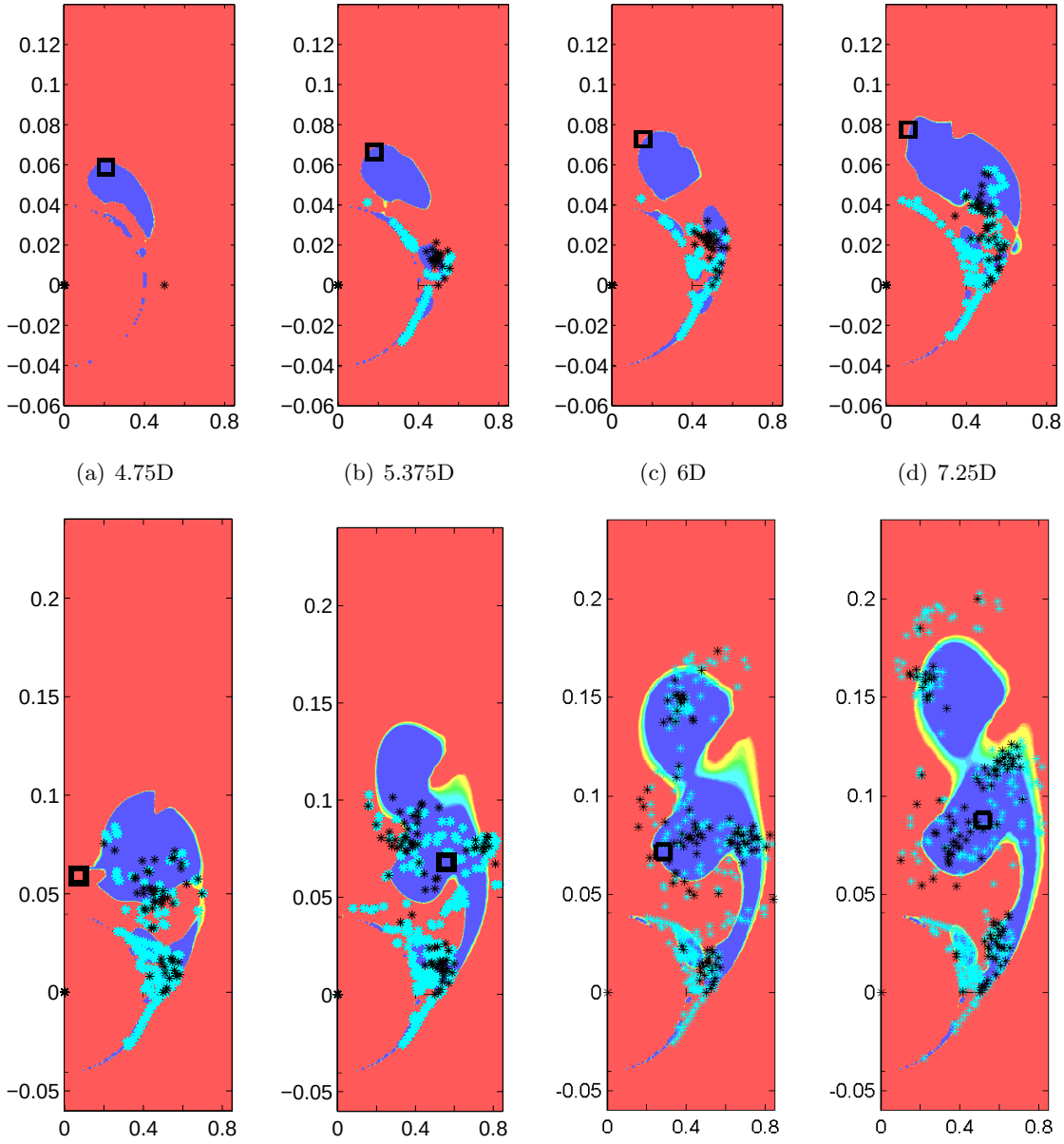

(a) 4.75D (b) 5.375D (c) 6D (d) 7.25D

(e) 8.5D (f) 11D (g) 13.5D (h) 14.75D

Figure 6.27: Vortex development for $\alpha = 20°$, potential+boundary layer at 5%

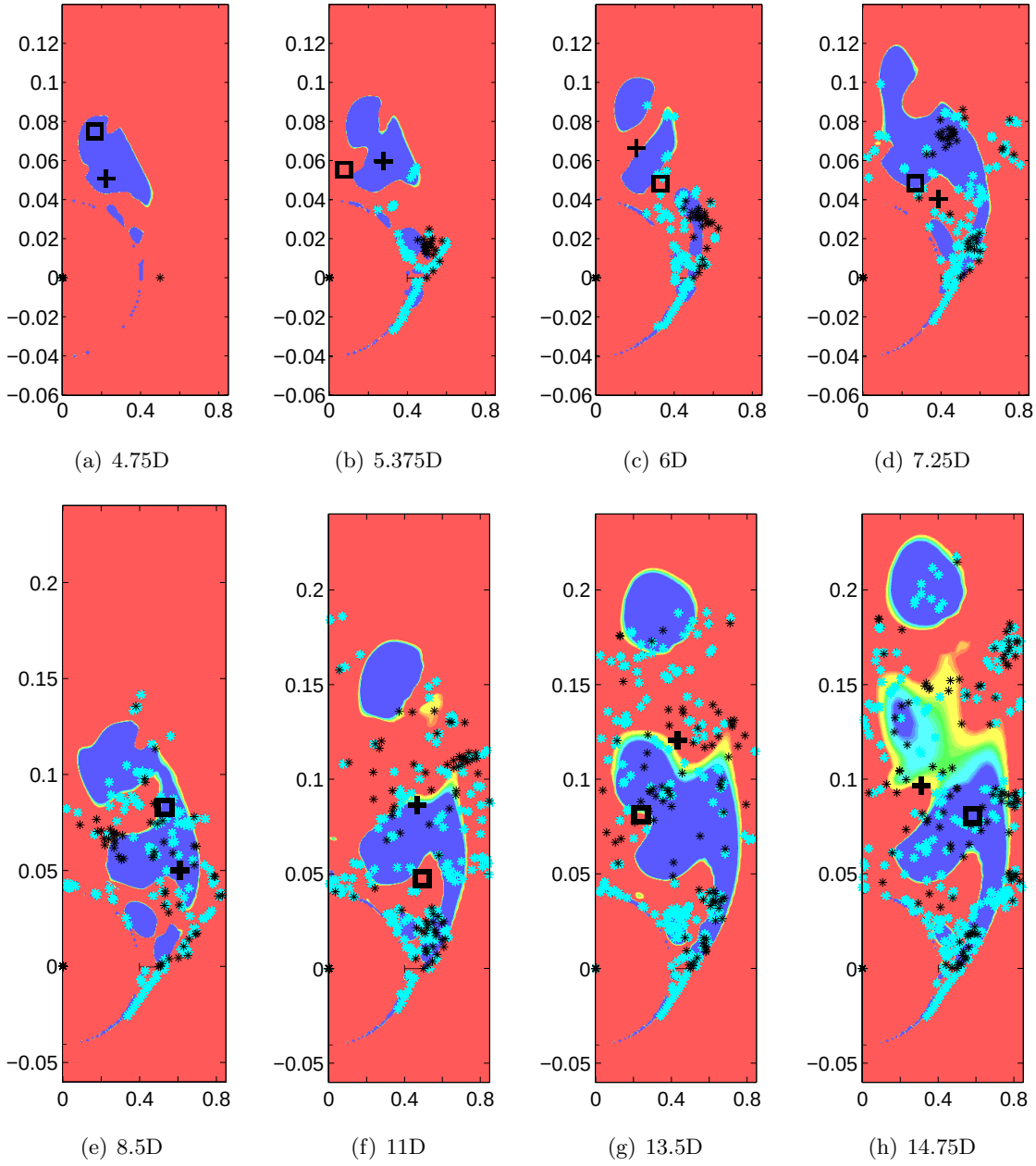

(a) 4.75D (b) 5.375D (c) 6D (d) 7.25D

(e) 8.5D (f) 11D (g) 13.5D (h) 14.75D

Figure 6.28: Vortex development for $\alpha = 25°$, potential+boundary layer at 5%

An alternative method of illustrating the position of the rolled up vortex sheet is shown in Figure 6.29 to Figure 6.38. Only the DVM potential method is plotted for angles greater than 10° because the inclusion of the boundary layer simulation results in vortex shedding and no single concentrated vortex is easily identified or can be plotted because multiple vortices exist. This is the particular case at the angles of attack above 15° where the discretised vortices are more diffuse. Of interest is the behaviour of the body vortices. Their trajectories deviate considerably from the CFD simulations (see Figures 6.34, 6.36 and 6.38). This is expected given that the 2D method does not combine vortices or model the coalescence of vortices in anyway.

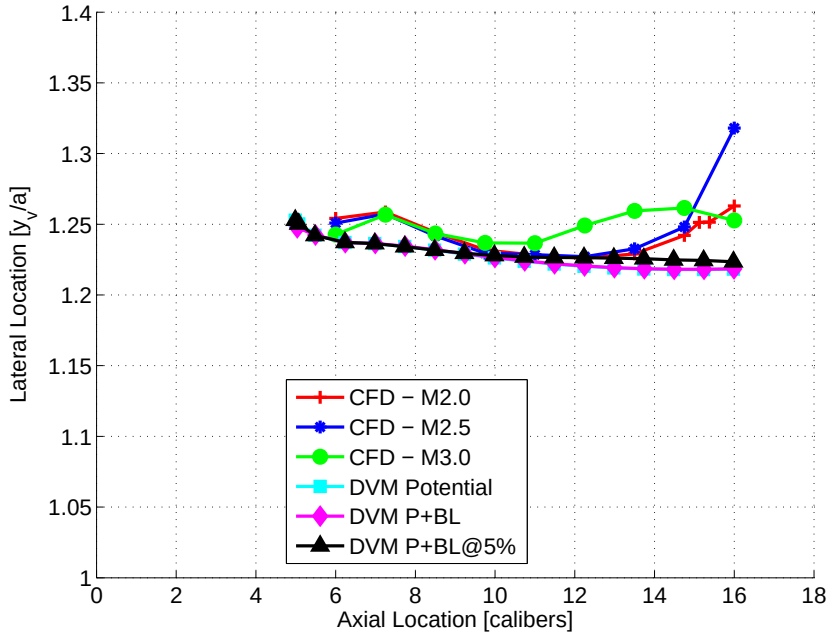

(a) Lateral

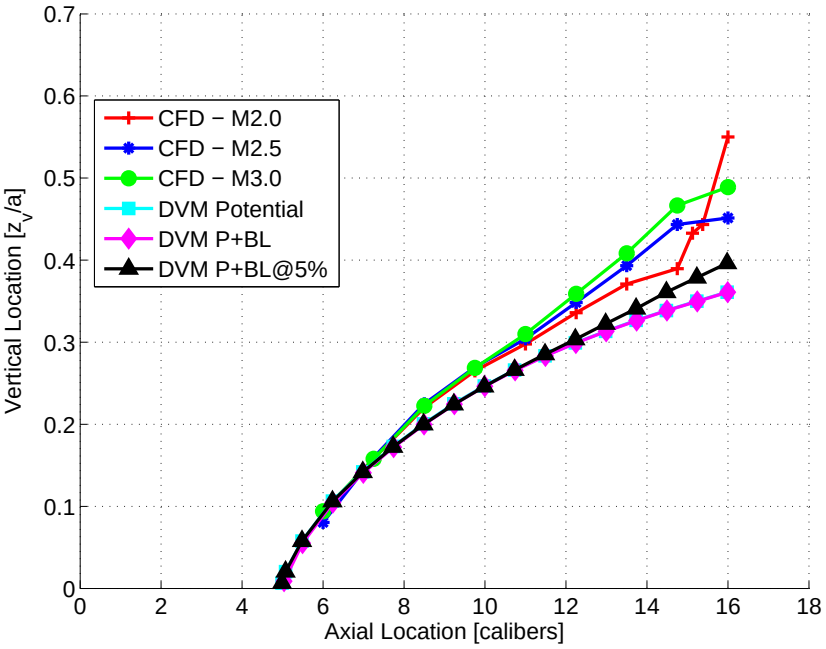

(b) Vertical

Figure 6.29: CFD and DVM concentrated vortex positions at $\alpha = 2°$

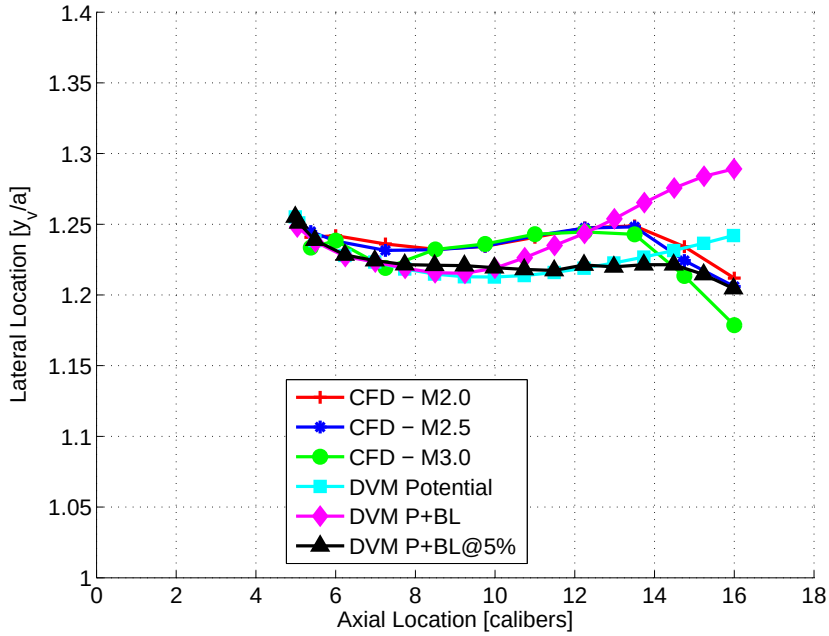

(a) Lateral

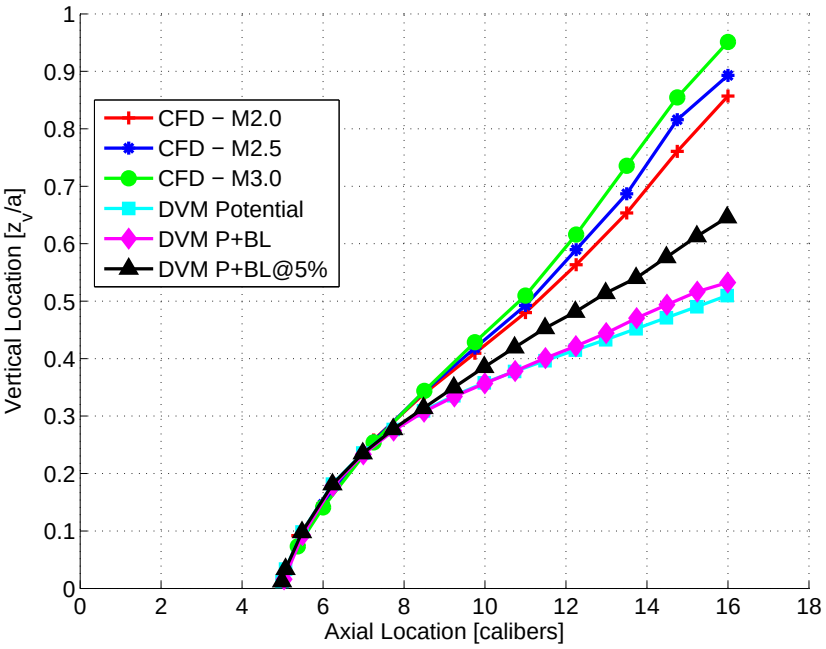

(b) Vertical

Figure 6.30: CFD and DVM concentrated vortex positions at $\alpha = 4°$

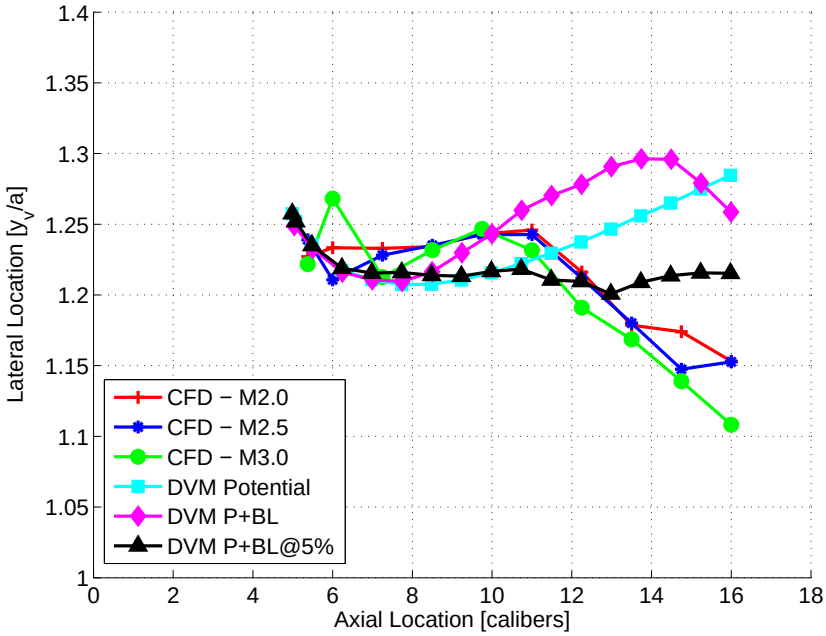

(a) Lateral

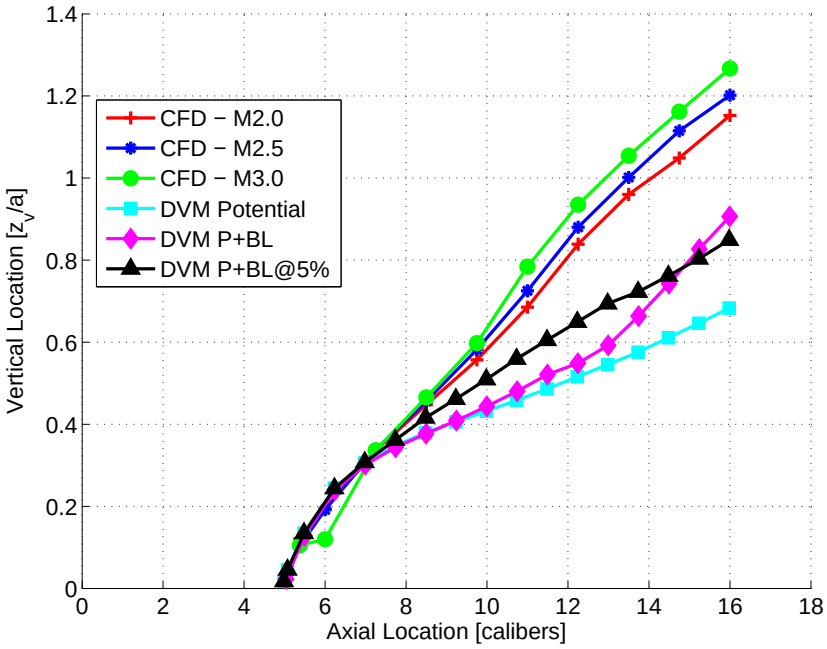

(b) Vertical

Figure 6.31: CFD and DVM comparisons of concentrated vortex positions at $\alpha = 6°$

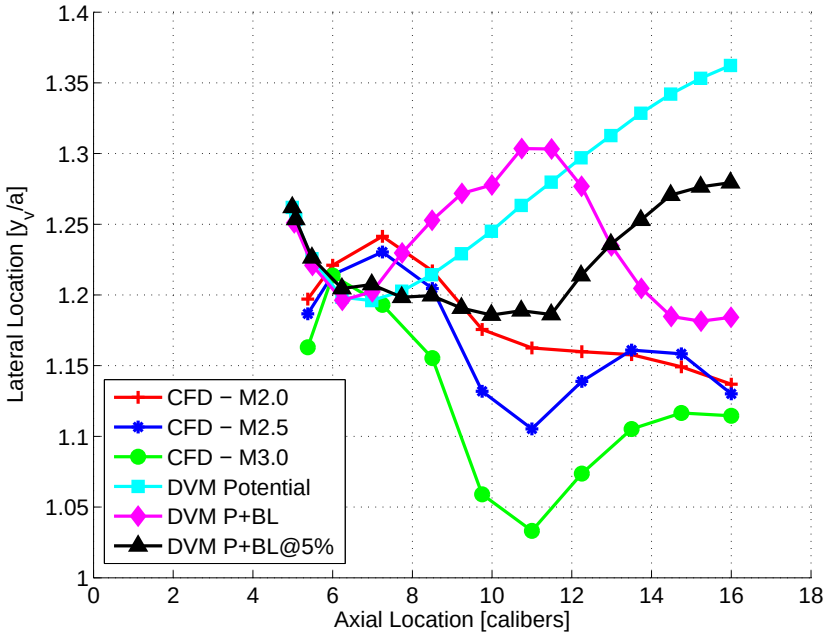

(a) Lateral

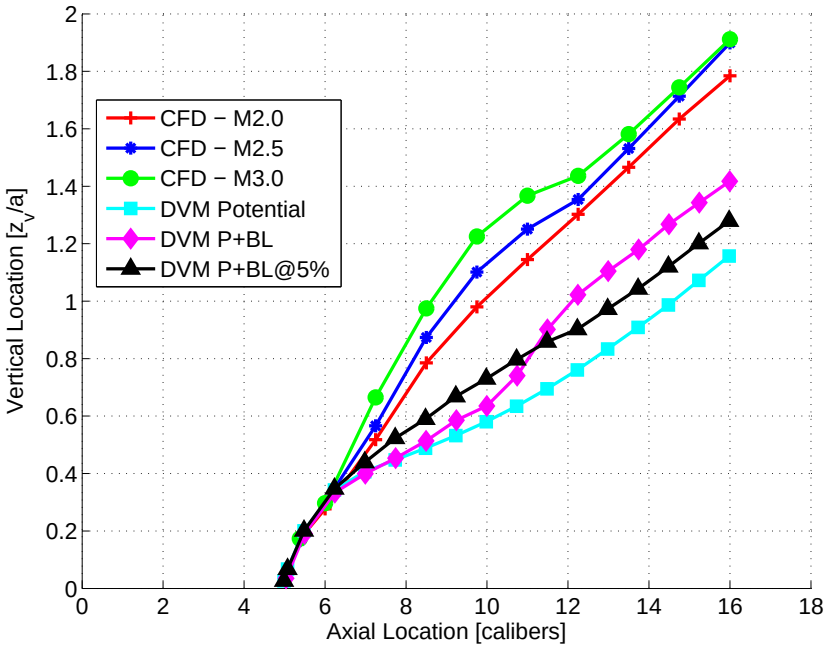

(b) Vertical

Figure 6.32: CFD and DVM comparisons of concentrated vortex positions at $\alpha = 10°$

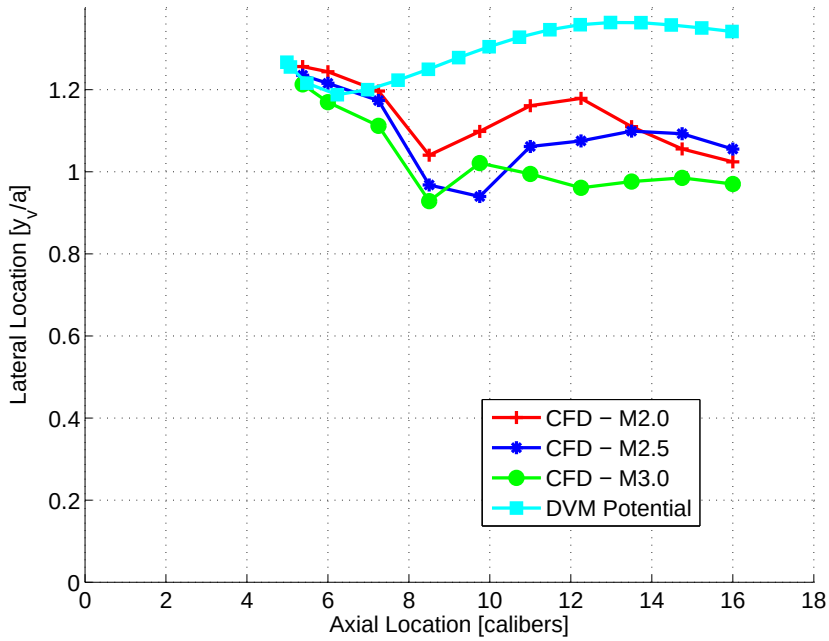

(a) Lateral

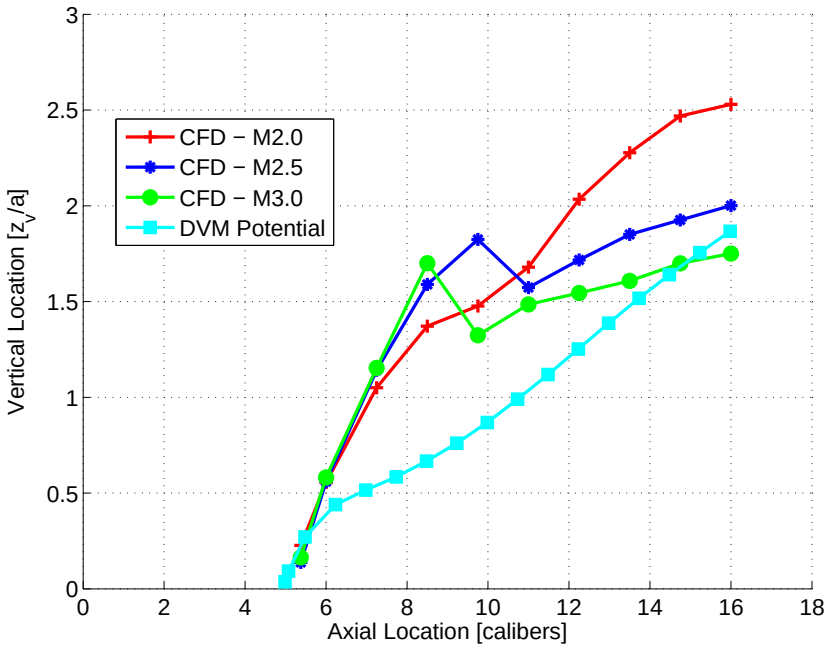

(b) Vertical

Figure 6.33: CFD and DVM comparisons of concentrated strake vortex positions at $\alpha = 15^\circ$

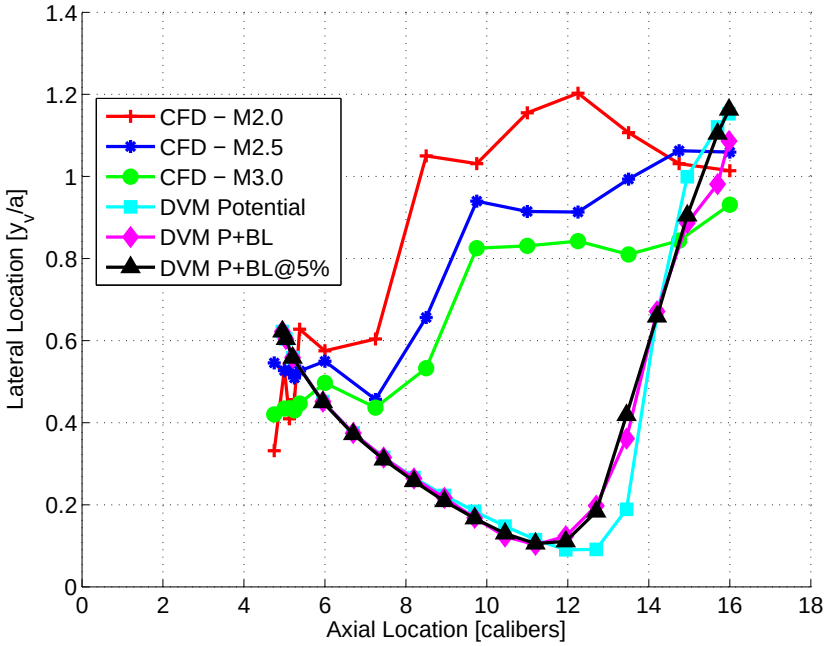

(a) Lateral

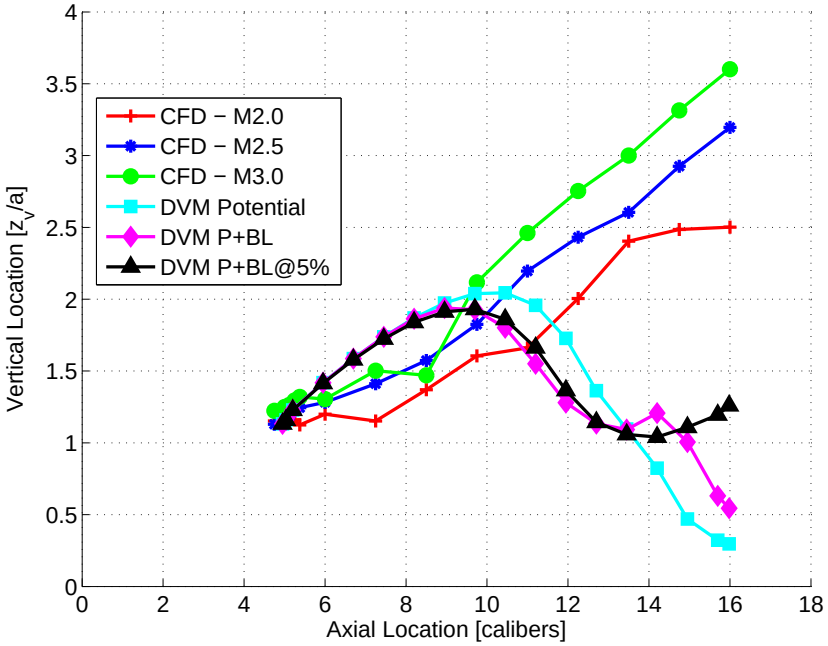

(b) Vertical

Figure 6.34: CFD and DVM comparisons of concentrated body vortex positions at $\alpha = 15°$

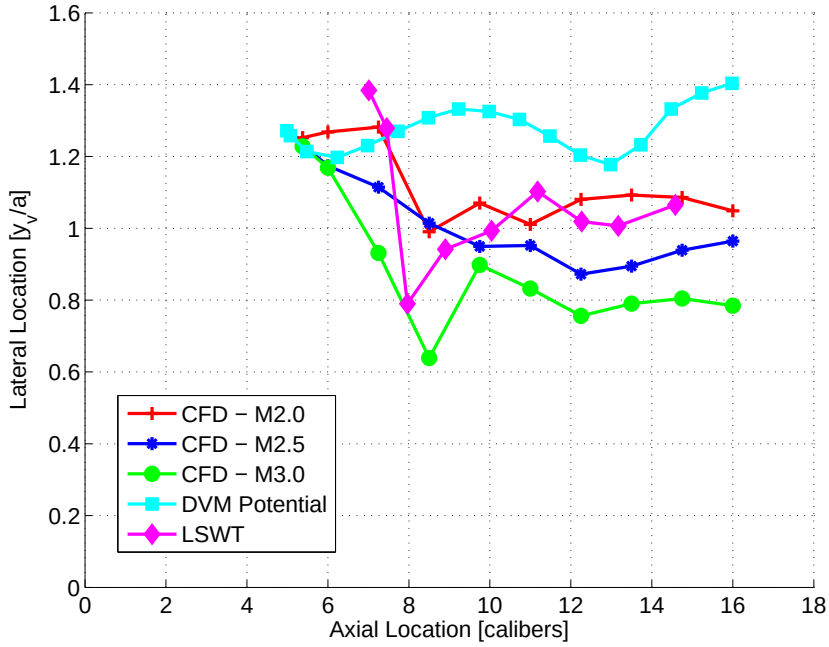

(a) Lateral

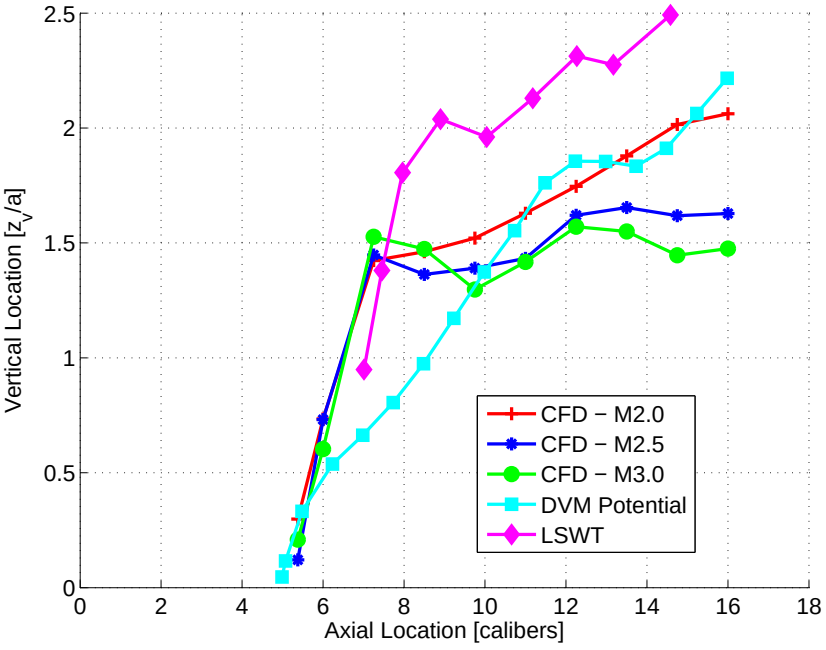

(b) Vertical

Figure 6.35: CFD and DVM comparisons of concentrated strake vortex positions at $\alpha = 20°$

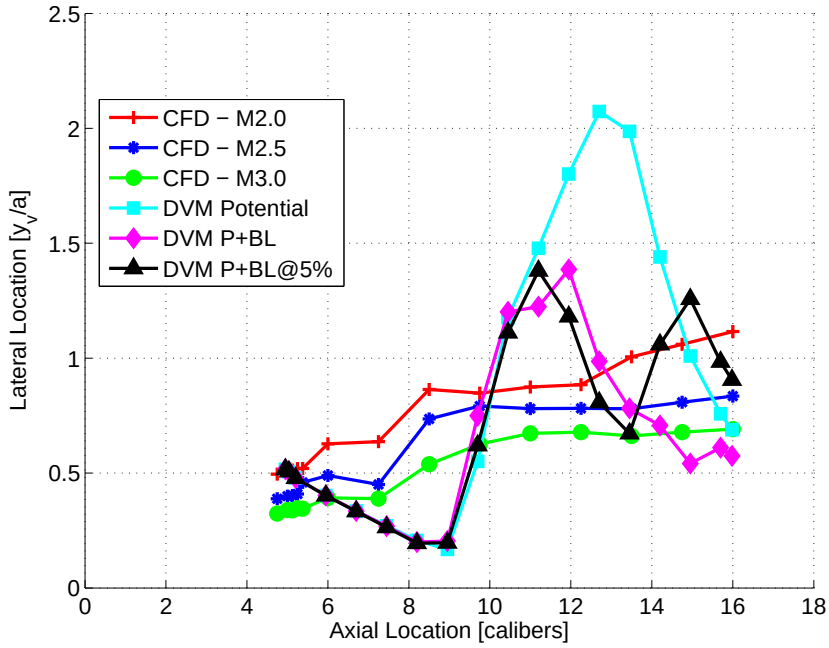

(a) Lateral

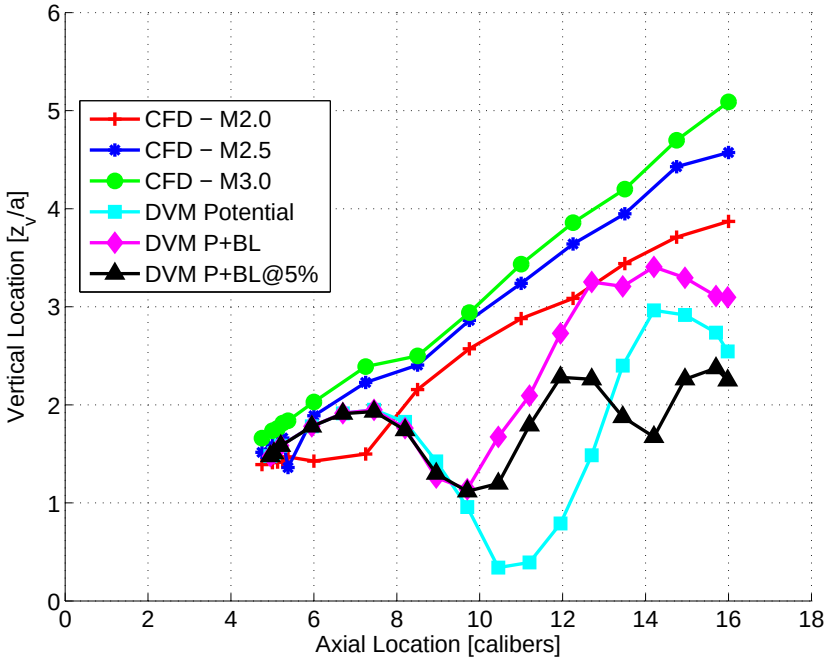

(b) Vertical

Figure 6.36: CFD and DVM comparisons of concentrated body vortex positions at $\alpha = 20°$

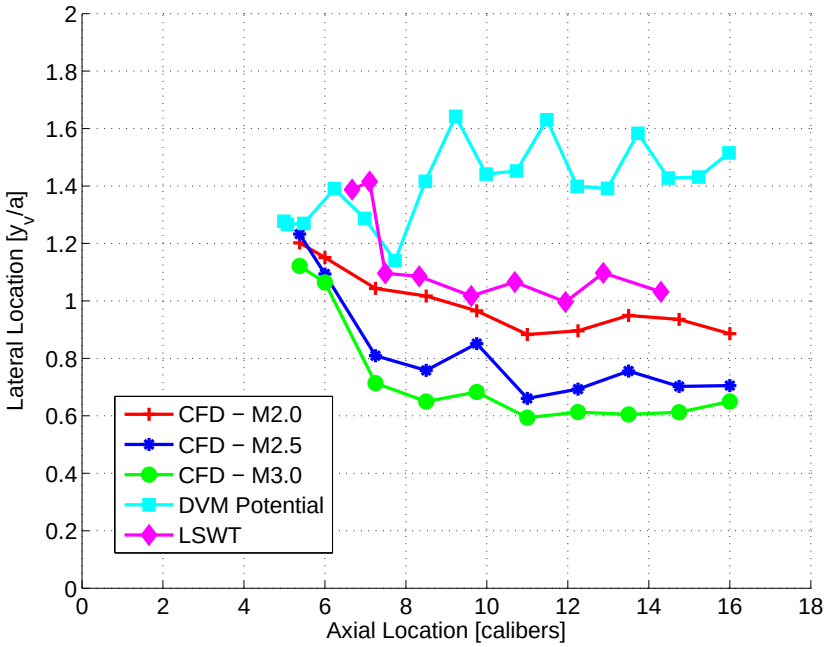

(a) Lateral

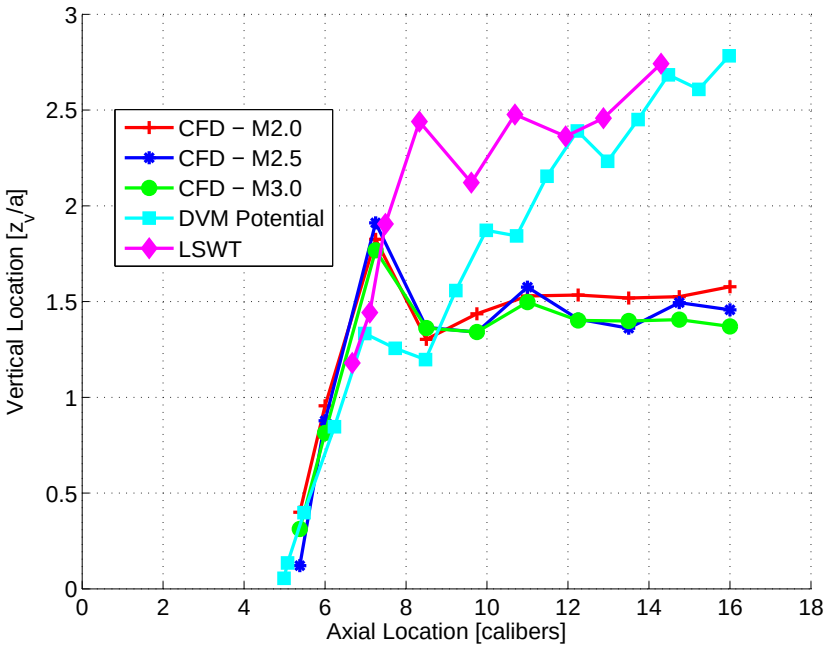

(b) Vertical

Figure 6.37: CFD and DVM comparisons of concentrated strake vortex positions at $\alpha = 25°$

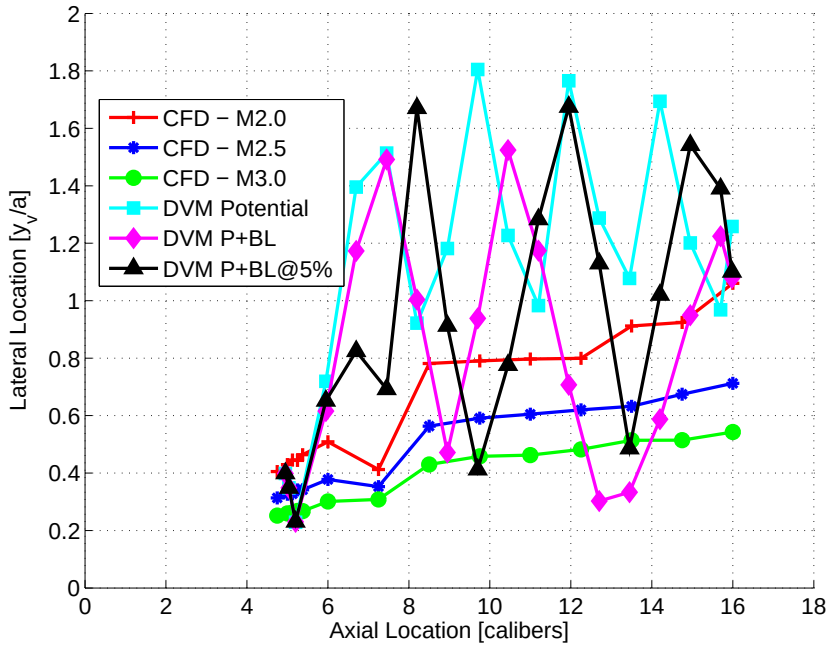

(a) Lateral

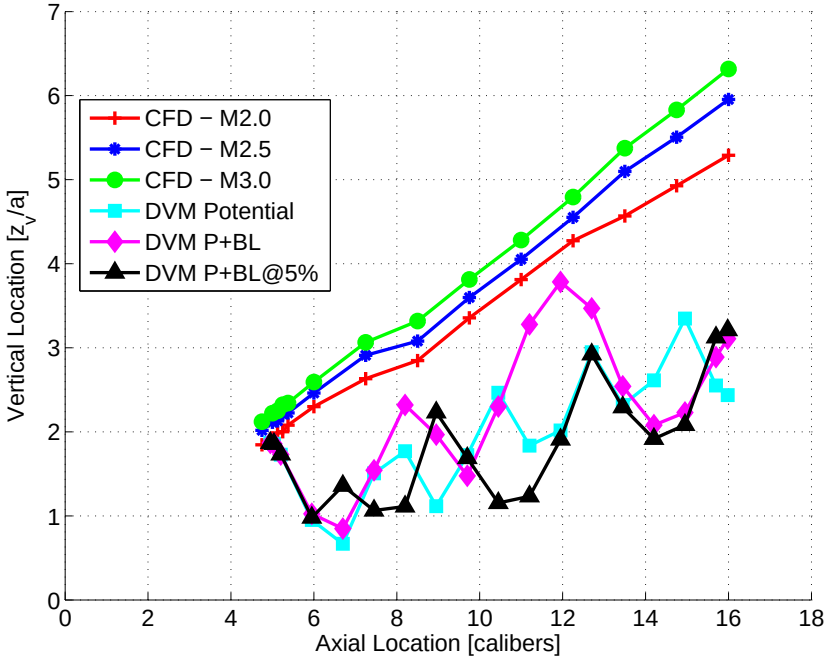

(b) Vertical

Figure 6.38: CFD and DVM comparisons of concentrated body vortex positions at $\alpha = 25°$

As for the SCV method, the concentrated vortex strength, Γ', is compared to the CFD simulations. Figure 6.39 to Figure 6.41 plot the CFD simulations against the DVM predictions for the angles of attack from 2° to 20°. All the angles of attack up to 15° show a good correlation with the CFD simulations. The 20° case (see Figure 6.41) clearly shows that the concentrated vortex strength is overpredicted, as would be the case for the 25° angle of attack.

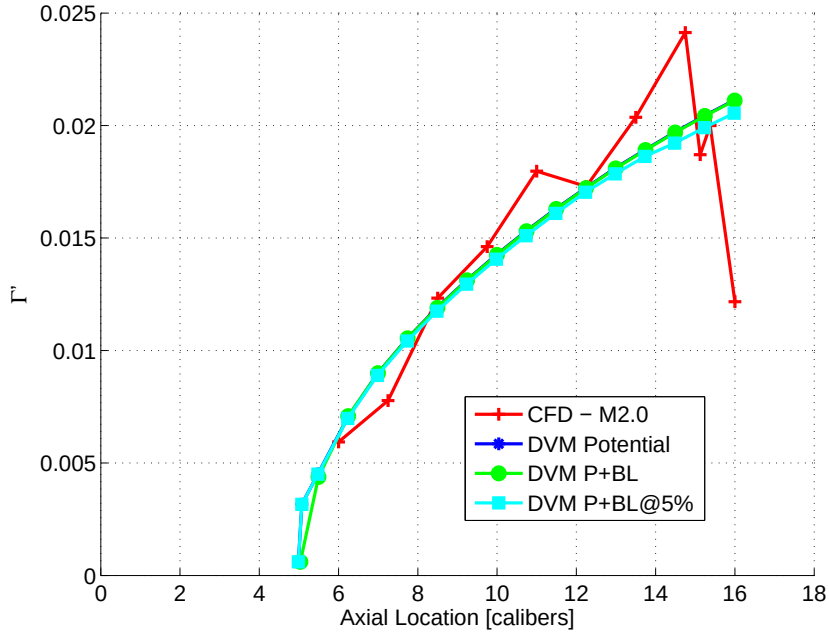

(a) 2°

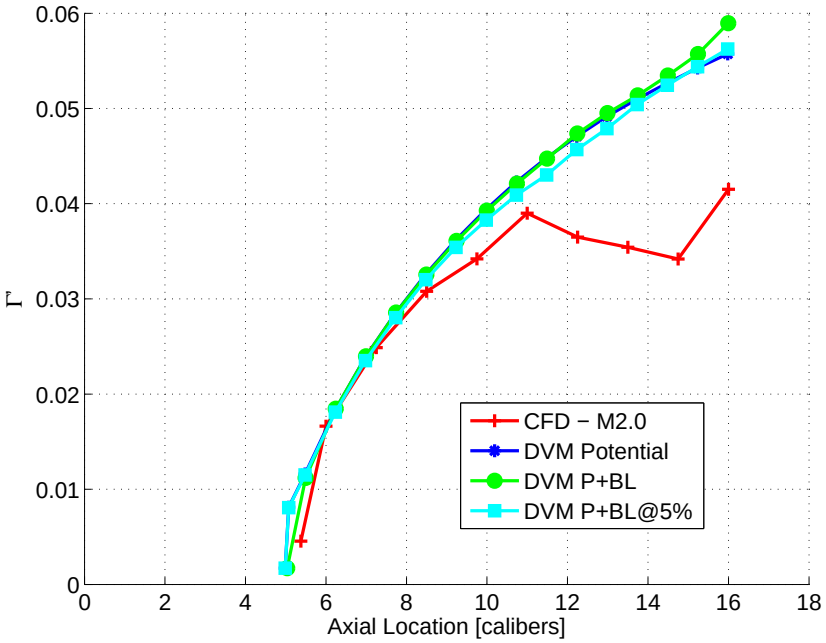

(b) 4°

Figure 6.39: CFD and DVM comparisons of the non-dimensionalised concentrated vortex strength for $\alpha = 2°$ and 4°

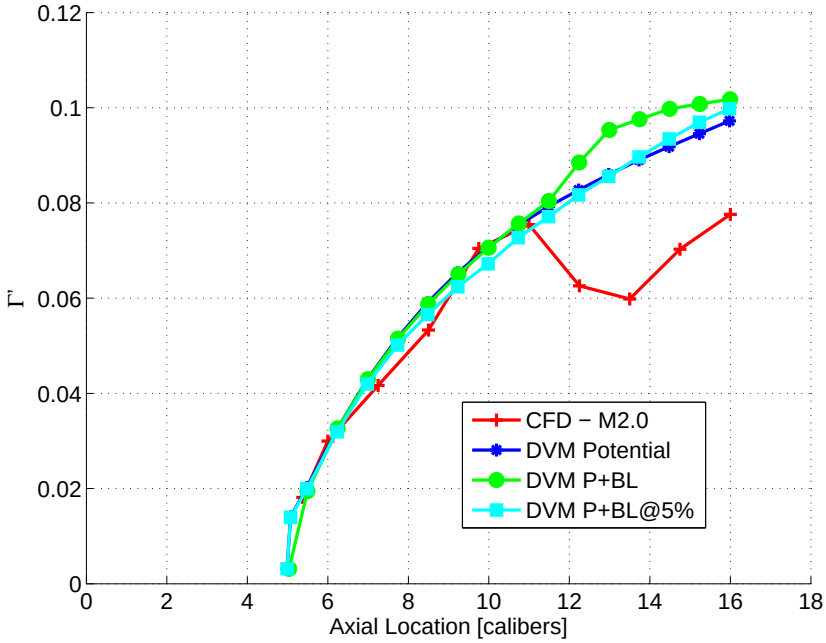

(a) 6°

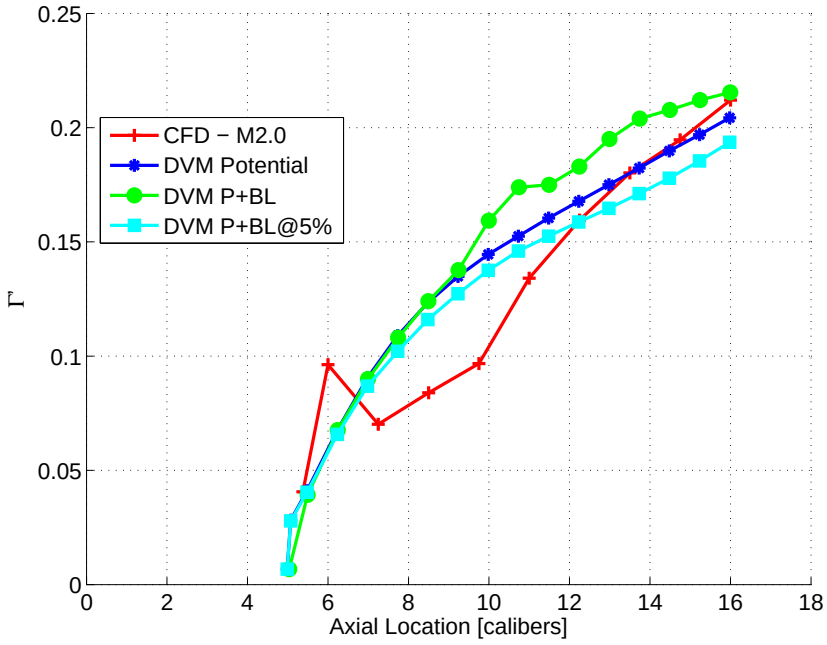

(b) 10°

Figure 6.40: CFD and DVM comparisons of the non-dimensionalised concentrated vortex strength for $\alpha = 6°$ and $10°$

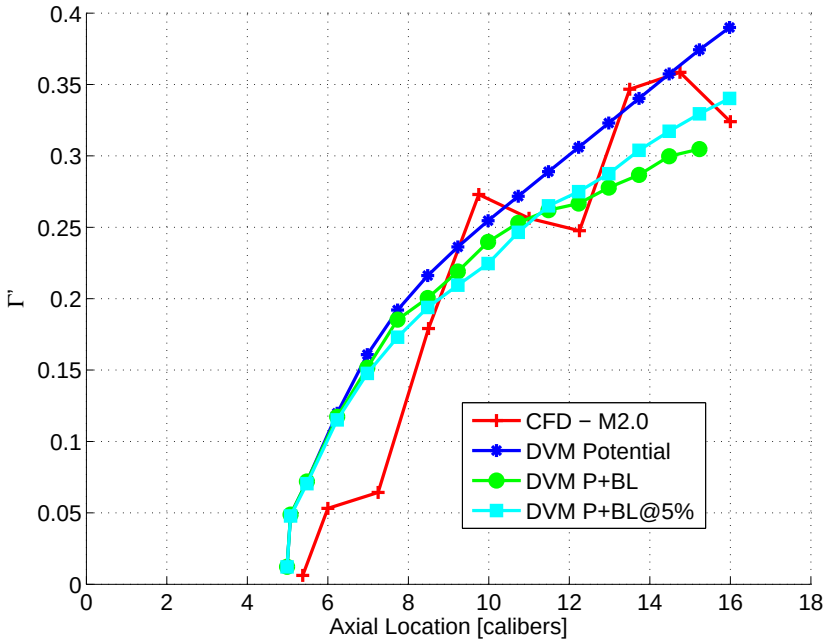

(a) 15°

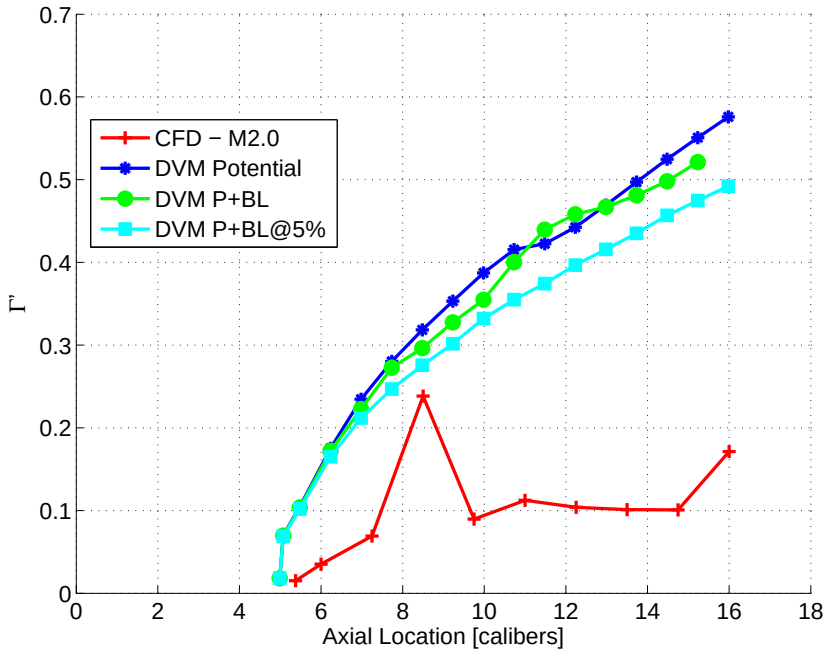

(b) 20°

Figure 6.41: CFD and DVM comparisons of the non-dimensionalised concentrated vortex strength for $\alpha = 15°$ and 20°

6.10 Discussion

From the flow development for the various angles of attack, the lee side flows for low angles of attack (up to 4°) are well captured by all the methods employed. This also manifests itself in the good correlation with the normal force coefficient. Above 4° the prediction of the position of the rolled up vortex sheet by the potential method deteriorates as the angle of attack increases. For the 6° to 15° angles of attack, the inclusion of the boundary layer separation model improves the prediction of the positions considerably. The potential only method does, however, predict at the intermediate angles of attack the loads and positions better than the SCV method. This implies that a single concentrated vortex has difficulty replicating the lee side flows at even moderate angles of attack because only two vortices are available to impose the Joukowski-Kutta condition for the two edges.

Both the boundary layer methods predict the establishment of the secondary vortex and it is debatable which method is better. The boundary layer separation vortices placed at 5% show better modeling of the vortex sheet, and can therefore be argued, in conjunction with the overall normal force predictions, to be the better method. Compared to the SCV method, the better predictions for 6°, 10° and 15°, for both loads and vortex positions demonstrate the effect of the secondary vortex on the strake edge condition. It can be concluded that the deviations in the SCV method correlate with the emergence of the secondary vortex and points towards the role of the secondary vortex in modifying the strake side edge condition.

The ability of the discrete vortex methods that employ a boundary layer model to better model the flow is on the other limited by the computational time required to solve the flow field of the configuration at hand. For this thesis, the code was not efficient in its implementation and no vortex merging was implemented such that a single angle of attack took over 6 hours to solve on a modern single core Intel CPU. On the other hand, the SCV method took less than 10 seconds to solve for the 25° angle of attack case. As the number of discrete vortices increases so does the computational time required. It is the opinion of the author that the time required for a solution of the DVM methods that utilise a boundary layer model do not make them feasible for engineering level use, especially when compared to the methods used by existing engineering codes.

Chapter 7

Free Vortex Model

7.1 Introduction

The approximate method presented in this thesis is based on the free vortex afterbody model developed by Hemsch *et al* [141] and the observation that the shed vortex sheet rolls up at higher positions that in potential only discrete vortex method. The vortices shed are idealised by the free vortex model (FVM) method as single concentrated vortices shed from the side edges of the wings/strakes.

The method, as for the DVM method, uses the tracking of vortices to determine the position of the vortex along the strake. The position coupled with the strength of the vortex, and using the vortex impulse theorem, determines the normal force and centre of pressure induced by the vortex on the configuration. The first significant difference between this method and the single concentrated vortex model based on the method of Bryson is that the Kutta condition is, in general, not satisfied at any point in the solution process. The second is that an external condition is required to solve the set of first order differential equations, which is the load that is imposed on the 2 dimensional cross section. The Newtonian impact method as devised by Jorgensen [31] is used to satisfy this condition. This method differs to other engineering methods used to track tip vortices in that the position of the vortex is dependent on the shed vorticity. Previous methods [141] have assumed a constant vortex strength and that the strength depends only on the total lift developed by the wing.

The presentation of the FVM method and it application to the configuration at hand begins with the continued theoretical development of this method as applied to cruciform wing-body configurations and is subsequently applied to the angles of attack of interest where upon the results are compared to the validated CFD simulations. As a test of the method to other aspect ratios and body diameter to stake span ratios, the method is then applied to other public domain cases and the results assessed.

7.2 Equation of Motion of Vortices

The movement of vortices, whether shed by the body or free, can be modelled as Lagrangian fluid particles. The initial theoretical development has been presented in Chapter 3.

For vortices of variable strength, assuming the shed vorticity is fed into a single vortex, an additional variable for each vortex is present. The treatment of such a system has already been performed by reference [141] and is reproduced for clarity.

In summary from equation 3.18, the transverse velocity of a j^{th} vortex, in the presence of other vortices can be written as

$$\begin{aligned} v_j - iw_j &= \left[-iV\sin\alpha e^{-i\phi_x}\left(1+\frac{r_o^2 e^{i2\phi_x}}{\nu_j^2}\right)+\frac{i\Gamma_j}{2\pi}\left(\frac{1}{\nu_j-\frac{r_o^2}{\bar{\nu_j}}}\right)\right. \\ &\quad \left. -i\sum_{k=1}^{n}\frac{\Gamma_k}{2\pi}\left(\frac{1}{\nu_j-\nu_k}-\frac{1}{\nu_j-\frac{r_o^2}{\bar{\nu_2}}}\right)\right]\left(\frac{d\nu}{d\sigma}\right)_{\sigma=\sigma_j} \\ &\quad -\frac{i\Gamma_j}{4\pi}\left(\frac{d\sigma}{d\nu}\right)\left(\frac{d^2\nu}{d\sigma^2}\right)_{\sigma=\sigma_j} \end{aligned} \tag{7.1}$$

For a circular body, for which this method was originally developed, the equations of motion for the j^{th} vortex is

$$\frac{dy_j}{dt} = v_j \text{ and } \frac{dz_j}{dt} = w_j \tag{7.2}$$

The cross-flow plane is moving down the body at a speed of $V\cos\alpha$. Thus

$$\frac{dx}{dt} = V\cos\alpha \tag{7.3}$$

The rate of change of the j^{th} vortex with body axial position is thus

$$\frac{dy_j}{dt} = \frac{v_j}{V}\frac{1}{\cos\alpha} \text{ and } \frac{dz_j}{dt} = \frac{w_j}{V}\frac{1}{\cos\alpha} \tag{7.4}$$

For vortices that are shed and are of variable strength, such as aftbody vortices, in an incremental distance, dx, the increments in the normal and side force are given by the vortex impulse theorem [148] as:

$$dF_N - idF_Y = d\left[\Gamma_L\left(\sigma_L-\frac{a^2}{\bar{\sigma_L}}\right)+\Gamma_R\left(\sigma_R-\frac{a^2}{\bar{\sigma_R}}\right)\right]\rho V \tag{7.5}$$

since

$$F_N - iF_Y = \rho V\Gamma\left(\sigma-\frac{a^2}{\bar{\sigma}}\right) \tag{7.6}$$

If the differential increments are due to the viscous cross-flow, then

$$dF_{N_v} - idF_{Y_v} = \left[d\Gamma_L\left(\sigma_L-\frac{a^2}{\bar{\sigma_L}}\right)+d\Gamma_R\left(\sigma_R-\frac{a^2}{\bar{\sigma_R}}\right)\right]\rho V \tag{7.7}$$

Assuming that the cross-flow drag is in the same direction as the cross-flow velocity yields

$$dF_{N_v} - i dF_{Y_v} = D_v \left(\sin\theta - i\cos\theta\right) \tag{7.8}$$

where

$$D_v = c_{d_c} q \sin^2 \alpha_{cr} 2a dx \tag{7.9}$$

and α_{cr} is the direction of the cross-flow angle of attack due to freestream velocity vector and the vortices, and θ is the cross-flow vector in the σ plane. Therefore

$$\rho V \left[\frac{d\Gamma_L}{dx}\left(\sigma_L - \frac{a^2}{\bar{\sigma_L}}\right) + \frac{d\Gamma_R}{dx}\left(\sigma_R - \frac{a^2}{\bar{\sigma_R}}\right)\right] = 2ac_{d_c} q_\infty \sin^2 \alpha_{cr} \left(\sin\theta - i\cos\theta\right) \tag{7.10}$$

The first order differentials for the vortices can then be integrated using standard routines in the same way as the position of the vortices to determine not only the path, but the strength as a function of the axial distance.

This method does not assume or predict the separation point and no separation condition is specified, only that the strength and position of the vortices is determined by the cross flow drag and imposing a no-net-force on the vortex. Indeed, the assumption made is that the vortex is free. Also implicit, as for the SCV method, is that no vortex sheet is modeled. Compared to the DVM and SCV method, the strength of the vortex is determined by the 2D load rather than through the Kutta condition. This is a direct application of the Allen heuristic methodology. Alternatively put, the shed vorticity is therefore a function of the 2D sectional loading. It should be noted that the difference between this method and the SCV method is that the vortices move as free fluid particles and the Kutta condition is not imposed on the edge explicitly.

7.2.1 Cruciform Wing-Body Configurations

The extension of the methodology from the previous section to cruciform wing-body configurations, and the thesis put forward, is to apply a transformation from the physical plane to the circle plane and then use the existing method as previously developed but applied to strake-body configurations rather than bodies only.

Velocities in the transformed plane, and hence trajectories in the transformed plane do not correspond to the physical plane because, as shown in reference [4], the velocities of the complex potential $W[\nu(\sigma)]$ are magnified by the term $\frac{d\nu}{d\sigma}$ and rotated by the angle $\arg\frac{d\nu}{d\sigma}$ because

$$v - iw = \frac{dW}{d\sigma} = \frac{dW}{d\nu}\frac{d\nu}{d\sigma} \tag{7.11}$$

The vortex strength differentials (and vortex strengths) are also the same in both the physical and transformed planes, thus requiring no additional terms. The governing equations then become

$$\rho V \left[\frac{d\Gamma_L}{dx} \left(\nu_L - \frac{r_o^2}{\bar{\nu_L}} \right) + \frac{d\Gamma_R}{dx} \left(\nu_R - \frac{r_o^2}{\bar{\nu_R}} \right) \right] = 2 c_{d_c} q \sin^2 \alpha_{cr} \left(\sin\theta - i \cos\theta \right) \tag{7.12}$$

The cross-flow drag term, c_{d_c}, is easily determined for a cylinder and has a value of 1.2 for subcritical cross flow Reynolds numbers and cross flow Mach numbers below 0.43. For body-strake configurations, the cross flow drag coefficient lies somewhere between that of a flat plate and a cylinder, depending on the strake to body diameter ratio. The two available sources for this information are that of the experimental data by Macha [107] or the Newtonian impact theorem implemented by Jorgensen [31]. For the purposes of this thesis, the Newtonian impact theory is used and is suitable over the span to diameter ratios being studied [157]. This does, however, not take into account Mach number effects as the experimental data of Macha does. The Newtonian impact theory predicts a drag ratio of:

$$C_D = C_{D_0} \frac{3}{2} \left(2 \frac{s_m}{a} - \frac{1}{3} \right) \tag{7.13}$$

For the configuration under consideration ($s_m/a = 1.25$) and assuming the drag coefficient of the cylinder is 1.2, the cross flow drag coefficient is 1.65, whilst Macha predicts approximately 1.5 for the cross flow Mach number of 0.6. A cross-flow Mach number correction based on the data of Macha is also applied using the average ratios for the data from reference [107]. For cross flow Mach numbers below 0.6, the same value as Mach 0.6 is used. The ratios as a function of cross-flow Mach number are listed in Table 7.1.

Table 7.1: Cross flow Mach number ratio

Mach	0.6	0.7	0.8	0.9	1.0	1.05
Ratio	1.0	0.971	0.9187	0.906	1.199	1.0

7.2.2 Initial Vortex Position and Strengths

The free vortex method presented so far requires initial vortex positions and strengths so that the first order differential equations can be solved. Being a method that does not impose boundary conditions and models the trajectory of the vortex as a Lagrangian fluid particle, in the initial stages of the solution process the initial vortex is close to the body resulting in the vortex traveling close to the body surface which is non-physical.

One starting point would be to use the criterion specified by the DVM method, create an initial vortex with a strength and then let the first order differential equations be solved in time. From Chapter 5, it was found that the SCV method was a good very low angle

of attack method. In this thesis this method is used to start the solution process for the FVM method. The SCV method is used simply because the solution is simple and does not involve multiple vortices as the DVM method. As previously shown, the initial solutions are sufficiently accurate to start the method, even though it is inaccurate along the rest of the length of the strake because the concentrated vortex enforces the Joukowski-Kutta condition. For this method, this is the only time when the Joukowski-Kutta condition is enforced. It should be noted that the SCV method used is taken directly from chapter 5 and no body vortex is therefore present in the formulation.

7.3 Body Vortex

As for the DVM implementation, the body vortex positions and strengths were estimated from the CFD simulations as defined in table 6.1. Because the method has an ability to model Mach number dependencies, even though it is only through the cross flow Mach drag coefficient, the positions and strengths for the Mach numbers 2.5 and 3.0 were also estimated from the CFD simulations in the same manner as for Mach 2.0 and subsequently used.

7.4 Test Matrix

As for the SCV and DVM methods, the conditions for which simulations were performed are the angles of attack of 1°, 2°, 4°, 6°, 10°, 15°, 20°and 25°.

7.5 Results

7.5.1 Global Loads

The normal force and centre-of-pressure comparison of the overall configuration is shown in Figure 7.1. The same method as the SCV and DVM predictions was used to determine the overall loads. Because the free vortex method does have a Mach number dependency, FVM predictions for the three Mach numbers are presented for comparison purposes. Compared to the SCV and DVM potential only methods, the normal force prediction is much better predicted. The centre-of-pressure predictions indicate an initial rearward movement of the centre-of-pressure and then a forward movement. The Mach 2.0 centre-of-pressure movement also has a small forward movement, though not as large as that predicted by the free vortex method. The trend is, however, well captured at the low angles of attack even though a constant offset exists.

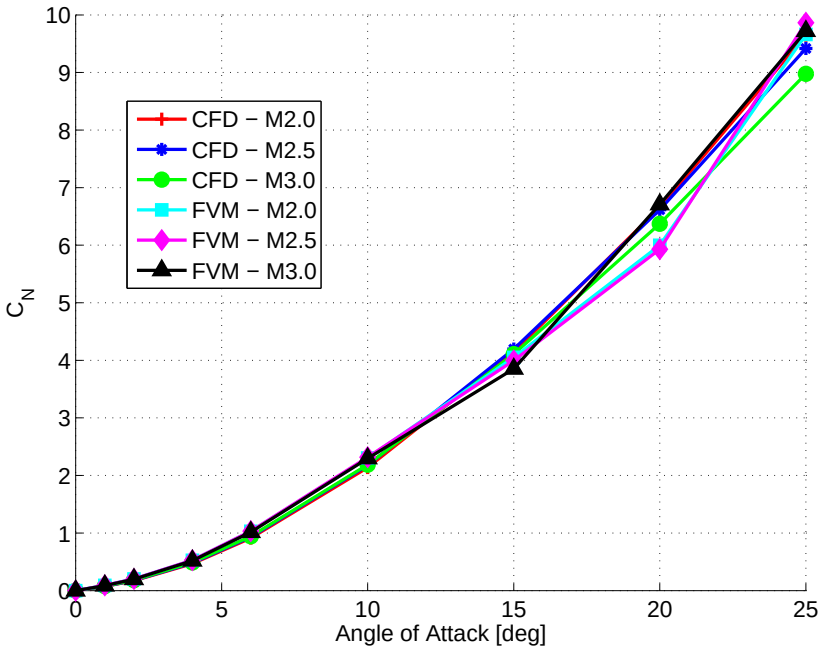

(a) Normal force

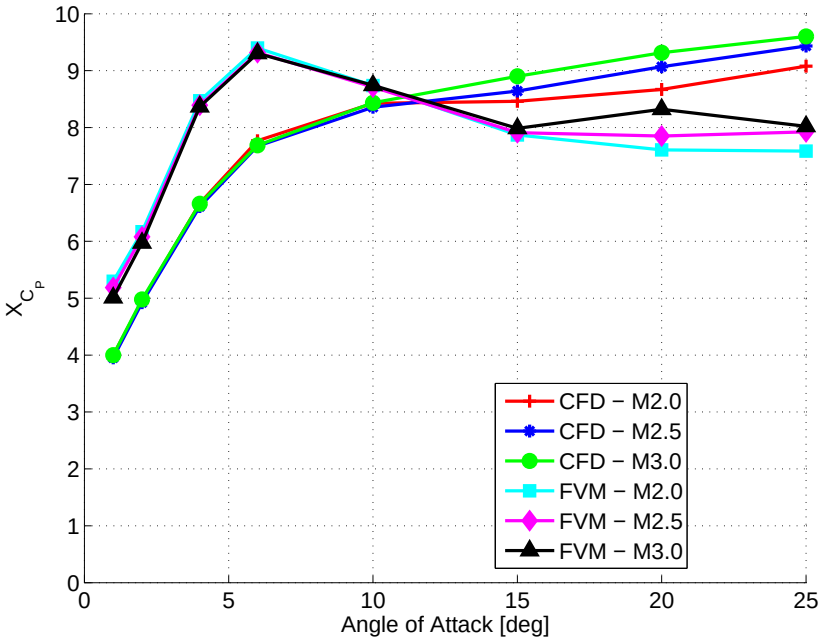

(b) Centre-of-pressure

Figure 7.1: CFD and FVM normal force and centre-of-pressure comparison

A closer investigation into the mechanism for this reveals that the normal force increment along the wing-body section is a function of angle of attack. Figure 7.2 plots the normal increment along the body length over the body-wing section for 4° and 10°. Of interest is the overall characteristic of the force increment along the length of the wing-body section. The initial drop in the force increment is due to the use of the SCV method which introduces a numerical artifact common to all angles of attack. As can be seen from the figures is that at the low angles of attack which is represented by the 4° case, the increment increases along the length of the wing-body section. The centre-of-pressure is toward the rear of the wing-body section. At 10° the centre-of-pressure is more forward, therefore explaining the centre-of-pressure characteristic seen for the overall configuration. This presents a current limitation in the method and is probably due to the assumption that the cross-flow drag coefficient is constant along the wing body section. It should be noted that the fore- and aftbody sections have centres-of-pressure that move rearward toward the planform centroid as the angle of attack increases. This also holds for the potential component of the isolated strake.

7.5.2 Detailed Flow Field

The flow field results of the simulations are shown in Figure 7.3 to Figure 7.10 and plots the position of the vortex for various axial locations in comparison to the CFD simulations. The FVM vortex position is denoted by the ◊ symbol. For the cases with a body vortex (i.e. 15°, 20°and 25°) the body vortex prediction is also plotted. For the cases with body vortices, the motion of these vortices are denoted by the □ and + symbols.

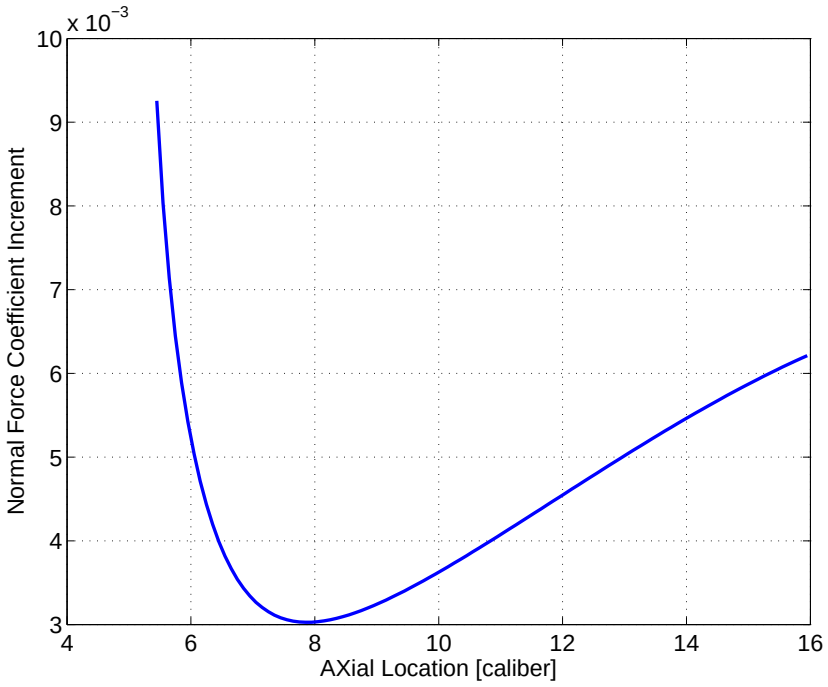

(a) 4°

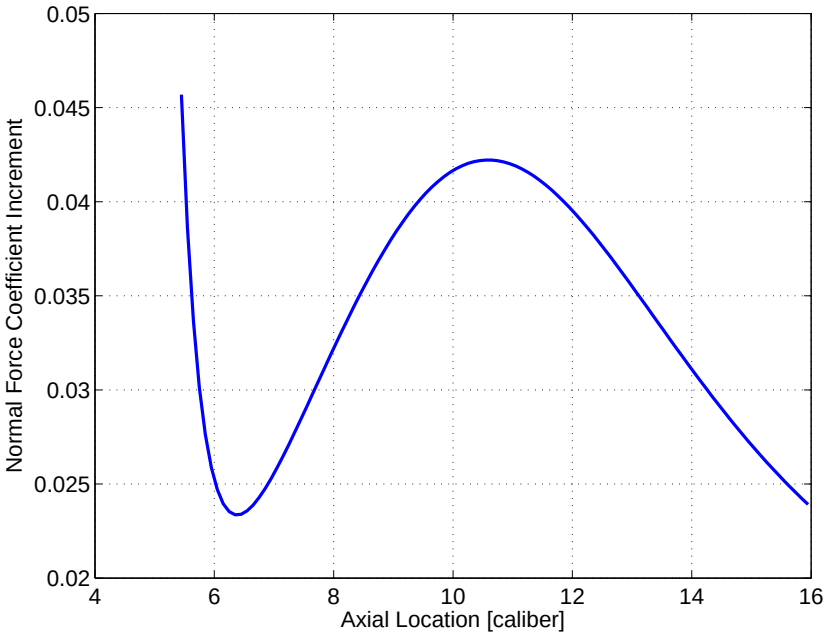

(b) 10°

Figure 7.2: Normal force coefficient increment at 4° and 10° along the body length

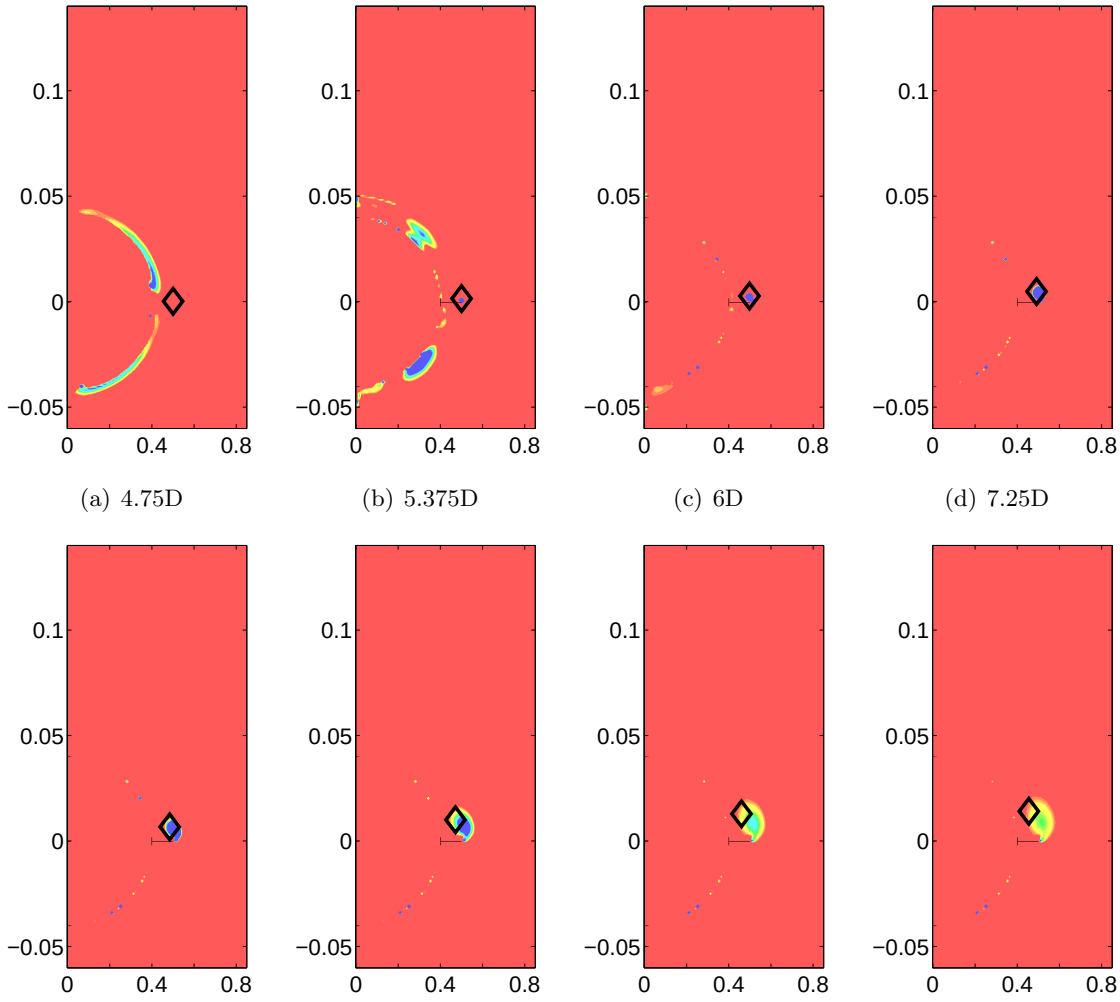

(a) 4.75D (b) 5.375D (c) 6D (d) 7.25D

(e) 8.5D (f) 11D (g) 13.5D (h) 14.75D

Figure 7.3: Vortex development for $\alpha = 1°$, FVM

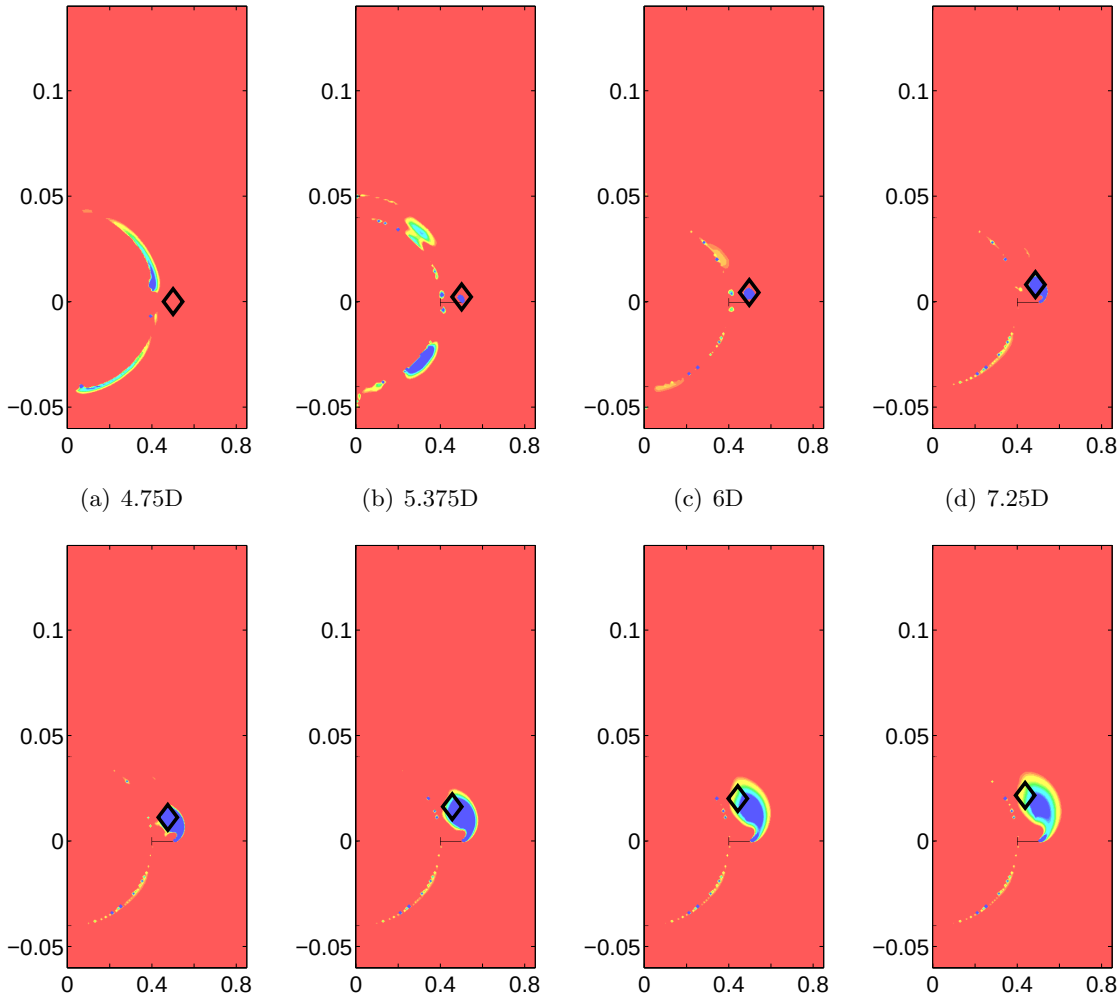

(a) 4.75D (b) 5.375D (c) 6D (d) 7.25D

(e) 8.5D (f) 11D (g) 13.5D (h) 14.75D

Figure 7.4: Vortex development for $\alpha = 2°$, FVM

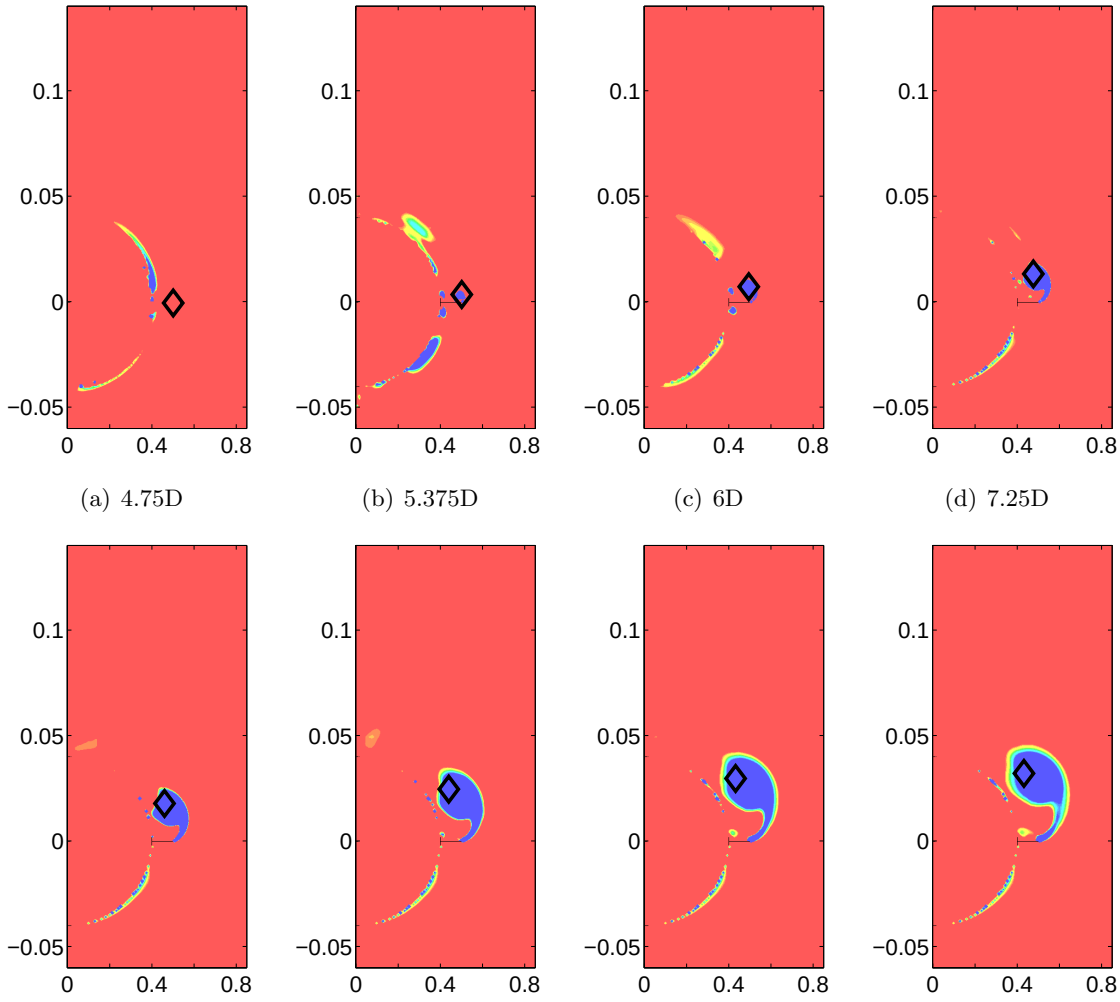

(a) 4.75D (b) 5.375D (c) 6D (d) 7.25D

(e) 8.5D (f) 11D (g) 13.5D (h) 14.75D

Figure 7.5: Vortex development for $\alpha = 4°$, FVM

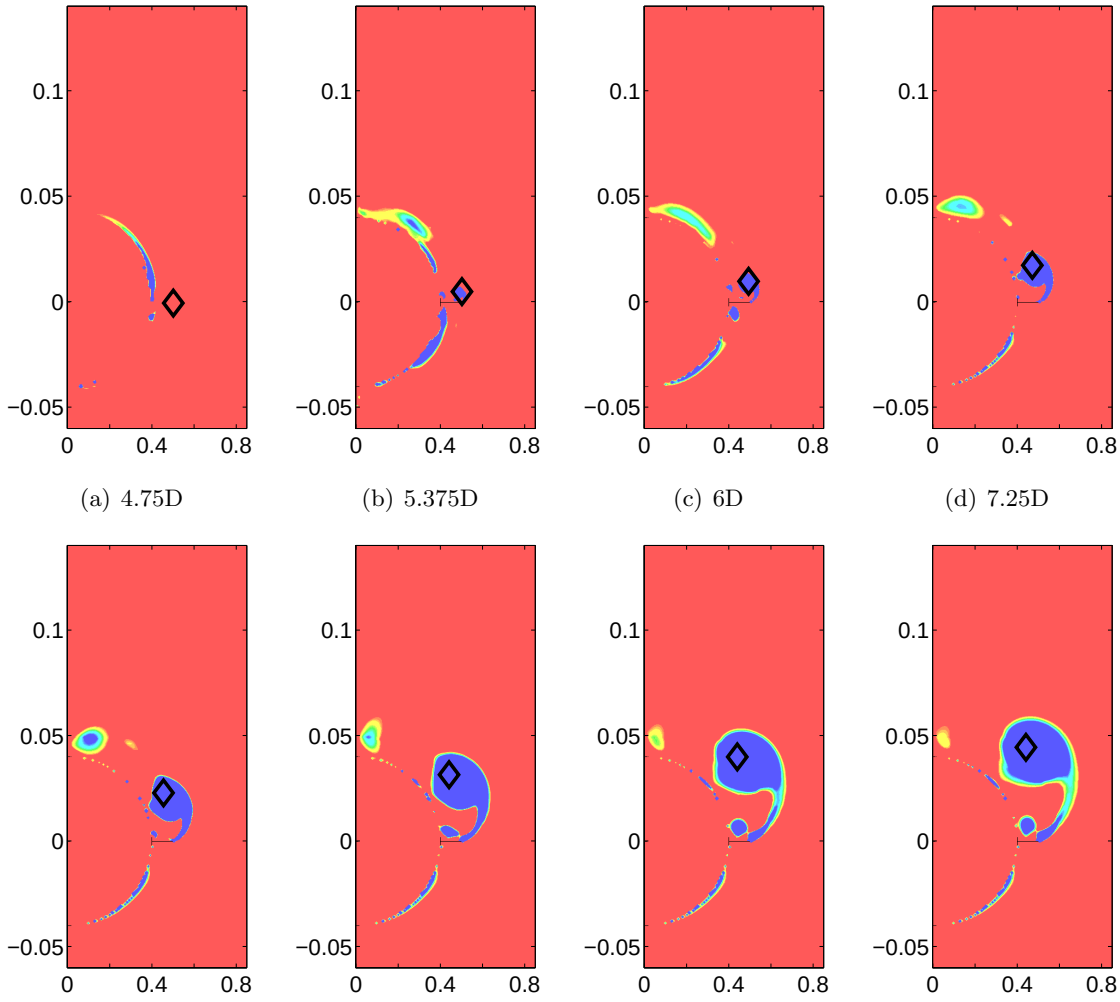

(a) 4.75D (b) 5.375D (c) 6D (d) 7.25D

(e) 8.5D (f) 11D (g) 13.5D (h) 14.75D

Figure 7.6: Vortex development for $\alpha = 6°$, FVM

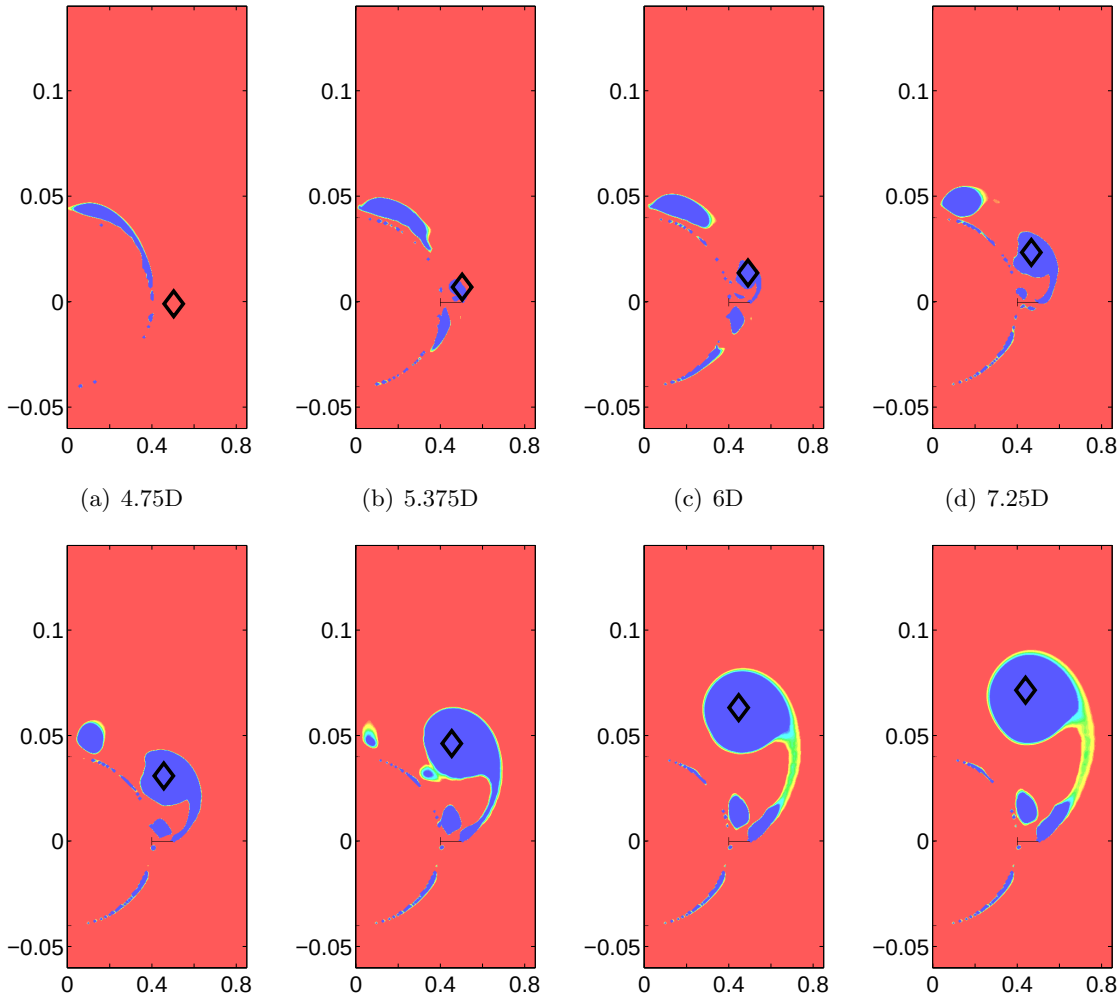

(a) 4.75D (b) 5.375D (c) 6D (d) 7.25D

(e) 8.5D (f) 11D (g) 13.5D (h) 14.75D

Figure 7.7: Vortex development for $\alpha = 10°$, FVM

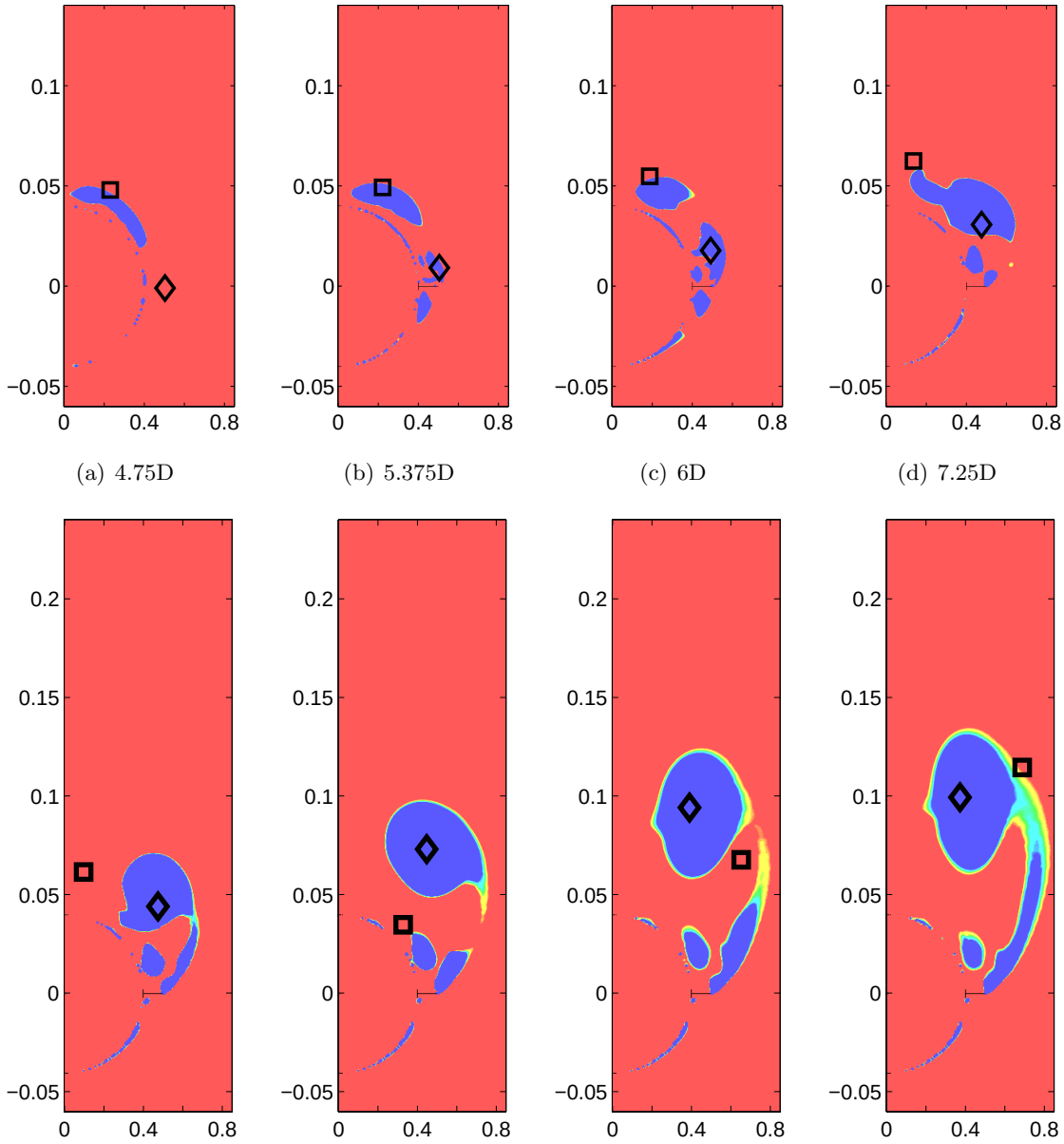

(a) 4.75D (b) 5.375D (c) 6D (d) 7.25D

(e) 8.5D (f) 11D (g) 13.5D (h) 14.75D

Figure 7.8: Vortex development for $\alpha = 15°$, FVM

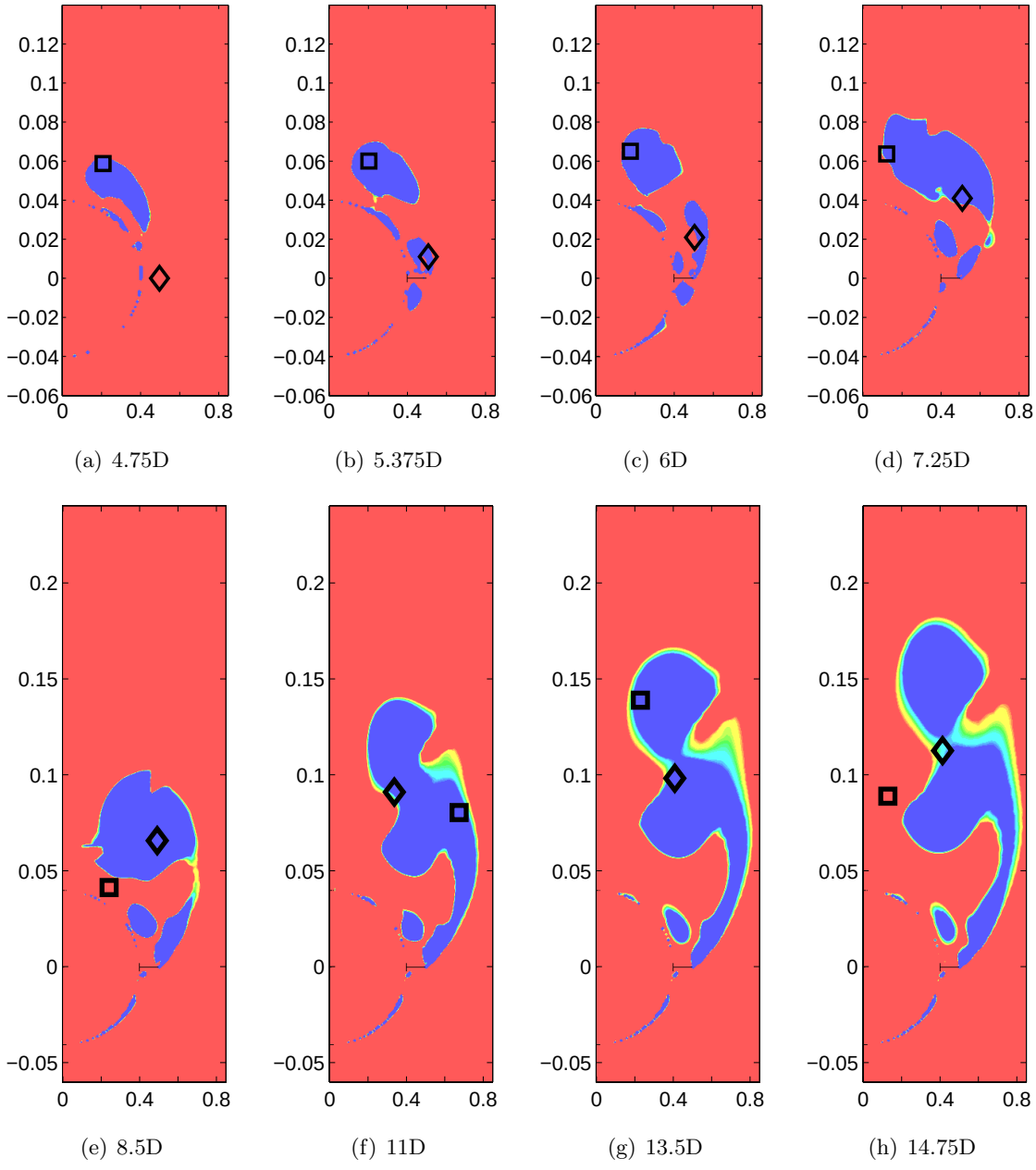

(a) 4.75D (b) 5.375D (c) 6D (d) 7.25D

(e) 8.5D (f) 11D (g) 13.5D (h) 14.75D

Figure 7.9: Vortex development for $\alpha = 20°$, FVM

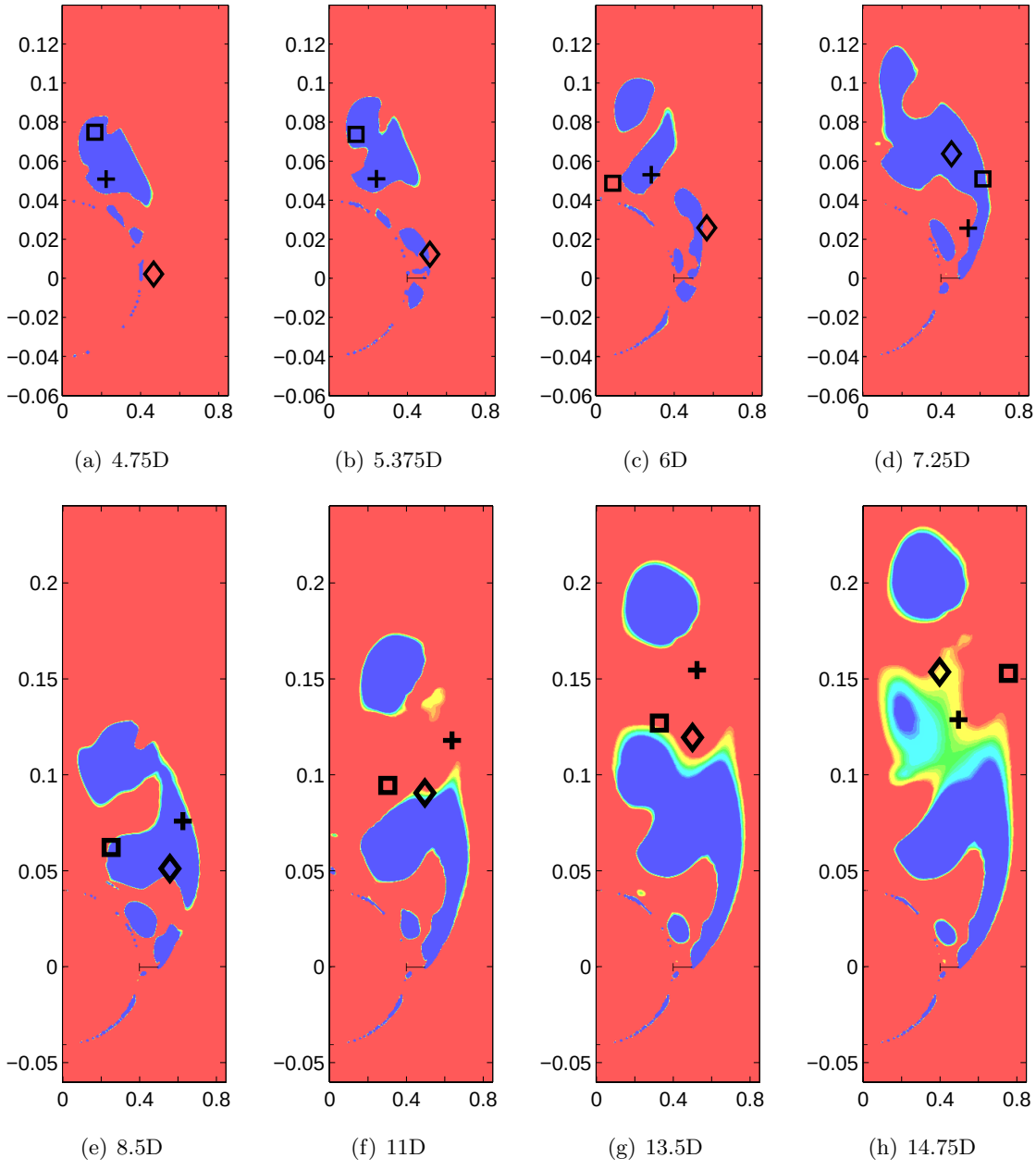

(a) 4.75D (b) 5.375D (c) 6D (d) 7.25D

(e) 8.5D (f) 11D (g) 13.5D (h) 14.75D

Figure 7.10: Vortex development for $\alpha = 25°$, FVM

As for the SCV and DVM methods, the alternative method of visualising the vortex trajectories are illustrated in Figure 7.11 to 7.20. The positions whilst not comparing well against the CFD simulations, compares well with the LSWT (subsonic) simulations in the vertical direction. The oscillatory nature of the strake vortex is due to the interaction of the strake vortex with the body vortex. As for the DVM simulations, no vortex coalescence is modeled and the body vortex trajectory is not limited by the physical presence of a vortex sheet.

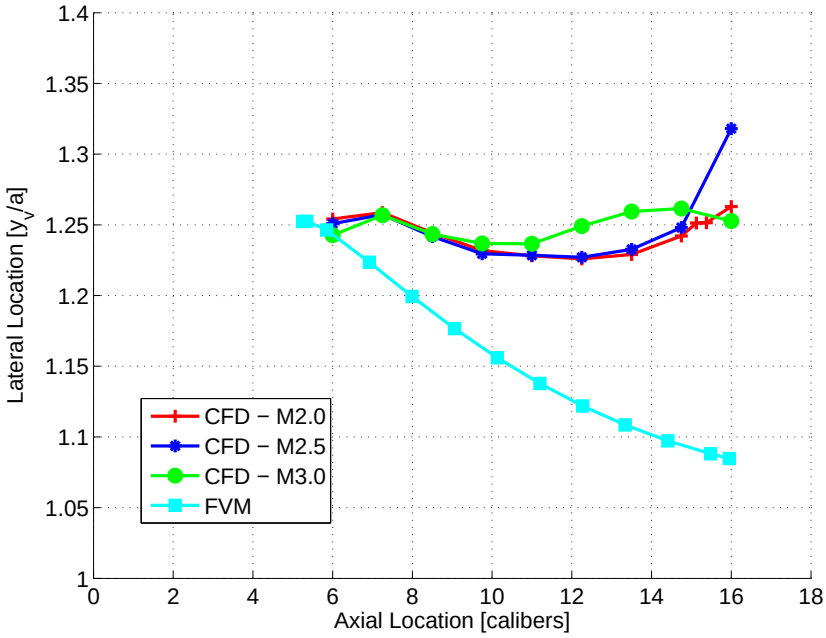

(a) Lateral

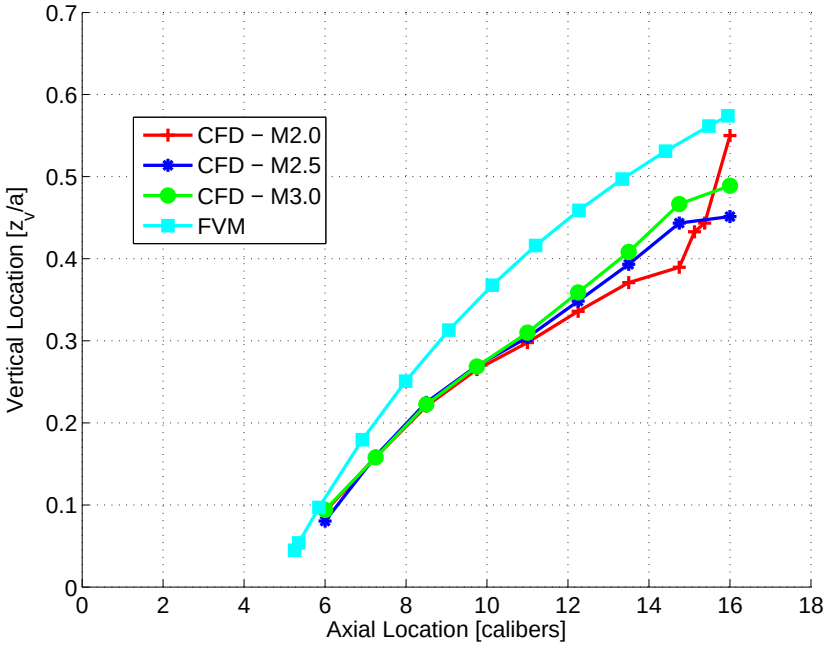

(b) Vertical

Figure 7.11: CFD and FVM concentrated vortex positions at $\alpha = 2°$

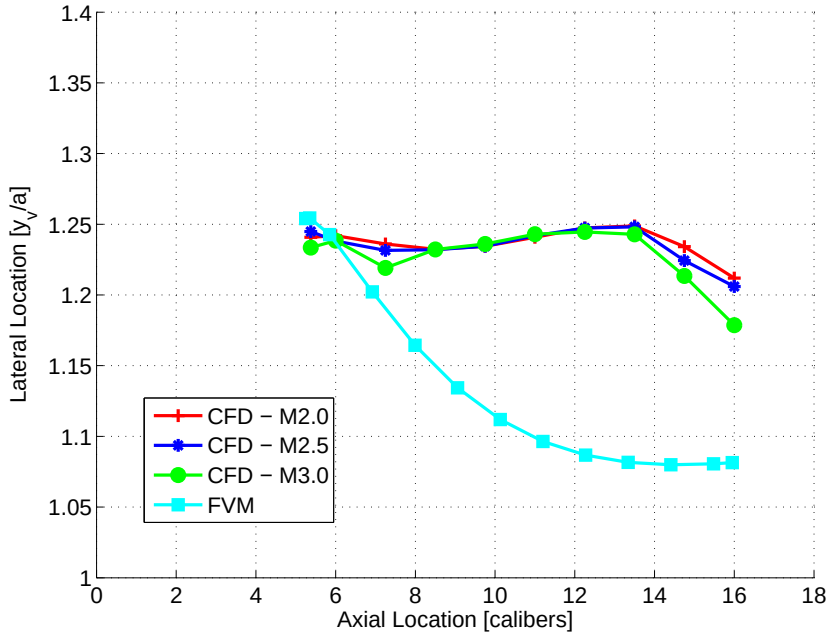

(a) Lateral

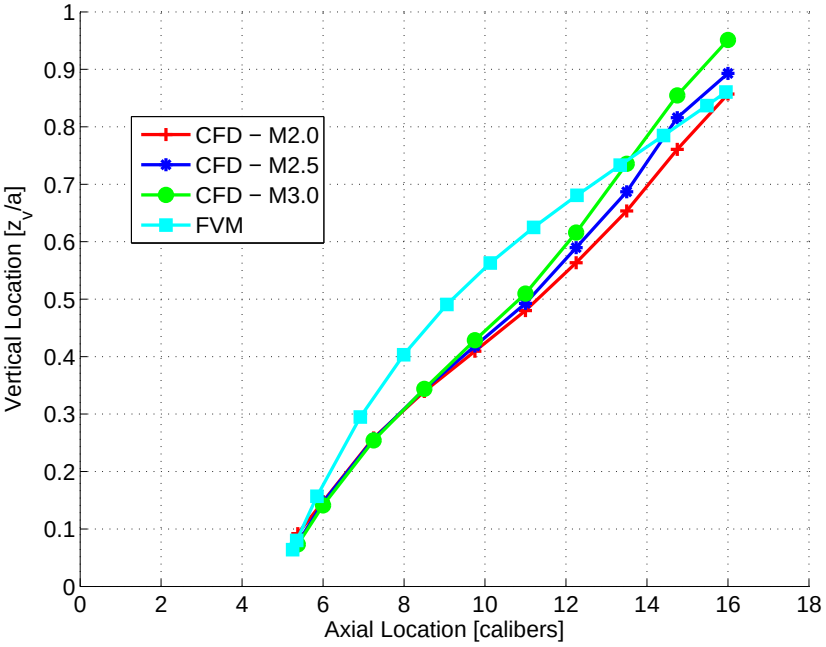

(b) Vertical

Figure 7.12: CFD and FVM concentrated vortex positions at $\alpha = 4°$

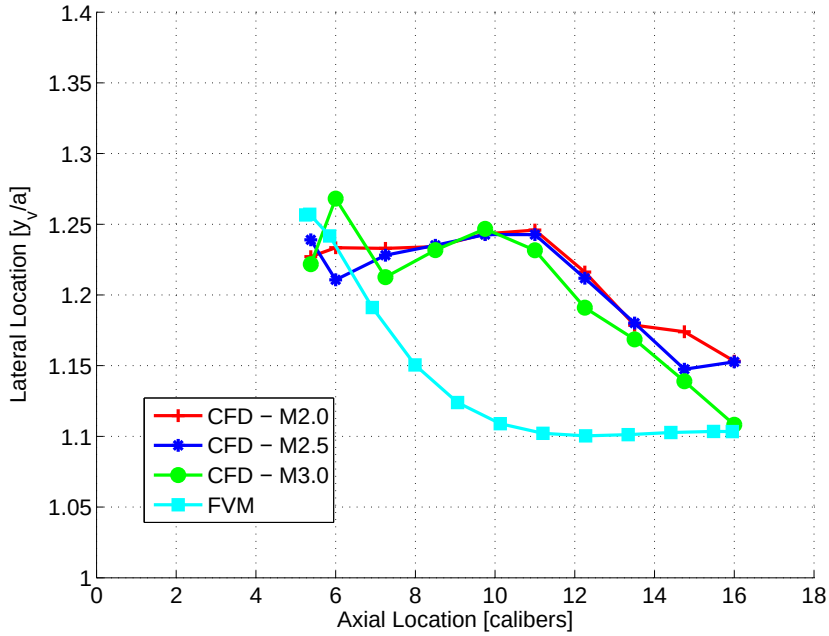

(a) Lateral

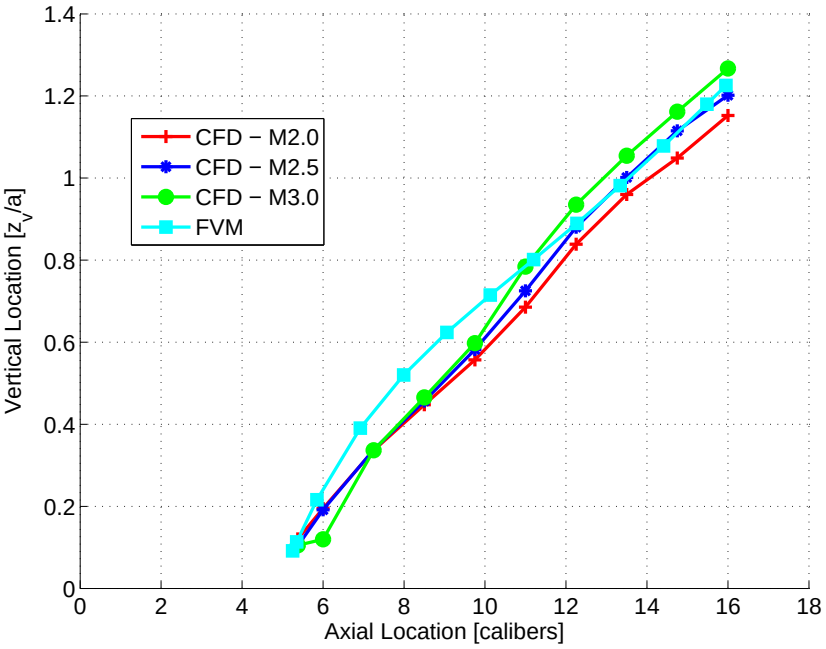

(b) Vertical

Figure 7.13: CFD and FVM comparisons of concentrated vortex positions at $\alpha = 6°$

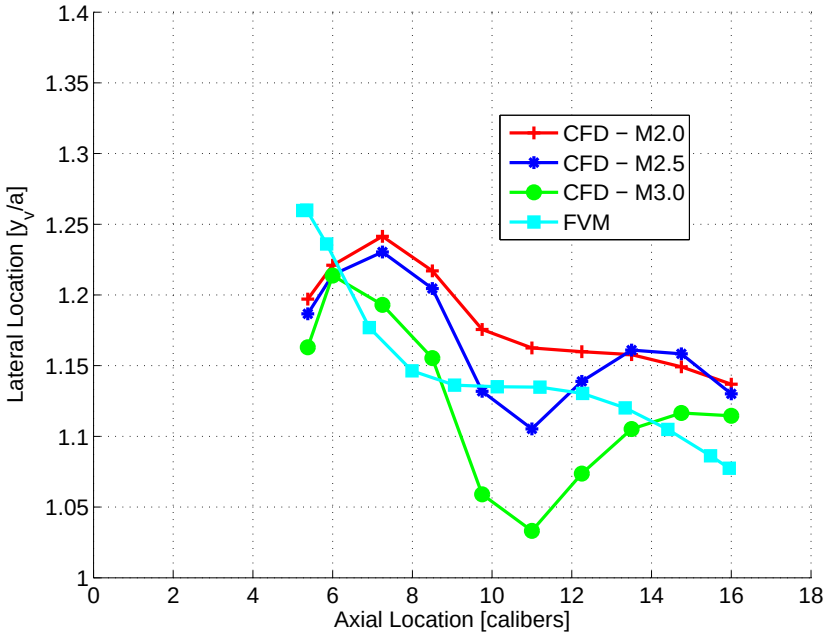

(a) Lateral

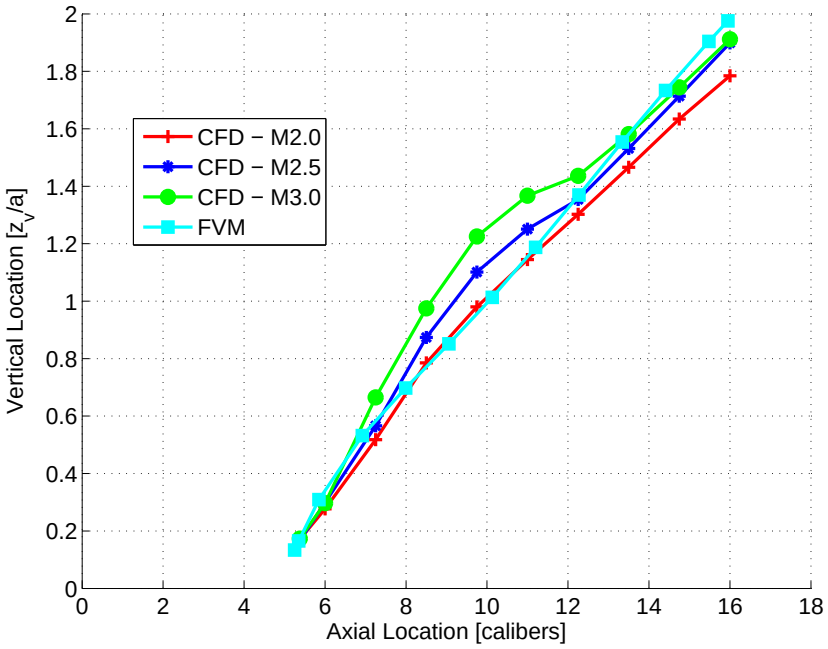

(b) Vertical

Figure 7.14: CFD and FVM comparisons of concentrated vortex positions at $\alpha = 10°$

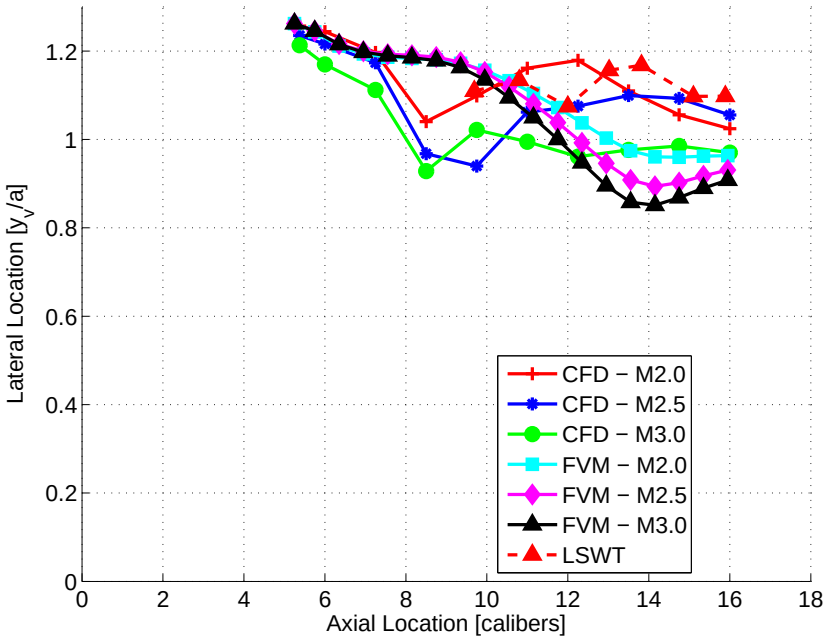

(a) Lateral

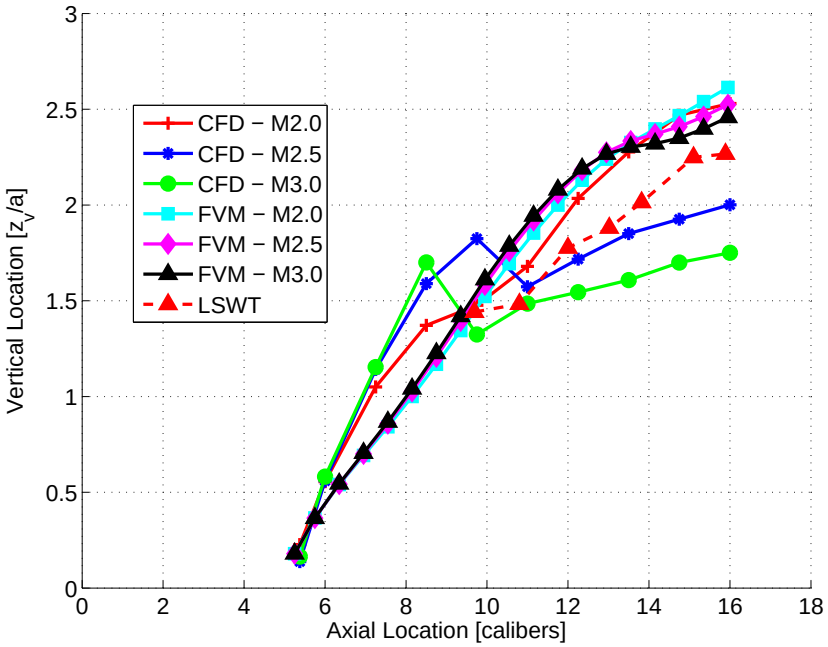

(b) Vertical

Figure 7.15: CFD and FVM comparisons of concentrated strake vortex positions at $\alpha = 15°$

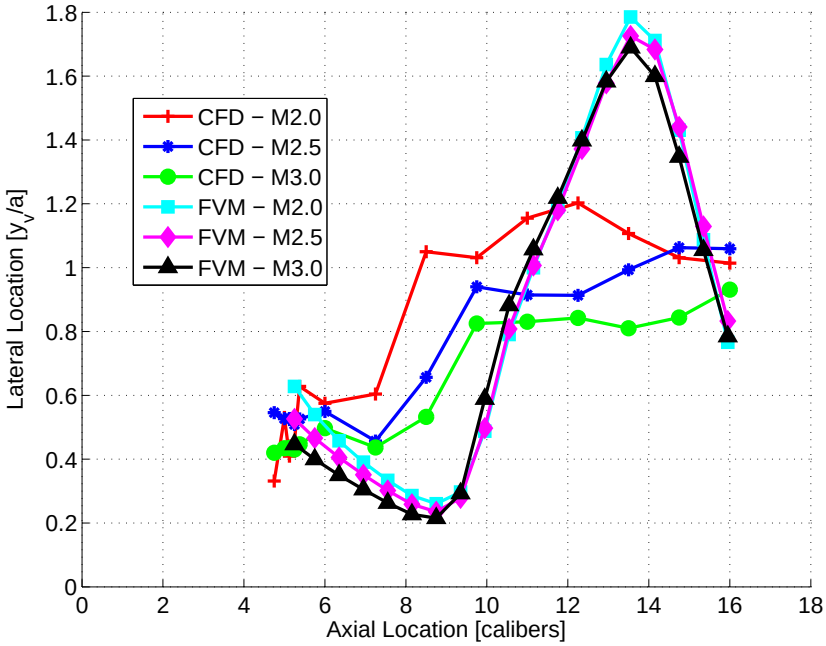

(a) Lateral

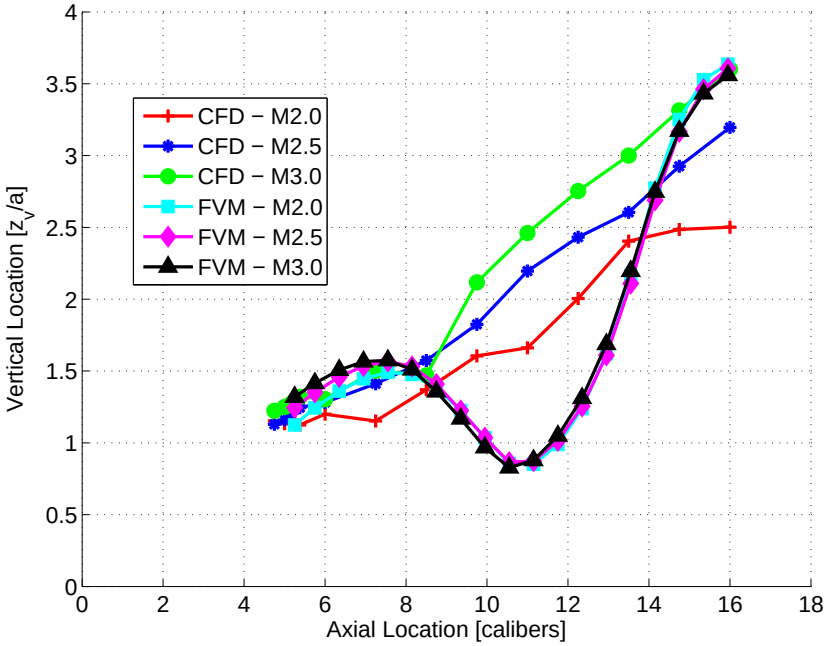

(b) Vertical

Figure 7.16: CFD and FVM comparisons of concentrated body vortex positions at $\alpha = 15°$

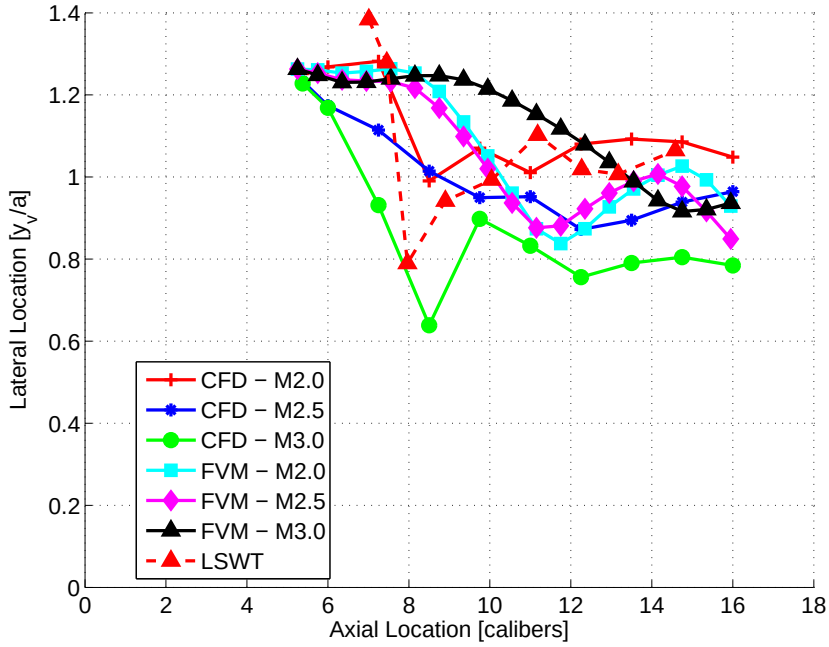

(a) Lateral

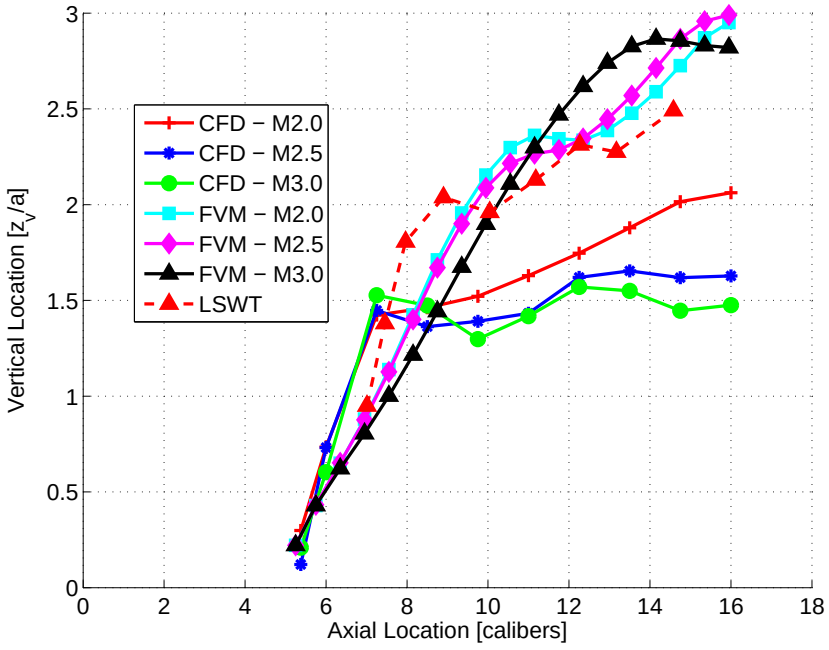

(b) Vertical

Figure 7.17: CFD and FVM comparisons of concentrated strake vortex positions at $\alpha = 20°$

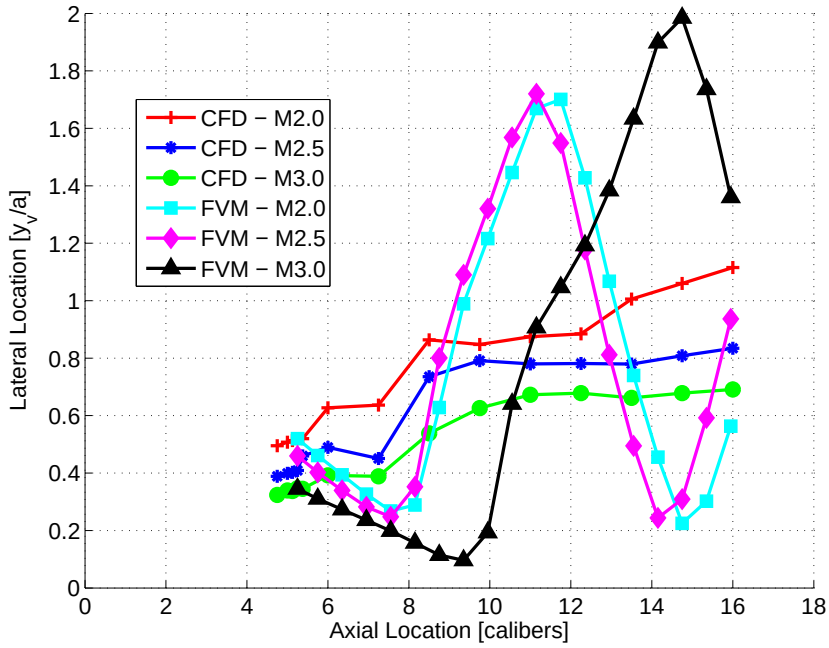

(a) Lateral

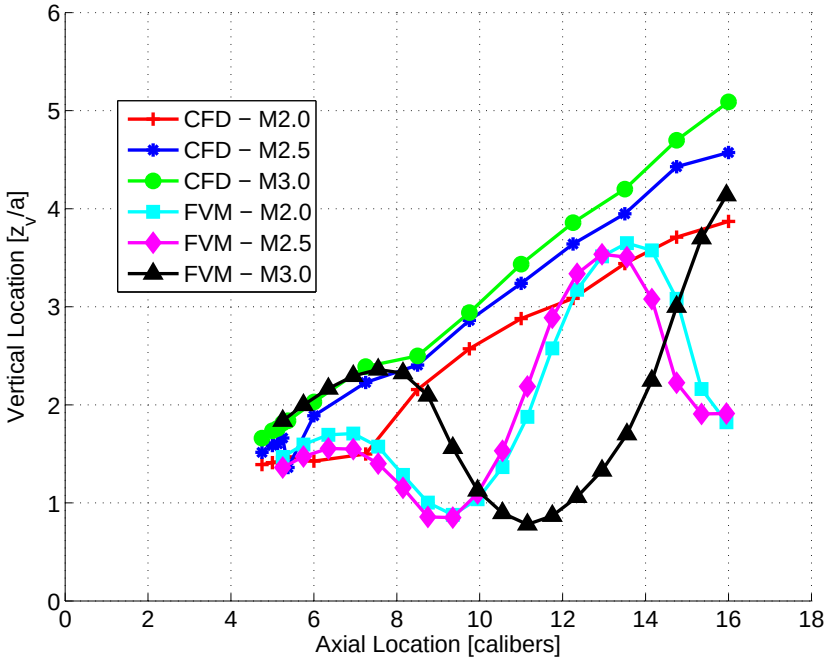

(b) Vertical

Figure 7.18: CFD and FVM comparisons of concentrated body vortex positions at $\alpha = 20°$

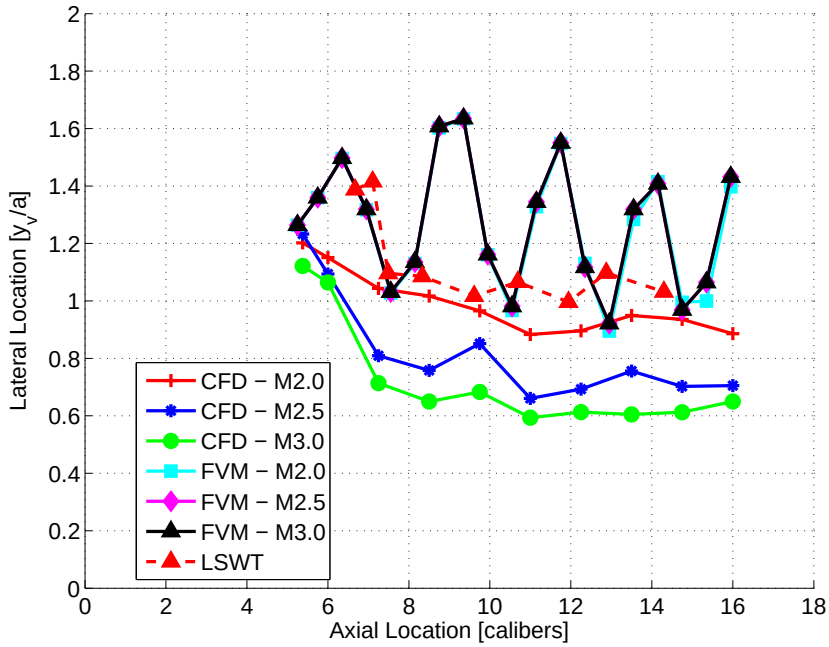

(a) Lateral

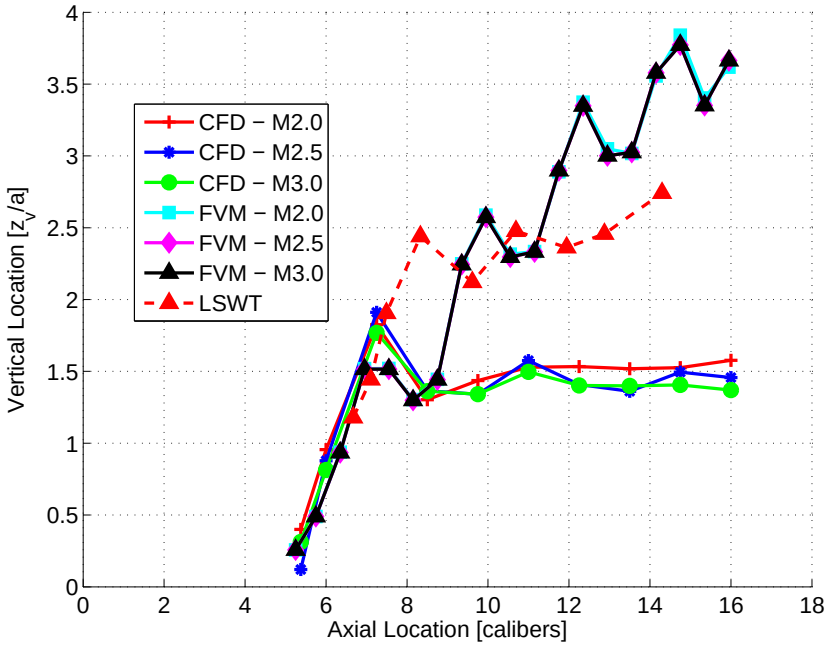

(b) Vertical

Figure 7.19: CFD and FVM comparisons of concentrated strake vortex positions at $\alpha = 25°$

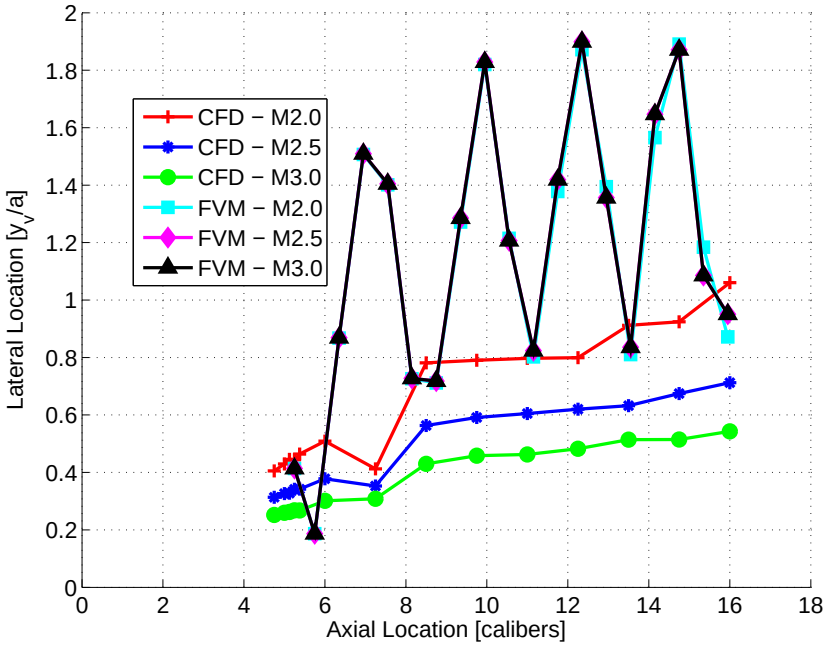

(a) Lateral

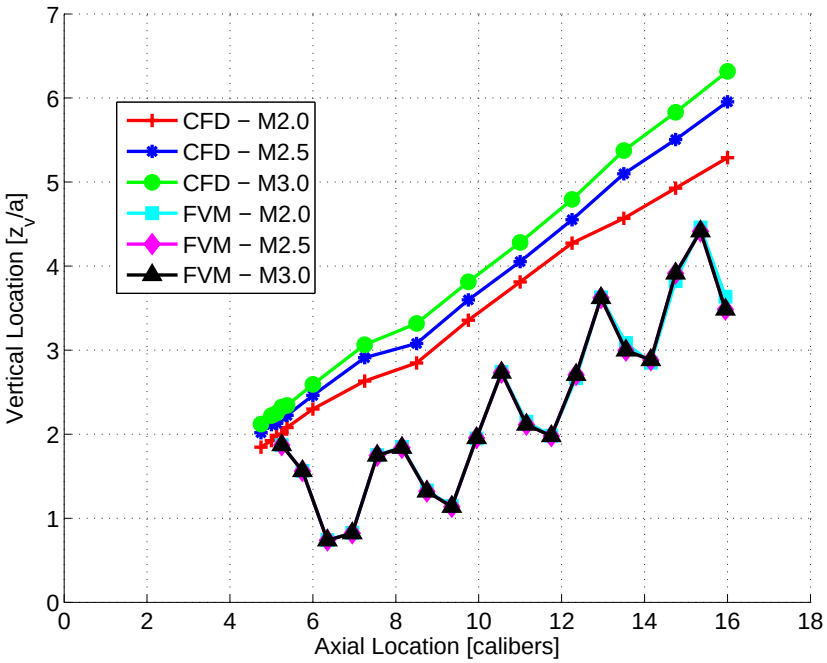

(b) Vertical

Figure 7.20: CFD and FVM comparisons of concentrated strake vortex positions at $\alpha = 25°$

As for the two previous methods, the concentrated vortex strength, Γ', is also compared to the CFD predictions for Mach 2.0. Figure 7.21 to Figure 7.23 plot the CFD simulations against the FVM predictions for the angles of attack from 2° to 20°. For 2°, the FVM underpredicts the vortex strength. The angles of attack 4° to 15° show good correlation with the CFD simulations in the vertical direction and reasonable correlations in the lateral direction. The 20° case clearly shows that the concentrated vortex strength (which is the vortex closest to the body) is overpredicted, and that the position is incorrect due to the vortex shedding. It is clear that when the Joukowski-Kutta condition dictates the separation characteristics that the FVM method is inadequate and that the shed vorticity is higher for the Joukowski-Kutta condition.

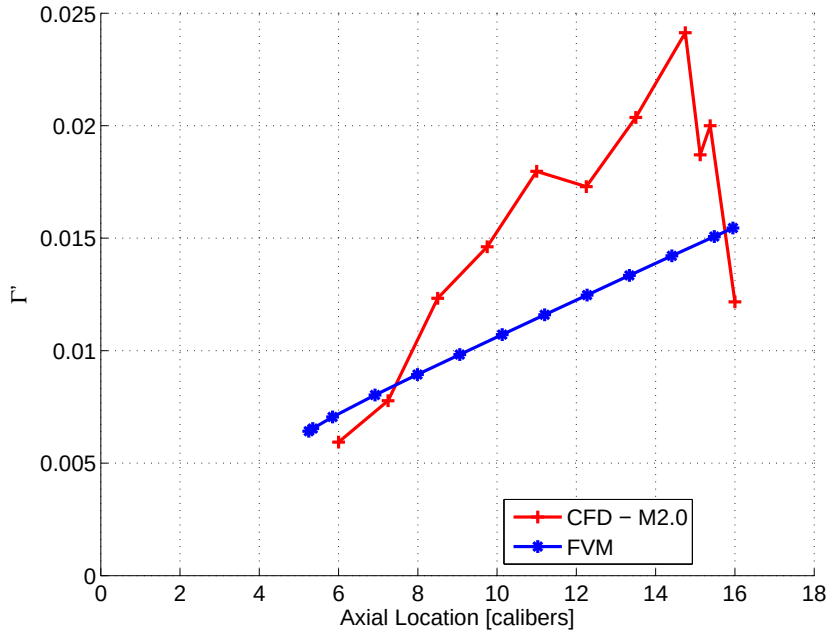

(a) 2°

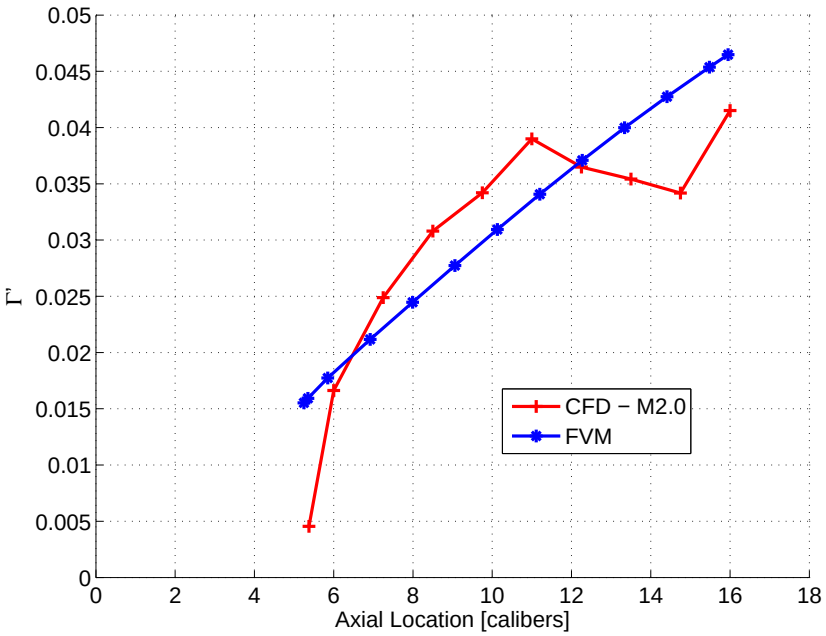

(b) 4°

Figure 7.21: CFD and FVM comparisons of the non-dimensionalised concentrated vortex strength for $\alpha = 2°$ and $4°$

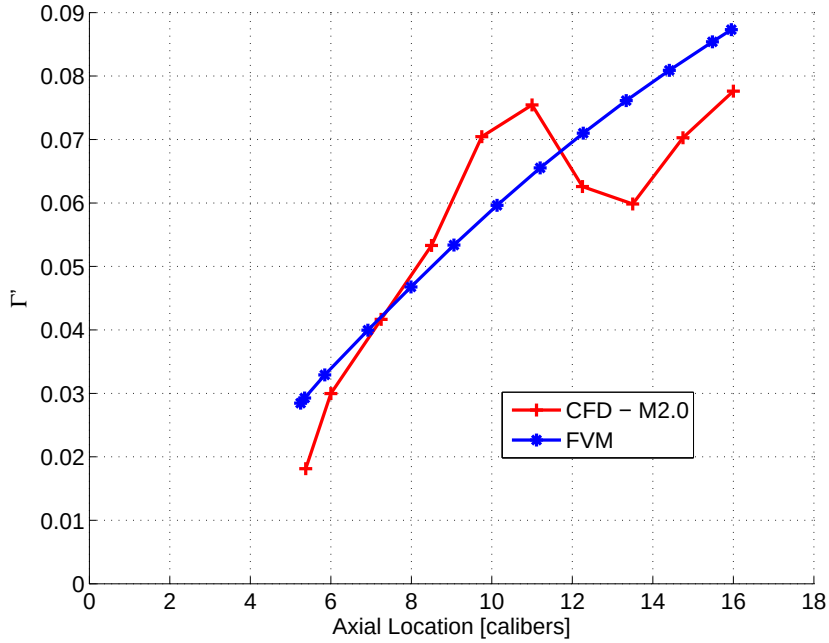

(a) 6°

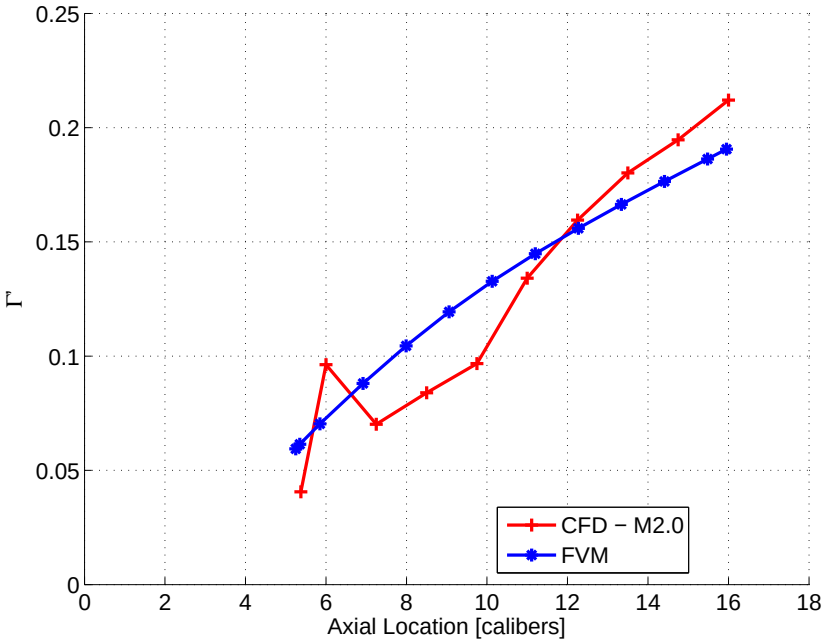

(b) 10°

Figure 7.22: CFD and FVM comparisons of the non-dimensionalised concentrated vortex strength for $\alpha = 6°$ and $10°$

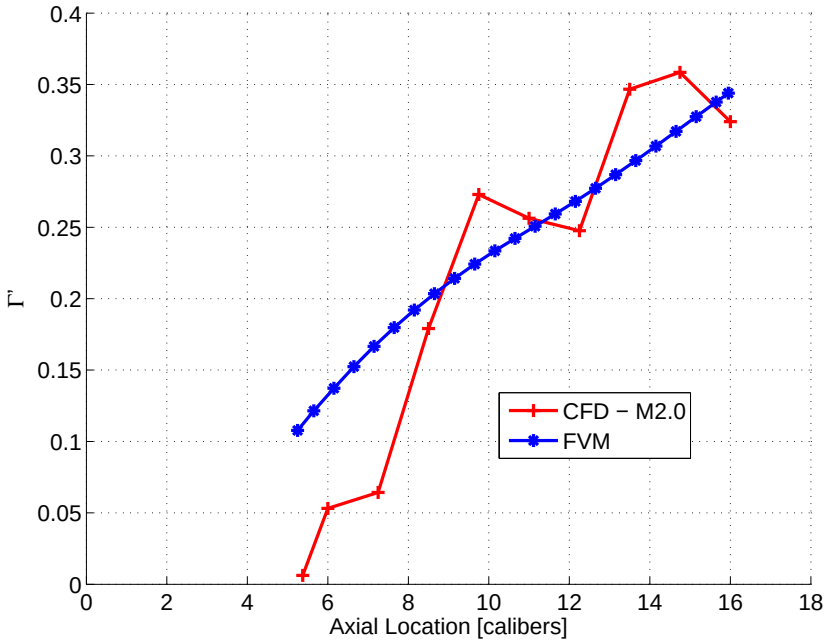

(a) 15°

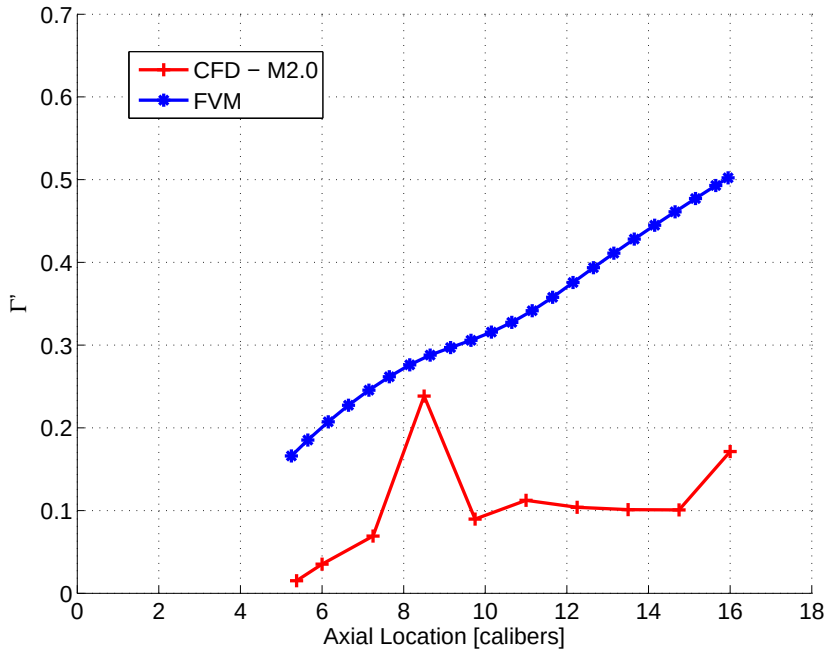

(b) 20°

Figure 7.23: CFD and FVM comparisons of the non-dimensionalised concentrated vortex strength for $\alpha = 15°$ and $20°$

7.5.3 Discussion

As seen from the results for angles of attack below 4°, the free vortex method predicts the position of the centre of the rolled up vortex sheet to be much higher than the CFD predictions. This is because the roll up vortex sheet position is dictated by the strake edge itself for low angles. For the angles from 6° to 15°, the position is well predicted, indicating that the roll up behaves as a free vortex rather than a bound vortex at the lower angles of attack. At 20° and 25°, the change in vortex structure due to shedding is not captured.

The normal force predictions are excellent for the lower angles of attack. At Mach 2.0 the predictions at moderate angles of attack are reasonable. As mentioned in the aerodynamic analysis of the configuration being studied (see chapter 4), when cross flow Mach numbers exceed 0.5 (and even possibly as low as 0.3) a drop in the realised vortex interference load occurs. For Mach 2.0 this occurs above 15°. For Mach 2.5 and 3.0 this is above 10°. As for the two previous methods, this method cannot account for transonic lee side effects and a limit of a cross flow Mach number of 0.55 is therefore placed on this method if vortex position predictions are to be used. The wing-body load prediction is, however, still reasonable for higher cross flow Mach numbers and can still be used as an engineering method. The implication is that the vortex position predictions should be better for a freestream Mach number of 1.5 and possibly lower, though other freestream effects may be present i.e. the flow may not be fully supersonic. The linearised 2D assumptions do not, however, predict any Mach number variation and this method is therefore applicable for Mach numbers ranging from low subsonic to high supersonic as long as the cross flow Mach number is less than or equal to 0.55. The predicted vortex position at the angles and Mach numbers when vortex shedding occurs is, however, not unreasonable compared to the CFD flow field and the position can be used when no other information are available.

Given that the method is a single concentrated model and that the method does not model the complex nature of the lee side flow and the contribution of the secondary vortex to the flow development, the ability of the method to predict the position of the vortex and the loads is remarkable.

The FVM method is similar to Sigal's "Unified Crossflow Concept" for predicting the loads, but utilises a 2D unsteady potential method rather than Allen's heuristic method, and therefore has the ability to predict the vortex positions, whereas the Unified Crossflow Concept is unable to do so and represents a method that provides more information than just the normal force and centre-of-pressure. The FVM method has the advantage of speed when compared to the DVM method that requires boundary layer separation simulation in order to accurately predict the loads and vortex positions. The method provides this speed advantage whilst providing accuracy levels for the normal force of within 10%, and therefore makes it imminently suitable for engineering level application.

The method is currently only applicable in the '+' orientation. An extension of the method to non-zero roll angles is recommended. No 2D cross flow data are currently available, especially for transonic speeds for cruciform wing-body configurations with very low aspect ratio wings so that the method can be validated for these orientations.

Finally, the method has been developed for bodies with constant diameter. The theoretical foundations for the method does, however, not limit its applicability to constants diameter bodies and the method can be extended to cone-strake configurations through the introduction of a term to account for the change in body diameter. This is recommended and its applicability for this configuration class tested.

7.6 Further Applications

Up to this point the FVM method presented has been applied to the configuration under consideration. A test of the applicability of this method is assessed in its application to other configurations and Mach numbers. The other configurations available are four public domain cases and a CFD simulation. The CFD case is a Mach 1.5 simulation of the configuration used in this thesis. The reason for not including the Mach 1.5 comparative data in the method development of this and previous chapters is the unvalidated nature of the data. The simulations were, however, performed with the same geometry and CFD mesh used for the Mach 2.0, 2.5 and 3.0 simulations, so some confidence in the predictions do exist, though strictly speaking no validation has been performed.

The ability to assess the performance of the free vortex method is limited by the few publically available tests for body-strake configurations [18]. From the available public domain cases only three are strictly applicable for body-strake configuration and speed range under consideration. The last case has been included even though it only has data for Mach numbers in the transonic and subsonic speed range (0.6, 0.9 and 1.2).

Other configurations have been excluded because the configurations either include tail fins or the strakes have a high sweep back angle and do not have any appreciable side edges i.e. taper ratio is approximately zero or less than 0.3.

7.6.1 Case : Mach 1.5

The Mach 1.5 case compares the FVM predictions with the CFD simulations for Mach 1.5 for the same configuration as in Chapter 4. The normal force and centre-of-pressures are compared in Figure 7.24. The same trend in the centre-of-pressure is predicted by both the CFD simulations and FVM method, with the differences therefore being the same as in the previous section. The normal force prediction is excellent throughout the angle of attack range.

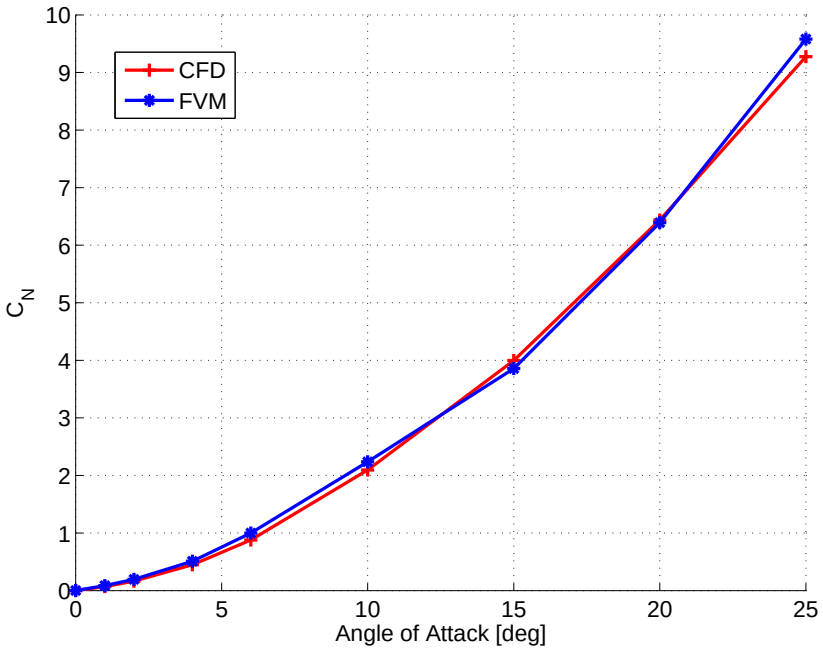

(a) Normal force

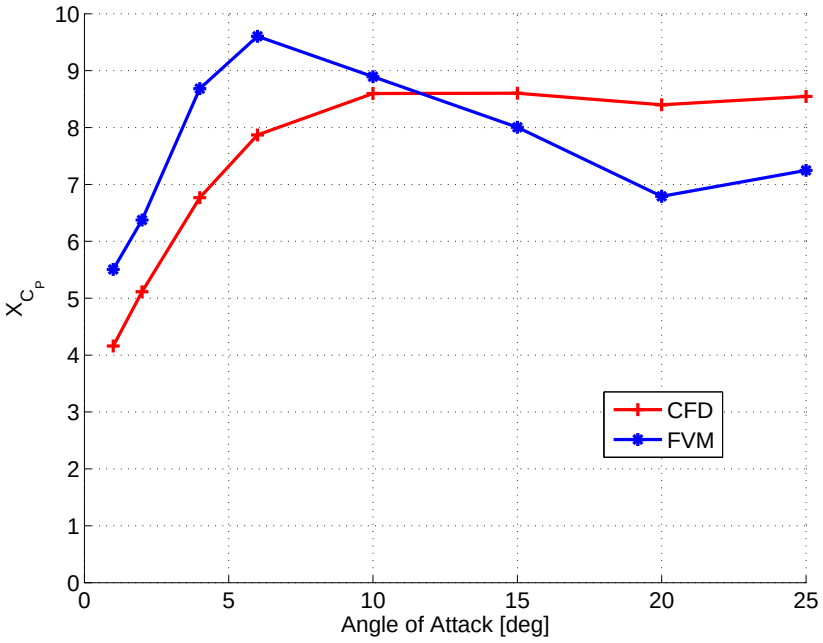

(b) Centre-of-pressure

Figure 7.24: CFD and FVM normal force and centre-of-pressure comparison for Mach 1.5

Because the data for the case was generated using CFD, flow field data exists, which allows the vortex positions to be compared. Very little difference between the Mach 1.5 and 2.0 simulations are present. A comparison of the vortex positions for 4° and 20° are presented in Figure 7.29 to Figure 7.25. It should be noted that the predictions up to 10° are the same as in the previous section because the cross flow Mach numbers remain low with no discernable change in results. The position of the vortex does have a Mach dependency (as predicted by the CFD) as already seen in the previous section and the correlation of the vertical vortex position is marginally poorer at the lower angles than for the Mach 2.0 predictions because the Mach 1.5 positions are predicted marginally lower than the Mach 2.0 positions. No significant difference in the lateral positions are present. As for the Mach 2.0 case, the CFD centre-of-pressure shows a small forward movement at the moderate angles of attack, and similarly for the free vortex method, the centre-of-pressure prediction is only reasonable for an engineering method.

Confirming the incompressible nature of the code is the prediction at 20°, where vortex shedding has just not started to occur yet (at Mach 1.5 the cross flow Mach number is 0.51). The CFD simulations indicate that the body and strake vortex coalesce into one vortex and its position is very well predicted by the FVM method. The LSWT predictions are also included to demonstrate the good correlation. The 25° prediction have not been presented because vortex shedding occurs in the CFD simulations which is consistent with the trends already presented.

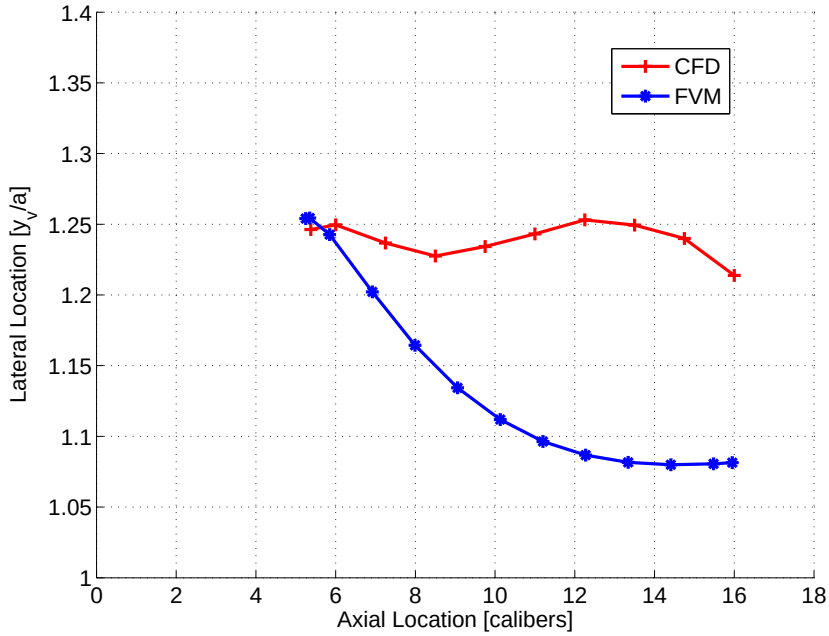

(a) Lateral

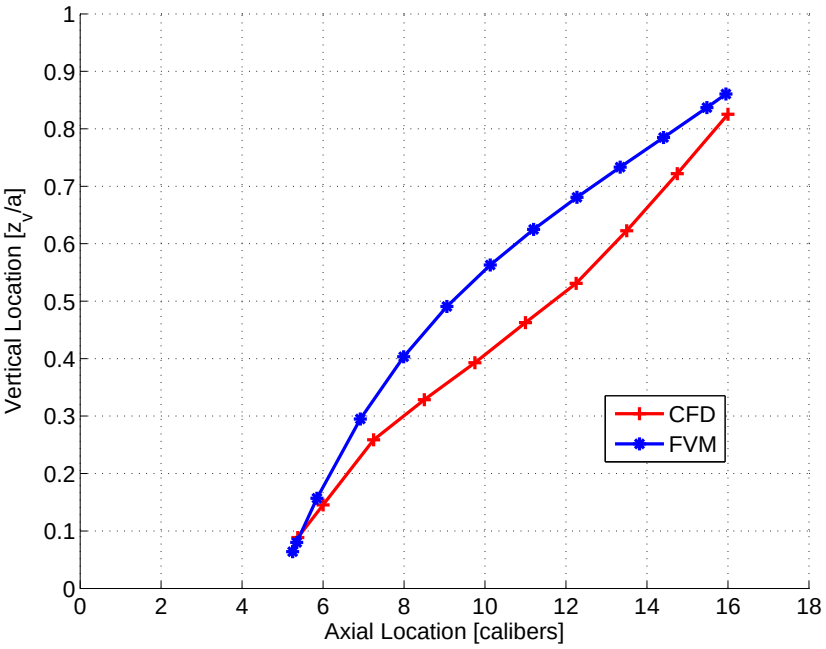

(b) Vertical

Figure 7.25: CFD and FVM concentrated vortex positions at $\alpha = 4°$ for Mach 1.5

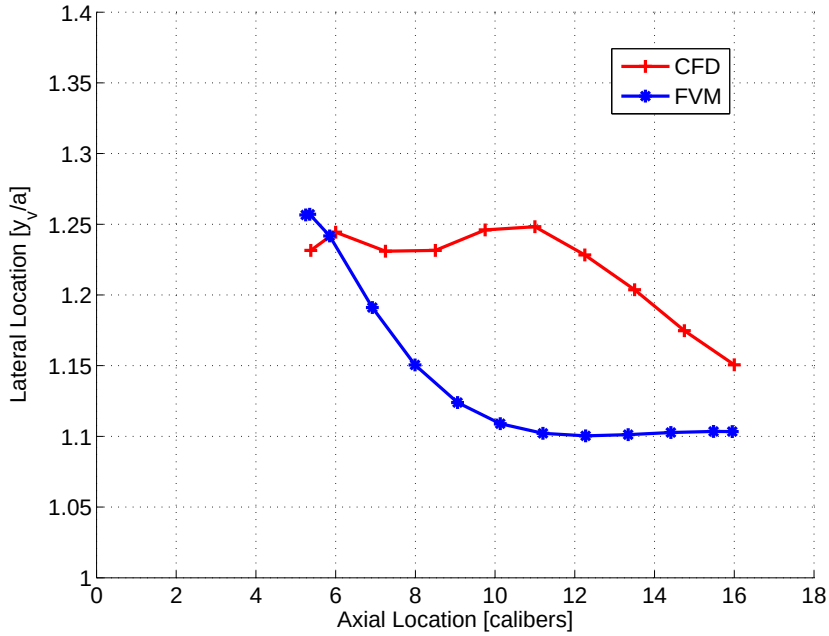

(a) Lateral

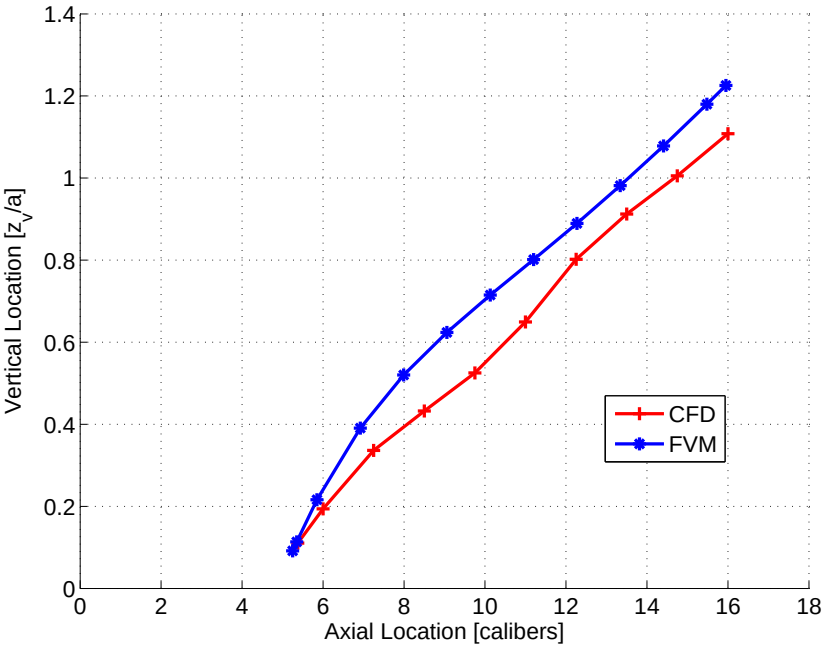

(b) Vertical

Figure 7.26: CFD and FVM concentrated vortex positions at $\alpha = 6°$ for Mach 1.5

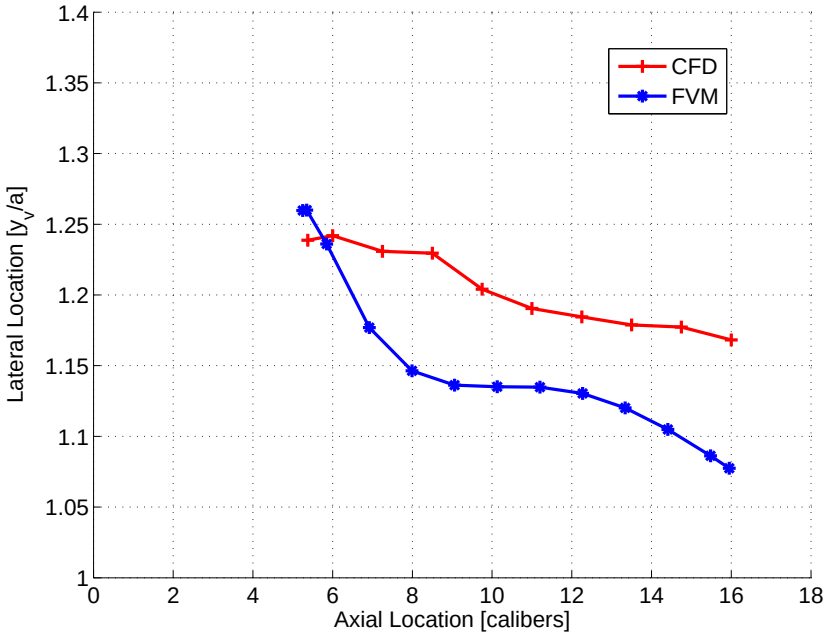

(a) Lateral

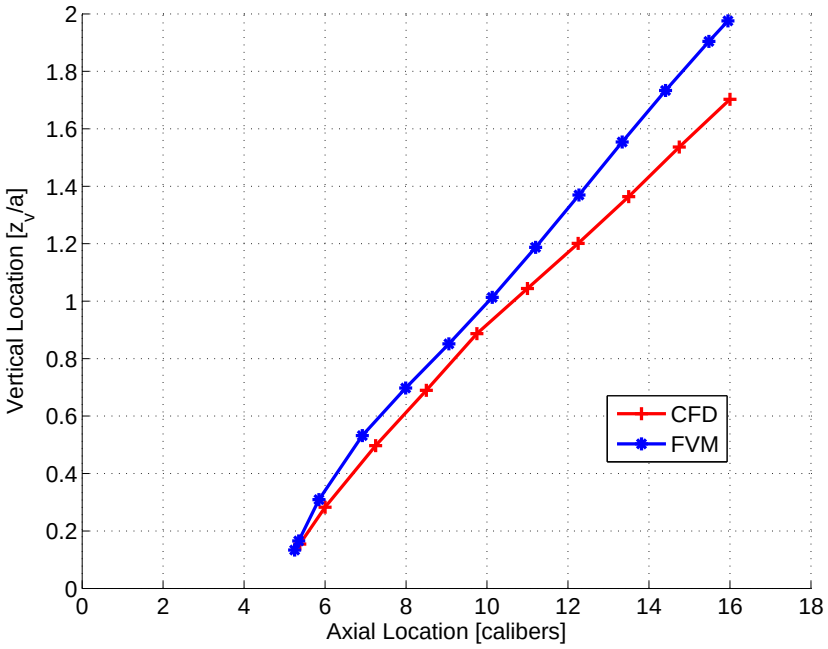

(b) Vertical

Figure 7.27: CFD and FVM concentrated vortex positions at $\alpha = 10°$ for Mach 1.5

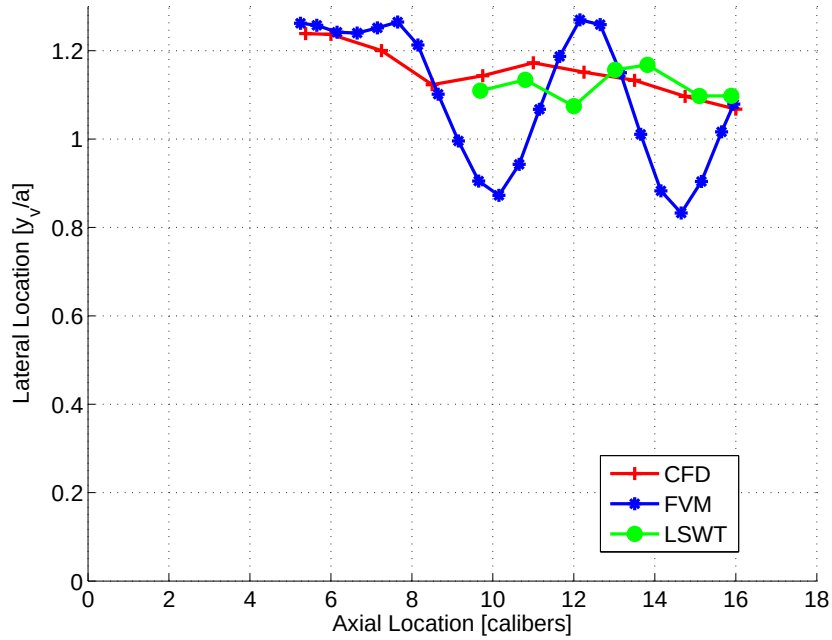

(a) Lateral

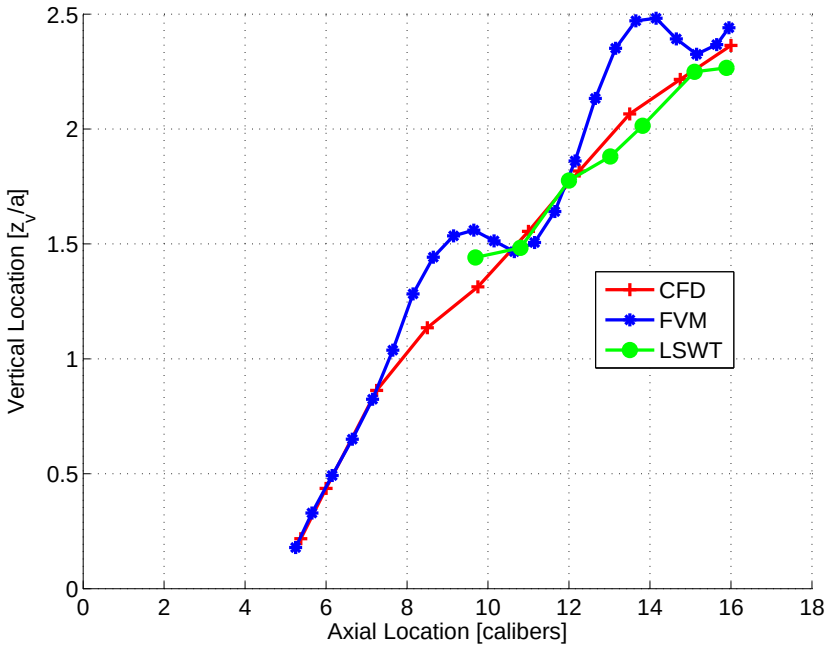

(b) Vertical

Figure 7.28: CFD and FVM concentrated vortex positions at $\alpha = 15°$ for Mach 1.5

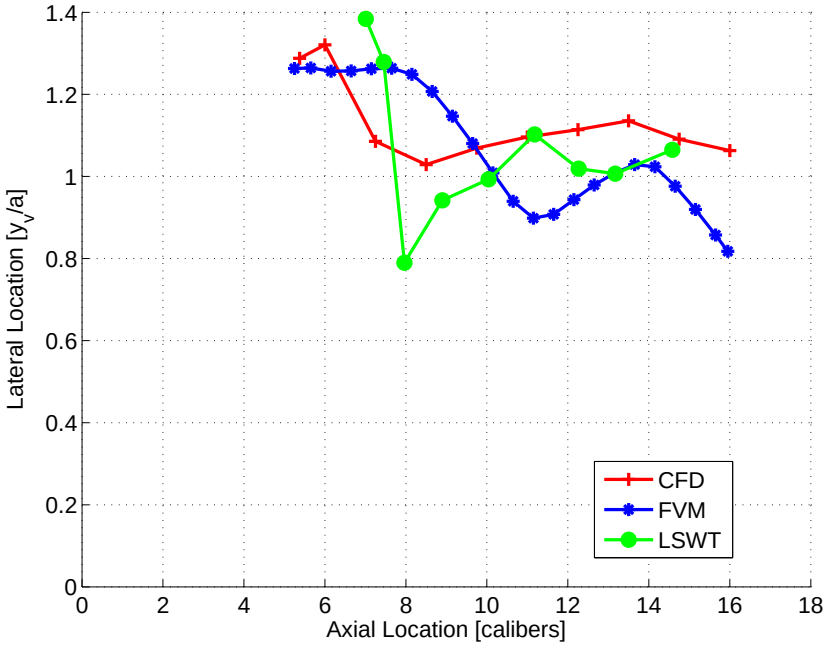

(a) Lateral

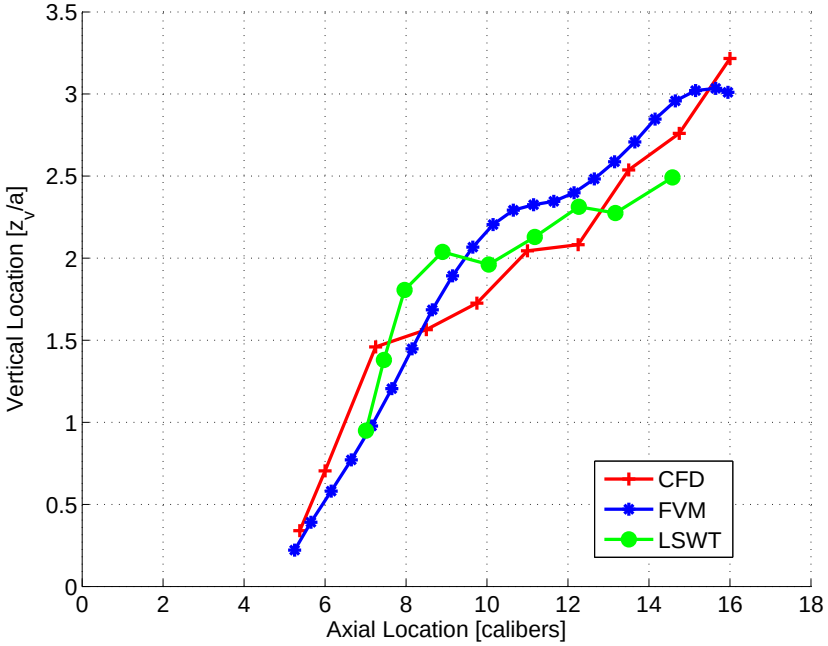

(b) Vertical

Figure 7.29: CFD and FVM concentrated vortex positions at $\alpha = 20°$ for Mach 1.5

7.6.2 Case : NASA TM-X-3130

The configuration of this test case of reference [158] is a planar wing-body configuration with a 3D tangent ogive nose and 7D strake-wing body section resulting in a 10D overall length, and no aftbody. The two available supersonic Mach numbers are 1.5 and 2.0. The configuration has a wing of aspect ratio of 0.0286, a span to body diameter ratio of 1.2. The configuration is shown in Figure 7.30.

The available data consists of five angles of attack (nominally 8°, 12°, 16°, 20°and 24°) for angles of attack less than 25°. The data have been digitised from the source documents, so errors exist when the comparisons are made. The normal force and centre-of-pressure errors have been estimated to be no more than 0.5 and 0.25 of a caliber respectively. Also the configuration used is a planar wing-body configuration rather than a cruciform wing-body configuration. Because of the very low strake span to body diameter ratio, no significant difference between the planar and cruciform configuration is expected.

The advantage of this particular case is that the nose vortices are of lower strength than for even the configuration used in Chapter 4. At angles above 10° vortices exist at the axial location where the strakes begin. Estimation of the vortex strengths and positions were determined from the CFD simulations in the same manner as that for the thesis configuration.

The normal force and centre-of-pressures are compared in Figure 7.31. The FVM method overpredicts the normal forces by up to 12% for Mach 1.5 and 15% for Mach 2.0. Whilst the differences are larger than the desired 10% limit they are still within that specified for engineering methods (see Table 2.2), and certainly within the digitisation accuracy. The centre-of-pressure position is predicted reasonably well given the limitations of the method.

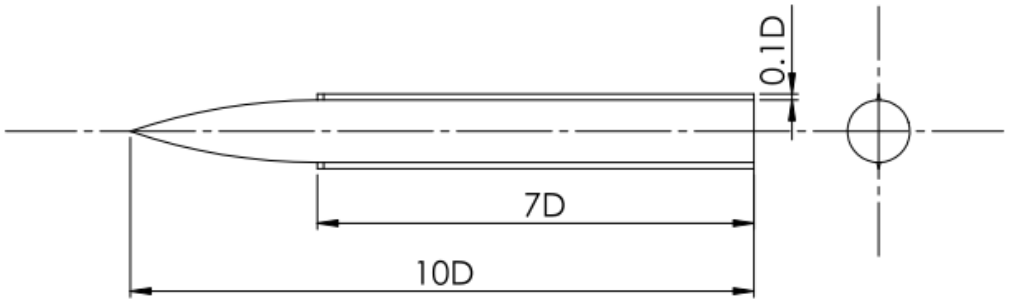

Figure 7.30: NASA TM-X-3130 model configuration

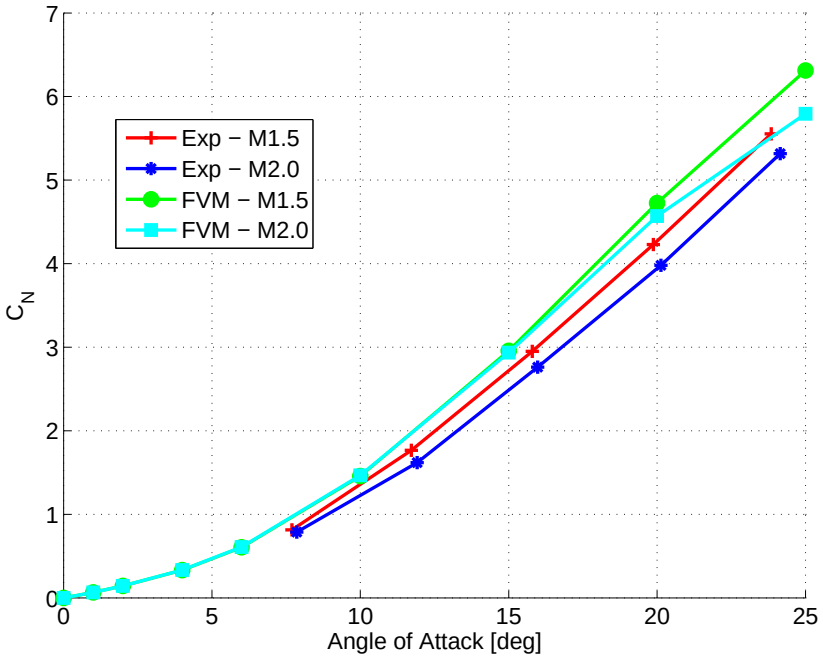

(a) Normal force

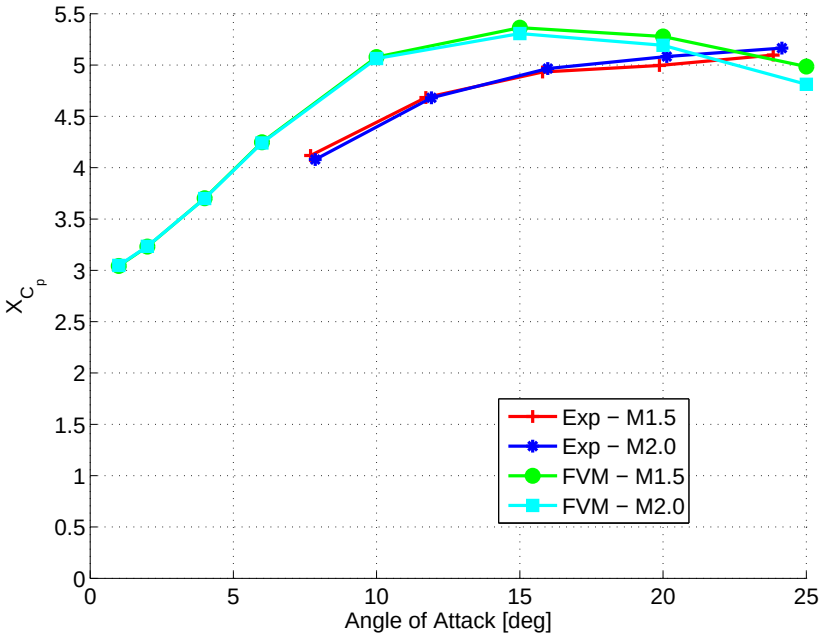

(b) Centre-of-pressure

Figure 7.31: CFD and FVM normal force and centre-of-pressure comparison for the NASA TM-X-3130 N1C1S configuration

7.6.3 Case : NASA TM-X-1839

The configuration of this test case of reference [105] is a 10D body with 3.5D nose and cruciform rectangular wings. The Mach numbers available for comparison purposes are 1.5, 1.9, 2.3 and 2.96. The Mach 2.96 condition was simulated as Mach 3.0. In contrast to the two previous cases, this model has a longer forebody and therefore greater strake vortex and body vortex interactions. Because no experimental or CFD data for the forebody or aftbody components exist, these have been estimated using the available engineering methods as defined in section 3.5. As for the previous configuration the experimental data have been digitised from the source documents. The configuration is shown in Figure 7.32. Whilst three different wings were experimentally tested only the small span wing is used because the aspect ratio is 0.0769 which can be considered very low and has a span to diameter ratio of 1.333. The next highest wing span aspect ratio is 0.154 (twice that of the smallest wing span) and is not considered very low aspect ratio. Finally, the proportion of the body length that the strakes occupy is only 43%.

The normal force and centre-of-pressure predictions are shown in Figure 7.33. The normal force prediction shows excellent correlation for the Mach numbers 1.5, 1.9 and 2.3. Unfortunately the Mach 3.0 FVM normal is overpredicted for angles of attack higher than 10°. The centre-of-pressure predictions are also good, with the experimental data showing considerable scatter at the low angles of attack because of the uncertainty associated with the discretisation of the graphs from paper.

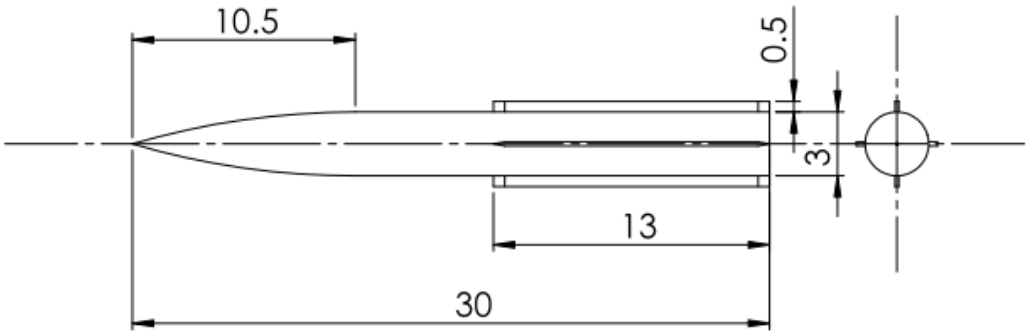

Figure 7.32: NASA TM-X-1839 model configuration, dimensions in inches

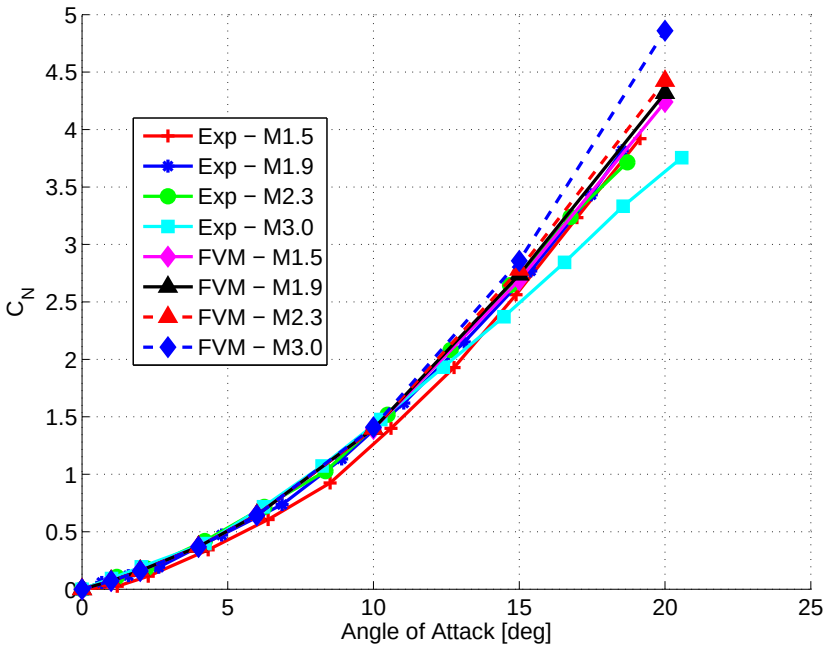

(a) Normal force

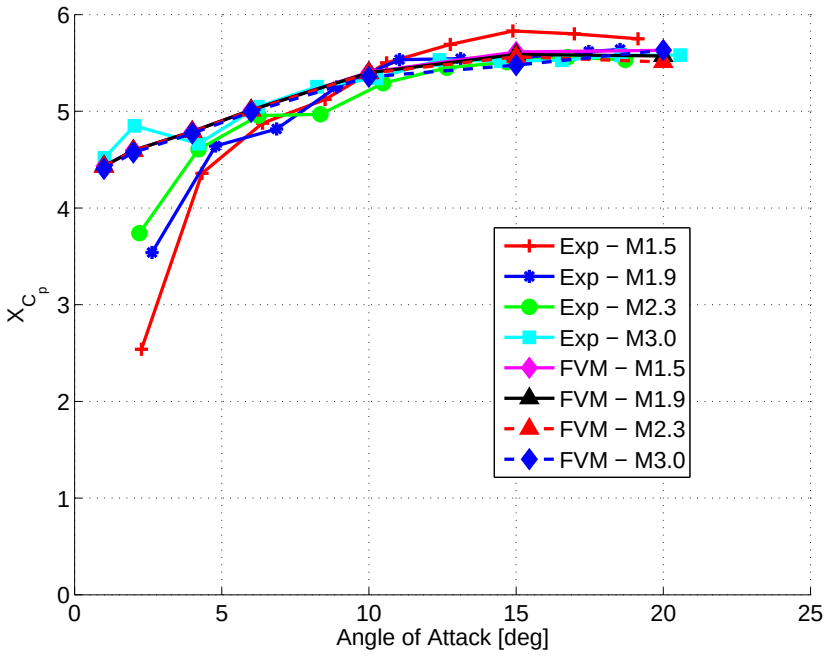

(b) Centre-of-pressure

Figure 7.33: CFD and FVM normal force and centre-of-pressure comparison for the NASA TM-X-1839 N1C1S configuration

7.6.4 Case : AIAA-2001-2410

The configuration of this test case of reference [13] was designated the B11AW22A3 configuration and was tested at a Mach 2.5. The configuration has a wing of aspect ratio of 0.067 and span to body diameter ratio of 1.6. The nose is 3D in length with a 3D aftbody. The strake has a 9.882D root chord and a taper ratio of 0.85, whilst the model had a 3.7" body diameter. As for the previous case, because no experimental or CFD data for the forebody or aftbody components exist, these have been estimated using the available engineering methods as defined in section 3.5. As for the previous configuration the experimental data have been digitised from the source documents. The configuration is shown in Figure 7.34.

The normal force and centre-of-pressure predictions are shown in Figure 7.35. The normal force prediction is very good except for the higher angles of attack where the FVM predictions are lower then the experimental data, though by less than 5%. The centre-of-pressure prediction demonstrates the same characteristics as previously observed, and is consistent with the limitations of the method.

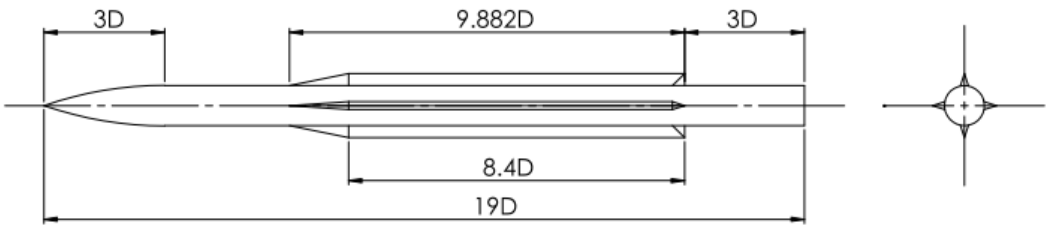

Figure 7.34: Simpson and Birch B11AW22A3 model configuration

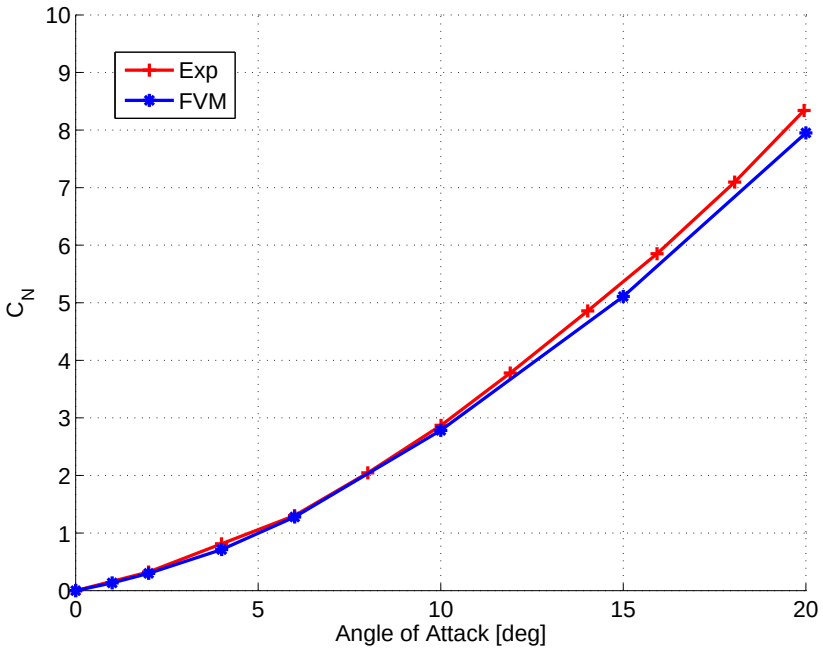

(a) Normal force

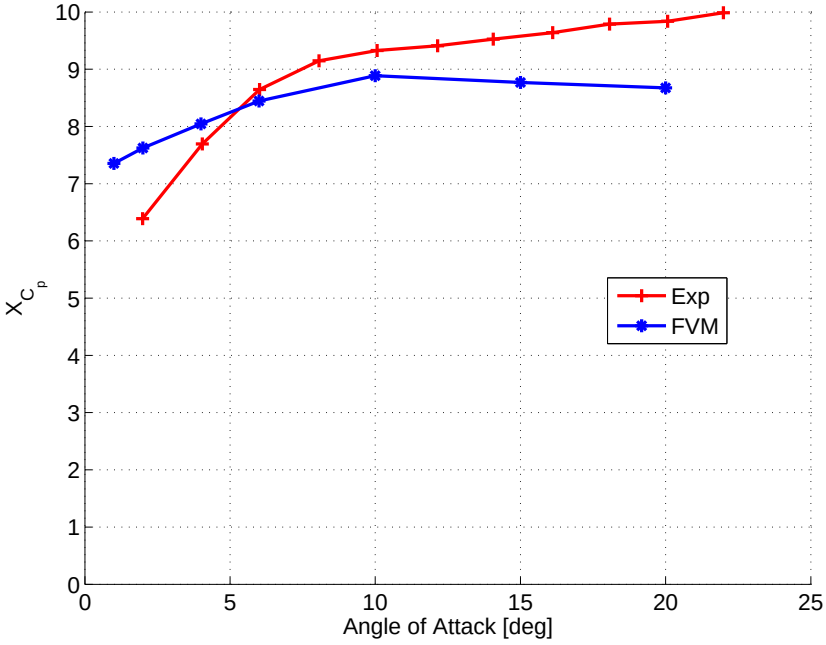

(b) Centre-of-pressure

Figure 7.35: CFD and FVM normal force and centre-of-pressure comparison for the W22 configuration

7.6.5 Case : NASA TM-2005-213541

The configuration in this case is a generic configuration supposedly representing the USA standard missile [104]. The data available for this model is only at Mach 0.6, 0.9 and 1.18 for the body-strake configuration. Comparisons are made against the Mach numbers 0.9 and 1.18 even though they are outside the range developed in this thesis (not supersonic, but transonic and subsonic). No Mach 0.6 simulations were performed because of the limitations in the body vortex prediction database of [41]. Whilst the span to body diameter ratio is 1.745, the wing aspect ratio is 0.144, which is higher than what would be considered a very low aspect ratio wing. The configuration is shown in 7.36. The data for this configuration was obtained from source with no digitisation errors.

The normal force and centre-of-pressure predictions are shown in Figure 7.37. As for the Simpson and Birch B11AW22A3 configuration the normal force is slightly underpredicted at the higher angles of attack. The centre-of-pressure is predicted further forward than the experimental data and is consistent with the current limitations of the method.

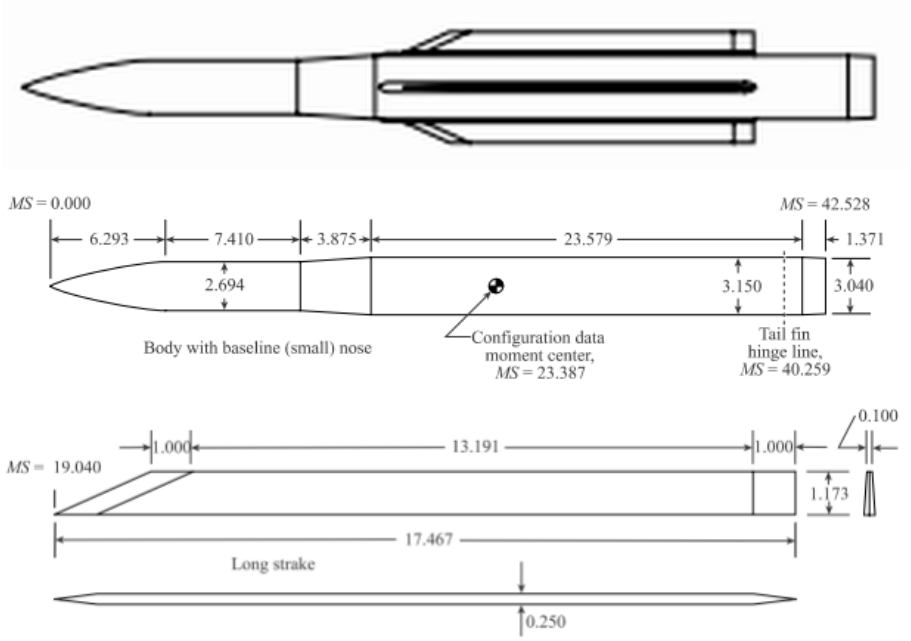

Figure 7.36: NASA TM-2005-213541 Triservice model configuration, dimensions in inches

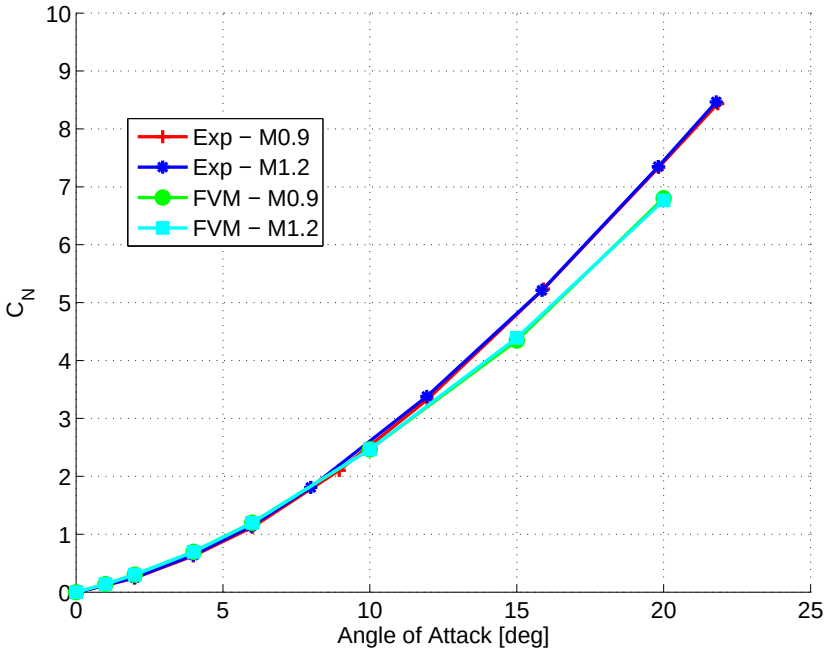

(a) Normal force

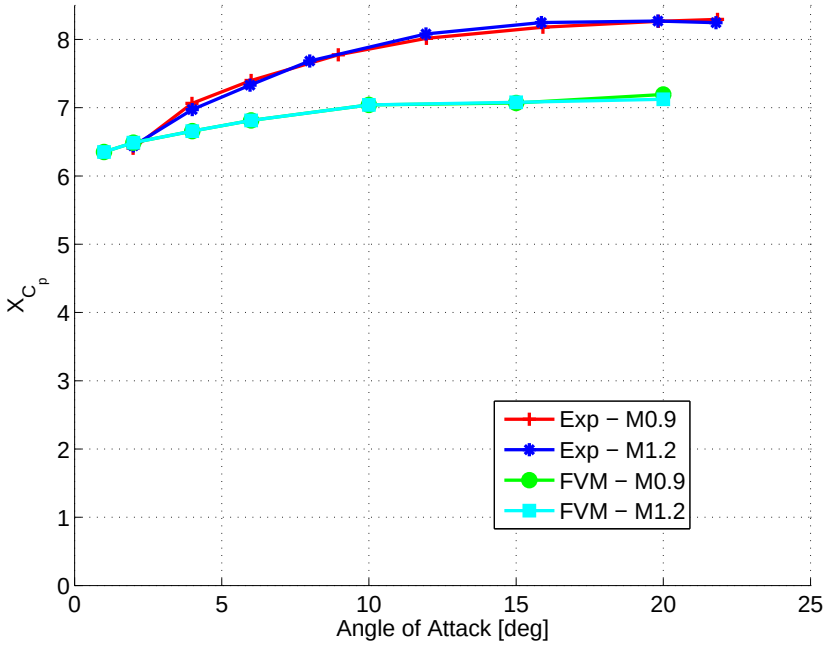

(b) Centre-of-pressure

Figure 7.37: CFD and FVM normal force and centre-of-pressure comparison for the NASA TM-2005-213541 Triservice configuration

7.6.6 Discussion

From the comparisons for the 5 cases presented, it can be seen that the free vortex method predicts the normal force very well for angles of attack up to 10° for all Mach numbers considered, even subsonic and transonic conditions. This applies even for the planar wing body configurations. The method tends to under predict the loads at the higher angles of attack i.e. $\geq 15°$, though the errors are less than 10%. The loads are, however, over predicted for the NASA TM-X-3130 case and excellent for the NASA TM-X-1839 case. Only two cases show poorer results, namely the TM-X-3130 Mach 2.0 and TM-X-1839 Mach 3.0 cases. The normal force predictions for Mach 1.5 show excellent correlation throughout the angle of attack range indicating its particular suitability at the low supersonic Mach numbers. The Triservice case demonstrates the applicability of the method to even high transonic speeds, high span to body diameter ratios approaching 2 and aspect ratios over 0.1.

The method, as for the SCV and DVM methods, is an incompressible method with some Mach dependency which manifests itself in the sectional drag coefficient. The method is good at low supersonic Mach numbers and is limited in its vortex position predictions by the vortex shedding due to supersonic reverse flow in the lee side of the configuration. At the higher angles where supersonic flow in the lee side is present, the position predicted by the method is better than that of the SCV method and can be used, though with caution.

The ability of the method to predict wing-body interactions, not only for global loads but the position of the concentrated vortex helps to improve the quality of overall missile loads and in particular the influence of the shed side edge strake vortex on downstream lifting surfaces and its consequential effect on the overall pitching moment (or centre-of-pressure).

Chapter 8

Conclusions and Recommendations

The following conclusions can be drawn:-

1. The lee side flow over a circular body with a wing of very low aspect ratio exhibits flow structures that at low angle of attack resemble the summation of the body and the wing, but at higher angles resembles that of the isolated body rather than a summation of the body and wing

2. The secondary vortex present in the body wing junction modifies the side edge and consequently the position of the side edge vortex and its interaction with the body vortex. The side edge vortex behaves more as a Lagrangian fluid particle along the body length rather than being constrained to impose the Joukowski-Kutta on the side edge.

3. Vortex shedding occurs for the lee side vortex when both the reverse flow region and the region outside the side edge vortex sheet are supersonic in the cross flow plane. The terminating normal shocks for both these regions triggers the vortex shedding.

4. The FVM method, utilising the SCV method to start the time stepping process, is a suitable engineering method that not only predicts the global normal force and centre-of-pressures but also the position of the rolled up side edge vortex sheet

5. The FVM should ideally be used in combination with the SCV method when vortex position predictions are important at low angles of attack (i.e. $< 4^{\circ}$)

8.1 Recommendations

1. Additional tests should be performed for non-zero roll angles ($0^{\circ} < \phi_x < 90^{\circ}$), to extend the database of Macha [107] on cruciform strake configurations for varying

strake span to diamater ratios. Following this, the FVM method can be tested with these data

2. Conduct 2D low speed tests to study the impulsively started vortex behaviour of cruciform strake configurations for the roll range of 0° to 90°.
3. Refine the centre-of-pressure prediction
4. Extend the FVM method to include symmetric vortex shedding
5. Assess the applicability of the FVM method to subsonic Mach numbers
6. Extend and assess the applicability of the FVM method to cone-strake configurations

Chapter 9

Contributions to the Field

The following contributions have been made to the field of applied engineering level aerodynamics for the circular body and cruciform strake configuration under consideration:

1. Modeling of a circular body and cruciform strake configurations using 2D potential methods with appropriate extensions for the cruciform configurations. These include:-

   (a) Modeling of a circular body and cruciform strake configuration using the discretised vortex method including lee side secondary (boundary layer) separation. Particular to this configuration is that the planform of strakes consist predominantly of a side edge rather than a leading edge.

   (b) Application of Bryson's single concentrated vortex model to the non-conical circular body and cruciform strake configuration

   (c) Application and extension of the free vortex trajectory method from cylinders to a circular body and cruciform strake configuration, and in particular, devising a method to start the solution

2. Identification of the conditions when symmetric vortex shedding occurs for circular bodies, strakes, and body and strake configurations

3. Identification of the significance of the lee side secondary separation on the development of, and positions/trajectories of the shed vortices

4. Development of an integrated engineering method for predicting normal force, centre-of-pressure and lee side vortex trajectories, and therefore the wing-to-body carryover factor

References

[1] Munk M.M. *The Aerodynamic Forces on Airship Hulls.* NACA Technical Report 184, 1924.

[2] Morikawa G. Supersonic Wing Body Lift. *Journal of the Aeronautical Sciences*, April 1951, pp. 217-228.

[3] Allen H.J. and Perkins E.W. *A Study of Effects of Viscosity on Flow over Slender Bodies of Revolution.* NACA Technical Reports 1048, 1951.

[4] Nielsen J.N. *Missile Aerodynamics.* Nielsen Engineering and Research, Inc, 1988.

[5] Allen H.J. *Estimation of the Forces and Moments Acting on Inclined Bodies of Revolution of High Fineness Ratio.* NACA-RM-A9I26, 1949.

[6] Jones R.T. *The Aerodynamic Forces on Slender Plane- and Cruciform-Wing and Body Combinations.* NACA Report 835, 1946.

[7] Pitts W.C, Nielsen J.N. and Kaattari G.E. *Lift and Center of Pressure of Wing-Body-Tail Combinations at Subsonic, Transonic and Supersonic Speeds.* NACA Rep. 1307, 1957.

[8] Vukelich S.R. and Williams J.E. Jr. Wing-Body Carryover at Supersonic Speeds with Finite Afterbodies. *AIAA Journal*, 19(5):661–664, May 1981.

[9] Vira N.R. and Fan D. Closed-Form Solutions of Supersonic Wing-Body Interference. *AIAA Journal*, pages 855–857, June 1982.

[10] Vira N.R. and Fan D. Supersonic Wing-Body Centre of Pressure with Finite Afterbodies. *AIAA Journal*, pages 1144–1146, August 1982.

[11] Hemsch M.J. and Nielsen J.N. Equivalent Angle-of-Attack Method for Estimating Nonlinear Aerodynamics of Missile Fins. *Journal of Spacecraft and Rockets*, pages 356–362, July-August 1983.

[12] Nelson H.F. and Bossi B.W. Aerodynamic Interference for Supersonic Low-Aspect-Ratio Missiles. *Journal of Spacecraft and Rockets*, 32(2):270–278, 1995.

[13] Simpson G.M. and Birch T.J. *Some Aerodynamic Characteristics of Missiles Having Very Low Aspect Ratio Wings.* AIAA 2001-2410, 2001.

[14] Hemsch M.J. and Nielsen J.N. *Tactical Missile Aerodynamics*, chapter Equivalent Angle-of-Attack Concept, pages 482–518. American Institue of Aeronautics and Astronautics, Inc, 1986.

[15] Froning H.D. Jr. *Aerodynamic Design of Slender Missiles for Bank-to-Turn Flight at High Angles of Attack.* AIAA 81-289, 1981.

[16] Moore F.G., McInville R.M. and Hymer T. The 1995 Version of the NSWC Aeroprediction Code: Part I - Summary of New Theoretical Methodology NSWCDD/TR-94/379, 1995.

[17] Rosema C., Underwood M. and Auman L. *Recent Fin Related Improvements for Missile DATCOM.* AIAA 2007-3937, 2007.

[18] Sigal A. and Blake W.B. Aerodynamic Analysis of Body-Strake Configurations AIAA 2007-3939. In *Collection of Technical Papers - AIAA Applied Aerodynamics Conference*, volume 1, pages 659–678, 2007.

[19] Sigal A. and Blake W.B. Comparative aerodynamic analysis of body-strake configurations AIAA 2010-4239. In *28th AIAA Applied Aerodynamics Conference*, 2010.

[20] Mendenhall M.R. and Nielsen J.N. *Effects of Symmetrical Vortex Shedding on the Longtudinal Aerodynamic Characteristics of Wing-Body-Tail Combinations.* NASA CR-2473, January 1975.

[21] Bollay W. A Non- Linear Wing Theory and Its Application to Rectangular Wings of Small Aspect Ratio. *Z. Angew. Math. Mech.*, (1):21–35, February 1939.

[22] Baker W.B. Jr. *Use of Semiempirical Aerodynamic methods for Preliminary Design.* NEAR Conference on Missile Aerodynamics, Oct. 31 - Nov. 2, 1988.

[23] Blake W.B. *Missile Datcom Applications to Projectiles.* AIAA 89-3370, 1989.

[24] Blake W.B. and Gillard W.J. Prediction of Vortex Interference on a Canard Controlled Missile. *Aerospace and Electronics Conference, 1988. NAECON 1988., Proceedings of the IEEE 1988 National*, Vol. 2:444–451, May 1988.

[25] Item 89008. *Royal Aeronautical Society, Engineering Sciences Data*, April 1989.

[26] Item 86009. *Royal Aeronautical Society, Engineering Sciences Data*, Jun. 1986.

[27] Item 83039. *Royal Aeronautical Society, Engineering Sciences Data*, Dec. 1983.

[28] Lesieutre D.J., Mendenhall M.R. and Dillenius M.F.E. *High Angle of Attack Missile Aerodynamics Including Rotational Rates.* AIAA 96-3392, Jul. 1996.

[29] Lesieutre D.J., Mendenhall M.R., Dillenius M.F.E. and Blair A.B. Jr. *Recent Applications and Improvements to the Engineering Level Aerodynamic Prediction Software MISL3.* AIAA 2002-0275, Jan. 2002.

[30] Denis P. *Le Code de Prevision Aerodynamique de l'ONERA : "MISSILE".* RTO AVT Symposium on "Missile Aerpdynamics", 11-14 May 1998.

[31] Jorgensen L.H. *Prediction of Static Aerodynamic Characteristics for Slender Bodies Alone and with Lifting Surfaces to Very High Angles of Attack.* NASA-TR-474, Sep 1977. Formerly issued as NASA-TM-X-73,123 with limited distribution.

[32] Lubard S.C. and Helliwell W.S. Calculation of the Flow on a Cone at High Angle of Attack. *AIAA Journal*, 12(7), July 1974.

[33] Levinsky E.S., Mei M.H.Y. and Su F.Y. *Nonconical Theory of Flow Past Slender Wing-Bodies with Leading-Edge Separation.* NASA CR-73446, October 1968.

[34] Nelson H.F. Wing-body Interference Lift for Supersonic Missiles with Elliptical Cross-Section Fuselages. *Journal of Spacecraft and Rockets*, 26(5):322–329, 1989.

[35] Jorgensen L.H. and Nelson E.R. *Experimental Aerodynamic Characteristics for Bodies of Elliptic Cross Section at Angles of Attack from* 0 deg *to* 58 deg *and Mach Numbers from 0.6 to 2.0.* NASA-TM-X-3129, Feb. 1975.

[36] Lin T.C. and Rubin S.G. Viscous Flow Over a Cone at Incidence, Part 2: Boundary Layer. *Journal of Fluid Mechanics*, 1:593–620, July 1975.

[37] Mendenhall M.R. and Perkins S.C. Jr. *Tactical Missile Aerodynamics*, chapter Vortex Cloud Model for Body Vortex Shedding and Tracking, pages 519–571. American Institue of Aeronautics and Astronautics, Inc, 1986.

[38] Pittman J.L., Miller D.S. and Siclari M.J. *Tactical Missile Aerodynamics*, chapter Supersonic Full-potential Method Applied to Missile Bodies, pages 632–668. American Institue of Aeronautics and Astronautics, Inc, 1986.

[39] Thomson K.D. and Morrison D.F. The spacing, position and strength of vortices in the wake of slender cylindrical bodies at large incidence. *Journal of Fluid Mechanics*, 50(4):751–783, 1971.

[40] Hemsch M.J., Nielsen J.N. and Dillenius M.F.E. *Method for Calcualting Induced Rolling Moments for Cruciform Canard Missiles at Angles of Attack up to 20Deg.* NWC-TP-5761, 1975.

[41] Nielsen J.N., Hemsch M.J. and Smith C.A. *A Preliminary Method for Calculating the Aerodynamic Characteristics of Cruciform Missiles to High Angles of Attack Including Effects of Roll and Control Deflection.* Office of Naval Research CR215-226-4F, Nov. 1977.

[42] Jorgensen L.H. *Prediction of Static Aerodynamic Characteristics for Space-Shuttle-Like, and Other Bodies at Anglews of Attack from* 0° *to* 180°. NASA-TN-D-6996, 1973.

[43] Ericcson L.E. and Reading J.P. *Tactical Missile Aerodynamics*, chapter Asymmetric Vortex Shedding from Bodies of Revolution, pages 243–298. American Institue of Aeronautics and Astronautics, Inc, 1986.

[44] Item 89014. *Royal Aeronautical Society, Engineering Sciences Data*, August 1989.

[45] Sarpkaya T. Separated Flow about Lifting Bodies and Impulsive Flow about Cylinders. *AIAA Journal*, (3):414, March 1966.

[46] Thomson K.D. Subsonic Wing-Body Interference for Missile Configurations at Large Angles of Attack. *Aeronautical Quarterly*, 28(pt 3):163–175, 1977.

[47] Van Dyke M.D. *A Study of Second Order Supersonic Flow.* NACA Report-1081, 1952.

[48] Van Dyke M.D. First- and Second Order Theory of Supersonic Flow Past Bodies of Revolution. *Jour. Aero. Sci.*, 18(3):161–179, March 1951.

[49] Ward G.N. Supersonic Flow Past Slender Pointed Bodies. *Quarterly J. Mech. and Appl. Math.*, page 94, 1949.

[50] Syvertson C.A. and Dennnis D.H. *A Second-Order Shock-Expansion Method Applicable to Bodies of Revolution Near Zero Lift.* NACA TN-3527, January 1956.

[51] Eggers A.J. Jr. and Savin R.C. *Approximate Methods for Calculating the Flow about Non-lifting Bodies of Revolution at Supersonic Speeds.* NACA TN-2579, December 1951.

[52] Rakich J.V. *A Method of Characteristics for Three-Dimensional Supersonic Flow with Application to Inclined Bodies of Revolution.* NASA TN-D-5341, October 1969.

[53] Jorgensen L.H. *Prediction of Static Aerodynamic Characteristics for Slender Bodies Alone and with Lifting Surfaces to Very High Angles of Attack.* NASA-TM-X-73,123, Sep 1977.

[54] Achenbach E. Influence of surface roughness on the cross-flow around a curcular cylinder. *Journal of Fluid Mechnaices*, pages 321–335, 1971.

[55] Fage A. and Warsap J.H. *The Effects of Turbulence and Surface Roughness on Drag of a Circular Cylinder.* Aeronuatical Research Committee, Reports and Memoranda No. 1283, October 1929.

[56] Bryson A.E. Symmetric Vortex Separation on Circular Cylinders and Cones. *Applied Mechanics*, 26:643–648, December 1959.

[57] Mello J.R. Investigation of Normal-Force Distributions and Wake Vortex Charactertistics of Bodies of Revolution at Supersonic Speeds. *Journal of Aeronautical Sciences*, (3):155–168, March 1959.

[58] Wardlaw A.B. *Prediction of Normal Force, Pitching Moment and Yawing Force on Bodies of Revolution at Angles of Attack up to 50 degrees using a Concentrated Vortex Flowfield Model.* NOLTR 73-209, October 1973.

[59] Fidler J.E. and Bateman M.C. *Asymmetric Vortex Effects on Missile Configurations.* AIAA 75-209, January 1975.

[60] Oberkampf W.L. Symmetric Body Vortex Wake Characteristics in Supersonic Flow. *AIAA Journal*, 18(11):1289–1297, November 1981.

[61] Angelucci S.B. A Multi-vortex Method for Axisymmetric Bodies at Angle of Attack. *Journal of Aircraft*, (12):959–966, December 1971.

[62] Marshall J.F. and Deffenbaugh F.D. *Separated Flow Over Bodies of Revolution Using An Unsteady Discrete-Vorticity Wake.* NASA CR-2414, June 1974.

[63] Mendenhall M.R. and Lesieutre D.J. *Predicted Voretx Shedding from Circular and Noncicular Bodies in Subsonic Flow.* NASA CR-4037, January 1987.

[64] Mendenhall M.R. Prediction of Vortex Shedding from Noncicular Bodies in Supersonic Flow. *Journal of Spacecraft and Rockets*, 18:385–392, Sept.-Oct. 1981.

[65] Mendenhall M.R. and Perkins S.C. Jr. *Predicted Vortex Shedding from Circular and Noncicular Bodies in Supersonic Flow.* NASA CR-3754, January 1984.

[66] Mostafa S.I.M. *Numerical Simulation of Unsteady Flows.* Ph.D. Dissertation, Naval Postgraduate School, ADA184132-3, June 1987.

[67] Siclari M.J. and Visich M. *Shock Fitting in Conical Supersonic Full-Potential Flows with Entropy Effects.* AIAA 84-0261, January 1984.

[68] Rakich J.V. and Lubard S.C. *Numerical Computation of Viscous Flows on the Lee Side of Blunt Shapes Flying at Supersonic Speeds*, Jan. 1975.

[69] Stahl W.H. *Aerodynamics of Low Aspect Ratio Wings.* AGARD LS-98, 1979.

[70] Szodruch J.G. and Peake D.J. *Leeward Flow Over Delta Wings at Supersonic Speeds.* NASA-TM-81187, April 1980.

[71] Stanbrook A. and Squire L.C. Possible Types of Flow at Swept Leading Edges. *Aeronautical Quartely*, XV:72–82, 1964.

[72] Stallings R.L. Jr. *Tactical Missile Aerodynamics*, chapter Low Aspect Ratio Wings at High Angles of Attack, pages 89–128. American Institue of Aeronautics and Astronautics, Inc, 1986.

[73] Stallings R.L. Jr. and Lamb M. *Wing-Alone Aerodynamic Characteristics for High Angles of Attack at Supersonic Speeds.* NASA-TP-1889, July 1981.

[74] Winter H. Stromungsvorgange an Platten und profilierten Korpern bei kleinen Spannenweiten, or Flow Phenomena on Plates and Airfoils of Short Span. *Forch. Ing-Wes.*, 6:40–50, 67–71, July 1935, also NACA Report 798.

[75] Sack A.H., Lundberg R.E. and Hanson C.W. *A Theoretical Investigation of the Aerodynamics of Slender Wing-Body Combinations Exhibiting Leading Edge Separation.* NASA CR-719, March 1967.

[76] Wickens R.H. *The Vortex Wake and Aerodynamic Load Distribution of Slender Rectangular Plates; The Effects of a 20-degree Bend at Mid-chord.* NAE-LR-458, 1966.

[77] Peake D.J. and Tobak M. *Three Dimensional Interactions and Vortical Flows with Emphasis on High Speeds.* NASA TM-81169, March 1980.

[78] Sarpkaya T. Inviscid Model of Two-Dimensional Vortex Shedding for Transient and Asymtptotically Steady Separated Flow Over an Inclined Plate. *Journal of Fluid Mechanics*, 68(pt 1):109–128, 1975.

[79] Legendre R. *Ecoulement Au Voisinage De La Ponte Avant D'Une Aile A Forte Fleche Aux Incidences Moyennes.* La Recherche Aeronautique Bulletin Bimestriel, No. 30, Nov-Dec 1952.

[80] Adams Mac C. Leading-Edge Separation from Delta Wings at Supersonic Speeds. *Journal of the Aeronautical Sciences*, 20:430, June 1953.

[81] Brown C.E. and Michael W.H. Jr. *On Slender Delta Wings with Leading Edge Separation.* NACA TN-3430, April 1955.

[82] Edwards R.H. Leading Edge Separation from Delta Wings. *Journal of the Aeronautical Sciences*, 21:134–135, November 1954.

[83] Pershing B. *Separated Flow Past Slender Delta Wings with Secondary Vortex Simulation.* TDR-269(4560-10)-4, August 1964.

[84] Scholz N. Kraft- und Druckverteilungsmessungen an Tragflachen kleiner Streckung. *Forch. Ing-Wes.*, 16:85–91, July 1949, also Journal of the Aeronautical Sciences, Vol 16, pp 637-638, 1949.

[85] Gersten K. Nichtlineare Tragflachentheorie fur Rechteckflugel bei inkompressibler Stromung. *Z. Flugwiss*, pages 276–280, 1957.

[86] Schlichting H. *Airfoil Theory at Supersonic Speed.* NACA TM-897, 1939.

[87] Gersten K. A Non-linear Lifting Surface Theory Especially for Low Aspect Ratio Wings. *AIAA Journal*, pages 924–925, 1963.

[88] Berlotserkovskiy S.M. *Calculation of the Flow Around Wings of Arbitrary Planforms in a Wide Range of Angles of Attack.* NASA-TT-F12291, 1969.

[89] Yermolenko S.D. *Nonlinear Theory of Small Aspect Ratio Wings.* Soviet Aeron. Vol. 9, 1966, pp. 5-11, NASA-TT-F10915, 1967.

[90] Polhamus E.C. *A Concept of the Vortex Lift of Sharp-Edge Delta Wings Based on a Leading-Edge-Suction Analogy.* NASA TN D-3767, 1966.

[91] Polhamus E.C. Predictions of Vortex-Lift Characteristics by a Leading-Edge Suction Analogy. *Journal of Aircraft*, 8(4):193–199, April 1971.

[92] Polhamus E.C. *Charts for Predicting the Subsonic Vortex-List Characteristics of Arrow, Delta, and Diamond Wings.* NASA TN D-6243, 1971.

[93] Lamar J.E. *A Modified Multhopp Approach for Predicting Lifting Pressures and Camber Shape for Composite Planforms in Subsonic Flow.* NASA TN D-4427, 1968.

[94] Lamar J.E. *Extention of Leading-Edge-Suction Analogy to Wings With Separated Flow Around the Side Edges at Subsonic Speeds.* NASA TR R-428, 1974.

[95] Lamar J.E. Prediction of Vortex Flow Characteristics of Wings at Subsonic and Supersonic Speeds. *Journal of Aircraft*, 13(7):490–494, July 1976.

[96] Moore F.G. and McInville R.M. Calculation of Wing-Alone Aerodynamics to High Angles of Attack. *Journal of Spacecraft and Rockets*, 32(1):187–190, 1995.

[97] White J.T. *A Method for Predicting Combined Dorsal Normal Force and Center-of-Pressure Location at Supersonic Mach Numbers.* AIAA 94-3466, 1994.

[98] Sigal A. *Aerodynamic Analysis of Body Strake Configurations.* AFRL Research Report, June 2006.

[99] Moore F.G., McInville R.M. and Hymer T. Aeroprediction Code for Angles of Attack Above 30 Degrees. *Journal of Spacecraft and Rockets*, 33(3):366–373, 1996.

[100] Moore F.G. and McInville R.M. and Hymer T. *An Improved Semiempirical Method for Calculating Aerodynamics of Missiles with Noncircular Bodies.* NSWCDD/TR-97/20, September 1997.

[101] Moore F.G. and McInville R.M. New Semiempirical Model for Wing-Tail Interference. *Journal of Spacecraft and Rockets*, 34(1):48–53, 1997.

[102] Jorgensen L.H. and Nelson E.R. *Experimental Aerodynamic Characteristics for A Cylindrical Body of Revolution with Various Noses at Angles of Attack from* 0 deg *to* 58 deg *and Mach Numbers from 0.6 to 2.0.* NASA-TM-X-3128, Dec. 1974.

[103] Jorgensen L.H. and Nelson E.R. *Experimental Aerodynamic Characteristics of a Cylindrical Body of Revolution with Side Strakes and Various Noses at Angles of Attack from 0 degrees to 58 degrees and Mach Numbers 0.6 to 2.0.* NASA TM-X-3130, March 1975.

[104] Allen J. *The Tri-Service Missile Database.* NASA TM 2002-211632, 2002.

[105] Spearman M.L. and Trescot C.D. *Effects of Wing Planform on the Static Aerodynamics of a Cruciform Wing-Body Missile for Mach Numbers up to 4.63.* NASA-TM-X-1839, July 1969.

[106] Robinson R.B. *Aerodynamic Characteristics of Missile Configurations with Wings of Low Aspect Ratio for Various Combinations of Forebodies, Afterbodies, and Nose Shapes for Combined Angles of Attack at Mach Number 2.01.* NACA RM L57D19, June 1957.

[107] Macha J.M. *A Wind Tunnel Investigation of Circular and Straked Cylinders in Transonic Cross Flow.* TAMU Rep. 3318-76-01, November 1976.

[108] Hirsch C. *Numerical Computation of Internal and External Flows.* John Wiley and Sons, 2001.

[109] Spearman M.L. and Robinson R.B. *Longitudinal Stability Characteristics at Mach Numbers 2.01, 4.65, and 6.8 of Two Hypersonic Missile Configurations.* NASA TM X-46, 1959.

[110] Jorgensen L.H. *Elliptic Cones Alone and With Wings at Supersonic Speeds.* NACA Report 1376, March 1963.

[111] Jeane J.R. *Missile Body Vortices and their Interaction with Lifting Surfaces.* AGARD Lecture Series No.121, 1982.

[112] Werle H. *Tourbillons de Corps Fuseles aux Incidences Elevees.* ONERA Note Tech., No. 175, 1971.

[113] Wardlaw A.B. *High-Angle-of-Attack Missile Aerodynamics.* AGARD LS-98, 1979.

[114] Nielsen J.N. *Quasi-cylindrical Theory of Wing-Body Interference at Supersonic Speeds and Comparison with Experiment.* NACA TR-1252, 1956.

[115] Nielsen J.N. and Pitts W.C. *Wing-Body Interference at Supersonic Speeds With an Application to Combinations with Rectangular Wings.* NACA-TN-2677, 1952.

[116] Browne S.H., Friedman L. and Hodes I. A Wing-Body Problem in a Supersonic Conical Flow. *Jour. Aero. Sci.*, 15(8):443–452, 1948.

[117] Nielsen J.N. and Kaattari G.E. *Method for Estimating Lift Inteference of Wing-Body Combinations at Supersonic Speeds.* NACA RM A51J04, 1951.

[118] Spreiter J.R. *The Aerodynamic Forces on Slender Plane- and Cruciform-Wing and Body Combinations.* NACA TN-1662, July 1948.

[119] Spreiter J.R. *Aerodynamic Properties of Slender Wing-Body Combinations at Subsonic, Transonic, and Supersonic Speeds.* NACA Report 962, 1950.

[120] Surkova E.M. Problem of Supersonic Flow Past a Slender Pointed Body with Tail. *Mosc Univ Mech Bull*, 29(5-6):43–49, 1974.

[121] Ferrari C. Interference Between Wind and Body at Supersonic Speeds - Theory and Numerical Application. *Jour. Aero. Sci.*, 15(6):317–336, 1948.

[122] Flax A.H. and Lawrence H.R. *The Aerodynamics of Low-Aspect-Wings and Wing-Body Combinations.* Third Anglo-American Aeronautical Conference.

[123] Schneider C.P. and Nikolitsch D. *Normal Force and Pitching Moment of Wing-Body-Combinations in the Non-Linear Angle-of-Attack Range at Subsonic Speeds.* AGARD CP-247, pp. 17. 1-27. 1.

[124] Lamar J.E. and Luckring J.M. *Recent Theoretical Developments and Experimental Studies Pertinent to Vortex Flow Aerodynamics.* AGARD CP-247, 1989.

[125] Levinsky E.S. and Mei M.H.Y. *Nonlinear Lift and Pressure Distribution of Slender Conical Bodies with Strakes at Low Speeds.* NASA CR-1202, October 1968.

[126] Mangler K.W. and Smith J.H.B. A Theory of the Flow Past a Slender Delta Wing with Leading-Edge Separation. *Proc. Roy. Soc.*, 251:200–217, 1959.

[127] Mendenhall M.R. and Lesieutre D.J. *Prediction of Subsonic Vortex Shedding From Forebodies With Chines.* NASA CR-4323, September 1980.

[128] Rosenhead L. The Formation of Vortices from a Surface of Discontinuity. *Proceedings of the Royal Society of London. Series A, Containing Papers of a Mathematical and Physical Character*, 134(823):170–192, 1931.

[129] Westwater F.L. *Rolling Up of a Surface of Discontinuity behind an Airfoil of Finite Span.* A.R.C R&M, 1935.

[130] Oberkampf W.L. *Prediction of Forces and Moments on Finned Missiles in Subsonic Flow.* AIAA 79-0365, January 1979.

[131] Oberkampf W.L. and Nicolaides J.D. Aerodynamics of Finned Missiles at High Angle of Attack. *AIAA Journal*, 9(12):2378–2384, December 1971.

[132] Oberkampf W.L. Prediction of Roll Moments on Finned bodies in Supersonic Flow. *Journal of Spacecraft and Rockets*, 12(1):17–21, January 1975.

[133] Est B.E. and Nelson H.F. Wing Vertical Position Effects on Wing-Body Carryover for Noncircular Missiles. *Journal of Spacecraft and Rockets*, 31(6):999–1006, 1994.

[134] Est B.E. and Nelson H.F. Wing-body Carryover for Noncircular Missiles. *Journal of Spacecraft and Rockets*, 32(3):426–432, 1995.

[135] Martin J.C. *The Calculation of Downwash Behind Wings of Arbitrary Plan Form at Supersonic Speeds.* NACA-TN-2235, July 1950.

[136] Heaslet M.A. and Lomax H. *The Calculation of Downwash Behind Aupersonic Wings with Applciation to Triangular Plan Forms.* NACA-TN-1620, June 1948.

[137] Lomax H. and Sluder L. *Downwash in the Vertical and Horizontal Planes of Symmetry behind a Triangular Wing in Supersonic Flow.* NACA-TN-1803, 1949.

[138] Mirels H. and Haefeli R.C. *Line-Vortex theory for Calcualtion of Supersonic Downwash.* NACA-TN-1295, 1949.

[139] Sacks A.H. Vortex Interference Effects on the Aerodynamic of Slender Ariplanes and Missiles. *Jour. Aero. Sci.*, 24(6):393–402,412, June 1957.

[140] Spahr J.R. *Theoretical Prediction of the Effects of Vortex Flows on the Loading, Forces and Moments of Slender Aircraft.* NACA TR-R-101, 1961.

[141] Hemsch M.J., Smith C.A., Nielsen J.N. and Perkins S.C. Jr. *Calculation of Component Forces and Moments of Arbitrarily Banked Cruciform Missiles with Control Deflections.* ONR-CR215-226-3, November 1976.

[142] Alksne A.Y. *Determination of Vortex Paths by Series Expansion Technique With Application to Cruciform Wings.* NACA TR-1311.

[143] Spreiter J.R. and Sacks A.H. *A Theoretical Study of the Aerodynamics of Slender Cruciform-Wing Arrangements and Their Wakes.* NACA TN-3528, March 1956.

[144] Sacks A.H. *Aerodynamic Interference of Slender Wing Tail Combinations.* NACA-TN-3725, January 1956.

[145] Gur I., Shinar J. and Rom J. Prediction of Roll Controllability of Slender Cruciform Canard Configurations. *J Spacecraft and Rockets*, 16(4):238–244, 1979.

[146] =Mendenhall M.R. and Lesieutre D.J. *Predicted Voretx Shedding from Circular and Noncicular Bodies at High Angles of Attack.* AIAA 79-0026, January 1979.

[147] Sarpkaya T. Lift, Drag and Added-Mass Coefficients for a Circular Cylindeir Immersed in a Time Dependent Flow. *Journal of Applied Mechanics*, page 130, March 1963.

[148] Sacks A.H. *Vortex Interference on Slender Airplanes.* NACA TN-3525, November 1955.

[149] Sarpkaya T. *An Inviscid Model of Two-Dimensional Vortex Shedding for Transient and Asymptotically Steady Separated Flow Over a Cylinder.* AIAA-79-0281, January 1979.

[150] *ANSYS FLUENT V12.0 Theory Guide*, April 2009.

[151] AIAA S-071A-1999. *Assessment of Experimental Uncertainty With Application to Wind Tunnel Testing*, 1999.

[152] AIAA G-045-2003. *Assessing Experimental Uncertainty Supplement to AIAA S-071A-1999*, 2003.

[153] Arevalo-Campillo M.A., Tuling S., Parras L., del Pino C., and Dala L. *Experimental Study of Very Low Aspect Ratio Wings in Slender Bodies.* Proceedings of ASME 2012 11th Biennial Conference on Engineering Systems Design and Analysis, ESDA 2012-82332, July 2-4, 2012.

[154] Alden H.L. and Schindel L.H. *The Calculation of Wing Lift and Moments in NonUniform Supersonic Flow.* M.I.T. Meteor Rep. 53, May 1950.

[155] Stratford B.S. *Flow in the Laminar Boundary Layer near Separation.* Aeronautical Reserach Council Reports and Memoranda No. 3002, November 1954.

[156] Stratford B.S. The Prediciton of Separation of the Turbulent Boundary Layer. *Journal of Fluid Mechanics*, July 1958.

[157] Macha J.M. Drag of Circular Cylinders at Transonic Mach Numbers. *Journal of Aircraft*, 16(6):605–607, June 1977.

[158] Jorgensen L.H. and Nelson E.R. *Experimental Aerodynamic Characteristics for a Cylindrical Body of Revolution with Side Strakes and Various Noses at Angles of Attack from* 0 deg *to* 58 deg *and Mach Numbers from 0.6 to 2.0.* NASA-TM-X-3130, March 1975.

[159] Jeong J. and Hussain F. On the identification of a vortex. *J. Fluid Mech.*, 285:69–94, 1995.

[160] Haller G. An Objective Definition of a Vortex. *J. Fluid Mech.*, 525:1–26, 2005.

[161] Hunt J.C.R., Wray A.A. and Moin P. Eddies, Streams, Convergence Zones in Turbulent Flows. *Proceedings of the Summer Program 1988, CTR-S88*, pages 193–207, 1988.

[162] Chong M.S., Perry A.E. and Cantwell B.J. A General Classification of Three-Dimensional Flow Fields. *Phys. Fluids. A*, 2:765–777, 1990.

Appendix A

The Definition of a Vortex Core

A.1 Definition Criteria

The determination of a vortex core is essential in the tracking of vortices in the CFD simulations. Four methods have been used to determine the location of the vortices in this thesis. These are:

1. Total pressure
2. Q-criterion
3. Δ-criterion
4. λ_2-criterion

The use of local pressure minima have been used in the past, though Jeong and Hussain [159] and Haller [160] indicate that these definitions and others based on pressure minima are readily refutable. The use of the total pressure definition has, however, been included due its historical usage and comparisons are made from a historical perspective.

Traditionally three Galilean invariant vortex definitions have been used. These are the Q-criterion [161], Δ-criterion [162] and the λ_2-criterion [159]. They are derived from various properties of the velocity gradient, ∇v. The velocity gradient, ∇v, can be decomposed into the strain rate, S, and vorticity, Ω, tensors, or:

$$\nabla v = S + \Omega \tag{A.1}$$

where

$$S = \frac{1}{2}\left[\nabla v + (\nabla v)^T\right] \tag{A.2}$$

and

$$\Omega = \frac{1}{2}\left[\nabla v - (\nabla v)^T\right] \tag{A.3}$$

The velocity gradient, ∇v, is simply:

$$\nabla v = \begin{bmatrix} \frac{du}{dx} & \frac{du}{dy} & \frac{du}{dz} \\ \frac{dv}{dx} & \frac{dv}{dy} & \frac{dv}{dz} \\ \frac{dw}{dx} & \frac{dw}{dy} & \frac{dw}{dz} \end{bmatrix} \tag{A.4}$$

The Q-criterion of Hunt, Wray and Moin [161] is defined as regions the the vorticity dominates the strain rate, or:

$$Q = \frac{1}{2}\left[|\Omega|^2 - |S|^2\right] > 0 \tag{A.5}$$

The Δ-criterion of Chong, Perry and Cantwell [162] is defined as:

$$\Delta = \left(\frac{Q}{3}\right)^3 - \left(\frac{\det\nabla v}{2}\right)^2 > 0 \tag{A.6}$$

The determinant of the velocity gradient is simply:

$$\det\nabla v = \frac{du}{dx}(\frac{dv}{dy}\frac{dw}{dz} - \frac{dw}{dy}\frac{dv}{dz}) - \frac{du}{dy}(\frac{dv}{dx}\frac{dw}{dz} - \frac{dw}{dx}\frac{dv}{dz}) + \frac{du}{dz}(\frac{dv}{dx}\frac{dw}{dy} - \frac{dw}{dx}\frac{dv}{dy}) \tag{A.7}$$

The λ_2-criterion of Jeong and Hussain [159] is defined as where the intermediate eigenvalue, λ_2, of the symmetric tensor $S^2 + \Omega^2$ is less than zero, or:

$$\lambda_2\left(S^2 + \Omega^2\right) < 0 \tag{A.8}$$

The intermediate eigenvalue, λ_2, of the charactertistic equation $\lambda_3 + P\lambda_2 + Q\lambda + R = 0$ is simply the negative of the trace, or:

$$P = -tr\left(S^2 + \Omega^2\right) \tag{A.9}$$

and after manipulating the strain-rate and vorticity tensors this results in:

$$\lambda_2\left(S^2 + \Omega^2\right) = \left(\frac{du}{dx}\right)^2 + \left(\frac{dv}{dy}\right)^2 + \left(\frac{dw}{dz}\right)^2 + 2\frac{du}{dz}\frac{dw}{dx} + 2\frac{du}{dy}\frac{dv}{dx} + 2\frac{dv}{dz}\frac{dw}{dy} < 0 \tag{A.10}$$

A.2 Comparison between Various Methods

A comparison between the various methods was performed to determine the most suitable for the types of flows encountered in this thesis. Two cases are typical, namely low and moderate angles of attack ($\alpha < 20°$), and higher angles of attack ($\alpha \geqslant 20°$) for Mach 2.0. For Mach 2.5 and 3.0, vortex shedding is initiated earlier.

For the low to moderate angles of attack all four criterion compared well in their location of the rolled up vortex sheet. This is shown in Figures A.1 and A.2. Whilst some differences were observed between the total pressure and the other three more rigorous criteria are present, the flow is characterised by a single concentrated vortex, resulting in

good correlation between all the methods. At higher angles of attack, where more than one vortex is shed, the total pressure provides a very poor indication of where vortices are present, especially when two or more vortices are in close proximity to each other. This is shown in Figures A.3 and A.4 for the prediction of the body vortex. For the purposes of this thesis the λ_2-criterion is used simply because it is the most recent formulation of the three methods.

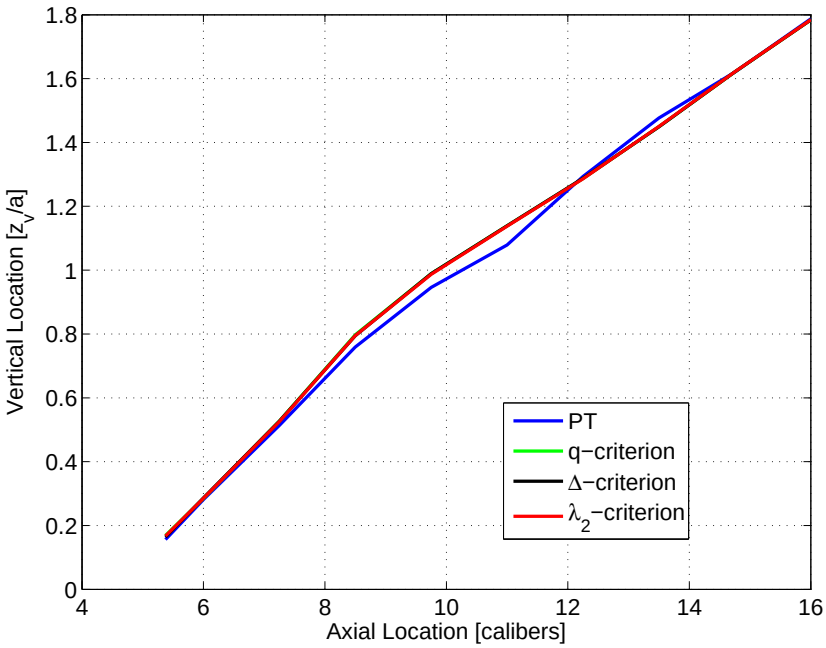

Figure A.1: Vertical vortex position predictions, $\alpha = 10°$

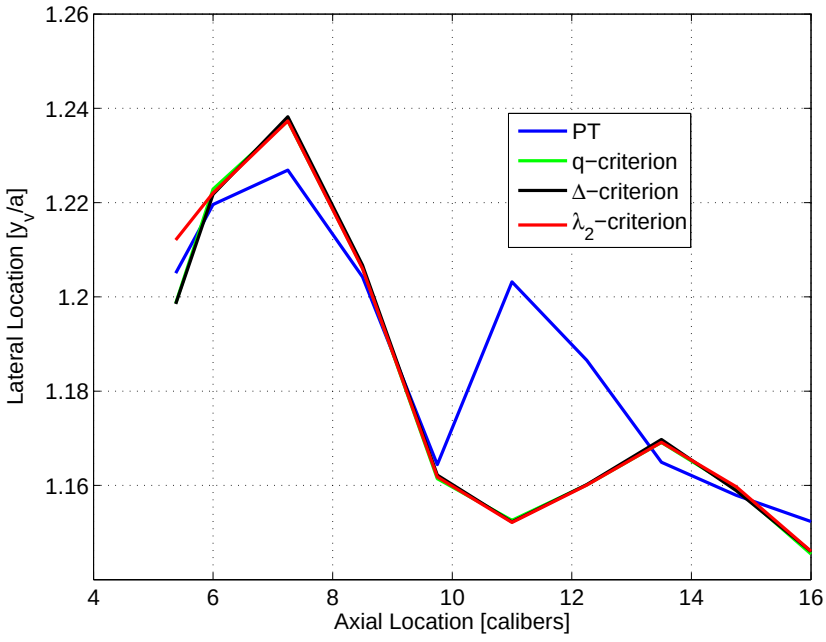

Figure A.2: Lateral vortex position predictions, $\alpha = 10°$

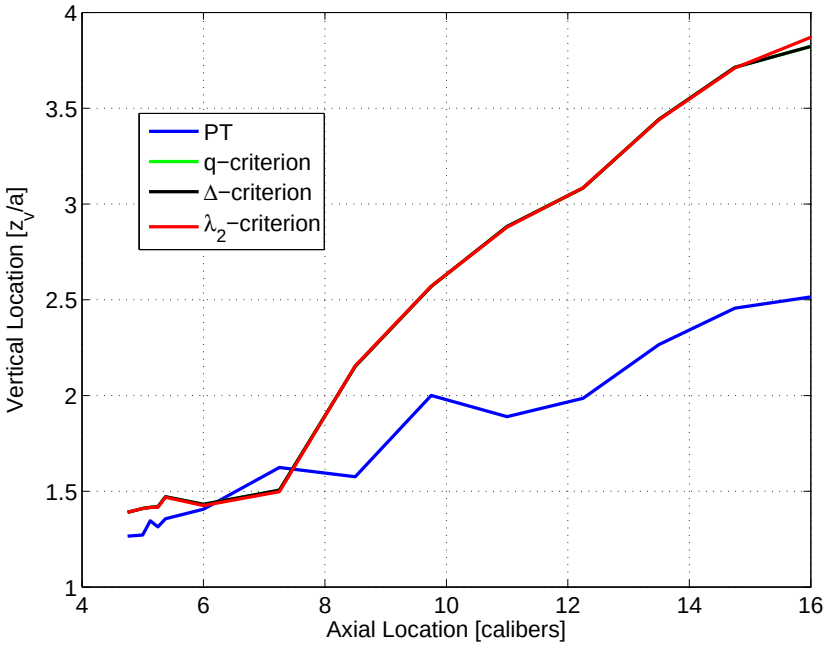

Figure A.3: Vertical vortex position predictions, $\alpha = 20°$

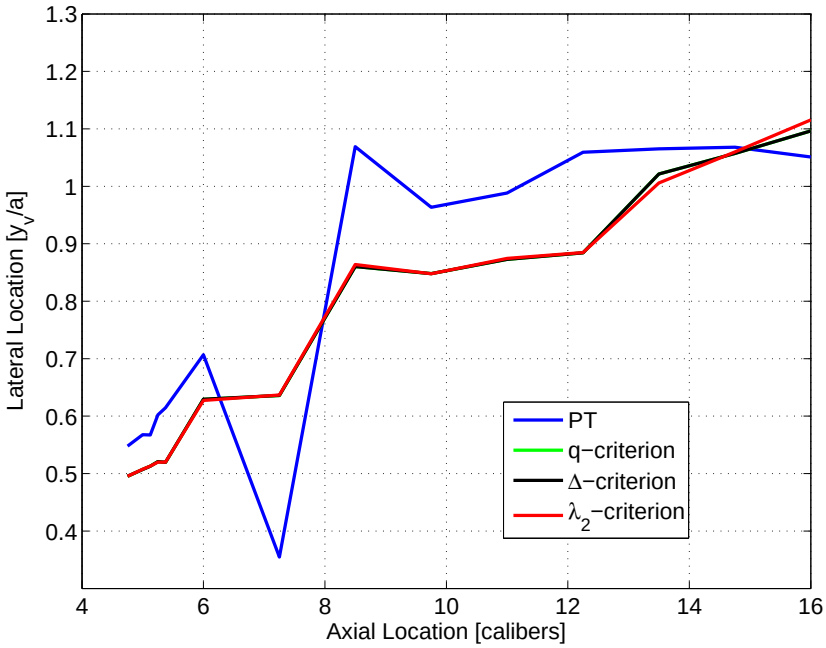

Figure A.4: Lateral vortex position predictions, $\alpha = 20°$

Appendix B

Published Papers

Two conference papers were published during the duration of the thesis, which also used the work in this thesis. They are

1. Tuling, S. and Dala, L. *Some Aspects of Modelling Very Low Aspect Ratio Wings in Slender Body Configurations*, Royal Aeronautical Society Applied Aerodynamics Conference, July 2010.

2. Arevalo-Campillos, M.A., Tuling, S., Parras, L., del Pino, C., and Dala, L. *Experimental Study of Very Low Aspect Ratio Wings in Slender Bodies*, Proceedings of ASME 2012 11th Biennial Conference on Engineering Systems Design and Analysis, ESDA 2012-82332, July 2-4, 2012.

Only the first paper has been included because the copyright for the second is held by the American Society of Mechanical Engineers.

Some Aspects of Modelling Very Low Aspect Ratio Wings in Slender Body Configurations

Mr Sean Tuling* and Dr Laurent Dala**

Abstract

The inclusion of very low aspect ratio wings or strakes of aspect ratio < 0.05 in slender body configurations are considered in this paper. A 19D tangent ogive body with a 3D nose, and two strakes of aspect ratio 0.0223 and 0.0336 and wing span to body ratio of 1.25, mounted in the 'plus' configuration, or zero roll, were studied. The data were generated in the commercial code Fluent and validation performed on a similar configuration for which experimental data were available. The Mach numbers considered were 2.0, 2.5 and 3.0. Results show that the wing-to-body factor, $K_{B_{(W)}}$, is significantly lower than that predicted by slender body theory at low and high angles of attack, indicating that the slender body theory has significant limitations for very low aspect ratio wings due to the complex interaction of the wing side edge and body vortex. An alternative methodology used to model inlets, developed by ONERA was also studied. Reasonably good correlations were obtained indicating the applicability of the ONERA inlet method to modelling body-strake configurations.

* (Corresponding Author) Council for Scientific and Industrial Research, South Africa. P.O. Box 395, Pretoria, 0001, South Africa, stuling@csir.co.za

** University of the West of England, Frenchay Campus, Coldharbour Lane, Bristol BS16 1QY, England, Laurent.Dala@uwe.ac.uk

Nomenclature

AR	Aspect Ratio
C_N	Normal force coefficient
D	Body diameter
i	Interference factor
k	Non-linear body and strake coefficient
K_1	Linear strake coefficient
K_B	Wing-to-body carry over factor
K_W	Body-on-wing carry over factor
L	Strake length
M	Mach number
ONERA	Office National d'Études et de Recherches Aérospatiales
s	wing span
S	Reference area, $\frac{\pi D^2}{4}$
SBT	Slender body theory
α	Angle of attack, °
β	Compressibility factor, $\sqrt{M^2-1}$
λ	Taper ratio

Subscripts

B	Body
eq	equivalent
T	Tail

W	Wing
v	vortex
$\alpha\alpha$	Non-linear, body and strake

Introduction

During the conceptual or early design phases of a slender body configuration such as a missile, engineering codes such as Missile Datcom or MISL3 are routinely used for the prediction of the aerodynamic performance of envisaged configurations, with overall accuracies of approximately 15-20%. These engineering codes are primarily based on linearised potential theory, and in the supersonic flight regime on slender body theory (SBT). Heuristic models [1] are used to account for viscous effects such as vortices that emanate from wings and the body. The addition of other lifting surfaces such as wings, tails or canards are generally accounted for by linear superposition principles and adding interference effects of, for instance, the body-on-wing and wing-on-body. Being based primarily on linearised potential theory, engineering codes are strictly applicable only at low angles with non-separated flow, though they have been successfully applied up to angles of attack of 20° to 25° in their original formulation, and in later years to higher angles of attack using the equivalent angle of attack method. Furthermore, the use of heuristic models are used to account for separated flow or viscous effects results in the class of codes being dependent on experimental or computational databases, for example, wings or tails tend to only be applicable for aspect ratios from 0.25 to 4.

The normal force coefficient for a slender body with wings and fins, using component buildup methodology, is typically defined as:

$$C_{N_{BWT}} = C_{N_B} + C_{N_{W(B)}} + C_{N_{B(W)}} + C_{N_{T(B)}} + C_{N_{B(T)}} + C_{N_{T(W)}} \quad (\ldots 1)$$

where $C_{N_{BWT}}$ is the normal force coefficient for the complete configuration (body-wing-tail), C_{N_B} is the body alone, $C_{N_{W(B)}}$ is the increment of the wing in the presence of the body, $C_{N_{B(W)}}$ is the increment of the body due to the presence of the wing and so forth. The contribution of the wing and increment of the body due to the presence of the wing has been formulated as a function of the interference factors and the wing alone aerodynamics and is normally formulated as

$$C_{N_{W(B)}} + C_{N_{B(W)}} = (K_{W_{(B)}} + K_{B_{(w)}})C_{N_W} \quad (\ldots 2)$$

The interference factors are traditionally obtained from the slender body theory and have performed reasonable well for low to moderate angles of attack, and at low to moderate supersonic speeds. The effect of no, limited or negative afterbodies have also been accounted for [2][3]. Additional factors such as vortices, either emanating from the body or upstream wings, have been modelled using simple [4] to complex vortex tracking methods and their influence on lifting surfaces such as tail fins and wings included using the tail interference factor, i_T [1].

In the 1970's the equivalent angle of attack method was introduced by Hemsch and Nielsen [5] allowing the low to moderate angle of attack methodology described above to be extended into the non-linear flight regime. The improvement emanated in the determination of the angle of attack that the wing would experience in the flow field of the body and vortices determining the normal force and pitching moment coefficients by considering the velocity components experienced by the wing/fin and reformulating the interference factors, such that

$$\tan(\alpha_{eq}) = K_W \tan(\alpha) + \tan(\Delta\alpha_v) \quad (...3)$$

Subsequently the components, $C_{N_{W(B)}}$ and $C_{N_{B(W)}}$, are thus

$$C_{N_{W(B)}} = C_{N_{W}(\alpha_{eq})} \quad (...4)$$

and

$$C_{N_{B(W)}} = \frac{K_{B_{(W)}}}{K_{W_{(B)}}} C_{N_{W(B)}} \quad (...5)$$

The modelling of very low aspect ratio wings, or strakes, that are added to slender bodies has been found to be poorly modelled by an engineering code such as Missile Datcom [6], given the modelling methodologies and limitation of the empirical databases. It was found that the wing-to-body interference factor, $K_{B_{(W)}}$, was overestimated by SBT, thus resulting in the codes predicting higher than expected normal forces. The aspect ratio of the wings (designated W22) considered was 0.067.

Particular to slender bodies with wings of aspect ratios lower than 0.1 and taper ratios above 0.8 is the question of whether the traditional component build-up methodology originally developed in the 1950's and 1960's, extended in the 1970's and refined in 1980's is suitable. This paper seeks to provide some insight into answering this question. Specifically the paper shall

- show that the original linearised theory based on SBT is unsuitable for body strake combinations
- show that for aspect ratios below 0.067, that $K_{B_{(W)}}$ remains significantly different to that predicted by SBT
- provide some insights into the flow phenomena dominating slender body and very low aspect ratio wing combinations
- point to alternative formulations methods for the modelling of slender bodies combined with very low aspect ratio wings

The speed range being considered is supersonic only, limiting the study to Mach numbers between 2.0 and 3.0. The configurations studied only considered the wings at zero roll (or the plus configuration). Furthermore, no pitching moment analysis has been performed, as the study concentrates on the prediction and modelling of normal force.

Methodology

The methodology used in this study was to generate aerodynamic data of two configurations in a component build up manner i.e. body alone, body and strakes and wing alone, numerically using CFD. These data were validated for the body alone and body and strake configuration against a similar configuration for which experimental were available.

The configuration chosen allows more generic studies to be performed. One of the reasons for performing the aerodynamic simulations in CFD was the difficulty in performing the wing alone simulations experimentally. Half wing tests would definitely require boundary layer suction complicating the experimental setup significantly due to excessive length of the chord compared to the span and growing boundary layer, while no easy method is available for mounting a full wing let alone measuring the wing loads.

Configurations

The two configurations both utilised a 19D tangent ogive body, with no boattail. The nose of the tangent ogive was 3D. The diameter used for this study was 80mm. For

each configuration a strake was mounted in the zero roll, or plus configuration. Both strakes had a span to body ratio of 1.25. The first strake had a length of 11.25D (or 900mm) and the second 7.5D (or 600mm). The strake leading edge had a sweep back of 45°, and a straight trailing edge. Both strakes started at the axial location of 4.75D (or 380mm) from the nose. The body and 900mm strakes are illustrated in Figure 1, while the resulting planform parameters for the strakes are listed in Tables 1 and 2.

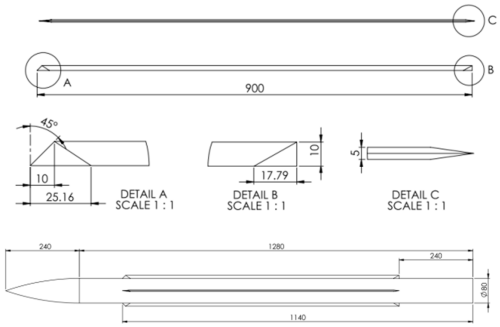

Figure 1. Body and strake dimensions in mm

Table 1. 900mm strake planform parameters

	Description	**Value**
AR	Aspect Ratio	0.0223
λ	Taper ratio	0.9889
b	Span	20mm

Table 2. 600mm strake planform parameters

	Description	**Value**
AR	Aspect Ratio	0.0336
λ	Taper ratio	0.9833
b	Span	20mm

CFD Simulations

The numerical simulations were performed using the commercial code Fluent solved using the Roe flux splitting scheme, spatially discretised using a second order upwind scheme. All simulations were performed using near wall treatment and the Spalart-Almaras turbulence model, using first order upwind spatial discretisation. The resulting meshes varied in size from 580000 for the body alone, ~3.8million for the strakes alone and ~3million for the body and strakes. Limited mesh sensitivity studies indicated no appreciable changes in results. Furthermore, the use of a second order discretisation for the Spalart-Almaras modelling also resulted in negligible changes in results.

Three Mach numbers were simulated namely 2.0, 2.5 and 3.0, while the angle of attack range was from 0° to 25°.

The CFD simulation methodology was validated against a similar configuration for which experimental were available. No experimental installed wing loads were, however, available for validation, other than from reference [6]. Given that the body-on-wing carryover factor, $K_{W_{(B)}}$, was satisfactorily modelled in reference [6] and that the wing semispan to body radius ratio is smaller than in reference [6], the same assumption has been made for the CFD simulations. A comparison of the body alone and body and strake between the experimental and CFD simulations are shown in Figure 2 for Mach 2.0, while the difference between the body and strake and body alone is compared in Figure 3.

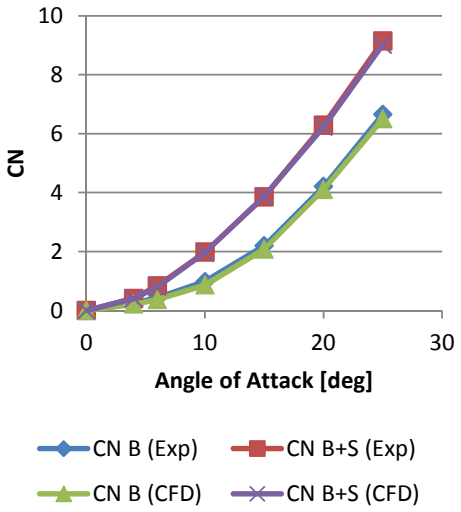

Figure 2. Body alone and body and strake comparison

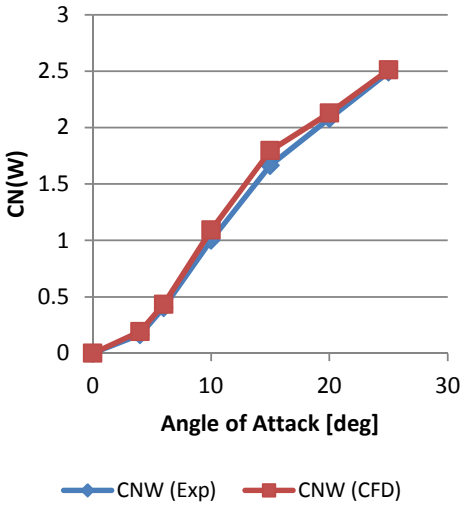

Figure 3. Installed strake comparison

Wing Alone Aerodynamics

As mentioned previously, the prevailing engineering prediction codes seem to provide sufficiently accurate results for wings of aspect ratio 0.25<AR<4. Wings of these aspects ratios show a relatively linear normal force characteristic at angles of attack from 0° up to until wing stalling starts to occur, which for the lower aspect ratios is around 40° to 50° at supersonic speeds. For the case described by Simpson and Birch [6], the wing designated W22 had an aspect ratio of 0.067 and taper ratio of 0.85, and a wing alone normal force characteristic as predicted by Missile Datcom version 1999 revision 3 as shown in Figure 4; this for a Mach number of 2.5. Performing a CFD analysis of the wing yielded a different characteristic, which is also plotted in Figure 4. The analysis was performed using Fluent, with the results confirmed by the experimental data available in [6].

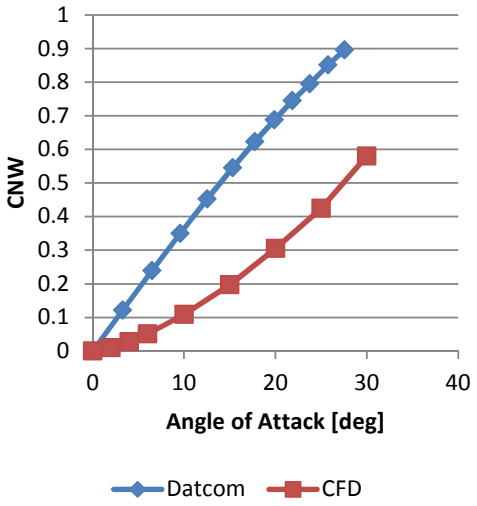

Figure 4. W22 normal force characteristics as predicted by Missile Datcom Rev 3/99 and Fluent

Inspection of the flow phenomena indicates that the flow on the leeward side is dominated by a side edge vortex, with the leading edge vortex being less significant than expected (at Mach 2.5 the leading edge is still subsonic). It is this side edge vortex that results in the non-linear behaviour of such low aspect ratio wings. The wing alone normal force characteristics of the strakes (900mm and 600mm) used in this study are shown in Figure 5. At the moderate angles of attack differences are noticeable which are dependent on the aspect ratio.

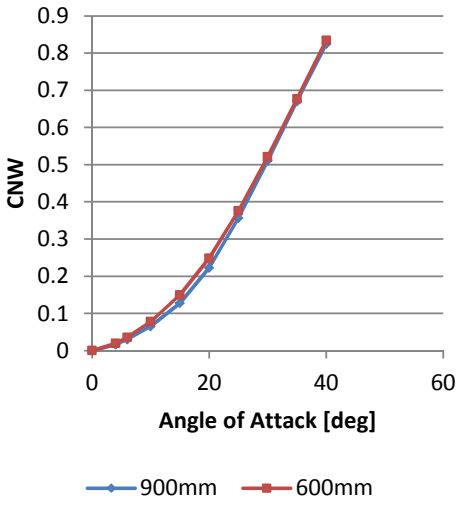

Figure 5. 900mm and 600mm wing normal force characteristics as predicted by Fluent at Mach=2.0

Given that the original component build-up methodology used lift curve slopes i.e. $C_{N_{\alpha_W}}$, the use of low aspect ratio wings can, by definition, only be modelled using the equivalent angle of attack method, because the linear potential lift curve slope is too low to predict any reasonable normal force coefficient. So while the equivalent angle of attack method was originally developed for non-linear characteristics at high angle of attack, conversely, non-linear wing characteristics at low angles of attack can be accommodated by the methodology, and indeed are required for very low aspect ratio wings.

Wing-to-Body Carryover Factor

With indications that the wing-to-body carryover factor, $K_{B_{(W)}}$, is significantly lower than that predicted by SBT [6], the simulations performed for the strake of 900mm (AR=0.0223). No simulations were performed for the 600mm strake (AR=0.0336). The body-on-wing factor, $K_{W_{(B)}}$, was also confirmed to be well predicted by Missile Datcom such that the equivalent angle of attack, taking into account the body vortex contribution was deemed sufficiently accurate to ascertain the wing normal force. This was achieved by comparing the wing installed loads to that of Missile Datcom using the predicted $K_{W_{(B)}}$ and resulting equivalent angle of attack.

The variation of $K_{B_{(W)}}$ as a function of angle of attack and Mach number are shown in Figure 6. It can be seen that at very low angles of attack $K_{B_{(W)}}$ is approximately zero, indicating that almost no wing loading is carried over to the body. However, the carryover increases rapidly, peaking at around 10° to 15° and then decreasing at the higher angles of attack.

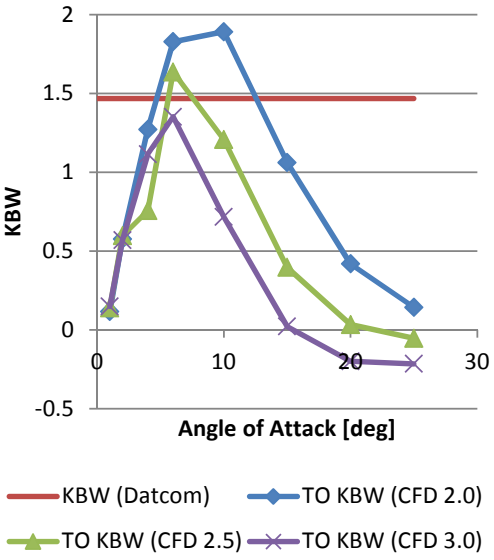

Figure 6. $K_{B_{(W)}}$ as a function of angle of attack at various Mach numbers

The behaviour of $K_{B_{(W)}}$ as a function of angle of attack is different to that found in reference [6]. This is primarily because the method of derivation used in this paper is different to that reference [6] which calculated their factor by only dividing the difference between the total configuration load and the sum of the body alone and installed wing loads by the installed wing load

(after removing body vortex interference effect) and not multiplying it by the body-on-wing carryover factor $K_{W_{(B)}}$ as previously defined in Equation 5.

Body-Strake Flow Phenomena

Some insight into the behaviour in the $K_{B_{(W)}}$ can be gained by the observation of the interaction of the flow structures occurring between the body and the strake, and in particular the body vortex and side edge vortex of the strake. At low angles of attack eg. 2°, no body vortex exists since the flow is primarily potential. The side edge vortex of the strake remains in approximately the same position as for the strake alone. This is illustrated in Figures 7 and 8, showing the vortex at body axial stations 6D and 13.5D.

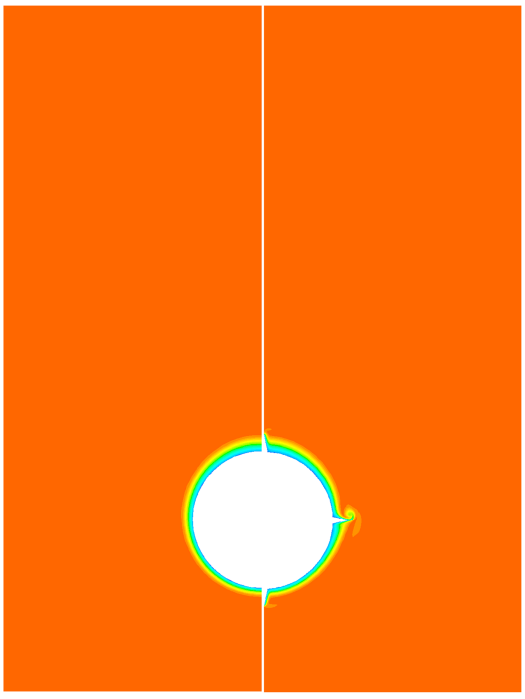

Figure 7. Vortices at 2°, plane 480mm

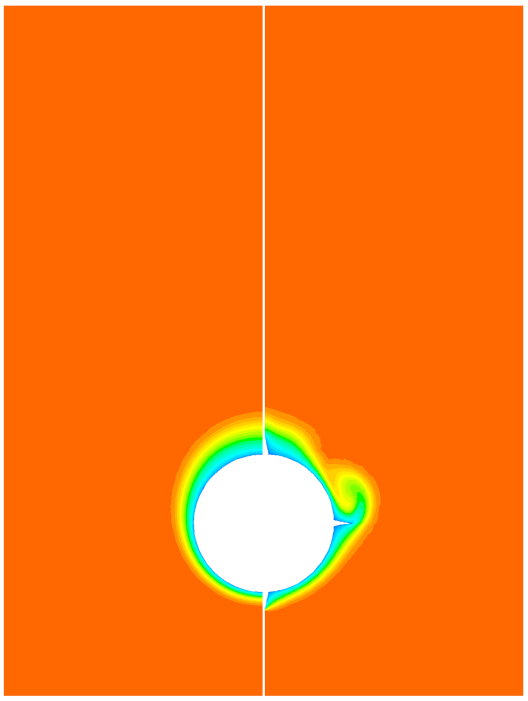

Figure 8. Vortices at 2°, plane 1080mm

At intermediate angles of attack eg. 10°, where $K_{B_{(W)}}$ is the greatest, the side edge vortex combine at a relatively early stage alone the body length. At 6D the side edge vortex remains distinct and separate from the small body vortex (see Figure 9). At 8.5D (see Figure 10) the side edge and body vortices are still distinctly separate, though the body vortex is diminished in strength. By 12.25D (see Figure 11) the body vortex and side edge vortex have coalesced. The position of the combined vortex is, however, at a similar position to where the side edge vortex would be should they have remained separated. At the plane of the end of strake or 16D (see Figure 12), the flow structures are well established and remain so until at least the end of the body.

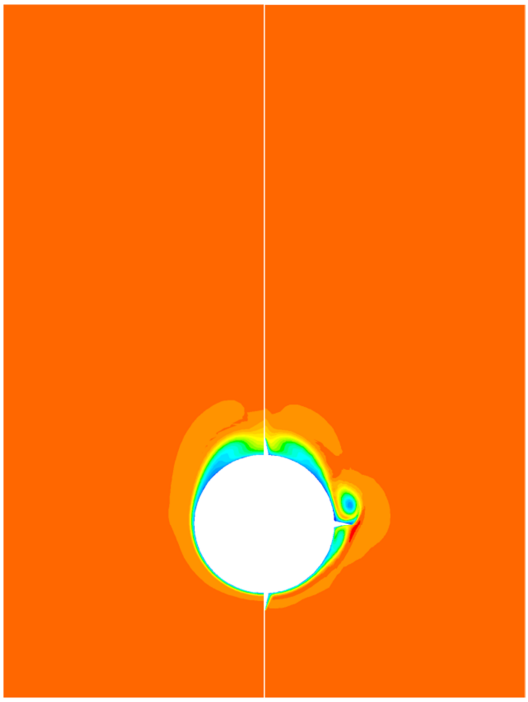

Figure 9. Vortices at 10°, plane 480mm

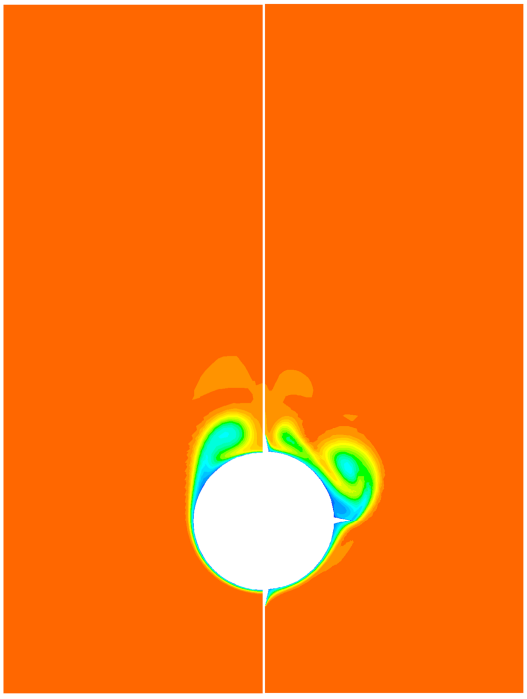

Figure 10. Vortices at 10°, plane 680mm

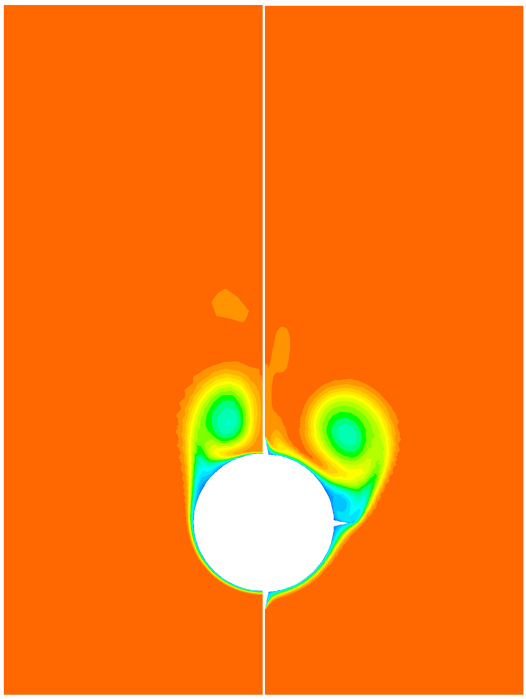

Figure 11. Vortices at 10°, plane 980mm

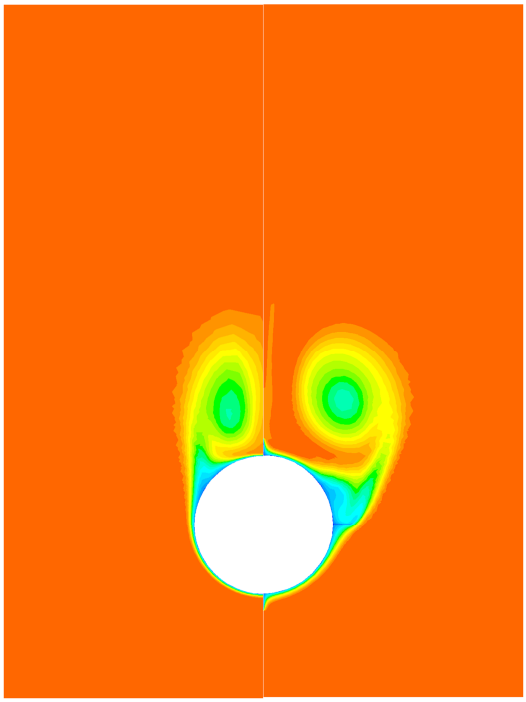

Figure 12. Vortices at 10°, plane 1280mm

At 25° angle of attack, the side edge vortex combines with the body vortex (as for the 10° case) but the resulting vortex does not move

out laterally as at 10° angle of attack. The side edge vortex seems to become part of the body rather than vice versa as for the 10° case. At 6D (see Figure 13) the side edge and body vortices are still separate. At 7.25D (see Figure 14) the two vortices interact but have not combined yet. At 8.5D (see Figure 15) the two vortices have almost coalesced but seems to remain distinctly separate. After this the two vortices combine into one and the vortex structure remains similar to that at the end of the strakes (see Figure 16). The reason for the body vortex dominating at 25° angle of attack is probably because of the higher strength of the body vortex at 25° compared to 10°.

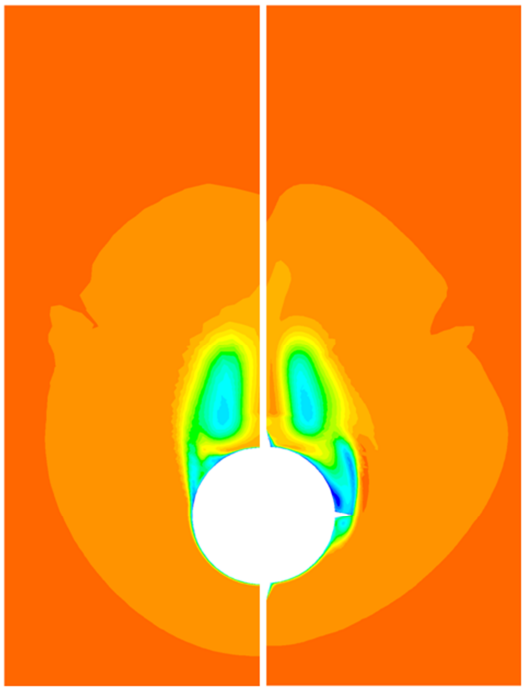

Figure 13. Vortices at 25°, plane 480mm

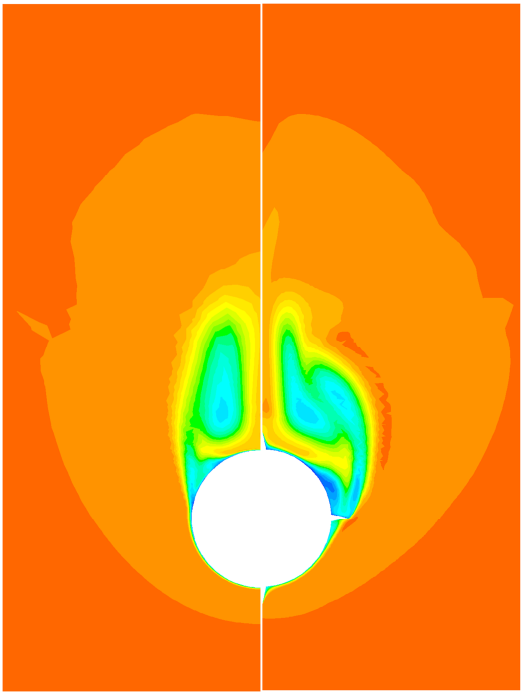

Figure 14. Vortices at 25°, plane 580mm

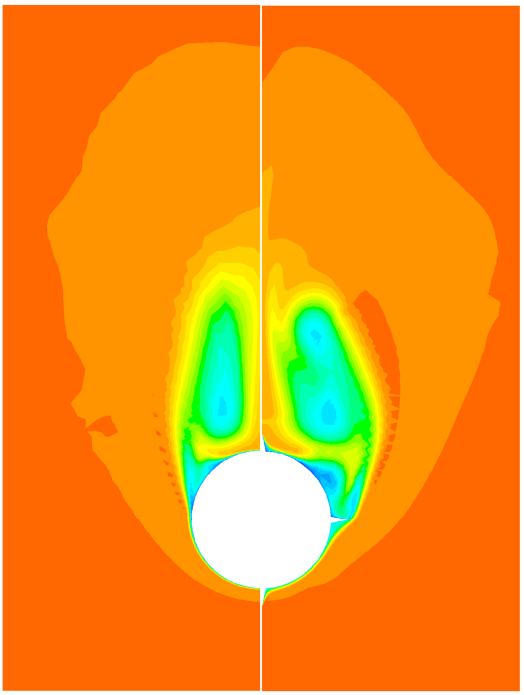

Figure 15. Vortices at 25°, plane 680mm

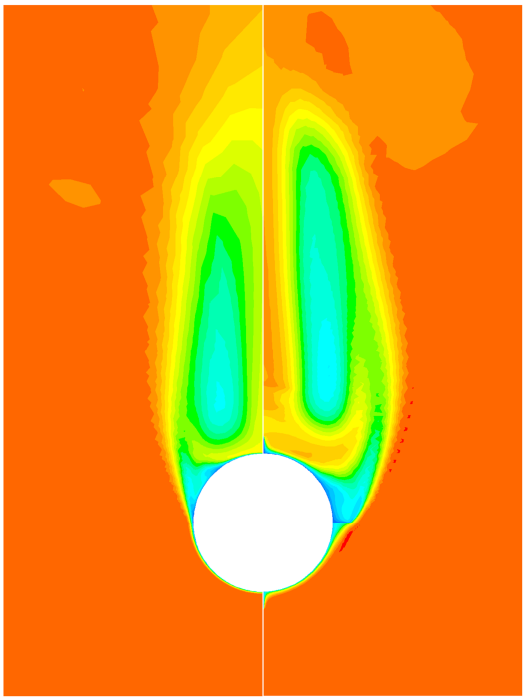

Figure 16. Vortices at 25°, plane 1280mm

Of particular interest for codes such as Missile Datcom is that the interaction between the body vortex and wing side edge vortex needs to be modelled. Missile Datcom does not model these interactions [7] and it appears that the simple models employed are not sufficient for wings of very low aspect ratio. A methodology of reference [8] assumes that for wings that have supersonic leading edges (as for the strakes in this study) that the lateral position of the body vortex remains fixed along the length of the wing. For the 10° angle of attack case this model is clearly invalid.

ONERA Inlet Methodology

An alternative methodology for predicting the normal force of a body strake combination is proposed, which utilises a formulation developed by ONERA for body inlet combinations [9]. Modelling the effect of the wings as inlets utilises a heuristic model based on the same form as a circular body, i.e. composed of a linear potential and non-linear component, with the resulting equation:

$$C_{N_{B+W}} = C_{N_B} + K_1[\frac{s}{D} - 1]^{1.6}\frac{\sin 2\alpha}{2} + C_{N_{\alpha\alpha}}\sin^{k}\alpha\,\frac{S_W}{S}$$

A comparison of the linear factor, K_1, (see Figure 17) of the wing and inlet shows that the potential component of the wing is smaller than for the inlet, though its applicability for engineering codes would still be suitable given the accuracy requirements of such codes. The non-linear factor, $C_{N_{\alpha\alpha}}$, is shown as a function of product $\beta.AR$ in Figure 18. The factor, k, was determined to be 1.65.

For K_1, from Figure 17, the two families of curves correspond to the 900m and 600mm length strakes, thus indicating that there may be a dependence on the relative length ratios that has not been sufficiently accounted for by the inlet method. The non-linear factor, $C_{N_{\alpha\alpha}}$, has a far better correlation. The error introduced by the poorer correlation for K_1 is, however, less than 2% for the overall configuration.

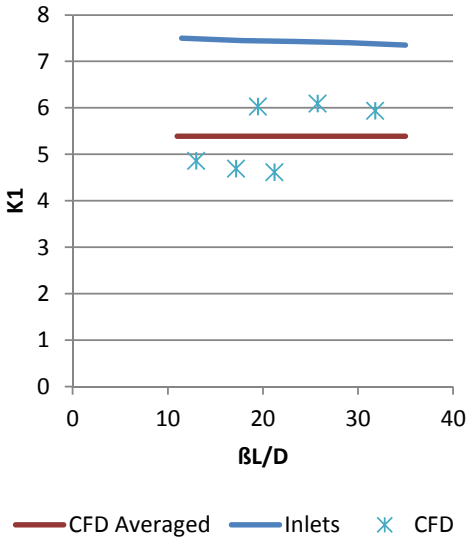

Figure 17. Linear factor K_1

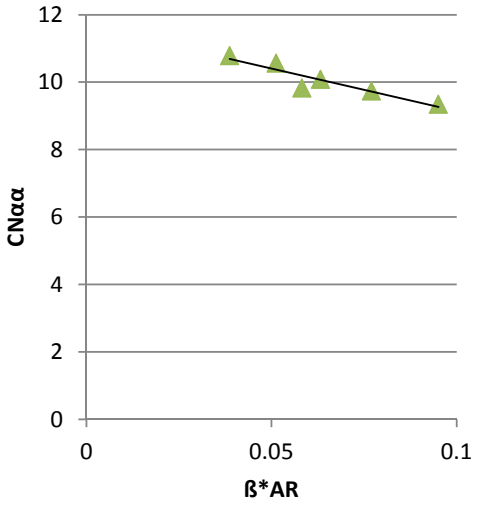

Figure 18. Non-linear factor $C_{N_{\alpha\alpha}}$

Conclusions

From the study it can be concluded that

- The component build up methodology can only be used successfully if the equivalent angle of attack method is employed.
- The modelling of extremely low aspect ratio wings (AR < 0.1) in body-wing configurations using the SBT interference factors has significant limitations at low and high angles of attack.
- The complex interaction of the wing side edge and body vortex results in the observed behaviour of the wing-on-body carryover factor, $K_{B_{(W)}}$, as a function of angle of attack.
- The model of keeping the body vortex at the same lateral and vertical location along the length of the wing is not valid for the intermediate angles of attack where the side edge vortex dominates.
- Modelling the wings as inlets provides an alternative solution to determining the normal force of body-wing combinations.

Acknowledgements

The authors would like to thank Stephen Gobey and Stiff du Toit for their enthusiastic support, and Janine Versteegh and Bhavya Vallabh for their help in keeping the CFD runs going.

References

[1] Nielsen J.N., *Missile Aerodynamics*, Nielsen Engineering & Research, Inc. 1988

[2] Vira N.R. & Fan D., Closed-Form Solutions of Supersonic Wing-Body Interference, *AIAA Journal*, June 1982, pp. 855-857

[3] Vira N.R. & Fan D., Supersonic Wing-Body Centre of Pressure with Finite Afterbodies, *AIAA Journal*, August 1982, pp. 1144-1146

[4] Pitts W.C., Nielsen J.N. & Kaattari G.E., Lift and Center of Pressure of Wing-Body-Tail Combinations at Subsonic, Transonic, and Supersonic Speeds, NACA TR-1307, 1957

[5] Hemsch M.J. & Nielsen J.N., Equivalent Angle-of-Attack Method for Estimating Nonlinear Aerodynamics of Missile Fins, *Journal of Spacecraft and Rockets*, Vol 20, Jul-Aug 1983, pp. 356-362

[6] Simpson G.M. & Birch T.J., Some Aerodynamic Characteristics of Missiles having Very Low Aspect Ratio Wings, *AIAA 2001-2410*, 19th Applied Aerodynamics Conference, June 2001.

[7] Blake W.B. & Gillard W.J., Prediction of Vortex Interference on a Canard Controlled Missile, *NAECON 88*, Proceedings of the IEEE National Aerospace and Electronics Conference, Dayton, OH; UNITED STATES; 23-27 May 1988. pp. 444-451. 1988

[8] Mendenhall M.R. & Nielsen J.N., Effect of Symmetrical Vortex Shedding on the Longitudinal Aerodynamic Characteristics of Wing-Body-Tail Combinations, NASA CR-2473, January 1975.

[9] Champigny P., Baudin D. & Gonidec P., Prevision Des Coefficidents Aerodynamiques de Missiles Munis de Prises d'Air, *Symposium AGARD/FDP sur l'Aerodynamique de Missiles*, 23-26 April 1990.